



Dedicated to building research infrastructure and the promotion of Science, Technology, Engineering and Math (STEM) education in West Virginia

2016–2017 STUDENT RESEARCH REPORTS

Summer Internships

Undergraduate Research Fellowship Program

Graduate Research Fellowship Program

NASA West Virginia Space Grant Consortium
G-68 Engineering Science Building
PO Box 6070
West Virginia University
Morgantown, WV 26506-6070
(304) 293-4099

www.wvspacegrant.org

Published December 2017



PREFACE

The National Space Grant College and Fellowship Program (also known as Space Grant) was first established under Title II of the National Aeronautics and Space Administration (NASA) Authorization Act of 1988 (P.L. 100-147). Space Grant is a unique national state-based network in 50 states, Puerto Rico and the District of Columbia. The program is a component of NASA's Education Directorate portfolio charged with carrying out effective education, research, and public outreach activities in science, technology, engineering and mathematics (STEM), particularly in fields most relevant to NASA's future workforce.

Currently, Space Grant is comprised of 52 consortia that engage over 1,000 affiliates nationally, including more than 600 colleges/universities, and state, industry, non-profit and federal partners, including NASA Centers. They work collectively to meet the nation's needs for developing and training a high-tech workforce to sustain a robust U.S. space science and space exploration program.

As one of the 52 university-based Space Grant consortia, the NASA West Virginia Space Grant Consortium (WVSGC or the Consortium) was established in August 1991. The Consortium is housed in the Benjamin M. Statler College of Engineering and Mineral Resources on the Evansdale Campus of West Virginia University in Morgantown, West Virginia. It is comprised of 12 West Virginia academic institutions and 8 corporate and scientific partners (a list of affiliates is listed on page 2). It is dedicated to building research infrastructure and promoting STEM education in West Virginia. The Consortium's programs focus on research, collaborations with high technology industries, student fellowships as well as K-12, and public outreach programs. This is consistent with the strategic vision for the state's participation in the nation's current and future endeavors in science and technology.

This publication is a compilation of student reports from summer internships, the NASA Undergraduate Research Fellowship Program and the NASA Graduate Research Fellowship Program for the 2016- 2017 fiscal year.

On behalf of the Board of Directors of NASA WVSGC, we would like to take this opportunity to express our appreciation to students who applied for these programs, the mentoring offered to West Virginia students by their faculty advisors in their research projects as well as the different internship locations that provided these opportunities. Without them, our internships and fellowship programs would not be where they are today: a crucial step in the workforce development pipeline for NASA and the high technology sector in the United States.

For additional information on our programs, please contact our office or visit wvspacegrant.org.

CONSORTIUM AFFILIATES

West Virginia University (Lead)

Bethany College

Bluefield State College

Community and Technical College System of WV

Fairmont State University

Glenville State College

Marshall University

NASA Independent Verification & Validation Facility

National Radio Astronomy Observatory

Polyhedron Learning Media, Inc.

Shepherd University

TechConnect WV

The Clay Center for the Arts and Sciences of West Virginia

TMC Technologies, Inc.

West Liberty University

WV High Technology Consortium Foundation

West Virginia State University

WVU Institute of Technology

West Virginia Wesleyan College

Wheeling Jesuit University

Table of Contents

| | |
|---|-----|
| 2016–2017 STUDENT RESEARCH REPORTS..... | 1 |
| PREFACE | 2 |
| CONSORTIUM AFFILIATES | 3 |
| Table of Contents | 4 |
| LIST OF PROGRAMS | 4 |
| I. SUMMER INTERNSHIPS | 4 |
| II. NASA WVSGC UNDERGRADUATE RESEARCH FELLOWSHIP PROGRAM | 5 |
| III. NASA WVSGC GRADUATE RESEARCH FELLOWSHIP PROGRAM..... | 7 |
| Summer Internships Reports | 9 |
| Barthelmess, Megan. West Virginia University. <i>Cost and effort estimation methodology</i> | 10 |
| Burks, Timothy. Bluefield State College. <i>Rocket and Payload Integration Development</i> | 18 |
| Dole, Bryan. West Virginia University. <i>International Space Station Low-Gravity Sloshing Experiment</i> | 25 |
| Kimble, Dustin. West Virginia Wesleyan College. <i>Polymer Blending Polylactade with Different Polymers</i> | 35 |
| Lopez, Scott. Wheeling Jesuit University. <i>Fabrication and Characterization of Novel Nanoporous Material for Space Applications</i> | 43 |
| Mardmomen, Nadia. West Virginia University. <i>The Impact of Climate Change on World Hurricane Energy</i> | 54 |
| Melroy, Samantha. West Virginia University. <i>Simulation to Flight-1 Outreach</i> | 63 |
| Milam, Olivia. Marshall University. <i>Investigation of Orionism: Multi-Puroise Crew Vehicle Simulation Software</i> | 71 |
| Tucker, Kody. West Virginia Wesleyan College. <i>A Study of Doping of Semiconductors on the Nanoscale Level</i> | 77 |
| Undergraduate Research Fellowships Reports..... | 87 |
| Adkins, Mark. Marshall University. <i>Improvements of application for predicting chemical concentrations and additional contaminants in waterways for rapid response to chemical spills</i> | 88 |
| Behnke, Grayce. Marshall University. <i>Modifications of the surface of zinc oxide nanoparticles in order to increase efficiency of solar cells</i> | 94 |
| Bonnett, Brittany. Fairmont State University. <i>Molecular dynamics investigations of factors influence self-assembly of detergent micelles</i> | 105 |
| Cipollone, Domenic. West Virginia University. <i>Direct writing of titanium dioxide nanoparticle inks for photoanodes in dye sensitized solar cell space applications</i> | 115 |

| | |
|--|-----|
| Clark, Kyle. Shepherd University. <i>Effects of acid mine drainage on plant communities in the central appalachians</i> | 123 |
| Conte, Justin. Marshall University. <i>Identification and mass spectral analysis of palmitoylated proteins and the potential link to insulin resistance and diabetes mellitus in obese subjects</i> | 136 |
| Garretson, Samantha. Marshall University. <i>Modification of nitinol nanoparticles with self-assembled alkylphosphonate films</i> | 147 |
| Hoffman, Sierra. Shepherd University. <i>Determining the growth response of quercus rubra along elevational and exposure gradients</i> | 147 |
| Hoffmaster, Marshall. Shepherd University. <i>Validation of marker genes for the rapid alkalization factor pathway in arabidopsis thaliana</i> | 168 |
| Moreland, Kerwin. West Virginia University. <i>Writing of inks for use in p-n junctions for optoelectronic applications</i> | 194 |
| Raub, Esther. West Virginia University. <i>Safe loading limits for the rotator cuff muscles</i> | 202 |
| Stiner, Emily. West Virginia University. <i>How many neutron star black hole binaries are in the milky way?</i> | 214 |
| Szeligo, Brett. Wheeling Jesuit Univeristy. <i>Preparation and stability of cis-dicarbonylbis(diorganodithiocarbamate)iron(ii) complexes</i> | 219 |
| Graduate Research Fellowships Reports | 226 |
| Amos, Debbie. Marshall Univesity. <i>Exercise regulates brain-adipose tissue crosstalk in the “stress less” mouse model</i> | 227 |
| Birt, Stephen. West Virginia University. <i>Numerical analysis of bird wing cross sections</i> | 240 |
| Boehm, Dylan. West Virginia University. <i>Characterizing the innate and adaptive responses of immunized mice to bordetella pertussis infection using in vivo imaging and transcriptomics analyses</i> | 250 |
| Lantto, Sean. West Virginia University. <i>Precise orbit determination using duty cycled gps data</i> | 274 |
| Murphy, Rachel. Marshall University. <i>Mechanisms of oxidative damage associated with tenofovir nephrotoxicity</i> | 281 |
| Osborne, Lynn Kasey. Marshall University. <i>“Fence-line” contrast soundscape study of forested lands in allegany state park and allegheny national forest: is there an impact of oil and gas development on an eastern forest soundscape?</i> | 298 |
| Parkman, Jacaline. Marshall University. <i>Diet-ifi202b interactions in a novel congenic mouse model of obesity</i> | 313 |
| Tehrani, Nathan. West Virginia University. <i>Characterization and flight testing of multi-antenna gnss, multi-sensor attitude determination for stratospheric balloon platforms</i> | 346 |
| Ward, Dakota. Marshall University. <i>Mechanisms of radiocontrast nephrotoxicity</i> | 362 |

LIST OF PROGRAMS

I. SUMMER INTERNSHIPS

For the 2016–2017 fiscal year, we have nine undergraduate students who successfully received internship opportunities. Below is a list of their names, the university they attend, the internship facility as well as their research topic. A copy of their research reports is included under Section I.

Barthelmess, Megan

University: West Virginia University

Location: NASA IV&V Facility

Research: *Cost and Effort Methodology*

Burks, Timothy

University: Bluefield State College

Location: NASA Langley Research Center

Research: *Rocket and Payload Integration Development*

Dole, Bryan

University: West Virginia University

Location: NASA Goddard Space Flight Center

Research: *International Space Station Low-Gravity Sloshing Experiment*

Kimble, Dustin

University: West Virginia Wesleyan College

Location: West Virginia Wesleyan College

University: *Polymer Bending Polylactade with Different Polyesters*

Lopez, Scott

University: Wheeling Jesuit University

Location: NASA Goddard Space Flight Center

Research: *Fabrication and Characterization of Novel Nanoporous Material for Space Applications*

Mardmomen, Nadia

University: West Virginia University

Location: NASA Goddard Institute of Space Science

Research: *The Impact of Climate Change on World Hurricane Energy*

Melroy, Samantha

University: West Virginia University

Location: NASA IV&V Facility

Research: *Simulation to Flight-1 Outreach*

Milam, Olivia

University: Marshall University

Location: NASA IV&V Facility

Research: *Investigation of Orionsim: Multi-puroise Crew Vehicle Simulation Software*

Tucker, Kody

University: West Virginia Wesleyan College

Location: West Virginia Wesleyan College

Research: *A Study of the Doping of Semiconductors on the Nanoscale Level*

II. NASA WVSGC UNDERGRADUATE RESEARCH FELLOWSHIP PROGRAM

The NASA WVSGC Undergraduate Research Fellowship Program provides support for undergraduate students under the supervision of their academic advisor. For the 2016-2017 fiscal year, we have fifteen undergraduate students who were awarded research fellowships. Below is a list of their names, the university they attend, their mentor as well as their research topic. A copy of their research reports is included under Section II.

Adkins, Mark

University: Marshall University

Mentor: Dr. Paulus Wahjudi

Research: *Improvements of Application for Predicting Chemical Concentrations and Additional Contaminants in Waterways for Rapid Response to Chemical Spills*

Behnke, Grayce

University: Marshall University

Mentor: Dr. Rosalynn Quiñones

Research: *Modifications of the Surface of Zinc Oxide Nanoparticles in Order to Increase Efficiency of Solar Cells*

Bonnett, Brittany

University: Fairmont State University

Mentor: Dr. Erica Harvey

Research: *Molecular Dynamics Investigations of Factors Influence Self-Assembly of Detergent Micelles*

Cipollone, Domenic

University: Fairmont State University

Mentor: Dr. Konstantinos Sierros

Research: *Direct Writing of Titanium Dioxide Nanoparticle Inks for Photoanodes in Dye Sensitized Solar Cell Space Applications*

Clark, Kyle

University: Shepherd University

Mentor: Dr. Mark Lesser

Research: *Effects of Acid Mine Drainage on Plant Communities in the Central Appalachians*

Conte, Justin

University: Marshall University

Mentor: Dr. Leslie Frost

Research: *Identification and Mass Spectral Analysis of Palmitoylated Proteins and the Potential Link to Insulin Resistance and Diabetes Mellitus in Obese Subjects*

Hoffman, Sierra

University: Shepherd University

Mentor: Dr. Mark Lesser

Research: *Determining the Growth Response of Quercus Rubra along Elevational and Exposure Gradients*

Garretson, Samantha

University: Marshall University

Mentor: Dr. Rosalynn Quiñones

Research: *Modification of Nitinol Nanoparticles with Self-Assembled Alkylphosphonate Films*

Hoffmaster, Marshall

University: Shepherd University

Mentor: Dr. Jonathan Gilkerson

Research: *Validation of Marker Genes for the Rapid Alkalinization Factor Pathway in Arabidopsis Thaliana*

Moreland, Kerwin

University: West Virginia University

Mentor: Dr. Konstantinos Sierros

Research: *Writing of Inks for Use in P-N Junctions for Optoelectronic Applications*

Raub, Esther

University: West Virginia University

Mentor: Dr. Ashish Nimbarte

Research: *Safe Loading Limits for the Rotator Cuff Muscles*

Stiner, Emily

University: West Virginia University

Mentor: Dr. Duncan Lorimer

Research: *How Many Neutron Star Black Hole Binaries are in the Milky Way?*

Szeligo, Brett

University: Wheeling Jesuit University

Mentor: Dr. Norman Duffy

Research: *Preparation and Stability of Cis-Dicarbonylbis(Diorganodithiocarbamate)Iron(II) Complexes*

III. NASA WVSGC GRADUATE RESEARCH FELLOWSHIP PROGRAM

The NASA WVSGC Graduate Research Fellowship Program provides funding for graduate students working on a thesis or dissertation with faculty from member institutions. For the 2016-2017 fiscal year, we have ten graduate students who were awarded research fellowships. Below is a list of their names, the university they attend, their mentor as well as their research topic. A copy of their research reports is included under Section III.

Amos, Debbie

University: Marshall University

Mentor: Dr. Nalini Santanam

Research: *Exercise Regulates Brain-Adipose Tissue Crosstalk in the “Stress Less” Mouse Model*

Birt, Stephen

University: West Virginia University

Mentor: Dr. Patrick Browning

Research: *Numerical Analysis of Bird Wing Cross Sections*

Boehm, Dylan

University: West Virginia University

Mentor: Dr. F Heath Damron

Research: *Characterizing the Innate and Adaptive Responses of Immunized Mice to Bordetella Pertussis Infection using In Vivo Imaging and Transcriptomics Analyses*

Lantto, Sean

University: West Virginia University

Mentor: Dr. Jason Gross

Research: *Precise Orbit Determination using Duty Cycled GPS Data*

Murphy, Rachel

University: Marshall University

Mentor: Dr. Monica Valentovic

Research: *Mechanisms of Oxidative Damage Associated with Tenofovir Nephrotoxicity*

Osborne, Lynne Kasey

University: Marshall University

Mentor: Dr. Anne Axel

Research: *“Fence Line” Contrast Soundscape Study of Forested Lands in Allegany State Park and Allegheny National Forest: Is there an Impact of Oil and Gas Development on an Eastern Forest Soundscape?*

Parkman, Jacaline

University: Marshall University

Mentor: Dr. Jung Han Kim

Research: *Diet-IFI202B Interactions in a Novel Congenic Mouse Model of Obesity*

Tehrani, Nathan

University: West Virginia University

Mentor: Dr. Jason Gross

Research: *Characterization and Flight Testing of Multi-Antenna GNSS, Multi-Sensor Attitude Determination for Stratospheric Balloon Platforms*

Ward, Dakota

University: Marshall University

Mentor: Dr. Monica Valentovic

Research: *Mechanisms of Radiocontrast Nephrotoxicity*

Summer Internships Reports

COST AND EFFORT ESTIMATION METHODOLOGY

Megan Barthelmess
NASA IV&V Facility
Industrial Engineering
West Virginia University
Morgantown, WV

ABSTRACT

The goal of this project was to develop a cost and effort methodology for the Independent Verification and Validation Office (IVVO) at the Independent Verification and Validation (IV&V) Facility located in Fairmont, WV. The IVVO is the office within the IV&V Program that primarily handles the IV&V of NASA missions. An accurate estimation tool will enable the IVVO to conduct effort and cost estimations in the early lifecycles of projects based on system characteristics, criticality of the software, and the scope of analyses to be performed. The IVVO can then use this methodology to update estimates later in the project lifecycle.

Choosing a tool that would be most beneficial to IVVO required an extensive amount of research. The research consisted of reviewing approximately twenty-five different estimation tools and techniques; these included commercial tools, in-house developed tools, and past estimation methods used by the Office. After the tools were narrowed down to four, the criteria for the tools were compared against the Technical Framework for IV&V, specifically, *Section 3.0 Verify and Validate Requirements*. The criteria also needed to include the Catalog of Methods that corresponded to Section 3.0.

The best option for the IVVO was found to be the Safety and Mission Assurance Support Office (SSO) Effort Estimate Tool, which is an in-house tool currently being utilized by the SSO. Using an in-house tool was especially advantageous for IVVO: it was easily customizable and had the ability to be changed in the future as the cost and effort estimation process evolves. Some recommendations were suggested in order to further customize the tool to suit the needs of the IVVO.

Historical data was also collected to populate the tool. This step was achieved by interviewing various project managers and leads, as well as utilizing monthly financial documents. Continual collection of historical data is necessary to finish populating the tool. Receiving a resource estimate from the Software Assurance Tool Team (SWAT) and working with SWAT daily to implement the tool will also be key for the completion of the implementation of this project.

INTRODUCTION

The IV&V Facility in Fairmont, WV, is primarily responsible for reviewing software for different NASA missions. Ensuring the software is correct, does what it's supposed to do, does not do what it is not supposed to do, and operates appropriately and safely is extremely important for NASA missions. Mission failures can have drastic effects, potentially resulting in loss of human life or loss of the mission. One component at IV&V is the Independent Verification and Validation Office (IVVO). The IVVO is mainly responsible for handling the IV&V of the NASA missions

at the Facility. Developing an accurate cost and effort estimation for the IV&V of different missions has been somewhat of a dilemma for the IVVO. A new method is needed to create reliable, consistent estimates that can be used throughout a project's lifecycle. The tool must be somewhat customizable and very dependable, as well as fit all of the IVVO's needs.

Cost is the dollar amount of a project, and effort is the amount of resources (people) a project needs. There is a uniform cost that is associated with a certain amount of effort at the IV&V Facility. If the effort for a project is calculated, the effort can simply be multiplied by this cost figure to receive a cost estimate.

BACKGROUND

For the past several years, the IVVO did not have an established method to develop cost and effort estimates for NASA missions and projects. For most of the previous estimates, a group of experts would gather and offer their opinions and best guesses based on their past experience with performing IV&V on similar missions. This method generally gave a somewhat realistic estimate, but there was no technique or historical, consistent way to support the estimate. A more meticulous tool needed to be developed to ensure more accurate and consistent estimates. An accurate estimate in the beginning of a project lifecycle would be beneficial throughout the entire project.

IV&V performs extremely specialized work, specifically the Verification and Validation of remarkably unique software. There are no commercial estimation tools available that fit the exact needs of IV&V, and the Office quickly realized this challenge. A vast amount of research would need to be performed in order to choose a tool. A more accurate means of estimation would also give the IVVO a way to review a Contractor's initial cost and effort estimate for a project.

MATERIALS AND METHODS

Research

There are hundreds of estimation tools that could suit the needs of the IVVO. Many types of these tools were considered as options for the Office throughout the project.

The first step was to become familiar with the Estimating Process. This was achieved by reviewing past and current estimation techniques that had been used by IVVO. One of the past techniques was Software Integrity Level Assessment Process (SILAP). SILAP required a list of all component parts of the project. From there, the components were scored based on different criteria categories. The categories are as follows:

| | |
|--------------------|--------------------------|
| <u>Consequence</u> | <u>Error Potential</u> |
| Human Safety | Development |
| Asset Safety | Process |
| Performance Safety | Software Characteristics |

Each section was then ranked to calculate the effort estimation. The current technique being used is Portfolio Based Risk Assessment/Risk-Based Assessment (PBRA/RBA). The first phase is PBRA and the second phase is RBA. Similar to SILAP, there are two categories in this technique:

| | |
|---------------|-------------------|
| <u>Impact</u> | <u>Likelihood</u> |
|---------------|-------------------|

Performance
Personnel Safety
Operational Software Control

Complexity
Testability
Degree of Innovation
Developer Characteristics

All sections are scaled on a scale of 1-5. Risk Analysis is then used to determine the estimate. After reviewing these two methods previously used by IVVO, a list of potential tools and techniques was created. This list was based on preliminary research, and it primarily consists of commercial tools and techniques that could be utilized by IVVO. Since there are various types of tools, a large amount of research was required to understand a brief background on how each tool works and if it could be applicable to the Office.

1. Analysis Effort Method
2. COCOMO 1
3. COCOMO 2
4. Putnam Model
5. COSYSMO
6. Evidence-Based Scheduling Refinement
7. Function Point Analysis
8. Parametric Estimating
9. SPQR/20
10. ESTIMACS
11. PRICE Systems Founders of Commercial Parametric Models
12. PROXY-Based Estimating (PROBE)
13. Program Evaluation and Review Technique (PERT)
14. SEER-SEM Parametric Estimation Effort, Schedule, Cost, and Risk
15. SLIM
16. Planning Game
17. Weighted Micro Function Points
18. Wideband Delphi
19. Expert Judgement Method
20. Estimating by Analogy
21. Top-Down Method
22. Bottom Up Method

After research was performed for the tools, the original list of twenty-two was narrowed down to seven tools.

1. COCOMO 2
2. COSYSMO
3. Function Point Analysis
4. SPQR/20
5. ESTIMACS
6. PERT

7. SEER- SEM

At this point of the project, an additional potential tool was introduced to the list: SSO Effort Estimate Tool. This tool was being developed in-house for Safety and Mission Assurance Support Office (SSO). The SSO Effort Estimate Tool was especially advantageous because it was an in-house tool: adjustments and customizations could be made more easily than with a commercial tool.

After additional, more in-depth research was performed, the top four tools were decided.

1. COCOMO
2. COSYSMO
3. SEER-SEM
4. SSO Effort Estimate Tool

Enough research had been conducted to have a strong understanding of the tools at this point. In addition to being reliable and customizable, the tool and its criteria also needed to fit well with NASA IV&V's Technical Framework. The Technical Framework is broken down into different sections and subsections. The main sections are as follows:

1.0 Management and Planning

2.0 Verify and Validate Concept Documentation

3.0 Verify and Validate Requirements

4.0 Verify and Validate Test Documentation

5.0 Verify and Validate Design

6.0 Verify and Validate Implementation

7.0 Verify and Validate Operations and Maintenance Content

Since there are seven different sections, it was decided that the focus for this project would be on *Section 3.0 Verify and Validate Requirements*, as well as its subsections. The subsections have a specific breakdown with descriptions for each: 3.1, 3.2, 3.3, 3.4, 3.5, 3.6, and 3.7.

To ensure each subsection is satisfied, there are specific documents referred to as the "Catalog of Methods." For each subsection, there are a series of corresponding Methods. A Method consists of a series of steps that must be completed in order to complete the subsection. Once a Method is completed, the subsection is also completed.

In order to see if the tool's criteria fit well to the Technical Framework and Catalog of Methods, a specific Method was chosen to focus on. The chosen Method was M-2 Version 1.3. The Method was broken down into simple and organized terms, and the different criteria of each tool were compared to it. This comparison gave the IVVO a better perspective of how the tool would fit into the already existing Technical Framework: How much change, if any, did the tool require? Were the existing criteria of the tool applicable to the Framework?

Historical Data

Another part of this project was collecting data from multiple project managers and project leads

about different missions conducted at IV&V. The data collected would be the first step of collecting historical data to populate the chosen tool. The missions included the following:

1. GSDO
2. ICESAT-2
3. Insight
4. JWST
5. MPCV
6. SLS
7. HEO
8. MARS2020

By interviewing different project managers, information on Requirements Analysis of the individual projects was collected. Some examples of questions include:

1. What is the most recent level of requirements completed?
2. How many total requirements are there?
3. How long did it take to complete the requirements analysis?

The goal of this was to gather a “baseline” for how many hours it took to complete a single requirement. However, this was a more difficult task than it seemed. Since projects and missions last several years, project managers often didn’t have the exact numbers needed. Because of this, monthly financial documents were used to gather information about the time spent on requirements for each mission.

For one specific mission, the Insight Mission, a baseline was found. Insight had a total of 3212 requirements and 4238 total hours spent analyzing the requirements. This averaged to 1.32 hours/requirement.

After further consideration, it was decided that different types of missions would require different amounts of analysis time. Different mission types include science missions vs. human-rated missions. The lifespan of the mission should also be considered. For example, a science mission that consists of a satellite flying in lower earth orbit would not take as long to complete as a human-rated mission going to Mars. There are different requirements involved for each specific mission.

RESULTS AND DISCUSSION

The Decision

After much consideration, the IVVO chose the SSO Effort Estimate Tool. Since the tool is currently under in-house development, it will be easier to make changes and adapt to the IVVO’s needs. Choosing a commercial tool would not have been as feasible. It would be difficult to adjust the tool and make changes as needed.

How the Tool Works

The tool requires the user to enter specific information to generate the estimate. Some of the most important information entered is scores of the criteria built into the tool. The criteria are:

1. Size

2. Complexity
3. Domain knowledge

The criteria are scored on a scale of 1-10. The user must also enter specific Tasks that the project must complete throughout the lifecycle. Each Task has Steps that must be completed in order for the entire Task to be finished. There is a task library that contains built-in Tasks and Steps. The estimation is then reported in in Person Days.

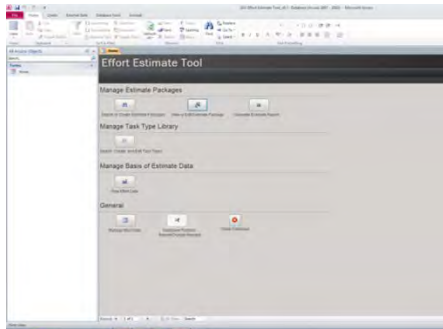


Figure 1: Home Screen

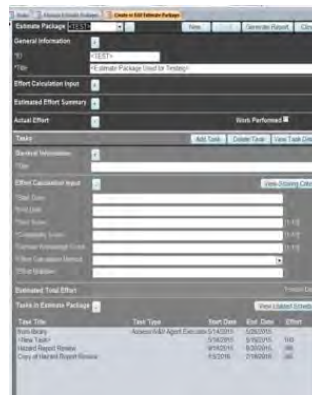


Figure 2: Search or Create Estimate Packages

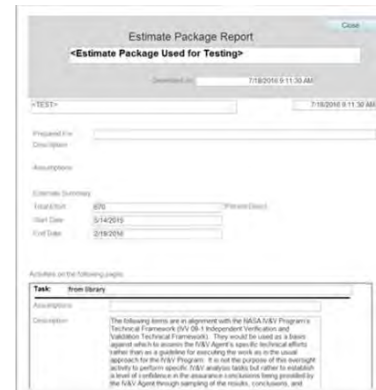


Figure 3: Generated Report

Recommendations

Although the SSO Effort Estimate tool is the best option, it does not entirely fit the needs of the IVVO. Some recommendations were needed in order to customize the tool and ensure it performs all designated, required tasks.

The following are recommendations:

1. Have a separate tool for the IVVO and the SSO

If a separate tool is not available, have different options within the tool in order to differentiate the different uses.

2. Add an additional five criteria to help create the estimate:
 - a. Testability
 - b. Degree of Innovation
 - c. Performance
 - d. Personnel Safety
 - e. Operational Software Control

The additional criteria come from the PBRA/RBA Risk Analysis. The total number of criteria would be eight. The original three criteria (Size, Complexity, and Domain Knowledge) would still be applicable. All eight criteria would be mandatory in order to use the tool. These original criteria could be scored at the Task level, while the additional five criteria could be scored at the Project Level.

By adding more criteria, the level of confidence of the estimate should slightly increase. With the

original three criteria, the estimate should be generated at approximately an 80% confidence level. With the addition of the extra criteria, the confidence level will increase, ideally to 85%.

- When the additional criteria are included, a unique scoring system will need to be developed for the tool.

Currently, the original three criteria have a scoring system built into the tool. The additional criteria can use a similar scoring system to PBRA/RBA, but it will still need to be modified for the tool.

- Have the Technical Framework and Catalog of Methods built into the Task Library. Different aspects of the Technical Framework could be assigned as “Tasks” (3.1, 3.2, 3.3, would each be separate tasks). The Catalog of Methods would be assigned as the “Steps.”



Figure 4: Manage Task Library



Figure 5: Task Details

These are the main recommendations that could be completed in order to implement the tool for the IVVO use. Additional recommendations with lower urgency were also considered. These include being able to access different tools readily available within this tool and allowing comment fields throughout the tool to document notes that are specific to a project.

OUTCOMES

The tool is now being discussed between the IVVO and SWAT (Software Assurance Tools Team) to ensure that all needs are capable of being met. The recommendations may need to be adjusted depending on SWAT’s input. The tool is currently based on Microsoft Access, but it will be a separate tool once the SWAT has completed it.

The tool could take up to a year to be fully implemented. Due to this development process, the tool could generate estimates at a larger level at first: 3.0, 4.0, etc. After further development, the tool could estimate at a more detailed level: 3.1, 3.2, 3.3, etc.

FUTURE PLANS

This project will not be complete after my internship ends. The IVVO must receive a resource (cost) estimate from SWAT for customizing the tool in order to fit the IVVO’s needs. After an estimate has been collected, the IVVO will assign resources to the tool as needed. These resources

will need to ensure that progress is being made throughout the project and work with SWAT daily to make sure needs are being met. The IVVO and SWAT will work together on the tool until it is implemented. Historical data will also have to be collected in order to populate the tool.

MOST VALUABLE ASPECTS

Throughout this summer, I learned several valuable lessons. I learned how to properly conduct research by analyzing multiple tools and choosing the best option based on my research. I also learned how to conduct myself in a professional setting – I’ve had to schedule and run meetings, as well as attend them. I also improved my communication and presentation skills. I enjoyed seeing teamwork between employees and interns in a real-life setting.

I also learned about the specifics of cost and effort estimation. There are numerous tools, techniques, and methods that can be used for the estimation. Collaboration from multiple teams is necessary, and experience in the field is absolutely essential. There is often not a single correct answer, but multiple options that could work well depending on the specific situation.

CONCLUSION

After much research, the IVVO chose the SSO Effort Estimation Tool to solve their estimation issues. This was the best choice for the office: it is developed in-house, reliable, and customizable. The recommendations suggested will only further strengthen the tool’s ability to estimate as well as increase the confidence level of the estimate. After SWAT implements the tool, IVVO will be able to update the tool as necessary and create accurate estimates for all missions.

ACKNOWLEDGEMENTS

I would like to acknowledge the West Virginia Space Grant Consortium for supporting me throughout this opportunity. I would also like to thank the NASA IV&V Facility in Fairmont, as well as my outstanding mentor Lisa Downs. An additional acknowledgement goes to Jess White for coordinating the internship program.

ROCKET AND PAYLOAD INTEGRATION DEVELOPMENT

Timothy Burks
NASA Langley Research Center
Electrical Engineering Technology
Bluefield State College
Bluefield, West Virginia

ABSTRACT

This summer internship provided valuable knowledge in the field of microprocessors, soldering, 3-D printing, Printed Circuit Board (PCB) layout, and payload integration. Various tasks were performed throughout the summer to give a better understanding of how these relate to the field of engineering. The knowledge gained from these tasks were then applied to teaching “at risk” teenagers during a summer camp in hopes of sparking an interest in a STEM-related field.

INTRODUCTION

As a member of Team RaPID (Rocket and Payload Integration Development) in the Game Changing Development program at Langley Research Center, there were three specific goals for the summer. The first goal required the team to complete the Rock On workshop at Wallops Flight Facility, on Wallops Island, Virginia. During this workshop, the objective was to construct and integrate a functioning circuit that would be launched into space to collect data. The second goal of this internship featured individual projects for each intern on Team RaPID. The specific task assigned to me required working with a point of contact from Orbital ATK to design a power distribution board that will be integrated into a sounding rocket that is scheduled to launch in December. The third and final goal of the summer required each intern to assist in designing a summer camp for “at risk” teenagers. This camp was designed for rising high school students, in hopes of sparking an interest in the science, technology, engineering and mathematics (STEM) field. The camp lasted four days and required the interns to be mentors as the teens learned the basics of 3-D printing, coding Arduinos, programming drones, and soldering electrical components.

GOALS

Rock On Workshop

The Rock On workshop began during the weekend following our second week of the internship. At this moment, the team was still getting to know each other, and the Rock On workshop helped immensely. The workshop was on a very tight schedule and required each team participating to finish in a timely manner to ensure that each circuit would be integrated onto the sounding rocket before launch.

The first few days of the Rock On workshop exposed each team member to many different sensors that we had never worked with before. Some of these sensors consisted of temperature/pressure and humidity sensors, accelerometers, and a Geiger counter. Most of the non-electrical engineering interns seemed to struggle a little more because they did not recognize the basic electronic

components that were being used as well. Some of the basic electronic components being used were LEDs, capacitors, transistors, voltage regulators, and resistors. Needless to say, the first few days were a learning experience for everyone involved.

Once the components of the circuit were soldered onto the board, programming came next. This area of the workshop provided the most informative lessons. Having never programmed anything before, our circuit was connected to the computer through a microprocessor called Arduino. The workshop provided very detailed slides, along with the Arduino software, to teach the importance of programming. Each team was able to program their circuits and test them to see if they were working properly. Some of the tests included touching the temperature sensor, breathing onto the humidity sensor, blowing onto the pressure sensor (through a straw), and testing the Geiger counter by disassembling a smoke detector, which featured a component that produced radiation. As each test was conducted, the Arduino software would display the changes in the data on the computer screen.

The final step of the workshop consisted of each team integrating their boards into a canister filled with other circuit boards. Once the boards were inside the canisters, NASA officials loaded the canisters onto the sounding rocket. The launch took place on the last day of the workshop and was retrieved hours later. The data, along with the physical hardware was given back to each team a few days later.

This workshop experience provided an amazing learning experience. Before this opportunity, I did not know what a Geiger counter or an Arduino was. I had never seen a pressure/temperature or humidity sensor before. I did not know how an accelerometer worked. The Rock On workshop took each of the above components and provided a very valuable lesson. It is clear that each of these sensors, along with many others, provide numerous amounts of data to NASA for space flights, or aerospace in general.

Printed Circuit Board (PCB) Layout

The Rock On workshop required the interns to work in teams. Once the workshop was completed, however, each intern was assigned a specific project to work on. The project assigned to me required designing a power distribution board that would intake a certain amount of voltage, and provide a set output voltage to different components. Orbital ATK had flown a very similar project the year prior, so the plan was to build a power distribution board similar to the previous one. The main difference between the two projects is that the newest project required less instrumentation, and featured a camera control circuit to capture footage during the flight.

Upon talking to the point of contact at Orbital ATK, the plan was to create a circuit that could intake up to 36 volts and provide a 28-volt output to a 25-pin connector, and a 5-volt output to the camera control circuit. The 25-pin connector would be on the output side of the power distribution board and would provide power to the sensors that were to be used.

After conducting research, it appeared that LM-317 voltage regulators along with properly sized capacitors and resistors could provide the best output voltages required for this particular circuit. A simulation tool, known as Multisim, was then downloaded onto the computer to construct the circuit to see if it would work as planned. Upon completion of the circuit, a test was simulated and

confirmed that the designed circuit would work properly.

The next step required physically testing the circuit through the use of a breadboard. Unfortunately, this never took place due to a few different reasons. The lone point of contact for this project took vacation during a critical time. The STEM-related summer camp happened around the same time and required two weeks' worth of work. These instances, along with the fact that the internship was coming to an end, forced the project to be handed-off to another intern. All information pertaining to this project was collected and will be provided to the available intern.

This individual project provided a very unique experience because I had no knowledge of PCBs prior to this opportunity. Working with a professional engineer to design a power distribution board has given me a better understanding of how an entire team works together. The reason for this is that something as small as a power distribution board can be critical to an entire flight. Working with something so small provides a better understanding of how important each person's job is.

Jr. Game Changers Camp

The final and most important goal of this internship came during week 8. A STEM-related summer camp for "at risk" rising high school students was conducted at Langley Research Center, Virginia, in hopes of sparking an interest in STEM-related fields. The name of the camp was Jr. Game Changers, and the goal was to teach the students how to 3-D print objects, code Arduinos, solder electrical components and program various drones to maneuver through obstacles.

The majority of the camp was planned by two interns on Team RaPID, Austin Fuller and Monty Noblezada. The other interns involved consisted of Marquis Burgess, Maggie Story, Maria Hovanessian, Scott Conklin, Maria McDougall, Betsy Wusk and myself. There were many officials from the Program office that assisted as well; however, the main contributors were Adelle Helble, Nancy Hornung, Carrie Rhoades and Mary Beth Wusk.

The students that participated in this camp were selected by their school. The camp was intended for rising 9th graders. However, there were a few sophomores in the mix. After the first day of the camp, a few seniors came as student ambassadors for the remaining three days. The turnout featured 30-35 students per day, with each day being a different number. This camp did not focus on minorities or a specific gender. It was open to any students that were allowed to come.

Prior to the camp, students were asked to take a Pre-camp survey to give an indication of knowledge on the subjects that were to be discussed. The camp began by separating the students into teams of three and performing team-building exercises to allow each of them to open up. The first lesson of the camp introduced the students to Inventor and 3-D printing. An activity was then given that required each team to work together to develop a specific structure on Inventor. Every intern acted like a mentor by walking around and assisting the students with any problems they encountered. Once each team completed their task they were rewarded with a pre-printed Space Shuttle for their hard work. The second activity of Day 1 introduced the students to various drones. Each team was given a drone and an iPad and instructed on how to properly maneuver it. Small obstacles were placed on the ground, and the teams were asked to maneuver around them. This task allowed each student to see how the drones operated differently.

Day 2 of the camp started with the construction of a programmable-robot, called the mBot. Each team was given an mBot and allotted a certain amount of time to build it from scratch. Once the construction was complete, the robots were connected to each computer and programmed to perform specific tasks. The programming for this robot came from a very simple coding software that allowed the students to drag-and-drop blocks of information, rather than typing in actual code. This made it easier for the students to see their robots perform the actions that were requested. The second lesson of the day proved to be our most troublesome task of the camp. After learning a little bit about code at a basic level, the next lesson involved working with Arduinos, which are microcontrollers. The lesson taught the students about coding that wasn't as simple to comprehend. The three Arduino examples used taught the kids how to say "Hello World," blink an LED, and read a temperature sensor. The students seemed to struggle with the tasks at first, but performed a lot better once mentors worked with them separately. The third and final lesson of the day featured another drone activity, but this time with a quadcopter. Teams were given a quadcopter and tasked to fly through small obstacles. Similar to the first day, the drones were driven by the students, manually.

The third day of the camp introduced the students to soldering, and required each team to prepare their drones for the final obstacle course on day 4. Due to a limited number of soldering kits, the students were split into separate rooms with half of them soldering and the other half programming drones. The students that were soldering were given a Drawdio, which is a small circuit attached to a pencil that makes a noise as you draw. The majority of components were pre-soldered for the kids prior to the camp; however, the students were allowed to solder a capacitor, resistor, and transistor. During the soldering class, the instructor taught the students about each of these components and how they work on an electrical circuit. The students in the other room were tasked with programming their drones for the final obstacle course. A course description was displayed, and each student began using their iPads along with an app called Tickle. Tickle is an easy-to-use programming tool that allowed each student to drag and drop lines of code to instruct their drones to perform specific tasks. Unlike the previous two days, the final obstacle course featured drones that were programmed rather than manually operated. The objective was to program a land drone that would navigate its way through a maze and stop at a certain location. This land drone would then send a signal to a quadcopter which would then lift off and fly up and over objects, through hoops and eventually land on a pad at a specific height.

The last day of the camp required each team to perform last-minute adjustments for their drones. The competition began, and the students had a blast. After each obstacle, the students were rewarded points, and the team with the highest amount of points was declared the winner. Unfortunately, no team made it entirely through the course, but there were plenty of teams that came close. Upon completion of the obstacle course, the students were given a post-camp survey. The pre- and post-camp surveys were eventually compared, with a conclusion that the camp was a success. Many of the students came into the camp with no knowledge of 3-D printing, coding, soldering, or programming drones. However, most of the students thoroughly enjoyed their time and left the camp with a genuine interest in STEM.

CONCLUSION

This internship has provided plenty of experience in different areas. The Rock On workshop exposed me to different types of sensors and provided a better understanding as to how and why they are used. The workshop also introduced me to Arduinos and coding, which was very new to me. Working with Orbital ATK took me out of my comfort zone, because I did not know what a Printed Circuit Board (PCB) was beforehand. However, after researching and spending plenty of time, I learned what a PCB was and how they're made. I also learned that there are many different types of software that will create a PCB layout for you. For example, at Bluefield State, we use Multisim (a circuit-simulating software) to build and test circuits. I was unaware that there is a feature that allows the circuit to be converted to a PCB. I discovered this while researching PCB software. Lastly, the Jr. Game Changers summer camp provided the most fun of the entire internship because it provided a feeling that none of other tasks did. Being able to teach these bright young teens provided an amazing feeling that words cannot describe. Overall, this summer was amazing! I am truly grateful to have had the opportunity to intern with one of the most prestigious organizations on Earth.

ACKNOWLEDGEMENTS

This internship would not have been possible without certain individuals. First and foremost I would like to thank my mentors Adelle Helble and Carrie Rhoades for selecting me as an intern this summer. Thank you for helping with every obstacle I came across. This internship would not have been possible without the two of you.

I would also like to thank the rest of the Game Changing Development office for helping me along the way. Working with the same program office for two consecutive summers has been a blessing.

I would like to take a moment and thank my fellow interns for their assistance along the way. I can only hope that I taught you as much as you taught me. The last nine weeks have brought each of us closer together, and I hope to see you all again.

Lastly, I would like to thank the West Virginia Space Grant Consortium for supplying the grant for my internship. Without this financial assistance, I would not be here. So for that, I thank you.

PICTURES

Rock On Workshop

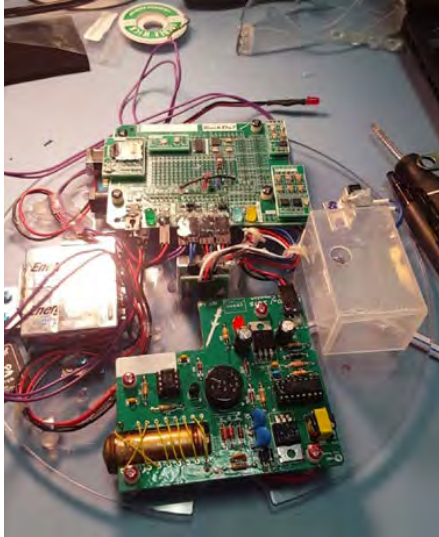


Figure 1: Completed Payload



Figure 2: Integrated Canister

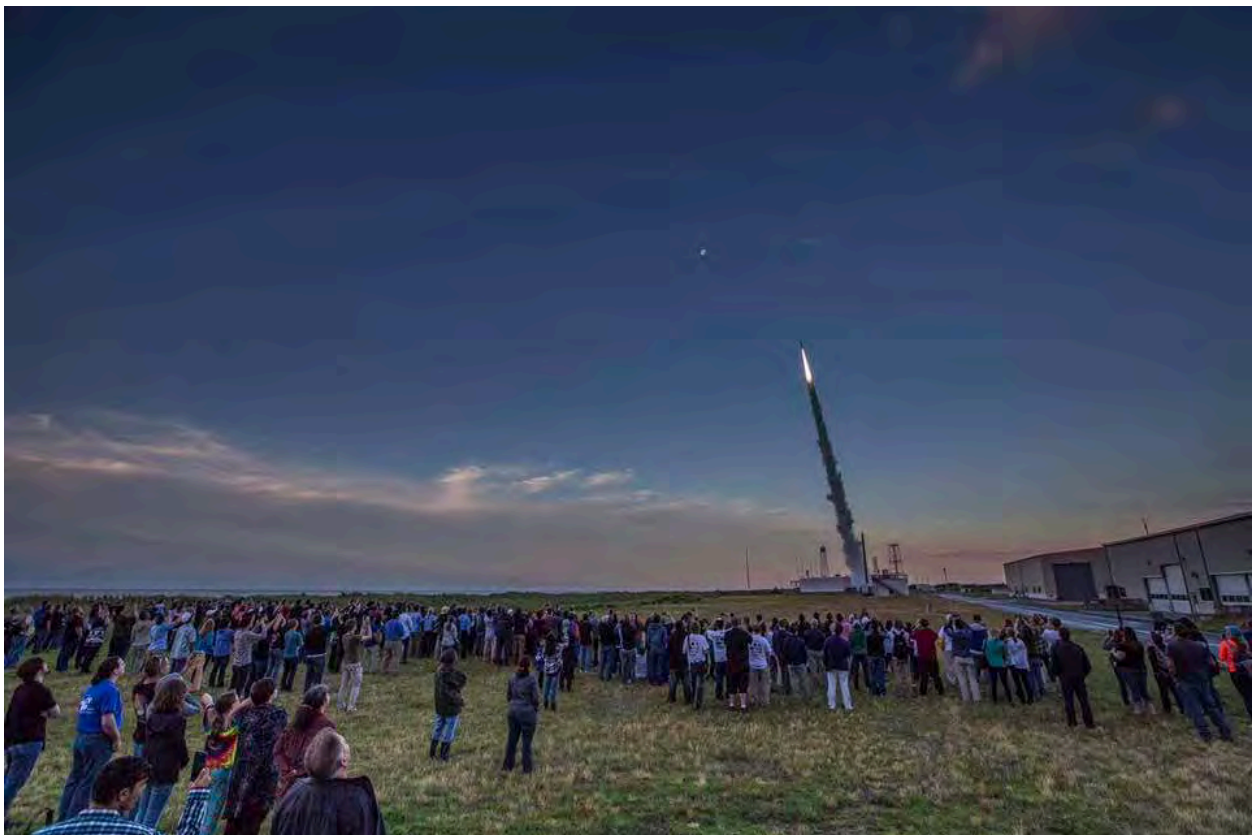


Figure 3: Sounding Rocket Launch

Jr. Game Changers Camp



Figure 4: mBot Programming



Figure 5: Drawdio Soldering



Figure 6: Jr. Game Changers Group Photo

INTERNATIONAL SPACE STATION LOW-GRAVITY SLOSHING EXPERIMENT

Bryan Dole
NASA Goddard Space Flight Center
Mechanical and Aerospace Engineering
West Virginia University
Morgantown, WV

ABSTRACT

During spacecraft steady flight and maneuvers, the propellant liquid inside of tanks used by the spacecraft undergoes sloshing, a movement of a liquid inside of a container that results in net forces and moments being applied on the tank as a whole. This can result in possible changes in mission trajectory, inefficient fuel consumption, and even, in extreme cases, mission failure. These behaviors are commonly analyzed and predicted using Computational Fluid Dynamics (CFD) analysis, based on theoretical dynamics. However, there is only a small amount of experimental work that has been conducted in order to verify CFD models.

A slosh tank enclosure has been designed in order to generate further experimental data in order to validate current CFD models. An experiment using the enclosure has been designed, required hardware for the enclosure has been researched and purchased, and two procedures have been designed: a procedure testing the position of camera and interior lighting and a ground test to verify enclosure hardware is accurate. Several force sensors and a pair of cameras in the enclosure will generate data that taken together will provide the magnitudes of forces and moments on the tank in the principal axes as well as give a visual of how the liquid is positioned through the duration of maneuvers. This information will then be compared to CFD methods to validate computational approaches.

INTRODUCTION

A slosh tank enclosure has been designed in order to generate further experimental data in regards to sloshing dynamics of a propellant tank undergoing spacecraft maneuvers. This data will be used to validate current CFD models used to analyze and predict fluid sloshing behavior in propellant tanks during low-gravity maneuvers. Nearly all computational analysis techniques rely on theory and do not have enough experimental data to prove their validity. In order to verify the accuracy of CFD models, an experiment using the enclosure has been designed, required hardware for the enclosure has been researched and purchased, and the enclosure has been constructed. The sloshing tank enclosure contains a propellant tank attached to groups of force sensors oriented in such a manner as to read the forces acting upon the tank in various coordinate axes. In addition, a pair of cameras are positioned at opposite ends of the enclosure in order to image the position of the liquid in the propellant tank. This data taken together will provide the magnitudes of forces on the tank in the principal axes as well as give a visual of how the liquid is positioned across through the duration of maneuvers. Both the force and moment magnitudes and images can then be compared to images and data obtained from CFD methods to validate computational approaches.

BACKGROUND

The term sloshing refers to the movement of a liquid inside of a container. Sloshing dynamics involve the forces and moments applied on a container as a result of interior liquid movement.^[1] During spacecraft steady flight and maneuvers, the propellant liquid inside of tanks used by the spacecraft undergoes interior sloshing. The orientation of the liquid throughout the duration of maneuvers occurs in three modes: a static mode in which the liquid is initially oriented due to static equilibrium, a dynamic mode caused by the spacecraft maneuver, and another static mode which shows the final orientation of the liquid in the tank once static equilibrium is again achieved.

Outside of the forces from the spacecraft maneuver itself, the slosh dynamics of the propellant tank ultimately depend on the dominant forces acting on the liquid to achieve static equilibrium. Two types of forces that have the greatest impact upon slosh dynamics are gravity and surface tension. Surface tension is the elastic tendency of a fluid surface to acquire the least surface area possible. This phenomenon is a result of boundary liquid molecules experiencing an inward attractive force. While interior liquid molecules are surrounded by other liquid molecules and thus experience equal forces in all directions that ultimately cancel out, boundary liquid molecules are surrounded by both liquid and gas molecules. When the liquid molecules attract more to other liquid molecules rather than gas, the boundary molecules experience a net inward force towards the liquid. In terms of energy, this attraction on the boundary molecules causes the boundary liquid molecules to possess a higher energy state than the interior liquid molecules. In order for the liquid as a whole to achieve the lowest energy state possible, it must minimize the amount of boundary liquid molecules and thus minimize the surface area of the liquid.^[2] On earth, gravity is much more dominant on the slosh dynamics in a tank. Body accelerations such as spacecraft maneuvers are dominant in space. However, surface tension plays a crucial role in determining the orientation of the liquid during the two static modes in the slosh dynamics problem.

DESIGN

An enclosure has been designed with the purpose of gathering data from propellant tank sloshing that can be sent to an outside source to be analyzed and compared to CFD models. The initial design is intended to provide a general layout of the different hardware required in the enclosure for different tasks for the experiment aboard the ISS. A propellant tank with a Propellant Management Device (PMD) inside the tank will be located in the center of the enclosure. The propellant tank is a transparent container, allowing video imaging of liquid slosh in the tank. The liquid used in the propellant tank for the slosh experiment will be water as it serves as a good approximation to hydrazine, a common propellant, in terms of sloshing behavior. The water in the propellant tank will be dyed a dark purple color to provide a larger contrast with the color of the enclosure walls. This contrast aids in producing a clear image from the cameras in the enclosure. The dimensions, final shape, and ends of the propellant tank have not been finalized.

A diagram of the top view of the initial propellant tank enclosure design is shown below in Figure 1. Several aspects of the enclosure design will need to be adjusted before a final design is created. The dimensions of the tank enclosure will need to be changed to account for the final dimensions and shape of the propellant tank. The placement of both the Raspberry Pi's and the LED light strips

will need to be adjusted based on results from the light testing procedure. A clamp between the propellant tank ends, and the force sensor arms will also need to be designed. This design will require knowledge of the shape and size of the ends of the propellant tank. The final design of the propellant tank enclosure will depend significantly on these changes.

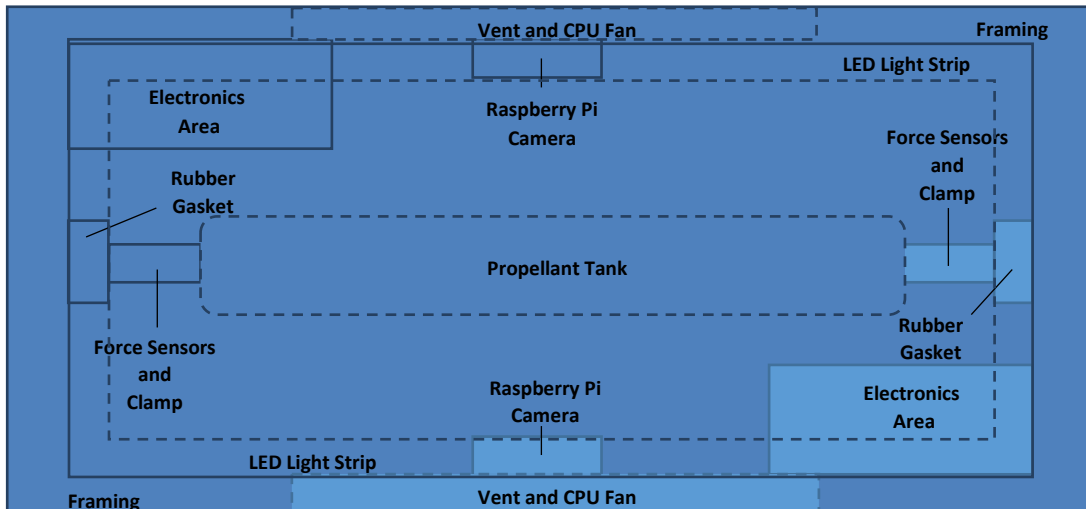


Figure 1: Initial Propellant Tank Enclosure Design (Top View)

Enclosure Framing

The outside framing of the propellant tank enclosure consists of 0.236” thickness white Polycarbonate sheet. The material has been used in past experiments aboard the ISS, so the material has been proven to be able to withstand the local conditions in which the propellant tank slosh experiment will take place. The white color of the framing was chosen in order to provide a strong contrast to the dark purple color of the water in the propellant tank. This allows the Raspberry Pi cameras to provide a clear image of the water in the propellant tank during the experiment.

A stress analysis has been conducted in order to ascertain an appropriate framing thickness that would survive max loading conditions with a sizable factor of safety while minimizing costs. Due to the complexity of a full plate bending analysis, the sides of the enclosure connected to the sensor arms have been approximated as four cantilever beams with the maximum load of the tank applied at the end of all four beams. The beams have been designed extending from the four corners of the enclosure framing side, meeting at the center where the force is applied to all four beams. The minimum thickness required for the enclosure framing to not exceed its yield strength was found for factors of safety of five, seven, and ten. The factors of safety were chosen to be higher because the stress analysis was an approximation of the true behavior of a plate under bending. Results of the stress analysis can be seen in Table 1. A full plate bending stress analysis is recommended before the final design is created.

| Factor of Safety | Maximum Bending Stress per Beam before | Minimum Frame Thickness (in.) |
|------------------|--|-------------------------------|
|------------------|--|-------------------------------|

| | Table 1: Framing Thickness Stress Analysis | |
|----|--|-------|
| | yielding (lbf/ft ²) | |
| 10 | 518400 | 0.27 |
| 7 | 740563 | 0.226 |
| 5 | 1036800 | 0.191 |

An enclosure framing thickness of 0.236” has ultimately been chosen for the propellant tank enclosure. The chosen thickness was a result of availability from different online vendors, minimization of framing costs, and a factor of safety between seven and ten, giving reasonable certainty that the framing will withstand maximum loads.

Force Sensors

Two sets of four force sensors will be used to gather force data throughout the duration of simulated spacecraft maneuvers as part of the ISS experiment. The force sensors gather data by having two surfaces press against each other, with the circular material of the force sensor located in between the two surfaces. In this design, the force sensors are located between the ends of the propellant tank and the clamp attaching the tank to the sensor “arms.” This ensures that all of the forces from the propellant tank are directed through the sensors so that the force data is an accurate representation of the loads from the tank. The force sensors will be oriented such that it will be easy to use the force data from each sensor to find the forces along the principal axes at a given point in time during the maneuver. A basic diagram for the setup of each force sensor is shown in Figure 2.

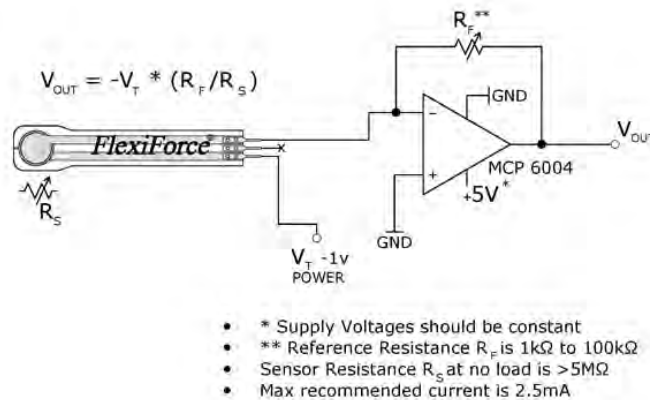


Figure 2: Basic Setup for FlexiForce Sensor

Raspberry Pi

Two Raspberry Pi cameras will be used in order to record video imaging of the propellant tank liquid throughout the duration of the simulated maneuvers. A camera module attached each Raspberry Pi will record images at set increments to give a visual of the orientation of the liquid over time throughout the maneuvers. Image capture via the camera module will be controlled

automatically through prepared Python code and the P910 motherboard. The Raspberry Pi's will send captured images to the motherboard through an Ethernet cable. The Raspberry Pi will also connect to the P910 motherboard through a USB 3.0 cable. The placement of the Raspberry Pi is subject to change in the final design based on results from the light testing procedure. A platform connected to the inner enclosure wall will have to be created and attached in order to provide a place for the Raspberry Pi to rest.

Rubber Gasket

A rubber gasket connects the propellant tank sensor "arm" to the side of the enclosure frame. The gasket helps to prevent shock loads from overloading and damaging the force sensors.

LED Light Strip

Two sets of LED light strips will serve as the sole lighting inside of the enclosure. The white color of the LED's has been chosen to provide maximum contrast to the dark tank liquid. The length and orientation of the LED light strips are subject to change in the final design based on results from the light testing procedure.

Vent and CPU Fan

Two pairs of vents on opposite sides of the entire will allow the enclosure to maintain a safe temperature for hardware. The vents must be designed so that air can travel through the vents, but light cannot enter or exit the enclosure. It is recommended that the vents are designed with two pairs of inclined surfaces perpendicular to each other within the enclosure framing. This would allow a passage for air but make it impossible for light to pass through.

A CPU fan will be placed inside of the enclosure in front of each vent. This will aid in circulating air into and out of the enclosure to aid in cooling. Referring back to Figure 1, in the initial design the CPU fans are placed directly below the Raspberry Pi and in front of the vents.

Electronics Area

All electronics not already mentioned will be attached to the enclosure in the areas designated in Figure 1. In addition, the force sensors, Raspberry Pi's, LED lights, and CPU fans will connect to the rest of the hardware located in the Electronics Areas in order to receive power and transmit data. Two sets of electronics areas are located in opposite corners of the enclosure and power one network of force sensors, Raspberry Pi, CPU fan, and LED light strip. The force sensors each connect to an Op-Amp circuit which then connects to the P910 motherboard to receive a power voltage and deliver a voltage reading corresponding to the force. The Raspberry Pi is connected to the P910 motherboard through both USB 3.0 for power and an Ethernet cable to transfer data. The LED light strips are connected to an 11.1V to 12V DC to DC converter which is powered through connecting to the P910 motherboard. The CPU fan is directly connected to the P910 motherboard for power. Figure 3 below shows the electrical layout of the electronics used in the propellant tank enclosure.

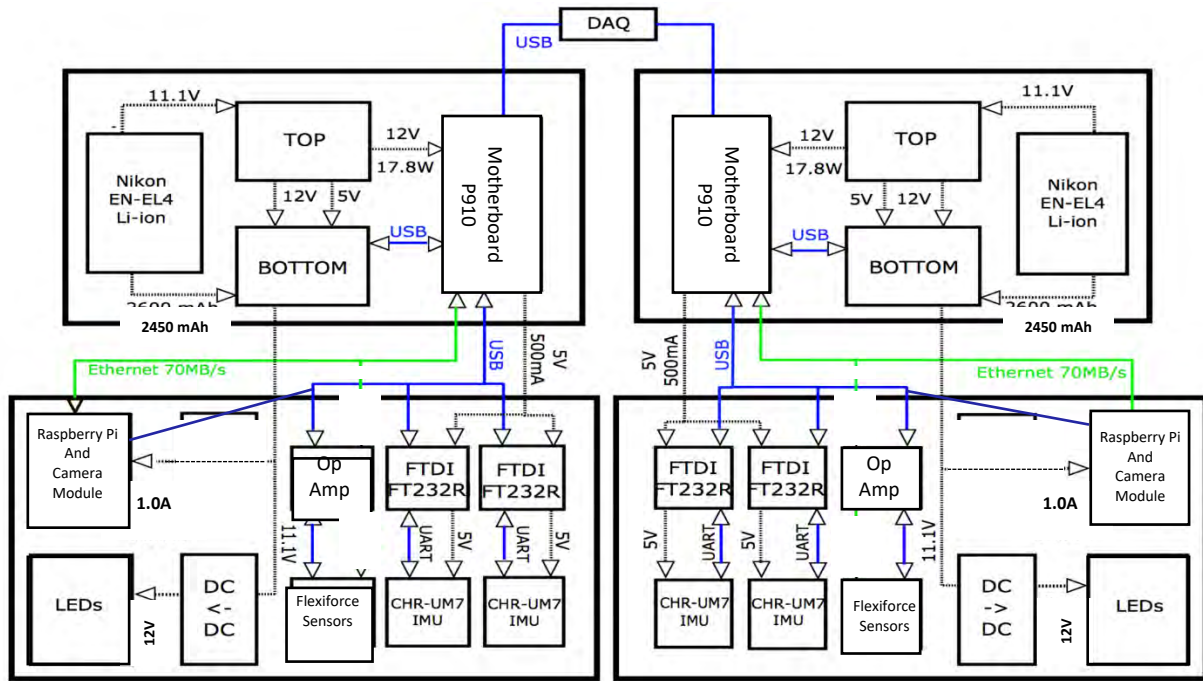


Figure 3: Electrical Layout of Propellant Tank Enclosure Hardware

P910 Motherboard

The P910 Motherboard is the center of the Electronics Area and controls all of the software processes and power throughout the enclosure. The motherboard itself is powered by a Lithium-Ion battery. The motherboard provides power to all other hardware and accessories within the enclosure through a variety of connections, seen in Figure 3. The motherboard also receives data from both the force sensors and the Raspberry Pi's. The motherboard can then send it wirelessly to ISS systems. The exact nature of the transfer between the enclosure and ISS computers has not been finalized. It is recommended for future work to look at SPHERES systems aboard the ISS as previous study was conducted on SPHERES. An expansion card will be attached to the motherboard to allow the use of USB 2.0 slots.

Inertial Measurement Unit (IMU)

IMU's are used in the enclosure in order to provide velocity, rotational, and GPS position data about the enclosure. They feature a collection of gyroscopes and accelerometers that provide data that is important for the development of CFD models. This data is sent through a FTDI controller that converts the data into information usable by the P910 motherboard. The IMU and controller system is both powered and transfers data through a USB cable.

Lithium-ion Battery

A Lithium-ion battery is used to provide power to the P910 motherboard is thus the entire electronics system. The battery is about to provide 2.45 amp-hours. Based on a preliminary power analysis, the battery will be able to power the entire system for 33-50 minutes. More work is required to calculate power requirement once electronics hardware has been solidified in the final design.

COST ANALYSIS

A propellant tank will be provided for use in the experiment. Previous work was conducted on a cost analysis for the propellant tank enclosure and all support equipment, and several types of hardware were recommended for purchase.^[3] The total cost from the initial recommendation, calculated by past interns, greatly exceeded the \$3000 budget for the propellant tank enclosure. Two major contributors to the total price were the Nano17 Force and Moment Sensors and the Aptica UI-5580CP Camera with unit prices of \$4300 and \$2292 respectively (not including support equipment).

A new cost analysis has been conducted to find additional pricing on equipment within the scope of the budget as well as pricing on additional components for the enclosure. Costs have been significantly reduced by replacing the Nano17 sensors with FlexiForce A201 Sensors and by replacing the Aptica UI-5580CP Cameras with Raspberry Pi 3 - Model B cameras. Two new budgets have been proposed: a full budget with two networks of sensors and cameras and a “light” budget using only one network of sensors and cameras. Both proposed budgets are within the \$3000 limitation. A comparison between the three budgets is shown in Table 2. The full and light budgets reflect two options in case a reduced budget is available at the time of purchase.

A secondary cost analysis has been conducted in order to evaluate additional support equipment needed for the propellant tank enclosure. Twenty-three additional pieces of hardware were identified as useful or necessary to the existing hardware for the enclosure. The additional hardware was \$352.68 in total. The total cost for all needed hardware was still under \$3000 for both the “full” and “light” budgets. The total cost of the additional hardware as well as revised budget costs can be seen in Table 2.

Table 2: Cost Analysis Budget Comparison for Enclosure

| Budget | Total Cost (dollars) |
|---------------------|-------------------------|
| Available | 3000 |
| Previous | 18953 |
| New (Full) | 2574 |
| New (Light) | 1795 |
| Additional Hardware | 353 |
| Revised (Full) | 2927 |
| Revised (Light) | 1999 |

PROCEDURE

Two separate experiments will be conducted: a preliminary experiment testing the lighting in a model of the enclosure and a ground test using the propellant tank enclosure. These two procedures are critical for shaping the final design of the propellant tank enclosure and ensuring that the hardware inside the enclosure functions as expected. Following the completion of both procedures and the implementation of feedback from the two experiments, a final procedure will need to be created for the final test aboard the ISS.

Light Testing Procedure

The goal of the Light Testing procedure is to find a position for the Raspberry Pi's and the LED lights within the enclosure that will produce an image that is both in focus and mostly devoid of shadow interference. A white cardboard box with a similar shape to the enclosure will be used as a model of the enclosure during the procedure. The propellant tank will be modeled by a clear water bottle. While the exact shape and size of the propellant tank may not be finalized when the procedure is conducted, these factors will not have a significant effect on the distance of the camera from the tank nor the generation of shadows within the enclosure. The type of liquid may have a greater effect on the generation of shadows, but the actual propellant tank inside the enclosure will use water as well. Thus a clear water bottle will serve as an effective model of the propellant tank during the procedure. The Raspberry Pi and LED light strips used in the procedure will be the same used in the enclosure.

The procedure is broken into three tasks: setup of equipment, camera focus testing, and camera lighting testing. During setup, the water bottled will be dyed a dark purple color. The amount of blue and red dye drops required to achieve the desired color will be recorded. This ratio of red to blue drops as well as the amount is useful as the propellant tank fluid will also be dyed to a dark purple color with the same dye. The LED light strips and Raspberry Pi will be placed in the box in an initial position based on the initial design in Figure 1. The Raspberry Pi will be connected to a monitor, keyboard, and mouse so it can be directly controlled. During camera focus testing, different distances between the Raspberry Pi and the water bottle will be tested until the image produced is clear. The ratio between this distance and the length of the water bottle will be useful to produce a focused image in the final design of the enclosure. During camera lighting testing, the orientation of the LED light strips in the cardboard box will be adjusted until minimal shadows are produced. This will help determine the orientation of the LED lights in the final design of the enclosure.

Propellant Tank Enclosure Ground Test

The ground test for the Propellant Tank Enclosure will ensure that all of the hardware within the enclosure is accurate and correctly functioning. The procedure will use the constructed final design of the enclosure based on feedback from the light testing procedure and dimension requirements. A ground CFD analysis will be used to validate data gathered from the enclosure. A large amount of testing and data for ground CFD models allow them to be used as a standard to compare the enclosure data against. The equipment used to simulate forces on the enclosure has yet to be finalized. To simulate maneuvers on the enclosure, the tank enclosure will be attached to either a vibration table or a hanging support mechanism. The ground test will compare the change in several variables including duration, magnitude, and direction of the force.

CONCLUSIONS

During the course of the internship, a design for the propellant tank enclosure was created while a cost analysis was performed in order to reduce costs to under \$3000 while capable of fulfilling design objectives. Procedures were also created in order to test different features of the enclosure in preparation for the final design and to ensure all equipment functioned correctly.

Some of the hardware needed for the Light Testing procedure did not arrive by the end of the internship. The final dimensions of the propellant tank also were not able to be ascertained by the internship's conclusion. As a result, neither procedures could be completed, nor was the final design created, nor the enclosure constructed. However, the remainder of the hardware needed for both procedures will arrive after the conclusion of the internship. The details of the two procedures are mostly documented. This will allow work to be easily continued in the future.

When work resumes on the project, all materials needed for the Light Testing procedure should be available. It is recommended that light testing should immediately commence, and feedback from the procedure used to create a final design of the enclosure. At that time, the dimensions and shape of the propellant tank should be finalized. Barring significant revisions to the enclosure design, all materials to construct the enclosure should already be acquired. Thus it is recommended for the enclosure to be built according to specifications of the final design. Following the creation of the physical enclosure, the Ground Test should then be conducted to verify all equipment is functioning and accurate.

Following completion of the Ground Test, work can begin on a final procedure for testing aboard the ISS. Details for transportation of the enclosure to the ISS as well as connecting the electrical systems of the enclosure to the ISS's computer will need to be finalized. This work will ultimately result in the enclosure being sent to the ISS for final testing to generate force and image data from sloshing. With the data acquired aboard the ISS, a CFD analysis can be conducted and compared to experimental data to ascertain their validity. This work may require additional research into modifying CFD modeling if experimental results differ from computational models significantly.

ACKNOWLEDGEMENTS

The NASA West Virginia Space Grant Consortium (WVSGC) deserves special thanks for their financial contribution to this internship. Without the aid from the grant provided by the Consortium, the internship and all work conducted during this time would not have been possible. Special thanks are also given to David J. Benson for acting as a mentor throughout the internship and providing significant aid in every phase of the propellant tank slosh project. Finally, special thanks are given to Joseph T. Miller for acting as a mentor and providing aid to the project during David Benson's temporary absence during the internship.

REFERENCES

1. Moiseyev, N.N. & V.V. Rumyantsev. "Dynamic Stability of Bodies Containing Fluid." Springer-Verlag, 1968.
2. White, Harvey E. (1948). Modern College Physics. van Nostrand. ISBN 0-442-29401-8.
3. Kosko, Steven A., and John C. Froehlich. "Copy of Cost Analysis" 2015. Microsoft Excel file.

POLYMER BLENDING POLYLACTADE WITH DIFFERENT POLYMERS

Dustin Kimble
West Virginia Wesleyan College
Petroleum and Natural Gas Geophysics
West Virginia Wesleyan College
Buckhannon, WV

ABSTRACT

A ramulaser was used to take Raman spectra of blends that consisted of PLA and PBT polyester and a blend that consisted of PLA and natural acetal. The spectra received revealed the crystallinity percentage found in each sample which was used to estimate the new melting point of the blend. The spectra of the blends produced anti-Stokes shifts which were the exact opposite when compared to the spectra of the three polyesters individually. The spectra of the blends all had the same number of anti-peaks that occurred at the same wavenumbers.

INTRODUCTION

The goals of this project were to increase the thermal stability and reduce the brittleness of the polymer polylactic acid. The PLA was blended with PBT (polybutylene terephthalate) polyester and natural acetal in order to achieve the proposed goals. The PLA was blended with the PBT polyester and the natural acetal in a lubricated Pyrex container using a hot plate and a stirring rod. A ramulaser was used to measure the crystallinity of the three polymers used to make the blends. The laser was also used to measure the crystallinity of the new samples. No computations were made besides determining the masses needed for each material in order to have multiple ratios to test. The ramulaser produced Raman spectra that displayed frequency shifts which have a direct correlation to the crystallinity of the materials. The PLA was blended with the PBT polyester and the natural acetal in a lubricated Pyrex container using a hot plate and a stirring rod. Both of the materials used to blend alongside the polylactade would, hypothetically, increase its thermal stability and reduce its brittleness. The samples were heated until in a molten state and then stirred together to create a more homogenous mixture. The hot plate was then slowly turned down to lower settings, allowing ample time for the mixture to also cool to the same temperature in order to promote crystal growth within the new blends. Many precautions had to be taken before working with the materials. The blends were made in a fume hood to prevent the inhalation of toxic fumes that may have been produced during the process. Gloves that resist heat were also used in order to prevent burns to the hands when mixing the polymers together.

BACKGROUND

Raman Spectroscopy

Raman spectroscopy is a common method in chemistry to identify chemical bonds in compounds in order to provide a fingerprint by which molecules can be identified. To map these molecular fingerprints a person observes vibrational, rotational, and other low-frequency modes in a system. Raman spectroscopy relies on the inelastic scattering, or Raman scattering, of light typically from

a laser in the visible, near infrared, or near ultraviolet range. The spectrometer used for the analysis part of this research was a Ramanprobe equipped with a ramulaser that emits a laser light at 785 nanometers manufactured by StellarNet, Incorporated. This laser uses a red laser and can be swapped with a green laser to show different data sets. The laser source is equipped with a dial in order to increase the intensity of the laser in order to penetrate the multiple materials clear down to the molecular level. The laser is transmitted through a fiber optic cable, and the returning photons are displayed as a spectrum within the software provided by the company that manufactured the spectrometer. This setup is referred to as tip-enhanced Raman Spectroscopy (TERS) which is preferred for bioanalysis of materials. The system works by using a laser light that interacts with molecular vibrations of the material that results in the photons from the laser being shifted up or down. After the laser light hits the material, photons are given off as inelastic light scattering, the sensor measures the energy state of the returning photons and determines whether the photons are of higher or lower energy than when they were emitted. If a photon comes back with a higher energy, shown as anti-peaks in the spectra, it is known as an anti-Stokes shift and results in a shift to a lower frequency. If a photon comes back with a lower energy, shown as peaks in the spectra, it is known as a Stokes shift and results in a shift to a higher frequency. The change in energy states leads to a shift in frequency away from the excitation wavelength, the Rayleigh line. Raman shift is another name given to Stokes and anti-Stokes shifts. A Raman shift is commonly documented in wavenumbers with units in inverse centimeters [cm^{-1}]. The software used to display the spectra automatically converts wavelengths into wavenumbers (Gardiner, Graves, Bowley 1989).

Polylactic Acid

Polylactic acid is frequently utilized as the material of choice for most 3D printers. The polylactade used during research was acquired from the departments own Dremel 3D printer. It is used for 3D printers because it is a thermoplastic. It is also an aliphatic polyester derived from mostly corn starch. Aliphatic means organic compounds consisting of carbon atoms linked in straight, open chains instead of containing a benzene ring. It has a chiral nature which is a presence of an asymmetric carbon atoms that causes several forms of polylactide. Poly-L-lactide (PLLA) and poly-D-lactide (PDLA) are the most commonly formed due to the chiral nature. The other forms are products resulting in the polymerization of different lactides. Once cooled, polylactide is relatively stiff and strong and, as such, does not bend well, but, instead, tends to break. For polylactade to be usable, it has to have a high molecular weight. Polylactic acid is made from lactic acid which can be catalyzed by various metals. The reaction creates mirror-image molecules allowing the PLA to reduce its stereoregularity compared to the starting material, corn starch. Another method of obtaining polylactade is through the direct condensation of lactic acid monomers. This process is carried out at a temperature less than 200 °C so that lactide monomers are not created. The reaction also produces one equivalent of water and the water produced can dramatically reduce the molecular weight of the material. PLA has a crystallinity of around 37%, a glass transition temperature of 60-65 °C, and a melting temperature between 95-100 °C. Glass transition temperature is the temperature at which materials transform from a hard, brittle state into a molten or rubber-like state. Due to its low maximum continuous use temperature, certain additives can be added to PLA to increase its heat-resistance resulting in the material withstanding a temperature of 110 °C before becoming deformed. PLA is soluble in chlorinated solvents, hot benzene, tetrahydrofuran, and dioxane. From other research, increasing the crystallinity of PLA also increases the amount of time it takes the material to degrade. (Södergård, Stolt 2002)

Polybutylene Terephthalate Polyester

The first polymer used to combine with the PLA during the research period was PBT polyester (polybutylene terephthalate). PBT polyester is a thermoplastic as well and is commonly used as an insulator in the electrical and electronics industries. It is used as an insulator is the reason it was chosen to be combined with the PLA. PBT polyester is a semi-crystalline polymer with a melting point of 223 °C. PBT is closely related polyethylene terephthalate (PET) except PBT has a slightly lower rigidity, better impact resistance, and a lower glass transition temperature. PBT polyester can be reinforced with glass fiber to increase heat resistance, and it can also be treated with flame retardants in order to make it noncombustible. PBT polyester is resistant to solvents such as chlorine and, as a result, would not be able to degrade as well as the polylactic acid. PBT is also more crystalline than PLA which would also increase the thermal stability of the new polymer. The crystallinity of the PBT polyester is estimated using the Raman spectrometer. The spectrum of the material showed a higher amount of energy while the Stokes shifts occurred. The increased levels of energy are found in materials with a higher percentage of crystallinity (The Editors or Encyclopedia Britannica 2015).

Polyoxymethylene (Natural Acetal)

The second polymer that was obtained in order to blend with the polylactic acid was polyoxymethylene. Also known as acetal, it is another oil-based plastic polymer that is commonly used to make ball bearings and small gear wheels used within the moving parts of high performance components. The material is also used in the manufacturing of frames for eyeglasses, ski bindings, fasteners, guns, knife handles, and lock systems. It is used in the automotive and consumer electronics industry. The acetal is more commonly known by the chemical firms that produce the material such as Delrin, Celcon, Rantol, Duracon, Kepital, and Hostaform. The acetal was chosen because of its high strength and hardness which would enhance the PLA's brittleness. The material also has a much higher crystallinity than both the polylactide and the PBT polyester. However, even with the higher crystallinity, the acetal has a lower melting point than the PBT polyester which is closer to the PLA. The acetal's melting point is about 175 °C which allows the acetal and PLA to be melted simultaneously and potentially create a better blend. Again, the effectiveness of the blends relies upon how slowly it can be cooled in order to promote crystal formation. Similar to PLA, acetal can be degraded by acids. Acetal has a high abrasion resistance, a low coefficient of friction, and high heat resistance (Ibeh 2011).

RESULTS

Polylactic Acid and PBT Polyester

In order to combine the PBT polyester and polylactide, a hot plate was used, and the materials were contained within a Pyrex glass container that was lubricated with canola oil for the purpose of reducing the amount of the new polymer that stuck to the surface. To combine polymers, they have to be melted and stirred together to make a blend. The difference in melting temperatures resulted in the polylactic acid melting way before the PBT polyester. The melting and blending of the samples was the easy part. Cooling the materials slow enough after the blend was created was more difficult. Due to a lack of a way to cool the new blend, the material developed into a glass like state that was more amorphous than crystalline. Slower cooling would have resulted in the formation of more crystals and a better material. All samples were taken at a mass percentage

meaning when 10% of the total mass was PLA the other 90% consisted of the PBT polyester. Nine samples were created each at different ratios that added up to a calculated mass. A final mass of the samples was not taken because it was unnecessary to the results of the experiment. When the samples were analyzed using the Raman spectrometer, it was discovered that each sample contained anti-Stokes shifts at the same wavenumbers. The shifts did not, however, go to the same frequency levels when compared. The shifts occurred at the following estimated wavenumbers [cm^{-1}]: 430, 540, 640, 680, 1350, and 1550. There is no discernible pattern of when the anti-Stokes shifts occur in each individual spectrum, only that they occur at the same wavenumbers in all samples. The reoccurring frequency shifts at the same wavenumbers could be a result from the inability to cool the new blend slow enough. There also is no pattern that coincides with the amount of counts received from each sample and the amount of a particular polymer that made up the blend. The samples containing 60% or less of the total mass in PLA, except for the 50-50 blend, do not have a plateau of max counts. In the samples that have these plateaus, they are all at the same number of counts while the samples that round off do so at different counts.

Polylactic Acid and Natural Acetal

The same process used to blend the polylactic acid and the PBT acid was also used to blend the PLA with the acetal. Multiple lubricated Pyrex glass containers held the samples while they blended. The same mass ratios used for the polylactade and PBT polyester were used with natural acetal resulting in nine samples. The same problem of an inefficient way to cool the blend also occurred during this set of samples. As a result, the blend most likely did not have the amount of crystal growth that it needs in order for the blend to maximized its potential. The samples appeared to be more amorphous. The biggest difference between the acetal samples and the PBT polyester samples is that the acetal had a lot fewer counts along the frequency line than the PBT polyester. This observation lines up with the original spectrums of the individual materials. The spectrum of the frequency of the acetal and PLA was much lower than the PBT polyester. The acetal samples had the same pattern as the PBT polyester. The samples all had anti-Stokes shifts at about the same wavenumbers. The anti-Stokes shifts were of the same magnitude as the anti-Stokes shifts observed with the PBT polyester. The frequency shifts occurred, surprisingly, at the same wavenumbers as the PBT polyester samples. In inverse centimeters, the wavenumbers are estimated to be 430, 540, 640, 680, 1350, and 1550. As of now, there is no explanation as to why these frequency shifts occurred at the same wavenumbers besides that the blends did not cool slow enough to allow for the growth of crystals within the structure. For the spectrums containing acetal, a pattern was noticed. The samples comprised of less than 50% of polylactade had much more background interference, which could indicate that the blend was able to form more crystals than those blends that consisted of at least 50% acetal.

RAMAN SPECTRA GRAPHS

(expand as needed; PLA percentage is always on left)

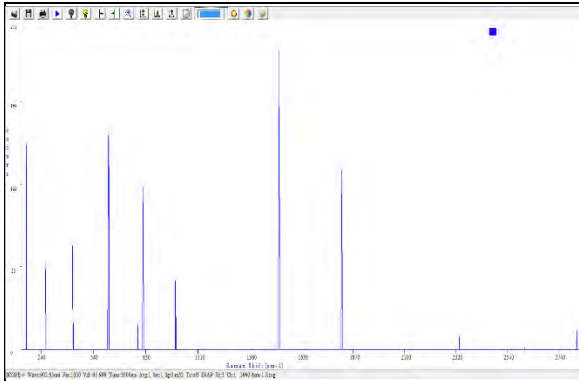


Fig. 1 Displayed are the spectrum of the PLA

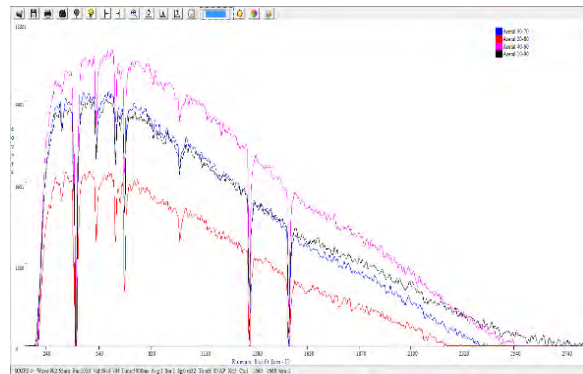


Fig. 2 Compared is the PLA-Acetal spectra with lower amounts of the polyactade

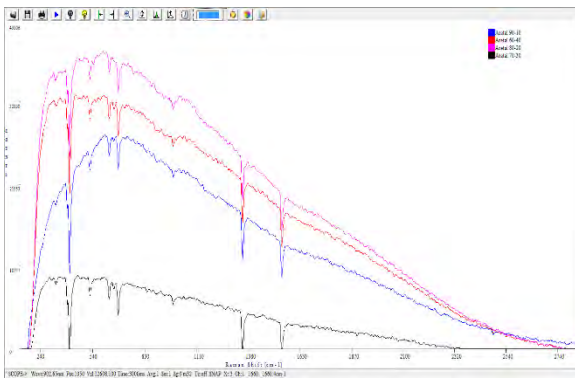


Fig. 3 Compared are the PLA-Acetal spectra with higher amounts of the polyactade

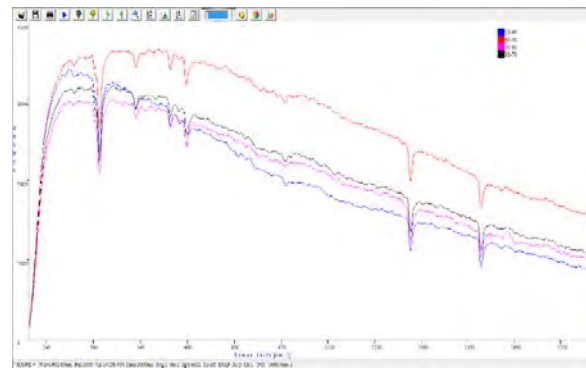


Fig. 4 Compared are four different blends of the PLA-PBT Polyester

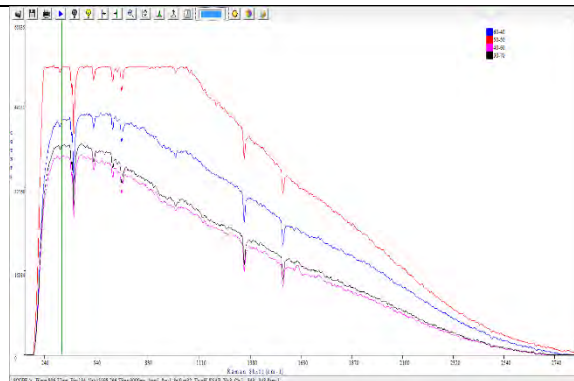


Fig. 5 Displayed are the spectra of another four blends of the PLA-PBT polyester

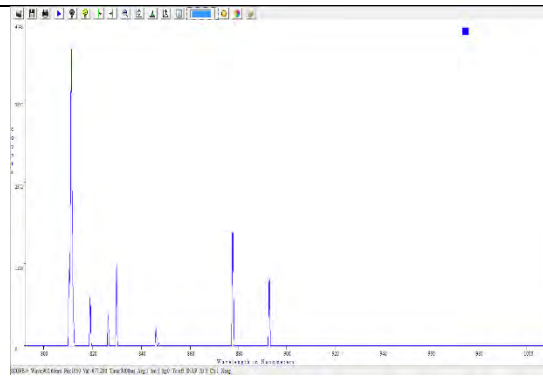


Fig. 6 Displayed is the spectrum of the Nature Acetal

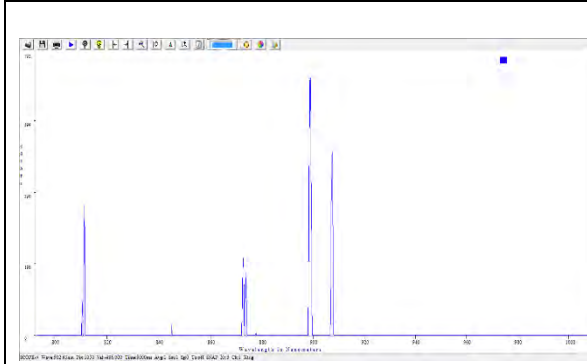


Fig. 7 Displayed is the spectrum of PBT Polyester

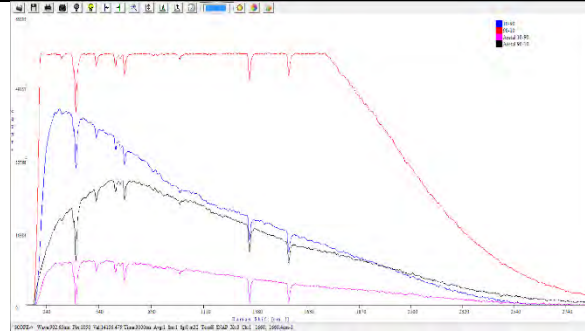


Fig. 8 Above is a comparison of spectra from the extremes of both the PLA-Acetal blend and the PLA-PBT polyester

FUTURE WORK

Future work and experimentation would consist of more in-depth studies of the molecular structures of the materials. To better research the materials an electron microscope is the best option. The electron microscope would allow the material to reveal its smallest structures and present a better representation of whether or not the materials contained any amount of crystal growth. Other things that could help the experiment is finding a way to cool the blends slower so that crystal growth is promoted. To do this, the experimental tool would need to be able to be closed and the heat adjusted manually. The max temperature of the engineering tool would have to be sufficient enough so that all of the material would be able to melt, so the temperature would have to reach 250 °C at the very least. Other tests for the blends would be to determine the melting temperature of the blends, and also to test their usability at higher temperatures for long periods of time. These experiments would go towards the observation of whether or not the maximum continuous use temperature increased which would result in an increase in the thermal stability of the original polylactic acid. The blends would have to be molded into other objects and replace a component that is subject to a high heat for long periods of time such as bearing in engines. Another set of experiments can be conducted in order to test the brittleness of the new blends. To conduct these experiments, the blends would first have to be molded into rods and/or plates. The rods and/or plates would then be bent by hand and by a press to observe if the material withstands that. The materials can also be placed into a machine that pulls on objects to measure their shear stress, and a Young's modulus can then be determined. A much longer experiment, or one that can be measured and estimated, would be the rate at which the materials degrade in nature and also the rate they degrade in a lab with a catalyst. The rate at which the materials degrade would provide whether or not they are still considered biodegradable. Other experiments that can be done to improve the heat stability of the PLA is combining it with other forms of polylactide such as PDLA and PLLA. Combining PLA with these other two would reinforce research that has already been accomplished for these polymer blends.

CONCLUSION

The research resulted in nine samples each of the PLA-PBT polyester blend and the PLA-acetal blend. Both sets of samples appeared to have glassy surfaces after being extracted from their containers. Both sets also displayed anti-Stokes shifts at the same wavenumbers. There were no distinctive patterns in individual data sets. No patterns and the lack of crystallization within the samples is most likely a result of poor cooling techniques for each specimen. To better cool the materials, the containers would need to be enclosed in some sort tool where the temperature is able to be controlled and reduced very slowly over a very long period of time. The slow cooling over ample amount of time would promote the amount of crystal growth in each sample resulting in better readings and possible patterns in the spectrum that corresponds to the amount of polylactic acid within the blend. Another error contributing to the lack of quality in the samples could be the amount of heat and energy loss while the sample was being created. To remedy this problem, the containers would have needed to be capped or enclosed and surrounded by insulators in order to minimize heat loss. Another possible error would be the release of gases from the melted materials. The release of gases could have caused a change in the molecular make-up of the blend resulting in the samples received. To diminish the amount of gas lost in future experiments, the utilization of a closed container that has all of the air vacuumed out of it would work the best. The

vacuum would ensure that no gases were lost to the atmosphere and a tool that analyzed gases could be used to reveal the exact amount of gas released during the blending of the two polymers. The most valuable aspect of the internship was the experience gained in learning how to do experiments and research over a long period of time. The knowledge gained during the research period will come in use when attending graduate school and assist with research during that time.

ACKNOWLEDGEMENTS

This research opportunity was possible through the benevolence of the NASA WV Space Grant Consortium and the grant they awarded me. Also, the advice and aid of West Virginia Wesleyan College's physics department's Dr. Joseph Wiest, Dr. Bert Popson, Dr. Eric Reynolds was greatly appreciated and beneficial.

REFERENCES

- Gardiner, D. J., P. R. Graves, and H. J. Bowley. Practical Raman Spectroscopy. Berlin: Springer-Verlag, 1989. Print.
- Ibeh, Christopher C. Thermoplastic Materials: Properties, Manufacturing Methods, and Applications. Boca Raton, FL: CRC, 2011. Print.
- "Polybutylene Terephthalate (PBT)." Encyclopedia Britannica Online. Encyclopedia Britannica, 1 Sept. 2015. Web. 18 July 2016.
- Södergård, Anders, and Mikael Stolt. "Properties of Lactic Acid Based Polymers and Their Correlation with Composition." Progress in Polymer Science 27.6 (2002): 1123-163. Web. 18 July 2016.

FABRICATION AND CHARACTERIZATION OF NOVEL NANOPOROUS MATERIAL FOR SPACE APPLICATIONS

Scott Lopez
NASA Goddard Space Flight Center
Chemistry
Wheeling Jesuit University
Wheeling, WV

ABSTRACT

Multilayered porous silicon is nanostructured silicon that could act as an optical filter and can enable scientists to better observe objects in outer space emitting in the mid-to-far infrared spectrum. Studying porous silicon using low resistivity wafers is a fairly well-understood field of interest, however, little has been done to examine the nanostructured material on high resistivity wafers. High resistivity porous silicon has a better optical transmission in the far infrared portion of the spectrum and is of interest for the construction of optical components and instruments. The current approach of making high resistivity multilayered porous silicon involves techniques such as bonding and or multilayer deposition. These methods are not ideal because of the differences in the thermal coefficients between the silicon and the added bonded or stacked material. Multilayer bonding can cause further problems since depositing a thick material onto a substrate does not always yield the desired thickness and could delaminate. Constructing a more efficient and repeatable method will begin by characterizing porous silicon to study its porosity, thickness and refractive index. The pivotal aspect of this approach is understanding what variables can be manipulated to yield a product that has the desired optical properties. The variables being surveyed in the experiments are current density and the amount of time etching porous silicon in a chemical bath. After changing these parameters the relationship between them and the porosity, thickness, and refractive index can be further analyzed. Once the relationship is defined, the conditions can be replicated to synthesize a multilayered nanomaterial using one silicon wafer in the same process. When this time efficient technique is clearly defined, it will allow for porous silicon to be made with a single material and thermal coefficient.

INTRODUCTION

The goal of the project was to characterize high resistivity porous silicon for the purpose of making of a product that could be used as an optical filter for transmission in the mid-to-far infrared region of the electromagnetic spectrum. The relationship between how current density and the duration of the experiment affects the thickness of the pores was successfully determined. This data will be used as a guide to other scientists who are exploring high resistivity wafers for the use of optical filters. Knowing which porosity and thickness yield a desired area of the electromagnetic spectrum, one would be able to replicate the experiment via the previous characterization of the material to obtain that optical filter.

The experiments were performed in the Detector Development Laboratory at NASA Goddard space flight center. The equipment used and learned during the internship where: single silicon

etching reactor, A.M.M.T (advanced micromachining tools) wet etching system, A.M.M.T porous silicon micromanaging software, HMDS vapor prime oven, photoresist spin coater, SUSS MA-6 (mask aligner), micro zone developer wet bench, spray developer, nitrogen gun, RIE-nonmetal etcher, profilometer, reflectometer, and scanning electron microscope. The chemicals used during the process was: acetone, isopropanol, S1811 photoresist, developer solution (1:1 by volume mixture of MF312:H₂O), nitrogen, piranha wafer cleaning solution (3:1 volume mixture of H₂SO₄:H₂O), porous silicon etching solution (1:1 by volume mixture of HF: C₂H₆O).

BACKGROUND

The Chemistry behind Porous Silicon

Silicon readily reacts with air to form a passivating native silicon dioxide layer (SiO₂) that does not allow etching to begin. The only silicon bond that is stronger than a silicon oxide bond is a silicon fluoride (SiF) bond. The stronger SiF bond is more spontaneously formed than the weaker SiO bond. Thus the formation of SiF is more favorable, and the reaction readily occurs to make silicon fluoride bonds. Because of the high electronegativity fluorine has with respect to silicon, the bond is more polarized and susceptible to a nucleophilic attack by fluorine molecules. At the end of the chemical reaction, the hydrophilic chemical silicon hexafluoride (SiF₆) is synthesized. The hexafluoride molecule dissociates into the aqueous solution allowing for the less reactive, more hydrophobic silicon hydride (SiH) molecule to form on the top layer of the silicon wafer. A lack of local polarization of the silicon hydride bond makes the silicon less susceptible to a nucleophilic attack. A silicon atom that has a silicon hydride bond can only be exposed to a nucleophilic attack when an electron vacancy called a 'hole' moves to the interface of the silicon and the hydrofluoric acid solution¹. When this situation arises in p-type or an n-type wafer it allows for a nucleophilic attack from fluoride on silicon to occur. SiH can react with HF without the use of holes. However, it is a slow process that decreases the overall thickness of the wafer. To speed up the reaction and make porous silicon, electricity and light were used to allow for the flow of the electrons to occur and the holes to move to the silicon-electrolyte interface. The chemical process continues until silicon hexafluoride is produced, leaves, and is replaced by silicon hydride once again. The process continues as long as the correct amount of light and current are available.

Types of Wafers

A wafer can have foreign atoms in its lattice structure, known as impurities, which increases the amount of electrons or holes in its structure and enables porous silicon etching. The addition of foreign atoms into the silicon wafers is called doping. If a phosphorous atom is implanted into the wafer during production, then a phosphorous atom takes the place of a silicon atom in the lattice structure of the wafer. This type of wafer is considered an "n-type" wafer because of an increase in negatively charged carriers caused by the extra valance electron of phosphorous. This extra electron will go to the conduction band and allow for the proper energy level to be met so that movement of electrons and holes can occur and etching can begin. The second type of wafer is a "p-type" wafer because it is doped with boron. A boron atom lacks an electron with respect to a silicon atom and thus creates a positively charged hole. The hole then contributes to the valance band, and the result is the movement of holes and electrons in the lattice structure of the silicon¹.

Wafer Orientation

The lattice structure of silicon can be arranged in either the $\langle 100 \rangle$ or the $\langle 111 \rangle$ direction. For the purpose of the experiments conducted the type of wafers used was oriented in the $\langle 100 \rangle$ direction. Electrochemical etching occurs on the (100) face of the wafer. This means that the direction of the chemical reaction is vertical with respect to the polished face of the wafer. Silicon can also be etched and not produce pores in a process called electropolishing which can occur if the current is too low, high, or if the concentration of HF is too low¹. When this occurs, no pores are formed but rather an overall thinning of the thickness of the silicon wafer. During pore formation, both the $\langle 111 \rangle$ direction (the side of the channel) and the $\langle 100 \rangle$ direction (the bottom of the channel) is exposed. The $\langle 100 \rangle$ direction is the direction of the electrochemical reaction that causes pores to get deeper and etch further. Because this is the path of least resistance for the holes to migrate to the wafer-electrolyte interface, etching can continue. Another reason that the $\langle 100 \rangle$ face is etched is that the hydrogens are angled in such a way that allows for a better nucleophilic attack. The sides of the channels, or the $\langle 111 \rangle$ direction, has hydrogen bonds that are perpendicular to the silicon thus hindering the electrolyte to perform a nucleophilic attack¹.

PROCEDURE

Both of the n-type and p-type wafers used were oriented in the $\langle 100 \rangle$ direction. The methodology throughout the project was changed until a technique was found that optimized high resistivity silicon etching. The method found was to combine an A.M.M.T wet etching system with a light source. After a single layer of the nanomaterial was made it was characterized and analyzed using a scanning electron microscope (SEM). The process used has been modified from previous work to save time and increase efficiency. Specifically, the final process was to: dip the wafer in hydrofluoric acid, HMDS vapor prime the wafers, spin 1811 photoresist, soft bake the wafer on a hot plate, expose the wafer to UV, hand develop the wafer in a developer solution, hard-baked, then etched in hydrofluoric acid in the A.M.M.T.

MATERIALS AND METHODOLOGY

The journey of the making of porous silicon from high resistivity wafers was a process that has not been vastly explored prior to this internship. The behavior of high resistivity porous silicon in this context was not known thus making the experimental setup to begin etching a challenge in itself. The starting point of etching high resistivity wafers was to use low resistivity wafer etching techniques.

The first method was to etch using the single silicon etching reactor. This reactor was used because of its capabilities to save material by etching small fragments of the total wafer. Instead of using an entire wafer for each experiment, many experiments could be performed on one wafer. The complication of this process was that etching did not occur because there was no current being put through the system. Without current, the initial electrochemical step was unable to occur, and the first step of etching could not begin. Various power sources with multiple output capabilities were investigated, however, no amount of current was able to run through the sample.

The second method explored involved using an A.M.M.T (advanced micromachining tools) wet etching system. The same problem with current was occurring at first, however, this system allowed for a lamp to be attached to its exterior. The lamp was shined through a built-in window as seen in figure one. The chemical reaction could take place because the light source allowed for photoexcitation of electrons. The excited electrons were able to move to the anode, and the holes were then able to reach the surface of the wafer and interact with hydrofluoric acid to allow etching to begin. Manipulation of the experiments could not be obtained since a full wafer did not allow for a wide range of currents to be passed through.

Geometry and Surface Area

Different geometries of the surface area were tested in order to see if a specific geometric pattern, shape, or size could allow for more current to pass through the wafer. The more current to be passed through the wafer at a given point could allow for a greater range of etching parameters to be tested. A combination of surface areas and geometries was tested and included rectangles, circles and squares. The conclusion was that a 1cm^2 surface area was able to optimize the current output when put into the shape of a circle and or square. One of the final 1cm^2 circle geometry is seen in figure six.

Light Source

After the correct geometry and surface area was determined, more current still needed to be pushed through the wafer. The solution was changing from a 100 watt light source to a 500 watt light source. This change substantially increased the output current going into the wafer. At this point in the project, we were able to now test the upper and lower limits of the experiment and a better understand the behavior of high resistivity porous silicon.

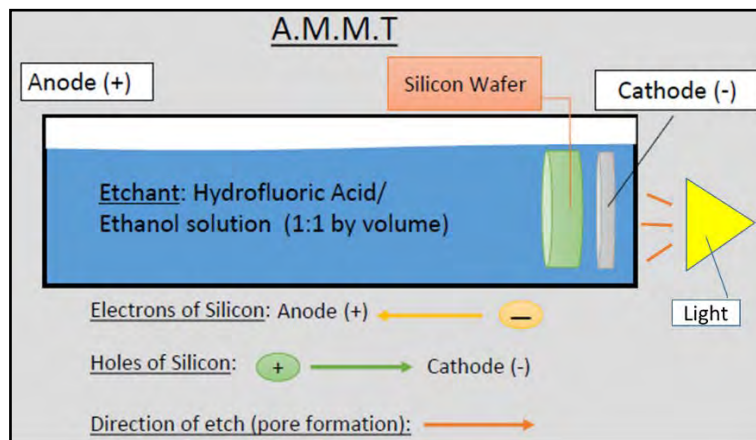


Figure One

Figure one (above) is a diagram of the A.M.M.T wet etching system used to etch porous silicon. The direction of the holes, electrons, and etch is illustrated above. This diagram is the final setup of the etching system and includes the addition of the light to the original A.M.M.T system.

RESULTS

Various experiments were run with both p-type and n-type wafers. Each type of wafer exhibited a different thickness behavior. The porosity has yet to be analyzed via optical microscope and SEM. The relationship between the amount of time etched and the current density compared to the thickness of the pores is seen in figures two, three, four, and five. As seen in figures two and three the pore thickness of the n-type wafer increases in response to a larger etch time and current density. The behavior of the p-type wafers is seen in figures four and five. The p-type wafer differs from the n-type wafer in that its thickness only increases as the total etching time increases. The current density is observed to have no effect on the thickness of the pores.

Two single and two multilayered samples were observed in the SEM. The single layer was observed at low and high current densities as is seen in figures seven and eight respectively. For the multilayered experiments, the two primary relationships observed were how the material behaved when exposed to different current densities and at various times. Figure nine shows a multilayered material that has first been exposed to a low current density then exposed to a high current density. Figure ten demonstrates the effect of exposing a high current density first followed by a low current density.

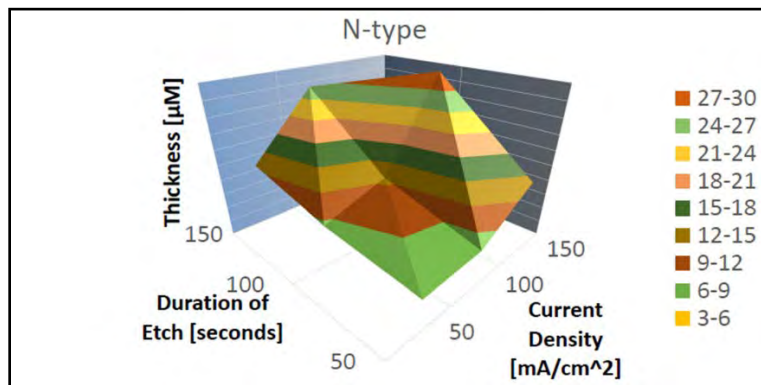


Figure Two

Figure two (above) is a three-dimensional graph demonstrating the etching behavior of a phosphorous doped, n-type wafer with <100> orientation. The graph shows the relationship between thickness and the etching time as well as the thickness and current density applied to the wafer.

| N-Type Wafer Data Table | | | |
|-------------------------|---|-------|-------|
| Duration of Etch [s] | Thickness [μM] | | |
| 150 | 12.78 | 26 | N/A |
| 100 | 8.443 | 12.55 | 30 |
| 50 | 6.3 | 7 | 14.14 |
| | 50 | 100 | 150 |
| | Current Density [mA/cm^2] | | |

Figure Three

Figure three (above) is a data table of a phosphorous doped, n-type wafer with $\langle 100 \rangle$ orientation. The data showed here is data that was used in figure two.

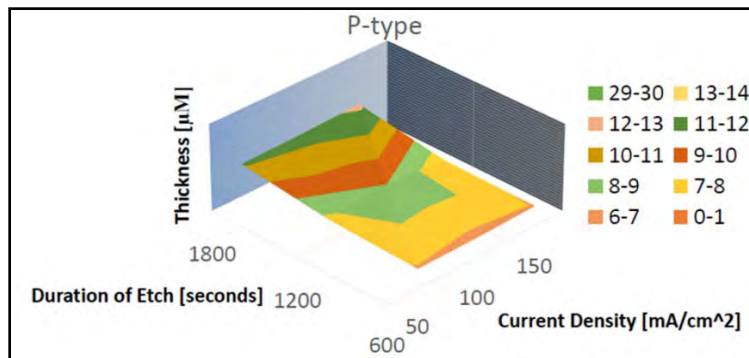


Figure Four

Figure four (above) is a three-dimensional graph demonstrating the etching behavior of a boron-doped, p-type wafer with $\langle 100 \rangle$ orientation. The graph shows the relationship between thickness and the etching time as well as the thickness and current density applied to the wafer.

| P-Type Wafer Data Table | | | |
|-------------------------|---|-------|-------|
| Duration of Etch [s] | Thickness [μM] | | |
| 600 | 11.11 | 11.46 | 12.26 |
| 1200 | 7.8 | 8.96 | 7.23 |
| 1800 | 6.92 | 6.75 | 6.92 |
| | 50 | 100 | 150 |
| | Current Density [mA/cm^2] | | |

Figure Five

Figure five (above) is a data table of a boron-doped, p-type wafer with a $\langle 100 \rangle$ orientation. The data showed here is data that was used in figure two.

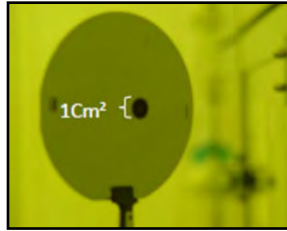


Figure Six

Figure six (above) is a picture of a boron-doped, p-type wafer with $\langle 100 \rangle$ orientation after it has been etched. The picture illustrates a 1 cm^2 circle as one of the final geometric shapes that optimize etching.

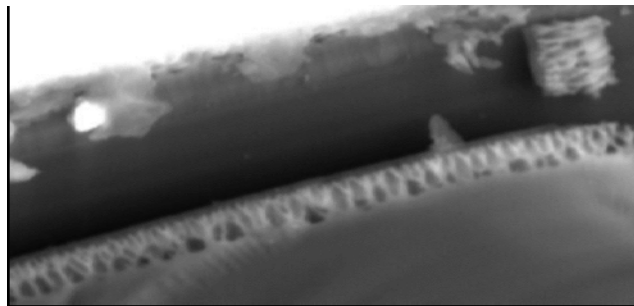


Figure Seven

Figure seven (above) is an image of single-layered porous silicon that was captured via scanning electron microscope. The wafer shown is a $\langle 100 \rangle$ orientated n-type wafer that was etched with a low current density of 50 mA for 100 seconds.



Figure Eight

Figure eight (above) is an image of single-layered porous silicon that was captured via scanning electron microscope. The wafer shown is a $\langle 100 \rangle$ orientated n-type wafer that was etched with a high current density of 150 mA for 150 seconds.

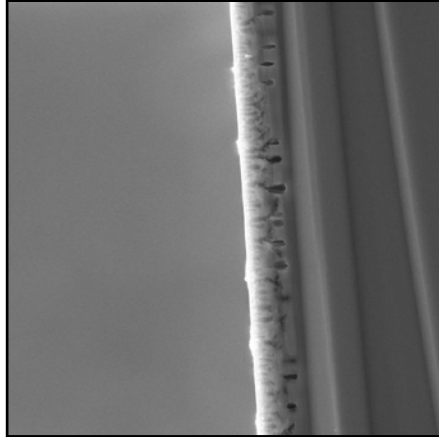


Figure Nine

Figure nine (above) is an image of multilayered porous silicon that was captured via scanning electron microscope. The wafer shown is a $\langle 100 \rangle$ orientated n-type wafer that was etched first with a low current density of 50 mA for 50 seconds then a high current density of 100mA for 100 seconds.

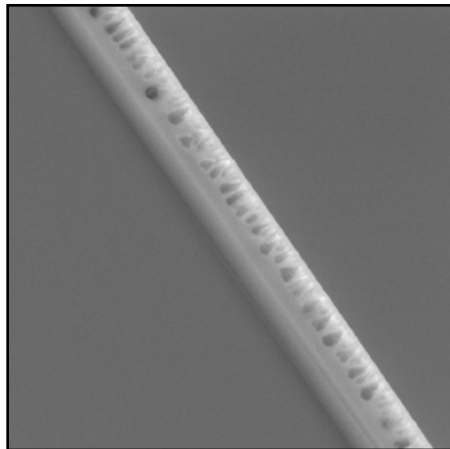


Figure Ten

Figure ten (above) is an image of multilayered porous silicon that captured via scanning electron microscope. The wafer shown is a $\langle 100 \rangle$ orientated n-type wafer that was etched first with a high current density of 100 mA for 25 seconds then a low current density of 50mA for 25 seconds.

DISCUSSION

The basis of the summer project was to see if high resistivity wafers could be characterized well enough to manipulate porous silicon's physical characteristics to transmit light into the mid-to-far IR region of the electromagnetic spectrum. As shown in figures two and three the pore thickness of the n-type wafer increases in response to a larger etch time and current density. Pore

morphologies were studied for low and high current density samples. These samples were seen to have different physical characteristics when examined by a scanning electron microscope.

Single Layer Porous Silicon

A sample with a low current density input shows an interconnecting branch- like network which differs from the high current density sample which shows distinct channels. This pore morphology in the low current sample could be due to the amount of available carriers at a given time at the silicon-electrolyte interface. If the current applied throughout the wafer is low, then the movement of the holes to the surface will be slow. The inconsistent arrival of holes to the interface indicates that the path of least resistance for hole movement is not clearly defined. Since the path of least resistance is not being explicitly followed the hole then ‘rises up’ to the interface with no clear direction. The channels observed in the high current density samples are believed to occur due to the increase in the applied current density. An increase in energy being put through the wafer allows the holes to move more rapidly to the silicon-electrolyte interface. The holes will naturally go to the path of least resistance because of the speed at which they are now traveling in the wafer. This trend can be seen in both low and high current density samples. In the low current density sample, some of the pores are larger at the bottom showing that those specific areas are in the path of least resistance. In the high current density sample, this trend is exploited further by the elongation of the pores in one direction forming a channel.

Multilayer Porous Silicon

Observing the behavior of multilayered porous silicon with different applied current densities yielded varying results. The results were not agreeable with the hypothesis that was formed based upon the behavior of the single layered experiments in figures seven and eight. The hypothesis for the low to high current density seen in figure nine was that the low current would create a shallow branched network and the high current density would make deep channels. As seen in figures seven and nine, when the low current was applied, it made the shallow net like structures. When exposed to high current right after the low current, deep channels formed as expected and passed through underneath the low current layer increasing the depth of the pores. When analyzing the high current density to low current density multilayered material in figure ten, the hypothesis was to invert the results seen in figure nine. The formation of deep channels followed by a shallow branched network underneath the first layer was expected but was not observed. When the wafer was exposed to a high current deep pores formed, however, when exposed to a low current density the shallow branched network formed on the top layer rather than the bottom. When the branched network morphology was applied to the top layer, the depth of the pores did not increase as seen with the other multilayered material. The porosity, or the number of pores in a given area, was increased because the shallow branched network added to the porosity that was previously made from the deep channels.

CONCLUSION

Outcomes and Future Work

Characterization of high resistivity porous silicon was accomplished. The characteristics of the nanostructure that was characterized were the thickness and morphology of the pores for both single and multilayered porous silicon. Single and multilayered high resistivity porous silicon was

successfully made in the A.M.M.T. The morphology and thickness of the nanostructures were done via a scanning electron microscope. For n-type wafers, the thickness was increased and was dependent upon the amount of applied current density to the sample and the duration of which the sample was etched in the chemical bath. Different behavior was seen in the p-type wafers. The thickness was only influenced by the applied current density and not the duration of the etch. This fascinating phenomenon of why the current density was observed to effect the thickness of the pores in only n-type wafers but not p-type wafers is still being investigated.

In the future, the single and multilayered porous silicon's optical properties will be measured via the Filmetrics reflectometer. Work is still being done with the company in order to get the software program properly calibrated to measure nanomaterials refractive index. This system will be able to calculate the materials porosity, thickness, refractive index, and transmittance. Once single layer porous silicon has been fully characterized with the reflectometer, the multilayered samples will be further examined. The test will show if there is an optical relationship between the single and multilayered porous silicon. If a correlation between the two can be exploited then manipulating the order and type of layer can thus yield the desired region of the electromagnetic spectrum. Studying the relationship of porosity and thickness to refractive index and transmittance is critical for the project. This relationship will allow for manipulation of the porous silicon in order to yield an optical component that can transmit regions in the near-to-far IR portion of the electromagnetic spectrum.

Reflection

The most valuable experiences of the program were being exposed to a level 100 clean room, studying new processes and applications of chemistry, having to critically think about experimentation/experiment set-up, and gaining new analysis techniques. Each day an outline was agreed upon in order to conduct experiments and understand why each experiment was taking place. The theoretical outcome of each new experimental setup was discussed as well as what chemical mechanisms were occurring by changing each parameter. The daily analyzation of the experiments allowed me to conduct research more independently and grow as an aspiring scientist. The financial support of the West Virginia Space Grant Consortium allowed for this amazing opportunity to happen. After this unique internship experience, I am able to more efficiently analyze real world problems in a variety of analytical, chemical, and engineering techniques.

ACKNOWLEDGMENTS

I would like to acknowledge the West Virginia Space Grant Consortium for funding my NASA internship at Goddard Space Flight Center. Also, a thanks to my mentor Larry Hess for allowing me to work on this project. My gratitude to co-worker Eliad Peretz for his contribution to the project as well as to the facility of code 500 for a memorable experience.

REFERENCES

¹Wiley-VCH - Sailor, M. J. - Porous Silicon in Practice, chapter one

THE IMPACT OF CLIMATE CHANGE ON WORLD HURRICANE ENERGY

Nadia Mardmomen
NASA Goddard Institute of Space Science
Biology
West Virginia University
Morgantown, WV

ABSTRACT

Tropical cyclones are among the most devastating natural disasters and are responsible for countless lives lost and millions of dollars in property damage. Because tropical cyclones acquire their energy from warm tropical water, cyclone energy is predicted to increase as ocean temperatures rise, as a result of recent climate change. Data was collected and analyzed by the National Oceanographic and Atmospheric Association (NOAA) Tropical Cyclone/National Hurricane Center Advisories. The data consists of hurricane position, wind velocity, air pressure, and status of the storm. Using the velocity of the wind for each hurricane, the total kinetic energy per unit of water vapor was calculated and analyzed since 1995 for every ocean. Most oceans have a strong correlation with ENSO, and this signal was removed in order to isolate the impact of climate change. The data was analyzed for trends at several time scales using statistical methods. No appreciable increase in the total cyclone kinetic energy was observed over the investigated time period.

INTRODUCTION

Recent spotlight on climate change has brought forth an urgent need study weather patterns because of the threat of natural disasters. Hurricanes, in particular, have become a forefront subject in the wake of the devastation left by Hurricane Katrina in 2005 and, more recently, Hurricane Sandy in 2012.

Hurricanes, also known as tropical cyclones, are storm systems that form in areas of warm water through means of convection (Weather Channel, 2015). Trade winds cause warm air and moisture at the ocean's surface to rise, leaving an area of low air pressure at sea level. Warmer air from surrounding areas flow down toward low sea surface pressure area and is heated by the warm ocean water. The heat causes this air to rise, which then creates another area of low pressure at the water's surface. As warm air rises from sea level, water evaporates and condenses to form dense storm clouds. This explanation can be visually seen in figure 1 below. Additionally, the intense winds cause the water beneath the storm to rise; creating a surge that can produce waves up to 33 ft (National Geographic Society, 2011).

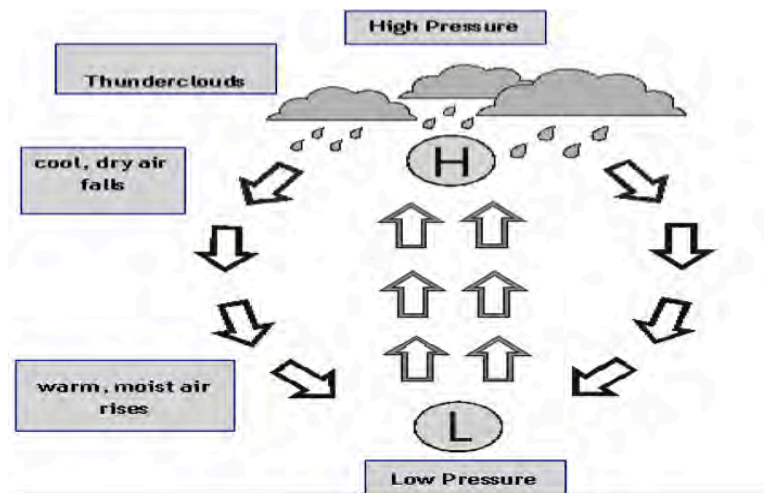


Figure 1. Formation of a hurricane.

The effects of a hurricane vary depending on the intensity and geography of the storm at landfall. However, the most common byproducts include heavy rainfall reaching up to 20 inches and wind gusts ranging from a minimum of 74 mph (Category 1) to over 155 mph (Category 5) (National Hurricane Center, 2012). These winds can have a severe impact on geography through flash floods, deep sediment erosion, and destruction of beaches.

Tropical cyclones are so heavily feared due to their disastrous nature, which creates a major concern as the globe warms from human impact. As the globe is warming, it is inferable that the ocean water is warming as well, causing it to readily evaporate and turn into dense rain clouds. Research has shown that the world has already increased by one and a half degrees Fahrenheit since preindustrial times (Sobel, 2015). Climate change and warmer ocean waters also impact the progression of hurricanes by increasing the rate of formation. The increase in sea surface temperature expedites the evaporation process, which accelerates storm cloud formation and strengthens the force of a hurricane (Emmanuel, 1987). Since climate change and warmer oceans are on the rise, it is plausible that warmer sea surface temperatures could cause hurricane activity to increase. Seeing this as a concern, specifically to the North Atlantic Ocean, an analysis of the total kinetic energy produced in each ocean (Atlantic, Pacific, and Indian) was performed to observe any patterns or changes in hurricane energy.

Additionally, ENSO data was observed in conjunction with kinetic energy to further understand the effects of climate change on hurricane activity. ENSO is a phenomenon in which sea surface temperatures in the Pacific Ocean are warmer than average, causing warmer water to accumulate in the East Pacific region and leaving dry, cool water in West Pacific (W. Pierce, 1997). However, the effects of ENSO are not only limited to the Pacific Ocean, as storm progression and regression are altered across all oceans. This difference results from the Coriolis effect, an ongoing occurrence in which the Northern Hemisphere's air currents force the northern hemisphere's water currents to circulate clockwise while the Southern Hemisphere's wind currents force the southern hemisphere's water currents to circulate counter-clockwise (Russell R, 2010). Therefore, an analysis of ENSO signal data was collected in conjunction with the kinetic energies of oceans worldwide.

METHODOLOGY

The total kinetic energy of three major oceans (Atlantic, Pacific, and Indian) was calculated on an annual basis based on a twenty-year time period. The time period observed was from 1996-2016, with six regions serving as areas of interest: the Atlantic, East Pacific, West Pacific, South Pacific, North Indian, and South Indian Ocean. The total kinetic energies were determined using the wind speed, allocated from the Unisys Weather Database, of hurricanes to calculate the storm velocities that occurred within a year. The kinetic energy of each storm was calculated by squaring the velocity and then finding the energy per kilogram of air due to the fact that the wind speeds were collected per kilogram of air. The kinetic energies of each storm were then totaled to determine the total kinetic energy for that specific year for each area of interest.

The energies were also compared with an ENSO signal to look for a relationship, or lack thereof, between the two sets of data. By looking for a relationship, correlation values were calculated between the two sets of data: individual oceans' kinetic energies versus ENSO. The ENSO signal that was used was from the NINO3 index. Before calculating correlation values, both the hurricane kinetic energy data and the NINO3 data set were scaled using the following equation: $(Y_i - Y_{avg})/\sigma$, in which Y_i is the total wind speed by year, Y_{avg} is the average wind speed of all years combined, and σ is the standard deviation. Once the two series were scaled, the relationship between the kinetic energy and the NINO3 data was determined by calculating a correlation value between zero and one with either a positive or negative, negative being an inverse, relationship. The oceans with the strongest correlation were subjected to the elimination of the signal to observe kinetic energy without an effecting factor. The Atlantic Ocean had the greatest correlation with ENSO, so the NINO3 signal was removed from the kinetic energy (the scaled ENSO data * the correlation value - the scaled kinetic energy) to calculate the kinetic energy without any effecting factors. All data was plotted on excel scatter plots.

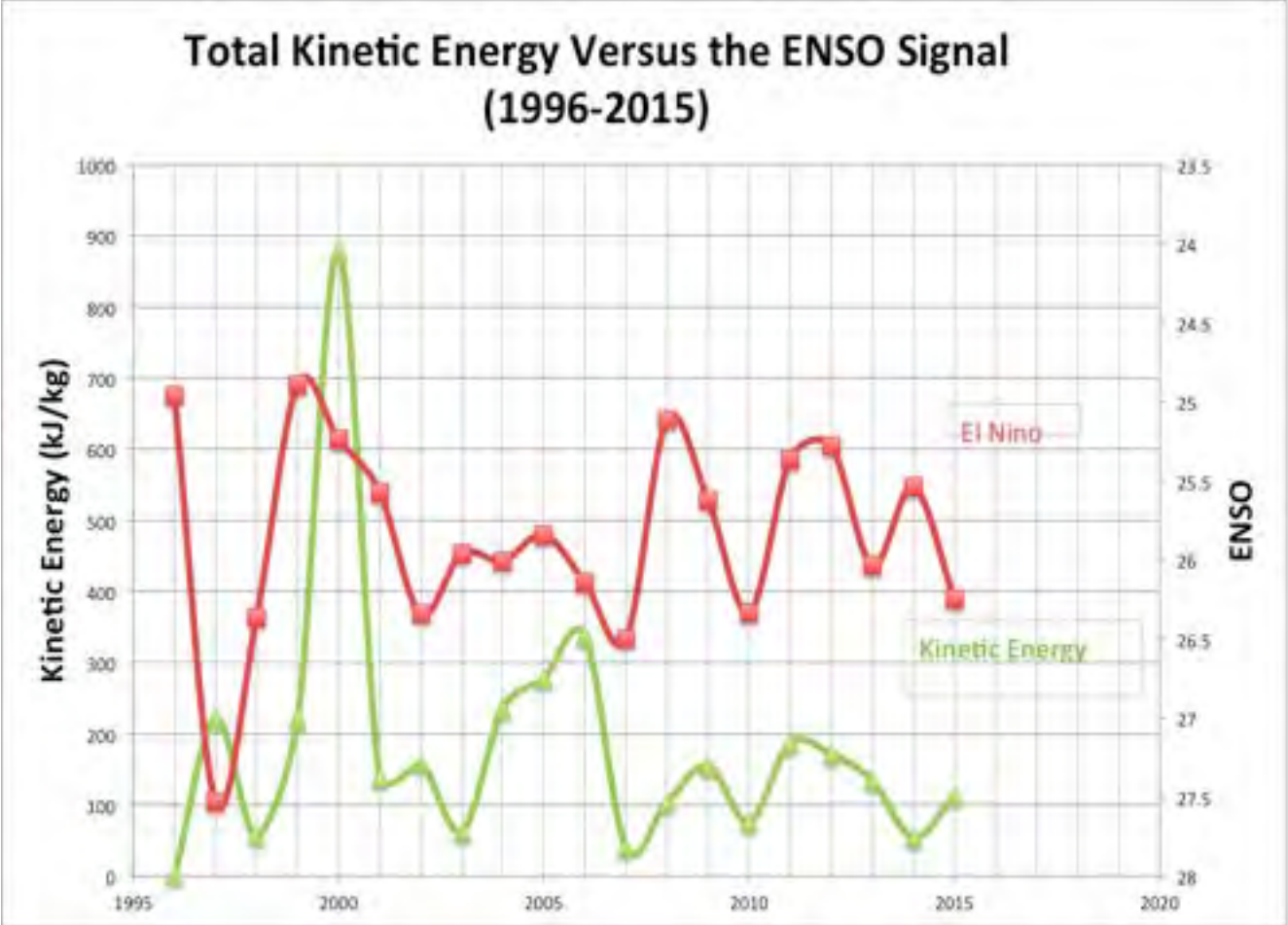
RESULTS

All correlation values between ENSO and each ocean can be seen in Table 1. After calculating the correlation values, it was seen that the effects of ENSO and the Atlantic region had the highest correlation with a negative value of about 47%. This value represented an inverse relationship between ENSO and hurricane activity. To show the inverse relationship, the two data sets were plotted against each other on the Graph 1 below.

| Oceans | Correlation |
|---------------|-------------|
| Atlantic | -0.47 |
| East Pacific | 0.32 |
| West Pacific | 0.02 |
| South Pacific | 0.35 |

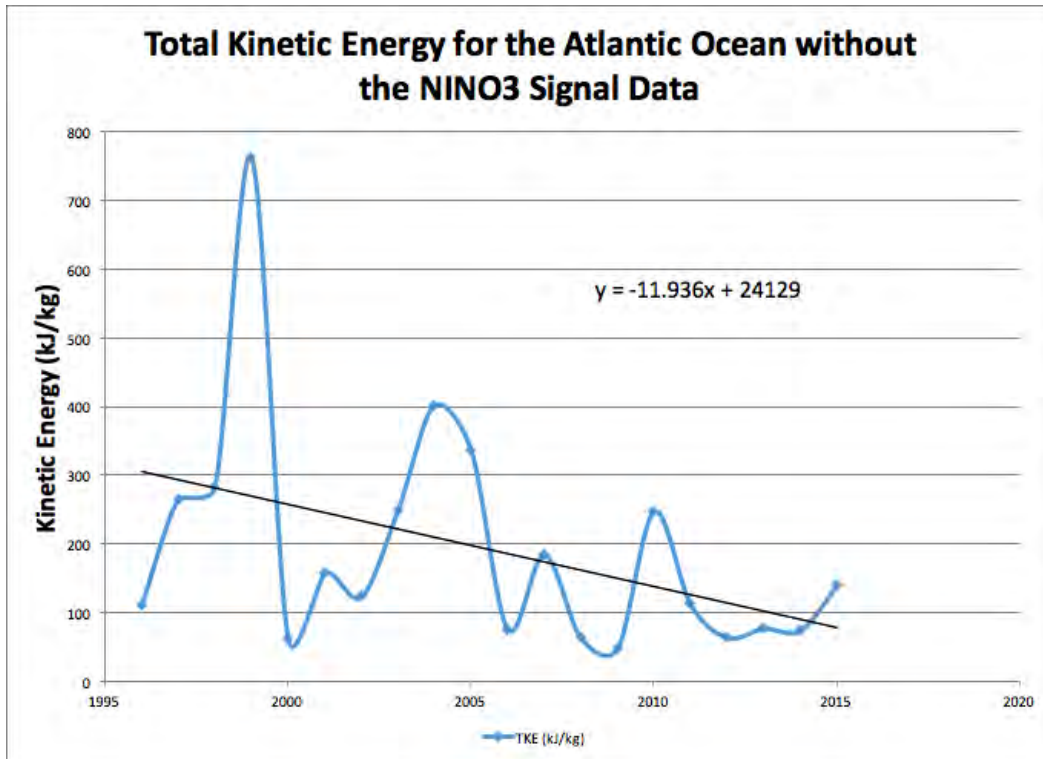
| | |
|--------------|-------|
| South Indian | -0.29 |
| North Indian | 0.07 |

Table 1. Correlation values between oceans' kinetic energies and ENSO signal



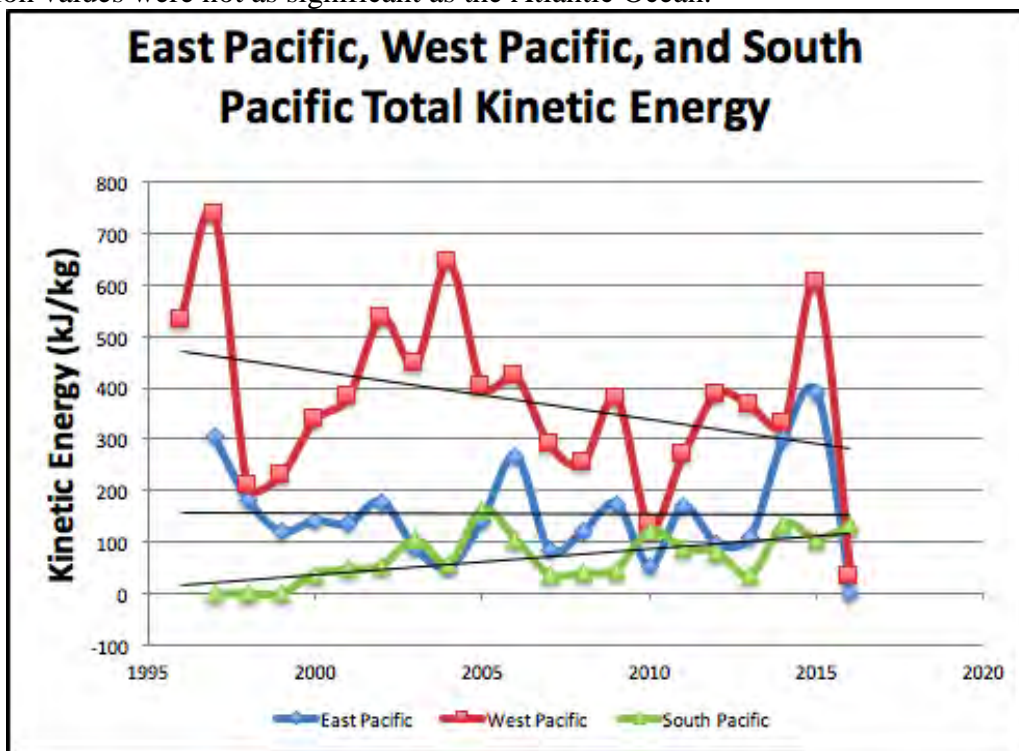
Graph 1. Unscaled kinetic energy of cyclones in the Atlantic Ocean vs. ENSO signal data set. In this image, the ENSO signal was plotted against the KE in order to see their inverse relationship. The y-axis for the ENSO signal was flipped in order to see how they are inversely related. If the y-axis was not flipped, it would be seen that as ENSO increases, KE decreases and vice versa.

Next, when ENSO signal data and the Atlantic Kinetic Energy data set were scaled in order to remove the signal, the data series produced a negatively sloped trendline. This data can be seen in Graph 2 below.

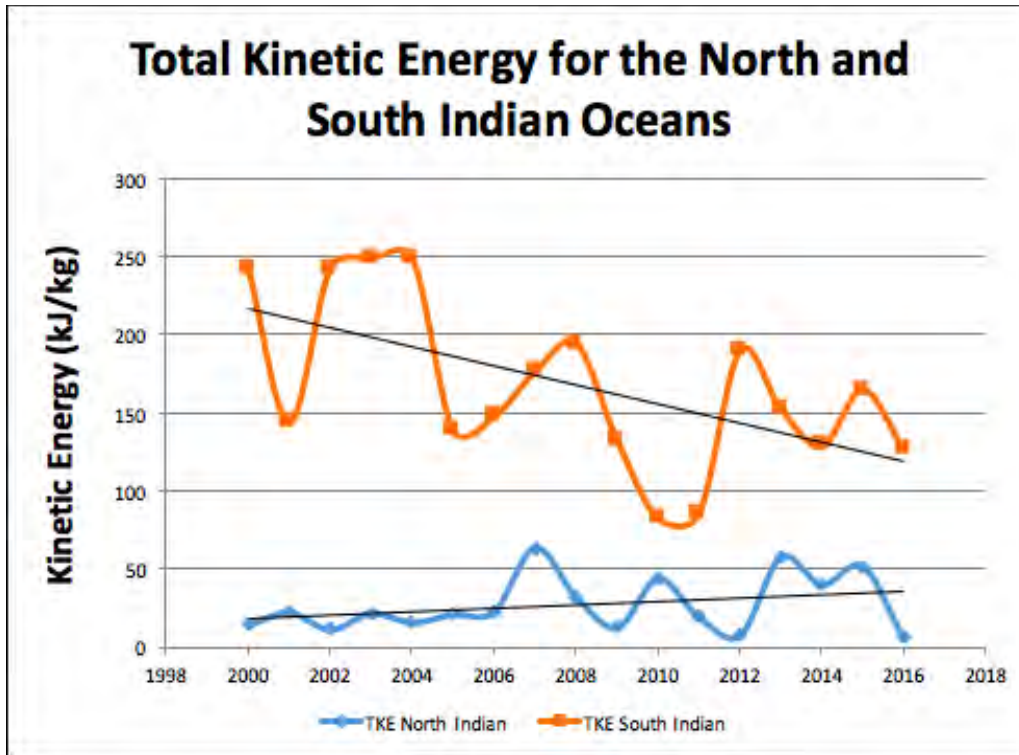


Graph 2. Total kinetic energy of Atlantic cyclones after removing NINO3 signal data.

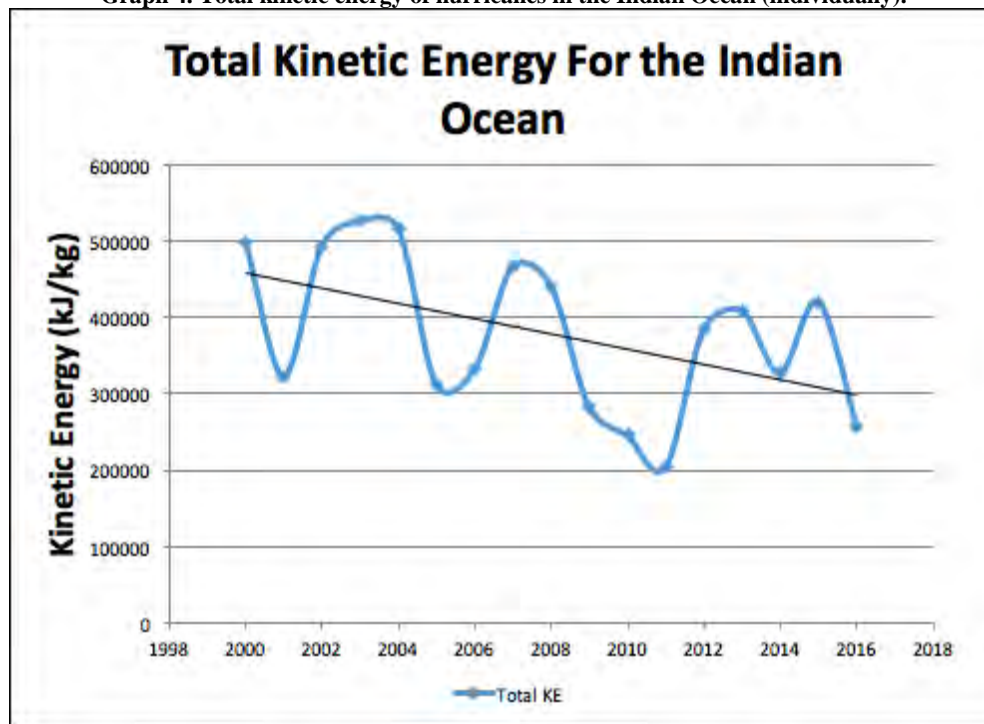
The graphs below represent all of the raw, total kinetic energy calculated using the average velocities. The ENSO signal was not removed from the Pacific or Indian Oceans because their correlation values were not as significant as the Atlantic Ocean.



Graph 3. Total kinetic energy of hurricanes in the Pacific Ocean



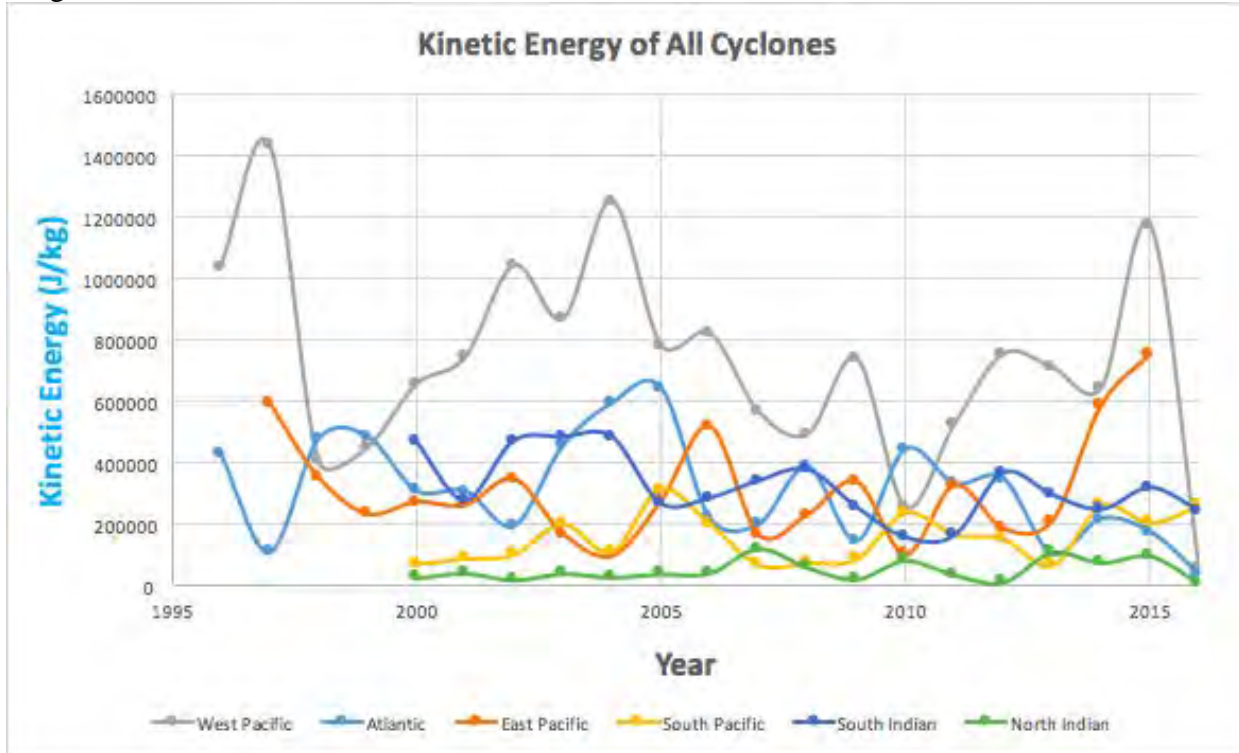
Graph 4. Total kinetic energy of hurricanes in the Indian Ocean (individually).



Graph 5. Total kinetic energy of hurricanes in the Indian Ocean (combined). When the two regions (North and South) are plotted together, they show an overall decreasing slope compared to when they are plotted individually.

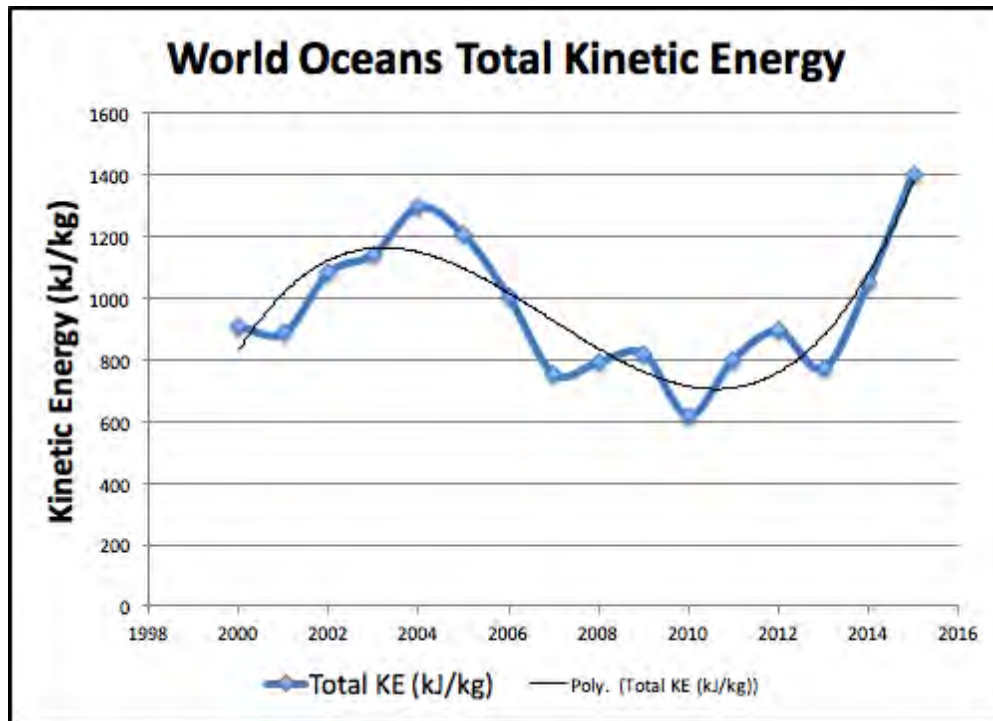
After plotting each individual ocean, all of the oceans were combined together to create a graph of total kinetic energy produced by hurricanes in the world. It was found that the West Pacific oceanic region had the highest average kinetic energy out of the six observed oceanic areas, with almost

double the amount of energy from the three out of the five other regions. This can be seen in the image below.



Graph 6. Total kinetic energies from tropical cyclones in all oceans from 1996-2016.

Aside from plotting each individual ocean on the same graph, each ocean's total kinetic energy was added together to be plotted as a whole. Below is the graph with the world's total kinetic energy as a whole.



Graph 7. Total kinetic energy of hurricanes of all oceans, with a polynomial trendline of order 3 included to show cyclic shape.

CONCLUSION

We calculated the total kinetic energy for each ocean that was analyzed for trends at several time scales using various statistical methods. No appreciable increase in the total cyclone kinetic energy was observed over the investigated time period. This observation served as inconclusive to the initial hypothesis of climate change increasing cyclone activity over time. One inference can be made that cyclone energy operates in a cyclic manner, which would explain the fluctuation in the total kinetic energy for all oceanic regions over the given time period. However, this hypothesis would have to be tested over a larger period of time, expanding forward or back in time to determine whether or not a strong cyclic function exists. Moreover, the strong correlation between the ENSO data and the kinetic energy in the Atlantic shows that there may be other larger factors in the progression of hurricane formation, such as air pressure and seismic activity, which should be considered in the continuation of this research.

FUTURE WORK

Future work for this project will entail collecting more data from a longer time series in order to build upon one possible conclusion that hurricanes may be going through a cycle. This time series in this study is only twenty years, and it not long enough to be able to make any definite conclusions.

ACKNOWLEDGEMENTS

This work was supported by:
NASA West Virginia Space Grant Consortium (WVSGC)
Dr. Paul Marchese, mentor
NASA Goddard Institute for Space Studies (GISS)
National Oceanic and Atmospheric Administration (NOAA)
Queensborough Community College

REFERENCES

- Emanuel, K.A., (1987). The dependence of hurricane intensity on climate. *Nature*, 326, 483 – 485
- .National Geographic Society. (2011, January 21). *Storm surge*. Retrieved August 2, 2016, from <http://nationalgeographic.org/encyclopedia/storm-surge/>
- National Hurricane Center. (2012). *Saffir-Simpson Hurricane Wind Scale*. Retrieved from <http://www.nhc.noaa.gov/aboutsshws.php>
- National Oceanic and Atmospheric Administration. *Hurricane/Tropical Data*. Retrieved from <http://weather.unisys.com/hurricane/index.php>
- National Oceanic and Atmospheric Administration. *NINO3 Timeseries*. Retrieved from http://www.esrl.noaa.gov/psd/gcos_wgsp/Timeseries/Data/nino3.long.data
- Pierce, D. W. (1997, June 25). *What is an El Niño, anyway?* Retrieved August 4, 2016, from <http://meteora.ucsd.edu/~pierce/elnino/whatis.html>

Russell, R., (2010, January 8). Cyclones and Anti-cyclones. *Windows to the Universe: National Earth Science Teachers Association*. Retrieved from <http://www.windows2universe.org/earth/Atmosphere/tornado/spin.html>

Sobel, A. (2016, July 15). *Where Are the Hurricanes?* Retrieved August 03, 2016, from http://www.nytimes.com/2016/07/15/opinion/where-are-the-hurricanes.html?emc=eta1&_r=1

The Weather Channel. (2015, August 6). *How do hurricanes form?* Retrieved from <https://weather.com/tv/shows/amhq/video/how-do-hurricanes-form>

SIMULATION TO FLIGHT-1 OUTREACH

Samantha Melroy
NASA IV&V Facility
Industrial Management Systems Engineering
West Virginia University
Morgantown, WV

ABSTRACT

Simulation-To-Flight 1 is West Virginia's first spacecraft. The spacecraft is merely the size of a loaf of bread but will take pictures of earth, study earth's atmospheric weather, experiment on electronic shielding and develop student interest in STEM (Science Technology Engineering and Mathematics), to name a few. This is part of NASA's CubeSat Launch Initiative where NASA wants all 50 states to launch a CubeSat into space. The NASA IV&V Facility, West Virginia University, and West Virginia Space Grant Consortium have teamed up to embark on the challenge. West Virginia's CubeSat, also known as STF-1, is planned to launch in June 2017. CubeSats are advanced technologies, and with these advancements, it is important for students to learn and get captivated by STEM. Advanced technology can become overwhelming which is why it is important to make science relatable, easy to understand and fun for students. Television shows like "How to Build...Everything" on the Science Channel brings what is an extremely complicated machine and breaks it down into a basic step by step process like that of building a cruise ship or a helicopter. It's made to fit a wide range of ages, backgrounds, and interests. The goal for STF-1 outreach is to get as many people drawn not only to STF-1 but to develop STEM knowledge. The objective of this summer outreach internship is to create an educational product for educators to take back to their classrooms and explore STF-1 with the development of STEM skills in students. The West Virginia Space Grant Consortium is funding the outreach portion of STF-1 to get students involved and excited about science.

INTRODUCTION

As with all NASA projects an outreach objective is required, the fulfillment of Simulation To Flight-1 outreach is described in the following sections. Simulation To Flight-1 (STF-1) summer internship outreach objective was to create products that would get students involved in STF-1 and STEM (Science Technology Engineering and Mathematics), encourage students to learn about science and give students' confidence in their ability to do STEM. The end goal of this internship was to make something that can be reputable by another individual with given materials.

The team's expectations of the internship included the creation of a presentation, a product for middle schoolers and videos/information for the STF-1 website. These products must also be able to be incorporated into classroom activities as well as future outreach endeavors. All of these objectives were met with the following products: 1) LEGO competition, 2) LEGO classroom activity, 3) STF-1 Presentation, 4) hands-on learning activity, 5) STF-1 coloring sheet and 6) STF-1 videos.

The target audience for a product was middle schoolers, ages 11-14 years old. For the middle school ages, the team wanted something relatable for students, and the main contributor to this

product included an EV3. An EV3 is a LEGO power system that is composed of motors, a light sensor, a gyro sensor and multiple building pieces. Other LEGO power systems include the NXT and the WeDo. These LEGO pieces are popular amongst school children with different types of power systems for a range of ages. These technologies are advancing and are part of the number one toy company in the world [1]. These products must be able to be incorporated into something that can be transferred around by the education facility, by a school club or by an outreach educator.

METHODOLOGY

To create a product that satisfies the STF-1 team's requirements multiple iterations were produced to create the final product. The main contributor to this was the LEGO EV3 STF-1. The first iteration was composed of regular LEGO blocks. The LEGOs were colored in blue and yellow to symbolize that this spacecraft was made in West Virginia. In the front of the LEGO CubeSat, a solar panel could be fitted into a slot and secured by LEGOs. There would be one solar panel for each cube and a volt meter to help students understand solar panel angles. Students were to attach LEGO power systems to the axle to make it do various tasks. An image of this first iteration LEGO CubeSat is shown in figure 1.

This LEGO CubeSat variation ended up not having as much opportunity to spread and reach out to students because it was an add-on to the LEGO EV3 and thus the LEGO EV3 CubeSat was created just by the parts in the EV3 box, see figure 2.

The second iteration of the LEGO CubeSat was created just out of EV3 materials. This allows for a future Educators Workshop to be run by the ERC (Educator Resource Center) at NAS IV&V (Independent Verification and Validation). The ERC has LEGO EV3s, WeDos and many other products that educators can rent out after taking an Educators Workshop on the product to bring it back to their classroom. This way people in the ERC can give a workshop to a few educators and they can take that knowledge back to their classroom to give it to 20 plus students per educator.

A small activity was discussed allowing to learn about Earth atmospheres and explain where STF-1 was to be located within Earth's layers. This was to be done with melting colored crayons and putting them in a thick straw for each layer, thus creating a thicker straw. This idea was created into something that will do the same but will require less assistance from the younger crowd. In the coming sections a bracelet/keychain product will be discussed and the impact it has on STF-1 outreach.

BACKGROUND

STF-1 has many objectives; the overall objective of CubeSats involve testing large-scale satellite functions in small scale to reduce the amount of clutter that is being put into orbit. STF-1 is a 3U satellite which means there are three 1U cubes stacked on top each other creating a larger satellite. Each 1U cube is 10x10x11.35cm. This is the standard dimensions for CubeSats. This standard allows for the same payload launching mechanism to deploy any CubeSat satellite into orbit around the Earth.

STF-1 has one primary and three secondary objectives. The primary objective is to demonstrate software only simulations environments. Secondary objective 1 includes GPS (Global Positioning System) and IMU (Inertial Measurement Unit) to advance CubeSat navigation systems which will approximate the performance of a higher quality IMU. The second objective for STF-1 is testing Magnetosphere-Ionosphere Coupling and Space Weather; this is to be done with West Virginia University. It will collect data in earth's atmosphere, specifically at the poles. The final objective includes testing the performance and durability of III-V Nitride-Based Materials' this will include testing electronic shielding from sun's rays. [2]

Figure 2 below is a screenshot of the STF-1 presentation slide describing STF-1 components. It displays the radio, memory, solid-state detector, antenna, camera, GPS, and 9volt battery. The antenna is retractable, similar to how a measuring tape works. In this picture, the antenna is retracted, but when extended it reaches up to 24 inches. This will send the data to earth. Next, we have the camera, the camera is important to take pictures of earth and will be something visual to see rather than a bunch of data. At the bottom of the satellite lays the battery which takes up a lot of space, almost a third of the CubeSat. A radio is used to send information to earth. The Solid-State Detector collects weather information. The 4 GB memory buffer is used to store the data, and once in the area the West Virginia satellites can retrieve the data and empty the memory on the STF-1. Finally the GPS, this will help improve CubeSat tracking and help learn how to increase IMU usage for future CubeSats.

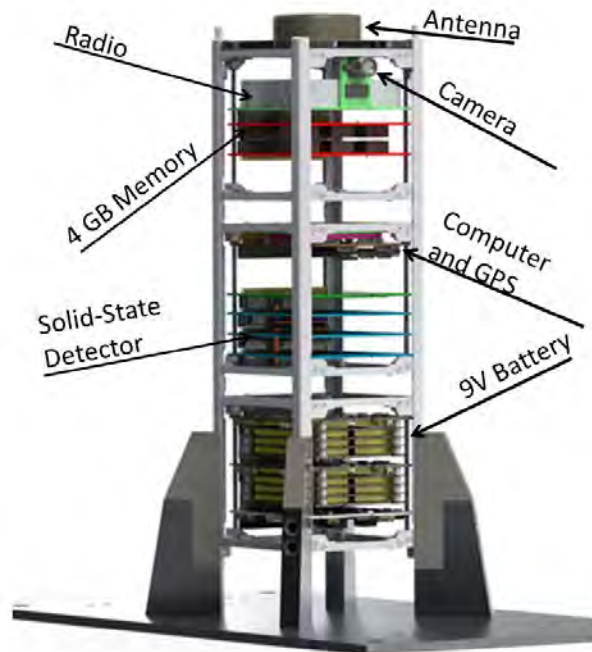


Figure 1: STF-1 Components

OUTREACH PRODUCT DESIGN

In this section, the design the products created for educational outreach will be discussed and described for the reasoning, as well as how they can be incorporated into schools, camps, and various other activities. The design for the STF-1 was taken from the presentation made for the students. The main components of STF-1 are explained in a way students can understand and relate to.

LEGO EV3 STF-1 Competition

To incorporate the actual STF-1 and the LEGO model it was important to explain the main contributions of satellites. Due to the limitations of LEGOs some objectives had to be left out but were discussed in another form. LEGO EV3 incorporates sensors and motors into its package thus incorporating it into the LEGO STF-1. This LEGO STF-1 created was to symbolize how small a CubeSat is by making it as close to the actual 10x10x11cm cube as possible, See Figure 3. Although STF-1 is composed of three cubes a simple explanation describing that this model is only one-third of the actual spacecraft will suffice. The audience intended for this product was middle and high schoolers. Many of these students, if not all, have experience playing with LEGO Mindstorms, or some other kind of LEGO power systems. This lets them get creative with what they want to do with their LEGO CubeSat code.

The LEGO STF-1 contains a light sensor and a gyro sensor. The light sensor is to act as a solar panel to display light at different areas of the room. The sensor will 1) show the orientation of the solar panel to the light to help learn how solar panels work and 2) understand that STF-1, and other satellites, have to use the sun to power itself to be fully self-sufficient. The gyro sensor is used to show the orientation of the satellite and help student understand the orientation of a solar panel to be the most efficient.

A medium motor is added to spin the LEGO STF-1. Students are to hold the axis to act as a stand to allow the satellite to spin, similar to how it will be in space. This challenges students to change the speeds, see how fast it can go and see how slow it can go. The high schoolers can learn about gears and the ratios between them. This is a great activity because there are only two gears involved in this gear reducer. A smaller gear drives a larger gear.

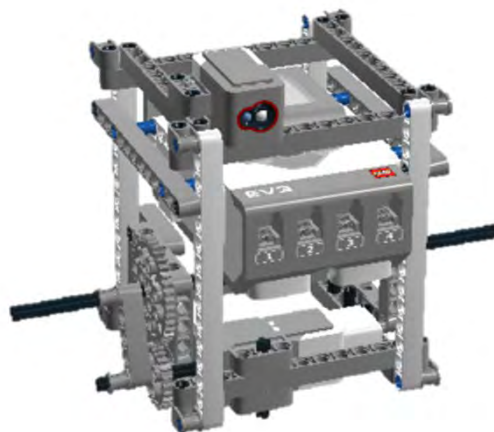


Figure 2: LEGO EV3 STF-1

All of these power functions plug into the LEGO brick at the top of the LEGO STF-1. This brick is the brain of the LEGO STF-1. With the use of a computer/iPad, the LEGO software gives students the ability to create their own code as to what they want their LEGO STF-1 to do. They can make it spin fast, slow. They can make spin to the highest light exposure and move it to specific angles. A direction booklet was created to instruct how to make this LEGO STF-1. This booklet includes fun facts about STF-1, NASA IV&V and suggested codes to try out. This was completed using LEGO Digital Designer (LDD).

A competition has been set up with the West Virginia Space Grant Consortium to develop students' knowledge on STF-1 and give the change to win a great prize for their school/family/FLL (First LEGO League) team. This competition involves the creation of a LEGO power system STF-1. Directions are given for NASA's LEGO EV3 model in Figure 3 on the STF-1 website as well as the West Virginia Space Grant website as a reference. This competition is for West Virginia students ages 9-14 with teams of 2-10 students. This competition has the same rules as FLL teams to coincide with their progress. The competition is geared towards classrooms, FLL teams and families that have students at the appropriate age level and access to LEGO power systems. Many schools now have LEGO classes or activities that allow them to have LEGOs in the classroom or for rent in the schools. Emails and ads have gone out to many people through the ERC and other sources to get as many student team submissions as possible. Each submission includes their own LEGO STF-1, the LEGO code and an essay describing what their LEGOS STF-1 mission was and what they want in future STFs. This is a great program to help students get their creative juices flowing and encouraging them to go towards STEM interests.

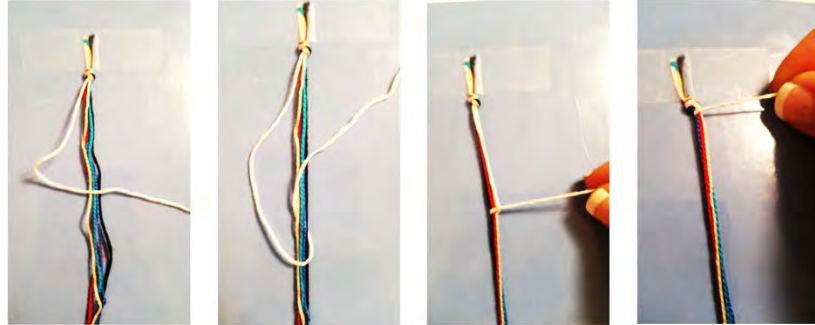
STF-1 Presentation

The STF-1 presentation was to describe why we have STF-1 and why we need STF-1. The presentation is a total of 30 minutes long but can be shortened for any circumstance. The presentation included information about why there are satellites, types of satellites and what we do with satellites. A comparison of how large the ISS (International Space Station) and how small a CubeSat is to show the comparison. A side by side picture of the ISS (which is the size of a football field) and a CubeSat (size of a loaf of bread) made the point of how vastly different they are in size. A transition into STF-1 was made to describe the main components as seen in figure 2. Additional information on the solar panels and components were made as well as describing the design process of STF-1. Many visuals were used to keep student's attention and get students to see actual STF-1 components/processes. This presentation was made similar to that of a SPOT (Space Public Outreach Team) presentation.

Hands-on Atmospheric Activity

A hands-on activity was created for a quick, easy, informational and inexpensive activity. This activity involves a scaled model of earth's atmospheres which will show where the STF-1 will be located using three square beads reading S-T-F. These beads will be located in the Thermosphere and will represent a 3U CubeSat while displaying the name STF. This activity will be making a bracelet/keychain by tying knots from yarn to create a long line of knots formed into a bracelet. This is a quick activity that can be performed in thirty minutes. To incorporate it into West

Virginia's first spacecraft the bracelet will be composed of blue yarn. This activity can be run by a teacher, engineer or anyone who has the supplies. The activity is on the STF-1 website for educator's purposes. Visual direction of how to make the keychain is shown in figure 4 along with the final product. One of the NASA IV&V educators, Jesse White, will be taking this to schools



to get students to learn about STF-1. This is a great activity for elementary schoolers all the way up throughout middle school.

It is difficult for students to wrap their head around how large something really is so this activity is great because each model is scaled to the correct proportion. The Troposphere is less than 10 miles, the Stratosphere and mesosphere are 22 miles each, the thermosphere (where STF-1 will be located) is 319 miles, and the Exosphere is 6,000 miles thick. This activity can be transformed into many other scaled activities such as distances of the planets or the phases of Mars [3].



STF-1 Coloring Page

Due to the LEGO EV3's being for students at a middle school level or higher a coloring page was created to help elementary school students learn about STF-1. This includes a description of STF-1 with fun facts on the back, and the coloring page is an outline of STF-1 with earth in the background displaying West Virginia on the map.

Figure 3: Bracelet/Keychain Activity

the presentation or given to teachers to use when there is a substitute or extra time at the end of the year.

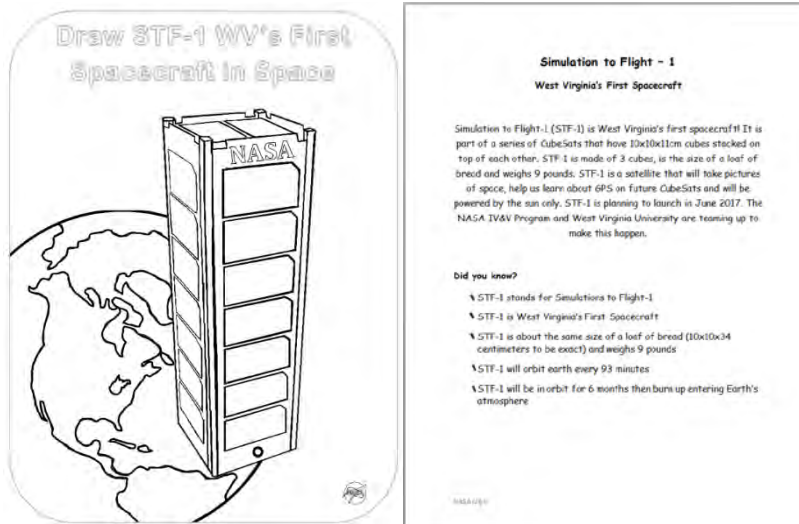


Figure 4: STF-1 Coloring Sheet; Front – Left, Back - Right

At the point of this writing, the STF-1 team is working on teaming up with Tailpipes, a restaurant in Morgantown, WV High Street, to create a space burger and use this coloring sheet to get kids to learn about STF-1. At Tailpipes, they frame colored coloring pages at each table, and one time it would be great to get STF-1 to be the coloring page. At this point they are interested, and hopefully, in the near future, STF-1 will be advertised in their restaurant.

STF-1 Videos

One of the objectives given by the STF-1 team was to create a few short videos that can be put on the STF-1 website. This was completed displaying the clean room, the structure of STF-1 and a tour of the components of STF-1. These videos were put on the website for student and teacher reference. The clean room is very interesting; there is a clean room for every satellite that goes into space. STF-1's clean room is relatively small compared to other satellite clean rooms, but obviously, not as much room is needed when there is a smaller spacecraft. When walking into the clean room, each person must walk on a sticky mat, put gloves on and depending on the level of sanitation a hair net to keep dirt and hair out of the electronics. The STF-1 structure was shown to relate the size to someone holding the structure. Finally, components were described that would go into space with STF-1. The people in these videos are experts and can get students to relate to STF-1. It is always more intriguing to have someone who is an expert to talk about their work.

CONCLUSION

The objectives set at the beginning of the internship have been met. The STF-1 team is satisfied with the products and has the ability to repeat all activities given. Activities have been given to all team members with suggestions on how to use them throughout the next year to teach about STF-1. To recap the objective of STF-1 outreach was to create a product to get young boys and girls interested in STEM and STF-1. The products produced included a presentation, LEGO competition, LEGO activity, videos and a hands-on activity, and a coloring sheet. These products were all given to the STF-1 team which is reputable. The electronic products including the presentation, LEGO Competition ad and information sheet, LEGO activity along with worksheets

for middle and high schoolers and directions, hands-on bracelet/keychain activity and the coloring sheet, were all sent via zip file. Along with the digital file of the bracelet/keychain activity, supplies were purchased, and 300 bracelets were cut and tied together for an educator to take to schools for students to learn about earth atmospheres and STF-1. This allows for less set up time.

As mentioned numerous times before all of these products are reputable and can be used by anyone with the given information. The STF-1 outreach objective products have been met. Currently, these products are available for schools, and a competition is ongoing until October 3rd, 2016. STF-1 is not set to launch until June of 2017 which gives the next school year for students to learn about STF-1.

ACKNOWLEDGEMENTS

I would like to thank West Virginia Space Grant Consortium for giving me this opportunity and my mentors Marcus Fisher, John Lucas, and Justin Morris. They have helped grow my educational experience and solidify my educational goals. I couldn't have asked for a better team. I would also like to acknowledge anyone I met at NASA IV&V, they always gave good feedback and encouraged the progress on STF-1 outreach.

REFERENCES

- [1] J. Davidson, "Lego Is Now The Largest Toy Company In The World," Time, 2014.
- [2] J. Morris and M. Grubb, *Simulation-to-Flight (STF-1) Proposal*, West Virginia: NASA, 2014.
- [3] J. White, Interviewee, *Hands on STF-1 Activity*. [Interview]. July 2016.

INVESTIGATION OF ORIONISM: MULTI-PURPOSE CREW VEHICLE SIMULATION SOFTWARE

Olivia Milam
NASA IV&V Facility
Computer Science
Marshall University
Huntington, WV

ABSTRACT

Successfully simulating a space vehicle's hardware is an important component of testing flight software. Flight software has many hardware inputs that must be simulated in order to test the software without the corresponding hardware. To perform meaningful tests using a simulator on the flight software, it is crucial for the simulator to provide responses that mirror what the real-life hardware would send to the flight software. Dynamic testers use the OrionSim simulation software during verification and validation procedures on the Orion Multi-Purpose Crew Vehicle's flight software. Goals of this investigation were to discover new uses and further document OrionSim. Understanding the tools used to verify and validate mission-critical software is an important component of assuring safe software and the safety of the Orion vehicle. The OrionSim investigators learned more about the system through reading source code, building sample simulations using the same Trick framework as OrionSim, observing the simulation in action, and interfacing with the software in new ways. The key to better understanding OrionSim was learning how the Trick Simulation Environment framework drove the simulation. This investigation resulted in a deeper understanding of an important testing tool. The significance of this investigation is that it contributes to the assurance that the simulation software is functioning as expected and that it is not behaving in unexpected ways. This knowledge helps increase the overall safety of the Orion Multi-Purpose Crew Vehicle.

INTRODUCTION

The goal of this project was to uncover information about OrionSim. OrionSim is a simulation software module that simulates the hardware of the Orion Multi-Purpose Crew Vehicle (MPCV). Simulating the hardware of Orion allows dynamic testers to test Orion's flight software. The reason OrionSim needs evaluation is that successful dynamic tests on the flight software are dependent on valid simulated hardware data. That is to say; the dynamic tests are only valid if the simulator is accurately emulating the hardware and providing valid data.

The investigators began evaluating OrionSim through reading the documentation, examining source code, building sample simulators, observing the simulator in action, and interfacing with OrionSim in new ways. The investigators read the documentation to gain an overview of what was currently known to NASA's Independent Verification and Validation (IV&V) program and what documentation was lacking. Examining source code allowed the investigators to find more specific information as to why certain things were occurring. Building sample simulators helped illuminate how the full OrionSim simulator worked. Observing the simulator also helped reveal key information about what was occurring. Finally, interfacing with OrionSim in new ways

further expanded the body of knowledge about the program. This project resulted in several deliverables. The first deliverable is a sample simulator that uses the Trick framework, just like OrionSim. This simulator is relatively simple. It simulates the physics of what would happen if a cannonball was fired using an analytical model of a cannonball. This sample program helped the investigators understand the bare essentials in Trick that are responsible for running OrionSim. This program was written in C++ and Python. Another deliverable was a client program that could connect to OrionSim in new ways. It created a TCP/IP socket to the variable server that Trick and OrionSim use. Users can use the program to send commands to OrionSim directly. This program was written in Java and was a useful starting point for a fellow intern who was working on a visualization program. Other deliverables include a log parser program written in Java, written documentation on Trick and OrionSim, and a training video on OrionSim for future investigators.

This investigation was an overall success. Basic information about OrionSim was uncovered that would lay the foundation for future investigations. The next big step in evaluating OrionSim will be examining the mathematical models that drive the Trick simulation. This task will be a time-consuming endeavor that requires domain knowledge about Orion, OrionSim, and environmental factors.

BACKGROUND

NASA's IV&V program helps assure the safety of the software used in NASA's space vehicles. It is imperative to examine the software with the same care and attention to detail that the physical components of the space vehicle are inspected with. This is especially true for the Orion Multi-Purpose Crew Vehicle (MPCV). Orion is the spacecraft that will replace the space shuttle and carry on new human spaceflight missions. Orion must, therefore, achieve a safety rating that permits human spaceflight. Verification and validation of software is an important step in achieving a human passenger rating. IV&V helps to assure that the software will behave as expected and not respond in unexpected ways. The independent aspect of NASA's IV&V testing further provide safeguards against conflicts of interest, financial issues, and groupthink, all of which could lead to missing potential problems. IV&V helps to assure the safety of the software running and guiding the spacecraft.

Evaluating complicated code, such as Orion's, requires many different test procedures with different objectives. For example, static code analysis examines the source code directly and attempts to find troubling areas in the code where a problem could occur. A potential problem could be a violation of the projects coding standards. An example of a coding standard is "variables cannot be mutable without justification." Static analysis then could entail looking for any mutable variable definitions that are defined as mutable without cause. This is different than dynamic testing. Dynamic testing involves running the program and observing what occurs when certain inputs are given to the program. The idea is to establish a nominal run of the program as a baseline and also search for potential problems that could only be found during run-time. An example of a run-time error would be a set of inputs that puts the flight-software into an infinite loop. Looking at the source code in dynamic testing is useful for identifying problematic areas, but its key focus is examining running software.

The type of testing this internship predominately supports is dynamic testing. OrionSim is a tool to help dynamically test the Orion flight software. OrionSim is a software mechanism of supplying Orion's flight software with inputs that simulates a phase of an Orion mission. OrionSim's responses should mirror what the real-life Orion hardware would send to the flight software. OrionSim has a few advantages over directly using the hardware. One advantage is that a software driver program is a relatively inexpensive way to test. That is, the Orion hardware is expensive, and only the most important tests can be run on the busy hardware rigs. A software simulator allows developers a chance to check that the code is running as expected and gives more testers the opportunity to check the flight software. OrionSim can also run faster than real time. This allows testers the ability to complete large batches of tests and do statistical analysis on the results. It is important to understand OrionSim in order to use it as a tool to perform meaningful dynamic tests. Testers need some level of assurance that the simulation software is approximating the hardware well enough to be meaningful and what the limits of the simulation are.

Assuring the accuracy of the simulator is an important step in evaluating the safety of Orion's software. If the simulation software is not feeding reliable data into the Orion flight software, then this tool is not useful for evaluating the run-time flight software responses. The purpose of this project was to begin an examination of the simulator.

PROJECT

The goal of this project was to explore OrionSim and document any findings. OrionSim is a component of a larger testing environment called SOCRATES. One of the aims of this project was to determine the role OrionSim plays in this larger environment. Much of the work on this project is foundational as it lays the groundwork for future research on OrionSim and its uses in dynamic testing. The reason relatively little information is known about OrionSim is that this toolset is not developed here. Furthermore, because it is a tool and not a product, there is also little documentation on it.

Trick was found to be a key element early on in the project. Trick is the underlying framework that runs the simulation. It is a toolkit that allows developers to focus on writing the mathematical simulation models instead of worrying about the backend drivers of the simulation. By documenting Trick, the stage is set for future investigators to work on the mathematical models that drive the simulation. Trick has also recently been released to the public. Understanding Trick is one of the first steps towards understanding OrionSim.

APPROACH

The main investigative approach to this project was conceptually deconstructing OrionSim into its foundational pieces. This was achieved through reading documentation, examining source code, building sample simulators using Trick, running OrionSim, and finding new ways to interface with it. Conceptually deconstructing OrionSim was the best option because there was not enough documentation to understand it as a whole out of the box. Furthermore, the source code for OrionSim was composed of hundreds of complicated C++ classes, making that as a sole approach tedious and unfruitful. Deconstructing OrionSim was the best option.

Reading the existing documentation on OrionSim was an essential starting point. Many of the first steps in the investigation came from reading the existing documentation. Some of the problems with the documentation were that they were out of date, referred to earlier editions of the software, or were from the perspective of a different testing environment. Even so, reading it provided the investigators a good overview of what was happening and what to look for.

Examining source code was another valuable step. This is the most direct way to determine how data is flowing in a program. However, because OrionSim is so massive and complicated, this approach only took the initial investigations so far. The mathematical models that drive the simulation require domain knowledge in many different areas including how the Orion vehicle works from a physical perspective, networking inside of Orion, and how the simulation works overall. Much of the work done by the end of this project lays the groundwork for better understanding of what is happening in the source code. For later investigations, examining the mathematical models will provide invaluable insight into the reliability and failings of the simulation.

Building sample simulators using Trick was one of the breakthrough moments of this project. Following the Trick tutorials and building a simple cannonball simulator revealed in simpler terms the basic mechanics of how the simulation worked. It clarified the role Trick plays in OrionSim and how many of the C++ classes are interacting with each other. Trick is one of the key layers within the program.

Observing OrionSim running also illuminated many facets of the program. Because of this program changes so often, sometimes it is difficult to know if it is running correctly. Part of what this investigation uncovered were markers that confirm the program is, in fact, running. Furthermore, observing the data OrionSim produces is valuable for determining if it is behaving as expected. This is another area that could be expanded upon in future investigations.

Finally, finding new ways to interact with OrionSim was an important part of this investigation. The MPCV team wanted to not only know the obvious uses for OrionSim, but also ones that may not be expected. Part of this investigation was delving deep within OrionSim and finding hidden tools and aspects. One such aspect that was utilized was its broadcasting variable server. The investigators wrote a program to connect to this variable server. This is a good first step for future programs interested in interfacing with OrionSim.

DELIVERABLES

The deliverables of this project include a sample Trick project, a TCP/IP client to connect to OrionSim, a log parsing tool, documentation, and a training video and presentation.

The sample Trick project was written in C++ and built using Trick 16. The object simulated was a cannonball. The mathematical model used was simple and only took into account essential requirements. Going through the process of making a simulation, even a simple one, provided insight into the inner workings of OrionSim. It also provided invaluable experience when writing the documentation that explains Trick. Additionally, it made it easier to understand many of the

components within OrionSim.

The TCP/IP client could not have been written without the experience gained after writing the sample Trick simulation. The TCP/IP client was built as a proof-of-concept that it is possible to connect to OrionSim and interface through other channels than the ones provided. The variable server is run by the Trick framework, and it accepts commands in Python. The client TCP/IP program was written in Java. The program checks the channel the variable server broadcast's its host and port location and connects to the specified host and port. Next, it sends commands and listens for a response. The sample program simply asks the client what version of Trick it is using and asks for the value of a few variables. This is a simple program, but it is the gateway to more exciting functionality. A fellow intern took an interest in this sample program used it as a jumping point for his project on 3D visualization.

The log parsing tool was a convenience tool written in Java to make it easier to read some of OrionSim's log files. These log files were long and not very human-readable. This program simply parses out the information on each line and rewrites it in a more readable format.

The most lasting deliverable for this project will be the documentation. This program was in need of more up-to-date documentation that was applicable to the IV&V program. This investigation produced documentation on OrionSim and Trick. The documentation encompassed many aspects of these programs and sought to be relevant to this program. Along with this documentation, a training video and presentation was produced. This information will make it easier for new investigators to continue examining OrionSim and begin the process of truly evaluating the use of this program as a dynamic testing tool.

CONCLUSION

This project uncovered and documented many aspects of OrionSim. In many ways, this project was a reconnaissance mission to find out more about a rapidly evolving tool and its uses. OrionSim could be a valuable tool for dynamically testing the Orion spacecraft's flight code. This tool needs to be evaluated so it can be relied on as a valid testing ground for Orion's flight code. Future long-term work would be an investigation to evaluate OrionSim's mathematical models that drive the software and designing test cases that make full use of OrionSim's capabilities.

VALUABLE ASPECTS OF THE PROGRAM

The financial support provided by WV Space Grant Consortium was essential for me to complete this internship. I am an older, financially independent, student and can only realistically undergo paid summer internships. I further appreciate the travel stipend. I noticed many of the interns here attend WVU or are else local. I think the travel stipend is a great way to encourage people from other parts of the state to complete internships at IV&V. The travel stipend helped offset the cost of gas to Huntington and the cost of a temporary apartment. I did not know about the I-79 High Technology Corridor until taking this internship and about all of the opportunities that match my degree available there. This internship has given me more insight into what STEM jobs are available in-state.

The experiences I gained at NASA IV&V further taught me how to think like an engineer. School

plays an important role in developing the skill of thinking from an engineering perspective; however, the actual practice of engineering teaches the more intuitive aspects of the skill. Practicing engineering is more intuitive because an investigator has to define the problem at hand by his or herself, without knowing what all of the relevant facts are. In school, most of the time, the problem is already defined. In real practice is difficult to filter down to the real issue without understanding the system at an intuitive level. This opportunity allowed me to practice the intuitive aspect of engineering on a complex domain. Furthermore, this internship was a unique opportunity to observe what it requires to work on a massive project. My previous internships focused on projects that could be completed by one individual. This is the first project I have had direct experience with that absolutely required a multitude of teams. Moreover, this experience helped develop more concrete skills. I examined vast amounts of professional level source code and learned new design patterns. I also wrote code to better understand the system I was working with and as a way to contribute software tools to the project. This project increased my knowledge of C++. I further gained firsthand experience of the software development lifecycle and especially the testing portion of this cycle. Typically the actual practice of verification and validation of code is not taught at an undergraduate level. This internship gave me an excellent overview of what is entailed when verifying and validating code.

ACKNOWLEDGEMENTS

Special thanks to the NASA WV Space Grant Consortium for making this internship possible. My mentor, Frederick Beamer, also was a valuable resource for helping me find the right path for my project and investigation. The yearlong MPCV intern, Katherine Reid, also gave me wonderful advice and tips.

A STUDY OF DOPING OF SEMICONDUCTORS ON THE NANOSCALE LEVEL

Kody Tucker

West Virginia Wesleyan College

Applied Physics

West Virginia Wesleyan College

Buckhannon, WV

ABSTRACT

During my research internship at West Virginia Wesleyan College, I studied semiconductors. For nine weeks, I performed a literature search of books, videos, and webpages, and with four variations of the silicon wafer. With one being undoped, I had two N-types and a P-type wafer.

INTRODUCTION

Semiconductors have an important role in society as they are used in many electrical applications ranging from diodes and transistors to logic gates and LED displays. Since their introduction in the 1900s, they began to alter the world of electronics and its everyday usage. Semiconductors paved the way for today's modern era which heavily relies on them as we see them in our phones, cars, planes, etc. My goal for this internship is to learn more about the common semiconductor is known as silicon. How is doping achieved, which type of dopant (p or n) enhances the semiconductor's conductance at best, and does an n-type dopant's position on the periodic table have any effect on conductance?

Even though there were previous applications, semiconductors didn't have much of an impact on the world until 1947. That year, American Physicists John Bardeen, Walter Brattain, and William Shockley implemented the transistor. This device amplified or switched electrical signals and power, and this technology would soon be used in computers, calculators, radios, etc. By utilizing transistors in these electrical appliances, smaller and cheaper versions became available.

In 1958, another technological breakthrough occurred. While employed at Texas Instruments, electrical engineer Jack Kilby demonstrated his integrated circuit. An IC consisted of circuit components placed onto a piece of a semiconductor. Kilby is credited as a co-inventor of the IC as another man named Robert Noyce worked on his version of the monolithic integrated circuit in 1959 while working for his company Fairchild Semiconductor. Eventually becoming known as the microchip, the ICs would be integrated in computers along with handheld calculators; it would later serve as a primary component in mobile phones and other electrical appliances.

Semiconductor materials are neither conductors nor insulators; however, they can be manipulated to act as them depending on the application needed. For example, at zero absolute temperature in Kelvin, they act very similar to insulators. In its early days, semiconducting technology were mostly made of the element Germanium including Kilby's integrated circuits. Eventually, due to the high cost and difficulty of obtaining Germanium underground, Silicon would replace it as the primary semiconductor in electronic devices as it was easily obtained from sand and much

cheaper. These elements are semiconductors as they have positive and negative charge carriers coexisting within them. The coexistence of the carriers grants the controlled modulation of conductivity and other electrical properties of that material. Electrically, this permits the fabrication of all sorts of electronic devices and circuits. (“timeline”)

PROJECT

A common process to alter the semiconductor’s properties is doping. This involves the introduction of an element impurities into the material in small portions as the process can drastically affect the conductivity of the material. Methods include using alloys, diffusion, and ion implantation; however, due to its disadvantages such as the cracking of the doped material, the alloy method is no longer used. Diffusion involves the transport of molecules from a region of higher concentration to an area of a lower concentration of molecules wherein a dopant molecule can fill in an empty space, move between the semiconductor’s atoms, or exchange with the other atoms as the material is heated to a certain temperature as the dopant molecules are transferred using a gas, liquid, or solid. Ion implantation involves the acceleration of charged dopant ions in an electric field and their penetration onto the semiconductor wafer. Done at room temperature, this process is accomplished using an implanter, and the penetration depth can be modified by adjusting the voltage to change the acceleration of the ions. This is preferable to diffusion.

These methods produce two types of doped semiconductors: p-type and n-type. A p-type semiconductor has a hole due to the semiconductor having one more valence (outer) electron than the dopant, and an example would be Boron-doped Silicon. In contrast, an n-type semiconductor has a free electron due to the dopant having one more valence electron than the semiconductor, and an example would be Arsenic-doped Silicon. The dopant concentration in the semiconductor varies by the relationship of the amount of dopant molecules versus the thickness of the material. The dopants increase the conductivity of the silicon, and a p-type and n-type semiconductor are used together to create a diode. (Halbleiter)

Also, there are semiconductors that are compounds of different elements. An example would be Aluminum Gallium Arsenide. Being an arsenide which is an anion with a negative charge of 3, this crystalline solid is used in lasers, LEDs, and photo-optics. The wavelengths reflected by these crystals are affected by the properties of that specific crystal as its properties are granted by the variation of the percentages of the elements in that crystal. The chemical formula is $Al_xGa_{1-x}As$, and the x represents a mole fraction which is the amount of an element expressed in moles divided by the total amount of all constituents. As such with a mole fraction of 0.36, the crystal’s formula would be $Al_{0.36}Ga_{0.64}As$; hence, the larger the concentration of Aluminum, the smaller the concentration of Gallium. These differences are responsible for the variance of the band gap energies within the crystal with the band gap range being between 1.42(GaAs) and 2.16 (AlAs) electron-volts. With different band gap energies, there will be a fluctuation in wavelengths. (NSM)

For my research project, I plan on studying the electrical properties of the silicon semiconductors at West Virginia Wesleyan College. Each wafer has a variation as I used undoped, Boron-doped, Phosphorus-doped, and Arsenic-doped wafers. For them, I performed multiple trials of increasing

applied voltages and measured the amperage flowing through them. Having an atomic number of 15, Phosphorus is the closest n-type dopant to Silicon ($z = 14$), and Arsenic ($z = 33$) would serve as a dopant farther away from Silicon on that table.

To observe the electrical properties of pre-doped and post-doped silicon, I ordered wafers from Virginia Semiconductor Inc. in Fredericksburg, Virginia. A wafer is a small round disc with varied sizes; Specifically, I ordered 2-inch diameter wafers with the exception of a 1-inch diameter arsenic-doped wafer provided by the college. All wafers were double-side-polished (DSP). DSP wafers are practical for semiconductor applications that require tightly controlled flatness characteristics, and it would be wise to keep all variations the same for a proper examination of the doping process. Every wafer has differences in categories of resistance, thickness, and doping concentration. Notably, these wafers can have different crystalline orientations of alignment when these wafers are created by the cutting of the silicon crystal, and they are designated by Miller indices numbers such as 100, 110, and 111; for simplicity, I will only be using the $\langle 100 \rangle$ orientation which has cube-structured lattice planes and directions. This orientation is distinguished by the angle between the wafer's primary and secondary flats. These flats are straight lines alongside the circumference of the wafer. For a p-type, there is an angle of 90 degrees whereas, for the n-type, there is a total of 180 degrees (in other words, parallel). I find this purchase to be simpler and cheaper since ion implantation and other processes are out of my budget. Interestingly, these wafers can be used to make multiple microchips as technological advancements have allowed certain sized wafers to be the platform for millions of transistors that will be connected together as part of the microchips.

First, what are the differences between conductors, semiconductors, and insulators? An insulator's valence band is completely full of electrons which impairs the material's ability to conduct current as the electrons must be free to excite; contrastingly, a conductor's valence band is only partially filled with electrons to allow the electrons to move freely and become conductive. A semiconductor has fewer partially filled valence bands than a conductor, limiting its conductivity; however, that can be changed by simply adjusting the temperature of the semiconductor.

Undoped semiconductors are referred to as intrinsic semiconductors. Even though there might be minimal traces of impurities, they seem to act so pure that the impurities' effects are negligible. Labeled i-type, intrinsic semiconductors mimic conductors and insulators when they are set to certain temperatures. For example at zero degrees absolute temperature in Kelvin, it is a perfect insulator as a result of having zero conductivity. As temperature increases, resistivity decreases and excited electrons move across an energy region with zero density into the conduction band. In the conduction band, they create conductivity. As this event occurs, empty states are left behind, and this allows the transpiring of free hole conductivity in the valence band. Add this to the conduction band conductivity to obtain the total amount of the semiconductor conductivity. By doping an intrinsic semiconductor, we modify it into an extrinsic one. Extrinsic semiconductors have properties that are strongly affected by impurities introduced to it during the doping process.

To distinguish the major difference between the extrinsic types of semiconductors, we must know the amount of electrons in both the dopant and the original semiconducting material. If the dopant

has less electrons, this will create positively-charged holes in the new material after the doping process. The valence electrons of the dopant ion are bonded with the valence electrons of the semiconducting element, but one valence electron of the original material is left unpaired. Since a covalent bond requires two electrons, it can be said that these areas of electron absence can be labeled 'holes.' Semiconductors with holes in their covalent bonds are classified as p-type. Another type of doped semiconductor involves the dopant having more valence electrons than the original material. This time, there are free electrons along with the covalently bonded ones. Semiconductors with free electrons are regarded as n-type. The doping process allows the introduction of impurities to increase the conductivity of a material which is also impacted by temperature. The greater the dopant concentration, the lower the resistivity. N-type dopant concentration such as Phosphorous has greater effect on lowering resistivity than p-types. Most likely, this is a result of the different methods of current flow and the properties of the extrinsic semiconductors. All experimentation was conducted at room temperature in the high 60s, low 70s degrees Fahrenheit range.

The current flow depends on the majority carrier. As the voltage is applied to a p-type semiconductor, current flows from the negative to positive terminal; however, for the electron 'holes,' they move toward the negative terminal due to the shifting of the covalently bonded electrons. As the holes are the majority carrier due to its great effect on current, this process explains the amperages of the Boron-doped semiconductors. In contrast to n-types, the electrons move toward the positive terminal as current flows as the free electrons are the majority carrier. This explains the functionality of the Phosphorus-doped and Arsenic-doped semiconductors.

RESULTS

After multiple trials of measuring amperage impacted by voltage focusing on the extrinsic semiconductors, I concluded that P-type semiconductors generally have greater resistivity allowing N-types to have greater conductivity with both still having better conductivity than the undoped type. Of course, this is all impacted by dopant type, dopant concentration, thickness, crystal structure, and diameter of the material. For a general explanation, let's claim that only dopant type and crystal structure varies. Recalling previous information, we know that N-types have additional electrons and P-types have holes in their valence bands. As voltage is applied to the material, current flows. In a P-type, it appears that the holes move backwards as the electrons accelerate. Realistically, the electrons are attracted to these positively charged holes and move in to fill them. As the electron leaves, another hole is created in its vacancy which attracts another electron; thus, current flow is a multistep process that happens very fast that it creates the illusion of the holes moving in a reverse direction. Contrastingly in an N-type, electrons are quickly replaced with another due to having additional free electrons. This is why N-type semiconductors are more conductive than P-types in general, and P-type is the more resistive of the two doped types. Considering that my experimentation found current to be roughly 11 nA for the I-type wafers at 5 volts which are less than all other amperages of the types of Silicon, this reflects my knowledge about the impact that the doping process has on this element.

My research also focused on variations caused by differences in thickness and resistivity. In the semiconductor industry, various wafers are made with specific measurements, qualities, and quantities to suit a particular job. For example, solar cell applications require a particular wafer

that possibly isn't acceptable for the common computer. Notice that I mentioned common, there are variations within these industries for certain equipment with price range also being a factor. Companies look at the quality and pricing of products and determine whether or not the product is efficiently useful for the job in respect to their budget. I experimented with two different thicknesses of Boron-doped Silicon. For this P-type, I utilized 250 and 500 micron (micrometer) thick wafers. After a few trials, I noticed that the thinner ones were able to conduct a greater amperage (2.7 mA) than the thicker ones (about 1 μ A or 0.001 mA). This huge difference is a result of their variations in resistivity (0.01-0.025, $>1 \Omega\text{-cm}$) which is impacted by dopant concentration in respect to thickness. The thicker the wafer, the more impurities needed to be added to reach a certain concentration in the 10^{14} - 10^{20} cm^{-3} parameter. Also, greater concentrations lessen majority carrier mobility. Defined, mobility is the ability to move freely and easily. To calculate the resistivity, dopant concentration and mobility is taken into account, or you can use graphs. For example, by using figure 1, P-types with a resistivity of $1\Omega\text{-cm}$ will have a dopant concentration of slightly more than $1 \times 10^{16} \text{ cm}^{-3}$. An N-type, such as Phosphorus or Arsenic-doped, would need less concentration to obtain equal resistivity.

Focusing on the N-type semiconductors, Phosphorus ($z=15$) is the nearest to Silicon and Arsenic is farther from it. From experimentation, I realized that Phosphorus-doped silicon is more conductive with less resistivity per doping concentration than the Arsenic-doped using 250 micrometer thick wafers. However, it turns out that the Arsenic dopant is preferable to Phosphorus in low resistivity applications such as integrated circuits with components including memory, microprocessors, and networking systems. Since both elements are in group 15 of the Periodic Table for having similar properties as they have five valence electrons, Arsenic is seen as a replacement for Phosphorus on the grounds of having a lower diffusion coefficient. (ESIA) For a quick analysis, I decided to layer an N-type wafer over a P-type. Using the Phosphorus doped and Boron doped Silicon, I measured their amperages. At five volts, my multimeter read an amperage of 0.3385 μ A. Alone, these specific wafers read approximately 2.33 and 0.095 μ A respectively. To me, it is very interesting that a combination didn't actually add amperage but rather fall within the range of the single wafers. For this specific result, the P-type was twice as thick as the N-type, and this contact of semiconductors has created a p-n junction. With their fermi levels not in equilibrium, diffusion occurs with electrons moving from the n-side to the p-side and holes would move in a reverse order from the p to the n. The diffused electrons have combined the junction region, and a steady state is soon achieved that diffusion is opposed by the electricity across the p-n junction created by the negatively charged acceptor ions of the n-side and the positively charged donor ions of the p-side caused by impurities. As a consequence, the fermi level is now continuous across the p-n junction. The p-n junction plays an important part in most semiconductor devices including diodes, transistors, solar cells, LEDs, and ICs. During the joining of the holes and free electrons in one p-n junction, the electron releases a photon which triggers the release of other photons. As the semiconductor material acts as a mirror, the photons bounce back and forth as it hits that material. This process continues until the junction is filled with laser light. Some of the light exits the back of the junction and hits the photo diode which uses the light to regulate the voltage applied to the diode. For the light emitting out of the front, it passes through a collimating lens to make the beam appear in a straight line. Without the lens, the light would appear like water being sprayed out of a spray hose nozzle. (EpicPhysics)

For a small side project, I focused on x-ray spectroscopy with semiconductor compounds.

Mentioning the aluminum gallium arsenide earlier, the crystal is composed of two elements from group III (Aluminum: $z=13$; Gallium: $z=31$) and one group V element (Arsenic: $z=33$ of the Periodic Table. With its chemical formula being $Al_xGa_{1-x}As$, the crystal can vary in wavelength. Notable wavelengths for this crystal include 670, 787, 889, and 907 nm. To obtain these crystals, I had to use diodes. Note that in the scientific world, these diodes are known as semiconductor lasers. Unfortunately for the diodes that I have, taking off the top portion consisting of glass would render their electrical properties, but the crystal inside is still useable for x-ray spectroscopy. Knowing this, I decided to only use the 889-nanometer diode. Rotating the counter from 11 to 90 degrees, I was able to find the peak number of counts. Of course, the angles previously stated is in reality regarded as twice the actual angle. As I move the counter, the holder containing the material is slightly adjusting its angle away from the counter. With the counter set to 400 volts, the peak number of counts was 429 at 36 degrees. I would then repeat the trial with a laser beam hitting the crystal. I picked three lasers: red, green, and blue. These lasers had impacted the results such that different angles had the peak number of counts. Using red, the highest number of counts was 309 at 67 degrees with most angles having counts in the 200s. Using blue, the highest peak was near 36 degrees with 353 counts; and for green, I obtained 333 counts at roughly 33.5 degrees. In general, these lasers increased the ability of the crystal to absorb x-rays with the red laser having the greatest impact on it. The wavelength of red is within the bounds of 625-740 nm which is longer than the wavelengths of green (500-565 nm) and blue (440-485 nm). According to my data, the closer the beam's wavelength is to the Aluminum Gallium Arsenide crystal's wavelength, the more likely it will alter the ability of that crystal. (Agrawal)

Semiconductors are very important in the modern world as we use them every day. As circumstances can alter them into conductors, I would like to find out more about them and the properties that allow us to have our electronic devices. Ranging in different forms from crystals to wafers whether doped or undoped, they are the basis for a lot of technology that we take for granted.

FUTURE WORK AND ACKNOWLEDGEMENTS

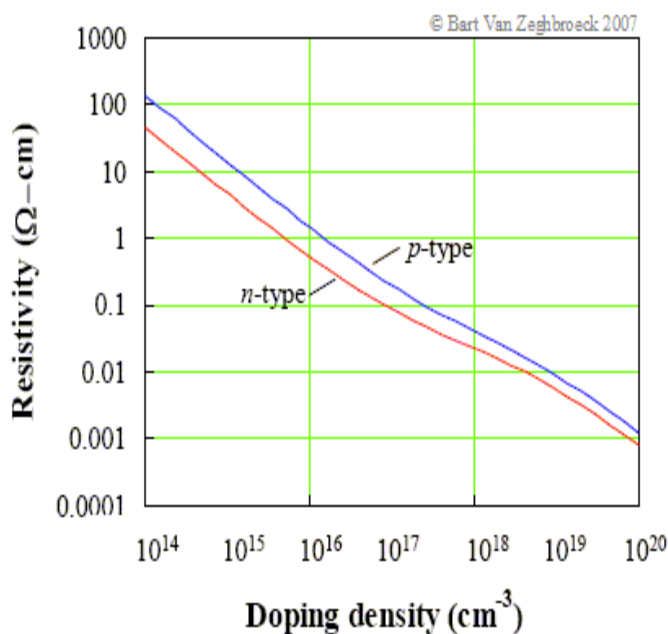
In the future, I plan on utilizing a transmission electron microscope to observe the crystalline structures of the silicon wafers. Originally, this was planned to occur within my nine-weeks of research here at the college, but our electron microscope became inoperable. The college hired a mechanic to fix it, and he has corrected a lot of issues. However, it still needs some finishing adjustments before I can use it. Hopefully, it will be completed by next spring so I can use it for my senior project; if not, I can set up an appointment with a department at West Virginia University to use theirs. I aim to continue my research by expanding the orientations of wafers. Since I only used $\langle 100 \rangle$ oriented wafers, I intend on ordering a few variations of the 110s and 111s and compare all of them.

My research was made possible by the financial support given by the NASA WV Space Grant Consortium and West Virginia Wesleyan College. I'd like to acknowledge Dr. Joseph Wiest, Dr. Bert Popson, and Bob Grose for their help in this project. Being my mentor, Wiest helped me find and set up equipment and materials as well as giving advice. Prior to sending this in, Popson read and checked this paper for errors; Grose disassembled the diodes for me so I can access the

crystal inside it. I'm also thankful for Chuck Coleman's continuing work on the electron microscope. I was figuring that I would be utilizing it within 8-weeks of the program, but things happen. Because of the repair, I completed experimentation with the aluminum gallium arsenide crystal in order to complete an extra week of work. Still, I'm very thankful that I was allowed to participate in this program because I learned about silicon and its uses to create microchips for electronics such as computers and other devices. Previously, I knew this to an extent, but this taken opportunity expanded my knowledge of this subject. Also, I was received a short experience of future classwork in the solid state / materials science lab that I will endure within the upcoming school year by using the x-ray spectroscopy equipment for my side project. I'm very grateful that I was able to work on this project.

Fig. 1: Dopant Concentration & Resistivity

Fig.2: Undoped (i-type) Silicon wafer



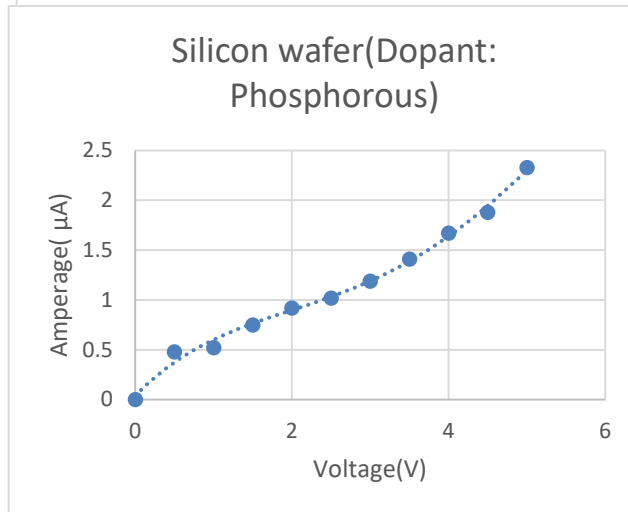
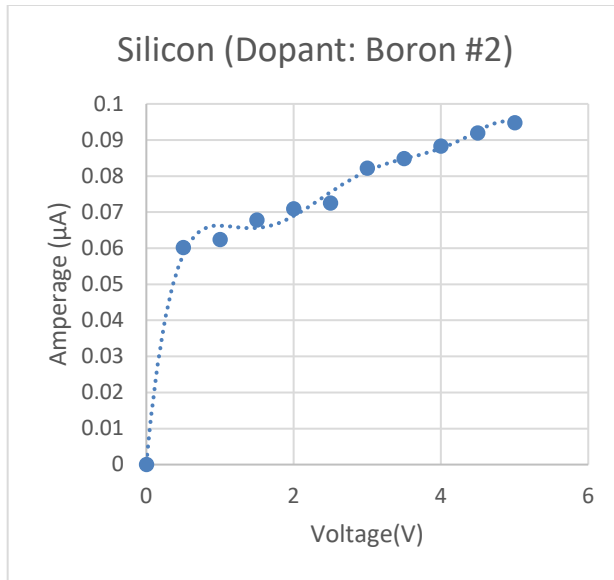


Fig.3: P-type Wafer; 500 microns thick

Fig.4: N-type Wafer; 250 microns thick

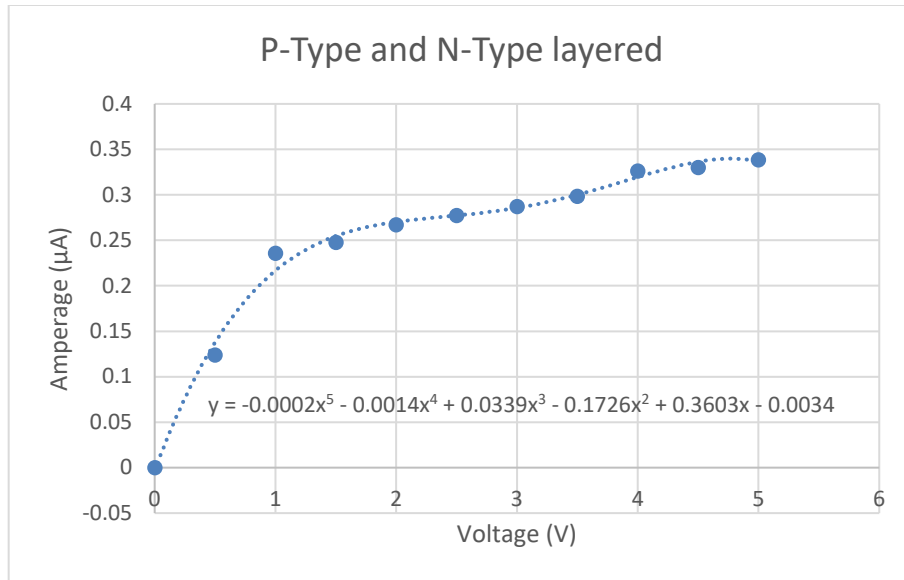


Fig. 5: P-type layered over N-type; Total Thickness: 750 microns

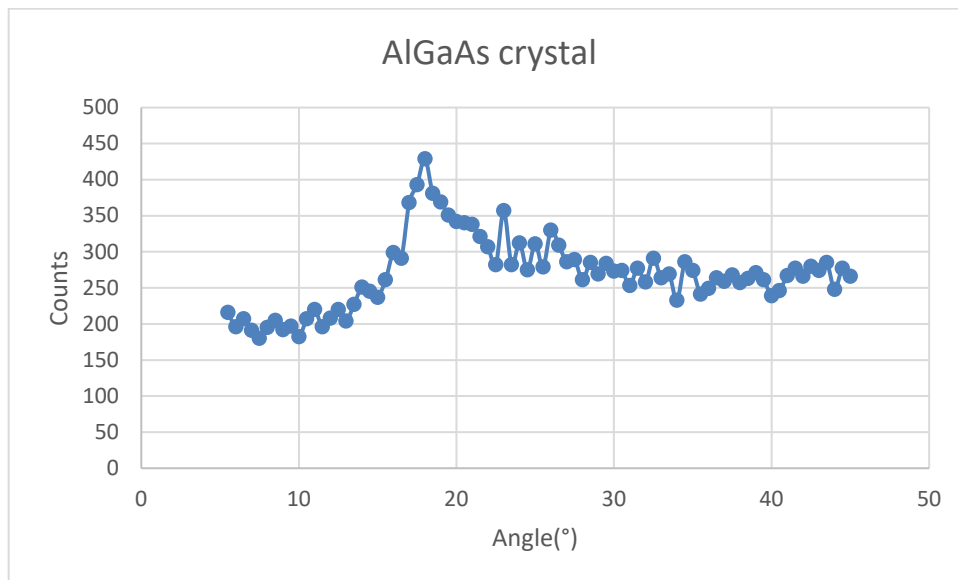


Fig. 6: Aluminum Gallium Arsenide Crystal from 889 nm diode

REFERENCES

Cplai. "How Do They Make Silicon Wafers and Computer Chips?" *YouTube*. YouTube, 05 Mar. 2008. Web. 01 June 2016. <<https://www.youtube.com/watch?v=aWVyhzuHnQ>>.

Hunter, Lloyd P., ed. *Handbook of Semiconductor Electronics; a Practical Manual Covering the Physics, Technology, and Applications of Transistors, Diodes, and Other Semiconductor Devices in Conventional and Integrated Circuits*. Third ed. New York: McGraw-Hill, 1970. Print.

Livingston, James D. *Electronic Properties of Engineering Materials*. p. 269-283. New York: Wiley, 1999. Print.

McKelvey, John Philip. *Solid State Physics for Engineering and Materials Science*. p. 372-439. Malabar, FL: Krieger Pub., 1993. Print.

"NSM Archive - Aluminum Gallium Arsenide (AlGaAs) - Band Structure and Carrier Concentration." *NSM Archive - Aluminum Gallium Arsenide (AlGaAs) - Band Structure and Carrier Concentration*. NSM. Web. 02 June 2016.

<<http://www.ioffe.ru/SVA/NSM/Semicond/AlGaAs/bandstr.html>>.

"Timeline." *The Silicon Engine: A Timeline of Semiconductors in Computers*. Semiconductor Special Interest Group. Web. 02 June 2016.

"Wafer Fabrication: Doping Techniques." *Halbleitertechnologie Von A Bis Z*. Halbleiter. Web. 01 June 2016.

Anderson, Hayley. "Transmission Electron Microscope (TEM) - Uses, Advantages and Disadvantages." *Transmission Electron Microscope (TEM) - Uses, Advantages and Disadvantages*. MicroscopeMaster, 2010. Web. 11 July 2016.

"Arsenic and Gallium Arsenide Are Fundamental to Semiconductor (Microchip) Manufacturing." *European Semiconductor Industry Association*. European Electronic Component Manufacturer's Association, Aug. 2007. Web. 7 July 2016.

Agrawal, Govind P. Dutta, Niloy K. *Semiconductor Lasers*. Second ed. New York: Van Nostrand Reinhold, 1993. Print.

EpicPhysics. "Laser Diodes - How It Works." *YouTube*. YouTube, 04 May 2012. Web. 10 July 2016.

Undergraduate Research Fellowships Reports

IMPROVEMENTS OF APPLICATION FOR PREDICTING CHEMICAL CONCENTRATIONS AND ADDITIONAL CONTAMINANTS IN WATERWAYS FOR RAPID RESPONSE TO CHEMICAL SPILLS

Mark Adkins
Computer Science
Marshall University
Huntington, WV

ABSTRACT

With the vast amount of chemical plants in the world, chemical spills are almost a guarantee in modern society. These chemical spills are a serious threat to the natural life surrounding them. In response to a chemical spill that affected the Elk River and surrounding areas, officials desired a less time-consuming, more lightweight application to simulate chemical spills in order to respond appropriately. As a result, previous students and faculty at Marshall University began working on an application that could provide this simple solution to public officials. Supported by the DOW chemical company, they developed a chemical simulator that was quick and required less training and expertise than the higher market tools. This is an expansion of that application that sought to include other containments and improve the accuracy of the simulation. After possibly considering including algae, we decided our model was not suitable and primarily focused on improving the accuracy of our results for chemicals.

INTRODUCTION

On January 9, 2014, around 5,000 gallons of MCHM leaked into the Elk River, impacting 300,000 customers [2]. Then, on January 14, 2014, the city of Cincinnati, OH closed off the water intakes while the spill passed by in the Ohio River [3]. Next, on January 17, 2014, the crisis was declared over, and the “Do-Not-Use” order was lifted [4]. Later, on January 27, 2014, the final Kanawha County water distribution site closed [5]. Lastly, and most unfortunately, on January 31, 2014, unacceptable, dangerous levels of MCHM were found in five schools in the affected area [6].

During this crisis, several problems occurred in the handling of important procedures. The officials had no quick way of predicting when the stream concentration would reach unacceptable levels [1]. Closing the water intakes 200 miles downstream showed perhaps too much caution [2]. The “do-not-use” ban was lifted prematurely [6]. There was also limited information available regarding the level of toxicity [1].

At the time, the U.S. Environmental Protection Agency provided several complex programs that could have predicted the chemical concentration [7]. However, many of these applications require not only specialization but a large time commitment to use [7]. As a result, many of these programs are unsuitable if a quick safety decision is needed from officials and first responders [1].

In response to this, Marshall University, with support from DOW, created a robust, lightweight application using Visual Studio to provide officials with the information needed to make a quick decision after a chemical spill [1]. The results are still inaccurate in regards to the complex programs; in particular, due to an inability to accurately calculate width, many of our test numbers

have fallen far outside the error margin. However, using Google Maps, the width of the river can be calculated as the distance between two points; this should improve the accuracy of the simulation.

Most of the setup for the application is the same from previous versions. The user provides the information for the spill, and then, they provide information for each point they select across the river [1]. However, when it comes time to enter the data for the river, there is now an option to open a Google Map at that specific point. From there, the user may click two points adjacent from one another on the river, and the width will be calculated as the distance between them. This may be done for each point as seen in figure 1.1.

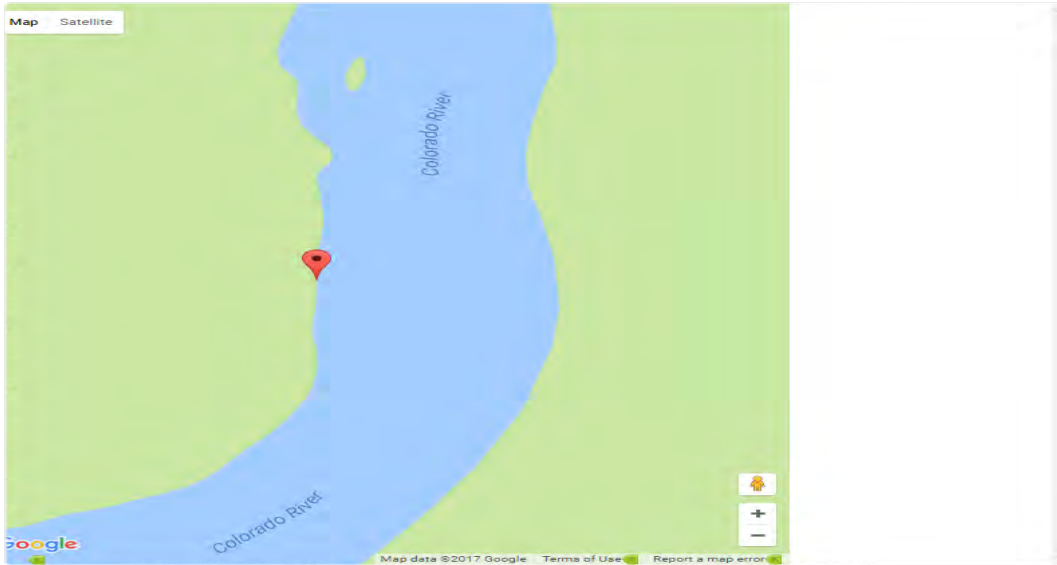


Figure 1.1 Google Maps before second point is selected for width calculation.

IMPLEMENTATION

Using the previous application, the implementation still uses the mathematical model described by Neely, Blau, and Turner [8]. The model uses the following equation:

$$V_n \frac{dC_n}{dt} = q(C_{n-1} - C_n) - k_e A C_n \quad | \quad n \geq 2$$

In this equation, C_n is the uniform contaminant concentration in the n th compartment at time t , V_n is the volume of the n th compartment, q is the volume flow of the river, k_e is the rate constant for the evaporation of the contaminant in units of depth/time, and A is the surface area of the compartment [8]. This equation has been implemented into the application already from previous versions.

These values are calculated across the app. First, you need the simulation time. This is how long one would like the simulation to last. One must also input how long each iteration will last in order to trace the spill across the river. For example, if the provided time was 24 hours, each iteration could last 30 minutes. This would allow the user to check the progress of each compartment at 30 minute intervals.

Next, the user will trace the desired spill route on a Google Maps. This allows the user to directly pinpoint the locations they wish to examine further should a spill occur. After selecting the path, the user must input the details for each marked point at every iteration. Conversely, the user may fill out one iteration and use those values for all others.

With the provided information above, we now calculate the river width, which is vital for both the volume and surface area of each compartment, using the Google Maps API method for calculating the physical distance between two latitude and longitude points expressed in meters. With this new addition, our results are closer to actual simulated results.

Afterwards, the user inputs the parameters for the spill including how many gallons and how long the spill occurred. This finishes all the needed variables for the mathematical model. The final page shows the results of the simulation and allows the user to proceed through each interval and examine how contaminated each marked point is.

RESULTS

We utilized a previous simulation to compare the results of the new width method.

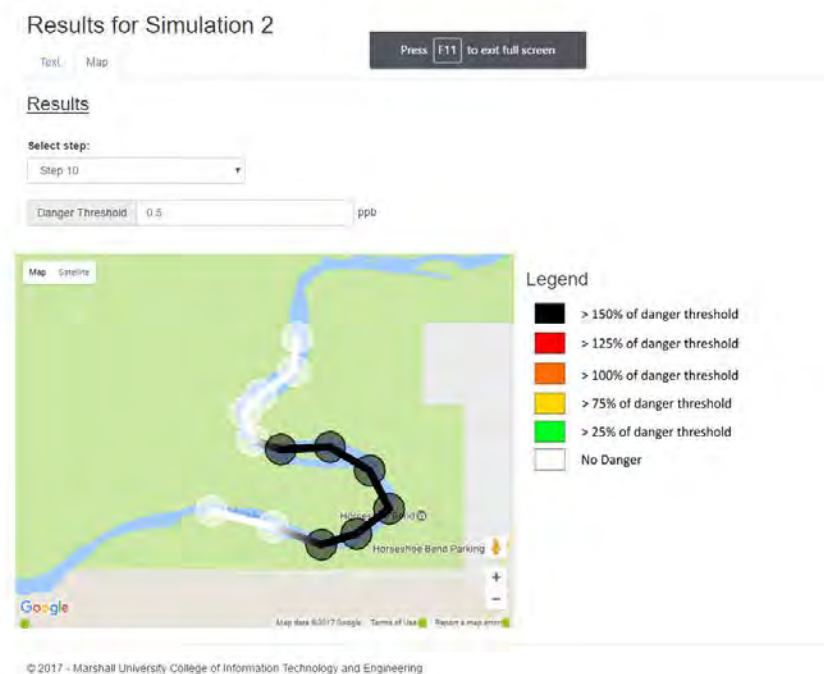


Figure 1.2 Results using hard-estimated width values.

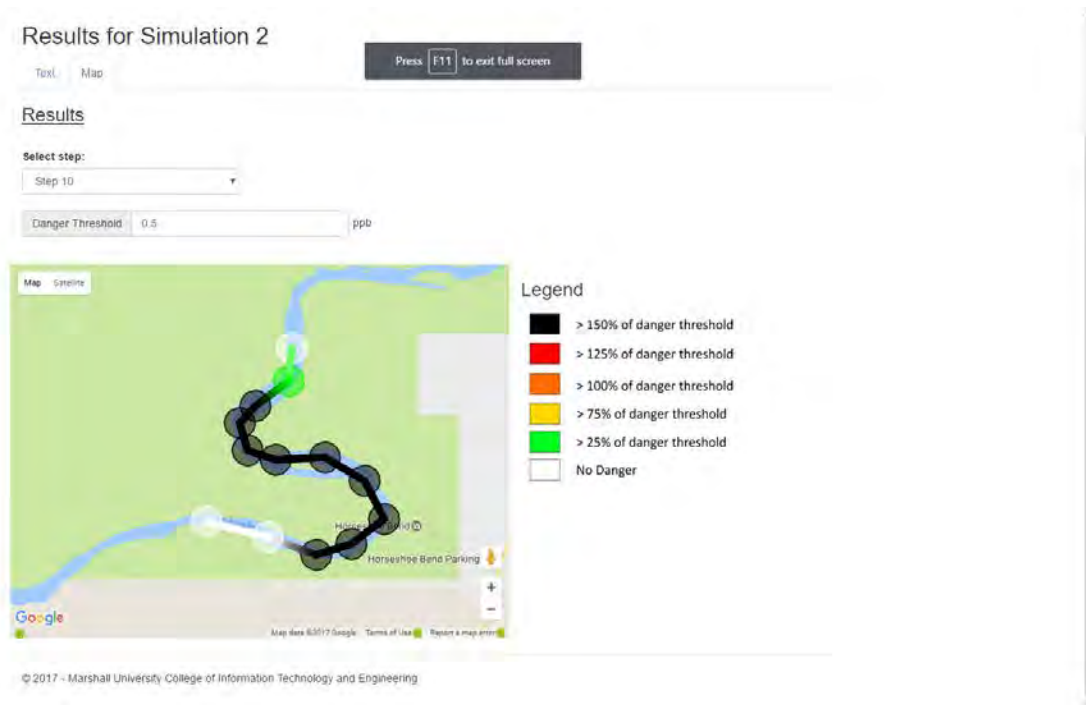


Figure 1.3 The simulation results after improving the width calculation.

The simulation in question for both figures 1.2 and 1.3 was of the Elk River. The chemical volume spilled in the simulation was 15000 gallons, and the simulated spill occurred for 3 hours. The river data was retrieved using USGS data. The width for figure 1.2 was estimated from a previous attempt while figure 1.3 was calculated using the new width method utilizing Google Maps. Both simulations are at step 10 with a danger threshold of 0.5 ppb.

DISCUSSION

Using the new method for finding river width, our average river width fell closer to the average provided by NASA's satellite calculations [9]. Originally, our river width measurements were highly underestimated. Now, they fall between the estimated values of 400-900 feet at different locations across the Elk River. This in turn has produced much better looking results as seen in figure 1.3.

Considering that the original estimates for the width of the river were below 100 feet, it is safe to assume that the second figure is more accurate in terms of how dangerous each compartment is. This is also verified by how the compartments are actually decreasing in danger instead of going straight from dangerous to safe. The new widths demonstrate progressive decreasing in how much of the dangerous chemical is present.

During the research project, the result of the investigation of the Freedom Industries spill was released to the public. We quickly found the public record and tried to use the water test found in the report to compare with our own [10]. Unfortunately, the report did not include the specifics of the river, so perfectly recreating the test was impossible. However, while not much, we did notice the general trend of our simulation matched the model from the report [10]. Without knowing the actual values used for the simulation, however, this leads to nothing conclusive.

While including a reliable method for calculating the width has strengthened the results, the overall time cost and real-world accuracy still leave a lot to be desired. The process could be streamlined to be more intuitive and less confusing for the user. Surprisingly, real world data for spill simulations is hard to find, so we lack a real basis to compare our results with. The current mathematical model could also be improved as it only always for one input. In a real crisis, there could possibly be several inputs of a chemical spill. There is still a lot of improvement for the application; however, with all our data closer in accuracy, we can be sure we are getting closer to simulating a real chemical spill.

CONCLUSION

With the addition of calculating width using Google Maps, the results of our chemical spill simulator grow closer to being more accurate and usable. However, a lack of test data leaves the actual results inconclusive. The user interface could use improvements, and the overall speed of the application needs improvement. While it still seems a less time-consuming application than the popular tools today, the application still requires a lot of time to properly utilize.

ACKNOWLEDGEMENTS

I would like to acknowledge and thank the NASA WV Space Grant Consortium for providing the grant and support.

I would also like to acknowledge and thank my research mentor Dr. Paulus Wahjudi for providing guidance throughout the project.

PRESENTATIONS

The application will be presented alongside a poster at the Marshall University CSSET event on April 25th, 2017.

REFERENCES

- [1] Davis, Daniel and Paulus Wahjudi. (2014). Simplified Concentration Prediction for Rapid Response to Chemical Spills. Retrieved January 20, 2017.
- [2] Ward, K. (2014, January 10). Freedom Industries cited for Elk chemical spill. The Charleston Gazette. Retrieved January 20, 2017.
- [3] Johnson, C. (2014, January 14). Spill posed no threat to Ohio River communities. The Herald-Dispatch.
- [4] LATEST: Do Not Use order lifted for remaining areas. (2014, January 27). West Virginia Illustrated. Retrieved January 20, 2017
- [5] Nuzum, L. (2014, January 27). Kanawha distributes final round of water. The Charleston Gazette.
- [6] Staff, M. (2014, January 31). Five schools tested show higher levels of MCHM. MetroNews.
- [7] Sharma, D., & Kansal, A. (2012). Assessment of river quality models: A review. Reviews in Environmental Science and Biotechnology, 12, 285-311.

- [8] Neely, W., Blau, G., & Turner, A. (1976). Mathematical models predict concentration-time profiles resulting from chemical spill in a river. *Environmental Science and Technology*, 10(1), 72-76.
- [9] NASA. (2015, July 9). A Satellite View of River Width. Retrieved on April 15, 2017. Retrieved from <https://earthobservatory.nasa.gov/IOTD/view.php?id=86172>.
- [10] U.S. Chemical Safety and Hazard Investigation Board. (2016). Chemical Spill Contaminates Public Water Supply in Charleston, West Virginia. Retrieved on November 4, 2016.

MODIFICATIONS OF THE SURFACE OF ZINC OXIDE NANOPARTICLES IN ORDER TO INCREASE EFFICIENCY OF SOLAR CELLS

Grayce Behnke
Forensic Chemistry
Marshall University
Huntington, WV

ABSTRACT

Self-assembled monolayers (SAMs) are molecules that bind to solids through adsorption and are incredibly useful due to their ability to greatly change the chemical and physical properties of surfaces, such as those of ZnO nanoparticles. ZnO specifically has a large variety of properties that are suitable for surface modification, including a wide band gap (3.37 eV), high exciton binding energy (~60 meV), and stable wurtzite structure. Through the process of SAMs, the surfaces of ZnO nanoparticles are modified with either 16-phosphonohexadecanoic acid or 11-phosphonoundecanoic acid and chemically bonded with 5-aminofluorescein, in order to serve as a fluorescent marker that can be used for determining the new properties of the modified surface. The sample concentration and use of “linker” molecules will be altered in order to determine the optimum conditions for the modifications to the ZnO surface and the success of modification will be determined using infrared spectroscopy, dynamic light scattering, zeta potential, ultraviolet-visible spectroscopy, scanning electron microscopy, and electrochemistry. Ultraviolet-visible spectroscopy was used to determine the band gap of the surface modified nanoparticles and initial results indicate a lower band gap, which would yield an increase in conductivity making ZnO ideal for solar cells.

INTRODUCTION

Self-assembled monolayers (SAMs) are molecules that bind to solids through adsorption. SAMs can be used as sensors for lethal bacterial enzymes, pH and conductivity indicators, biological imaging, limitation of corrosion, and as a biomaterial substrate.³⁻⁹ SAMs are incredibly useful in facilitating the binding of molecules to the surface of a metal, like zinc oxide (ZnO) which can significantly change chemical and physical properties of the metal oxide.¹⁰ ZnO specifically has a large variety of properties that can be altered through surface modification. These properties include a wide band gap (3.37 eV), high exciton binding energy (~60 meV), and stable wurtzite structure.¹⁰ After binding an organic compound to a ZnO surface, a fluorescein, specifically 5-aminofluorescein, will be attached to the organic molecule in order to serve as a visual method

for determining the new properties of the modified surface.⁸ 5-aminofluorescein has a maximum wavelength of absorption at 496 nm, which can shift the absorption of our complex into the visible region, allowing for new and unique characteristics. By changing the properties of the ZnO surface layer, solar cell efficiency can be increased in order to improve conduction and decrease corrosion.

Solar cells, such as the inverted, heterogeneous solar cell seen in Figure 1, are important for improving the

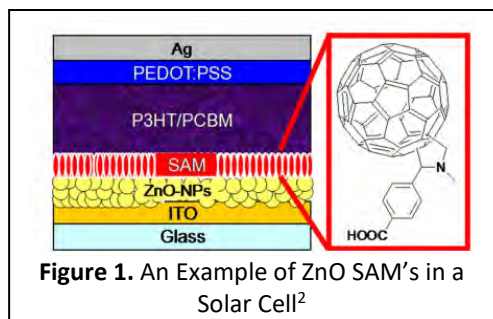
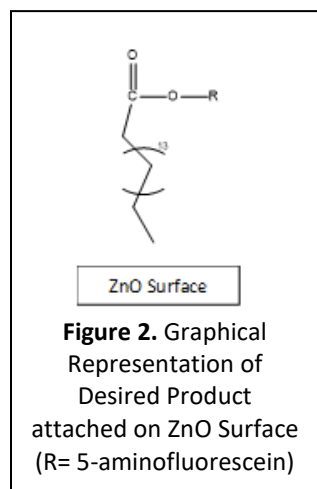
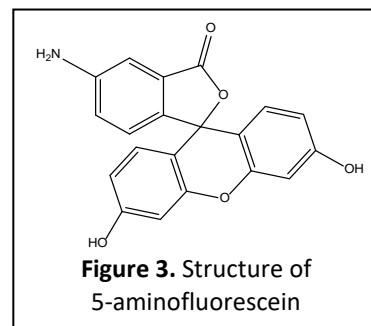


Figure 1. An Example of ZnO SAM's in a Solar Cell²

environment. They require no additional fuel sources beyond the energy required to construct them, as they rely on energy from the sun. While several alternative energy sources exist, all have major disadvantages when compared to solar power. Using solar power reduces the power needed from fossil fuel power plants, which produce dangerous emissions. In West Virginia, a main source of energy is coal, but coal mining leaves behind large amounts of waste that are devastating to the local environment. Increasing the United States' usage of solar energy would allow more independence from the nations that are currently relied upon to provide fuel sources such as oil.¹¹ Using solar power also reduces the power needed from nuclear plants reducing dangerous nuclear waste, which is difficult to dispose of due to its long half-life and shielding needs. The United States is currently the world's largest producer of nuclear power and accounts for more than 30% of worldwide nuclear generation of electricity. There are currently 100 nuclear reactors in the United States that produced over 798 billion kilowatts of energy per hour in the year 2014, creating large amounts of nuclear waste in the process.¹² While solar cells already exist and are being used, there are significant improvements to current technology that can be made in order to increase power efficiency. Several major companies, such as SunPower, Panasonic, Sanyo, SolarCity and Suniva are all in competition to produce the most efficient solar cells. As recently as October 2, 2015, SolarCity issued a press release indicating they have created the world's most efficient solar panel that utilizes an oxide as the middle layer of the solar cell that utilizes thin film passivation layers.¹³ Increasing the efficiency of solar cells through the usage of SAMs is a very prevalent area of study that will allow independence from fuel sources that damage the environment or are not locally available. The surface modifications of ZnO will increase efficiency by changing the properties of the solar cell and will decrease the corrosion that occurs, while maintaining a cost-efficient reaction process.



There are several possible ways to conduct the binding of molecules to the surface of ZnO. The binding of 16-phosphonohexadecanoic acid (16-COOH-PA) and 11-phosphoundecanoic acid (11-COOH-PA) to the surface of the ZnO nanoparticles occurs as self-assembled monolayers.^{6-7, 10} Of the two different phosphonic acids, 16-COOH-PA is thought to be the best option to bind to the ZnO surface as it has a longer carbon chain, which will allow for more intermolecular forces, stabilizing the surface of the nanoparticle. After the 16-phosphonohexadecanoic acid is attached to the surface, a 5-aminofluorescein will be attached through nucleophilic substitution (Figure 2). The 5-aminofluorescein (Figure 3) will be used to perform additional tests to determine the properties of the modified surface, such as the type of attachment that has occurred. The 5-aminofluorescein will also be used to create a correlation of pH increasing with fluorescence.⁹ If this does not work, then the alternative is to attach a 5(6)-carboxyfluorescein to the 16-phosphonohexadecanoic acid, but the heavy atom effect will prevent this method from yielding the best results. While there are several methods to modify the surface of the ZnO solid, the 16-phosphonohexadecanoic acid and 5-aminofluorescein path is expected to yield the highest efficiency and limit corrosion of the solar cells.



EXPERIMENTAL SECTION

Materials

16-phosphonohexadecanoic acid (16-COOH-PA, 97% purity), 11-phosphonoundecanoic acid (11-COOH-PA, 96% purity), fluoresceinamine (pure), and ZnO nanopowder were purchased from Aldrich. The reported average particle size of the ZnO nanopowder is less than 100 nm with a BET surface area of 15-25 m²/g. Tetrahydrofuran (THF, Optima grade) and ethanol (190 proof) were purchased from Pharmo-Aaper. All chemicals were used without further purification.

Formation of the Monolayers

SAMs were formed on the surface of the nanoparticles by sonicating 300 mg of ZnO nanopowder in 30 mL of THF for 15 minutes. A surfactant solution, formed by sonicating 7.5 mM of either 11-COOH-PA or 16-COOH-PA in 6 mL of THF for 15 minutes, was prepared. The well-dispersed nanopowder was added to the surfactant solution and then the nanoparticle/surfactant solution was sonicated without heat for 15 minutes. The sample was left to stir under a fume hood overnight with the lid on and then the lid was removed and the sample was allowed to stir for another 24 hours. A 10 mM solution containing 5-aminofluorescein was created in 10 mL of THF in a vial wrapped in aluminum foil to prevent light from entering the sample. The mixture was added to a dried ZnO-11-COOH-PA or ZnO-16-COOH-PA and sonicated for 15 minutes in the dark. Then the solution was allowed to stir on ice for 2 hours. Following this procedure, the solution was vacuum centrifuged at 30°C for 1 hour. Since a physically adsorbed layer can be formed, the modified particles were rinsed and sonicated again in 15 mL of THF for 15 minutes and then centrifuged to remove weakly bound molecules from the ZnO surface.¹⁴

Attenuated Total Reflectance Infrared Spectroscopy (ATR-IR)

ATR – IR was performed using a Thermo Scientific Nicolet iS50 FT-IR and was used to analyze the alkyl chain ordering and bonding motif of the molecules to the surface. The unmodified ZnO nanoparticles were used to collect a background spectrum for analysis purposes. Typically, 256 scans were collected with a resolution of 2 cm⁻¹.

X-Ray Photoelectron Spectroscopy (XPS)

XPS measurements were performed with a PHI 5000 VersaProbe ESCA Microprobe system (ULVAC-PHI) using a focused Al K-Alpha X-ray source at 1486 eV energy and 25 W with an X-ray spot size of 100 μm. The take-off angle of the photoelectron was set at 45°. An analyzer pass energy of 117.4 eV was used for a survey scan, and high-resolution scans for zinc, oxygen, and carbon elements were carried out at an analyzer pass energy of 23.5 eV. The XPS spectra were referenced to the C1s peak at a binding energy of 117.40 eV.

Scanning Electron Microscope with Energy-Dispersive X-ray Spectroscopy (SEM/EDS)

SEM/EDS was performed with a JEOL 5310-LV (Low Vacuum) with Backscattered Electron Detector, Cathodoluminescence Detector, and Oxford Instruments Pentafet X-Ray Detector (EDS) with Isis Analysis Hardware/Software. The SEM uses Printerface Image Capture Software. Samples were prepared individually in pin stubs and sputtered with a 10-nm thin coat of gold/palladium. SEM/EDS was used to analyze the surface composition of the nanoparticles and obtain information about particle size and elemental composition. The size distribution of the nanoparticles was calculated from the size measurements of 20 nanoparticles using ImageJ.

Dynamic Light Scattering (DLS) and Zeta Potential Measurements

A Brookhaven ZetaPlus Potential Analyzer (90Plus PALS) was used to perform DLS and zeta potential measurements of the unmodified and modified ZnO nanoparticles. The measurements were performed at 25 °C in water and THF. For DLS, at least three measurements were made for each sample and the collected values were averaged. For zeta potential, 10 measurements were made for each sample and the collected values were averaged. The Zeta Potential Analyzer was employed to determine the direction of particles under the influence of an electric field, allowing the estimation of the zeta potential of the ZnO suspensions under water and THF.

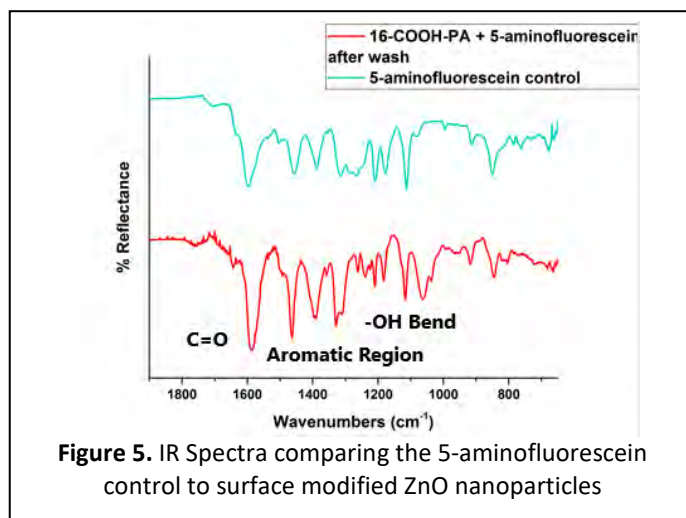
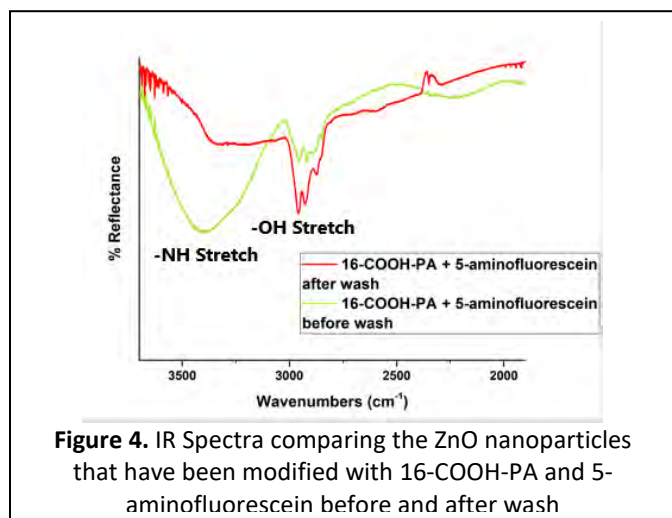
Ultraviolet-Visible Spectroscopy (UV-Vis)

An Agilent Cary 50 Bio UV-Visible Spectrophotometer was used to perform band gap analysis of unmodified and modified ZnO nanoparticles. 5 mg of sample was dissolved in 10 mL of dimethyl sulfoxide and diluted so that the absorbance was less than 1. Three measurements were made using a scan rate of 4800.0 nm/min and a scan wave range of 225-600 nm and results were averaged.

RESULTS AND DISCUSSION

Attenuated Total Reflectance Infrared Spectroscopy (ATR-IR)

The vibrations obtained from ATR-IR are the fastest way to determine if the surface of a molecule has been altered. An IR spectra obtained from the combination of the ZnO surface and the 16-COOH-PA would not yield any bands in the aromatic region as there are no aromatic structures present prior to the addition of 5-aminofluorescein. However, bands would appear as an O–H stretch from 3300-2500 cm^{-1} , a C=O stretch from 1760-1690 cm^{-1} , a C–O stretch from 1320-1210 cm^{-1} , and an O–H bend from 1440-1395 and 950-910 cm^{-1} due to the carboxylic acid at the unbound end of the 16-COOH-PA. An IR spectra obtained of the final product should yield bands in the aromatic region around 3030 cm^{-1} and between 1600 and 1500 cm^{-1} due to the attachment of 5-aminofluorescein. As seen in Figure 4, after modification and subsequent rinsing in order to ensure a strong adsorption, there is still a peak in the N-H region, which indicates that the amine group from the 5-aminofluorescein has remained intact. Additionally, as seen in Figure 5, two new peaks emerge, that do not exist in the 5-aminofluorescein control, after the 16-COOH-PA and 5-



aminofluorescein are attached to the ZnO surface, which proves that a bond has in fact formed between the amino group of the 5-aminofluorescein and the carboxylic group of the 16-COOH-PA.

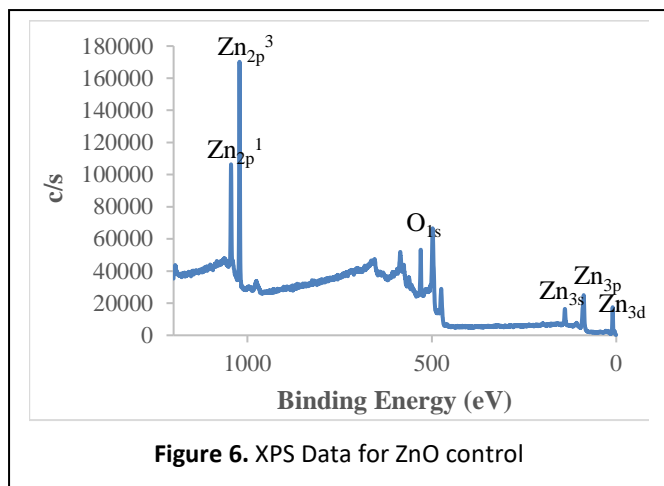


Figure 6. XPS Data for ZnO control

X-Ray Photoelectron Spectroscopy (XPS)

XPS uses soft x-rays (with a photon energy of 200-2000 eV) to examine core-levels of molecules and the way in which they are chemically bound. Figure 6, which is the ZnO control spectra, only shows peaks for Zn and O as is expected. In Figure 7, which is the ZnO-11-COOH-PA-5-aminofluorescein, a carbon peak is present due to the 11-carbon chain. The nitrogen and phosphorous peaks are not present, which may be due to the fact that relative to the structure of the molecule, there are fewer nitrogen and phosphorous

atoms, which could lead to shadowing by another element which is present in a larger quantity.¹⁵

Scanning Electron Microscope with Energy-Dispersive X-ray Spectroscopy (SEM/EDS)

SEM/EDS assisted in the visualization of the ZnO nanoparticles and identified the elemental composition of the modified ZnO nanoparticles. The SEM images (Figure 9A, 9B, and 9C) indicate a distribution of particle sizes with typical particle diameters < 250 nm and no visible change in the spherical morphology of the nanoparticles after the modifications. The diameter of the modified nanoparticles is larger than the diameter of the unmodified nanoparticles and the results are summarized in Table 1. The ZnO nanoparticles modified with either 11-COOH-PA or 16-COOH-

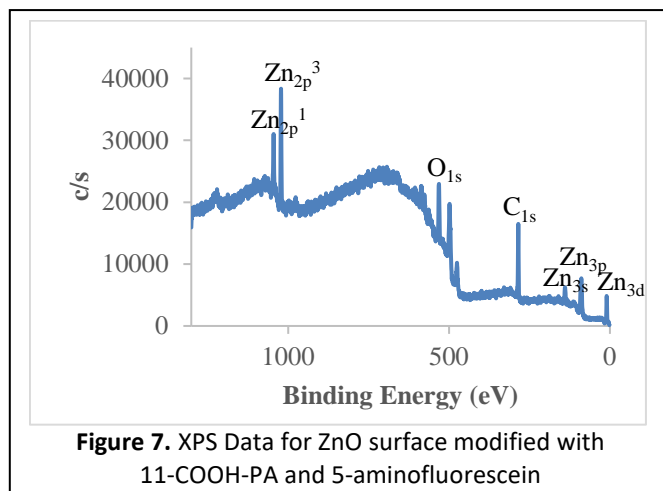
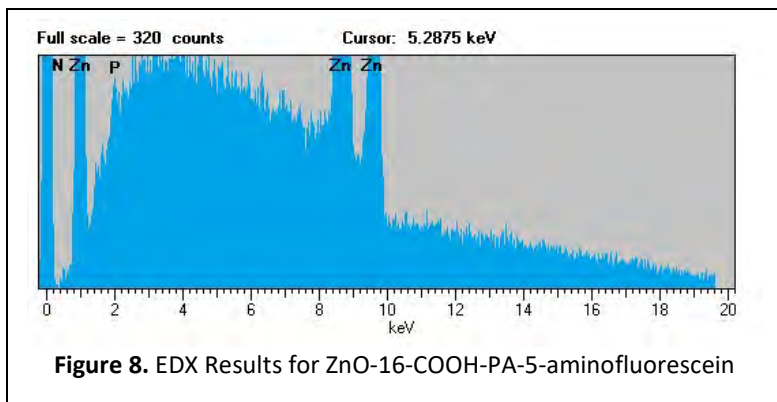


Figure 7. XPS Data for ZnO surface modified with 11-COOH-PA and 5-aminofluorescein

Table 1. Average Particle Sizes obtained using SEM

| Modifications | Average Particle Size(nm) | Particle Distribution (± nm) |
|-----------------------------------|---------------------------|------------------------------|
| ZnO | 167 | 31 |
| ZnO-11-COOH-PA | 189 | 62 |
| ZnO-16-COOH-PA | 223 | 56 |
| ZnO-11-COOH-PA-5-aminofluorescein | 227 | 62 |
| ZnO-16-COOH-PA-5-aminofluorescein | 239 | 75 |

PA are larger than the ZnO control nanoparticles, with the 11-COOH-PA being slightly smaller than the 16-COOH-PA, which is expected due to the shorter carbon chain. Following modification with 5-aminofluorescein, the particle size is again seen to increase. This is likely due to the fact that another layer, one that is highly rigid and aromatic, has been added to the surface of the nanoparticles.

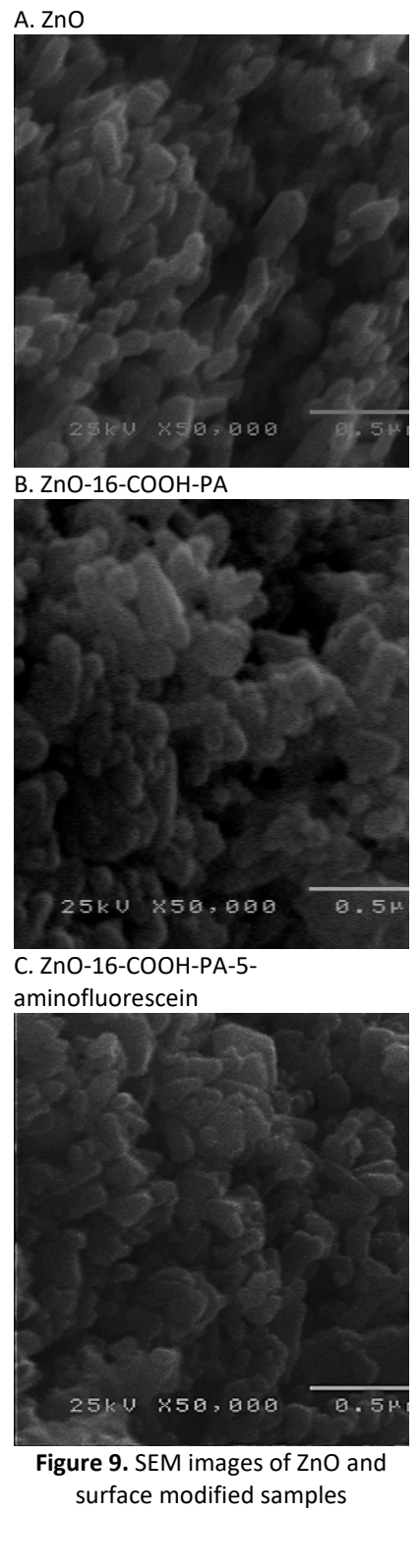


Following modification using the 5-aminofluorescein in both 11-COOH-PA and 16-COOH-PA an increase in particle sizes is seen. The particle agglomeration from the modified particles is likely due to an increase of interaction between the particles and the charge on the surface of the particles, which was confirmed using zeta potential analysis (see below). Furthermore, as the films are closely packed, breaking the particle agglomerations becomes difficult, affecting the particle distribution.¹⁶

EDS elemental analysis obtained in conjunction with the SEM images revealed the presence of zinc in the control ZnO samples and the phosphonic acid modified samples revealed the presence of phosphorous, indicating that attachment has occurred. In addition, the samples modified with 5-aminofluorescein indicate a small peak that may be indicative of the presence of nitrogen as observed in Figure 8. However, the analyzer has a beryllium filter on it, meaning that anything smaller than Na will not be effectively detected or identified.¹⁷

Dynamic Light Scattering (DLS) and Zeta Potential

DLS was used to measure the particle sizes of the unmodified and modified nanoparticles in water, ethanol, and THF. Ethanol, THF and water were selected due to their differing polarities. In addition, ethanol and water are polar protic and THF is polar aprotic. By observing the surface modified nanoparticles in several different solvents, we are able to determine how solvent dependent the particle size and zeta potential are. The SEM measurements indicate that the particles are significantly smaller (167 to 239 nm) than the results from DLS (245- 497 nm). These discrepancies may be due to the different methods and mathematical models used, the Brownian particle displacement of the particles in solution and the hydrodynamic diameter.^{16, 18} The hydrodynamic diameter is the



diameter of the particle and ligands, ions, or molecules that are associated with the surface and travel along with the particle in colloidal solution, increasing the average particle size.¹⁹ In the SEM images, the particles are on a solid surface, which essentially eliminates the counter ion effects and/or electrostatic interactions causing smaller particle sizes than those obtained from DLS (Table 2).

Table 2. Comparison of Particle Sizes using Different Solvents and Concentrations

| | Water | | THF | | Ethanol | |
|---------------------------------------|--------------------|---------------------|--------------------|---------------------|--------------------|---------------------|
| | Particle Size (nm) | Zeta Potential (mV) | Particle Size (nm) | Zeta Potential (mV) | Particle Size (nm) | Zeta Potential (mV) |
| ZnO | 497.2 +/- 12.2 | -11.09 +/- 0.42 | 413.2 +/- 18.0 | -11.48 +/- 4.40 | 306.9 +/- 4.0 | -28.12 +/- 0.60 |
| 11-COOH-PA | 245.5 +/- 5.7 | -16.95 +/- 0.34 | 431.3 +/- 17.0 | -18.40 +/- 4.48 | 297.1 +/- 1.3 | -36.50 +/- 0.81 |
| 11-COOH-PA -5-aminofluorescein | 247.6 +/- 4.6 | -22.31 +/- 0.37 | 258.1 +/- 1.2 | -53.67 +/- 2.50 | 273.0 +/- 1.0 | -36.87 +/- 1.02 |
| 16-COOH-PA | 339.0 +/- 9.8 | -23.48 +/- 0.41 | 282.5 +/- 1.1 | -42.55 +/- 2.40 | 300.0 +/- 2.7 | -36.67 +/- 0.92 |
| 16-COOH-PA -5-aminofluorescein | 279.3 +/- 10.6 | -23.26 +/- 0.29 | 323.4 +/- 3.4 | -42.23 +/- 1.98 | 330.9 +/- 1.7 | -35.75 +/-0.69 |

Zeta potential is the electrostatic potential difference between a rotationally averaged point at the shear plane and an average point within the liquid and can be correlated to the surface charge of the particle and the nature and composition of the surrounding medium in which the particle is dispersed.²⁰ It is calculated using Smoluchowski's equation: $\mu_{ep} = \epsilon_0 \zeta / \eta$ where μ_{ep} is the electrophoretic mobility, ϵ_0 is the dielectric constant of the liquid, ζ is the zeta potential, and η is the viscosity of the liquid. Due to surface modification, the zeta potential values became more negative, indicating greater stability. The phosphonic acid modifications were negatively charged, imparting a negative charge to the dispersed nanoparticles causing electrostatic repulsion between molecules, leading to increased stability.²¹⁻²² The zeta potential was highly solvent dependent as can be seen in the greatly varied zeta potential values for both the unmodified ZnO and the surface modified samples. The 11-COOH-PA-5-aminofluorescein samples were more stable than the 11-COOH-PA samples, according to the zeta potential values. The 16-COOH-PA-5-aminofluorescein samples had very little variation from the 16-COOH-PA samples, however, there was still a greater stability than the values obtained for unmodified ZnO.

Ultraviolet-Visible Spectroscopy (UV-Vis)

UV-Vis can be used to determine the band gap of a substance, which is the minimum energy required to excite an electron that is in its bound state into a free state in order to participate in conduction.¹⁰ Zinc oxide (bulk material) has a band gap is 3.3 eV and a large exciton binding energy (60 meV).¹⁰ By lowering the band gap, conductivity can occur more easily and as such this is ideal for solar cells. The maximum wavelength of absorption for 5-aminofluorescein is 496 nm. As can be seen in Figure 10, the maximum wavelength of irradiance of light from the sun is around 500 nm, which is why 5-aminofluorescein has been selected as the chromophore for this project. Additionally, dye-sensitized solar cells, with the sensitizer or chromophore being one of the key components, have attracted attention, due to their low cost and high sunlight-to-electric power-conversion efficiencies.²³

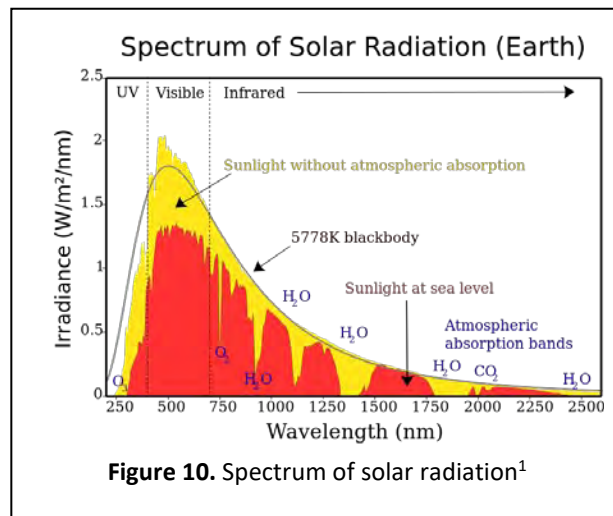


Figure 10. Spectrum of solar radiation¹

The data in Table 2 was obtained using Formula 1 and Tauc plots, which can be used to determine the optical band gap. It can be seen that mathematically the averages of the data obtained is lowest for the ZnO that was surfaced modified using both the phosphonic acids and the 5-aminofluorescein, which is indicative of potential increased performance if used in a solar cell.

$$E(eV) = \frac{hc}{\lambda} \times \left(6.242 \times 10^{18} \frac{eV}{J} \right)$$

Formula 1: Band gap calculation

Table 2. Average band gap data obtained mathematically and graphically

| Compound | Mathematical (eV) | Graphical (eV) |
|---------------------------------|-------------------------|------------------------|
| 16-COOH-PA + 5-aminofluorescein | 3.34 +/- 0.00252 | 3.08 +/- 0.0368 |
| 11-COOH-PA + 5-aminofluorescein | 3.34 +/- 0.00380 | 3.08 +/- 0.0262 |
| 11-COOH-PA | 3.34 +/- 0.00326 | 3.02 +/- 0.0163 |
| ZnO Control | 3.35 +/- 0.00266 | 3.07 +/- 0.0125 |
| 16-COOH-PA | 3.35 +/- 0.00609 | 3.09 +/- 0.0125 |

CONCLUSION

Zinc oxide nanoparticles were modified using 16-phosphonohexadecanoic acid, 11-phosphonoundecanoic acid, and 5-aminofluorescein through self-assembled monolayers. Using ATR-IR spectroscopy and XPS data, the phosphonic acid and 5-aminofluorescein molecules were found to attach and form strong, uniform covalent bonds on the surface of the ZnO nanoparticles. SEM and DLS were used to demonstrate the effects of the surface modifications on

the size of the ZnO nanoparticles before and after surface modification. Zeta potential was used to determine the stability of the nanoparticles in solution. This project proves that surface modification to ZnO nanoparticles can be accomplished easily in order to tailor the surface of ZnO to desired physical and chemical properties. After the attachment of the 5-aminofluorescein, the band gap was lower, which indicates that less energy would be required to excite electrons into a conductive state, leading to increased efficiency of potential solar cells.

Future work includes electrochemistry in order to determine if corrosion was decreased by making a stable product. This will be achieved using cyclic voltammetry and electrochemical impedance spectroscopy. After the attachment of 5-aminofluorescein there will be activity in the redox region in a cyclic voltammogram and if the peak current for the return potential scan is equal to the peak current for the forward potential scan then the product is stable. Electrochemical impedance spectroscopy can help to determine corrosion and semi-conductor abilities.

The surface modification of ZnO by 16-phosphonohexadecanoic acid and 5-aminofluorescein will increase efficiency by changing the properties of the ZnO nanoparticles and will decrease the corrosion that occurs, while maintaining a cost-efficient reaction process. By increasing the efficiency of solar cells, the usage of other more environmentally damaging power sources, such as fossil fuel and nuclear power, can be decreased. Solar power is a clean and renewable source of energy that is dependent on energy from the sun.

The most valuable aspects of this program were the hands-on-experience and opportunities to meet and interact with professionals in my field through funded travel, which has allowed me to network with people who have helped me immensely.

ACKNOWLEDGEMENTS

- NASA West Virginia Space Grant Consortium
- Marshall University Chemistry Department
- Dr. Rosalynn Quiñones
- West Virginia University Shared Research Facilities
- Marshall University SURE Program
- Marshall University Molecular and Biological Imaging Center
- Kentucky - West Virginia Louis Stokes Alliance for Minority Participation

PUBLICATIONS/PRESENTATIONS

Accepted Publication

- Quinones, R., Garretson, S., **Behnke, G.**, Fagan, J., Mueller, K. (2017) "Fabrication of Phosphonic Acid Films of Nitinol Nanoparticles by Dynamic Covalent Assembly." *Thin Solid Films*.

Presentations of Research

- Undergraduate Research Day at the Capital- February 24, 2017 (Poster)
- KY-WV LSAMP Symposium- March 4, 2017 (Oral)

- 253rd American Chemical Society National Meeting & Exposition- April 2-6, 2017 (Poster)

REFERENCES

1. Spectrum of Solar Radiation. Wikipedia, Ed. 2013.
2. Hau, S. K., Yip, Hin-Lap, Ma, Hong, Jen, Alex K.-Y, High performance ambient processed inverted polymer solar cells through interfacial modification with a fullerene self-assembled monolayer. *Applied Physics Letters* **2008**, *93*.
3. Frisk, M. L., Tepp, William H., Johnson, Eric A., Beebe, David J., Self-Assembled Peptide Monolayers as a Toxin Sensing Mechanism within Arrayed Microchannels. *Analytical Chemistry* **2009**, *81* (7), 8.
4. Zhou, Y. L., Zhi, J. F., Wang, P. F., Chong, Y. M., Zou, Y. S., Zhang, W. J., Lee, S. T., Surface functionalization of cubic boron nitride films for biological sensing applications. *Applied Physics Letters* **2008**, *92*, 3.
5. Manhat, B. A., Brown, Anna L., Black, Labe A., Ross, J.B. Alexander, Fichter, Katye, Vu, Tania, Richman, Erik, Goforth, Andrea M., One-Step Melt Synthesis of Water-Soluble, Photoluminescent, Surface-Oxidized Silicon Nanoparticles for Cellular Imaging Applications *Chemistry of Materials* **2011**, *23*, 12.
6. Quiñones, R., Gawalt, Ellen S., Polystyrene Formation of Monolayer-Modified Nitinol Effectively Control Corrosion. *Langmuir* **2008**, *24* (19), 7.
7. Raman, A., Gawalt, Ellen S., Self-Assembled Monolayers of Alkanoic Acids on the Native Oxide Surface of SS316L by Solution Deposition. *Langmuir* **2007**, *23* (5), 5.
8. Bidmanova, S., Hlavacek, Antonin, Damborský, Jiri, Prokop, Zbynek Conjugation of 5(6)-carboxyfluorescein and 5(6)-carboxynaphthofluorescein with bovine serum albumin and their immobilization for the optical pH sensing. *Sensors and Actuators B* **2011**, *161*, 7.
9. Miao, R., Mu, Lixuan, Zhang, Hongyan, Xu, Haitao, Zhou, Bingjiang, She, Guangwei, Wang, Pengfei, Shi, Wensheng, Facile Method for Modification of the Silicon Nanowires and Its Application in Fabrication of pH-Sensitive Chips. *ACS Applied Materials & Interfaces* **2013**, *5*, 6.
10. Quiñones, R., Rodriguez, Kate, Iuliucci, Robbie J., Investigation of phosphonic acid surface modifications on zinc oxide nanoparticles under ambient conditions. *Thin Solid Films* **2014**, *565*, 10.
11. Callahan, R. Why Are Solar Panels Important in Our Society <http://www.livestrong.com/article/151450-why-are-solar-panels-important-in-our-society/> (accessed 10/2/2015).
12. Nuclear Power in the USA. <http://www.world-nuclear.org/info/Country-Profiles/Countries-T-Z/USA--Nuclear-Power/> (accessed 10/8/2015).
13. Wesoff, E. Is SolarCity's New PV Module the 'World's Most Efficient Rooftop Solar Panel'? <http://www.greentechmedia.com/articles/read/Is-SolarCitys-New-PV-Module-the-Worlds-Most-Efficient-Rooftop-Solar-Pane> (accessed 10/2/2015).
14. Quiñones, R.; Rodriguez, K.; Iuliucci, R. J., Investigation of phosphonic acid surface modifications on zinc oxide nanoparticles under ambient conditions. *Thin Solid Films* **2014**, *565* (0), 155-164.
15. Berlin, J., Analysis of Boron with Energy Dispersive X-ray Spectrometry. *Imaging & Microscopy* **2011**, *13*, 19-21.

16. Feichtenschlager, B.; Pabisch, S.; Peterlik, H.; Kickelbick, G., Nanoparticle Assemblies as Probes for Self-Assembled Monolayer Characterization: Correlation between Surface Functionalization and Agglomeration Behavior. *Langmuir* **2012**, *28* (1), 741–750.
17. McCarthy, J., Friel, John, Camus, Patrick, Impact of 40 Years of Technology Advances on EDS System Performance. *Microscopy and Microanalysis* **2009**, *15*, 484-490.
18. Ling, X. Y.; Reinhoudt, D. N.; Huskens, J., Ferrocenyl-Functionalized Silica Nanoparticles: Preparation, Characterization, and Molecular Recognition at Interfaces. *Langmuir* **2006**, *22* (21), 8777-8783.
19. Kasva Anuradha, P. B., and Sunkara Sakunthala Madhavendra, Macromolecular Arabinogalactan Polysaccharide Mediated Synthesis of Silver Nanoparticles, Characterization and Evaluation. *Macromol. Res.* **2015**, *24* (2), 152-162.
20. Sizovs, A.; Song, X.; Waxham, M. N.; Jia, Y.; Feng, F.; Chen, J.; Wicker, A. C.; Xu, J.; Yu, Y.; Wang, J., Precisely Tunable Engineering of Sub-30 nm Monodisperse Oligonucleotide Nanoparticles. *J. Am. Chem. Soc.* **2014**, *136* (1), 234-240.
21. Schmitt Pauly, C.; Genix, A.-C.; Alauzun, J. G.; Guerrero, G.; Appavou, M.-S.; Pérez, J.; Oberdisse, J.; Mutin, P. H., Simultaneous Phase Transfer and Surface Modification of TiO₂ Nanoparticles Using Alkylphosphonic Acids: Optimization and Structure of the Organosols. *Langmuir* **2015**, *31* (40), 10966-10974.
22. Oueiny, C.; Berlioz, S.; Patout, L.; Perrin, F. X., Aqueous dispersion of multiwall carbon nanotubes with phosphonic acid derivatives. *Colloids Surf., A* **2016**, *493*, 41-51.
23. Seo, K. D., Song, Hae Min, Lee, Myung Jun, Pastore, Mariachiara, Anselmi, Chiara, Angelis, Filippo, Nazeeruddin, Mohammad K., Grätzel, Michael, Kim, Hwan Kyu, Coumarin dyes containing low-band-gap chromophores for dye-sensitised solar cells. *Dyes and Pigments* **2010**, *90*, 304-310.

MOLECULAR DYNAMICS INVESTIGATIONS OF FACTORS INFLUENCE SELF-ASSEMBLY OF DETERGENT MICELLES

Brittany Bonnett
Chemistry
Fairmont State University
Fairmont, WV

ABSTRACT

Although surfactants are used in a variety of applications (e.g., drug delivery, oil recovery, membrane protein solubilization), the molecular interactions that lead to their physical properties remain poorly understood. Our goal is to obtain a more thorough understanding of the underlying energy landscape of the self-assembly of detergent molecules in aqueous solution. All-atom molecular dynamics simulations of two detergent systems, n-dodecyl- β -D-maltoside (DDM) and a closely-related (epimeric) stereoisomer of DDM, were carried out to investigate factors influencing self-assembly of micelles. Explicitly solvated systems for each detergent range from 60 to 220 detergent molecules. The effects of starting configuration (pre-formed micelle, inverse micelle, and random assembly) and initial packing density have also been characterized. Analysis included aggregation number (AN), radius of gyration (R_g), moment of inertia (I), solvent accessible surface area (SASA), asymmetry parameter (α), and packing parameter (P). Our results show that system size and starting configuration have significant and sometimes unexpected effects on simulation time and observed micelle properties.

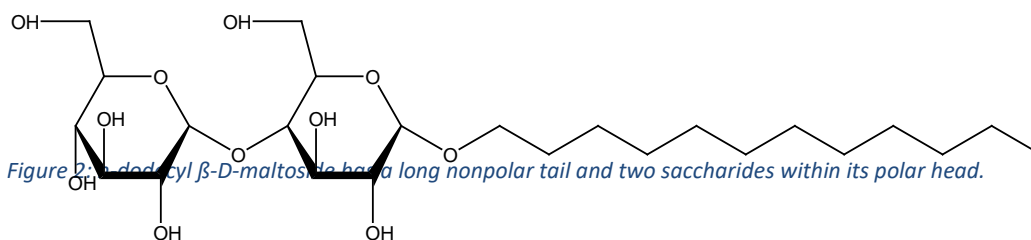
INTRODUCTION

The goal of this research project is to model selected micelles in order to validate the force field for detergent assemblies, as well as to investigate micelle configurations that will hold the bacterial membrane protein proteorhodopsin (PR). PR (Figure 1) is a photoactive protein that is primarily found in marine bacteria and acts as a proton pump.¹ The detergents chosen for study include n-dodecyl β -D-maltoside (DDM, Figure 2) and its stereoisomer n-dodecyl 1,4- β -D-allosyl-allose (DDAA, Figure 3), packed into configurations including pre-formed micelles, random assortments, and inverse micelles (Figure 4). Simulation jobs were submitted to West Virginia University's High Performance Computing (HPC) servers and, following stabilization, the resulting micelles were analyzed. All work was performed on the WVU HPC servers, a personal computer running Windows 10, and Bishop, a high-performance computer at Fairmont State University with a Linux-based operating system.



Figure 5: Proteorhodopsin is a membrane protein that acts as a proton pump.²

Avogadro, an open-source molecular-editing software, was initially used to build DDM. The software had its limitations, and it was discovered during the summer term that the detergent built was not DDM, but DDAA. As seen in a comparison between Figures 2 and 3,



DDM's saccharide rings have hydroxyl groups in an R-S-R conformation, while DDAA's hydroxyl groups have an R-R-R conformation. Analysis of various DDAA configurations was completed over the summer, and results were compared with those of a graduate student at West Virginia university working with DDM.³ It was discovered that DDAA tended to form micelles roughly within DDM's literature aggregation number range of 80-150 molecules⁴ with smaller clusters present, while the graduate student's DDM configurations formed micelles with no smaller clusters no matter the number of detergent molecules present. Because the initial DDAA configurations and the initial DDM configurations had possessed two different packing tolerances (distance between each detergent molecule) of 5 Å and 2 Å respectively, the focus of the fall research was investigation of the factors influencing self-assembly of the micelles.

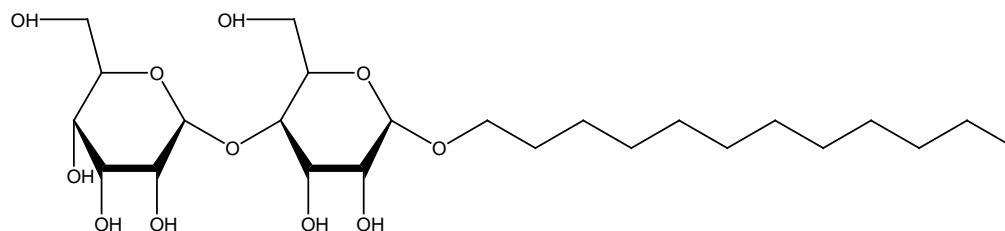


Figure 3: n-dodecyl 1,4- β -D-allosyl-allose has a very slight conformational difference from that of DDM. The hydroxyl groups have an R-R-R configuration instead of an R-S-R as seen in DDM.

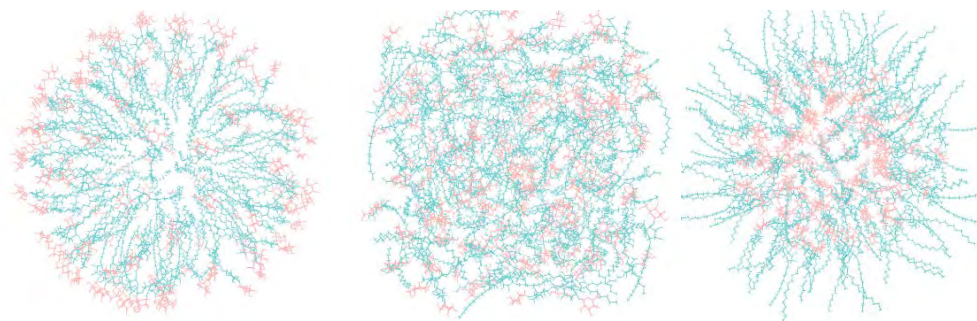


Figure 4: From left to right: a pre-formed micelle, a random assortment, and an inverse micelle of DDM.

Due to difficulties building the proper conformation of DDM in Avogadro, a DDM PDB from the Royal Society of Chemistry Protein Data Bank was downloaded and packed into micelles and random assortments in PackMol, a molecule-packing software.⁵ These configurations included the following: 60-molecule pre-formed micelle, 60-molecule random assortment, 80-molecule pre-formed micelle, 110-molecule random assortment, 130-molecule pre-formed micelle, and 200-molecule pre-formed micelle. More configurations were prepared by other undergraduate students

in the research group. The assemblies were prepared for simulations with VMD, a molecular graphics program that is used to visualize molecular structures,⁶ using the PSFgen extension, which generates a PDB (a file in Protein Data Base format that stores atomic coordinates and velocities) and a PSF (a file that stores a protein's structural information) of the system.⁷ The DDM configurations were ionized and solvated in VMD and heated to 310 K using NAMD, an open-source MD software package.⁸ Once the configurations were prepared, the simulation jobs were submitted to WVU's HPC servers with PBS scripts, which contains the code needed to queue jobs on the servers.⁹ Analysis was performed on configurations that have achieved ample simulation time using VMD's TKConsole, and data analysis extensions, and a rewrapping tool that centered the micelle within its periodic cell boundaries.

RESULTS

After roughly 150-200 nanoseconds of simulation time, the DDM micelles were analyzed using VMD extensions. Results of the analysis are collected in Table 1.

| Configuration and tolerance | Simulation time (ns) | AN | Average R_g (Å) | Average SASA ($\times 10^4 \text{ Å}^2$) | Average α | P |
|------------------------------------|-----------------------------|-----------|-------------------------------------|--|------------------------------------|----------|
| 60 pre-formed micelle, 2 Å | 206 | 60 | 18.7 ± 0.2 | 1.73 | 0.091 | 0.48 |
| 60 random assembly, 2 Å | 206 | 60 | 18.7 ± 0.4 | 1.17 | 0.10 | 0.48 |
| 80 pre-formed micelle, 2 Å | 206 | 80 | 20.3 ± 0.2 | 1.91 | 0.087 | 0.53 |
| 110 random assembly, 2 Å | 206 | 110 | 22.5 ± 0.2 | 2.34 | 0.11 | 0.59 |
| 130 pre-formed micelle, 2 Å | 182 | 130 | 23.7 ± 0.2 | 2.70 | 0.13 | 0.62 |
| 200 pre-formed micelle, 2 Å | 159 | 200 | 27.5 ± 0.2 | 3.40 | 0.20 | 0.72 |

Table 1 details the results of the analysis of the DDM configurations. Included are the simulation times in ns, AN (aggregation number), average R_g (radius of gyration), average SASA (solvent accessible surface area), average α (asymmetry parameter), and average P (packing parameter).

Plots of R_g , SASA, and α against time in ns were created in order to investigate micelle stability, which we are identifying as the point when the measured parameter levels out. Because this levelling behavior is most easily observed in plots of R_g versus time, it was determined that radius of gyration (the radius of the x, y, and z planes of the entire system in units of Ångstrom around the central axis of the micelle) was the most favorable parameter for defining stability. Calculated values of R_g for the DDM micelles (18-28 Å) are comparable with literature values of 23-26 Å.⁴ The R_g values that fall below literature values are theorized to arise from the fact that our R_g calculations do not include the water of hydration around the micelles.¹⁰ A strong upward trend is observed, with average R_g increasing with aggregation number.

R_g over time can be compared to visual representations of the micelle throughout the course of the simulation. In Figure 5, the radius of gyration of the 110 random assembly (**A**) has a spike at 115 ns, illustrated by the micelle breaking up in **B**. The R_g stabilizes again as the assembly forms a micelle (**C**).

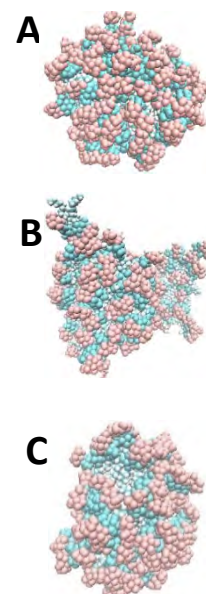
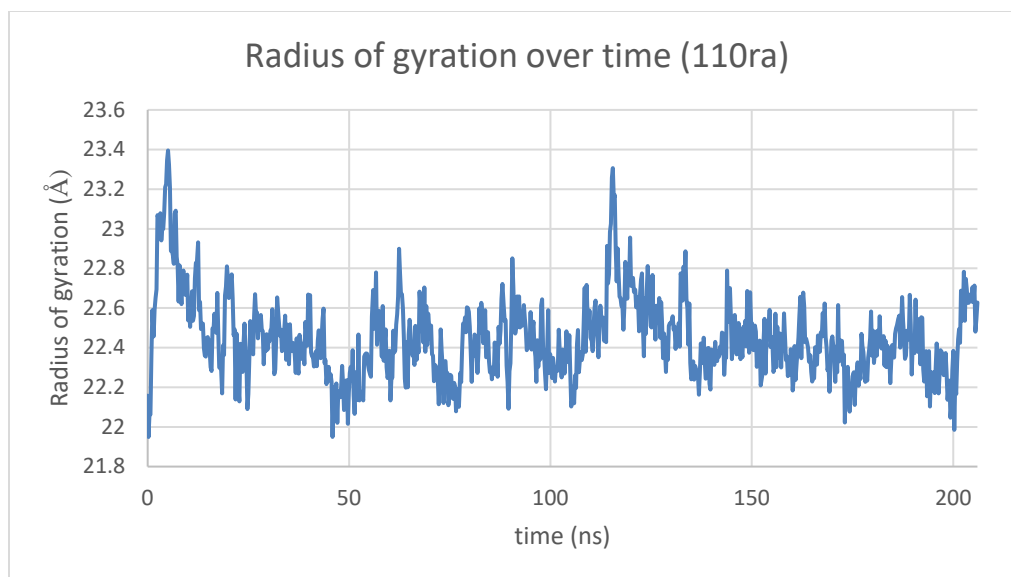


Figure 5: The radius of gyration of a 110-molecule DDM random assortment over time. This configuration (A, 0 ns) stabilizes rather quickly after a R_g spike at 115 ns (B), forming a micelle (C, ~125 ns).

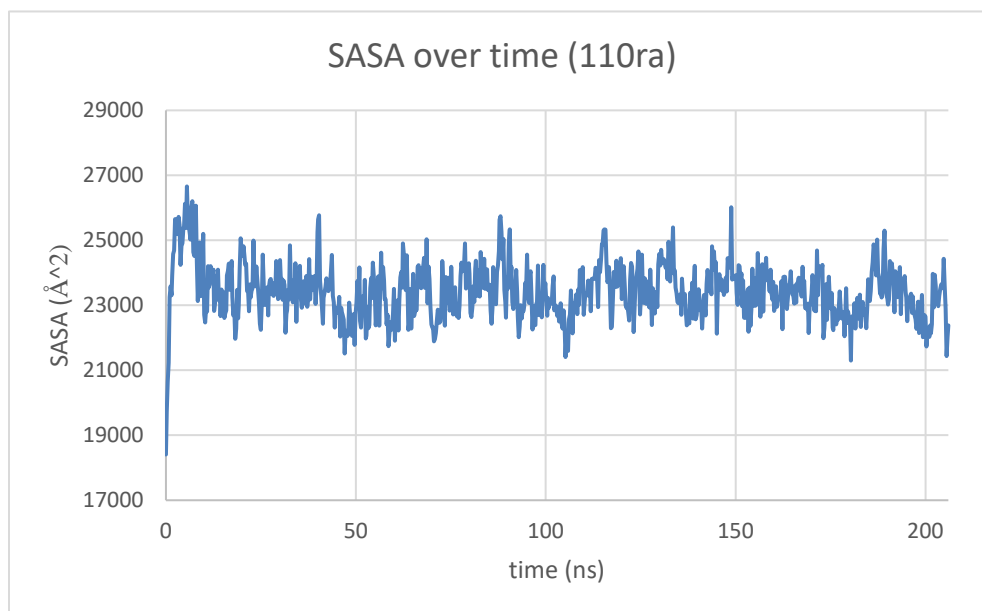


Figure 6: The solvent accessible surface area of a 110-molecule DDM random assortment over time.

Solvent accessible surface area (SASA, the surface area of the micelle exposed to water) was also used to investigate micelle stability. SASA values were calculated with a VMD extension and plotted over time, but the point at which the micelle stabilizes is not as obvious as with R_g . Like R_g , a correlation between average

SASA and aggregation number is observed, with SASA increasing with micelle size.

Another type of analysis used to determine stability of micelles was the calculation of moment of inertia eigenvalues. Three eigenvalues (X, Y, and Z) for each micelle were determined with VMD, which in turn led to the calculation of the asymmetry parameter, α , with the equation $(2X-Y-Z)/(X+Y+Z)$. The closer α is to 0, the more perfectly spherical the micelle is.¹⁰ With the DDM configurations, α tends to increase with aggregation number.

The asymmetry parameter can be compared to each configuration's packing parameter (P). P is dependent upon the number of carbon atoms in the detergent's nonpolar tail and the number of detergent molecules in the system. The closer P is to 1/3, the more spherical the micelle, while a P value of 2/3 indicates a more ellipsoidal shape. Plotting both α and P against aggregation number allows for an observation of the relationship between the two parameters. In

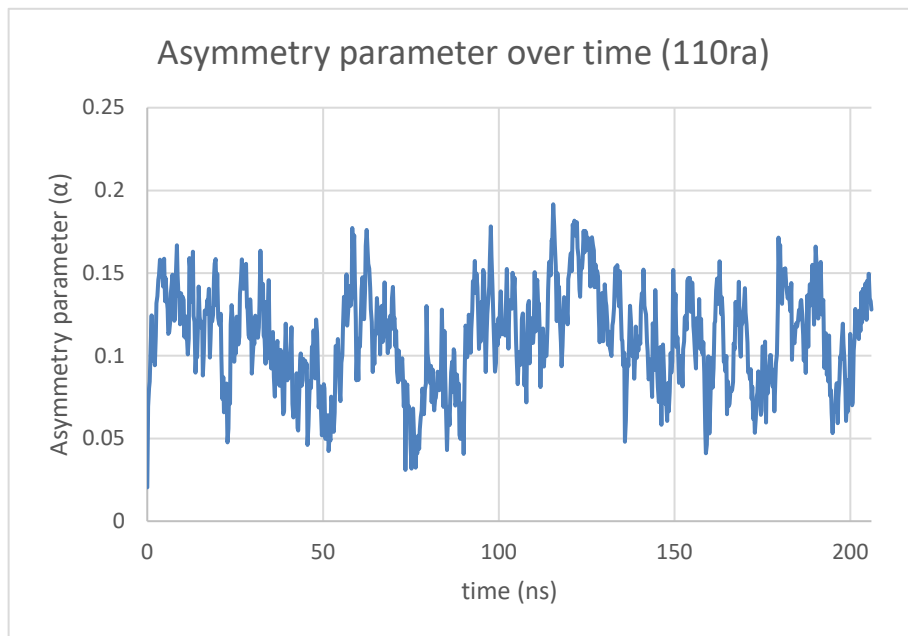


Figure 7: The asymmetry parameter over time for the 110-molecule DDM random assortment rapidly oscillates, but its relatively low average value indicates micelle sphericity.

Figure 8, α and P both increase with micelle size, with the smaller micelle being more spherical and the larger micelle being more ellipsoidal. The medium micelle falls somewhere between these characteristics. This indicates that larger micelles may lack the stability of the smaller, more spherical micelles, and that micelles falling into the lower literature aggregation number range could possibly be the most suitable candidates for study with PR.

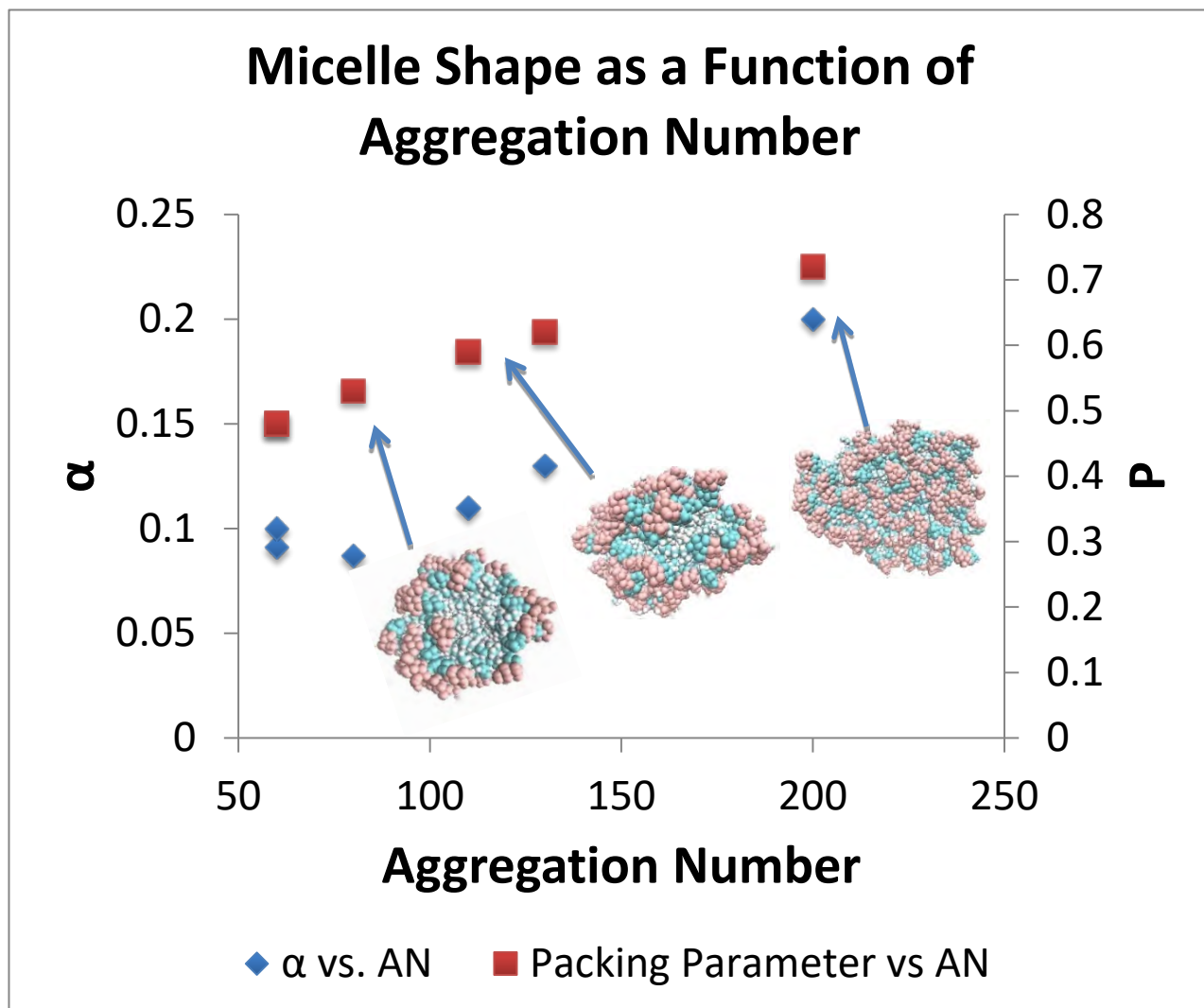


Figure 8: Micelle sphericity as a function of aggregation number. Shown are snapshots of DDM micelles, from left to right: AN= 60, 110, and 200.

Results from analysis of the DDAA micelles are compiled in Table 2.

| Table 2: Simulation results of various DDAA configurations | | | | | | |
|--|----------------------|-----|---------------|---|--------------|------|
| Configuration and tolerance | Simulation time (ns) | AN | Avg R_g (Å) | Avg SASA ($\times 10^4$ Å ²) | Avg α | P |
| 60 pre-formed micelle, 5 Å | 30 | 22 | 39.4 ± 4 | 2.69 | 0.41 | 0.48 |
| 60 inverse micelle, 5 Å | 127 | 60 | 25.6 ± 4 | 2.09 | 0.26 | 0.48 |
| 60 random assembly, 5 Å | 422 | 60 | 33.4 ± 4 | 2.06 | 0.44 | 0.48 |
| 80 pre-formed micelle, 5 Å | 15 | 80 | N/A | N/A | N/A | 0.53 |
| 80 inverse micelle, 5 Å | 95 | 80 | 21.9 ± 3 | 2.07 | 0.094 | 0.53 |
| 110 random assembly, 5 Å | 237 | 110 | 23.3 ± 0.2 | 2.32 | 0.11 | 0.59 |
| 130 pre-formed micelle, 5 Å | 44 | 64 | 32.3 ± 3 | 3.61 | 0.32 | 0.62 |
| 130 inverse micelle, 5 Å | 128 | 130 | 28.3 ± 2 | 3.38 | 0.53 | 0.62 |
| 200 random assembly, 5 Å | 72 | 200 | 28.6 ± 0.6 | 4.05 | 0.21 | 0.72 |
| 200 pre-formed micelle, 2 Å | 77 | 200 | 28.1 ± 0.5 | 3.67 | 0.21 | 0.72 |

Table 2 includes the DDAA simulation data for the runs performed over the summer. Shaded rows indicate that the micelle never stabilized.

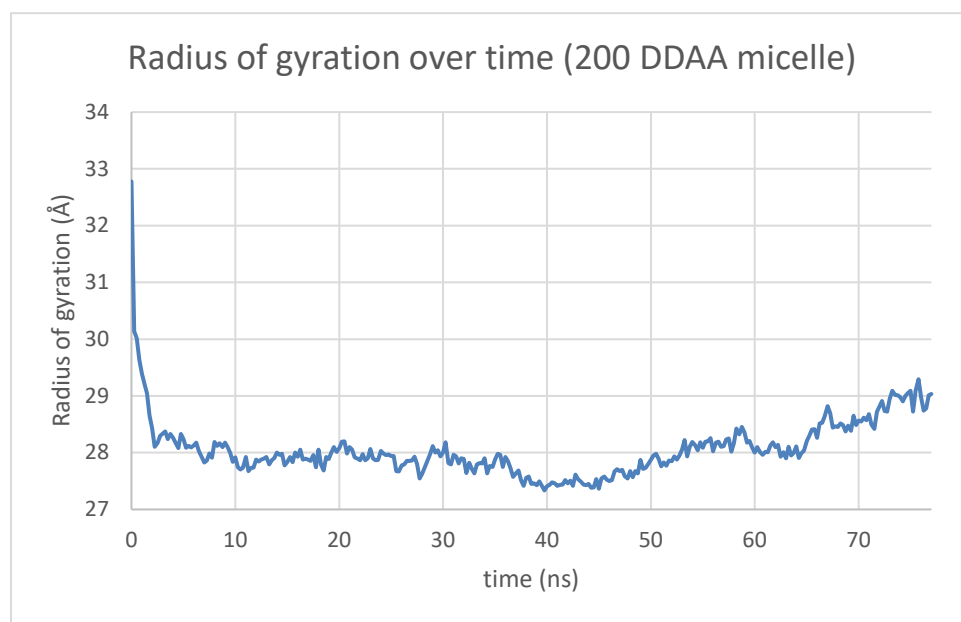


Figure 9: The radius of gyration over time for the 200-molecule pre-formed DDAA micelle indicates that stabilization was rapid. A small spike in R_g is present near the end of the simulation.

Unlike the DDM simulations, the DDAA configurations have no clear correlations between aggregation number and R_g , SASA, or α . An interesting data point, however, is the 200-molecule pre-formed DDAA micelle. This configuration had an initial packing tolerance of 2 Å, and stabilized very quickly. Similar to the DDM

simulations, the 200-molecule pre-formed DDAA micelle has an aggregation number above literature values, and its average R_g (28.1 Å), SASA (3.67×10^4 Å²), and α (0.21) values are comparable to those of the 200-molecule pre-formed DDM micelle (27.5 Å, 3.40×10^4 Å², and 0.20 respectively).

CONCLUSIONS

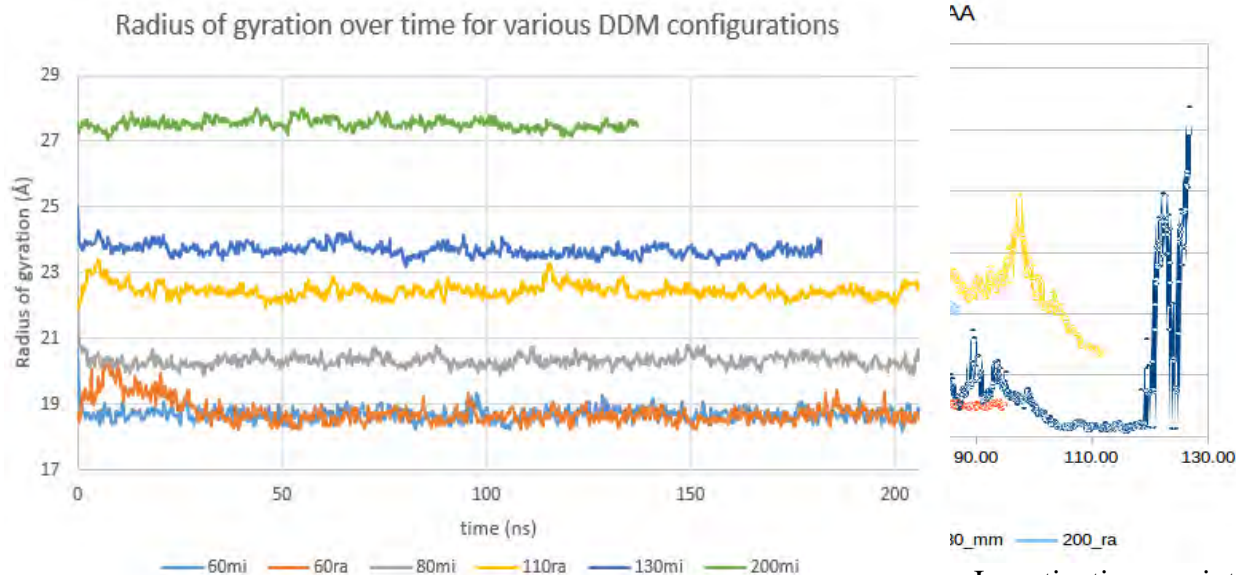


Figure 10: The radius of gyration over time for DDM configurations of 60 pre-formed (60mi), 60 random (60ra), 80 pre-formed (80mi), 110 random (110ra), 130 pre-formed (130mi), and 200 pre-formed (200mi).

Investigations into the discrepancies between the DDM and DDAA configurations of different initial

packing tolerances raise an important question about molecular dynamics: is the tolerance used when initially creating detergent assemblies more important than the stereochemistry and structure of a detergent molecule? Comparison between R_g values of the 2 Å DDM configurations (Figure 10) and the 5 Å DDAA configurations (Figure 11) can shed some preliminary light on this question. In Figure 10, the R_g for DDM stabilizes quickly, similar to the results for the 200-molecule pre-formed DDAA micelle with a 2 Å initial tolerance. However, in Figure 11, the R_g values rapidly fluctuate with little correlation with system size. Figure 9 is more similar to the R_g trend in Figure 10 despite the fact that the detergent used was DDAA. This is an indication that packing tolerance has a much larger effect on micelle stability and behavior than detergent stereochemistry. Packing tolerance also has an effect on the number of water molecules (and therefore the number of total atoms) in the system, with more loosely packed systems possessing a larger number of water molecules.

Because of this incongruity, future experiments are necessary to investigate the factors that influence micelle self-assembly. Suggestions for future work include DDM simulations consisting of various packing tolerances, system sizes, and detergent configuration. Tolerances will range from 2 to 5 Å, with possible investigations into micelles with much larger packing tolerance values. System sizes will range from 20 to 200 (and possibly more) DDM molecules to study aggregation number effects. This will also allow for investigation into micelle behavior of configurations consisting of DDM molecules above or below literature aggregation numbers. Configurations will consist of pre-formed micelles and random assortments, as well as inverse micelles (which are interesting due to the fact that they tend to stabilize quicker than pre-formed micelles or random

assortments, according to Table 2), in order to determine if initial configuration has a significant effect on micelle stabilization.

ACKNOWLEDGEMENTS

I would like to thank the NASA West Virginia Space Grant Consortium for their funding of this project through the Undergraduate Research Fellowship. Without their financial support, this project would not have been possible. Because of funding through the NASA WVSGC, this research project has also advanced much further along than before, and meaningful data has now been able to be consistently acquired.

I would also like to thank Fairmont State University College of Science and Technology for additional support, as well as access to their resources. I would especially like to extend my thanks to my research mentor, Dr. Erica Harvey, for her excellent guidance and direction on this project.

West Virginia University has also made this project possible. I would like to thank Dr. Blake Mertz, who heads the molecular dynamics research at West Virginia University and is responsible for the direction and development of our investigations. In addition, I want to acknowledge Sadegh Faramarzi, a graduate student at WVU under Dr. Mertz, for his assistance throughout the year. WVU's High Performance Computing Shared Research Facility has also made our research possible by allowing us access to their servers.

PRESENTATIONS

1. "Molecular Dynamics Investigation of Factors Influencing Self-Assembly of Detergent Molecules." Brittany Bonnett, Carl Scaggs, Lucas Freeze, Sadegh Faramarzi, Blake Mertz, and Erica Harvey, presented at the Southeastern Regional Meeting of the American Chemical Society, October 24, 2016 in Columbia, SC.
2. "Molecular Dynamics Investigation of Detergent Micelle Properties." Ashley Hoffmaster, Brittany Bonnett, Sadegh Faramarzi, Lucas Freeze, Danielle Grodi, Blake Mertz, and Erica Harvey, presented at the Central Eastern Regional Meeting of the American Chemical Society, May 18-21, 2016 in Covington, KY.
3. "Molecular Dynamics Investigation of Detergent Micelle Properties." Oral presentation by Brittany Bonnett, Ashley Hoffmaster and Lucas Freeze Celebration of Student Scholarship, Fairmont State University, April 19, 2016.
4. "Molecular Dynamics Simulations of Detergent Micelles." Brittany Bonnett, Ashley Hoffmaster and Erica Harvey, presented at the West Virginia Academy of Science meeting on April 9, 2016 at Marshall University. Won second prize in the Undergraduate Poster division.
5. "Molecular Dynamics Simulations of Detergent Micelles." Ashley Hoffmaster, Brittany Bonnett, and Erica Harvey, presented at the West Virginia Academy of Science meeting on April 9, 2016 at Marshall University.

REFERENCES

1. Bamann, C., Bamberg, E., Wachtveitl, J., & Glaubitz, C. (2014). Proteorhodopsin. *Bioenergetics*, 1837(5), 614-625.
2. Reckel, S., Gottstein, D., Stehle, J., Loehr, F., Takeda, M., Silvers, R., Doetsch, V. (2010, November 29). 2L6X: Solution NMR Structure of Proteorhodopsin. RCSB Protein Data Bank. <http://www.rcsb.org/pdb/explore/explore.do?structureId=2L6X>
3. Mertz, J.B. et al., manuscript in preparation, Fall 2016.
4. Abel, S., Dupradeau, F., Raman, E., MacKerell, A. D., Jr., & Marchi, M. (2011). Molecular Simulations of Dodecyl-maltoside Micelles in Water: Influence of the Headgroup Conformation and Force Field Parameters. *J. Phys. Chem. B*, 115, 487-499.
5. RCSB Protein Data Bank. (2016). Dodecyl-beta-D-maltoside. <http://ligand-expo.rcsb.org/pyapps/ldHandler.py?formid=cc-index-search&operation=ccid&target=LMT>
6. Stone, J. (2012, February). Using VMD. <http://www.ks.uiuc.edu/Training/Tutorials/vmd/vmd-tutorial.pdf>
7. Isgro, T., Phillips, J., Sotomayor, M., Villa, E., Yu, H., Tanner, D., & Liu, Y. (2012, February). NAMD Tutorial: Unix/MacOSX Version. <http://www.ks.uiuc.edu/Training/Tutorials/namd/namd-tutorial-unix.pdf>
8. Fairmont State University MD Simulations (2016). Ionization, Solvation, and Heating. <https://sites.google.com/site/mdsimulationsatfsu/software/what-is-vmd/ionization-solvation-and-heating>
9. WVU Research Computing HPC Wiki (2016, June 1). Running Jobs. https://wiki.hpc.wvu.edu/hpc_wiki/index.php/Running_Jobs
10. Israelachvili, J.N. (2011). *Intermolecular and Surface Forces*, third edition (Elsevier).

DIRECT WRITING OF TITANIUM DIOXIDE NANOPARTICLE INKS FOR PHOTOANODES IN DYE SENSITIZED SOLAR CELL SPACE

APPLICATIONS

Domenic Cipollone
Mechanical Engineering
West Virginia University
Morgantown, WV

ABSTRACT

Dye-sensitized solar cells are a low-cost alternative to the traditional Silicon based cells. The materials, especially the semiconducting foundation of TiO_2 , required to fabricate this generation of the solar cell are non-toxic, abundant, and eschew the need for high energy processing. This research focuses on the development of functional TiO_2 inks compatible with the direct writing process and low-temperature processing, in order to improve system manufacturability and compatibility with extraterrestrial applications.

INTRODUCTION

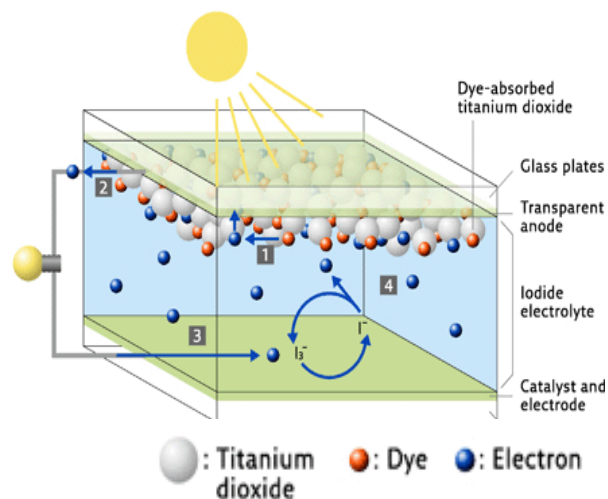


Figure 6: Current-driving mechanism of DSSC

Titanium dioxide (TiO_2) is a relatively abundant, non-toxic material with both semiconducting and photocatalytic properties. The semiconducting abilities of this material are utilized in dye-sensitized solar cells (DSSCs) and serve as the foundational element of the cell. This study begins to explore the deposition and fabrication of DSSC photoanodes in extraterrestrial settings through the formulation, synthesis, characterization, and deposition of water-based semiconducting TiO_2 inks compatible with direct writing. Initially, the work outlines the development of several functional TiO_2 inks. The effects of the mixing process and ink constituent components on the synthesized material are characterized and explored through contact angle

measurements, rheological characterization, and transmission electron microscopy (TEM). The inks are then directly written onto glass and ITO/PET substrates. Next, the processing-properties-microstructure relationships are studied through the surface characterization of directly written thin films. From this data, maps relating the printing parameters such as speed, pressure, and distance to the substrate to the film's features are created, allowing for the systematic production of a thin film, mesoporous TiO_2 using direct writing.

BACKGROUND

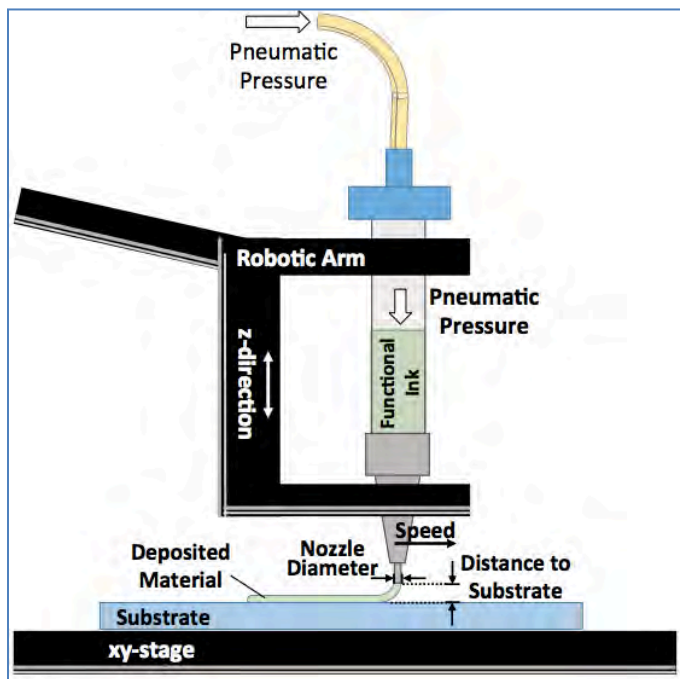


Figure 7: Schematic of direct writing system

Currently, the Flexible Electronics for Sustainable Technology (FEST) laboratory at West Virginia University explores the use of direct writing to fabricate DSSCs. These solar cells generally consist of two transparent substrates coated with conducting electrodes sandwiching a catalyst layer, an electrolyte, a sensitizer, and a TiO_2 semiconducting layer. Of crucial importance is the dye monolayer situated on the surface of the TiO_2 , which initiates the electron injection into the TiO_2 network upon photoexcitation, driving current through the cell.¹ See Figure 1.

In comparison to the established methods of TiO_2 deposition, direct writing is a non-energy intensive process and requires no special condition, such as that of a vacuum.

Furthermore, this process deposits a continuous filament, as compared to ink-jet printing, which deposits individual drops in sequence. This core difference results in a more conductive film due to the material's continuity. Essentially, the direct writing process uses pneumatic pressure to extrude ink as a continuous filament through a nozzle onto pre-defined substrate locations. As a result, this technique provides a deposition route that produces virtually no material waste, a pivotal element in an extraterrestrial environment with limited resources. Moreover, because direct writing enables the deposition of materials in ambient conditions, the process is capable of large area patterning on glass and polymer substrates, lending the process to scalability both in terrestrial and extraterrestrial settings.

As NASA plans to colonize Mars and plans further deep-space missions, the capability to manufacture solar cells and solar cell components will prove critical. Expeditionary groups that travel immense distances with limited resources will have the ability to manufacture energy devices as need be, providing crucial energy to the space craft or colony. With further research and development, this generation of solar cell combined with the additive manufacturing approach of direct writing has the potential to replace Silicon-based solar cells in extraterrestrial applications.

EXPERIMENT

TiO₂ Ink Synthesis



Figure 8: TALH TiO₂ ink

The non-toxic, water-soluble TiO₂ inks consist of crystalline TiO₂ nanoparticles, an organic titanium dioxide precursor, Titanium(IV) bis(ammonium lactato)dihydroxide (TALH), water, and a polymer-agent, either Polyacrylic Acid (PAA) or Poly(vinylpyrrolidone) (PVP). To synthesize the TiO₂ ink, water, and a polymer-agent are set to mix until homogenous. Next, the TALH solution is added to water and stirred. Upon mixing, crystalline TiO₂ particles are added to the solution, mechanically stirred, and then sonicated for 15 minutes. The resulting solution is then stirred for 15 minutes, and the polymer solution added drop wise. The ink is then sonicated for an additional 15 minutes to improve particle dispersion and to prevent agglomeration, and again set to stir for a minimum of 1 hour.

Four formulations of the ink following the above process are synthesized and directly written. These formulations differ through variation of the polymer-agent (PAA or PVP) and by varying the TALH to crystalline TiO₂ ratio. The formulations are as follows: 1:6 PVP, 1:6 PAA, 1:12 PVP, and 1:12 PAA.

Ink Characterization and Deposition

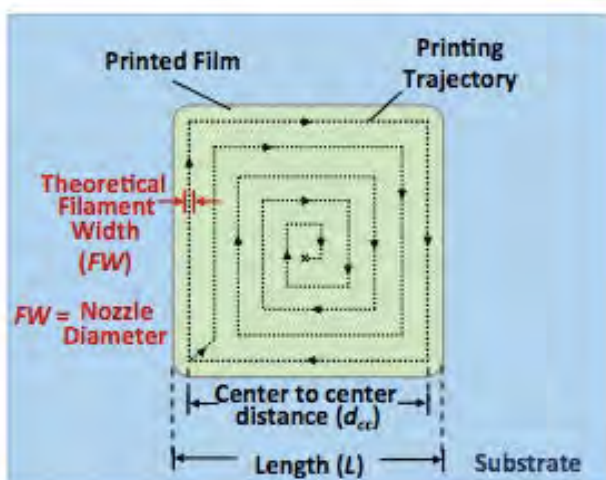


Figure 9: Schematic of film printing pattern for use in DSSCs

The as-synthesized ink is characterized through contact angle and viscosity measurements, which quantify the effects of the polymer agent and effect of varying the ratio of TALH to crystalline TiO₂. Next, the material is directly written onto glass or ITO/PET using a Nordson robotic deposition system and a 100- μ m-diameter nozzle. Predefined areas for material deposition are chosen through the construction of a series of points, creating a continuous path for the nozzle to follow. In order to create a continuous film, a spiral is programmed, allowing the natural spreading of the deposited lines to slightly merge.

These thin films are then either left to dry naturally, or post-processed through a 4 hour UV treatment or 30 minutes at 150°C. After drying, a small area of the film is imaged using TEM, showing the effects of the organic precursor, TALH.

Additionally, the printed films are judged as acceptable qualitatively. Features such as large spreading, prominent cracking, or discontinuities deem the films unacceptable. The acceptable films are then taken for profilometry measurements, which determine the film height and surface roughness. Finally, maps relating the film height and spreading to the printing parameters such as speed, pressure, distance to the substrate, and nozzle diameter are created.

RESULTS AND DISCUSSION

Viscosity and Contact Angle

It is found that as the ratio of organic precursor TALH to crystalline TiO_2 increases, the viscosity of the ink increases. Additionally, the inclusion of the polymer agent increases viscosity. Figure 5a shows that the 1:12 ink has approximately one order of magnitude greater initial viscosity than that of the 1:6 ink. Moreover, the PVP and PAA inks have a higher viscosity than that of the no-polymer formulation. It is also important to note that all inks demonstrate the shear-thinning behavior.

The polymer agent, either PAA or PVP, serves to improve the printing fidelity of the inks. The polymers help to reduce agglomeration of the TiO_2 nanoparticles, which prevents clogging when extruded through the nozzle. Moreover the inclusion of the polymer agent reduces the drying time of the water-based ink, in turn further preventing clogging.

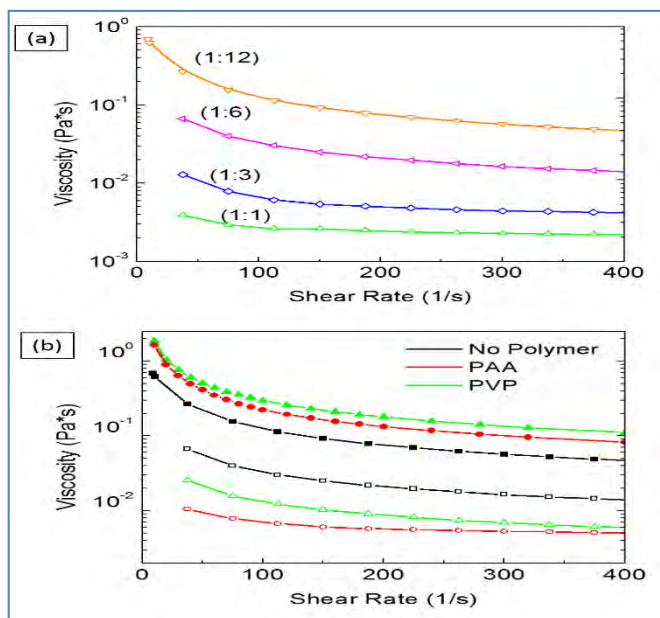


Figure 10: Viscosity for (a) different particle loading inks and (b) different polymer formulated inks

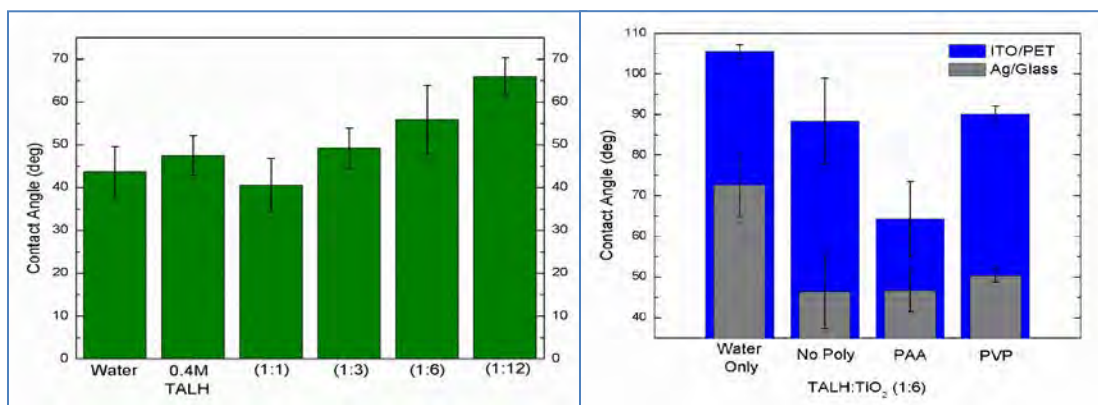


Figure 11: (left) Contact angle for different particle loading inks and (right) contact angle for different polymer formulated inks

The inclusion of the polymer agent and increase of

TALH: TiO_2 ratio not only alter the viscosity, but also change the contact angle of the ink. Figure 6 demonstrates that as one increases the particle loading, the contact angle increases. Furthermore, as one introduces PAA to the formulation, a noticeable decrease in contact angle is noted from that of the no polymer solution, though the addition of the PVP results in no obvious change in contact angle. The changes in both viscosity and contact angle will be seen to significantly impact the

printing fidelity of the materials.

TEM

Upon low-temperature sintering at 150°C and UV exposure, the organic precursor TALH begins to decompose and form amorphous TiO₂ that situate in between the larger, crystalline TiO₂ nanoparticles. These bridges eschew the need for typical high temperature sintering (~500°C) which would degrade a polymer substrate such as ITO/PET. As such, the presence of the TALH helps to combat issues with conductivity and electron mobility that would result from a lack of high temperatures post-processing. Figure 7 shows TEM images of particles from as-purchased particles and then from the post-processed films deposited by direct writing.

In the as received TiO₂ particles (Figure 7a), no bridge or bridge element can be seen. Following a 4 hour UV and treatment at 150°C for 30 minutes (Figures 7b & 7c), bridging elements can be seen making amorphous connections between larger the Anatase TiO₂ particles.

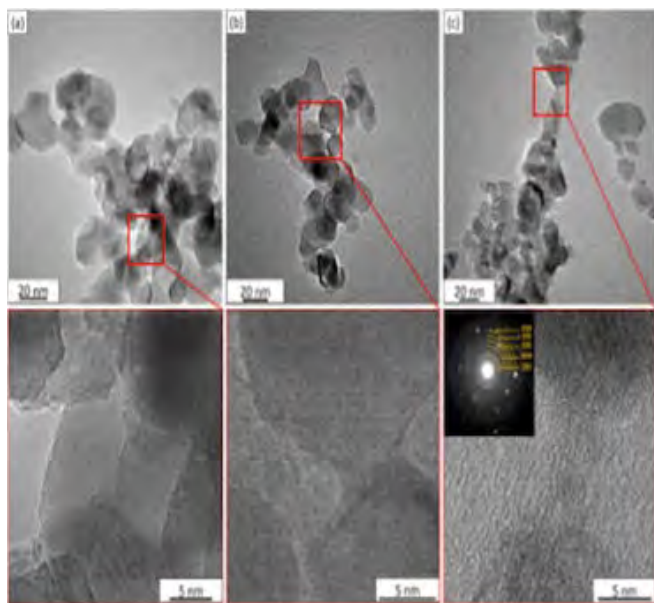


Figure 12: (a) as received TiO₂ particles (b) TALH:TiO₂ 1:6 PAA ink after 4 hour UV exposure and (c) TALH:TiO₂ PAA 1:6 after 150 C for 30 minutes

Direct Writing and Mapping

Four formulations of the TiO₂ were directly written: 1:6 PVP, 1:6 PAA, 1:12 PVP, and 1:12 PAA. The inks were directly written with a 100µm diameter tip and approximately 80 µm from the substrate. With those parameters constant, various writing speeds and pressures were used to deposit films using the predefined spiral pattern.

As one increases the pressure, more material is extruded through the nozzle, resulting in a thicker film. On the contrary, as one increases the writing speed, less material is extruded resulting in a thinner film. These parameters were optimized in this mapping process to deliver as thin a film as possible with minimal visible cracking.

The 1:6 inks being less viscous than the 1:12 inks suffer from significantly more clogging. This is the result of agglomeration from the particles due to lesser dispersion and the result of faster drying in the nozzle. In terms of substrate adhesion, the 1:6 inks also have more spreading and a less degree of hydrophobicity when compared to their 1:12 counterparts. The lower contact angle results in a greater percent spreading and less retention of the intended deposition pattern.

It must be noted that the 1:6 PAA ink features both less clogging and less spreading as compared to the 1:6 PVP ink. This is the cause of the PAA's acidity, which slightly etches the substrate, resulting in better substrate adhesion, particularly on the polymer substrate. With the 1:6 PVP formulations, the deposited ink tends to coalesce and lose semblance of a pattern.

Overall, the 1:12 inks have better printability. The improved printability is attributed to the increased viscosity, which lessens the drying time and improves particle dispersion. Those two factors significantly mitigate the clogging issues present in the 1:6 systems. Due to their higher viscosity, the 1:12 inks tend to spread less and produce more continuous films.

In regards to direct writing capability and printing fidelity, the 1:12 PAA ink is the optimal formulation. This ink adheres well to both glass and polymer substrates with limited spreading and features the least clogging and spreading. The maps shown in Figure 8 demonstrate the wide regime of printability. With this range available, a variety of features can be produced in regards to a specific application.

The films deposited on ITO/PET were judged as acceptable by examination of the film surface features and spreading of the material. If the predefined shape was lost or significant cracking resulting in harmful discontinuities were present on the surface, the film was not taken for profilometry and surface characterization. Following the film characterization of height and spreading, maps were created which relate those properties to the deposition parameters. Regions of the map where discontinuities or significant clogging exist are documented as well, giving a full description of the potential deposition range.

Figure 8 details the relationships between pressures and direct writing speed and film qualities such as spreading, film thickness, and surface roughness for the 1:12 PAA system. One can see that the regions of high pressure and low speed result in overflow, which leads to cracking. Conversely, regions with high writing speed and low pressure result in discontinuities or no ink extrusion. Printing regimes with insignificant pressure never produce a film. Moreover, the far right regions of the map lead to the most spreading and a higher roughness.

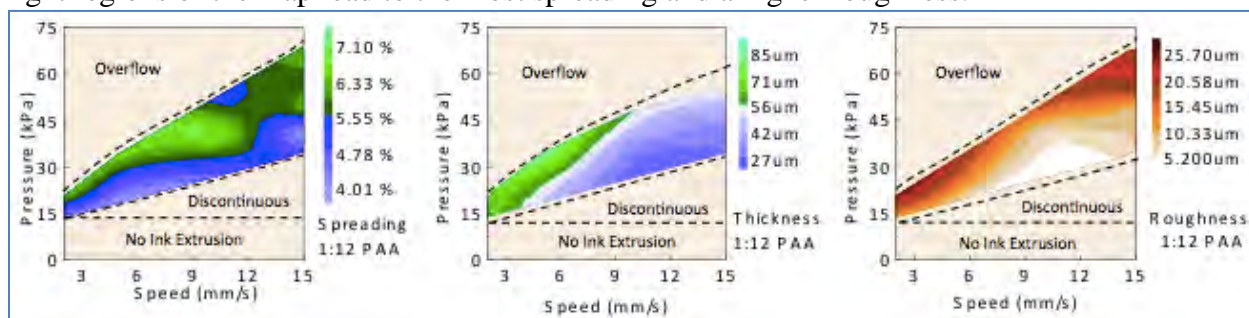


Figure 13: Printed feature variation with printing parameters for the TALH:TiO₂ (1:12) PAA ink on ITO/PET substrates

For DSSCs, ideally one wants as thin a film as possible. The thin films allow for improving electron mobility and higher opacity, allowing more light to enter and excite the sensitizer. With this in mind, the optimal film thickness produced by direct writing is found at 10 mm/s and 25 kPa for the 1:12 PAA system. Those parameters combined with a 100 μ m diameter tip and deposition height of approximately 80 μ m results in the thinnest continuous film of \sim 27 μ m with negligible cracking. Additionally, the spreading of the film at with those conditions is around 4%, leading to minimal material waste and retention of the intended pattern.

CONCLUSION

This study lays the groundwork for extraterrestrial solar cell manufacturing through the exploration of the synthesis, formulation, deposition, and characterization of TiO₂ formulations compatible with low-temperature processing and the direct writing system. The inks and direct writing system allow for the precise deposition of semiconducting material on both glass and polymer substrates, limiting material waste. Additionally, with the potential for low-temperature processing, the energy requirements for post-processing will be notably reduced. As NASA plans more deep space and extraterrestrial missions, the importance and capability of manufacturing energy producing devices cannot be understated.

The constituent components of the TiO₂ have been shown to impact not only the final formulation of the ink but also the direct writing compatibility. Increasing the particle loading leads to an increased viscosity, which in turn improves printability of the system due to improved particle dispersion and a reduction in drying time. Furthermore, inclusion of a polymer agent, most notably PAA, helps to further reduce clogging and drying time. Importantly, the inclusion of the organic precursor TALH provides a route for low-temperature sintering and subsequent deposition on flexible polymer substrates by forming amorphous TiO₂ bridges upon decomposition.

The printing parameters, such as speed, pressure, and distance to the substrate, are shown to have a quantifiable effect on the physical properties of the deposited films. As one increases pressure and extrudes more material, cracking and spreading tend to increase, resulting in a functional failure. To print as thin a film as possible, one must optimize speed and pressure to minimize cracking as well as spreading. In particular, the 1:12 PAA ink shows the highest printing fidelity. Due to its relatively high viscosity and the inclusion of the polymer agent PAA, both drying and clogging of the system are reduced, resulting in continuous, thin, and reproducible thin films that adhere well to polymer substrates.

To further improve the manufacturability of the system in extraterrestrial applications, further work will be done to incorporate the sensitizer into the TiO₂ ink formulation. The dyeing process is typically the longest, requiring anywhere from 12-24 hours.³ With this co-dyeing, the direct writing system will enable the one-step fabrication of the photoanode, drastically reducing DSSC fabrication time.

This undergraduate fellowship from the WVSGC was most valuable for me in that it allowed me to fully immerse myself in undergraduate research. It greatly developed me in my writing style and critical thinking. The financial support is critical in my opinion because it allows students to engage fully without worrying about a paycheck from a job or financial security. Furthermore, the relationships I formed with the graduate students in the lab are long lasting and have helped elevate my mentality. Finally, because I am going to graduate school next year, this project has put me at an advantage in terms of technical ability and personal confidence, and I now feel more comfortable and ready to take on future independent and team projects.

ACKNOWLEDGEMENTS

This work acknowledges the funding provided by the West Virginia NASA Space Grant

Consortium, as well as the help of my academic advisor Dr. Konstantinos Sierros and the FEST laboratory.

PUBLICATIONS/ PRESENTATIONS

- 1) Undergraduate Research Day at the WV Capitol Poster Presentation
- 2) ACS Applied Materials & Interfaces publication
- 3) SURE Poster Presentation
- 4) Fall 2016 MRS Meeting & Exhibit
- 5) WVU Welcome Week Poster Presentation

REFERENCES

1. Wang, P., Zaekeeruddin, S. M., Exnar, I., Gratzel, M. 24 Oct 2002. "High efficiency dye-sensitized nanocrystalline solar cells based on ionic liquid polymer gel electrolyte." *Chem. Commun.*, (24), 2972-2973
2. M. Torres, A. Andrade, D. Cipollone, L. Grant, D. Korakakis, K. Sierros. 21 Sept 2016. "[Robotic Deposition of TiO₂ Films on Flexible Substrates from Hybrid Inks: Investigation of Synthesis–Processing–Microstructure–Photocatalytic Relationships.](#)" *ACS Appl. Mater. Interfaces*. **8** (2016)

EFFECTS OF ACID MINE DRAINAGE ON PLANT COMMUNITIES IN THE CENTRAL APPALACHIANS

Kyle Clark
Biology
Shepherd University
Shepherdstown, WV

ABSTRACT

Acid mine drainage, one of the major environmental complications in West Virginia. AMD is when abandoned mines leak heavy metals into streams and rivers. AMD leaches into the groundwater, which in turn may have implications on plant community composition and health. Abandoned mine field sites in West Virginia were identified and all necessary permissions to conduct research at the sites were obtained. In Tucker County, field work consisted of laying out two transects radiating outwards from a high wall at five mine sites approximately 200 meters. Sites were chosen based on time remediation of reclaimed to unreclaimed. Established plots included identification of all mature trees and soil properties such as pH. Measures of species composition, diversity, and richness were calculated and modeled against soil properties. Water samples were collected to find an estimate of iron concentration.

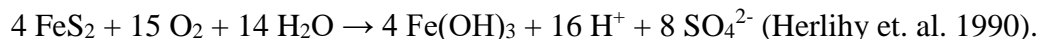
Data suggests that the effects of groundwater contamination did not have a negative impact on community composition, diversity, and within species performance. Community composition was predicted to shift from the dominance of low pH tolerant species to less tolerant species, and within species, performance was expected to rise with distance from mine. Data shows no significant differences between soil pH, species richness, and diversity. This study was important for understanding which tree species are able to inhabit acidic soils and if there were any differences with soil pH of mine that has been reclaimed and one that is not.

INTRODUCTION

Acid mine drainage, also known as acid rock drainage, is one of the major environmental complications in West Virginia. Acid mine drainage is when abandoned mines leak heavy metals into the streams and rivers that turn them into the orange colored acidic water (United States Geological Survey 1998). Fool's gold, iron sulfide, is mixed with the air and the water and creates a chemical reaction to make sulfuric acid (USGS 1998). Acid generation rate consists of a plethora of factors such as temperature, pH, bacterial activity, and oxygen concentration in the water (Akcil and Koldas 2006). Acid mine drainage affects the groundwater, which in turn affects other water sources that a lot of biotic and abiotic parts of the ecosystem depend upon. Acid mine drainage has affected at least 484 streams for a total of 2,852 stream miles in West Virginia alone (WVDEP 1995). Excessive amounts of iron in the soil could have damaging effects on individual plant life or effects on a community level due to disruptions of various cell functions (Marschner 1995). Studies show that excessive iron concentrations in a plant could damage it at a cellular level (Bienfait 1989). The Appalachian region of the eastern USA is more than 80% forested, but large forest areas have been lost due to numerous impacts including coal surface mining. In Appalachia, more than 600,000 ha have been mined for coal under the USA's national coal mine reclamation law, the Surface Mining Control and Reclamation Act (SMCRA), and >10,000 additional ha are

being mined each year (Angel et. al. 2011).

It has been documented that Zn, Fe, Cu, Mn or Ni are directly involved in protein synthesis in plants (Neagoe et al. 2005). When iron II sulfide is oxidized, it releases hydrogen ions in the water. Iron III is established, which in turn, hydrolyzes in the water to form iron III hydroxide (Herlihy et al. 1990). A chemical reaction below shows how much hydrogen ions are imported when finished.



This formation results in what is commonly known as yellow boy, but will only form when the pH levels are approximately 3.5 or below. *Acidithiobacillus ferrooxidans*, a species of bacteria, has been known to help in the chemical reaction process that forms yellow boy (Akcil and Koldas 2006). *Acidithiobacillus ferrooxidans* thrive mostly in acidic water with a pH of less than 3.2 (Akcil and Koldas 2006). However, limestone is a very common solution to buffering the acidic water. One technique that involves the limestone would be to create a lining of limestone so that it would cause the flowing acidic water to buffer as it is flowing over the limestone (Akcil and Koldas 2006). Another chemical reaction below shows step-by-step processes (Kuyucak 2002).

Species richness is able to inform us of the abundance of species in a given community. Species richness can be used to compare the differences between sampling sites of which trees are most abundant there but only through the same plot sizes. The diversity of a community can tell us which sampling sites were more diverse through the species that were included in the sample plots. In most reclaimed mines, there are trees that were used specifically to help better the soil and the different species of trees that were planted (Burger 2001). Looking at the data collected, diversity of certain species that help the quality of the soil and growth of other trees should be included.

Reclamation efforts have been taken after the mining process through the Forestry Reclamation Approach (FRA). The FRA has been used by coal mining companies to ensure the safety of the environment by restoring mine soils and planting native trees. Efforts like the FRA keep our ecosystems stable and safe for everyone and everything by looking towards improving the water quality, wildlife habitat, watershed protection, wood production, and wood production (Angel et al. 2011).

Arbuscular mycorrhizal fungi is a certain type of obligate plant symbiont that forms with the roots of 80-90% of land plants (Smith and Read 2008). Mycorrhizae act as extensions for root systems to pass through into the bulk soil and uptake nutrients (Chapin III, Matson, Mooney 2002). This fungus is highly important for plants, as it protects the roots from metal toxicity (Smith and Read 2008), and without this fungus, plants are vulnerable to iron chlorosis (Beinfait 1989). However, the arbuscular mycorrhizal fungi were found less in reclaimed sites than non-mined sites (Cumming & Levy 2011). Previous studies have shown that iron toxicity plays a direct role in plant protein synthesis and could play a major role in the growth performance of plants (Marschner 1995). This means that on contaminated sites mycorrhizae are even more essential to plant performance, but are themselves less abundant, thereby making the contamination issues even more intense for the plant (Chapin III, Matson, Mooney 2002).

It is hypothesized that plant composition, richness, and diversity will be different comparing reclaimed and unreclaimed mine sites. Remediated mine sites are expected to have higher richness, diversity, and pH. There are not many studies based on acid mine drainage on woody plants and is important to understand the correlation between the two. In this research study we hope to learn the outcome of tree species through diversity and species richness of trees that inhabit acidic soils. This research contributes to ecological studies that have not yet conducted research on abated and unabated mining sites in the community of woody plants diversity and richness.

METHODS

Tucker County, WV is home to many coal mines. With its rich reserves of coal, mining the resource skyrocketed in the early 1900's. Our sample sites included Snyder Run Highwall 1 and 2, Long Run Highwall, Pendleton Creek Highwall 1, and Blackwater Manor.

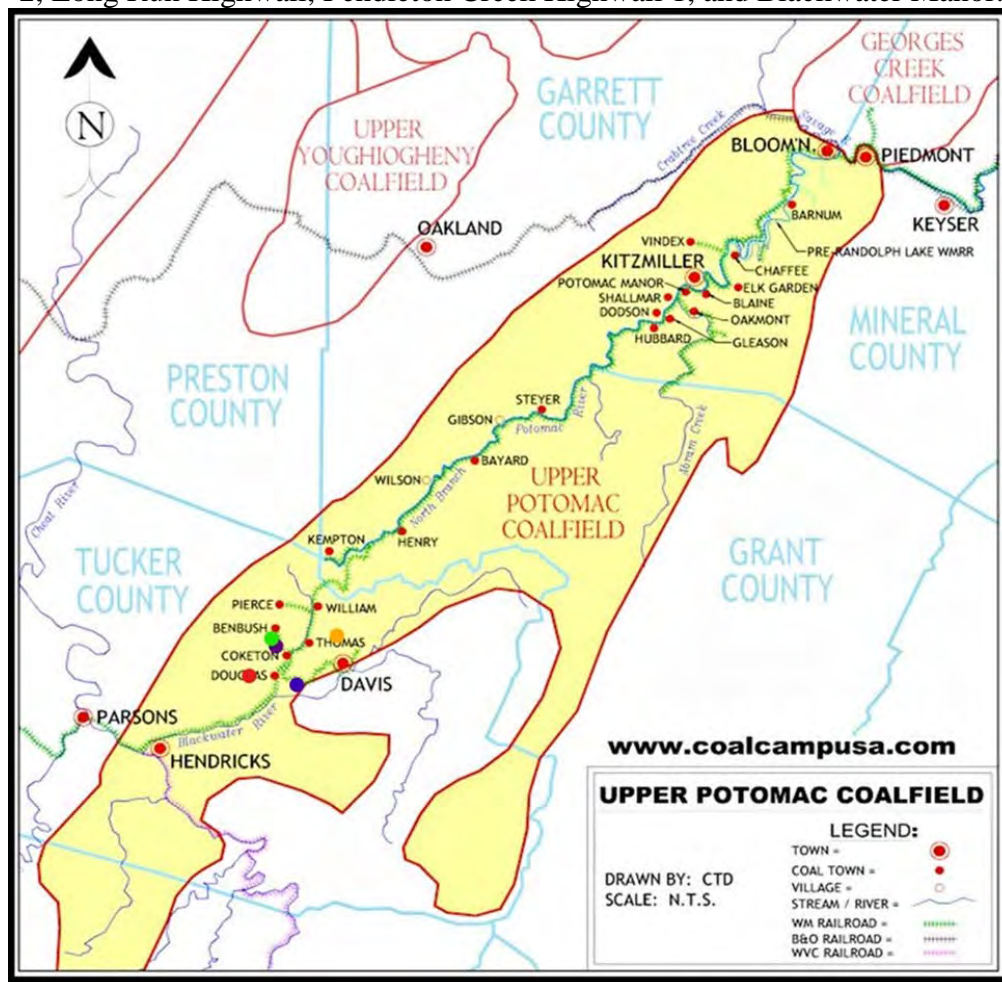


Figure 1. Map of the region of study. Colored dots show the locations of each mine site.

Pendleton Creek Highwall (yellow), Blackwater Manor (blue), Long Run (red, to the left of Blackwater Manor), Snyder Run Highwall 1 (green), Snyder Run Highwall 2 (purple).

Snyder Run Highwall 1 consisted of mostly of red maple (*Acer rubrum*), sourwood (*Oxydenrum arboretum*), black locust (*Robinia pseudoacacia*) and red pine (*Pinus rubra*) species. Tall grass

present in all plots with dew on the plants, the soil was soft in some areas with little to no shale. Snyder Run Highwall 2 was dominated by a combination of sourwood, hemlock (*Tsuga canadensis*) and yellow birch (*Betula alleghaniensis*) trees. Tall grass was present in some plots but others there were patches of dead leaves. The soil was soft with little to no shale in some spots.

Blackwater Manor was mainly comprised of sourwood and hemlock trees. Blackwater Manor had lots of rhododendron species through some of our plots. Tree cover was present and dead organic matter on the ground at all plots. Long Run Highwall was rich with hemlock, red maple, and yellow birch trees. Leaf litter was found in all plots with shade cover. Lots of rhododendron bushes were found in the plots nearest the high wall. Pendleton Creek Highwall was rich with red maple and sourwood trees in all plots. Leaf litter was found in all plots and shade cover in all plots as well.

Sample design was having two plots nearest the high walls and both were radiating outwards approximately 200 meters where a plot was made at the ends. There were four total plots for each mine site. Sampling began with finding a suitable spot for a plot that included a sufficient number of trees along each high wall. Once a spot was located, a 25X50 meter plot was made using a retractable measuring tape, and at every corner, a tree was flagged with a red flagging tape. Materials for sampling consisted of a spade, ground auger, soil pH probe, water bottle for cleaning the probe after every use, data sheet for recording soil pH, diameter tape. Soil pH sampling was conducted by sampling ten random spots within the 25X50 meter plot. Every soil pH recorded required a hole to be dug approximately 10 cm deep. The ground auger would be used to make a small hole in the soil and then switch to the other end to enlarge the hole for the probe to be inserted. Samples of woody plants were taken first through tree identification and then by retrieving the diameter of all trees at breast height (DBH) using a diameter tape. With this data in each plot area, we can calculate the species richness and the diversity of tree species within each plot, transect, and mine. Soil pH that was taken at every plot area can be combined with the data of tree species for examination to see if pH levels had any significance for how diverse and rich species were in the central Appalachians. Water samples were collected at mine sites for testing iron concentrations through the use of a LaMott's chemical kit. Samples included just water and samples with sediment inside.

RESULTS

Data analysis shows that all recordings of pH levels were low. The range of iron content collected varied between 0.5 ppm to 2ppm and 9 ppm to +10 ppm between samples with and without sediment. There was no real significance with the diversity of species.

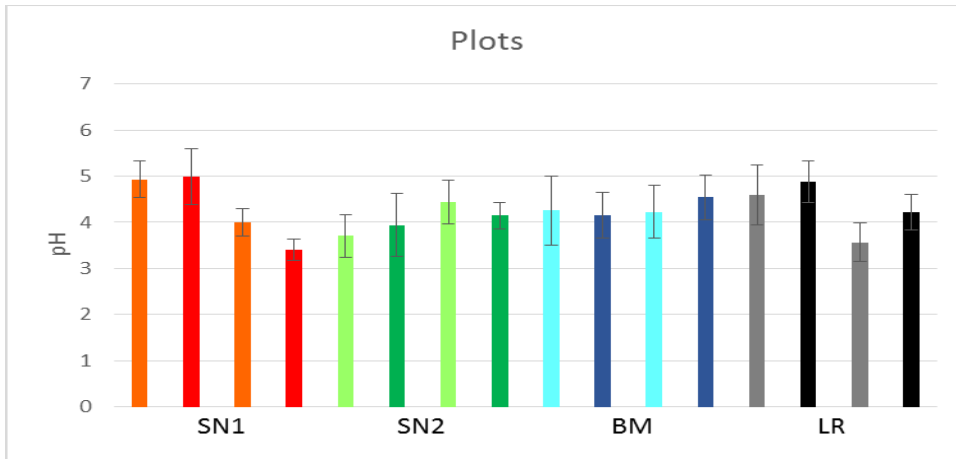


Figure 1. Shows the relationship between soil pH of Snyder Run Highwall 1 (SN1) in red and orange, Snyder Run Highwall 2 (SN2) in green and lime green, Blackwater Manor (BM) in blue and sky blue, and Long Run Highwall (LR) in black and gray.

All lightly colored bars indicate the plot site nearest the high walls and the darker colored bars indicates the plot site furthest from the high walls. The pH levels of all plots across these mines never reached over a pH of 5 indicating that the soil pH was all acidic. However, Long Run is the only mine site that shows acidity increasing the further the plot is from the high wall on both transects. No additional data were obtained for the Pendleton Creek high wall.

Table 1. Common names of all the species that were found and their abbreviations that are used. Abbreviations were made with the first two letters of the genus name and first two letters of the species name. Example: *Acer Rubrum* is the scientific name for Red Maple. Take AC from *Acer* and RU from *Rubrum* = ACRU.

| Common Species Name | Species Abbreviation |
|---------------------|----------------------|
| Red Maple | ACRU |
| Striped Maple | ACPE |
| Black Locust | ROPS |
| Hemlock | TSCA |
| Autumn Olive | ELUM |
| Yellow Birch | BEAL |
| Service Berry | AMAR |
| Aspen | POGR |
| Sour Wood | OXAR |
| Red Pine | PIRU |
| Sugar Maple | ACSA |
| Norway Pine | PIAB |
| White Pine | PIST |
| American Beech | FAGR |
| White Ash | FRAM |
| Hop Tree | PTTR |
| Witch-Hazel | HAVI |
| Black Cherry | PRSE |

There were a total of 18 species of woody plants that were recorded. Seeing sourwood trees gives some insight to what the pH levels are going to be like since they are known to be a woody plant that thrives in acidic soils.

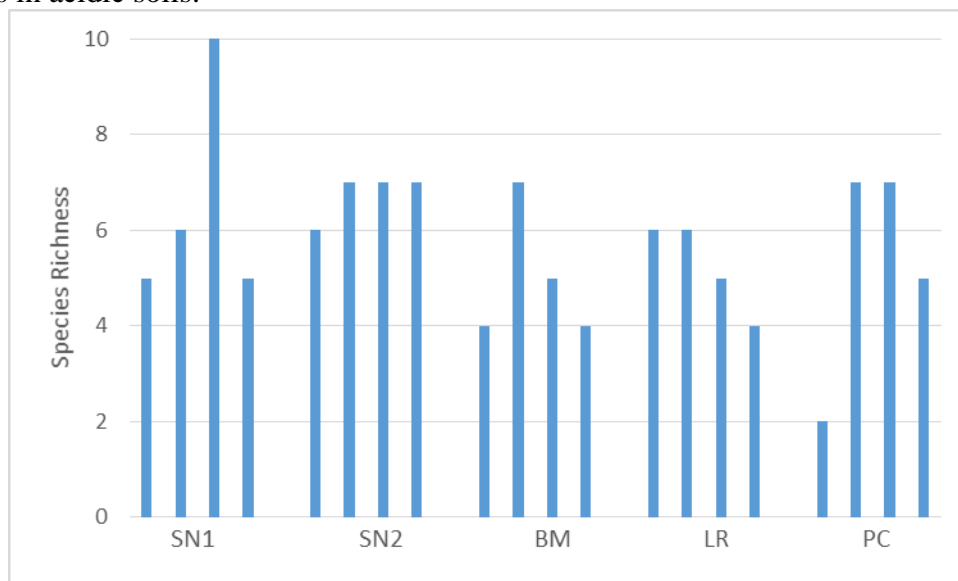


Figure 5. Shows the species richness of all plots across all mine sites.

Plots starting from left to right are transect 1 and plot 1, then plot 2, then transect 2 and plot 1, then plot 2. Snyder Run 1 transect 2 and plot 1 had the most species richness while Pendleton Creek transect 1 and plot 1 had the least species richness.

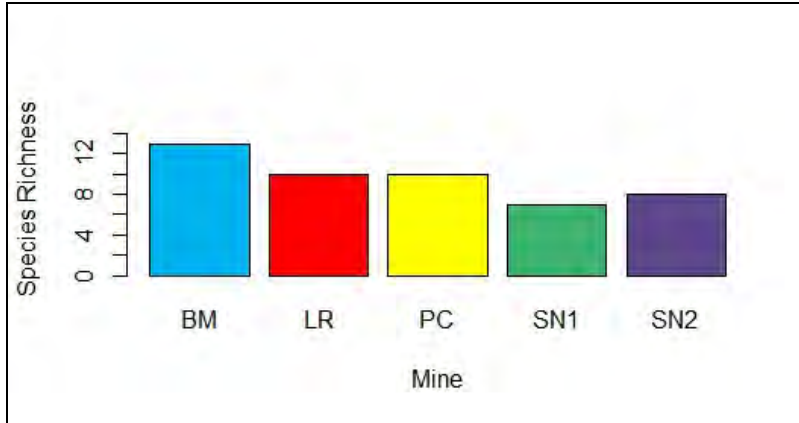
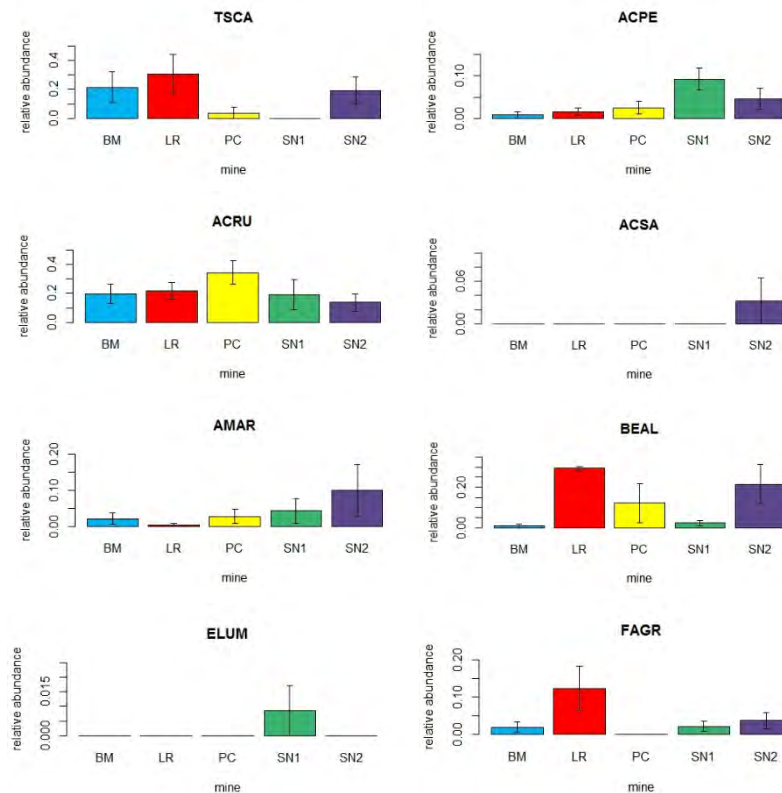


Figure 6. Shows the total amount of species richness in all of the mines.

Snyder Run 1 had the most species richness compared to all the other mine sites with Long Run having the lowest amount of species richness. The total species richness between the mine sites and when comparing them by plots is quite similar. There was expectations to Blackwater Manor, Long Run and Pendleton Creek having a higher species richness since they have been reclaimed sites compared to Snyder Run 1 and 2 which have not been reclaimed yet. Data shows that there is no significance between mine sites for species richness.



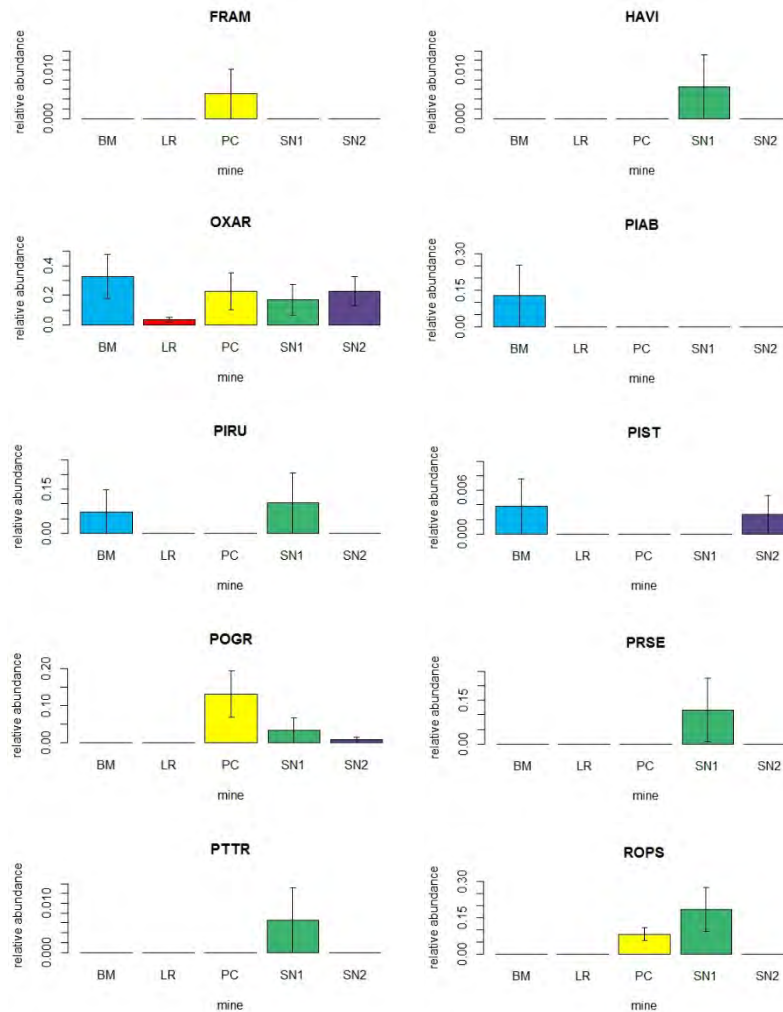


Figure 3. Shows the standard error of relative abundance across all mines for every species. Sourwood, yellow birch, service berry, striped maple, and red maple are found in all sites.

Sourwood, yellow birch, service berry, striped maple, and red maple are found in all sites. In all of the mining sites, maples were found and a couple of white ash were found in Pendleton Creek. Sourwood is a species of woody plants that like to grow in acidic soils and is not surprising to see that they are found at all mine sites where the pH levels are all low. Species of trees that appear in one to three of the mines do not usually show any significance whereas the species that appear in four to all of the mine sites are found to be significant in relative abundance.

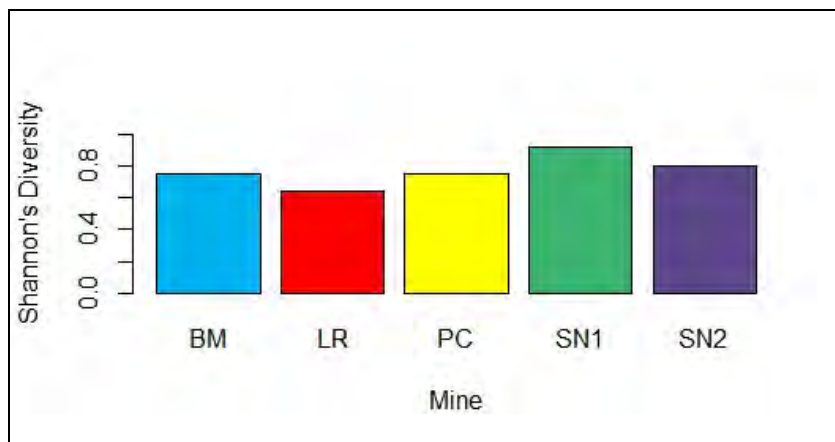


Figure 7. Graph shows Shannon's Diversity across all mine sites.

There is little difference between the mines except Long Run which has the lowest diversity. However, Snyder Run 1 and 2 having the highest diversity is not what was expected since these two mine sites are the unreclaimed mines. Data shows that there is no significant differences between mines for diversity.

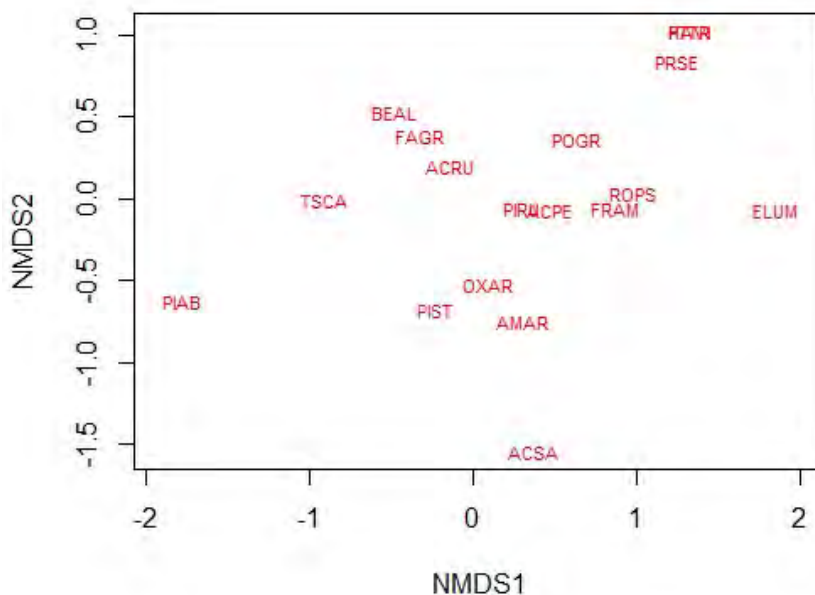


Figure 4. Nonmetric multidimensional scaling that shows each species of tree and how spatially different they are from each other.

Species that overlap each other are the red pine (PIRU) and striped maple (*Acer pensylvanicum*) (ACPE) which are located on the 0 y-axis and 0.4 on the x-axis. Hoptree (*Ptelea trifoliata*) (PTTR) and Witch-Hazel (*Hamamelis virginiana*) (HAVI) overlap and are located at the very top on the 1 y-axis and 1.3 x-axis.

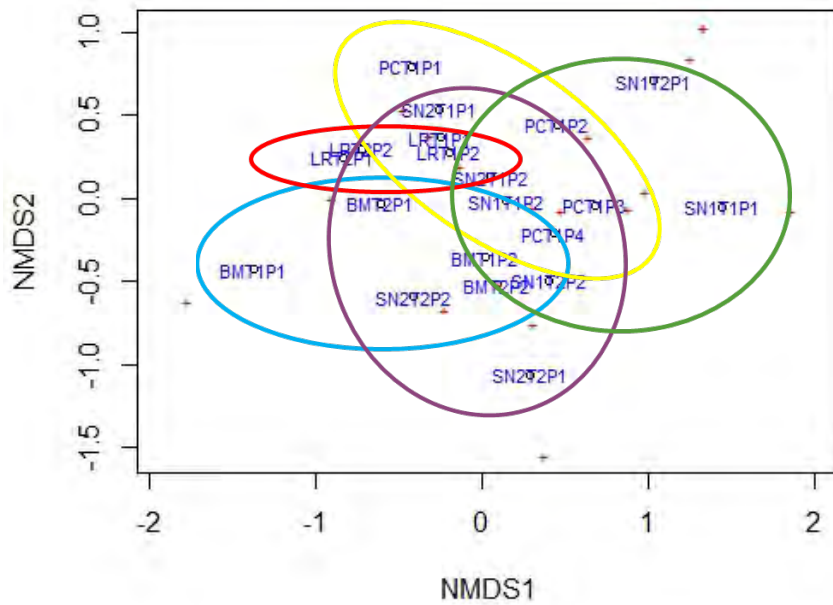


Figure 4. Nonmetric multidimensional scaling that shows each plot that was made.

This nonmetric multidimensional scaling graph indicates that there is no spatial significance between mines due to excessive overlapping of mines. Long Run may be so compacted compared to the others because how close the plots were to each other which could show the same species of trees.

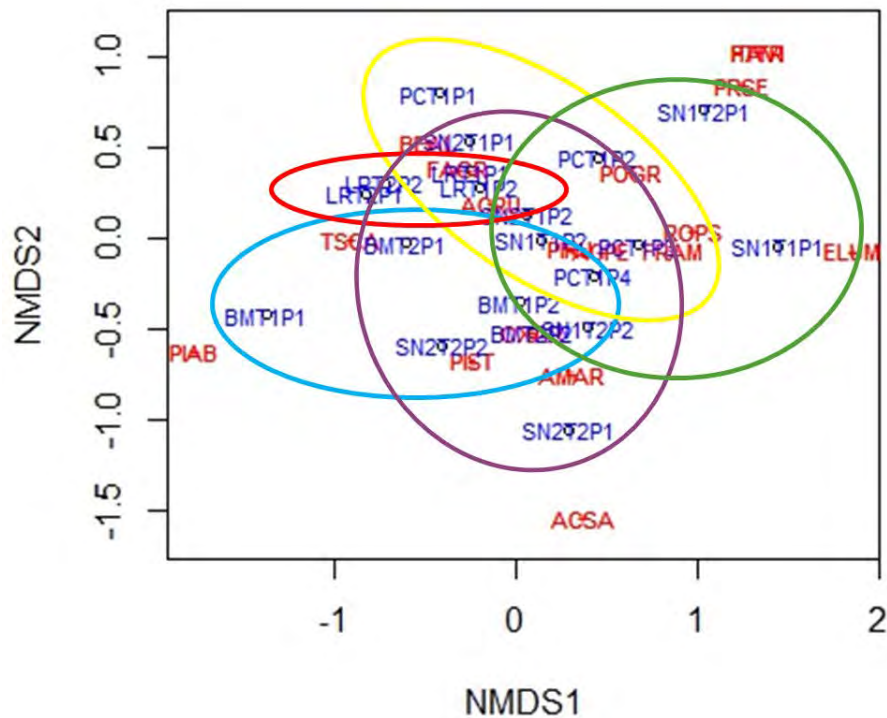


Figure 4. Nonmetric multidimensional scaling that tells us the relationship between each plot (blue) and each species of tree (red).

The closer a plot is to a species then that is where the species would be most commonly found in compared to the other plot sites. The consistent overlapping of mine sites shows that there is no spatial significance between mines.

DISCUSSION

The goal of the study was to find out if remediation efforts had any significance when comparing mine sites with each other that have been reclaimed and unreclaimed. Data shows that there were no significant differences between mine sites in species richness and diversity. Relative abundance showed no significance except in sourwood which likes acidic soils, red maples and striped maples. The nonmetric multidimensional scaling shows no significant spatial differences between mine sites due to overlapping of all the mine plots. Iron concentrations were high from 9 ppm to >10 ppm in samples with sediment and some without sediment. The null hypothesis is accepted in which remediation efforts did not improve plant community composition, diversity and richness.

Information of every mine site sampled is in courtesy to Jonathan Knight of the WVDEP. Pendleton Creek Highwall 1 was a mine operated during the WWII era as a dragline to excavate minerals. Later on, the highwall became a reclaimed site in 2010. Reclamation efforts for

Pendleton Creek Highwall 1 includes a reconstructed channel for their small tributary to flow into the Pendleton Creek. Long Run was a mine site that involved surface and underground mining but was reclaimed in 1996. Reclamation efforts for Long Run included the highwall to be backfilled, a refuse was covered with a soil cap, underdrains that were installed to capture AMD and then transport it off of the site, treatment systems were installed to treat AMD as well. However, the treatment systems are either no longer functioning or never functioned well at all in the first place. Blackwater Manor was a mine site dating back to the early 1900's and was reclaimed in 1997. There were three mine portals sealed and included a water treatment (Pavlick, Hansen, and Christ 2005). Snyder Run Highwall 1 and 2 were mine sites involving underground mining in the early 1900's. Both of these highwalls are unreclaimed sites and therefore have no reclamation efforts in place (Knight 2017). Grass/legumes are planted by the WVDEP as ground cover but also has remediation effects for the soil. Agricultural liming by the WVDEP buffers the acidity of the soil, increasing the pH (Knight 2017).

In some reclamation efforts, certain commonly planted woody species, including the native black locust (*Robinia pseudoacacia*) and the non-native and invasive autumn olive (*Elaeagnus umbellata*), were able to proliferate on SMCRA-reclaimed landscapes (Zipper et. al. 2007). This was not seen in the mine sites where autumn olive was only seen once and black locust in two mine sites. Crop trees are long-lived species that are characteristic of the region's mature forests and produce saleable forest products. Yellow poplar (*Liriodendron tulipifera*), oaks (*Quercus* sp.), ash (*Fraxinus* sp.), maple (*Acer* sp.), and other native deciduous species are commonly planted as crop trees on mines reclaimed using the FRA (Angel et. al. 2011).

Sourwood trees could be outcompeting the autumn olives and black locusts because of the pH conditions of the soil even though that black locusts and autumn olives are considered invasive species. Better installments of treatments would help greatly in lowering AMD since some of their installments from before hardly or don't work at all. It is imperative that the plant community health be taken care to prevent direct and indirect conflicts with other species. One AMD prevention tactic would be to use an anoxic limestone drain that involves the AMD being treated below the ground surface using alkalinity to buffer the pH level (Kuyucak 2002). Individual plant health may be because of the vesicular arbuscular mycorrhizae that limit the iron intake (Smith and Read 2008). Planting trees like black locust with white ash and can help promote growth (Burger 2001). We can see that there are black locust species and white ash in the Pendleton Creek mine site. According to Pavlick, there is an AML Trust Fund that the WVDEP set up but they have been slow in their priorities of lowering the risks of AMD. It is clear in Pavlick's study that reclamation efforts should be of high importance and in eleven years since the study the reclamation efforts have not changed Long Run nor Blackwater Manor.

ACKNOWLEDGEMENTS

The author would like to thank the NASA West Virginia Space Consortium for the funding they provided, Shepherd University for funding WVAS in 2016 and 2017, Shepherd University Biology Department, Dr. Mark Lesser, Jonathan Knight of the WVDEP, Western Pocahontas for allowing permission to be on their property, Demian Nunez and Stacey Jones for helping with field work.

PUBLICATIONS

Clark, K. and Lesser, M. 2017. Effects of Acid Mine Drainage on Plant Communities in the

Central Appalachians. West Virginia Academy of Sciences (WVAS). Glenville State College, WV.

Clark, K. 2017. Effects of Acid Mine Drainage on Plant Communities in the Central Appalachians. Biology capstone presentations. Shepherd University, Shepherdstown, WV.

REFERENCES

Akcil, A., & Koldas, S. (2006). Acid Mine Drainage (AMD): causes, treatment and case studies. *Journal of Cleaner Production*, 14(12-13 SPEC. ISS.), 1139–1145. <http://doi.org/10.1016/j.jclepro.2004.09.006>

Angel, P. N., Barton, C. D., Davis, V., & Franklin, J. A. (2011). Restoring Forests and Associated Ecosystem Services on Appalachian Coal Surface Mines, 751–765. <http://doi.org/10.1007/s00267-011-9670-z>

Bienfait, H. F. (1989). Prevention of stress in iron metabolism of plants. *Acta Botanica Neerlandica*, 38: 105–129. doi: 10.1111/j.1438-8677.1989.tb02035.x

Burger, J. A., Zedaker, S. M., & Zipper, C. E. (2001). Woody Species Diversity, Forest and Site Productivity, Stumpage Value, and Carbon Sequestration of Forests on Mined Lands Reclaimed Prior to the Passage of the Surface Mining Control and Reclamation Act of 1977.

Chapin III, F. S., Matson, P. A., Mooney, H. A (2002). *Principles of Terrestrial Ecosystem Ecology*. Springer. NY, New York U.S.A.

Herlihy, A. T., Kaufmann, P. R., Mitch, M. E., & Brown, D. D. (1990). Regional estimates of acid mine drainage impact on streams in the mid-Atlantic and southeastern United States. *Water, Air, & Soil Pollution*, 50(1), 91-107.

Kuyucak, N. (2002). Role of microorganisms in mining: generation of acid rock drainage and its mitigation and treatment. *ejmp & ep (European Journal of Mineral Processing and Environmental Protection)*, 2(3), 179-196.

Levy, M. A., & Cumming, J. R. (2014). Development of Soils and Communities of Plants and Arbuscular Mycorrhizal Fungi on West Virginia Surface Mines. *Environmental Management*, 54(5), 1153–1162. <http://doi.org/10.1007/s00267-014-0365-0>

Marschner, H., 1995. *Mineral Nutrition of higher Plants*, second ed. Academic Press, London.

Neagoe, A., Ebenå, G., & Carlsson, E. (2005). The effect of soil amendments on plant performance in an area affected by acid mine drainage. *Chemie Der Erde - Geochemistry*, 65(SUPPL. 1), 115–129. <http://doi.org/10.1016/j.chemer.2005.06.009>

Smith SE, Read DJ (2008) *Mycorrhizal symbiosis*. Academic Press, Waltham, MA.

Pavlick, M., Hansen, E., & Christ, M. (2005). Watershed based plan for the north fork Blackwater River Watershed, West Virginia. *Downstream Strategies, Morgantown, WV*.

Zipper CE, Burger JA, McGrath JM, Amichev B (2007) Carbon accumulation potentials of post-SMCRA coal-mined lands. In: Barnhisel RI (ed) 24th Annual national conference of the American Society of Mining and Reclamation, Lexington, pp 962–980.

IDENTIFICATION AND MASS SPECTRAL ANALYSIS OF PALMITOYLATED PROTEINS AND THE POTENTIAL LINK TO INSULIN RESISTANCE AND DIABETES MELLITUS IN OBESE SUBJECTS

Justin Conte
Chemistry
Marshall University
Huntington, WV

ABSTRACT

Historically, an inverse relationship has been observed between the concentration of free fatty acids (FFAs) and cellular glucose uptake. Evidence strongly indicates that the FFAs found in abundance in obese individuals somehow contribute to insulin resistance and ultimately the onset of type II diabetes mellitus. Unfortunately, little is known to date about the mechanism. Similarly, the reversible fatty-acylation, S-palmitoylation, has yet to be characterized to the same extent as other well-known post-translation modifications. Using mass spectrometric techniques, this project attempts to establish an effective protocol for the *in vitro* identification of S-palmitoylated proteins, and use this protocol to evaluate the potential of the human tyrosine kinase insulin receptor to undergo the modification. Spectral data for the tryptic mass fingerprint suggests that the protein is susceptible to non-enzymatic palmitoylation at C1083 in the tyrosine-kinase domain; however, the CAD spectrum for the tryptic peptide containing this residue did not provide a sufficient number of landmark peaks necessary for the sequencing of the peptide, and thus the amino acid modification site has yet to be confirmed—although it has been localized to a peptide within the active site of the receptor.

INTRODUCTION

It is hypothesized here that a high intracellular and plasma concentration of free fatty acids has the potential to inhibit insulin signaling via the palmitoylation of cysteine residues within the amino acid sequence of the human tyrosine kinase insulin receptor—consequently altering the structure and function of the protein.

Several proteins—especially transmembrane proteins—have been found to undergo palmitoylation. S-palmitoylation is a reversible post-translational acylation that involves the addition of the FFA substituent palmitate to the cysteine side chain of peptides.⁴ The reaction occurs via a nucleophilic substitution with the

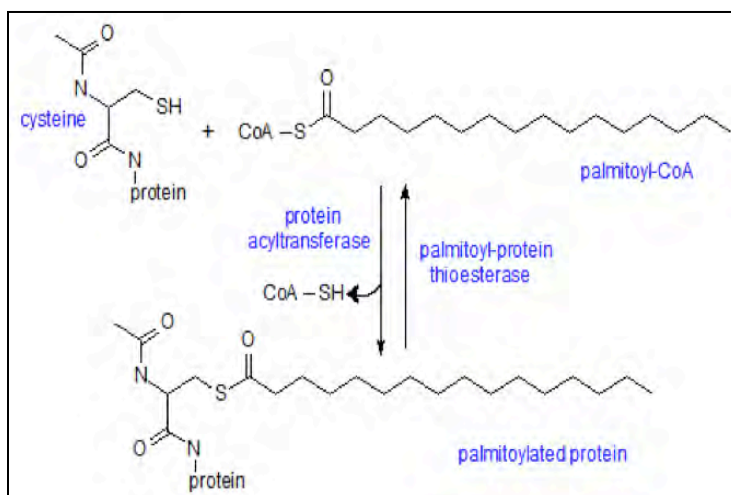


Figure 1: The enzymatic reaction of the cysteine side chain with palmitoyl CoA.

cysteine's thiol acting as the nucleophile and palmitoyl-CoA acting as the substrate as shown in Figure 1.¹⁶ Palmitoyl CoA is a key intermediate in the beta-oxidation of fatty acids that consists of a long hydrocarbon chain with a thioacyl CoA group at the terminal end.¹⁰ Under normal physiological conditions, the free fatty acid concentrations are too low for non-enzymatic palmitoylation to proceed, so the process most commonly occurs through an enzymatic pathway with the assistance of palmitoyl acyltransferases or protein acyltransferases (PATs)—23 of which are present in humans and are characterized by DHHC motif amino acid sequences and an abundance of cysteine residues in the catalytic domain.⁴ These enzymes demonstrate considerable specificity and serve to transport palmitoyl CoA to the thiol of cysteine residues where the palmitoyl group is attached.¹³ The two proposed mechanisms of enzymatic S-palmitoylation are shown in figure 2. The first mechanism involves the acylation of a cysteine residue within the active site of the enzyme, then an acyl exchange with the protein substrate via a substitution reaction in which the protein contributes its own cysteine thiol group to act as a nucleophile.⁹ The second mechanism involves the initial binding of coenzyme A to the acyl transferase, then a subsequent nucleophilic substitution in which the coenzyme A leaving group remains bound to the enzyme after the acylation of the protein substrate.⁹ Depalmitoylation is also an enzymatic process mediated by proteins known as acyl protein thioesterases (APTs) that hydrolyze the thioester bond that links the cysteine residue to the palmitoyl substituent.³ The active sites of these enzymes contain the characteristic SHD catalytic triad of a serine hydrolase—the same catalytic triad also found in the serine proteases trypsin and chymotrypsin.¹ To date, few of these proteins have been observed in the human body, leading researchers to believe that these enzymes are relatively versatile or that there are more that have yet to be found.³

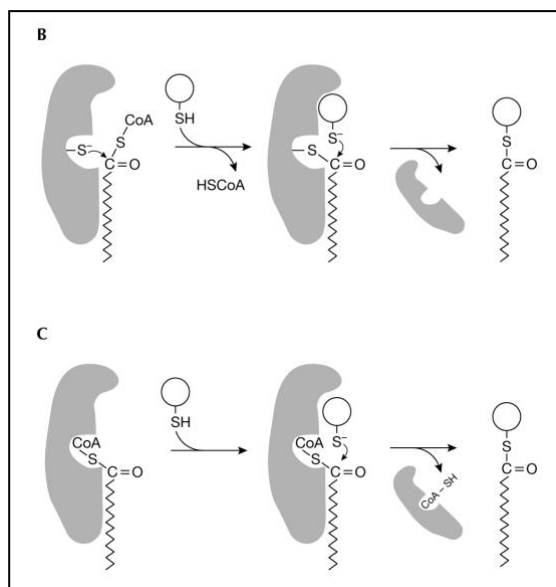


Figure 2: Proposed mechanisms of enzymatic S-palmitoylation via palmitoyl acyltransferase.⁹

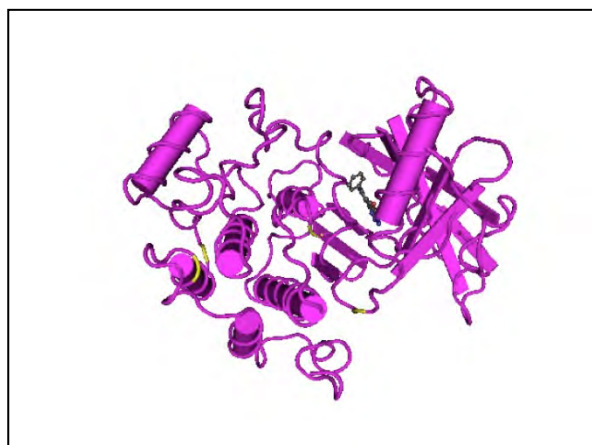


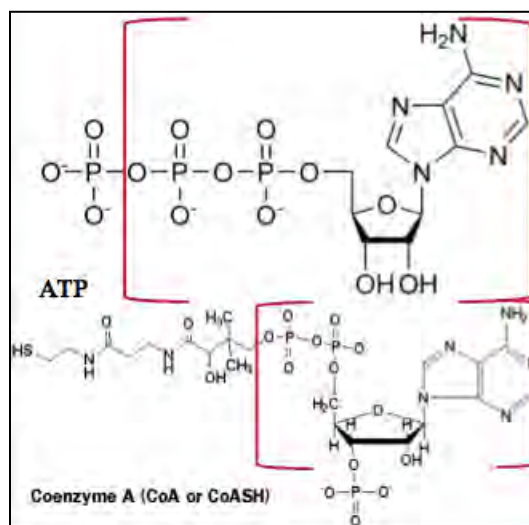
Figure 3: The tyrosine kinase domain of the human insulin receptor β -subunit with cysteine residues highlighted in yellow.

Although normal physiological concentrations of FFAs are too low for S-palmitoylation to proceed through a non-enzymatic pathway,⁴ it has been widely observed that FFA concentrations are elevated in obese individuals due to the limited capacity of adipose tissues.⁵ It is possible that the nucleophilicity of cysteine's thiol group combined with an increased availability of palmitoyl CoA both create a favorable environment for the reaction to occur even in the absence of a PAT.¹⁶ It is also possible that the high energy C—SCoA bond drives the reaction in a manner similar to the nature of ATP hydrolysis in other cellular processes.

Palmitoylated cysteine residues have been found at multiple regions during the analysis of different proteins. These characteristic locations include the carboxy and amino terminal regions of membrane-soluble proteins, internal regions, regions close to other lipid-modified side chains, and cytosolic regions near the domains of other transmembrane proteins.¹³ Six of the cysteine residues present in the cytosolic beta subunit of the human insulin receptor fit one or more characteristic descriptions of this profile. C1008 is found in the juxtamembrane position; C1083, C1165, C1261, and C1272 are found in the active site (figure 3); and C1335 is found in the C-terminal region. It has been proposed that the beta-subunit contains only one free thiol group. Although it is unclear at which precise point in the signaling pathway FFAs interfere with glucose transport, the effects of cysteine modification on the human insulin receptor's activity have been tested, and results have demonstrated both an inhibitory and activating effect on autophosphorylation and kinase activity depending on the reagent used to modify the cysteine residue. This suggests that the free thiol group is located near the ATP binding site. Although it is unknown which of the six cysteine residues contributes this free thiol, it is known that C1008 and C1272 both lie in regions that are vital to the proper function of the receptor.¹² Here, it is easily comprehensible that the addition of a large hydrocarbon substituent to this region could block the ATP binding site or otherwise alter the conformation of the protein and thus render the receptor dysfunctional. Considering the leaving group, Coenzyme A, the competitive inhibition of ATP binding is also a possibility as the two molecules share structural similarities. These structural similarities are highlighted in figure 4. Note the common nitrogenous base, ribose unit, and the phosphate groups attached to carbon 5 of the ribose sugar.

Palmitoylation can also impact the localization of proteins in the cell. It is an essential signaling modification required for the localization of the N and H isoforms of Ras proteins—key points of regulation in the mitogen-activated protein kinase (MAPK) signal transduction pathway that regulates cell growth and differentiation.⁸ The hydrophobic properties of the palmitoyl group may also promote protein association with lipid rafts—cholesterol-rich microdomains of the plasma membrane that mediate endocytosis. In fact, palmitoylation has been found to be a partial trigger of massive endocytosis³—a recently observed form that involves the ingestion of up to 70% of the plasma membrane and a clear impediment to the efficacy of the body's signaling mechanisms that rely on cell-surface interactions.¹¹

Elevated concentrations of the FFAs have been known to interfere with the proper protein folding and trafficking function of the endoplasmic reticulum (ER) by inducing ER stress.¹⁴ Under these conditions, unregulated or widespread palmitoylation has the potential to cause unprocessed peptides to aggregate or anchor into the ER membrane. During the lifetime of this modification, it makes the peptides essentially inaccessible for folding or degradation and may leave the ER unable to resolve the stress. If the stress is not relieved after a period of time, apoptosis may commence. This phenomenon is known to occur in the pancreatic β -islets responsible for producing insulin peptide hormone.²



A general goal of this project is to develop an effective protocol for the positive identification of S-palmitoylated proteins and their modification sites, but ultimately, the objective is to assess the *in vitro* palmitoylation state of the human tyrosine kinase insulin receptor and identify the site(s) of modification.

Figure 4: The molecular structures of ATP and Coenzyme A with the similar regions shown in brackets.

EXPERIMENTAL METHODS

Instrumentation

Two different mass spectrometers were used in this project. A Bruker Autoflex II matrix-assisted laser desorption/ionization time-of-flight (MALDI-TOF) mass spectrometer equipped with an N₂ laser was mostly used for analysis of protein digests. Large chemical species like polypeptides are normally susceptible to multiple charging. This makes mass analysis tedious and time consuming due to the different mass-to-charge ratios that any single polypeptide can have; however, matrix-assisted ionization restricts polypeptides to single charging. Therefore, the peaks in the MALDI-TOF mass spectrum of a protein digest are directly representative of the peptide molecular weights. This makes identification of modified peptides much easier and more time-efficient. An $n(+238$ Da) mass shift is an indication that a particular peptide has undergone the modification—where n is some positive integer less than or equal to the number of cysteine residues within a particular peptide.

A Thermo-Finnigan LCQ mass spectrometer equipped with an electrospray ionization source and quadrupole ion trap was mostly used for the fragmentation and sequencing of peptides. Analytes were injected into the instrument via a C₁₈ microcapillary flow column that allows for chromatographic separation. It was expected that this would facilitate greater retention times for palmitoylated peptides and make them more easily distinguishable from unmodified peptides with similar molecular weights. The instrument's collision-activated-dissociation (CAD) fragmentation mechanism involves bombarding charged peptides with helium atoms and breaking the amide bonds at different locations along the peptide backbone. The location of fragmentation is dependent upon the location of the resonant charge in the amide backbone at the time a helium atom makes contact. *De novo* peptide sequencing—based on the m/z of the b and y ions—was used to confirm the identity of the peptide at a particular m/z and ultimately determine the amino acid modification site. Unlike MALDI, electrospray ionization results in the multiple charging of peptides and makes the analysis more tedious. The anticipated shift for a modified fragment is dependent upon its charge state. For a modified +1 fragment, a shift of $+n(238$ $m/z)$ is expected, while a modified +2 fragment is expected to exhibit a $+n(119$ $m/z)$ shift.

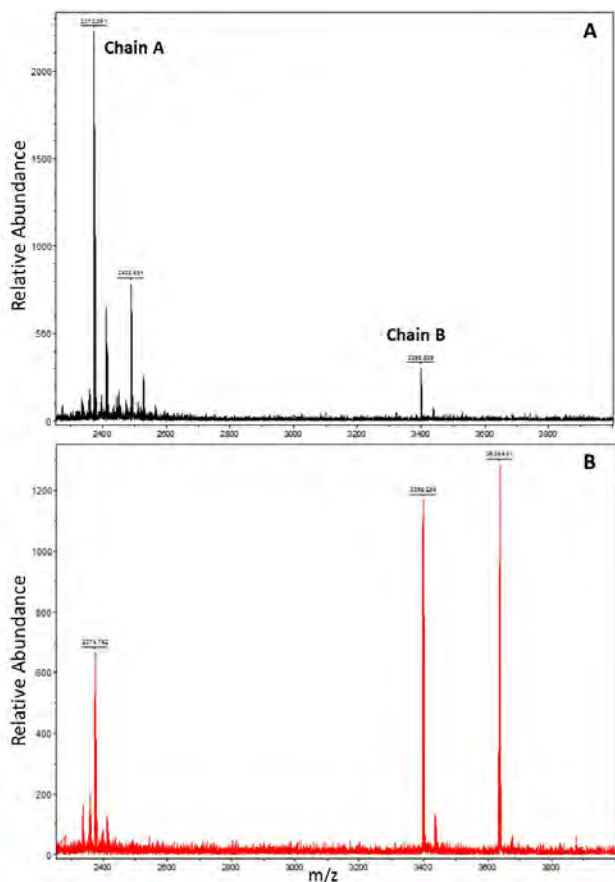
Human Insulin Peptide Hormone Incubation and Mass Analysis

1 μ L of 1 nmol/ μ L insulin peptide hormone was incubated for 24 hours at 37°C with 5 μ L of 300 mM HEPES buffer (pH 7.4), 2 μ L of .04 M DTT in HEPES, 5 μ L of 2.0 mM Palmitoyl-CoA in PBS, and 12 μ L of distilled water. After incubation, 4 μ L of the sample was purified using C₁₈ ZipTips® in accordance with the manufacturer's instructions and 1 μ L of the purified sample was spotted onto to the steel sample plate with .8 μ L of saturated α -cyano-4-hydroxycinnamic acid/50% acetonitrile/50% trifluoroacetic acid matrix solution. The solutions were mixed on the

plate, and the mass spectrum was obtained for the intact protein under reducing conditions in the MALDI-TOF mass spectrometer. Afterwards, the rest of the original sample was left to digest at room temperature (25°C) for another 24 hours with 1 μL of .25 $\mu\text{g}/\mu\text{L}$ chymotrypsin solution and 30 μL of 25 mM NH_4HCO_3 . After the 24 hour period, the peptides were purified using C₁₈ ZipTips® in accordance with the manufacturer's instructions. After the 24 hour period, the digestion was stopped using 3 μL of glacial acetic acid (>99%). A 1 μL aliquot of the purified digest was then pipetted onto the steel sample plate followed by a .8 μL aliquot of saturated α -cyano-4-hydroxycinnamic acid/50% acetonitrile/50% trifluoroacetic acid matrix solution. The solutions were mixed on the plate, and the chymotryptic mass fingerprint was obtained in the MALDI-TOF mass spectrometer.

Human Insulin Receptor Incubation and Mass Analysis

10 μL of .1 $\mu\text{g}/\mu\text{L}$ recombinant human tyrosine kinase insulin receptor of Baculovirus infected sf9 cell origin was incubated for 24 hours at 37°C with 2 μL of 10 mM Palmitoyl CoA in PBS and 13 μL of .01M PBS. After incubation, the samples were left to digest at room temperature (25°C) for another 24 hours with 1 μL of .2 $\mu\text{g}/\mu\text{L}$ trypsin solution and 30 μL of 25 mM NH_4HCO_3 . After the 24 hour period, the digestion was stopped using 3 μL of glacial acetic acid and the peptides were purified using C₁₈ ZipTips® in accordance with the manufacturer's instructions. A 4 μL aliquot of the purified digest was mixed with approximately 20 μL of X M acetic acid and injected into the LCQ mass spectrometer via the LC flow column. The tryptic mass fingerprint was taken, and the m/z of any peak of interest was noted. The CAD spectrum was taken for any peak of interest by selecting for its m/z, and the peptide at this m/z was sequenced to ensure that it was the expected tryptic peptide. Any amino-acid modification sites were determined from this spectrum.



In the stock solution, other than the insulin receptor fragment (amino acids 1011-1382), there were also other reagents present: 25% Glycerol, 50 mM Tris HCl, 150 mM NaCl, .25 mM DTT, .1 mM EGTA and .1 mM EDTA (chelating agents), and .1 mM PMSF (protease inhibitor).

RESULTS AND DISCUSSION

Analysis of the insulin peptide hormone samples suggests that the B chain of the peptide has the potential to undergo palmitoylation. The mass spectrum of the control sample in Figure 5 shows two prominent peaks at 2,378 m/z and 3,396 m/z. Respectively, these peaks are indicative of the presence of the A and B chains. Also shown in Figure 5, the mass spectrum of the experimental sample shows the same prominent peaks as the control sample; however, another prominent peak is shown at 3,634 m/z. This is a

Figure 5: The control (A) and experimental (B) MALDI-TOF mass spectra for the insulin peptide hormone under reducing conditions.

+238 Da shift from the B chain peak and thus is a positive indication that palmitoylation has occurred at a single

site. The chymotryptic peptide mass fingerprint shown in figure 6 also suggests that the modification has occurred. Note the parent peak at 2839 m/z that corresponds to the B chain peptide FVNQHLGSHLVEALYLVCGERGFF in both the experimental and control spectra. In the experimental spectrum, two other relevant peaks are shown—one shifted up by approximately 238 Da to 3078 m/z and the other shifted up by approximately 476 Da to 3316 m/z. The peak at 3078 m/z is indicative of the aforementioned peptide being palmitoylated at a single site, while the peak at 3316 m/z is indicative of the peptide being palmitoylated at two sites. The experimental spectrum also exhibits a significant peak at 2069 m/z, which is shifted 238 Da up from the anticipated m/z for the B chain chymotryptic peptide containing C7, FVNQHLGSHLVEALY. While both the peptide mass fingerprint and the original spectrum of the protein under reducing conditions are positive indications of the modification, only the peptide mass fingerprint suggests that the B chain can be modified at both cysteine residues, C7 and C19. This modification is unlikely to occur outside of the reducing conditions used for incubation, as the six cysteine residues

within the A and B chains all participate in the formation of disulfide bridges—illustrated in figure 7.¹⁷ On the other hand, palmitoylation of the peptide may occur prior to folding in the ER lumen—especially in the β -cells of the pancreatic islets where the hormone is produced. Here, unregulated palmitoylation may contribute to ER stress and activate the unfolded protein response that ultimately ends in apoptosis if unmitigated.⁶

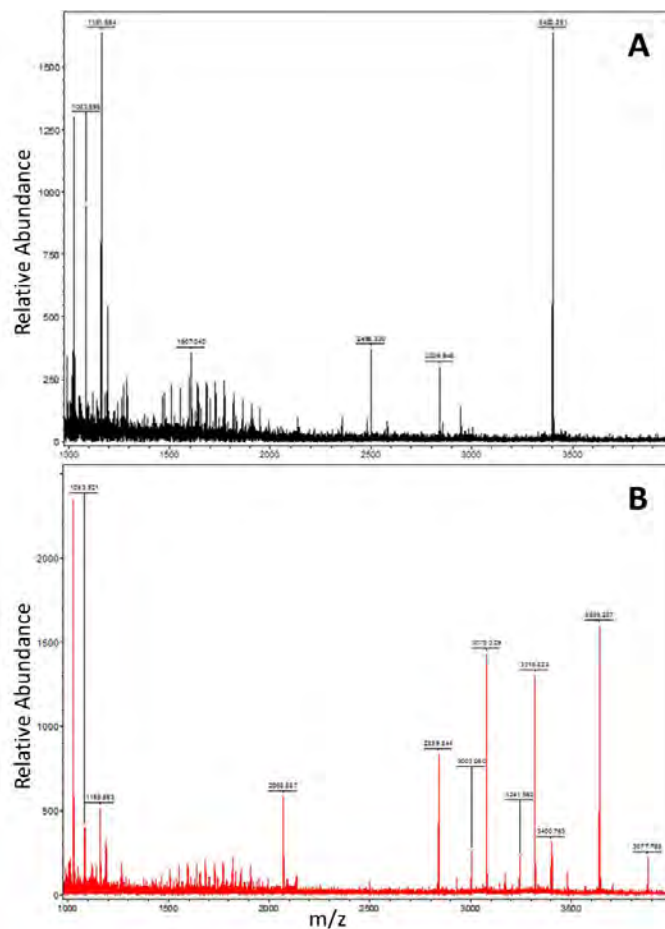


Figure 6: The chymotryptic peptide mass fingerprint for the control (A) and experimental (B) samples of the insulin peptide hormone.

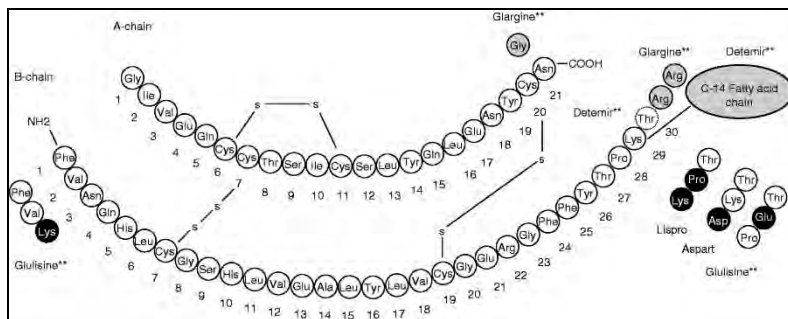


Figure 7: The amino acid sequence of the human insulin peptide hormone showing the A and B chains linked by disulfide bridges between cysteine residues.¹⁷ Note that the fatty acyl substituent attached via K29 in the B chain is not a part of the native structure and should be disregarded for the purposes of this illustration.

did not seem to compromise the relative abundance of the peptide, as the peak at 1278 m/z in figure 8C was among the most intense in the spectrum. The peptide's CAD spectrum shown in figure 9 did not provide a sufficient number of landmark peaks needed for sequencing and therefore the precise amino acid modification site was unable to be confirmed.

Figure 8C shows the tryptic mass fingerprint obtained during analysis of the human insulin receptor at 1.20 minutes, with the 1278 m/z peak being a positive indication for the $(M+2H)^{2+}$ palmitoylated peptide containing C1083. The receptor's tryptic mass fingerprint at .98 minutes shown in figure 8B does not contain this peak. Noting the longer retention time for the palmitoylated peptide and the liquid chromatogram in figure 8A, this data suggests that the palmitoylated peptide associates with the C₁₈ stationary phase in the instrument's liquid chromatographic (LC) column prior to mass analysis. This

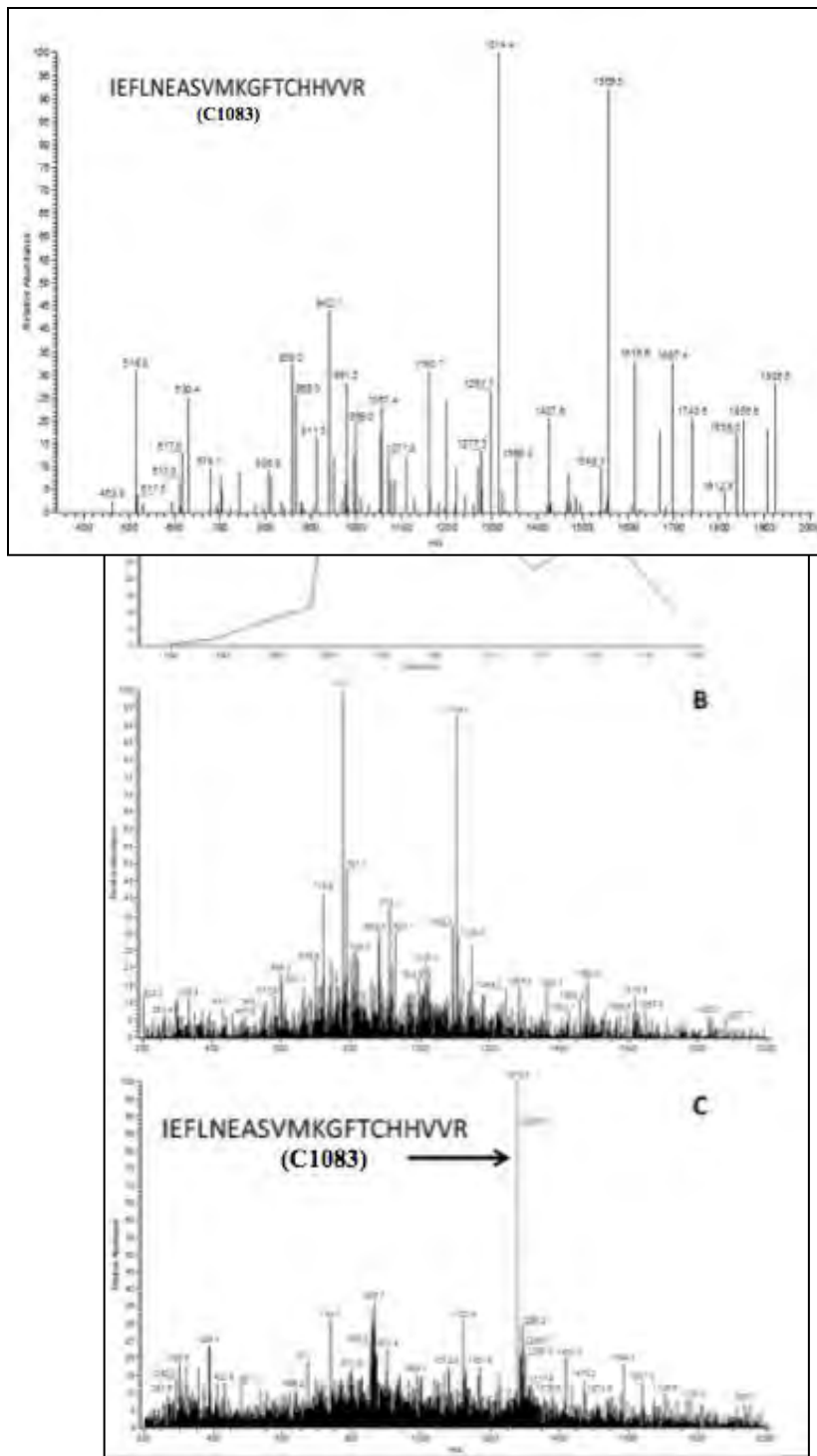


Figure 8: The liquid chromatogram (A), tryptic mass fingerprint at .98 minutes (B), and tryptic mass fingerprint at 1.20 minutes (C) for the human tyrosine kinase insulin receptor.

Figure 9: The CAD spectra of the $(M+2H)^{2+}$ ion for the tryptic peptide containing C1083.

CONCLUSION

Results varied with the composition of the matrix solvent. 50% Acetonitrile/50% trifluoroacetic acid was used until 50% ethyl acetate/50% trifluoroacetic acid was later substituted. The behavior of ethyl acetate upon elution onto the steel MALDI plate allowed the analyte to accumulate at the boundaries of the cell. This seemed to improve resolution of spectra in many cases and was also more convenient: it seemed to be slightly more volatile and thus required less drying time before analysis. The physical properties of the modified cysteine residues and the control residues still raise a few concerns. In many trials, the mass fingerprint spectra obtained using MALDI exhibited low intensities for small cysteine containing peptides. This may suggest that even though they are not detected, there may be modified cysteine residues present that are not desorbing from the MALDI plate due to some non-covalent interaction—perhaps aggregation of the hydrophobic tails in the modified cysteine side chains. This hydrophobic character is illustrated by the spectra in figure 8, as the palmitoylated chymotryptic peptide exhibited a greater retention time than most other peptides when the insulin receptor sample was injected through the LC flow column. For whatever reason, the peptides may also fail to ionize, which is essential for the detection of a chemical species in any mass spectrometer. It is also suggested that the electrospray ionization mechanism used to obtain the CAD spectrum and the typical serine-protease digestion protocol both have the potential to cleave the palmitoyl substituent off of a modified peptide.¹⁸ The active sites of the palmitoyl-cleaving APT and serine protease digestion enzymes contain the same catalytic triad, so palmitoylated cysteine residues near a serine-protease cleavage site may be susceptible to palmitoyl-loss. Alternatively, palmitoylated cysteine residues proximal to a cleavage site may actually prevent binding to the digestion enzyme in some cases. In fact, the palmitoylated tryptic peptide of the human insulin receptor illustrated in figure 8C contains a cysteine that is four residues away from an internal trypsin cleavage site; therefore, this suggests that palmitoylation of cysteine residues adjacent to protease cleavage sites may induce miscleavage during standard digestion protocol. To reduce the susceptibility of modified peptides to palmitoyl-loss in future trials, treatment with a mild reducing agent for the reduction the carbonyl in the acyl side-chain may be preferable. By reducing the electrophilicity of the modified side chain, this should prevent any further possibility of nucleophilic attack and substitution during digestion. Furthermore, liquid chromatographic separation prior to mass analysis indeed seems to be preferable for the identification of palmitoylated peptides, as their longer retention times may make them less likely

to be mistaken for other unmodified peptides of similar molecular weight.

While the specific amino-acid palmitoylation site in the human tyrosine kinase insulin receptor has yet to be confirmed, the modification site has been localized. C1083 is found in the active site of the receptor. This supports the hypothesis that palmitoylation may have the ability to interfere with the autophosphorylation of the insulin receptor's tyrosine kinase domain by blocking the ATP binding site. Furthermore, palmitoylation of this residue may still inhibit receptor dimerization via anchoring the individual monomers in the cell membrane. C1083 seems to be a notably favorable modification site, with the pKa of the residue being inevitably lowered by the two adjacent histidine residues, H1084 and H1085, making it more likely that the side chain is found in the more-nucleophilic thiolate form at physiological pH. It should be noted that one of the B chain palmitoylation sites of the insulin peptide hormone, C7, is also located proximal to two basic residues: H5 and H10. Results from this study seem to suggest that palmitoylation may have the potential to play a role in the ER stress response that ultimately leads to pancreatic β -cell death due to the high susceptibility of the insulin peptide hormone to undergo the modification. The data also suggests that there is also a possibility that the modification may induce the onset of insulin resistance under elevated FFA concentrations; however, future work should focus on reproducing these results under *in vivo* conditions with an objective to isolate modified insulin receptor proteins from model organism hepatocytes and adipocytes. This lab considers the Zucker rat to be a suitable candidate for *in vivo* trials. If successfully isolated, an activity assay should be conducted measuring the effect of palmitoylation on the receptor's function.

ABBREVIATIONS

CoA= Coenzyme A

ATP= Adenosine Triphosphate

CAD= Collision-Activated Dissociation

HEPES= 4-(2-hydroxyethyl)-1-piperazineethanesulfonic acid

PMSF= Phenylmethylsulfonyl Fluoride

m/z= mass to charge ratio

Amino Acid Single-Letter Identifiers= A(Alanine), C(Cysteine), D(Aspartic Acid), E(Glutamic Acid), F(Phenylalanine), G(Glycine), H(Histidine), I(Isoleucine), K(Lysine), L(Leucine),

M(Methionine), N(Asparagine), P(Proline), Q(Glutamine), R(Arginine), S(Serine),

T(Threonine), V(Valine), W(Tryptophan), Y(Tyrosine)

ACKNOWLEDGEMENTS

Thank you to Dr. Leslie Frost of Marshall University for allowing me to be a part of this project and providing to me her valuable time, resources, and guidance during my tenure in her lab. I would also like to thank the NASA West Virginia Space Grant Consortium for its sponsorship and the financial support that made it possible for me to dedicate more of my time to completing the objectives of this research.

REFERENCES

1. Audagnotto, M.; Ho, S.; Sandoz, P.; Andenmatten, N.; van der Goot, G.; Dal Peraro, M. New

- Insight into the Catalytic and Inhibition Mechanism of the Human Acyl Protein Thioesterase. *Biophysical Journal*. 2016, 110(3): 547a-548a.
2. Baldwin, A.C.; Green, C.D.; Olson, L.K.; Moxley, M.A.; Corbett, J.A. A Role for Aberrant Protein Palmitoylation in FFA-Induced ER Stress and β -Cell Death. *American Journal of Physiology-Endocrinology and Metabolism*. 2012, 302(11): E1390-1398.
 3. Blaskovic, S.; Adibekian, A.; Blanc, M.; Van der Goot, G.F. Mechanistic effects of protein palmitoylation and the consequences thereof. *Chemistry and Physics of Lipids*. 2015, 180: 44-52.
 4. Blaskovic, S.; Blanc, M.; Van der Goot, F.G. What does S-palmitoylation do to membrane proteins? *FEBS Journal*. 2013, 280(12): 2766-2774.
 5. Boden, G. Obesity and Free Fatty Acids (FFA). *Endocrinology and Metabolism Clinics of North America*. 2008, 37(3): 635-646. 6. Boden, G.; Chen, X.; Ruiz, J.; White, J.V.; Rossetti, L. Mechanisms of fatty acid-induced inhibition of glucose uptake. *Journal of Clinical Investigation*. 1994, 93(6): 2438-2446.
 6. Boden, G.; Chen, X.; Ruiz, J.; White, J.V.; Rossetti, L. Mechanisms of fatty acid-induced inhibition of glucose uptake. *Journal of Clinical Investigation*. 1994, 93(6): 2438-2446.
 7. Cassel, R.; Ducreux, S.; Alam, M.R.; Dingreville, F.; Berle, C.; Burda-Jacob, K.; Chauvin, M.A.; Chikh, K.; Paita, L.; Al-Mawla, R.; Crola Da Silva, C.; Rieusset, J.; Thivolet, C.; Van Coppenolle, F.; Madec, A.M. Protection of Human Pancreatic Islets from Lipotoxicity by Modulation of the Translocon. *PLoS One*. 2016, 11(2): e0148686.
 8. Chamberlain, L.H.; Lemonidis, K.; Sanchez-Perez, M.; Werno, M.W.; Gorieku, O.A.; Greaves, J. Palmitoylation and the Trafficking of Peripheral Membrane Proteins. *Biochemical Society Transactions*. 2013, 41(1): 62-66.
 9. Dietrich, L.E.P.; Ungermann, C. On the mechanism of protein palmitoylation. *EMBO reports*. 2004, 5(11): 1053-1057.
 10. Faergeman, N.J.; Knudsen, J. Role of long-chain fatty acyl-CoA esters in the regulation of metabolism and in cell signaling. *Biochem. Journal*. 1997, 323: 1-12.
 11. Hilgemann, D.W.; Fine, M.; Linder, M.E.; Jennings, B.C.; Lin, M. Massive endocytosis triggered by surface membrane palmitoylation under mitochondrial control in BHK fibroblasts. *eLife*. [Online] 2013,2:e01293. <http://elifesciences.org/content/2/e01293/article-info> (accessed Sep 27 2015).
 12. Macaulay, S.L.; Polites, M.; Frenkel, M.J.; Hewish, D.R.; Ward, C.W. Mutagenic structure/function analysis of the cytoplasm cysteines of the insulin receptor. *Biochem. Journal*. 1995, 306: 811-820.
 13. Ohno, Y.; Kashio, A.; Ogata, R.; Ishitomi, A.; Yamazaki, Y.; Kihara, A. Analysis of substrate specificity of human DHHC protein acyltransferases using a yeast expression system. *Molecular Biology of the Cell*. 2012, 23(23): 4543-4551.
 14. Pagliassotti, M.J.; Kim, P.Y.; Estrada, A.L.; Stewart, C.M.; Gentile, C.L. Endoplasmic Reticulum Stress in Obesity and Obesity-Related disorders: An Expanded View. *Elsevier*. 2016, 65(9): 1238-1246.
 15. Patel, P.S.; Buras, E.D.; Balasubramanyam, A. The Role of the Immune System in Obesity and Insulin Resistance. *Journal of Obesity*. [Online] 2013, 2013: 616193. <http://www.ncbi.nlm.nih.gov/pubmed/23577240> (accessed Sep 27 2015).
 16. Resh, M.D. Fatty acylation of proteins: new insights into membrane targeting of myristoylated and palmitoylated proteins. *BBA-Molecular Cell Research*. 1999, 1451(1): 1-16.

17. Varewijck, A.J.; Janssen, J.A.M.J.L. Insulin and its Analogues and their Affinities for the IGF1 Receptor. *Endocrine Related Cancer*. 2012, 19: F63-F75.
18. Yuhuan, J.; Leymarie, N.; Haeussler, D.J.; Bachschmid, M.M.; Costello, C.E.; Lin, C. Direct Detection of S Palmitoylation by Mass Spectrometry. *Analytical Chem*. 2013, 85(24): 11952-11959.

MODIFICATION OF NITINOL NANOPARTICLES WITH SELF-ASSEMBLED ALKYLPHOSPHONATE FILMS

Samantha Garretson

Biology

Marshall University

Huntington, WV

ABSTRACT

Nitinol (NiTi) nanoparticles, which are a fifty-fifty metal alloy of nickel titanium, are valued because of their corrosion resistance and superelasticity. NiTi is best known for its shape memory, as the bulk metal can physically change shape when transitioned by heat or pressure between the austenite and martensite forms. NiTi has potential in biomedical tools, nanofluids, and nickel alkaline batteries. To be able to utilize the NiTi nanoparticles, the surface requires modification, specifically by phosphonic acids. The metal oxide surface readily adheres to these acids, forming self-assembled alkylphosphonate films. In this study, phosphonic acids, including 16-phosphonohexadecanoic acid, octadecylphosphonic acid, and 12-aminododecylphosphonic acid are used to form an ordered self-assembled monolayers on the NiTi nanopowder.

These surface modifications could be used in the preparation of nanofluids in order to improve their suspension. NiTi nanofluids have the ability to change electrical and thermal conductivity at the transition temperature, producing a smart nanofluid. Initially, isoelectric point was found by creating a series of nitinol solutions ranging from pH 2 to pH 12. Zeta potential was used to find the isoelectric point of the NiTi nanofluids, which was expected to be around four and eleven based on the known isoelectric points of nickel and titanium. The isoelectric point, based on the experimental data, was at four and nine to ten.

Following the experimentation with the isoelectric point, NiTi nanofluids were made and tested with dynamic light scattering (DLS) for 31 days. The experiment required two groups, where one was sonicated and ran in DLS every day, and the other was sonicated only once at the beginning of the experiment and ran in DLS every day. As suggested by literature, the nanoparticles that were sonicated every day were larger than the nanoparticles that were not sonicated. Possible explanations include aggregation due to over-sonication, as well as the more likely proposition that the larger nanoparticles were able to settle out in the non-sonicated group.

INTRODUCTION

While space travel is already very dangerous due to the effects of gravity on physical health, the risk of flight denoted by former accidents, and the hazards of micrometeorites and other debris. The purpose of protective gear is to reduce the exposure to these dangers, not to expose these scientists to more threats such as free radicals. Nitinol at optimum function could make helmets and resistant to leaks and the effects of ever-changing gravity, spacecraft that are resistant to extreme heat and puncture bearings that can withstand the force of take-off, and research equipment that can handle the very different temperatures and atmospheric pressure of other moons and planets.

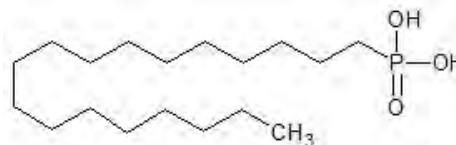
The plight of nitinol falls in that the nickel is still very reactive. Many people suffer from nickel allergies, and there is a high chance that the metal could even be cariogenic. To prevent the chance of free radicals escaping from the surface of the metal, a self-assembled monolayer must be produced to oxidize the reactive ions. To produce this, the nanopowder must be modified. The method proposed employs the use of acids to increase the phosphorous content of the metal alloy.² Through this project, the goal is to modify the nanoparticles in a way that their vital properties are not lost, but the fallacies are improved. NASA has already contributed immensely to the production of nitinol with the non-invasive tweezer, specialized eyeglass frames, and needle wire localizers that can mark the exact location for an anticipated surgery.¹ These products would be much safer and last even longer if a self-assembled monolayer were to be effectively applied.

PROJECT DESCRIPTION

Octadecylphosphonic acid (Figure 1), 16-phosphonohexadecanoic acid, and 12-aminododecylphosphonic acid will be used in this project as an organic modifier on the nitinol surface.⁶ Phosphonic acids contribute wetting, adhesion, and friction to the surface of the substance, assembling through hydrogen bonding and van der Waals forces.⁶ The incredible strength of this bond accounts for the protective characteristic of the self-assembled monolayer, completed via submersion in octadecylphosphonic acid, or a similar solution, such as the carboxylic acid to be employed concurrently and during the summer.⁷ Phosphonic acids are the most useful due to the low acid dissociation constant, making carboxylic phosphonic acid more likely to react with the free nickel oxide radicals.

Figure 1. Octadecylphosphonic acid structure.

NiTi nanoparticles also have the potential to form nanofluids which can advance the thermal conductivity of fluids in the form of a “smart” nanofluid. These advanced thermal properties come from the nitinol’s ability to undergo a controlled shape change. Currently, nanofluids are being produced in a lithium hydroxide/potassium hydroxide solution to encourage suspension of the particles. Particles are analyzed daily over the course of 31 days with dynamic light scattering at different weight percents. One set of nanofluids are sonicated daily, while another set is left undisturbed.



Another form of analysis currently in use is zeta potential, which is a measure of the attraction between particles when suspended in solution. Zeta potential varies with pH values, and therefore, can be used to find the isoelectric point of a particle. The isoelectric point is the pH in which a molecule possesses no net electrical charge. Samples of nitinol in water ranging from pH one to twelve were analyzed for zeta potential. Titanium typically carries an isoelectric point of four, while nickel’s ranges from eleven to twelve. Nitinol’s isoelectric point was found at four and twelve, so the results matched conclusions drawn from previous literature.

EXPERIMENT

To modify the nanoparticles, phosphonic acids are added to the nitinol powder in low concentrations. Following IR scans of the unrinsed modified nitinol, a rinsed sample of the concentration must be prepared using sonication and a vacuum centrifuge. This procedure helps to remove molecules physically attracted to the surface. Infrared spectroscopy is used in the

project to monitor the extent to which the acid bonds to the surface of the nitinol.⁸ Energy dispersive x-ray spectroscopy and x-ray photoelectron spectroscopy has provided information about the presence of phosphorous in the modified samples.

Cyclic voltammetry is used to characterize the ability of the substance to participate in reduction-oxidation reactions at the surface. A control of the nitinol has been analyzed, and from there, different concentrations of the acids can be compared to the unmodified nanoparticles. Thus far, the nitinol has proven to be significantly less corrosive when modified, but further investigation and employment of electrical impedance spectroscopy will help to confirm this (Figure 2). Additional cyclic voltammetry data must also be collected within a nanofluid solution. Therefore, nanofluids must be produced. Thus far, a nitinol control nanofluid has been created and analyzed with dynamic light scattering. Nanofluids of the modified nitinol must be produced, which will require a significant amount of samples and a modified base solution.

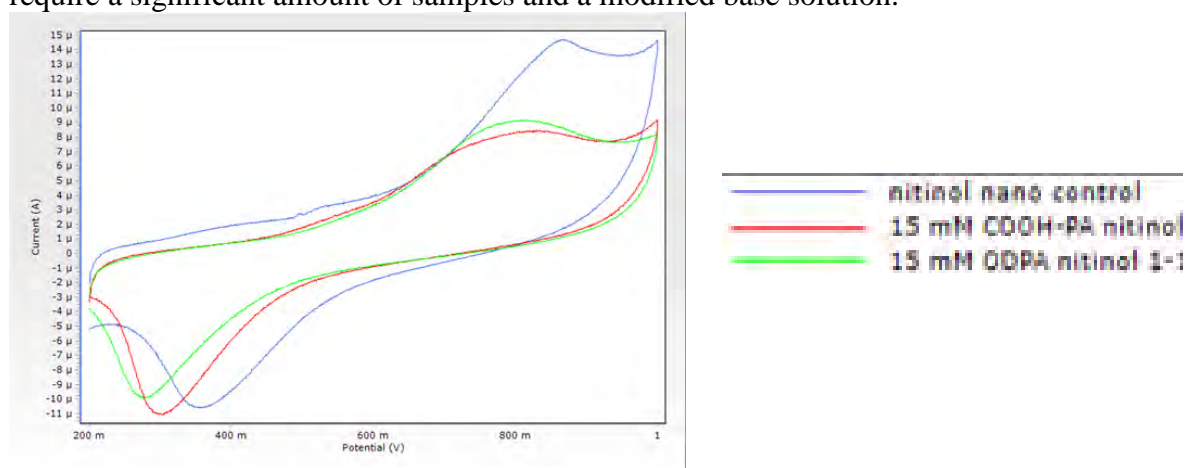
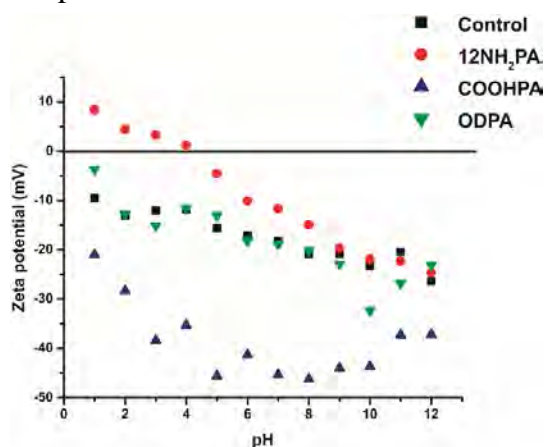


Figure 2. Cyclic Voltammetry data for unmodified particles, particles modified with 15 mM COOH-PA, and particles modified with 15 mM ODPA.

Isoelectric point was found on the nitinol nanoparticles by finding the zeta potential at a series of pH values ranging from two to twelve. The experiment was performed on the unmodified nanoparticles to serve as a control and the nitinol modified with phosphonic acids. The isoelectric point is typically the point at which the nanoparticles have no net electric charge at the surface. The isoelectric point of nitinol changes upon modification with acid (Figure 3).



The isoelectric point of nitinol changes upon modification with acid (Figure 3).

Figure 3. Isoelectric point of nitinol nanoparticles, including the unmodified nitinol, nitinol modified with 12-NH₂PA, nitinol modified with COOH-PA, and nitinol modified with ODPA.

Further investigation is being done to apply the nitinol to a biological concept, in which the nanoparticles will be examined for their ability to promote cell adhesion to surfaces. A collaboration with Dr. Nadja Spitzer in Marshall University's Department of Biological Sciences has allowed the opportunity to unmodified nitinol to B35 cells via coverslips treated with deionized water, ethanol, and polylysine and then coated with a nitinol-ethanol solution. The cells modified by the nitinol-coated coverslips are analyzed for morphological changes through fluorescent microscopy. The cells will also be analyzed quantitatively for evidence of toxicity through comet assays. The cells will be applied to a thin agar, and a high-alkaline solution will be added to strip away the cell membrane, leaving on the cell's DNA. When subjected to electrophoresis, the DNA from the nucleus will migrate. Large segments of DNA from cells that are healthy will not travel far through the agar. Smaller segments, fragmented in the process of apoptosis or necrosis, will travel farther through the agar. The DNA can then be stained with 4,6-diamidino-2-phenylindole (DAPI) and imaged. The proportion of DNA that has been segmented can be compared quantitatively to the amount of DNA that is not segmented through the olive tail moment, calculated using the OpenComet plugin on ImageJ (NIH). This will help to determine if the nitinol is toxic to the cells. Further analysis will be done by adding a nitinol solution to cells that have already been plated to see if there is a difference in morphology, compared to the cells grown on plain or nitinol-modified coverslips.

CONCLUSION

Phosphorous has appeared in energy dispersive X-ray and X-ray photoelectron spectroscopy, proving that 16-phosphonohexadecanoic acid and octadecylphosphonic acid is binding to the surface of the nanoparticles. There is a CH peak in the infrared spectroscopy, so there is evidence of the acid, even in low concentrations. The powder x-ray diffraction scan of the modified nanoparticles are consistent with the expected results of an austenite sample as given by the manufacturer. The cyclic voltammetry data suggests that the modification of the nanoparticles decreases redox reactions on the surface of the nitinol based on the decreasing area of the graph from unmodified to modified nanoparticles of moderate concentrations of either 16-phosphonohexadecanoic acid, octadecylphosphonic acid, or 12-aminododecylphosphonic acid. Solid-state nuclear magnetic resonance data demonstrates little peak shift between the control acid samples and the nitinol modified with acid, suggesting a monodentate binding at the surface. Experimentation with nitinol nanoparticles in B35 cells have yielded only preliminary results, but thus far, it has been concluded that the cells can grow in the presence of nitinol. Additionally, it has been concluded that rinsing with ethanol for sterilization does not affect the size of the nanoparticles via DLS. Given that the nitinol is of expected composition, the head group of the self-assembled monolayer is present, the organic component of the acid is present, and the redox activity has decreased on the surface of the modified nitinol nanoparticles, the project is progressing significantly. In the future, the data from the B35 cells will be analyzed with a confocal microscope and comet assays. Further investigation will be done with cyclic voltammetry in a nitinol solution to further test for corrosion resistance. More nanofluids will be made with modified nitinol to compare to the nanofluid created with the nitinol control.

ACKNOWLEDGEMENTS

- NASA West Virginia Space Grant Consortium
- Marshall University, Chemistry Department
- Marshall University, Geology Department
- Marshall University, Biological Imaging Center
- Marshall University, Department of Biological Sciences
- DOW-Marshall University STEM Partnership
- Summer Undergraduate Research Experience (SURE)
- West Virginia University Shared Research Facilities
- Pennsylvania State University, Chemistry Department
-

PUBLICATIONS

Accepted Publication

- Quiñones, R., **Garretson, S.**, Behnke, G., Fagan, J., Mueller, K. (2017) “Fabrication of Phosphonic Acid Films of Nitinol Nanoparticles by Dynamic Covalent Assembly.” *Thin Solid Films*.

Research Presentations

- 13th Annual Undergraduate Research day at the Capitol (URDC), Charleston WV - Thursday February 25, 2016 (Poster)
- 47th American Chemical Society Central Regional Meeting, Cincinnati, OH - May 18-21, 2016 (Poster)
- Marshall University Undergraduate Summer Research Program Final Symposium, Huntington, WV - July 22, 2016 (Oral Presentation)
- Summer Undergraduate Research Experience Final Presentation, Huntington, WV- July 27, 2016 (Oral Presentation)
- 253rd American Chemical Society National Meeting & Exposition, San Francisco, CA- April 2-6, 2017 (Poster)

REFERENCES

- (1) Files, B. *NASA Technical Reports Server* 2000, 1.
- (2) Quiñones, R.; Gawalt, E. S. *Langmuir* 2008, 24, 10858.
- (3) *Materials Characterization and Chemical Analysis*; Wiley-VCH Inc., 1996.
- (4) I., J. *Stockholms University* 2012, 33.
- (5) Roy, S.; Quiñones, R.; Matzger, A. J. *Crystal Growth & Design* 2012, 12, 2122.
- (6) Nie H., W. M., and McIntyre N. *Surface Science Western*. 2006, 1.
- (7) Nie H., M. D., Francis M., and McIntyre N. *Surface Science Western*. 2006, 1.
- (8) Quiñones, R.; Gawalt, E. S. *Langmuir* 2007, 23, 10123.

DETERMINING THE GROWTH RESPONSE OF *QUERCUS RUBRA* ALONG ELEVATIONAL AND EXPOSURE GRADIENTS

Sierra Hoffman
Biology
Shepherd University
Shepherdstown, WV

ABSTRACT

How tree species perform across the breadth of their realized niche is essential for understanding their response to changing environmental conditions. This is especially relevant in topographically heterogeneous landscapes, where changes in elevation, exposure, slope and aspect all interact to determine how a particular species will perform at any given location. We focused on growth performance in *Quercus rubra* (red oak) in the Shenandoah National Park. We established 4 transects that spanned >700 meters of elevation change. Each transect encompassed an exposure gradient from a stream-side to a ridgetop location, and were positioned on opposing aspects. Along each transect we cored five mature trees at six equally spaced points. Tree cores were prepared using standard dendroecological methods. Climate data from 1965-2016 was obtained from National Climatic Data Center for seven weather stations surrounding the Park. Elevational lapse rates were calculated for temperature data to adjust regional temperature to accurately represent coring locations. Ring width was modelled against climatic and topographic variables to determine which variables were important to red oak growth.

Results showed spring and autumn precipitation and temperature from current and previous year were associated with growth. Growth was maximized at low elevations at moderate distances from stream, however as elevation increased red oak performed better at greater distances from streams. At high elevations, growth was higher on ridgetops pre-1990 and has become more similar along the entire exposure gradient post-1990. As temperature continues to increase, optimal growth of red oak will shift to higher elevations and nearer stream environments.

INTRODUCTION

An important question in forest ecology is how tree species will respond to ongoing climate change (Nogues-Bravo et al., 2007, Hayhoe et al. 2008), the IPCC Second Assessment Report (IPCC, 1996) states that future research is necessary to predict climate effects on mountainous regions. Every species responds in a distinctive manner and it is difficult to determine one response for one species and apply that to the entire heterogeneous tree community (Candel-Pérez et al., 2012; Iverson & Prasad, 1998). One way to measure how species will respond to rapidly changing climate is to determine annual growth and examine the conditions the tree is under. Dendroecology provides a way to answer these questions through the analysis of the tree-rings. Disturbance history, climatic conditions influencing growth, and annual growth increment can all be determined through dendroecological methods (Fritts & Swetnam, 1989).

In this study, I will focus on determining climatic conditions and other abiotic factors that influence annual growth, to provide answers to how trees will respond to rapid warming. It is also important to research and analyze tree growth responses to climatic factors along elevational and topographic gradients (Adams & Kolb, 2005). In the IPCC Fifth Assessment Report (IPCC, 2014), it confirms that with high confidence levels, climate change is proportionally more perceptible at high

elevations, thus making high altitudes more sensitive to climate change (Beniston et al., 1997). In landscapes which have a lot of topographic variation (i.e. the Central Appalachians) tree species may experience changes in growth performance across very small spatial scales (i.e. <1km). This gives me the opportunity to compare results across fine-scales and apply them to larger landscape levels to determine how and why trees optimally grow in specific areas.

Oak-dominated forests are widespread throughout the Appalachians. Red oak forests are one of the most common in Shenandoah National Park (henceforth referred to as the Park); making red oak is possibly the most common tree in the Park (Mazzeo, 1974). This makes red oak an important species in the Central Appalachians and in Shenandoah, and an excellent study species for this research. *Quercus rubra* (Red Oak) is native across much of the eastern United States and Canada stretching from the southern Appalachians to Nova Scotia in the north (Figure 1). It grows in elevations up to 1070m (3,500 ft) in West Virginia and approximately 1680m (5,500 ft) in the southern Appalachians (Sander, 1990). The mean annual precipitation in this distribution, ranges from 760mm- to 2030mm (30in-80in) and mean annual temperature ranges from 4°C- 16°C (40°F- 60°F) (Sander, 1990). Red Oak is known to grow over all varying topographic positions but it optimally grows in aspects facing north or east, coves and deep ravines, and well-drained valley floors (Sander, 1990).

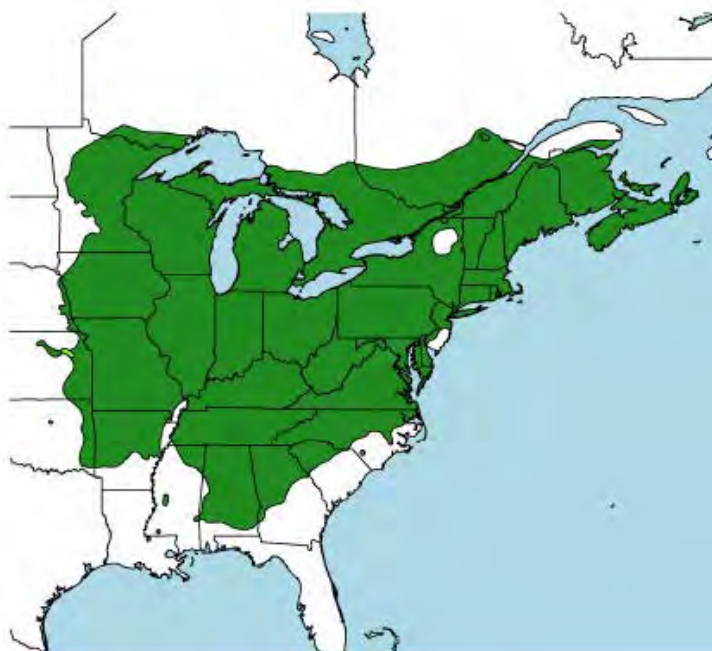


Figure 1. The figure shown above is a representation of the distribution of *Quercus rubra* across eastern North America.

Further, studies show, that red oak is most sensitive to precipitation, soil moisture and air temperature in the central and southern Appalachians (Pan et al., 1997). Pan et al., (1997) showed that previous year precipitation is the most significant variable that affects growth of northern red oak. They found that because of the negative and positive relationships with their climatic variables that red oak favors below-average temperature during summer and winter but above-average temperature and moisture during early growing season. All species in this study showed inverse

relationships with temperature of the current growing season because higher temperatures will cause water stress and reduce photosynthesis (Pan et al., 1997; Rosenberg et al., 1983).

White et al., (2011) performed an experiment in the southern Appalachians and determined that tree growth was highly correlated with growing season precipitation. They also determined that at lower elevations there was more of a varied response to climatic variables; insinuating that oak climate stress increases in variability with a decrease in elevation and latitude (White et al., 2011). Terrell & LeBlanc (2002), performed a study of 71 *Quercus rubra* populations that were spread across the eastern USA, and found that radial growth was mostly sensitive to climatic conditions in the early growing season (May to June). These studies help to reveal some answers about how red oak responds to its climate, and tells scientists how diverse red oak's niche space can be. However, it remains unclear where within this range performance is maximized, the niche centroid is located, and how complex elevational and topographic gradients will affect that performance (Siefert et al., 2015).

I propose to study red oak in the central Appalachians using transects that span major topographic gradients within the landscape so that I can determine how growth response is related to fine-scale changes in climatic and other abiotic factors that exist across these gradients. I will then use these results to make larger generalizations about the total population of red oak. Climate is rapidly changing and it is important to understand how tree species and entire forest communities are going to react to that change.

METHODS

Study site and design

My field site is located within the Central Appalachia in Virginia. Shenandoah National Park (Hereafter referred to as the Park) is ideal for the study of red oak because it encompasses the geographic requirements for this study and is close in proximity to Shepherd University. The Central Appalachian Mountains are known to offer a very diverse habitat for all species, due to the exclusive array of topographic features, soil, and climate (temperature, precipitation etc.) (Landscape, 2017). The Park's elevational range is 160m-1,235m (530 feet-4,051 feet) which provides ample topographic conditions to map out the study design. In order to capture all major topographic conditions I set up transects, specifically close to hiking trails for ease of access, that span contrasting features of the Park. Specifically, two transects span the lower half of the total elevation gradient. These two lower transects are on opposing aspects and each span a cove-to-ridge transition. The next two transects for the higher elevation are also on opposing aspects and also span a cove-to-ridge transition. The first two transects range from approximately 294m (cove) to 757m (ridge). The next two transects will range approximately from, 825m (cove) to 1022m (ridge). This encompasses our full elevational and exposure gradient which enabled me to analyze the differing climatic factors that affect red oak radial growth (Table 1, Figure 2).

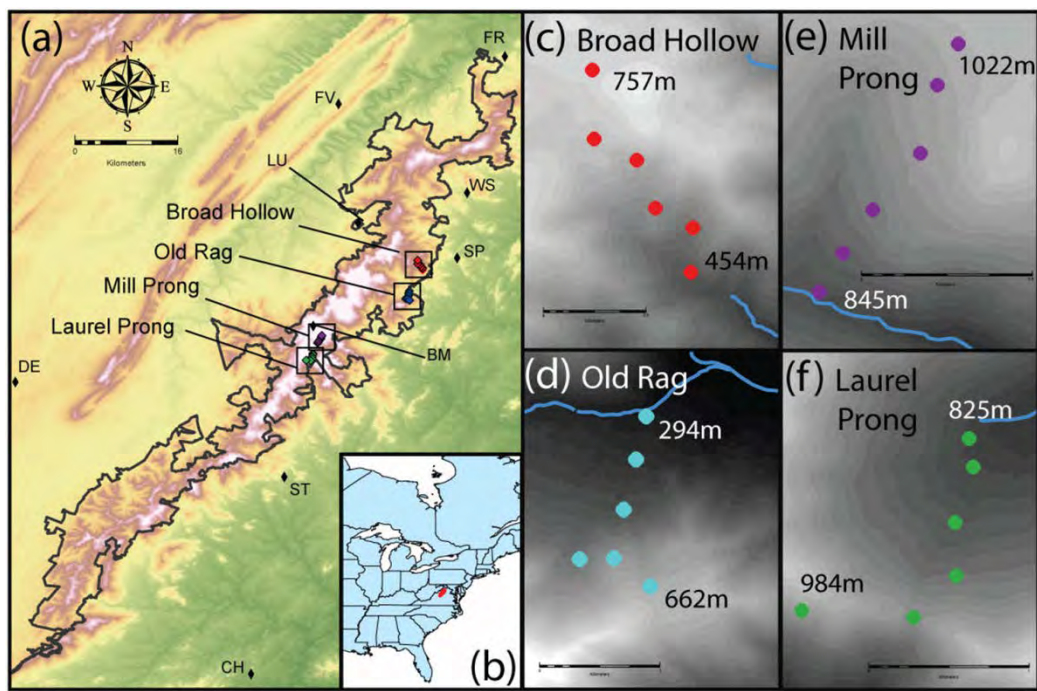


Figure 2. a) Representation of our 4 transects and 9 weather stations we used for data within and around Shenandoah National Park b) Shenandoah National Park in relation to the eastern part of the United States c-f) station location and elevation range along each transect.

Within each individual transect (total of 4) there were 6 stations equally spaced throughout. At each station we randomly selected and cored up to 5 mature red oak trees with a diameter at breast height (d.b.h) greater than 10cm, which were within roughly 20 meters from the station center. When choosing the trees to core at each station, we avoided any trees that appeared to be unhealthy or have insect damage. To core the trees we used a Haglof 5mm diameter increment tree borer (Haglof Company, 2017). We cored each tree about 2ft from the base and aimed the increment borer toward the center of the tree. At each station, we were able to core at least one tree, but most stations we were able to core the maximum amount (Table 1). At more than half of the 24 stations, we were able to core our maximum amount, which was 5. Only a select few stations we could not core our maximum goal. We cored approximately 120 trees in total (4 transects, 6 stations at each, and roughly 5 trees within each station).

Table 1. A summary table of the topographic variables for each station at all 4 transects. The average diameter at breast height (dbh) for each station was calculated and the corresponding latitude and longitude is given for each station.

| Transect | Station | Elev. (m) | Aspect | Dstream (m) | # of trees | Avg. dbh (cm) | Longitude (W) | Latitude (N) |
|--------------|---------|-----------|--------|-------------|------------|---------------|---------------|--------------|
| Broad Hollow | 1 | 454 | South | 46.48 | 2 | 62.45 | 78.281831 | 38.599374 |
| | 2 | 540 | South | 389.03 | 5 | 51.26 | 78.281682 | 38.602489 |
| | 3 | 581 | South | 521.28 | 3 | 37.67 | 78.284313 | 38.603873 |
| | 4 | 665 | South | 911.42 | 1 | 47.1 | 78.285622 | 38.607239 |
| | 5 | 697 | South | 1169.51 | 5 | 48.7 | 78.288621 | 38.608729 |
| | 6 | 757 | South | 1638.72 | 5 | 61.34 | 78.288747 | 38.613569 |
| Laurel Prong | 1 | 825 | North | 133.48 | 3 | 23.37 | 78.436016 | 38.482608 |
| | 2 | 831 | North | 292.37 | 3 | 88.3 | 78.435784 | 38.48101 |
| | 3 | 837 | North | 649.51 | 5 | 65.1 | 78.436806 | 38.477892 |
| | 4 | 913 | North | 975.60 | 5 | 46.32 | 78.4367744 | 38.47489 |
| | 5 | 954 | North | 1273.14 | 5 | 41.62 | 78.439136 | 38.472564 |
| | 6 | 984 | North | 1483.21 | 5 | 95.15 | 78.445412 | 38.472948 |
| Mill Prong | 1 | 845 | South | 50.89 | 5 | 36.48 | 78.429333 | 38.497337 |
| | 2 | 880 | South | 250.96 | 5 | 42.76 | 78.428348 | 38.49897 |
| | 3 | 926 | South | 481.01 | 5 | 37.64 | 78.427095 | 38.500798 |
| | 4 | 986 | South | 796.97 | 5 | 43.6 | 78.425086 | 38.503183 |
| | 5 | 999 | South | 1110.24 | 5 | 27.16 | 78.424371 | 38.506052 |
| | 6 | 1022 | South | 1317.63 | 5 | 33.34 | 78.423489 | 38.507788 |
| Old Rag | 1 | 294 | North | 52.41 | 5 | 60.34 | 78.300573 | 38.570285 |
| | 2 | 365 | North | 408.75 | 5 | 61.5 | 78.301334 | 38.567055 |
| | 3 | 397 | North | 824.22 | 5 | 52.54 | 78.302261 | 38.563307 |
| | 4 | 505 | North | 1255.19 | 5 | 50.82 | 78.305558 | 38.559601 |
| | 5 | 579 | North | 1216.57 | 5 | 50.92 | 78.302699 | 38.559669 |
| | 6 | 662 | North | 1465.70 | 5 | 42.22 | 78.300274 | 38.557554 |

Analysis-laboratory data preparation

Once the cores were collected we brought them back to the lab and mounted and prepared them using standard dendroecological methods (Fritts & Swetnam, 1989). We initially started the preparation by mounting them and using a vibratory hand sander of progressively higher grit sand paper sheets starting with 80-, 120- and 240-. The cores were then hand sanded using sandpaper of 320-, 400- and 600-. The annual rings were measured from 1965-2015, using a Velmax measuring bench (Velmax Inc., 2016) and dissecting microscope. The program used to measure the tree rings was MeasureJ2X (MeasureJ2X, 1998). Once all cores were measured, we cross-dated the cores, using COFECHA (Grissino-Mayer, 2001) to ensure no missing or false rings (Cook & Kalriukstis, 1990). Tree cores that didn't cross-date well (had a negative or very low correlation (<10%) to the rest of the cores in that particular series), were not included in further modelling. Only several trees were taken out of the data set using this threshold. By eliminating several negatively correlated cores, and other cores that were broken/unable to effectively measure, all subsequent analysis includes 97 red oak trees. The overall correlation of our 4 transects were; Broad Hollow series was 26.5%, Laurel Prong series was 32.4%, Mill Prong was 44.6% and Old Rag was 48.4%.

Detrending the tree cores is important to standardize the data set (Cook et al., 1990). Specifically, to account for noise such as competition and light exposure that may mask the signal of how the tree is responding to the topographic position it is growing in. We used the spline method to detrend the chronologies. To detrend the cores, we used R programming (Team R, 2016) language and the

following packages; detrendeR and dplR (Campelo, 2012; Bunn & Korplela, 2015). The spline graphs of each tree were analyzed to make sure there were no errors/outliers that would need further analysis.

Analysis- climate data preparation

Climate data was prepared using National Oceanic and Atmospheric Administration (NOAA) weather station data. Weather station data was obtained from 7 weather stations in and surrounding the Park (Figure 2a). The climate data was from 1965-2016. Temperature variables were adjusted to more accurately reflect the transect stations by modeling daily weather station temperature values against weather station elevation. The slope and intercept of these simple linear models were then used to correct temperature at each transect station based on its elevation. This provides a more accurate fine-scale temperature that the trees at each location are actually experiencing, than the regional weather station data alone accounts for. Climate variables include maximum and minimum monthly temperature, seasonal temperature, monthly precipitation, as well as growing degree days and frost free days. The topographic variables that were included in the model were elevation (elev), distance from stream (dstream), and aspect (Table 1).

Analysis- modelling

Once each variable was established, we used the R program (Team R, 2016) to create a local polynomial regression fitting (LOESS) model of the ring widths and the interaction between distance from stream and elevation. The interactions between these two variables were studied to look at general trends in the ring widths averaged across the entire time span. I was also able to create plots made through time based on sub-setting the data by distance from stream and elevation. This allowed us to assess the trends through time at different topographic positions (Figure 4 and 5).

The final analysis included standardized variables to assess relative importance, by building a mixed model. The model was framed using fixed and random variables, an autocorrelation term and variable transformation. The fixed effects were all of our current and previous year climate variables (as listed in earlier methodology). It's important to include previous year data into the model because it is when the tree is storing all of the energy to go into the next years growing season. Random effects were included in the model to account for variation between trees, between stations and between transects that can't be accounted for in our other variables. The autocorrelation term was used to account for temporal autocorrelation between years in the model. We used a generalized linear model (glm) with an information criterion (AIC) value of 1901. We used this AIC criteria and a combination of stepwise AIC to initially select variables from the full list. This was then further refined by removing variables with high variance inflation factors (VIF) scores to take out each variable that had the highest VIF value and rerun the glm with a backward step AIC. Finally we removed variables that were not significant at the 0.05 level. To assess the relative importance of the retained variables we standardized them and ranked them based on the standardized coefficients. Each variable was assessed for biological importance and significance level using a threshold of a square root value less than 2 (Hadi et al., 2000).

The final variables that were retained in the model are shown in the table 3. In this study, we had the transformation variable log of distance from stream. This is to account for the non-linear relationship between growth and exposure. Using R program, we calculated the mean, minimum

and maximum of our logged data set. These values were used to outline the criteria for near the stream and further from the stream. The mean of the data set was 6.4 and this was used to determine if the distances were <6.4 , they were considered close to the stream and if the distances were >6.4 , they were considered to be far from the stream. Our minimum value was 3.839 and maximum was 7.402. The square root transformation of ring width data was to account for heteroscedasticity in the data. were not significant at the 0.05 level. To assess the relative importance of the retained variables we standardized them and ranked them based on the standardized coefficients. Each variable was assessed for biological importance and significance level using a threshold of a square root value less than 2 (Hadi et al., 2000).

The final variables that were retained in the model are shown in the table 3. In this study, we had the transformation variable log of distance from stream. This is to account for the non-linear relationship between growth and exposure. Using R program, we calculated the mean, minimum and maximum of our logged data set. These values were used to outline the criteria for near the stream and further from the stream. The mean of the data set was 6.4 and this was used to determine if the distances were <6.4 , they were considered close to the stream and if the distances were >6.4 , they were considered to be far from the stream. Our minimum value was 3.839 and maximum was 7.402. The square root transformation of ring width data was to account for heteroscedasticity in the data.

RESULTS

Ring width

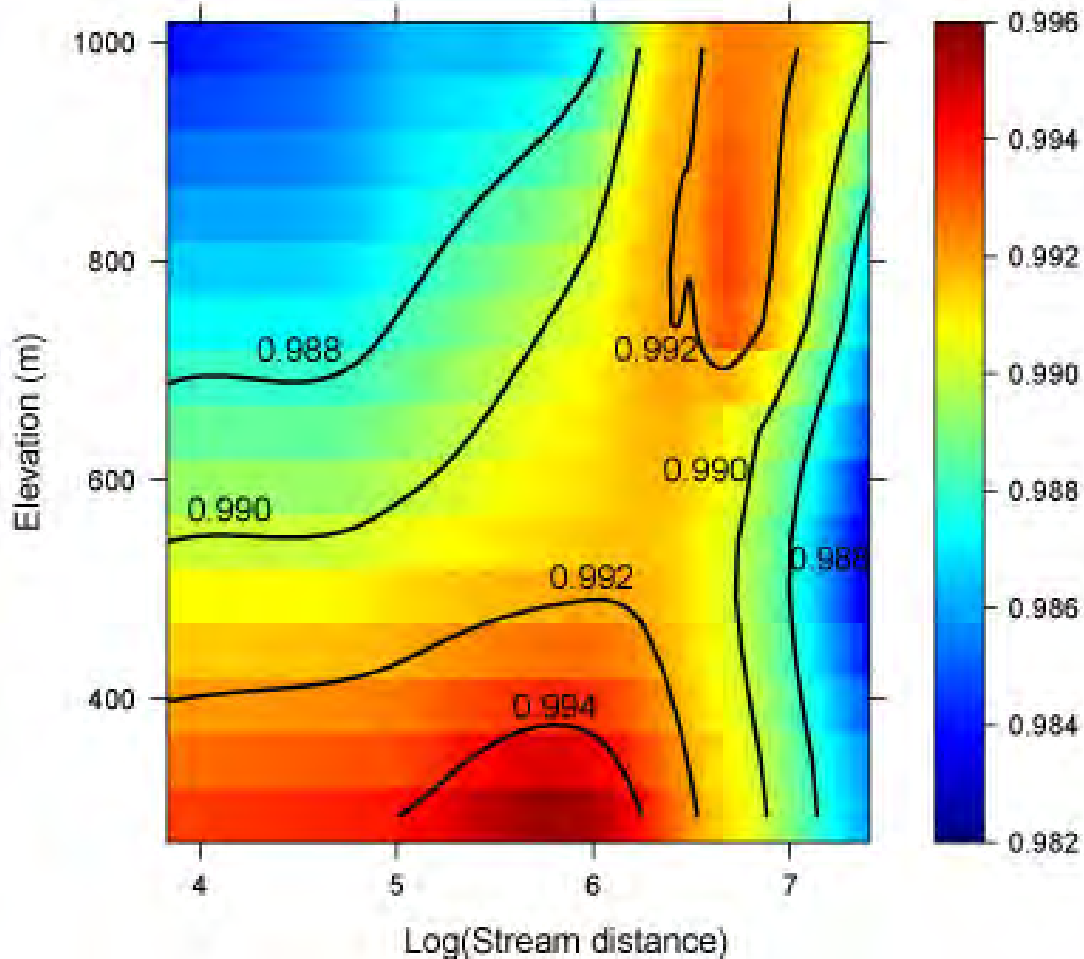


Figure 3. Results of LOESS model of detrended average ring width growth against elevation (m) and log of stream distance extrapolated across all landscape positions.

The legend on the right shows that the more red/burgundy a cell is on the graph, the bigger the predicted ring width is. The legend shows that the more blue a cell is on the graph, the smaller the ring width is.

The loess regression model showed that even though red oak grows in all elevations that we measured in the Park, growth is maximized at certain locations. There is a strong correlation with larger ring width at lower elevation levels and moderate distances from stream, approximately 601.84m (5-6). Ring widths at these cells are 0.994, and are the highest values for this model. It is interesting to note that maximum growth is shifted along the distance from stream axis. This is why there is a somewhat 'diagonal' pattern associated with this figure. With increasing elevation, greater ring widths were found at distances further from streams (near ridgetops). However, the

lower ring widths for red oak occur at higher elevations and close distances to stream and lower elevations and further distances from the stream (Figure 3).

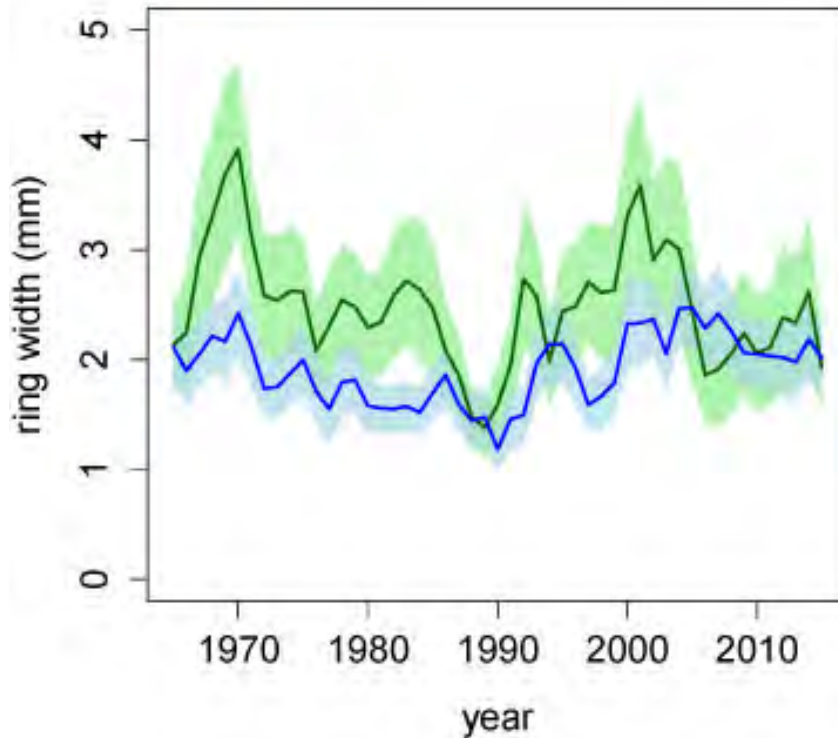


Figure 4. Average ring width for high elevation (>600m) trees (blue) and low elevation (<600m) trees (green). Shading indicates the 95% confidence interval.

Before the 1990s red oak grew better at lower elevations. Around the 1990s, both low and high elevations had a substantial decrease in ring width. After this decrease, red oak growth was more variable and didn't grow better in one geographic location or the other. This confidence interval shows that pre-1990 there is minimal overlap between the two curves. However, post-1990 is where most of the overlapping occurs. Since both of the confidence intervals are mostly overlapping throughout this graph, this suggests that this is not a significant relationship.

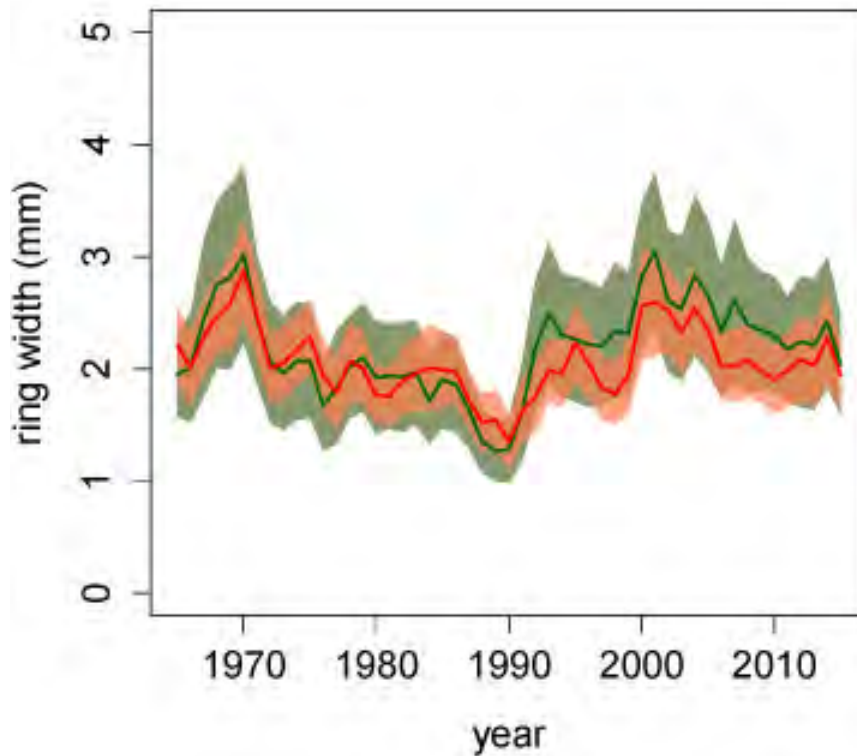


Figure 5. The figure shown above is a graphical representation of near (<601.84m) to the stream (green) and far (>601.84m) from the stream (red) confidence level, showing transparency to denote the range of each transects ring width within each category.

Proximity of being near or far from a stream to red oak prior to the 1990s made no significant difference to growth. The red (far) and green (near) lines prior to the 1990s are almost in sync with each other and don't have much differences. However, after the 1990s, the red (far) line shifts and is somewhat lower than the green (near) line. Since our two confidence intervals have so much overlap, this relationship is not significant.

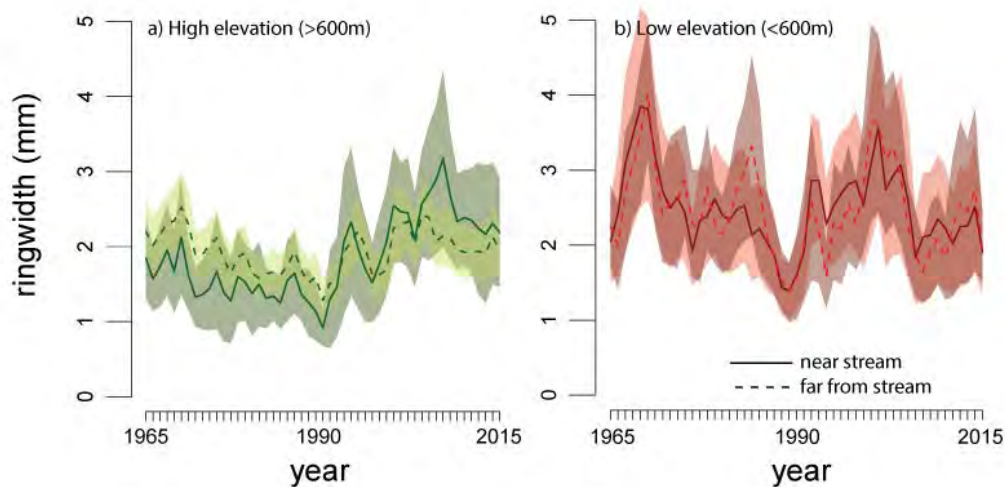


Figure 6. a) Ring widths from 1965 to 2015 at high elevations (>600m). The dotted line and light green shading shows ring widths that are far from the stream (>601.84m). The dark green and solid line curve represents ring widths that are near to the stream (<601.84m). b) Ring widths from 1965 to 2015 at low elevations (>600). The dark red and dotted line curve shows ring widths are far from the stream (>601.84m). The light red and solid line curve shows ring widths that are near the stream (<601.84m).

This is a synthesis of both distance from stream and elevation. We separated high and low elevation by setting a criteria of < or > 600m. We separated close to and far from the stream by setting criteria of < or > the mean of the logged data set, which is 601.84m. At high elevations before the 1990s, ring widths are higher when red oak is far from the stream (Figure 6a). After the 1990s there is more variation between the two geographic locations of red oak at higher elevations. After the 1990s, there was a shift in which location red oak grows best at. Since the 1990s, ring width has been increasing at both near and far from the stream, but there is still more variation and no clear differences along the distance from stream gradient (Figure 6a). The graph appears to have a steady increase which indicates this relationship is over time. Without factoring in the distance from stream lines, overall, trees at lower elevations are growing better than at higher elevations, ring widths are larger (Figure 6b). At lower elevations, red oak growth seems to be more variable throughout the entire record but over the last decade or so, ring widths appear to be consistently lower as they have been through the time span.

Table 3. Summary of the final variables that are included in our model for determining the factors that affect red oak. The scaled coefficients column shows the relationship that each variable has with growth performance. Attached to this column shows the level of significance to the model. The last column shows the standard error of each variable.

| Model Term | Scaled coefficients ^a | | Standard error |
|--------------------------------------|----------------------------------|-----|----------------|
| log(dstream) | -0.0083 | | 0.0052 |
| Previous Aug. min temp. | -0.0073 | *** | 0.0018 |
| Previous Aug. precip. | -0.0068 | | 0.0061 |
| March max temp. | -0.0038 | *** | 0.0007 |
| Previous Oct. precip. | -0.0038 | *** | 0.0006 |
| Previous Sept. min temp. | -0.0033 | ** | 0.0015 |
| Previous Nov. max temp. | 0.0015 | ** | 0.0007 |
| Previous Aug. precip. * log(dstream) | 0.0021 | ** | 0.0009 |
| Previous Oct. max temp. | 0.0027 | ** | 0.0012 |
| June max temp. | 0.0029 | ** | 0.0009 |
| June precip. | 0.0029 | *** | 0.0007 |
| May min temp. | 0.0048 | *** | 0.0008 |
| Aug. precip. | 0.0083 | *** | 0.0012 |
| Intercept | 0.9873 | *** | 0.0502 |

a: 3 stars represent p-value <0.0001, 2 stars represent p-value<0.05 and 1 star represents p-value<0.1

Our model initially started out with 26 climate and topographic variables. Thirteen of the variables were retained and of those, 11 were significant (Table 3). The two variables that don't show statistical significance are log (dstream) and previous August precipitation. However, the interaction between the two variables is significant, thus we have to leave the two individual variables in the model. Of these model variables, 7 were temperature variables that represents fall, spring and summer. The variable that has the lowest positive correlation value of 0.0015 is previous November maximum temperature. Whereas, previous September minimum temperature has a coefficient value of -0.0033 and has the smallest negative correlation.

Our model contains 4 precipitation variables that focus on current year fall and summer and previous fall. The highest positive correlation in the model is August precipitation, with a value of 0.0083. Our model contains one topographic variable; log of distance from stream, which as the strongest negative correlation value (-0.0083) in our model. Our temperature variables were corrected for the elevational difference from the weather stations. Therefore, even though the elevation variable itself isn't in our model, it is accounted for with the temperature variables.

DISCUSSION

In this study, we found that red oak growth was optimal: 1) at low elevations and moderate distances from stream, and 2) at high elevations growth was higher at ridgetops pre-1990, but has become more similar along the entire exposure gradient post-1990 (Figure 3). Our model suggests that this isn't due to the actual proximity to the stream that is allowing red oak to optimally grow in specific geographic locations but it is the climate that is driving these patterns. Current and previous year spring and autumn temperature and precipitation are driving these patterns. Temperatures specifically affect these circumstances because trees that are at the cove of a mountain and near streams are experiencing cooler temperatures. Whereas, trees that are at ridgetops and far from the streams are experiencing warmer temperatures. Generally, as altitude increases, temperature decreases. Therefore, anticipated increases in temperature may continue to

shift optimal growth of red oak to higher elevations and nearer streams (cooler) environments. It is important to note that red oak is still able to persist and grow at all locations within the Park that we studied, however these are the positions in which red oak experiences more optimal growth.

Pan et al., (1997) performed a dendroclimatological study on major forest species in the central Appalachians. One of the species that was included in their study was northern red oak. Their results have similar attributes to our study because we share many of the same relationships with our climate variables. Of the final 13 variables in our model, we share 6 that have the same positive/negative effect on red oak growth: May temperature, previous November temperature, March temperature, August temperature, August precipitation and June precipitation. Of these 6 common variables, 5 are significant in both studies. March temperature isn't significant in their study, however it is for ours. From this study, they concluded that relatively warm autumn and winter may favor growth of some species the next year and based on this, Pan et al., determined that warm weather in late season may be responsible for an increase in photosynthesis and food accumulation.

White et al., (2011) performed a study on the climatic response of oak species across an environmental gradient in the southern Appalachians. The climate data for their study is somewhat similar to our climate data. For example, current year June precipitation is significant in our study and theirs. The relationship that this variable has on the model is also similar because it has a positive association. May and June temperature are also significant in both our studies. However, in their study these two variables have a negative effect on their model, whereas in our model, they have a positive association. White et al. made the conclusion that since they had high correlations between tree growth and precipitation and inverse relationships with temperature that moisture availability was the greatest influence on red oak in the southern Appalachians. They also hypothesized that from their results, oak climate stress increases in variability with a decrease in elevation and latitude.

These are great examples to compare my study to, because while moisture availability is important to red oak, temperature seems to be the driving factor for red oak growth in the central Appalachians. We have more temperature variables showing significance in our model than precipitation variables. These examples prove that even when studying the same species, they still respond differently depending on their location. This is why more research like this should be conducted because the response of trees at all locations will be dependent on the current conditions the tree is under.

The IPCC (2007) reports that by the end of this century, the global mean temperature will increase by 2.4 to 6.4 degrees Celsius. Climate, specifically temperature, is a major factor that controls where tree species and other plants are able to persist (McKenney et al., 2007). As the climate continues to change, trees will have to account for this change somehow. In many cases, many trees have already started to shift their distribution and will continue as the environment does so as well. It is very evident in our results that since the 1990s there have been a lot of shifts. Current Forest inventory and Analysis (FIA) shows that red oak surrounding the Park has importance values ranging from 4-20. However, the HadleyCM3 (A1F1, "Harsh") shows a sudden shift where red oak's distribution is almost, if not completely, eliminated in many parts of the south eastern and mid-western areas of the United States. Red oak's distribution is shifted north where the importance values have decreased and specifically surrounding the Park has decreased to about 0-

3 (Iverson et al., 2008).

Future research should focus on refining the amount of moisture that each individual station gets. Our study could potentially not be accurate because we are putting a big window over each of the gradient saying that all stations receive the same amount of moisture. Better moisture accountability will show how much moisture each station is actually receiving because it should be different from each opposing aspect (i.e. cove to ridgetop).

ACKNOWLEDGEMENTS

I thank Dr. Mark Lesser for mentoring me throughout this research, data collection, analysis, guidance in the laboratory and figure production. I thank Mr. Rodney Dever for helping with work in the field and the data collection process. I would like to thank Amaris Jalil for helping me with the field work, data collection, and analysis. I am thankful for the National Park Service for giving me the opportunity and approving my research in the Shenandoah National Park. I was able to present these findings to the West Virginia Academy of Sciences with the help and funding of Shepherd University. Funding for this research opportunity was provided by the NASA West Virginia Space Grant Consortium.

PUBLICATIONS

- Hoffman, S., Jalil, A., and Lesser, M. 2017. Determining the growth response of *Quercus rubra* along elevational and exposure gradients. West Virginia Academy of Sciences (WVAS). Glenville State College, WV.
- Hoffman, S., Jalil, A., and Lesser, M. 2017. Determining the growth response of *Quercus rubra* along elevational and exposure gradients. US-IALE Baltimore, MD.
- Hoffman, S. 2017. Determining the growth response of *Quercus rubra* along elevational and exposure gradients. Biology capstone presentations. Shepherd University, Shepherdstown, WV.

REFERENCES

- Adams, H. D., & Kolb, T. E. (2005). Tree growth response to drought and temperature in a mountain landscape in northern Arizona, USA. *J. of Biogeography*, 32(9), 1629–1640.
- Andy Bunn, Mikko Korpela, Franco Biondi, Filipe Campelo, Pierre Mérian, Fares Qeadan and Christian Zang (2015). dplR: Dendrochronology Program Library in R. R package version 1.6.2. <http://CRAN.R-project.org/package=dplR>
- Beniston, Martin, Henry F. Diaz, and Raymond S. Bradley. "Climatic change at high elevation sites: an overview." *Climatic Change at High Elevation Sites*. Springer Netherlands, 1997. 1-19.
- Candel-Pérez, D., Linares, J. C., Viñebla, B., & Lucas-Borja, M. E. (2012). Assessing climate growth relationships under contrasting stands of co-occurring Iberian pines along an altitudinal gradient. *Forest Ecology and Management*, 274, 48–57.
- Cook, E. R., & Kalriukstis, L. a. (1990). Methods of Dendrochronology. *Methods of Dendrochronology*, 97–104.
- Cook, E. R., Meko, D. M., Stahle, D. W., & Cleaveland, M. K. (1999). Drought reconstructions for the continental United States. *Journal of Climate*, 12(4), 1145–1163.

- Decagon. (2016). Decagon Devices. Retrieved from www.decagon.com
- Filipe Campelo (2012). detrendeR: Start the detrendeR Graphical User Interface (GUI). R package version 1.0.4. <http://CRAN.R-project.org/package=detrendeR>
- Fritts, H. C., & Swetnam, T. W. (1989). Dendroecology: A Tool for Evaluating Variations in Past and Present Forest Environments. *Advances in Ecological Research*, 19(C), 111–188.
- Grissino-Mayer, H.D. 2001. Evaluating crossdating accuracy: A manual and tutorial for the computer program COFECHA. *Tree-Ring Research* 57(2):205-221.
- Hadi, A.S., Chatterjee, S., Price, B., (2000). *Regression analysis by example*. John Wiley & Sons, 3, 236-244.
- Haglof Company Group. 2017. Retrieved from <http://www.haglofco.com/index.php/en/products/instruments/survey/389-increment-borers>
- Hayhoe, K., Wake, C., Anderson, B., Liang, X. Z., Maurer, E., Zhu, J., Wuebbles, D. (2008). Regional climate change projections for the Northeast USA. *Mitigation and Adaptation Strategies for Global Change*, 13, 425–436.
- IPCC: 1996, Watson, R. T., Zinyowera, M., and Moss, R. H. (eds.), *Climate Change 1995, The IPCC Second Assessment Report*, Cambridge University Press, Cambridge and New York, p. 862.
- IPCC Intergovernmental Panel on Climate Change 2007. *Climate Change 2007: The Physical Science Basis. Summary for Policy Makers* (13 November 2007; www.ipcc.ch/).
- IPCC, 2014: *Climate Change 2014: Synthesis Report. Contribution of Working Groups I, II and III to the Fifth Assessment Report of the Intergovernmental Panel on Climate Change* [Core Writing Team, R.K. Pachauri and L.A. Meyer (eds.)]. IPCC, Geneva, Switzerland, 151 pp.
- Iverson, L. R., & Prasad, A. M. (1998). Predicting abundance of 80 tree species following climate change in the Eastern United States. *Ecological Monographs*, 68(4), 465.
- Iverson, L. R., A. M. Prasad, S. N. Matthews, and M. Peters. 2008. Estimating potential habitat for 134 eastern US tree species under six climate scenarios. *Forest Ecology and Management* 254:390-406. <http://www.treesearch.fs.fed.us/pubs/13412>
- Landscape. (2017). Central Appalachian Forest Ecoregion. Retrieved February 20, 2017, from http://www.landscape.org/explore/natural_geographies/ecoregions/Central%20Appalachian%20Forest/
- Mazzeo, P.M, 1974. *Trees of Shenandoah National Park in the Blue Ridge Mountains of Virginia*. The Shenandoah Natural History Association, Inc. Luray, Virginia.
- McKenney, D. W., Pedlar, J. H., Lawrence, K., Campbell, K., & Hutchinson, M. F. (2007). Potential impacts of climate change on the distribution of North American trees. *BioScience*, 57(11), 939-948
- MeasureJ2X (1998). VoorTech Consulting. Retrieved from <http://www.voortech.com/projectj2x/>
- Nogues-Bravo, D., Araujo, M. B., Errea, M. P., & Martinez-Rica, J. P. (2007). Exposure of global mountain systems to climate warming during the 21st Century. *Global Environmental Change*, 17(3-4), 420–428.
- Pan, C., Tajchman, S. J., & Kochenderfer, J. N. (1997). Dendroclimatological analysis of major forest species of the central Appalachians. *Forest Ecology and Management*, 98(1), 77–87.
- Roseberg, N.J., Blad, B.L., Verma, S.B., 1983. *Microclimate the Biological Environment*. Wiley,

- New York.
- Sander, I. L. (1990). *Quercus rubra*. Pages 727-733 in Burns, R. M., & Honkala, B. H. editors. *Silvics of North America, volume 2. Hardwoods*. USDA Agriculture Handbook 654, United States Department of Agriculture, Washington, D.C., USA
- Siefert, A., Lesser, M. R., & Fridley, J. D. (2015). How do climate and dispersal traits limit ranges of tree species along latitudinal and elevational gradients? *Global Ecology and Biogeography*, 24(5), 581–593.
- Tardif, J. C., Conciatori, F., Nantel, P., & Gagnon, D. (2006). Radial growth and climate responses of white oak (*Quercus alba*) and northern red oak (*Quercus rubra*) at the northern distribution limit of white oak in Quebec, Canada. *Journal of Biogeography*, 33(9), 1657-1669.
- Team, R. development core. (2016). *R: A language and environment for statistical computing*. R Foundation for Statistical Computing. Vienna
- Terrell, M. & LeBlanc, D. (2002) Spatial variation in response of northern red oak to climate stresses in eastern North America. *Dendrochronology, environmental change and human history*, 6th International Conference on Dendrochronology, Universite-Laval, Quebec City, August 22–27, 2002, pp. 340–343
- Thermochron. (2016). Thermochron Temperature Logger. Retrieved from <http://thermochron.com>
- Velmax. (2016). Velmax Measuring Systems. Retrieved from <http://www.velmax.com/index.html>
- Whalley, W. R., Ober, E. S., & Jenkins, M. (2013). Measurement of the matric potential of soil water in the rhizosphere. *J. of Experimental Botany*
- White, P. B., van de Gevel, S. L., Grissino-Mayer, H. D., LaForest, L. B., & Deweese, G. G. (2011). Climatic response of oak species across an environmental gradient in the history, 6th International Conference on Dendrochronology, Universite-Laval, Quebec City, August 22–27, 2002, pp. 340–343.
- Thermochron. (2016). Thermochron Temperature Logger. Retrieved from <http://thermochron.com>
- Velmax. (2016). Velmax Measuring Systems. Retrieved from <http://www.velmax.com/index.html>
- Whalley, W. R., Ober, E. S., & Jenkins, M. (2013). Measurement of the matric potential of soil water in the rhizosphere. *J. of Experimental Botany*
- White, P. B., van de Gevel, S. L., Grissino-Mayer, H. D., LaForest, L. B., & Deweese, G. G. (2011). Climatic response of oak species across an environmental gradient in the southern Appalachian Mountains, USA. *Tree-Ring Research*, 67(1), 27–37.

VALIDATION OF MARKER GENES FOR THE RAPID ALKALINIZATION FACTOR PATHWAY IN *ARABIDOPSIS THALIANA*

Marshall Hoffmaster

Biology

Shepherd University

Shepherdstown, WV

ABSTRACT

Most studies involving plant hormones has revolved around the study of small molecule hormones. Although signaling mechanisms for these are well understood, signaling mechanisms involving peptide hormones remain understudied. Our studies center on Rapid Alkalinization Factor (RALF), that when applied exogenously to plants causes rapid alkalization of the cell's apoplast which inhibits cell growth and elongation. RALF consensus sequences have been found in all plant lineages examined, suggesting RALF plays a fundamental role in plant biology. The mechanisms by which RALF mediates its effects remain to be elucidated. We hypothesized, that like other plant signaling molecules, RALF influences plant growth in part by effecting transcriptional changes. This study aims to define the AtRALF1 transcriptional response in *Arabidopsis thaliana* and to establish bonafide RALF marker genes for molecular characterization of the pathway. Two microarray time-course experiments were performed, one with exogenously applied AtRALF1 and another with estrogen-inducible AtRALF1 transgenic lines. Over a 24-hour time-course with exogenous peptide and estrogen-induction, 4799 and 1128 genes significantly changed expression (p -value < 0.05 , with a \log_2 fold difference of ± 1), respectively. We performed cluster and gene ontology analysis on those genes to elucidate what biological processes RALF influences and determined calcium signaling, membrane modifications, and defense responses to be significant. Comparing the time-courses for overlap identified a set of genes we think is the early transcriptional response for this pathway. Three of these genes were subjected to validation by qPCR.

INTRODUCTION

Cell to cell signaling is paramount to any biological system. Without this crucial component, all organisms would fail to develop properly as cells would be unable to differentiate. Currently, cell to cell communication/signaling occurs by four methods: endocrine, paracrine, juxtacrine and autocrine. Although biomedical researchers have been able to characterize these signaling methods, they are still faced with many important questions regarding how these signals induce different cellular responses through their signal cascade events. These crucial questions are proving to be especially difficult to answer in humans due to their high complexity.

In efforts to answer these questions, simpler multicellular organisms, such as plants, have been utilized in studies involving cell signaling. Currently, most research involving plant signaling has only focused on phytohormones (Murphy and De Smet, 2014). Some of these heavily studied phytohormones include brassinosteroids, auxins, jasmonates, and gibberellins. Out of these four classes of phytohormones, brassinosteroids have been the most heavily characterized. The

brassinosteroid (BR) family contains around 40 members as well as 4 conjugates (Clouse, 2002). Although plant species may have different endogenous levels of brassinosteroids, the effects BR's exert on plants appear to be consistent across species. Currently, BR's have been shown to influence stem elongation by promoting growth of the epicotyl, hypocotyl, and peduncle. Furthermore, BR's also increase the rates of cell division, accelerate senescence, cause membrane hyperpolarization, increase ATPase activity, and alter cortical microtubule orientations. Brassinosteroids also appear to follow a more canonical signaling pathway as opposed to the three other classes.

Currently, the initial perception of brassinosteroids is believed to be a result of an interaction between brassinosteroids and BRI1 (Brassinosteroid Insensitive 1), a leucine-rich repeat receptor kinase (Li and Chory, 1997). BRI1 appears to be localized to the cell membrane in all organs in young plants, thereby allowing it to induce a variety of cellular changes. Upon BR binding, BKI1 (brassinosteroid kinase inhibitor) disassociates from the plasma membrane, thereby allowing BKI1 to interact with BAK1 (brassinosteroid associated kinase 1). After the phosphorylation of BKI1, further signal transductions eventually lead to the inactivation of BIN2 (brassinosteroid insensitive 2). Upon inactivation, BSU1 (BRI1 suppressor 1) will dephosphorylate BRF (brassinosteroid response transcription factor), thereby allowing BRF to initiate the transcription of various genes associated with plant growth (Belkhadir and Chory, 2007).

Auxins are the next class of heavily characterized phytohormones, which also effect cell growth as well as have a variety of impacts on plant development. Regarding gene expression, auxin has been shown to induce changes within minutes of its perception. Much of the genes affected fall into a family of genes aptly named Aux/IAA (Auxin/Indole-3-acetic acid) genes and auxin response factor (ARF) genes, which consists of 29 and 23 members respectively and are found in *Arabidopsis thaliana* (Teale et al., 2006). Current research has yet to fully elucidate the overall function of each member of the Aux/IAA family. However, each member of the family is thought to contribute individual functions needed to induce certain cellular responses. While these functions remain elusive, it seems that most of these members are destined for the nucleus, as proteins encoded have a nuclear localization signal and are transcribed within minutes of auxin exposure (Teale et al., 2006). Auxin has also been shown to induce cell wall changes and hyperpolarization (Teale et al., 2006). Specifically, auxin influences genes encoding proteins for cell wall degradation, expansins, arabinogalactans, and class III peroxidases. Furthermore, auxin also appears to influence cell division by mediating protein degradation pathways. However, the link between degradation and cell division remains elusive.

Jasmonates are a family of oxylipins that play paramount roles in plant defense responses to both biotic and abiotic stresses (Acosta and Farmer, 2010). In this family, jasmonic acid (JA), methyl jasmonate (MeJA), jasmonoyl-isoleucine (JA-Ile), Oxo-phytodienoic acid (OPDA), and dinor-OPDA are among the most heavily studied. Regarding plant defense, jasmonates appear to have the biggest influence on wound and insect related damage, influencing approximately 67-85% of genes related to leaf damage. In addition, jasmonates can also induce wounded plants to form smaller petioles, as well as cause new leaves to have more trichomes. Additional defense responses include protection from necrotrophic pathogens, bacterial pathogens, root pathogens and symbionts, and protection from detritivores.

Jasmonate signaling is proposed to follow a five step model, with signaling and synthesis tightly regulated (Acosta and Farmer,2010). In step 1, lipoxygenases located in the plastids first produce 13-hydroperoxyfatty acids. These acids then undergo further modification until OPDA and dinor-OPDA are formed. Upon formation, these compounds then exit the plastid and are transported to the peroxisome. In step 2, OPDA and dinor-OPDA are modified in the peroxisome to form jasmonic acid, where it then moves into the cytosol. Step 3 is optional, and JA may undergo further modification to form JA-Trp and JA-Ile. In step 4, JA will bind to a nuclear receptor known as COI1 (Coronatine insensitive 1), which is complexed with a SCF(Skp1, Cullins, F-box proteins) ubiquitin E3 ligase . Upon binding, the active E3 ligase then targets JAZ(Jasmonate ZIM-Domain, a negative regulator of jasmonate responsive genes) proteins for degradation, thus allowing the previously bound transcription factor to initiate gene expression.

The final class of phytohormones are gibberellins (GA), which also control growth and various developmental processes along with responses to abiotic stress. When studying gal-3(a gene crucial in GA biosynthesis) knock outs, plants were shown to have short stature, bushier and have darker green leaves(Richards et al., 2001). Along with influencing plant growth, GA is also crucial for proper development, as gal-3 KO seeds fail to germinate, have delays in flowering, and even exhibit male sterility. When certain species of plant are subjected to different abiotic stresses, GA has also been shown to play vital roles in plant responses. These responses can include growth restriction, tolerance to submergence, shade avoidance, cell expansion, and regulation of shoot growth (Colebrook, 2014).

Although plant hormone signaling has been well categorized, signaling involving peptides has recently only come into light over the past decade. Recent studies have shown that plant growth, especially cell elongation, can be affected by both steroid hormones as well as small peptides (Singh and Savaldi-Goldstein, 2015). However, the responses of peptide mediated growth remain undiscovered (Marshall et al.,2011). In recent years, studies have been conducted involving the use of a newly discovered small peptide from tobacco, Rapid Alkalinization Factor (RALF). Application of this 5kDa cysteine rich peptide exogenously to growing seedlings results in growth arrest of shoots and roots, while over-expression of RALF genes results in semi-dwarf plants (Pearce et al.,2001). RALF genes are present throughout the entire plant kingdom, suggesting a fundamental role of RALF in various plant processes (Pearce et al.,2001). Experiments have revealed that different RALF peptides present in various plant species play key roles in cell growth as well as development. Specifically, RALF has been linked to various activities such as: increasing cytoplasmic Ca²⁺ levels, inhibiting proton pump activity, inhibiting pollen germination, inducing strong alkalinization of growth medium, as well as inhibiting pollen tube elongation (Murphy and De Smet, 2014). As the years have passed, characterization of the RALF family, and similar peptides, has increased greatly. As of now, the cysteine rich peptide family now includes RALF, Epidermal Patterning Factor(EPF1), EPF2, Tapetum Determinat1 (TPD1), Stomagen/EPF-Like9 (EPFL9) and Early Nodulin (Murphy and De Smet, 2014). However, this study will only focus on the further characterization of RALF.

RALF begins as a 115 preprotein, with RALF being located at the C-terminus(Pearce et al.,2001). How RALF is processed to its active form consisting of only 49 amino acids has yet to be fully elucidated. Although exact processing enzymes are still to be determined, what has been discovered is that an up-stream dibasic site is crucial for RALF to be processed correctly. This

discovery resulted from studying various mutations in the AtRALF1 (At1g02900) gene in *Arabidopsis thaliana* (Matos et al., 2008). Specifically, 35S:AtRALF1(R69A) inducible lines presented a normal phenotype regarding root and leaf growth as well as an accumulation of the mutated peptide. Furthermore, 35S:AtRALF1 inducible lines appeared to be semi-dwarfed. In addition, these inducible lines had very little processed peptide in a crude extraction. This observation suggests that when processed correctly, RALF has a quick turnover rate as a way to control its activity. Even though no processing enzymes have been identified, these observations suggest that there could be an involvement of a kexin-like convertase, as they tend to recognize either RR or KR sites when processing certain proteins (Matos et al., 2008).

Soon after, further studies discovered that the RR (di-arginine) sequence in the RALF gene was a recognition site for the proteolytic enzyme, AtS1P (Site 1 Protease) which separated the propeptide, liberating RALF (Murphy and De Smet, 2014). This discovery also served to further address how RALF is processed, as AtS1P is a Golgi localized enzyme, suggesting that final RALF processing may need to take place in the Golgi. However, AtS1P can also be transported to the apoplast of cells and process RALF extracellularly. Interestingly, RALF peptides have also been shown to have very few post-translational modifications, and only need four conserved cysteine residues in order to fold into the functional protein (Bedinger et al., 2010).

How RALF induces its responses is still an ongoing topic, however, one possible RALF receptor for regulating cell expansion has been identified. This discovery was FERONIA, a receptor-like kinase, which binds RALF according to co-immunoprecipitation experiments (Haruta et al., 2014). Specifically, it was shown that when RALF was bound to FERONIA, a phosphorylation cascade was initiated that inhibited AHA2 (*Arabidopsis* plasma membrane H(+) -ATPase isoform 2), caused an increase in apoplastic pH, and reduced plant cell elongation.

In order to fully understand the mechanisms of RALF as a whole, RALF's influence on gene expression must also be known. Unfortunately, there has been very little research done on RALF's influence on plant transcriptomes. However, this study serves to provide answers to this crucial question. The study presented here combined various physiological, genomic, and molecular approaches to gain a better understanding of RALF1's transcriptional influence in the model system *Arabidopsis thaliana*. Firstly, a comparison was made between estrogen-inducible *Arabidopsis* microarray data to that of exogenously applied RALF1 microarray data to find overlapping genes. Secondly, these marker genes underwent validation by means of qPCR. Validation of the microarray data from both systems (exogenous treatment and estrogen-induction) will allow for the generation of true RALF1 pathway marker genes. Establishment of these marker genes will then be used in future studies geared towards the characterization of *Arabidopsis* mutants resistant to the effects of RALF1 and examination of the RALF1 pathway in other plants.

MATERIALS AND METHODS

Normalization of Estrogen and Exogenous RALF1 time-course array data

Normalization of the estrogen time course array data was carried out by first averaging all previously collected microarray data for each of the samples in both the exogenous and estrogen arrays. Once the average log₂ expression value was calculated for each of the samples, a normalized log₂ fold difference was determined by calculating the difference between the average

RALF log₂ value and the average Citrine log₂ value at each respective time point. Using a gene annotation document retrieved from Affymetrix, proper Arabidopsis Genome Initiative numbers (AGI's) were paired with their respective Affymetrix Probe ID's. These data were then ranked by order of decreasing log₂ fold changes at each respective time point.

Normalization of the raw exogenous microarray data followed similar methodology during the initial processing. As with the estrogen data, previously collected Chipster data for the exogenous RALF time-course was averaged together for the 30min mock samples, and all samples for RALF at the 30min, 60min, 120min, 180min, 12hr, and 24hr time points. Normalization of the data was carried out manually by taking the difference between each RALF log₂ fold difference at each time point and the mock 30min time point.

Creation of Top table lists using R

Creation of top table lists for both the up and the down-regulated RALF1 genes were created using the free software R (R Core Team, 2016). Specifically the R packages, AffyLmGUI (Gautier, 2004) and Linear Models for Microarray Analysis, Limma (Ritchie, 2015), and bioconductor (Gentleman, 2003) were utilized. Estrogen targets were first normalized by means of Robust Multi-Array Average (RMA) and a linear model fit was calculated. Individual contrasts were then calculated between the RALF1 and Citrine samples for each individual time point. Contrast data was then used to create individual top tables for the 0(mock), 6, 12, and 24 hour time points. These tables were created under the following parameters: All genes were present, the Holm–Bonferroni (HOLM) method was used for adjustment, and the tables were ranked by P-value.

Raw top tables for the exogenous data were created using the same parameters as the estrogen data, however, contrasts were made by taking the difference between RALF log₂ differences at each time point and the 30min mock.

Creation of Up and Down Regulated Gene Lists using Top Tables

Creation of unique up regulated gene lists for both the estrogen and exogenous time- courses first involved the sorting of all genes in accordance to their M (log₂ fold difference) value in descending order. Any genes that fell below a log₂ fold difference of 1 were then removed during the creation of up regulated list. Creation of the down-regulated list utilized a cut off of -1 or less, as such, any genes above -1 were removed. Both lists were then resorted in accordance to their p-value and removed if their p-value exceeded 0.05. Creation of both up and down regulated gene lists for all other time points in both the estrogen and exogenous time-courses were created using the same methodology.

Further modification of the both the up and down regulated lists for the 6, 12, and 24-hour estrogen time points was required in order to remove any overlap with the mock. Using a free online Venn diagram creator, Venny (Oliveros, 2015), separate comparisons were made between the mock up and down list and the 6, 12, and 24 hour up and down lists. A new file was then created that contained genes lists with the mock overlap removed for all time points in both the up and down regulated lists. This modification was not required for the up and down regulated gene lists for the exogenous time-course.

Using Venny, the 6, 12, and 24-hour time point lists for all the up-regulated genes were compared.

A new file was then created that contained gene lists unique to various time points as well as lists that contained genes that overlapped between the various time points. All down regulated gene lists were analyzed and compiled following the same methods. Lastly, Venny was used to make a final comparison of all up and down regulated genes, any duplicated genes were removed.

The up and down gene regulated lists for the exogenous time-course also underwent a similar comparison using Venny. However, only the 30,60,120, and 180 minute lists were compared to one another and any overlapping genes as well as genes unique to a specific time-point were recorded.

Creation of estrogen gene clusters using Mfuzz

Cluster analysis of all genes both up and down regulated by RALF1 was conducted using Mfuzz(Carlisle and Futschik,2005), a software package located within R. Initial processing (pre-processing) of the RALF expression tables was carried out using the following defaults: missing values were filtered using a threshold value of 0.25, missing values were filled with a K value of 10 while using the median averaging method, and the table was standardized using the normal SD based method. The gene list was then clustered using the Fuzzy C-means soft clustering method using 12 centers and m value of 1.25. Lastly, a cluster analysis was carried out using a minimum membership (acore) value of 0.5 and the resulting list was exported for later use.

Analysis of estrogen cluster data using GO-DAVID

In order to ascertain as to which biological pathways are represented by each Mfuzz cluster, the gene ontology toolkit from the Database for Annotation, Visualization and Integrated Discovery (DAVID) (Huang, 2009) was utilized. Clusters 1-12 were analyzed separately according to the following parameters: genes were searched using AGI (TAIR_ID) numbers, using the *Arabidopsis* ATH1-121501 Genome Array as the background. Functional annotation charts were then created which contained information from all of the following search terms: GOTERM_BP_FAT, Interpro, SP_PIR_Keywords, and Fold enrichments.

Hierarchical clustering and heat mapping of estrogen and exogenous genes

Hierarchical clustering and heat mapping was carried out using the free online program, MultiExperiment Viewer (Saeed, 2003). When loading the initial tables, the annotation data came from *Arabidopsis thaliana* and the array setting was set to ath1121501. Hierarchical clusters and heat maps were created for overlapping up-regulated genes as well as down-regulated using the default settings for MultiExperiment Viewer's clustering function.

The two clusters were then analyzed separately for any genes that showed similar expression values between the 6hr estrogen time point, as well as the 30,60,120, and 180min exogenous time points. Any overlapping up or down regulated genes between the various time points were noted and compiled for later use in the final selection of marker genes.

Time course using Estrogen inducible RALF1 and Citrine Arabidopsis lines

Two different estrogen inducible *Arabidopsis* lines were utilized in this time course, one line induced Citrine, while the other induced RALF. Seedlings were first surface sterilized using 1ml of a prepared solution containing 30% concentrated Clorox bleach and 0.1% Triton-X 100 for 10 minutes. The seeds were then washed 10 times using sterile water and then left to imbibe in 5ml

of 0.5X Linsmaier and Skoog (LS) (Caisson Labs: Cat. No: LSP03-1LT) growth media for 2 days. A total of 12 60x15 mm petri dishes (Falcon Ref. No: 351007) were needed for each transgenic *Arabidopsis* line, for a final total of 24 plates. To plate the seeds, 1ml aliquots of seeds continued in the LS media were spread evenly around the perimeter of the plates. Three biological replicates were plated for each time-point that was to be assessed in this study, a 1hr treatment, a 3hr treatment, a 6hr treatment, and a mock. Seeds were grown under continuous light and 22°C for 11 days with an additional 0.5ml of LS media being added to the seeds on day 9. To begin treatment of the seeds, a 18ml solution of 1uM β -estradiol was created (Sigma #F2758). Seedlings to be tested for 1hr, 3hrs, or 6hrs each received 1ml of 1uM β -estradiol, while each mock sample received 1ml of LS media. Tissue samples were then flash frozen in liquid nitrogen. RNA was extracted from samples done in biological triplicate, biotin labeled with affymetrix 3' IVT kit (Affymetrix 902416), and hybridized to ATH1 chips (Affymetrix 900385).

Time course using Exogenous AtRALF1 peptide

Seven day-old *Arabidopsis* seedlings grown in liquid culture were treated with 10 uM RALF peptide, purified from *E. coli*, over a 24 hour time-course and samples collected at 0, 0.5, 1, 2, 3, 12, and 24 hours after treatment. RNA was extracted from samples done in biological triplicate, biotin labeled with affymetrix 3' IVT kit (Affymetrix 902416), and hybridized to ATH1 chips (Affymetrix 900385).

RNA Extraction

A total of 24 tissues samples were collected from the treated seedlings. Total RNA was extracted using the protocol for the Rneasy Plant Mini Kit (Qiagen Lot No.151038416). To ensure RNA purity, an additional Dnase step was performed for 10 minutes, followed by a spin-column purification. The total RNA was quantified by means of optical density, and then all samples were adjusted to 200ng/ul.

cDNA Synthesis for qPCR

A total of 2.5ug of RNA was reversed transcribed according to the protocol found in the First Strand cDNA Synthesis Kit by Thermofisher (Lot No. K1642). Before use in qPCR 200ul of a 1:10 dilution was created for each sample.

Quantitative PCR with SYBR Green

The standards used in all qPCR runs were created by first combing 25ul of cDNA from all samples into a single tube. This mixture then underwent 6 serial dilutions to create the final standard curve mixture. Working dilutions of cDNA were created by creating 100ul of a 1:2 dilution of the 1:10 stocks. The SYBR mix needed for each run was created by combining 8ml of nuclease free water, 10ml of DMSO (Life Technologies Lot No. 1076C053), 400ul of 10mg/ml BSA (Ambion Lot No. 1609068), 200ul of Tween 20 (Sigma Lot No. SLBR6201V), and 20ul of SYBR Green (Life Technologies Lot No. 1825741). Each PCR reaction consisted of 20ul containing 2ul of 10x ExTaq Buffer containing 15mM MgCl₂, 2ul of SYBR Green Mix, 2ul of 10mM total dNTP mix (Invitrogen Lot No. 1736450). 1.0ul of 10uM forward and reverse primers, 1.8ul of nuclease free water, and 0.2ul of Bio Pioneer Taq. Real time qPCR was run on the Mini Opticon System by Bio-rad. The cycling consisted of 1 cycle of denaturation at 95.0°C/3 minutes, followed by 40 cycles of amplification (95.0°C/ 10s, and 60.0°C/ 30s). A melt curve was also created after the 40th cycle which ranged from 55.0°C – 95.0°C while increasing in increments

of 0.5°C after 10s. Tests were performed on a 48-well plate with each biological sample run in triplicate and each standard run in duplicate.

RESULTS

Analysis of Estrogen Microarray Data

Before marker genes could be selected for validation by means of qPCR, an analysis of previously collected data using the estrogen inducible lines was required. *Arabidopsis* seedlings were treated for 6 hours, 12 hours, and 24 hours with a mock included and the overall transcriptome was assessed by means of DNA microarray. This initial analysis therefore expanded upon this and served to determine if any genes were unique to certain time-points. Analysis of the microarray data for the previous estrogen time course was carried out in the statistical package R, specifically using the Afflmgui package. All data for the 22,747 probe sets were normalized by means of robust multi-array analysis (RMA), and a linear fit model was computed, and contrasts were performed for all time-points. Genes were then sorted based on a p-value less than 0.05 and if their log₂ value was either greater than 1 or less than -1. Before comparing all time-points, the total number of significantly up or down-regulated genes for each time-point were graphed (Figures 1 and 2).

Regarding up-regulated genes, a total of 543 genes were up-regulated at the 6 hour time-point, 541 were up-regulated at the 12 hour time-point, and 33 were up-regulated at the 24 hour time-point (Figure 1). As for the down-regulated genes, 104 genes were down-regulated at the 6 hour time-point, 221 at the 12 hour time-point, and 14 at the 24 hour time-point (Figure 2). These up and down regulated gene lists, excluding the mock overlap, were then analyzed for overlap (Figure 3). Analysis determined that out of 1,118 up-regulated genes, a total of 794 genes changed over the time course (Figure 3A.) Of the 794 genes, 228 genes were unique to the 6hr time-point, 224 genes were unique to the 12hr time-point and 23 genes were unique to the 24 hour time-point. In addition, 309 genes were found to overlap between the 6hr and 12hr time-points, 2 genes overlapped between the 6hr and 24hr time-points, 4 genes overlapped between the 12hr and 24 hour time-point, and 4 genes overlapped between all time-points. As such, any genes that were not unique to certain time-points were excluded from the final marker gene selection. Also, genes in the 24 hour time point would also not be used in the final marker gene selection due to RALF eliciting more early responses.

A total of 413 significantly down regulated genes were established during the analysis. Of these 413 genes, 337 genes total changed over the time course (Figure 3B.) Out of these 337 down regulated genes, 178 genes were unique to the 6hr time-point, 221 genes were unique to the 12 hour time-point and 14 were unique to the 24 hour time-point. Furthermore, 73 genes were found to overlap in both the 6hr and 12hr time-points, 1 gene overlapped between the 6 and 24 hr time-points, and 2 genes overlapped between the 12hr and 24hr time-point. There were no down regulated genes that overlapped between all time-points. Lastly, there were 4 genes that overlapped between both the up and down regulated lists. This resulted in 1128 genes that we either significantly up or down regulated were established for the estrogen microarray.

Cluster Analysis of Significantly Up and Down Regulated Estrogen Genes Using Mfuzz

In order to elucidate how RALF elicits its effects on cells, a Mfuzz cluster analysis and GO-DAVID (Gene Ontology) analysis was performed on the 1128 significantly up or down regulated genes isolated from the estrogen array data. Resulting Mfuzz clustering generating a total of 12 clusters (Figure 4). Each cluster contained a certain set of genes that followed a similar expression pattern over the entire 24 hour time course. Cluster 1 contained a total of 65 genes that appeared to be significantly down-regulated at the 12hour mark, with an overall expression change of -1.5. In addition, only a certain number of genes appeared to be up-regulated at the 6hr mark, but the overall expression change for the genes at this point ranged from 0- 1.5. The high degree of variability in the expression of these 65 genes at the 6hr time-point further supports that these genes are mostly affected by RALF at later times. A GO-DAVID analysis of this clustered revealed that these 65 genes are mostly involved in abiotic stress responses, specifically at the level of transcription. Cluster 2 contained a total of 148 which were significantly down-regulated at both the 6 and 12 hour marks and then returned to normal expression around the 24 hour mark. Unlike cluster 1, there was little variability in the overall expression changes between all 148 genes as all genes appeared to have equal expression changes throughout the entire time course. A GO-DAVID analysis of the clustered revealed that these 148 genes were associated with cellular growth specifically involving nucleotide metabolism. In addition, these genes were also involved with cell wall modification.

Cluster 3 contained a total of 42 estrogen genes that appeared to be significantly up-regulated at the 12 hour time-point with little changes in the 6hr and 24hr time-points. GO-DAVID analysis revealed that these 42 genes are mainly involved in defense against biotic factors, auxin metabolism, hormone biosynthesis, cell wall modification, calcium binding, and aromatic amino acid metabolism. Cluster 4 contained a total of 158 genes that were up-regulated between 6 and 12 hours and returned to basal levels at 24 hours. In addition, there was little variability in expression, and all genes tightly followed this pattern throughout the time course. GO-DAVID revealed that these 158 genes are also involved in calcium signaling and cellular defense. These genes are also involved in MAPK(Mitogen activated protein kinase) activity, Salicylic acid (SA) signaling, indole metabolism, camalexin and phytoalexin metabolism, and apoptosis.

Cluster 5 contained a total of 93 genes that were significantly up-regulated at the 6hr mark and then proceeded to return to basal levels thereon after. GO-DAVID revealed that these 93 genes are involved in wound and stress response, ethylene biosynthesis and metabolism, calcium signaling, and protein phosphatase activity. Cluster 6 contained a total of 91 genes that were significantly down regulated at the 12 hour mark with an overall expression change of -1.5. GO-DAVID revealed that these genes were involved with cell membrane modification, various lipid metabolism and biosynthesis, cell growth, brassinosteroid metabolism, cuticle metabolism, and nitrate assimilation.

Cluster 7 contained a total of 126 genes that were up-regulated between 6 and 12 hours, with little expression variation within that time. Accordingly, these genes appeared to be involved with calcium transport through channels and pumps, purine and ribonucleotide metabolism, ion transport, ATP metabolism and biosynthesis, and ATP pump activity. Cluster 8 contained a total of 83 estrogen genes that are up-regulated at 12 hours, but also significantly down-regulated at 24 hours. Genes appeared to have some variability in their overall expression changes until the 12 hour mark, but after the 12 hour mark they are relatively consistent in expression. These genes are

involved with defense responses, vesicle transport, hydrogen peroxide catabolism, carbohydrate catabolism, protein kinase activity, and apoptosis.

Cluster 9 contained a total of 65 genes that were up-regulated at 6 hours, but significantly down regulated at 12 hours. Accordingly, these genes are involved in various stimuli responses(carbohydrate, organic, hormonal) , ethylene biosynthesis, auxin signaling, RNA metabolism, and transcription. Cluster 10 contained 106 genes that were significantly up-regulated at 12 hours and returned to normal levels after. GO analysis revealed that these 106 genes are involved in defense responses, cell wall modification, carbohydrate metabolism, innate immune responses, SA signaling, aromatic amino acid biosynthesis, and response to hypoxia and changes in oxygen levels. Cluster 11 contained a total of 84 genes that were down regulated at 6 hours, but significantly up-regulated at 24 hours with some variability in expression between 6 and 24 hours. Genes contained within this cluster appear to be involved with cell wall modification, expansin activity, chromatin remodeling, and histone assembly. Lastly, cluster 12 contained 92 genes that were slightly up-regulated at 6 hours, but were significantly down-regulated at 24 hours. GO analysis revealed that these 92 genes are involved in kinase activity, Calmodulin signaling, MAPK activity, vesicle transport, ER nuclear signaling, pollen tube development, alternative splicing, and protein chaperone activity.

Comparing Estrogen and Exogenous RALF1 Microarrays

As with the estrogen array, genes either significantly up or down-regulated were compiled graphically before being compared to each other and the estrogen data (Figures 5 and 6). Regarding the up-regulated genes, a total of 789 were up-regulated at the 0.5 hour time-point, 1134 at the 1 hour time-point, 1719 at the 2 hour time-point, 1756 at the 3 hour time-point, 938 at the 12 hour time-point, and 250 at the 24 hour time-point (Figure5). A total of 197 genes were down-regulated at the 0.5 hour mark, 582 at the 1 hour mark. 1394 at the 2 hour mark, 1734 at the 3 hour mark, 954 at the 12 hour mark, and 236 at the 24 hour mark(Figure 6).

An initial comparison of RALF response genes from both the estrogen and exogenous data was made (Figure 7). When examining the 2439 up-regulated genes from the exogenous array to the 794 up-regulated genes from the estrogen array, it was determined that 626 genes overlapped (Figure 7A). As for the down regulated genes, a total of 234 genes overlapped between the 2463 exogenous array genes and the 337 estrogen array genes (Figure 7B). As a result, a total of 860 possible RALF marker genes were established.

The same methodology was used to create lists depicting the 4799 significantly up-regulated and down-regulated genes for each time-point (mock, 0.5hr, 1hr, 2hrs, 3hrs, 12hrs and 24hrs) for the exogenous RALF microarray data. Due to analysis of the estrogen data, it was suspected that genes affected by RALF would overlap in the early time-points in both the estrogen and exogenous RALF arrays. To confirm this a comparison was made between unique up regulated genes for the 6hr and 12hr estrogen data and the unique 0.5hr, 1hr, 2hr, 3hr, 12hr, and 24hr time-point for the exogenous RALF data (Figure 8). When comparing the 6 and 12hr estrogen genes to that of the 0.5hr and 1hr exogenous genes, 183 of the 1543 total up-regulated genes overlap (Figure 8A). When comparing the 6 and 12hr estrogen genes to the 2 and 3hr exogenous genes , a total of 262 of 2141 total up-regulated genes overlapped (Figure 8B). Lastly, comparing the 6 and 12hr estrogen genes to that of the 12 and 24hr exogenous genes, it was determined that only 19 of the

1438 genes overlapped (Figure 8C.) Based on the poor overlap between the 6 and 12hr estrogen and the 12hr and 24hr exogenous gene lists, a decision was made to exclude genes from the 12 and 24hr time-points in the final marker gene selection.

Hierarchical Clustering and Heatmapping of RALF Early Response Marker Genes and Marker Gene Selection

In order to select probable candidates for qPCR validation, each of the 626 up-regulated and the 234 down-regulated early response genes were subject to hierarchical clustering and heatmapping (Figure 9 and 10). Selection of marker genes was determined by selecting certain genes that shared relatively equal expression values in between both the exogenous RALF and the estrogen induced lines. Regarding the up-regulated genes, it was determined that a total of 324 genes had a relatively equal expression value during the early time points in both study (Figure 9). Specifically, these genes shared equal expression during the 6hr time-point in the estrogen lines, and in the 30min, 60min, 120min and 180min time-points in the exogenous time course. Although these genes are also subsequently located in the estrogen 12hr time-point, there is, however, more variability in their expression, further indicating RALF tends to elicit more early responses (Figure 9). These 324 genes were then ordered based on decreasing expression values and as a result, 10 up-regulated marker genes were chosen as candidates for qPCR validation (Table 1).

Out of the 234 down-regulated genes, only a total of 13 genes appeared to share similar expression values over the early estrogen and exogenous time course (Figure 10). Due to the small number of available down-regulated genes, all genes were used as possible marker gene candidates and were subject to qPCR validation (Table 2). As before, these genes appeared to varying levels of expression in the later time-points as was noted in the up-regulated gene cluster (Figure 10). However, unlike the up-regulated genes, the overall expression change in these genes is not as pronounced as it is in the up-regulated gene cluster, which can be an indication of how RALF can affect transcription.

Validation of Marker Genes by Quantitative Polymerase Chain Reaction

Three of the most highly induced up-regulated genes isolated from the heatmap were then subjected to validation by qPCR (Figure 11). In addition to the marker genes, AtRALF1 (At1g0900) was also analyzed to ensure estrogen induction was successful. Induction of RALF was successful in the transgenic RALF lines, as RALF was induced approximately 1500% over the respective zero mock, while only reaching 150% in the transgenic citrine lines. This induction also held steady well onto 6 hours where the induction was 913% when compared to the mock (Figure 10). Marker 1, At4g30280, appeared to be induced identically in both the RALF and citrine plant lines at the 1 and 3 hour markers, correlating to 1300% and 580% over the zero mock (Figure 10). At 6 hours, At4g30280, did appear to be induced more in the RALF lines at 500% when compared to the citrine lines where the induction was only 63%. Marker 2, At2g32190, appeared to share similar expression values with regards to the 1 hour time-point in both plant lines, with an overall induction of 270% (Figure 10). However, at the 3 and 6 hour RALF time-points, marker 2 was repressed as the induction was now only 23% and 30%. This observation was not seen in the citrine lines (Figure 10). Marker 3 also had the highest induction at the 1 hour time-point in both lines, with inductions of 130% and 144% respectively. As with marker 2, marker 3 was also repressed at the 3 and 6 hour time-points in the RALF lines as well as the 6 hour time-point in the citrine lines (Figure 10).

DISCUSSION

Before the discovery of RALF, studies focusing on peptide signaling centered around a small post-translationally modified peptide isolated from tobacco known as systemin (Murphy and De Smet, 2014). Further investigation of systemin revealed that it is responsible for primary wound defense (Pearce and Ryan, 2003). Since then, systemin now falls into the systemin family with other peptides based on their small size, amino acid composition, and their roles in defense signaling (Pearce and Ryan, 2003).

Systemin does appear to share some similarity with RALF1 as they both induce the rapid alkalization of the apoplastic space located in plant cells. However, unlike RALF, the signaling pathway of systemin has been heavily characterized (Pearce and Ryan, 2003). To elicit its effects, systemin first binds to a cell surface receptor kinase known as SR160(systemin cell-surface receptor 160). Upon binding, the intracellular kinase domain then proceeds to activate a MAPK. The activated MAPK then serves two purposes, the rapid alkalization of the apoplast by inactivating the proton ATPase and the activation of phospholipase. Upon activation of phospholipase, membrane phospholipids are hydrolyzed and linolenic acid is released and is subsequently converted into Jasmonic acid and other oxylipins which then initiate transcription of various defense genes. In addition, the JA produced through the systemin pathway only serves to amplify the pre-existing JA signal. However, this interaction between systemin and JA has yet to be fully understood.

As systemin was discovered in tobacco, so too was RALF. Due to RALF's ability to cause rapid apoplast alkalization and root growth inhibition, it too was thought to be involved in plant systemic defense, although it did not appear to induce defense-signaling pathways (Constabel and Haruta, 2003). Due to this observation, it appears RALF's discovery has now led to even more questions regarding as to how the plant kingdom regulates development as well as interactions with the surrounding environment.

Therefore, this studied served two main purposes; the establishment of true bonafide RALF1 marker genes in *Arabidopsis thaliana* and the initial characterization of the biological processes influenced by RALF. Marker genes were established through the analysis of previously collected microarray data, one array utilized exogenously applied RALF1 purified from bacteria while the other array utilized RALF1 produced endogenously by utilizing an estrogen receptor-based transactivator within transgenic *Arabidopsis* lines. Genes that had significant expression changes in response to RALF1 in the estrogen inducible lines were subject to gene ontology to gather this preliminary data on the biological processes influenced by RALF.

A total of 22,747 genes were subject to LIMMA analysis in the estrogen microarray. Analysis revealed that a total of 1128 genes were either significantly up-regulated ($p < 0.05$ and $\log_2 > 1.0$) or down-regulated ($p < 0.05$ and $\log_2 < -1.0$) (Figure 1). A preliminary gene ontology analysis revealed that RALF appeared to elicit early and late responses in the estrogen treated time-course. Genes that are up-regulated early in the time-course are mainly associated with biotic defense, protein phosphorylation, calcium mobilization and binding, ATPase activity, ribonucleotide metabolism, ion transport, ethylene signaling and biosynthesis, transcription, cell wall

modification, aromatic amino acid metabolism, and MAPK activity. Genes that are up-regulated at a later time were mainly associated with cell wall modification, transcription, expansin activity and chromatin remodeling, and apoptosis. Genes that were down-regulated early were found to be associated with cellular growth, cell wall modification, brassinosteroid metabolism, and membrane modification. Lastly, genes down-regulated at later time-points were found to be associated with protein phosphorylation, MAPK activity, ER-signaling, and vesicle transport. Although this is only preliminary data on how RALF1 influences the transcriptome of *Arabidopsis*, the patterns observed in the clusters as well as the gene ontology analysis can allow for initial characterization of the RALF response.

The initial response to RALF does appear to be the rapid alkalization of the cell's apoplast, due to the inhibition of the H⁺ ATPase pump located on the cell membrane. This rapid alkalization thereby inhibits cell wall extension, preventing cell expansion and elongation. According to the acid growth theory, protons act as the primary mediators of plant cell growth as they alter the activity of expansins, which act to break hydrogen bonds between the cellulose chains (Staal et al., 2011). However, due to RALF's ability to block H⁺ influx into the apoplastic space, expansin activity will be drastically reduced due to the rapid rise in apoplastic pH. Thus, cell walls will remain rigid and will be unable to undergo any modification. In addition, RALF may also affect growth by interfering with proper ion homeostasis by mediating ion movements across the cell membrane. In addition, it was also noted that at later time-points, RALF appeared to induce genes associated with programmed cell death. These two observations may be linked as studies have shown that certain plants may undergo apoptosis in response to ion disequilibrium (Huh, 2002). Secondly, RALF may also affect plant cell growth due to altering protein kinase activity as well as calcium signaling and mobilization. Both calcium and protein phosphorylation are paramount to various signal transduction pathways as they modulate the activity of various other targets downstream. Furthermore, like systemin, RALF may interact with ethylene, a potent inhibitor of plant growth (Burg, 1973).

Lastly, later RALF response genes both up and down-regulated are responsible for more long term and slower effects, as opposed to short term and rapid response occurring during the early response. Long term RALF responses may include the remodeling of chromatin, which can either cause up-regulation of certain genes, or the down-regulation of genes associated with growth. Also, RALF may interfere with the brassinosteroid signaling pathway, as genes affecting its synthesis are down-regulated, which may help to strengthen the growth inhibiting effects of RALF.

Although there appears to be a variety of ways in which RALF influences plant growth, how and what RALF uses to induce these effects is still to be elucidated. These results only serve as an initial characterization and studies involving gene knockouts utilizing the established marker genes will provide more conclusive data on the RALF pathway and response.

In order to select probable RALF marker genes, analysis of two different microarrays was required. One microarray utilized exogenously applied RALF1 while the other used RALF1 induced by means of an estrogen inducible promoter. Each array was first compared separately to establish a set of significantly up or down-regulated genes. Analysis of the estrogen microarray yielded 794 genes that were significantly altered while the exogenous array yielded 4799 genes. Due to the sheer difference in genes altered, utilizing gene expression data from one array alone would not

suffice in marker gene selection. Depending on how RALF is introduced to samples, certain issues may arise. Firstly, the RALF used in the exogenous array was purified from *E. coli*. A consequence of this purification method is that certain endogenous bacterial peptides may inadvertently be co-purified along with RALF. Therefore, gene expression as well as genes that are affected may be in response to the bacterial peptides and not RALF (Mueller et al. 2012).

Secondly, RALF1 applied exogenously may reach more tissue types than that of induced RALF, which may be the reason as to why RALF1 appeared to up and downregulate more genes in the exogenous array as opposed to the estrogen array. Another alternative method of RALF1 delivery, is the induction of the RALF1 gene by using a promoter that binds estrogen. Estrogen is an animal steroid hormone and is therefore absent from plants, as such, it does not appear to play a role in plants which makes this an ideal system for an inducible, endogenous, expression of RALF in plants (Zuo et al. 2000). Although this system prevents unwanted effects from other proteins, it still can cause undesired responses from plants. This issue stems from the inability to control how much RALF is induced upon treatment with estrogen. As such, if RALF1 were to be induced to a high degree, the excess RALF1 may cause undesired transcriptional responses from treated specimens. By comparing both arrays, each utilizing different methods of RALF1 delivery, it was possible to eliminate some of these undesired results. Comparing both arrays yielded a total of 860 overlapping up and down-regulated early response genes. These genes were then used to select possible marker genes as it was hoped that these genes only responded differently to the presence of RALF1 and not due to either bacterial peptides or a possible overabundance of the RALF1 peptide, as well as the estrogen.

In order to select true candidates for validation by qPCR, a heatmap and hierarchical cluster was created for the 626 up and 234 down-regulated gene lists. When conducting an analysis of microarray data it can be difficult to elucidate particular gene expression patterns, which is paramount to final marker gene section. If a certain gene group shares a similar expression patterns in both arrays, then these genes may be specific targets during the RALF response (Wang, 2005). Although cluster analysis can be an ideal tool for selecting functionally related genes, there arises certain drawbacks. Firstly, clustering is purely an exploratory technique, true conclusions about the RALF response genes cannot be made. Secondly, there are a variety of approaches that can be utilized in order to create these clusters, some of which may result in different gene relationships. Lastly, clustering is not specific to a certain data set, therefore any dataset may be used and clusters may therefore be random (Wang, 2005). Heatmapping and clustering of the 626 up-regulated genes revealed that 325 genes shared similar expression patterns in the 6hr time-point in the estrogen array, and the 0.5 to 3hr time-points in the exogenous array (Figure 9). In addition of the 234 down-regulated genes, only 14 genes shared similar expression patterns. As such, it would appear that RALF appears to alter gene expression mainly by upregulating certain genes, but only to a certain point, as the trends observed are transient. However, if both time courses were run using similar time-points, more reliable marker genes may have been selected, as the earliest time-point in the estrogen array was only 6 hours while it was 0.5hours in the exogenous array.

Out of the 339 up and down-regulated marker genes selected, only three of the most highly up-regulated genes were subjected to validation by means of qPCR. In addition to these markers, AtRALF1 (At1g02900) was also tested in order to ensure proper function of the estrogen inducible system. Overall, treatment of the transgenic RALF lines with 1ml of 1 μ M β -Estradiol did appear

to induce RALF to 1500% over the mock at 1 hour with a steady induction up to 6 hours with a final induction of 900% (Figure 10). This was further confirmed as RALF showed almost no induction in the transgenic citrine lines when treated with 1ml of 1 μ M β -estradiol. Although RALF was induced in the RALF lines, there was no significance between the induction of the markers in the RALF lines and the citrine lines. Thus, the expression data from the microarrays could not be validated. In addition, some markers also showed trends in expression that were not observed in the microarrays. One such trend is Marker 2, as it appeared to be induced at the 1 hour mark in the RALF lines but then appears to be repressed thereon after, a pattern not observed in the microarray data. Although these data conflict with the data in the microarray, these marker genes should not be rejected. It should be noted that unlike the seedlings used in the microarray experiments, the seedlings used in this time-course study were in poor health. Due to the age of the seeds used in this study, their overall health and germination was poor, resulting in a low yield of RNA and subsequent cDNA. Also, the incubator in which the seeds were grown was unable to fully mimic the ideal growing conditions of *Arabidopsis*. Lastly, there were many technical errors regarding the proper functioning of the Mini-Opticon system. Therefore, the combination of these errors may be the reason as to why data from the qPCR validation appear to conflict with the data from the microarrays. In order to rectify this conflict, a repeat of this experiment should be conducted, using healthier seedlings, a new qPCR machine, as well as a new means of incubation.

Although this study is only an initial characterization of the RALF1 response, it does set foundations for future studies that will serve to elucidate true RALF response genes and targets by means of gene knockouts. As with systemin, RALF1 too appears to interact with another growth hormone, ethylene. Therefore, studies examining the RALF1 response to plants treated with an ethylene inhibitor can be used to examine any connections between RALF1 and ethylene. Also, RALF1 is only one of the 40 RALF peptides, therefore, studies characterizing the other members of the RALF family are also needed. In addition, the estrogen inducible system should also be subjected to different concentrations of estrogen to examine any possible links between estrogen concentration and the overall induction of RALF.

ACKNOWLEDGEMENTS

I thank Dr. Jonathan Gilkerson for mentoring me through this independent research, data collection and analysis, as well as laboratory guidance and figure creation. This work was supported by a NASA WV Space Grant Consortium Undergraduate Research Fellowship to MH, a NASA WV Space Grant Consortium Research Enhancement Award to JG, and an NIH NRSA award (1F32GM096610) to JG.

REFERENCES

- Acosta, I., & Farmer, E. (2010). Jasmonates. *The Arabidopsis Book*, 1-13.
- Bedinifer, P. (2010). RALFs: Peptide regulators of plant growth. *Plant Signaling and Behavior*, 1342-1346.
- Belkhadir, Y., & Chory, J. (2007). Brassinosteroid Signaling: A Paradigm for Steroid Hormone Signaling from the Cell Surface. *Science*, 1410-1411.

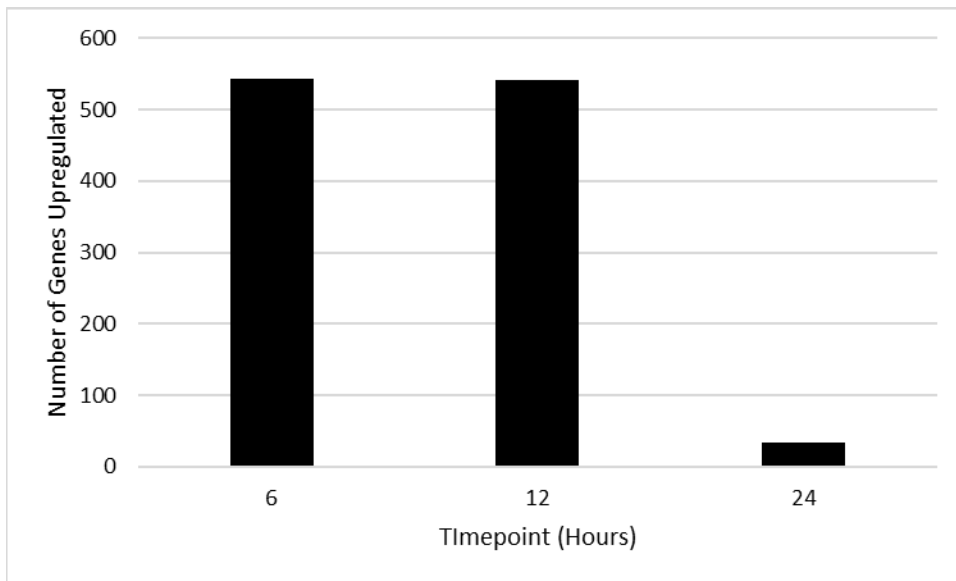
- Burg, S. (1973). Ethylene in Plant Growth. *Proceedings of the National Academy of Sciences of the United States of America*, 591-597.
- Carlisle B. and Futschik M. (2005). "Noise robust clustering of gene expression time-course data." *Journal of Bioinformatics and Computational Biology*. 965-988.
- Clouse, S. D. (2002). Brassinosteroids. *The Arabidopsis Book*, 1-23.
- Colebrook, E. H. *et al.* (2014). The role of gibberellin signalling in plant responses to abiotic stress. *Journal of Experimental Biology*, 67-75.
- Constabel, P., & Haruta, M. (2003). Rapid Alkalinization Factors in Poplar Cell Cultures. Peptide Isolation, cDNA Cloning, and Differential Expression in Leaves and Methyl Jasmonate-Treated Cells. *Plant Physiology*, 814-823.
- De Smett, I., & Murphy, E. (2014). Understanding the RALF family: a tale of many species. *Trends in Plant Science*, 1360-1385.
- Gautier, L. *et al.* 2004. affy---analysis of Affymetrix GeneChip data at the probe level. *Bioinformatics* 20, 3 (Feb. 2004), 307-315.
- Gentleman R, Carey VJ. Visualization and annotation of genomic experiments, in Parmigiani G, Garrett ES, Irizarry RA, Zeger SL, eds. *The Analysis of Gene Expression Data*, NY: Springer, 2003.
- Haruta, M. (2014). A Peptide Hormone and Its Receptor Protein Kinase Regulate Plant Cell Expansion. *Science*, 408-411.
- Huang DW *et al.* (2009). Systematic and integrative analysis of large gene lists using DAVID Bioinformatics Resources. *Nature Protoc*, 4(1):44-57.
- Huh, G.-H. *et al.* (2002). Salt causes ion disequilibrium-induced programmed cell death in yeast and plants. *The Plant Journal*, 649-659.
- Li, J. and J. Chory. (1997). A putative leucine-rich repeat receptor kinase involved in brassinosteroid signal transduction. *Cell* 90:11929-938.
- Marshall, E. (2011). Cysteine-Rich Peptides (CRPs) mediate diverse aspects of cell-cell communication in plant reproduction and development. *Journal of Experimental Botany*, 1677-1686.
- Matos, J. (2008). A conserved dibasic site is essential for correct processing of the peptide hormone AtRALF1 in *Arabidopsis thaliana*. *The Federation of European Biochemical Societies Letters*, 3343-3347.
- Mueller K *et al.* (2012) The flagellin receptor FLS2 is blind to peptides derived from CLV3 or Axt1 but perceives traces of contaminating flg22. *Plant Cell* 24: 3193-3197.
- Oliveros, J.C. (2015) *Venny*. An interactive tool for comparing lists with Venn's diagrams.

- Pearce, G. (2001). RALF, a 5-kDa ubiquitous polypeptide in plants, arrests root growth and development. *Proceedings of the National Academy of Sciences of the United States of America*, 12843-12847.
- Pearce, G., & Ryan, C. (2003). Systemins: A functionally defined family of peptide signals that regulate defensive genes in Solanaceae species. *Proceedings of the National Academy of Sciences of the United States of America*, 14577-14580.
- R Core Team (2016). R: A language and environment for statistical computing. R Foundation for Statistical Computing, Vienna, Austria.
- Richards, D. *et al.* (2001). How Gibberellin Regulates Plant Growth and Development: A Molecular Genetic Analysis of Gibberellin Signaling. *Annual Reviews in Plant Physiology and Plant Molecular Biology*, 67-88.
- Ritchie, M.E *et al.* (2015). limma powers differential expression analyses for RNA-sequencing and microarray studies. *Nucleic Acids Research* 43(7), e47.
- Saeed A.I. *et al.* (2003). TM4: a free, open-source system for microarray data management and analysis. *BioTechniques*. 34:374–378.
- Singh, A., and Savaldi-Goldstein, S. (2015) Growth control: brassinosteroid activity get context. *J Exp Bot*, 66(4): 1123-32.
- Staal, M. *et al.* (2011). Apoplastic Alkalinization Is Instrumental for the Inhibition of Cell Elongation in the Arabidopsis Root by the Ethylene Precursor 1-Aminocyclopropane-1-Carboxylic Acid. *Plant Physiology*, 2049-2055.
- Teale, W. D. *et al.* (2006). Auxin in action: signaling, transport and the control of plant growth and development. *Nature Reviews Molecular Cell Biology*, 847-859.
- Wang, Y. *et al.* (2005). Hykgene: a hybrid approach for selecting marker genes for phenotype classification using microarray gene expression data. *Bioinformatics*, 1530-1537.
- Zuo, J., Niu Q., and Chua, NH. (2000). Technical advance: an estrogen receptor-based transactivator XVE mediates highly inducible gene expression in transgenic plants. *Plant J*, 24 (2) 256-73.

PUBLICATIONS

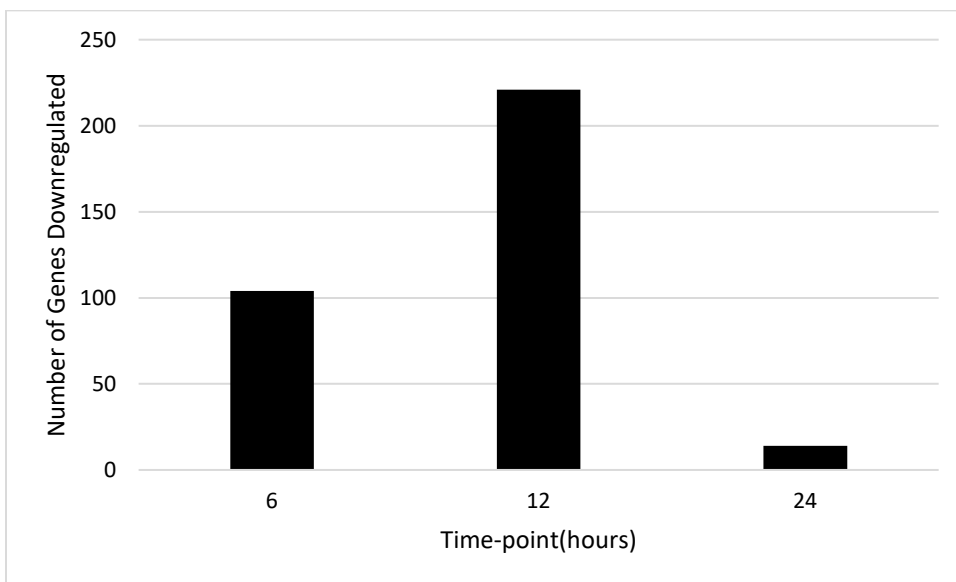
This research was presented at the 92nd annual West Virginia Academy of Sciences meeting at Glenville State College on April 8, 2017. Another presentation will be given at the Mid-Atlantic American Society of Plant Biologists meeting on April 29 at Salisbury University in Salisbury, MD. Finally, this research will also be presented orally to the Shepherd University biology department on April 13. In addition, we are in the process of having this research published in the proceedings of the West Virginia Academy of Science.

TABLES AND FIGURES



Figure

1: Total number of genes that were significantly up-regulated in the estrogen microarray. Gene lists were created using the R statistical packages AffyLmgui and Limma. Raw expression data was first normalized by Robust Multi-Array Average (RMA), and a linear fit model was computed. Contrasts were then performed on each time-point to their respected mock. Final up-regulated gene lists contained only genes with a p-value<0.05 and a Log₂ value >1.



Figure

2 Total number of genes that were significantly down-regulated in the estrogen microarray. Gene lists were created using the R statistical packages AffyLmgui and Limma. Raw expression data was first normalized by Robust Multi-Array Average (RMA), and a linear fit model was computed. Contrasts were then performed on each time-point to their respected mock. Final down-regulated gene lists contained only genes with a p-value<0.05 and a Log₂ value <-1.

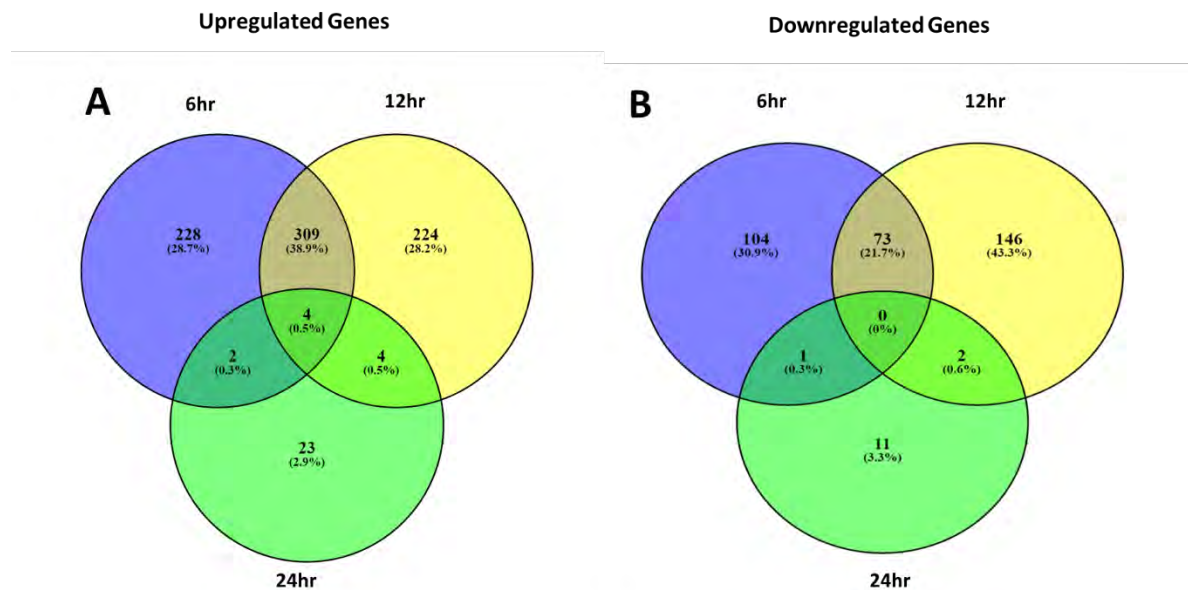


Figure 3: Venn diagram comparing genes all 1,531 up-regulated and down-regulated genes, (a) and (b) respectively, from the endogenous RALF array. Venn diagrams were created using the online freeware Venny. A total of 1,117 up-regulated genes were compared, 543 genes from the 6 hour time-point, 541 from the 12 hour time-point, and 33 from the 24 hour time-point. A total of 413 down-regulated genes were compared, 178 from the 6hr time-point, 221 from the 12 hour time-point, and 14 from the 24 hour time-point.

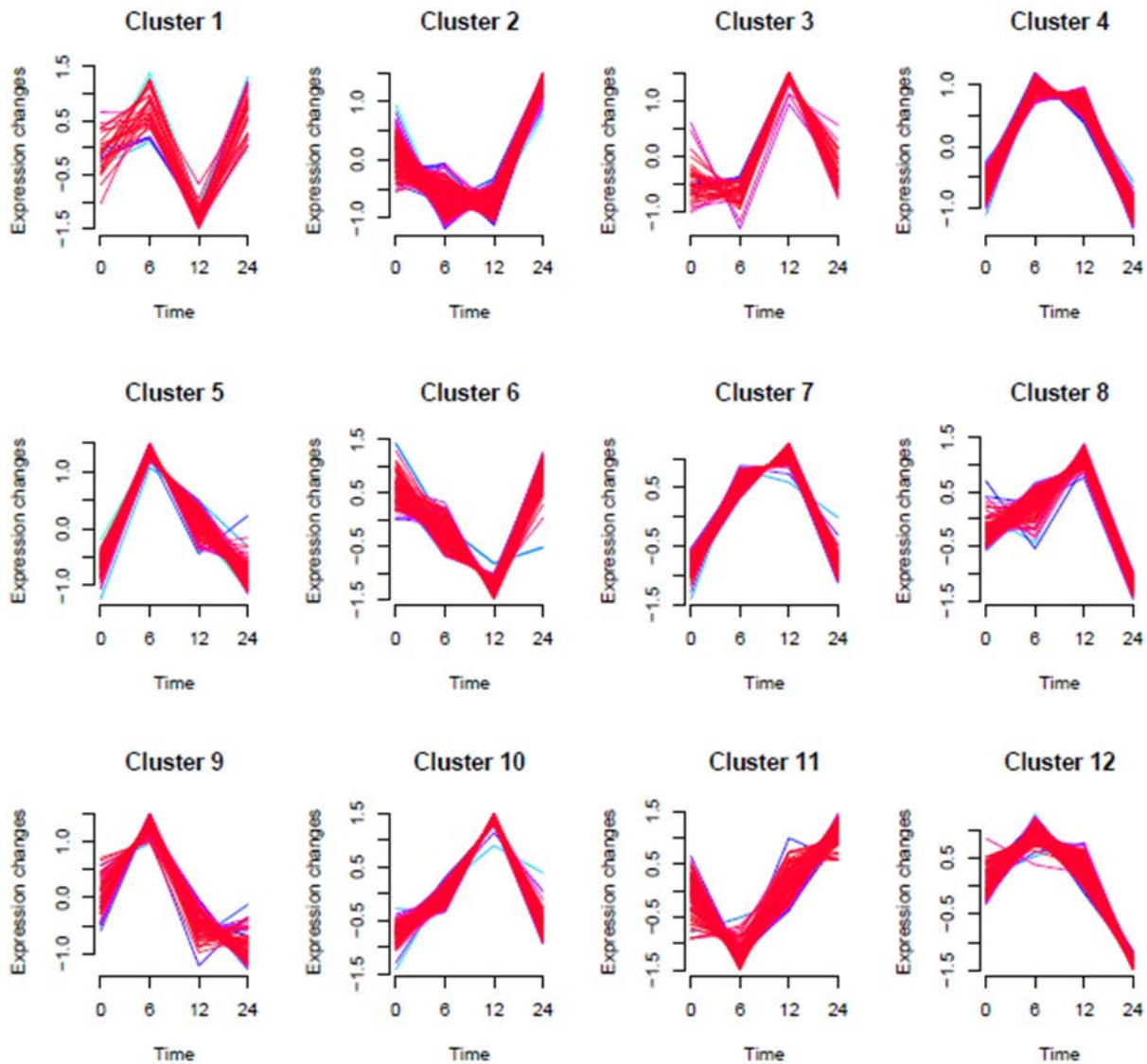


Figure 4: Cluster analysis of the 1,131 significantly up and down-regulated genes isolated from the estrogen microarray. Clusters were created utilizing the R software package Mfuzz. A total of 12 clusters were created using an M score of 1.25. Additional clustering parameters included a cluster(cores) value of 0.5, and using the soft clustering method. Clusters 1 through 12 respectively contained a total of 65, 148, 42, 158, 93, 91, 126, 83, 65, 106, 84, and 92 genes. Genes from each cluster then underwent gene ontology to create functional annotation charts using the online freeware GO-DAVID. Parameters for GO-DAVID included searching by AGI, GOTERM_BP_FAT, Interpro, SP_PIR_Keywords, and a fold enrichment was also added to each chart.

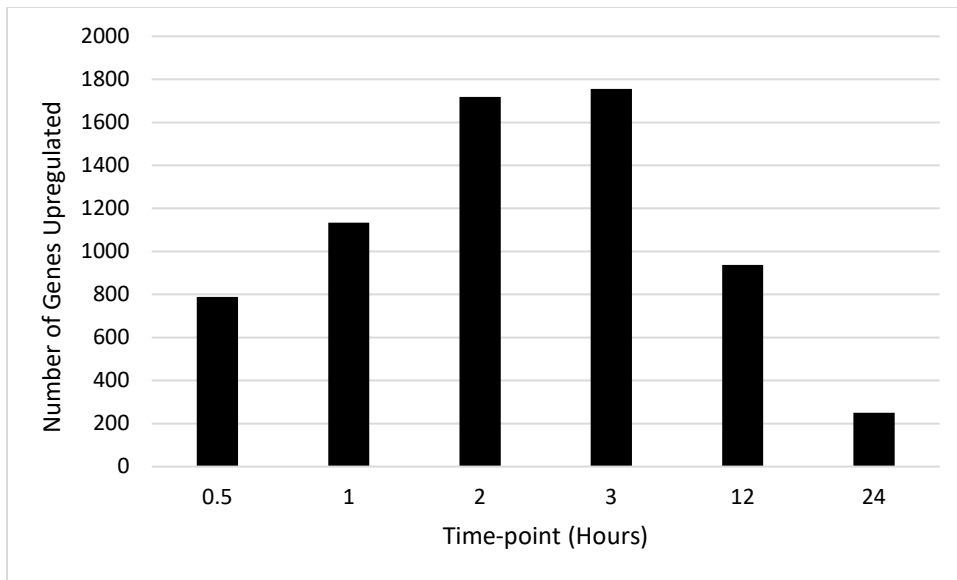


Figure 5: Total number of genes that were significantly up-regulated in the exogenous RALF microarray. Gene lists were created using the R statistical packages AffyImgui and Limma. Raw expression data was first normalized by means of Robust Multi-array Average (RMA), and a linear fit model was then computed. Contrasts were then performed on each time-point. Final up-regulated gene lists continued only genes with a p-value<0.05 and a Log₂ value >1.

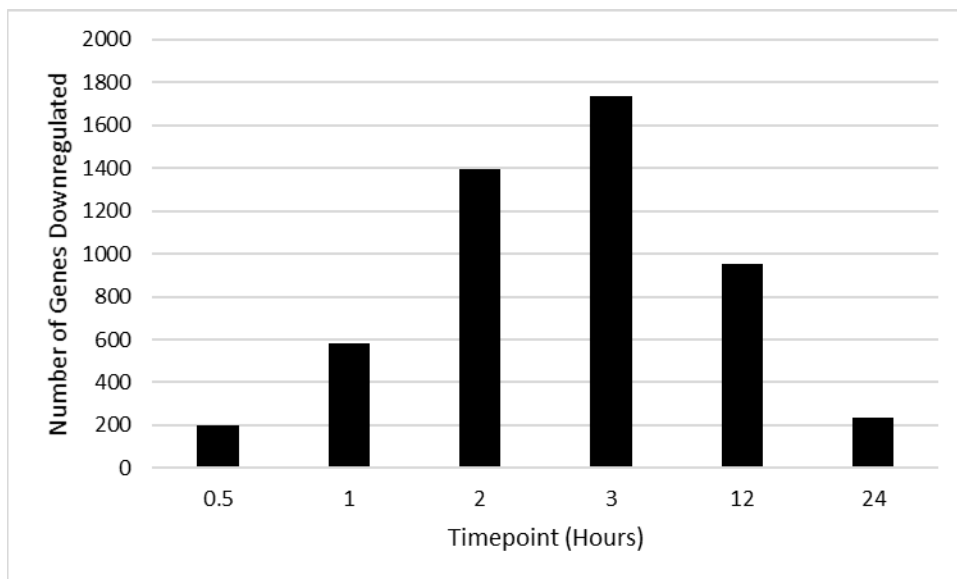


Figure 6: Total number of genes that were significantly down-regulated in the exogenous RALF microarray. Gene lists were created using the R statistical packages AffyImgui and Limma. Raw expression data was first normalized by means of Robust Multi-Array Average (RMA), and a linear fit model was then computed. Contrasts were then performed on each time-point. Final down-regulated gene lists continued only genes with a p-value<0.05 and a Log₂ value <-1.

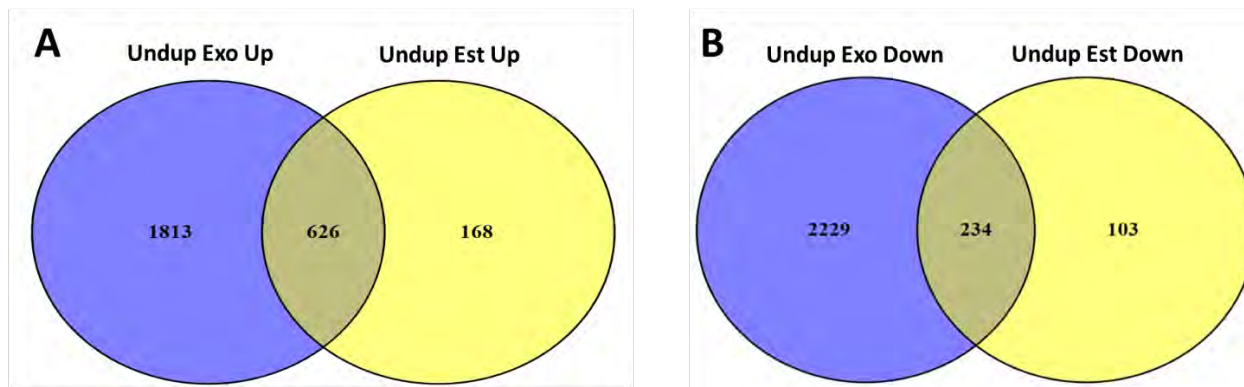


Figure 7: Venn diagrams depicting gene overlap between the significantly up (a) and down-regulated (b) genes isolated from the estrogen and exogenous RALF microarrays. Venn diagrams were created using the online freeware Venny. Before the comparisons, all duplicate genes from each array were removed. For the up-regulated genes, a total of 2,439 exogenous genes were compared to 794 estrogen genes. Regarding the down-regulated genes, 2,436 exogenous genes were compared to 337 estrogen genes.

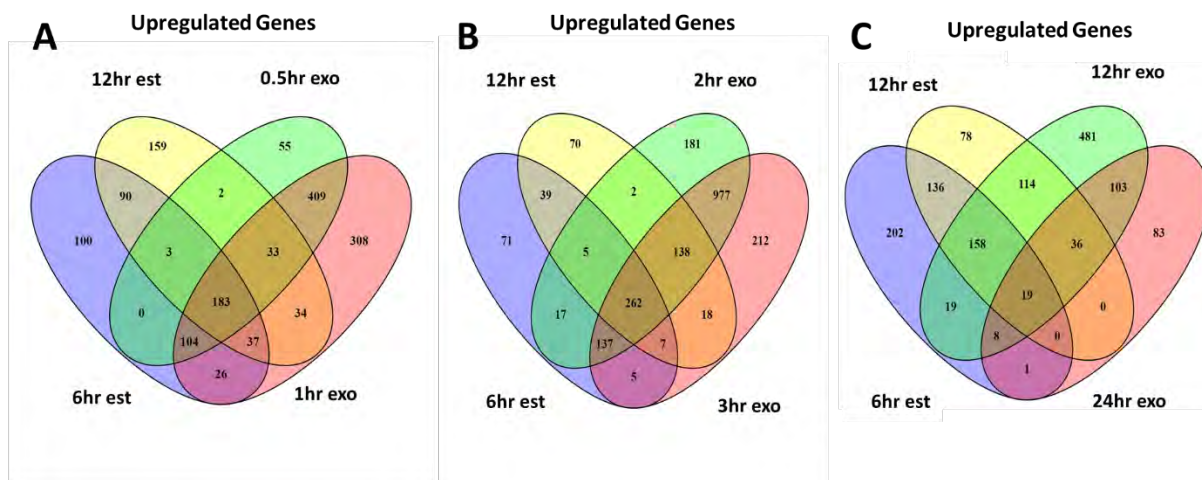


Figure 8: Venn diagrams depicting the overlap between up-regulated genes from the 6 and 12 hour estrogen time-points with all time-points from the exogenous array. Venn diagrams were created using the online freeware Venny. A total of 1543 genes were analyzed in panel A, 2141 were analyzed in B, and 1438 were analyzed in C. Significant overlap occurred between the 6 and 12hour estrogen and the 0.5, 1, 2, and 3 hour exogenous time-points, while little overlap occurred between the 12 and 24hour exogenous time-points.

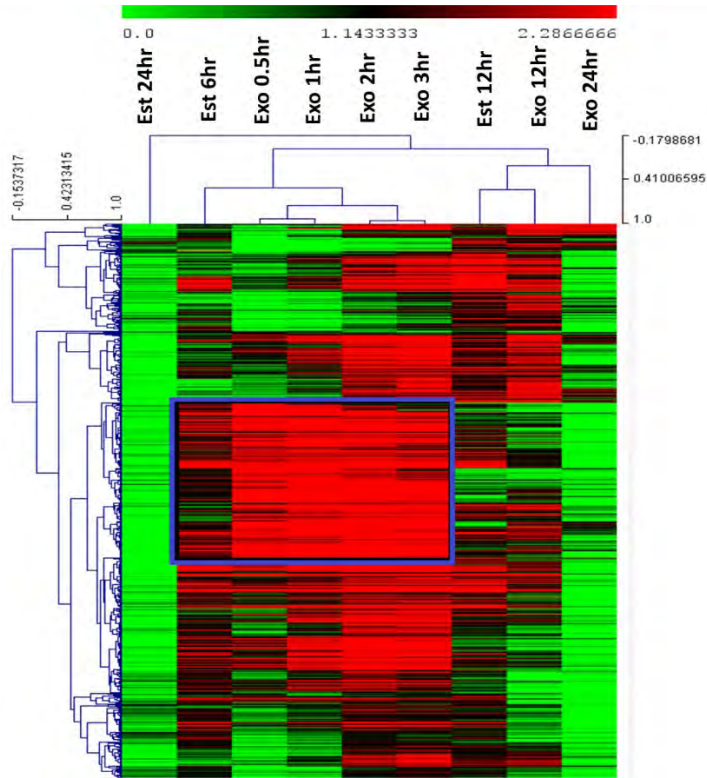


Figure 9: Heatmap and hierarchical cluster of overlapping up-regulated genes between the estrogen and exogenous microarrays. This heatmap and hierarchical cluster was created using the freeware program Mutiexperimentviewer. Parameters included using *Arabidopsis thaliana* for the organism and using ath1121501 for the array setting in addition to default clustering settings. A total of 626 up-regulated genes were heat mapped and clustered according similar expression values throughout the time-course. A total of 325 genes were isolated as possible RALF marker genes.

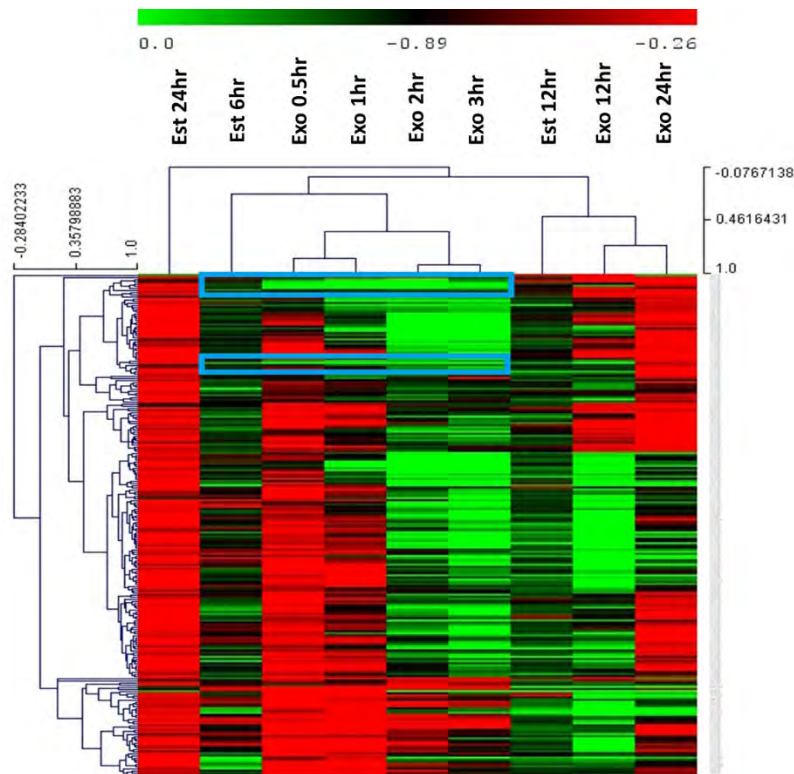


Figure 10: Heatmap and Hierarchical cluster of overlapping down-regulated genes between the estrogen and exogenous microarrays. This heatmap and hierarchical cluster was created using the freeware program Mutiexperimentviewer. Parameters included using *Arabidopsis thaliana* for the organism and using ath1121501 for the array setting in addition to default clustering settings. A total of 234 down-regulated genes were heat mapped and clustered according similar expression values throughout the time-course. A total of 14 genes were isolated as possible RALF marker genes.

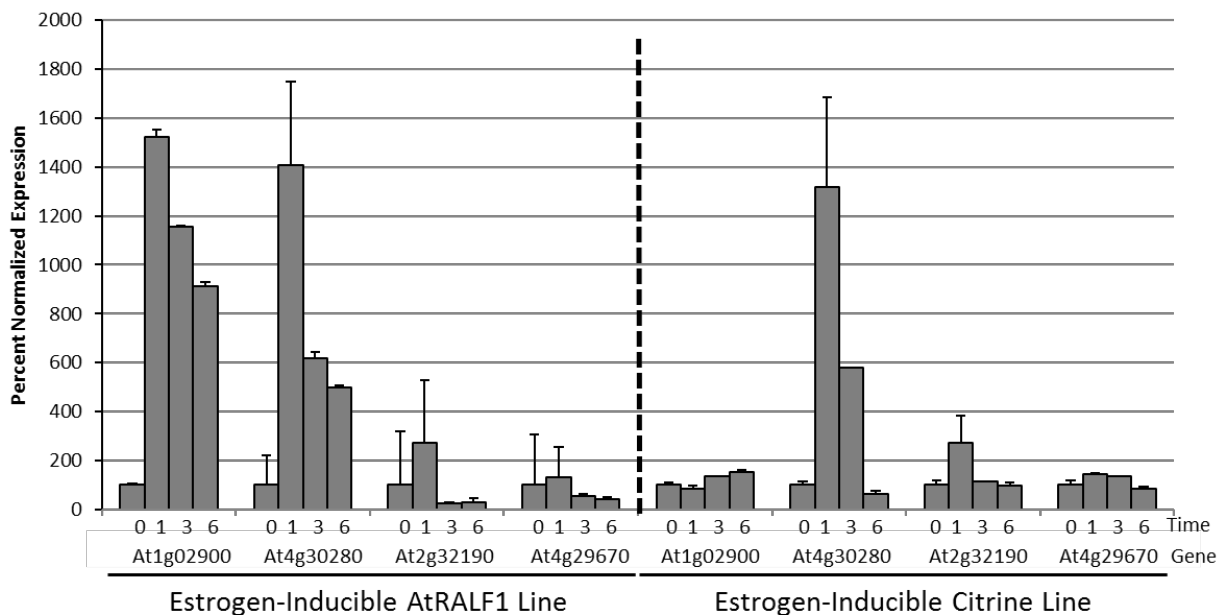


Figure 11. Validation of three of the most highly induced up-regulated marker genes by means of qPCR. To ensure the effectiveness of the estrogen inducible system, the expression of AtRALF1 (At1g02900) was also analyzed. Samples were first normalized to two control genes Actin and IPP2, and were then normalized to their respective zero mock. Error bars represent the standard error of the mean of 3 biological and 3 technical replicates at each respective time-point.

Table 1: Up-regulated RALF marker genes subject to validation by qPCR

| Marker Gene (Up Regulated) | Function |
|-----------------------------|--|
| At4g30280 | Cell wall biogenesis and organization |
| At2g32190 | Molecular function unknown |
| At4g39670 | Glycolipid transport |
| At1g66090 | Signal transduction in defense responses |
| At3g50930 | Apoptosis and SA signaling |
| At2g32210 | Molecular function unknown |
| At1g56060 | Molecular function unknown |
| At4g12720 | Defense response signaling |
| At4g08040 | Ethylene biosynthesis |
| At2g34930 | Defense response signaling |

Table 2: Down-regulated RALF marker genes subject to validation by qPCR

| Marker Gene(Down Regulated) | Function |
|------------------------------------|---|
| At1g66890 | Molecular function unknown |
| At3g52070 | Function unknown, integral Membrane Protein |
| At3g63210 | Response to abscisic acid and seed dormancy processes, encodes a novel zinc-finger protein with a proline rich N-terminus |
| At4g38840 | Auxin responses |
| At4g28290 | Molecular function unknown |
| At2g40610 | Involved in plant cell wall loosening, involved in nematode-induced syncytia in roots |
| At3g63200 | Involved in lipid catabolism |
| At2g21210 | Auxin Responses |
| At1g72200 | Protein ubiquitination |
| At3g01190 | Response to oxidative stress |
| At2g24150 | Response to oxidative stress |
| At1g12845 | Molecular function unknown |
| At2g34490 | Sterol biosynthesis |

WRITING OF INKS FOR USE IN P-N JUNCTIONS FOR OPTOELECTRONIC APPLICATIONS

Kerwin Moreland
Mechanical Engineering
West Virginia University
Morgantown, WV

ABSTRACT

Optoelectronics have been an important area of research for the past few decades, and this zone of interest for various applications continue to grow in popularity amongst scientists and researchers around the world. Many applications optoelectronics are currently being used for includes LCD displays, infrared displays, photo detectors, solar panels, and assorted types of sensors. The potential for newer and better technologies that lies in the materials that compose these devices is exciting because they're continuously being improved, and a shift towards transparent electronics seems to be forthcoming.

In today's world, almost every electronic system uses a key component called the diode, which play a vital role in the function of optoelectronics. Diodes work in a way that combines two semiconductor materials with different kinds of doped features. One of the two materials is of the n-type, and the other of the p-type, which makes for varying electrical properties. A material of the n-type is sometimes referred to as the donor region, which means that it possesses an excess amount of electrons. The p-type material has inhabitants of "holes" in its region of the junction, which makes it electron accepting. When materials that exhibit strong traits of being n-type and p-type are brought together, a p-n junction is created. The area between these two materials is then formed as well, which is a zone known as the depletion region, which can be manipulated using different types of materials in varying amounts, and can also have a wide range of effects when in forward or reverse-bias. The ideal scenario that is created within this device makes it act as a diode, which allows electrical current to flow in a single direction, but not so in the opposite.

The research that has been concluded in this work is the investigation of printing these p-n junctions using p-type semiconductor components in conjunction with an n-type material: zinc oxide (ZnO). Although literature review has backed the feasibility of printable n-type material not only in this work, but in a great many others as well, the p-type material is still an area to be perfected for fully operational 3D printed devices (Choi, Yun-Hyuk, et al). The key point of looking into creating p-n junctions to form a diode for devices such as solar cells is important because being able to print the fundamentals of these electronic components makes for a fast and convenient method for manufacturing. The greater key challenge in printing p-type inks is being able to formulate polymers and precursors in the material with the same features and functionality as rigid vacuum-based techniques, which are currently time consuming, and can be much more expensive (Abdelfatah, Mahmoud, et al).

INTRODUCTION

The focus of the work in this research project was looking at printing both p and n-type materials in combination for small optoelectronic devices. First, a plan was set for formulating the n-type

material based from ZnO, since it is a more well-known semiconductor material with excellent optical traits. Once this was done, multiple inks were made of varying amounts of the dopant, which was aluminum in this project. The next step was to configure the robot used for the direct writing of the inks, which included experimenting with various pattern types while taking into consideration the nozzle size. A pattern type to fit material in a 1x1cm square was chosen, which were then printed on cleaned glass slides 2.54cm square. After this was complete, the ZnO inks were annealed one layer at a time, while comparing their electrical properties and viscosities across a range of dopant added. Not only was this done, but layers were then printed on top of the ones that were annealed prior, and the same process was repeated to see what kind of impact a thicker film would have on bringing out the desired qualities of a semiconductor. The main properties looked upon were each film's ability to carry a current across a range of applied bias voltages. This was explored extensively, and the planning phases for executing a good quality copper-based p-type material were investigated via literature review. This was not something that could be done during the time period, but an idea of how it will be executed in the future was established. This part of the project was very challenging, as there are not many examples currently that show copper-based films exhibiting excellent optical traits, especially using a 3D printing approach (Bai, Yun and Christopher B. Williams).

BACKGROUND

Prior to beginning this project, the author's interests included 3D printing and materials research. The combination of the two yielded the idea of pursuing a project that would create the goal of 3D printing optoelectronic devices. The first step towards this goal was to create a p-n junction, which is the main component in functioning devices.

The 3D printing, or direct writing method of depositing materials to form objects of variable geometries is carried out after formulating inks with proper viscosity for extrusion through a fine tip, which must also exhibit near fluid-like properties in order to create different layer patterns. Vertical integration within these devices is a key concept to pay attention to because it means that the creation of devices with changing functionality within themselves could possibly be within reach. Also, directly depositing the ink onto a substrate via a nozzle tip-based method allows for large area manufacturability of devices while avoiding the limits of other techniques, such as thermal evaporation, or pulsed laser deposition. These methods have been explored extensively in this area of research, as well as others. But the printing technique seen in this work only uses air pressure for deposition, whereas the other methods may require higher energy to yield results of similar outcomes. The 3D printing principle here uses pressure to extrude material stored in a syringe, and then through the nozzle's tip, which can be performed in a wide range of settings. Variables include differing nozzle sizes, multiple printing speeds, z-offset positions for varying layer thicknesses, and in some cases, even adjustable temperature settings. On the other hand, another example of a less flexible technique includes vacuum deposition, which can require complex setups for operation, and does not make for the most versatile setup for further use in space or zero gravity applications.

EXPERIMENT

In this experiment, preparation of aluminum doped zinc oxide (ZnO:Al) inks was completed as

the first major step in the project. Materials for formulation included zinc acetate dihydrate (ZAD), aluminum nitrate nonahydrate ($\text{Al}(\text{NO}_3)_3 \cdot 9\text{H}_2\text{O}$ (dopant source), 2-methoxyethanol (stabilizer), ethanolamine (0.453g) (stabilizer), and polyvinylpyrrolidone (PVP). The mixture was then stirred for 2 hours at 65°C . The PVP was utilized for controlling the mixture's viscosity to a point where it would be easy to extrude through the nozzle used for printing. An atomic weight percentage of 20 (20 at. wt. %) was used in this experiment because the material showed to exit the nozzle without clogging issues, and it also proved to maintain the integrity of the printed shape without spreading. For the ZAD, 1.714g was held consistent across all solutions. To produce films with a varying amount of dopant, 1.029, 0.087, 0.146, and 0.205g of $\text{Al}(\text{NO}_3)_3 \cdot 9\text{H}_2\text{O}$ was used for 1, 3, 5, and 7 at. wt. % inks, as well as a batch of pure ZnO solution, which utilized no $\text{Al}(\text{NO}_3)_3 \cdot 9\text{H}_2\text{O}$.

The substrates used in this experiment were 1x1in. cut glass slides, which were cleaned prior to use using a combination of ethanol, acetone, and deionized water. When printing was executed, cleaned nozzles of 0.3mm tip diameter were utilized while material was held in a plastic syringe. Each ink was stored at room temperature and sealed in the vials so ambient air could not affect the solutions. Inks were then extruded at a pressure of approximately 20psi for best results at a printing speed of 5mm/s with the nozzle at a height of 1mm above the surface of the substrate. The nozzle screwed directly into the bottom of the syringe, and the tube supplying air pressure at the top, as all parts were made to fit with one another in conjunction with use during the robot operation.

Once inks were printed using a diagonal line method of operation, one layer of each concentration of the ink was annealed at 500°C starting at room temperature, ramping up to temperature by $2^\circ\text{C}/\text{min}$, holding peak condition for two hours, and ramping down at the same pace. Films were then characterized by viscosity range before printing, and electrical properties after the annealing process. Electrical properties were observed using a two-point probing method at a distance of 3mm between probes at a bias voltage range of -10 to 10 volts. A Brookfield LVDV-II+ Pro rotational rheometer was used to determine the viscosities of all inks produced.

METHODS

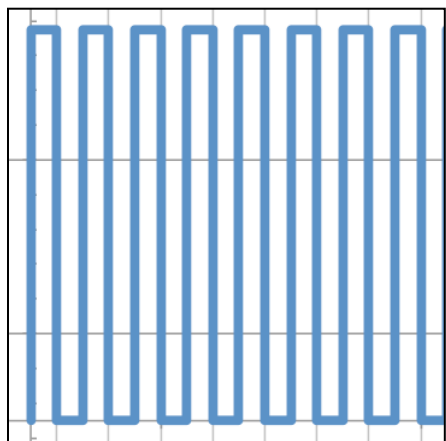
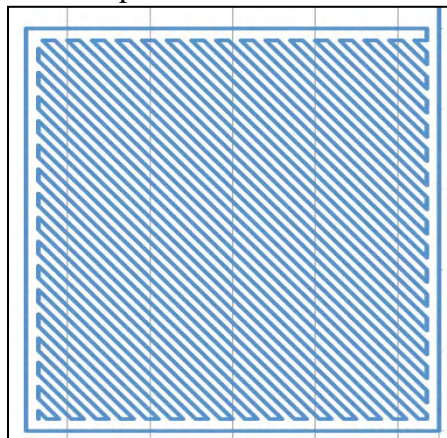


Figure 1. Example of initial pattern style of parallel lines.

Once inks were prepared, films were printed with a pattern type that would reduce the amount of surface roughness due to spacing between each line of extruded material. At this point in the process, this was simply a trial and error type of procedure. First, lines were printed parallel to one another in a square shape, which can be seen in figure 1. But it was observed that although the material was continuous, a wavy pattern could be seen with the naked eye on the surface of the material. The trial step in elimination of this inconsistent surface feature was printing an initial perimeter of the square, followed by filling in the rest of the area using diagonal lines. Spacing between lines was a key step in determining how this was to be modeled, where this value was kept at the value of the nozzle's diameter. From this point, using a simple slope-distance equation could be used to determine the pattern. The

robot used in this experiment can be told when to extrude material and move in 3-dimensions in a

step-by-step manner using a manually inputted program. Importing the coordinates from an excel file, and choosing to extrude material at all points along the pattern at a constant pressure made this feat possible.



As stated in the section prior, one layer of each concentration of ink was deposited on a glass substrate and annealed. Following this, another layer was printed on top of the previous layer and annealed again. This was done until pure ZnO and 1, 3, 5, and 7 at. wt. % films were printed up to 5 layers. At this time, a comparison of electrical properties was investigated to determine which was the most optimal thickness for continuation for use in an actual device. It was also ensured that glass slides were rinsed in ethanol, cleansed with acetone, and soaked in deionized water to remove any unwanted material from affecting the deposited material before annealing, during annealing, or during electrical conductivity trials.

Figure 2. Example of final pattern design using diagonal lines.

Viscosity was tested using a Brookfield LVDV-II+ Pro rotational rheometer. The torque constant (TK) for this device was a set value of 0.09373, the spindle multiplier constant (SMC) was 9.922, and the shear rate constant (SRC) was 2. These values are necessary for viscosity calculation, and are dependent on the rheometer model being used. Below, equation 1 describes the calculation for shear rate, and equation 2 shows how to obtain the full-scale viscosity range, measured in centipoise (cP). These values shown on the graphs following this section this explanation were obtained directly from the rheometer.

$$\text{Equation 1:} \quad \text{Shear Rate} \left(\frac{1}{\text{sec}} \right) = \text{SRC} * \text{RPM}$$

$$\text{Equation 2:} \quad \text{cP} = \text{TK} * \text{SMC} * \frac{10,000}{\text{RPM}}$$

RESULTS

Upon measuring the viscosity of each of the inks manufactured, the following results can be seen in figure 3 below. The range of viscosities shows to stay consistent with ZnO:Al inks of 3, 5, and 7 at. wt. %, but not as close a resemblance was seen with pure ZnO and ZnO:Al of 1 at. wt. % concentration. This may have been due to the fact that even a slight addition of $\text{Al}(\text{NO}_3)_3 \cdot 9\text{H}_2\text{O}$ to the rest of the mixture can cause a variation in the viscosity seen here. Overall, the properties each ink showed during physical extrusion during the printing process were nearly identical, and films were nearly identical in appearance.

As for the electrical properties observed in this experiment, testing was only done on films that were printed with 4 and 5 layers of material. The problem that occurred while trying to manage a complete inspection of finer films was the production of gaps in the annealed product. These voids made it impossible to allow a current to flow through the material, and although this was especially true for films of 1 layer, it was still seen in films of 2 and 3 layers, where gaps were finally filled in the 4th layer of printed material. The reason for so much degradation of material was due to the

fact that such high temperatures reached in the furnace caused evaporation of most of the films. An example of finer films can be observed in figure 4, while a comparison of what thicker films looked like can be seen in figure 5.

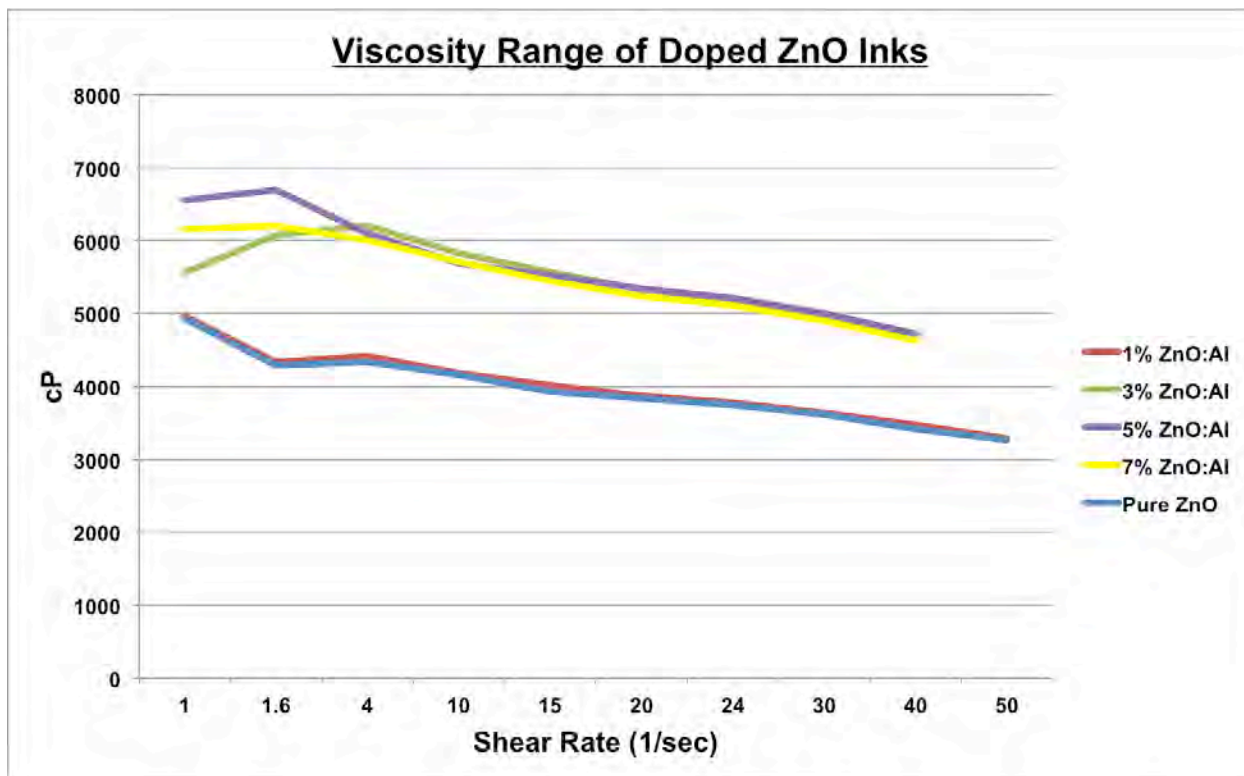


Figure 3. Range of viscosities for each concentration of doped ZnO ink.

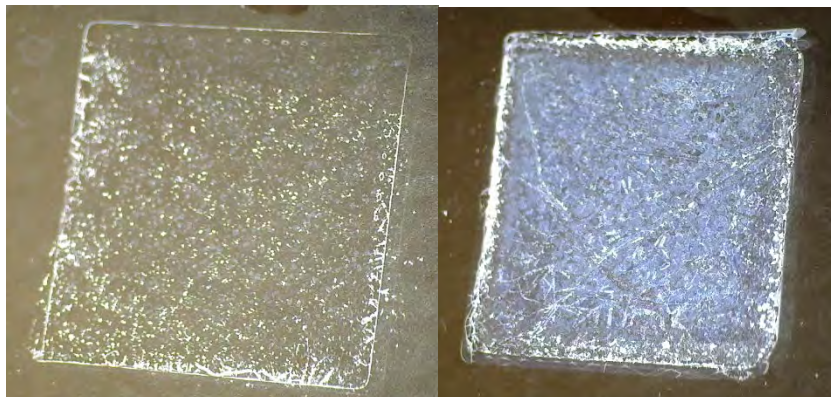


Figure 4 (left). Example of a 2-layer film of 3 at. wt. % ZnO:Al after annealing. Small yellow dots can be seen on the surface of the film, which is leftover evaporated material that had stuck to the surface. Removal via an air hose of this leftover material proved to be difficult to remove without damaging the films.

Figure 5 (right). Example of a 5-layer film of 3 at. wt. % ZnO:Al after annealing. A more solid structure can be seen in this film, while most of the evaporated material on the immediate surface is mostly removed.

Electrical conductivity was done by probing the surface of each film with small pins connected to a power source, where the amount of voltage applied could be controlled manually for testing. Below are the results from testing the conductivity of all concentrations of 4 and 5 layer films at a

distance of 3mm distance between probes (seen in figures 6 and 7). It was observed that both films of 4 and 5 layers exhibited similar behavior, while films of lower concentrations of aluminum doping seemed to have a more drastic jumps in current flow at voltages near zero. Films of higher concentrations showed more linear behavior, acting in a near resistive manner, even at a voltage close to zero. This is especially true for films of 4 layers, but 5 layer films all acted nearly the same in the bias voltage range of -10 to 10 volts.

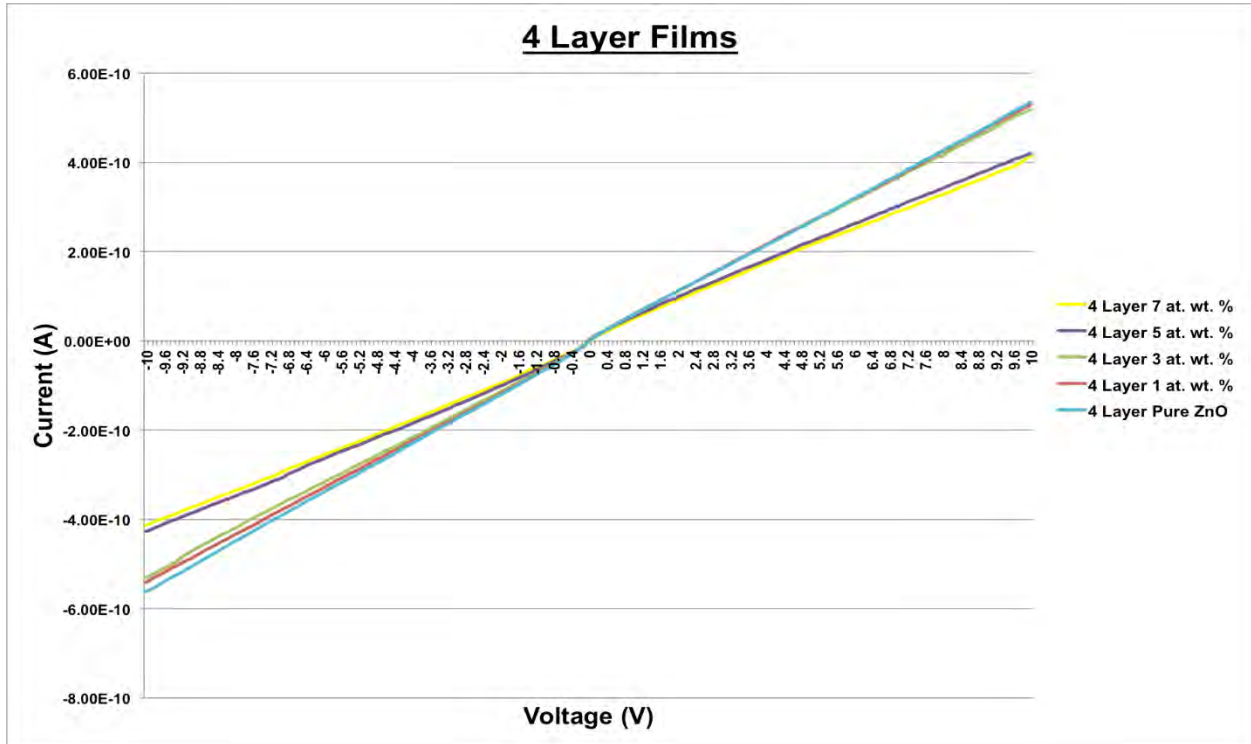


Figure 6. Electrical characterization of 4 layer films of varying concentration.

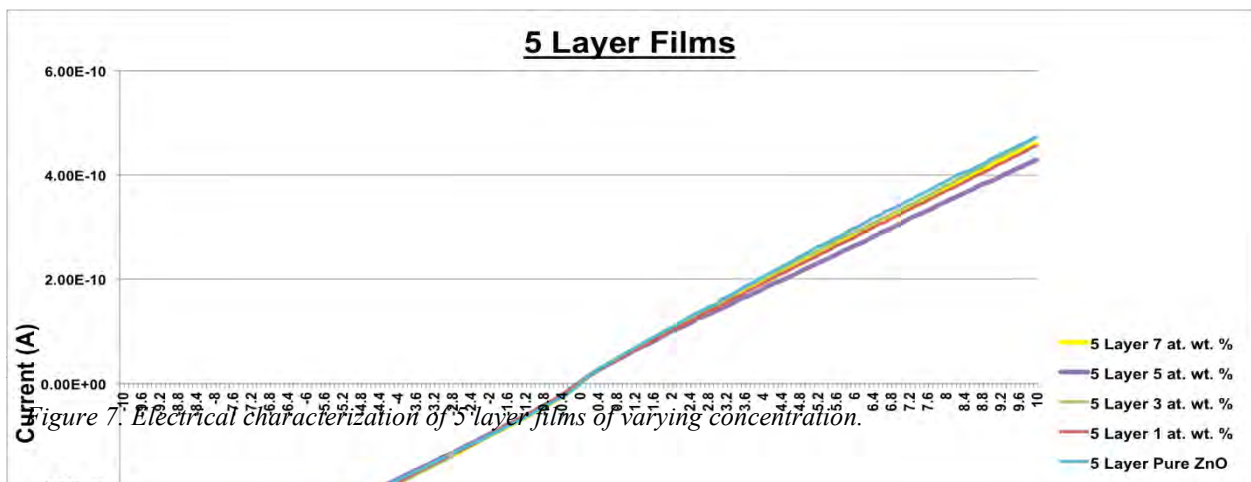


Figure 7. Electrical characterization of 5 layer films of varying concentration.

CONCLUSION

The conclusion of this work shows that finding a method in which printing semiconductor materials for use in optoelectronic applications for use in p-n junctions was successful. Films of ZnO:Al were created of varying amounts of dopant added, as well as varying layer thicknesses. Comparing these traits showed that films of 4 to 5 layers were best in providing the proper semiconductor qualities in this experiment. The desired response when applying a voltage across the device would be to see a high resistance in one direction, while noticing a low resistance in the other. As for the n-type material separately, the ideal situation would be to see a level trend at a wide range of bias voltages, while noticing a steady increase in the voltage through a specific range. It was seen in this experiment that the films of both 4 and 5 layers across all doping types had a slight resemblance to this trend, making it feasible for use in p-n junctions.

EXPERIENCE

The experience gained through this project was one that made for well-learned self-reliance in the lab. With thorough two-way communication in the lab with others, and a group of people willing to assist in the learning process through the laboratory experiments, made for a more self-confident role as a researcher. Having such good peers and teachers showed to have a large impact, and definitely went a long way, as there is greater belief in being self-sufficient in doing a solo project. Another aspect of the project (from an engineering viewpoint) was having to be able to solve problems that were not very typical in standard practice. What is meant in this explanation is that having to figure out problems in which a standard mechanical, electrical, or industrial engineer without research experience, for example, may have to face in order to figure out some sort of difficulty. Having a new type of research proposal gives engineers a chance to look at critical thinking in a new light, and gives inspiration to new ideas. This is how discoveries are made, and having worked on a difficult project such as this one was an experience that could not have been done alone.

FUTURE WORK

After conclusion of the work period, it has been decided that more literature review in the area of

p-type copper-based material will be explored for further use in optoelectronics. The major milestone in completion of this task will be to come up with an ink solution that will exhibit quality optical traits. As for the n-type material, it is thought that a more in depth look into lowering the annealing temperature may be of use for controlling the amount of evaporated material. The effect on the electrical properties of films afterward may have a better influence on these traits, and could be of major importance later on. Another area of emphasis for continual exploration would be figuring out a better method for cleaning the evaporated material from the annealed films, which would certainly increase optical traits, making for even thinner, transparent films.

ACKNOWLEDGEMENTS

A big thanks goes to the NASA West Virginia Space Grant Consortium for the award, as well as the opportunity to pursue this area of research. Another thank you to Dr. Konstantinos Sierros for providing invaluable knowledge as mentor during the research period. To Ioannis Kortidis for being a short-term mentor during the beginning of the project, and to Maria Torres, Guy Cordonier, and Derrick Banerjee for their assistance in the lab. With the help and mentoring of all mentioned here, the project really turned out to be a great learning experience.

PRESENTATIONS

An expected outcome of this award for the research conducted was to present all findings at Undergraduate Research Day at the Capitol in Charleston, WV. However, this fell through, as the work was not accepted for participation during the event in February of 2017, but the concluded work was presented at the Materials Research Society at WVU, as well as in front of the other members working in the same laboratory.

REFERENCES

- Abdelfatah, Mahmoud, et al. "Fabrication and Characterization of Low Cost Cu₂O/ZnO:Al Solar Cells for Sustainable Photovoltaics with Earth Abundant Materials." *Solar Energy Materials & Solar Cells*, vol. 145, Feb2016 Part 3, pp. 454-461. EBSCOhost, doi:10.1016/j.solmat.2015.11.015.
- Bai, Yun and Christopher B. Williams. "An Exploration of Binder Jetting of Copper." *Rapid Prototyping Journal*, vol. 21, no. 2, Mar. 2015, pp. 177-185. EBSCOhost, doi:10.1108/RPJ-12-2014-0180.
- Choi, Yun-Hyuk, et al. "Direct Printing Synthesis of Self-Organized Copper Oxide Hollow Spheres on a Substrate using Copper(II) Complex Ink: Gas Sensing and Photoelectrochemical properties." *Langmuir*, vol. 30, no. 3, 28 Jan. 2014, pp. 700-709. EBSCOhost, search.ebscohost.com/login.aspx?direct=true&db=a9h&AN=94135486&site=ehost-live.

SAFE LOADING LIMITS FOR THE ROTATOR CUFF MUSCLES

Esther Raub
Industrial Engineering
West Virginia University
Morgantown, WV

ABSTRACT

Rotator cuff injuries are very common in astronauts due to the pressurized nature of astronaut suits, the suit design itself and the physics of zero gravity environments. In the NASA Tiger Team report, EVA training at the Natural Buoyancy lab caused over 60% of astronauts to report some degree of shoulder pain. [Williams, 2003] Other research has been done in the area of shoulder muscles, but safe loading limits for the rotator cuff muscles have never been developed. This paper discusses the design and implementation of an experiment to analyze fatigue development in the rotator cuff muscles under different joint demands. From analysis of the data collected in this experiment, safe loading limits were approximated at 30% of maximum voluntary contraction (MVC) by using statistical measures and linear regression to study the trends of subject fatigue. The data collected from this study can be combined with current publications to improve the understanding of the rotator cuff muscles. The results and experimental process can also be incorporated into future research to aid in the development of new safety standards for the shoulder muscles.

INTRODUCTION

The goal of this project was to develop and conduct an experimental study to measure muscle fatigue under different joint demands in ten, male subjects. This was accomplished by selecting four, evenly spaced loading levels (15%, 30%, 45%, 60% of subject's maximum) and measuring the electric activity in the subject's muscles when exerting the given torque value over a period of 60 seconds. The muscles studied in this experiment were the supraspinatus, infraspinatus, and teres minor. The order of the muscles and loading levels was randomized and subjects were given a rest period between each trial to ensure that prior trial fatigue was not a primary concern in the data. Analysis of the EMG data showed a negative relationship between force level and the slope of the median frequency line at loading levels below 60% in all muscles.

BACKGROUND

When training for work on the International Space Station, many astronaut candidates reported shoulder injuries and the development of shoulder musculoskeletal diseases. Fourteen percent of the astronaut candidates surveyed reported needing surgical procedures to treat their shoulder injuries. Of this fourteen percent, none of the candidates had a prior history of shoulder injuries or musculoskeletal diseases. These injuries can lead to crippling pain and severe short- and sometimes even long-term health problems for those who suffer from them. [Williams, 2003]

However, rotator cuff injuries are not only common in astronauts, but also in the workplace. Shoulder injuries are a costly and miserable experience for both workers and employers. Almost every employee is susceptible to a shoulder injury as most common tasks place stress on the

shoulder joint in some way. Reaching to obtain a bolt, lifting a heavy box, and even grasping a tool and pulling it towards oneself can all fatigue the shoulder muscles when performed repetitively. Not only are shoulder injuries a highly common workplace hazard, but these injuries are also one of the slowest to recover. According to the Bureau of Labor Statistics shoulder injuries were responsible for a median of 26 days away from work. This is over twice as long as the median for all other body parts at 10 days! [BLS, 2015] Even after 6 months, only 50% of shoulder injuries are fully recovered. [Croft Petal, 1996] In addition to being painful for the worker, if injured on the job, workers can be eligible for workers compensation benefits which can be costly for the employer. In the state of Maryland the average compensation per shoulder injury was \$25,378 as opposed to \$22,447 for back injuries. [MDWC, 2017] For these reasons it is imperative that fatigue development in the shoulder complex be studied to aid the development of strict safety standards for the shoulder and rotator cuff muscles.

PROJECT

Project Team

This research project was completed by a team of students led by Dr. Ashish Nimbarte, Associate Professor of the Industrial and Management Systems Engineering department at West Virginia University. The team members include Esther Raub who is an undergraduate student at West Virginia University and majoring in Industrial Engineering. She is the author of this paper, and the focus of each section is on the work that she directly participated in. Hossein Motabar and Iman Nabiyouni are PhD students in the Industrial and Management Systems Engineering department at West Virginia University and were also members of the project team.

Approach

The data was collected using a lab-based study and human subjects. The experiment began by determining the maximum torque level (maximum voluntary contraction or MVC) of each subject in three postures. The subjects were then instructed to perform each exertion at four different percentage torque levels to study fatigue development in the rotator cuff muscles. The muscle activity of the subjects during these exertions was measured using surface electromyography. The force and muscle activity data were recorded and analyzed to quantify safe loading limits.

Variables

For this study, the independent variable is the force exerted by the test participant. Each participant was instructed to apply four levels of torque: 15% of MVC, 30% MVC, 45% MVC and 60% MVC. Subjects were instructed to hold the given value by reading a biofeedback display which showed the current torque level experienced by the dynamometer. If the subject began to exhibit any inconsistencies in the torque value the subject was told to stop by the HUMAC operator, and the EMG data recording was ended. This would occur when the subject began to fatigue at high percentages of MVC and could not maintain the given torque level. Each exertion was performed for a maximum duration of 1 minute.

The dependent variable for this research project is the muscle fatigue developed by the participant. During the shoulder exertions, the muscle activity data was recorded continuously using the EMG system. The muscle activity data was analyzed to estimate muscle fatigue.

Posture determination

The original proposal for this research specified that the MVC postures and actions listed below in Table 1 would be used. These positions were selected due to common usage by other researchers in the field. However, due to the nature of these positions, particularly the supraspinatus, measurement of the torque level would be extremely difficult to accomplish and monitor. For this reason current publications were analyzed to see if any alternate positions were available.

| Table 1 Muscle name, posture and action of rotator cuff muscle MVCs as mentioned in original research proposal | | |
|---|--|--|
| Muscle | MVC posture | MVC action |
| Supraspinatus | Arm will be abducted at 20 degrees in frontal plane; elbow will be flexed at 90 degrees; and no shoulder flexion. | Arm will be resisting the abduction, while subject will sit on a chair and will push against a wall. |
| Infraspinatus | Arm will be abducted at 50 degrees in frontal plane; elbow will be flexed at 90 degrees; and hand will be in 90 degrees pronation. | Arm will be resisting the External rotation of the shoulder. |
| Teres minor | Arm will be abducted at 50 degrees in frontal plane; elbow will be flexed at 90 degrees; and hand will be in 90 degrees pronation. | Arm will be resisting the Internal rotation of the shoulder. |

Several alternative postures were found and tested using the HUMAC system and EMG data collection. The resulting data was analyzed to determine which MVC posture and action created the highest level of muscle activity in each muscle. The resulting postures can be seen in table 2 below and these were the postures used in the experiment. Photos of these postures as positioned in the HUMAC can be seen in figures 1 through 3 below. To protect subject confidentiality, these images were taken during pilot testing and not during the actual data collection.

| Table 2 Muscle name, posture and action of rotator cuff muscles as studied in this research project | | |
|--|---|---|
| Muscle | MVC posture | MVC action |
| Supraspinatus | The shoulder abducted in the scapula plane to 90° with elbow rotated internally to 45 degree. | Arm abduction with resistant force applied at wrist. |
| Infraspinatus | The shoulder flexed in frontal plane to 125 degree. | The participant will resist a force applied above the elbow toward the inferior angle of the scapula. |
| Teres minor | The shoulder 45° abducted and elbow 90° flexed. | The participant will internally rotate their arm with a resistive force applied at the wrist. |



Fig. 1 Supraspinatus MVC posture

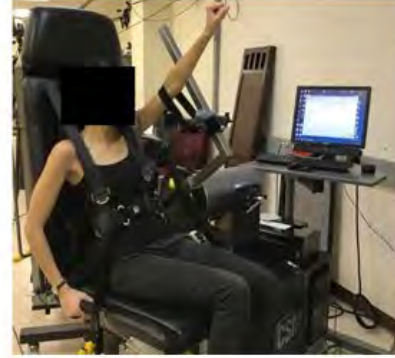


Fig. 2 Infraspinatus MVC posture



Fig. 3 Teres minor MVC posture

Sensor Location

Based on the technology available in the laboratory, the researcher decided that surface electromyography would be used for data collection. Since surface EMG does not penetrate the skin, deep muscles cannot be studied with these sensors. There are only three rotator cuff muscles which are located near the surface of the skin. These muscles are the teres minor, supraspinatus, and infraspinatus. Methods for locating these muscles were researched and practiced by all members of the project team. Because the MVC postures used in this study are also the MVC postures for the deltoid muscle, sensors were also attached to the anterior, medial, and posterior deltoid. One reference sensor was placed on the forehead, due to the low amount of muscle fibers present in this region. The sensor locations can be seen in figures 4 through 6. To protect subject confidentiality, these images were taken during pilot testing and not during the actual data collection.



Fig. 4 Front sensor view



Fig. 5 Side view of sensor locations



Fig. 6 Rear sensor view

Data file creation

An excel workbook containing several spreadsheets was created to record and organize experimental information from each data collection trial. To ensure that fatigue from previous trials would not bias the overall results, the three rotator cuff muscles to be tested for each subject were set in a random order. This was done by listing each patient and the three muscles to be tested. Next, a column of random numbers was generated in Excel next to each muscle set. The muscles were then sorted from largest to smallest using the randomly generated numbers in the spreadsheet shown in figure 7 below. Since the randomly generated numbers changed every time the document was modified, the number columns were deleted after sorting.

| | A | B | C | D | E | F | G | H | I | J | K | L | M | N | O | P | Q | R | S | |
|----|-----------------|---------------|----------|---------------|----------|---------------|----------|---------------|----------|---------------|----------|---------------|----------|---------------|----------|---------------|----------|---------------|----------|-------|
| 13 | Muscles: | Subject 1 | | Subject 2 | | Subject 3 | | Subject 4 | | Subject 5 | | Subject 6 | | Subject 7 | | Subject 8 | | Subject 9 | Subje | |
| 14 | Infraspinatus | Teres Major | 0.586026 | Infraspinatus | 0.190588 | Supraspinatus | 0.225589 | Teres Major | 0.810812 | Teres Major | 0.20349 | Teres Major | 0.126544 | Supraspinatus | 0.388597 | Teres Major | 0.157659 | Teres Major | 0.633835 | Supra |
| 15 | Supraspinatus | Infraspinatus | 0.646129 | Supraspinatus | 0.314889 | Infraspinatus | 0.996164 | Supraspinatus | 0.597445 | Infraspinatus | 0.380136 | Supraspinatus | 0.728211 | Infraspinatus | 0.714224 | Supraspinatus | 0.415964 | Infraspinatus | 0.138579 | Teres |
| 16 | Teres Major | Supraspinatus | 0.728134 | Teres Major | 0.368031 | Teres Major | 0.612941 | Infraspinatus | 0.669048 | Supraspinatus | 0.641676 | Infraspinatus | 0.20902 | Teres Major | 0.40419 | Infraspinatus | 0.102918 | Supraspinatus | 0.57016 | Infra |
| 17 | | | | | | | | | | | | | | | | | | | | |
| 18 | | | | | | | | | | | | | | | | | | | | |

Fig. 7 Randomization of muscle order for each subject

A separate spreadsheet, shown in figure 8 below, was created to determine the order of the subject muscle percentages. These were also randomized to minimize the influence of fatigue in the data. Since changing the position of the HUMAC system is quite time-consuming, the percentages were only changed within each muscle, meaning all four percentages were completed consecutively for the same muscle. The percentages were sorted using the column heading PiMj where i=subject number (1-10) and j=muscle number (1, 2, or 3).

| 1 | Percentages: | P1M1 | P1M2 | P1M3 | P2M1 | P2M2 | P2M3 | P3M1 | P3M2 | P3M3 | P4M1 | P4M2 | | | | | | | | | | | |
|---|--------------|------|----------|------|----------|------|----------|------|----------|------|----------|------|----------|----|----------|----|----------|----|----------|----|----------|----|----------|
| 2 | 15 | 45 | 0.252848 | 60 | 0.907492 | 30 | 0.609967 | 60 | 0.363943 | 60 | 0.809627 | 15 | 0.84492 | 15 | 0.446388 | 60 | 0.11059 | 45 | 0.779774 | 60 | 0.287761 | 60 | 0.723533 |
| 3 | 30 | 60 | 0.091897 | 45 | 0.315279 | 60 | 0.669234 | 15 | 0.053448 | 30 | 0.517234 | 60 | 0.608186 | 45 | 0.680974 | 30 | 0.477199 | 15 | 0.11196 | 30 | 0.342036 | 45 | 0.652406 |
| 4 | 45 | 30 | 0.509537 | 30 | 0.562946 | 45 | 0.461405 | 30 | 0.516979 | 15 | 0.29152 | 30 | 0.285357 | 30 | 0.110765 | 45 | 0.936742 | 30 | 0.776811 | 15 | 0.646217 | 15 | 0.425654 |
| 5 | 60 | 15 | 0.1632 | 15 | 0.561859 | 15 | 0.678124 | 45 | 0.691714 | 45 | 0.117093 | 45 | 0.043646 | 60 | 0.051843 | 15 | 0.112463 | 60 | 0.977422 | 45 | 0.682362 | 30 | 0.29556 |

Fig. 8 Randomization of muscle percentage for each subject

A master spreadsheet titled “Subject Trial Details” which combined the results from the randomizer for the muscle order and the muscle percentages was created. This spreadsheet also included columns to record the patient’s target MVC percentage value (the value the subject is instructed to hold using the biofeedback display), Borg C-10 (pain/ discomfort) rating for that trial, and any additional comments. At higher MVC percentages most subjects were unable to maintain the required torque level for the entire 60 seconds. For this reason, the comments section was often used to record the duration of the subject’s trial.

| | | Target/ MVC | C10 | Comments | | Target/ MVC | C10 | Comments |
|----|---------------|-------------|-----|----------|---------------|-------------|-----|------------------------|
| 1 | S1 | | | | S6 | | | |
| 2 | Teres Major | 23.3 | | | Teres Major | 24 | | |
| 3 | 15 | 3.495 | 3 | 60 | 45 | 10.8 | 3 | 16 |
| 4 | 45 | 10.485 | 4 | 60 | 60 | 14.4 | 3 | 20 |
| 5 | 30 | 6.99 | 6 | 60 | 30 | 7.2 | 4 | 29 |
| 6 | 60 | 13.98 | 8 | 30 | 15 | 3.6 | 5 | 43 |
| 7 | Supraspinatus | 11 | | | Infraspinatus | 32.33333 | | |
| 8 | 45 | 4.95 | 7 | 16 | 60 | 19.399998 | 7 | 60 |
| 9 | 60 | 6.6 | 7 | 12 | 45 | 14.5499985 | 4 | 60 |
| 10 | 30 | 3.3 | 6 | 23 | 30 | 9.699999 | 7 | 60 |
| 11 | 15 | 1.65 | 8 | 30 | 15 | 4.8499995 | 4 | 60 |
| 12 | Infraspinatus | 32.3 | | | Supraspinatus | 10 | | |
| 13 | 60 | 19.38 | 7 | 11 | 30 | 3 | 10 | 22 |
| 14 | 30 | 9.69 | 6 | 17 | 60 | 6 | 7 | 11 |
| 15 | 15 | 4.845 | 4 | 33 | 45 | 4.5 | 8 | 21 |
| 16 | 45 | 14.535 | 6 | 30 | 15 | 1.5 | 8 | 30 |
| 17 | S2 | | | | S7 | | | |
| 18 | Supraspinatus | 15 | | | Infraspinatus | 39 | | |
| 19 | 30 | 4.5 | 4 | 60 | 60 | 23.4 | 9 | 45 ignore first 3 secs |
| 20 | 60 | 9 | 5 | 35 | 15 | 5.85 | 6 | 60 |
| 21 | 45 | 6.75 | 6 | 30 | 30 | 11.7 | 7 | 60 |

Fig. 9 Subject trial details spreadsheet

The final spreadsheet created for the master data file was the MVC calculator shown in figure 10 below. This was created to ensure that at least three of the subject’s MVC trial values were within 10% of one another. A simple IF statement ($=IF(ABS((B\$2-B4)/B\$2)<=0.1, 1, 0)$) was used to calculate and evaluate each of the data points. Additional rows were added to the table in the case that more MVC trials than normally mandated were required to achieve the desired 10% margin. This spreadsheet and the subject trial details were filled out by the EMG operator during the experiment.

| Trial # | Plateau value for trial | % Error w/ trial 1 | % Error w/ trial 2 | % Error w/ trial 3 | % Error w/ trial 4 | % Error w/ trial 5 | % Error w/ trial 6 | Average if 3 trials are within 10% of each other |
|---------|-------------------------|--------------------|--------------------|--------------------|--------------------|--------------------|--------------------|--|
| 1 | 10 | | | | | | | 9.5 |
| 2 | 15 | 0 | | | | | | |
| 3 | 12 | 0 | 0 | | | | | |
| 4 | 9 | 1 | 0 | 0 | | | | |
| 5 | 9.5 | 1 | 0 | 0 | 1 | | | |
| 6 | - | #VALUE! | #VALUE! | #VALUE! | #VALUE! | #VALUE! | #VALUE! | |
| 7 | - | #VALUE! | #VALUE! | #VALUE! | #VALUE! | #VALUE! | #VALUE! | |

Fig. 10 MVC calculator to ensure that all three trials averaged were within 10% accuracy

DATA COLLECTION

Equipment

Mechanical system: The researchers selected the HUMAC NORM for use as the dynamotor system because had many different adapters available for use as the moment arm, and it provided real-time torque graphs.

Electrical system: The Delsys electromyography system was selected for its reliability. When a sensor became loose or detached the Delsys system produced a beeping noise, warning the researchers. Since this was a common occurrence during data collection which could destroy the integrity of the data if unnoticed, this feature was an essential function.

Pilot Testing

To prepare for subject data collection, the team worked together to set up and test the data collection process. The purpose of this pilot testing was for the researchers to familiarize themselves with the procedure and to find any possible errors that could arise during the experiment. The EMG data collected during these trials was recorded and placed into Matlab to ensure that the Delsys was working properly. This data was not used in the official data analysis or results

Procedure

Subjects were recruited for this experiment by word of mouth. Before establishing a data collection time, all potential subjects were informed of the risks and basic procedure of the experiment. All subjects were required to read and sign a West Virginia Institutional Review Board consent form before beginning any data collection. Participants also completed a questionnaire stating that there was no history of musculoskeletal or serious health concerns (such as heart disease or seizures). Subjects were not given any direct benefits for participating in this study, and were allowed to leave at any point of the data collection process.

First, the demographic information (height, weight, and age) of each participant was collected. The researcher explained the basic procedure of the experiment to the subject and then located the muscles on the subject's back and right arm. Sensors were attached to the participant's skin using stickers and were then plugged into the input model. Next, the input model was connected to the main amplifier. The participant was told to hold the MVC postures listed in table 2 while one of the researchers watched the EMG data. If the EMG readings were excessively low, the sensors, power supply, and amplifier would be checked one at a time.

Next, the subjects were seated in the HUMAC NORM and secured to the chair to ensure that no external movements could affect the results. The length of the HUMAC adapter was measured and recorded in the subject portfolio. The participants were given a minimum of 3 MVC trials for each position. Each trial had a duration of 7 seconds and a rest period of 2 minutes afterwards. Participants were informed not to reach their maximum torque value too rapidly as this could lead to muscle strain. The subject's maximum voluntary contraction was found by identifying the highest value held for approximately 3 seconds in the trial. This value can also be called the plateau. The MVC trials were repeated and the values stored in the MVC calculator spreadsheet until 3 trials were within 10% of each other. The MVC plateau for these three trials was averaged and input into the subject trial details spreadsheet. Four percentages (15%, 30%, 45%, and 60%)

of the MVC were calculated and assigned to the subject in a random order as determined in figure 8.

Participants were asked to hold a specified MVC percentage value for a maximum of 60 seconds. Progress could be observed by watching the real-time torque level graph given on the HUMAC monitor. A researcher was stationed next to the monitor to warn the EMG collector to cease data collection if the subject's torque value exceeded or dropped below the specified value. This often occurred due to fatigue at higher MVC percentages. The duration of the trial was recorded in the subject trial details spreadsheet. Participants were also asked to rate the discomfort experienced at the final moment of the trial on the Borgs C-10 scale where 0 represents no noticeable fatigue and 10 represents maximum fatigue. After each percentage trial the subject was given a two minute rest period. During this time removal of the arm from the HUMAC adapter was allowed. If additional time was necessary to recover, it could be requested by the subject.

Each subject completed at least three MVC trials and four percentages for each of the three MVC postures. This totals to twelve 60 second long percentage trials and a minimum of nine 7 second long MVC trials. The order of each posture was randomized for each subject as shown in figure 7 above. Once all trials had been completed, the researcher checked to ensure that all EMG files had been recorded. At this time the participant was detached from the HUMAC and allowed to remove the sensors.

Subjects

Since this experiment involved human subjects, a CITI training course was completed by all researchers who would be in contact with the participants. This course discussed the protections of human subjects and the ethical guidelines of research. A proposal and consent form were also sent to the Internal Research Board for approval. This was completed to ensure that all testing and procedures completed in this experiment were ethical and involved only minimal risk for the subjects.

The original research proposal suggested that ten subjects be selected for this data collection. This included five male and five female subjects. After pilot testing, it was discovered that male subjects and female subjects showed high variation in trial duration. This meant that male data and female data should not be mixed until after further testing. It was concluded that five subjects would be too small of a sample to make any conclusive predictions. During pilot testing, male subjects were able to hold the MVC postures for longer durations. Male subjects generally also possessed a lower body fat percentage. This led to less interference during the surface EMG data collection. For these reasons, female subjects were eliminated from this experiment and only male subjects were recruited.

Ten, right hand dominant males between the ages of 18 and 40 with no prior history of musculoskeletal diseases or other serious health concerns were selected for this experiment. To minimize sensor interference, all subjects selected had a BMI less than 30 (obese). The average and standard deviation of the subject demographics can be seen in table 3 below.

Table 3 Subject demographics

| | Age (yrs) | Height (in) | Weight (lbs) | BMI (lbs/in ²) |
|--------------------|-----------|-------------|--------------|----------------------------|
| Average | 24.2 | 70 | 172.7 | 24.79 |
| Standard Deviation | 5.1 | 2.1 | 17.2 | 2.63 |

DATA

ANALYSIS

The raw electromyography data for all percentage exertions was saved in c3d format and full-wave rectified. “This EMG data was then transformed to frequency domain using fast Fourier transformation to estimate median frequency. The one minute exertion was divided to 10 divisions and then median frequency was calculated for each division.” When the data exhibits a decrease in median frequency, it is considered to be a sign of muscle fatigue [Chowdhury and Nimbarte, 2015].

RESULTS

Analysis of the data showed that when compared solely on duration, all three muscles behave similarly to force increments. According to figure 11 below, as the percentage MVC (or force exerted) increases, the duration of the trial decreases. Only at 15% infraspinatus were all 10 subjects able to hold the given torque level for a full minute. The slope of the regression lines does vary between each of the muscles. Teres minor shows the least change in duration with a slope of -5.5 whereas infraspinatus shows the largest change with a slope of -9.2.

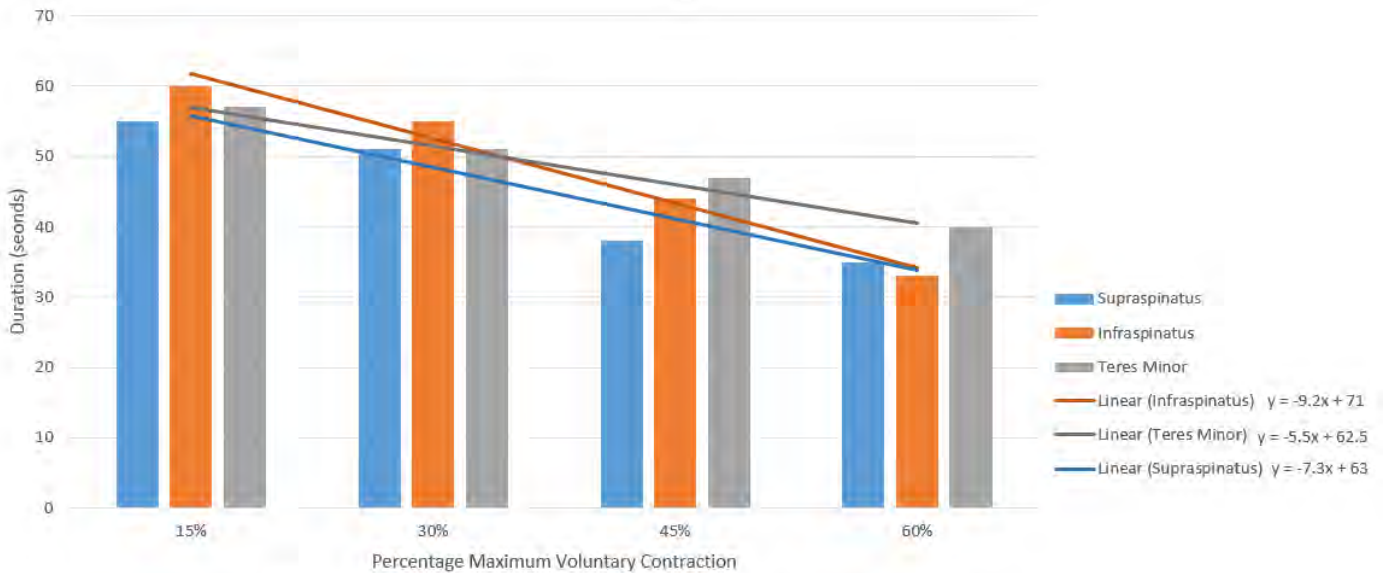


Figure 11 Average duration by muscle and percentage MVC with regression analysis

The slope of the median frequencies was also examined. For most trials, as the percentage MVC increases the median frequency slope decreases. In all three muscles the largest percentage decrease was between 15% and 30% MVC as shown in table 4 below. In the teres minor and supraspinatus the slope became slightly less negative between 45% and 60%. This

may be due to the shorter trial durations. As the percentage MVC increases the subject must hold a higher torque value. Many times the subjects had difficulty finding and maintaining the heavy torque level over an extended time period. This could have led to variation in the independent variable, the MVC percentage. As soon as any variation was noticed the HUMAC operator instructed for the trial to be terminated; however, this also provided less time for muscle fatigue to develop.

Table 4 Percentage change in median frequency slope between consecutive MVC percentages

| Supraspinatus | | | Infraspinatus | | | Teres Minor | | |
|---------------|---------|---------|---------------|---------|---------|-------------|---------|---------|
| 15%-30% | 30%-45% | 45%-60% | 15%-30% | 30%-45% | 45%-60% | 15%-30% | 30%-45% | 45%-60% |
| -0.235 | -0.198 | 0.044 | -0.170 | -0.121 | -0.069 | -1.090 | -0.092 | 0.067 |

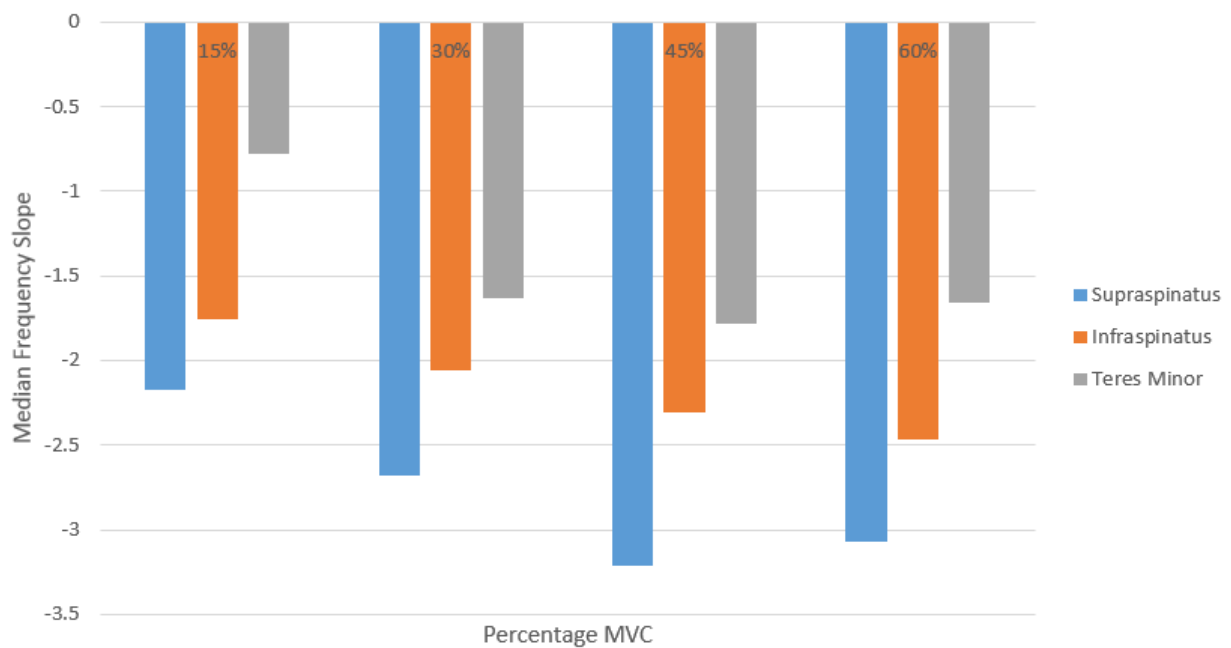


Figure 12 Median frequency slope by muscle and percentage MVC

CONCLUSION

Based on the data collected, the greatest change in median frequency slope occurs between 15% and 30% MVC. This leads to the conclusion that a safe loading limit for the rotator cuff muscles would be near 30% of the subject's maximum for male subjects. This percentage could be recommended as a safety factor in workplace settings. The results of this research can be added to the current body of work concerning the rotator cuff muscles and fatigue development in human subjects. [Teyhen, 2008] When combining this research with other related studies in the future, it will possible to establish definite loading limits for the rotator cuff muscles. These limits can be used to improve both astronaut and worker health and safety in industry and minimize the risks of rotator cuff injuries.

An area for future study would be a repetition of this experiment in female subjects. Since the

sample size of this experiment was 10 subjects, the female study should also consist of 10 subjects between the ages of 18-40. The participants should also be free of musculoskeletal diseases or other serious health conditions. If completed successfully, the results from both studies could be compared to determine if males and females exhibit fatigue at various loading levels in the same way.

ACKNOWLEDGEMENTS

The research discussed in this paper was funded by an undergraduate fellowship awarded by the West Virginia Space Grant Consortium. Dr. Ashish Nimbarte served as my research mentor for the duration of this project and helped to lead the project team. Without his patience and guidance this project would not have been possible.

PRESENTATIONS

The results of this research were compiled into a technical paper and presented at the Institute of Industrial and Systems Engineers mid-Atlantic regional conference in Knoxville, TN. The presentation consisted of a 15 minute PowerPoint and 15 minutes of questions from the judges. Esther Raub received first place for her paper and presentation and was awarded a \$500 prize.

REFERENCES

1. Atsushi, Yamamoto. "Prevalence and Risk Factors of a Rotator Cuff Tear in the General Population." *Journal of Shoulder and Elbow Surgery* 19.1 (2010): 116-20. Print.
2. BLS (2014). Nonfatal occupational injuries and illnesses requiring days away from work, 2013 [online]. Bureau of Labor Statistic. Available from <http://www.bls.gov/news.release/pdf/osh2.pdf> [Accessed 09 Jan 2017]
3. Bureau of Labor Statistics (BLS), (2015). Nonfatal occupational injuries and illnesses requiring days away from work, Retrieved from: <http://www.bls.gov/news.release/pdf/osh2.pdf> [Accessed 09 Jan 2017]
4. Chowdhury, S., & Nimbarte, A. (2015). Comparison of fourier and wavelet analysis for fatigue assessment during repetitive dynamic exertion. *Journal of Electromyography and Kinesiology*, 25(2), 205-213. doi:10.1016/j.jelekin.2014.11.005
5. Croft, P., Pope, D., & Silman, A. (1996). The clinical course of shoulder pain: Prospective cohort study in primary care. *BMJ: British Medical Journal*, 313(7057), 601-602.
6. Deydre S. Teyhen, Joseph M. Miller, Tansy R. Middag, and Edward J. Kane (2008) Rotator Cuff Fatigue and Glenohumeral Kinematics in Participants Without Shoulder Dysfunction. *Journal of Athletic Training*: Jul/Aug 2008, Vol. 43, No. 4, pp. 352-358.
7. Scully, D., Ph.D. (2008) Full Wave Rectifier. [online] Tufts University. Available from <http://www.eecs.tufts.edu/~dsculley/tutorial/diodes/diodes3.html> [Accessed 19 Jan 2017]
8. Templehof, Siegbert. "Age-related Prevalence of Rotator Cuff Tears in Asymptomatic Shoulders." *Journal of Elbow and Shoulder Surgery* 8.4 (1999): 296-99. Web.
9. Warnken, LLC. (2017). "Value of Shoulder Cases." *Maryland Workers Compensation Value of Shoulder Cases Comments*. MDCompLaw.com, n.d. Web. 19 Jan. 2017.
10. Williams, David R., and Brian J. Johnson. "EMU Shoulder Injury Tiger Team Report." *NASA/TM 212.058* (2003): 1-104. *Nasa.gov*. NASA. Web. 18 Apr. 2017.

HOW MANY NEUTRON STAR BLACK HOLE BINARIES ARE IN THE MILKY WAY?

Emily Stiner

Physics

West Virginia University

Morgantown, WV

ABSTRACT

Among the many milestones eagerly awaited in pulsar astronomy is the discovery of a pulsar in orbit around a stellar-mass black hole. The purpose of this experiment was to analyze how many neutron star black hole binaries potentially exist in the Milky Way. Using software packages that simulate pulsar populations, we used pulsar and black hole orbital parameters given via collaborators, and compiled the resulting time of arrival pulses as a function of time for a year's worth of data. Then, by fitting and isolating the black hole orbital parameters to the simulation, we looked at the observational signatures that black hole binaries might have in pulsar timing data. When the black hole was fit to the data, the simulation produced white-noise timing residuals centered around zero, which is to be expected. However, when the black hole parameters were excluded in fits to the data, the residuals resembled the red noise signals frequently characterized as timing noise. Thus, we offer the bold suggestion that some of the observed pulsar timing noise may be a result of a black hole signature.

INTRODUCTION

There are currently about 2500 known pulsars [1], and we expect there are more to be discovered. Pulsars are highly magnetized neutron stars, often with rotations on the order of milliseconds. Of the known pulsar population, at least a dozen has been recognized as a double neutron star binary system. With LIGO's discovery of gravitational waves from a black hole binary [2] unambiguously proving the existence of black holes, the obvious conclusion must be raised: there are intermediate systems in nature that form a binary system of a neutron star and black hole. This system would derive from a pulsar binary, with the primary pulsar more massive than the secondary pulsar. As the primary pulsar goes supernova, it results in a black hole. Due to the smaller mass of the secondary pulsar, its supernova results in a neutron star. Thus, the system that remains is the binary system we are attempting to quantify. Of the 2500 currently known radio pulsars, our task was to quantify how many would have an observable black hole companion.

PROJECT

Modeling

The first stage of the experiment was to implement existing models of black hole neutron star binaries from collaborators to predict a sample of the targeted binary system and their orbital parameters. This was done by utilizing the StarTrack Population Synthesis code, which is designed with special emphasis on compact object modeling, especially for black holes and neutron stars [3]. Then, we used PsrPopPy, a Python-based program that simulates pulsar populations and distributions [4], to generate a fake catalog of pulsars. Ten pulsars were randomly selected, and paired with a corresponding black hole, also randomly selected. The important parameters required

for the timing calculations are given below: the spin period P of the pulsar in milliseconds, its corresponding unitless spin-derivative, the dispersion measure DM, and S1400, its flux density measured at 1400 MHz. The masses of both the neutron star NS and black hole BH are listed in terms of their solar masses, with their eccentricity e of their orbit, semi-major axis parameter a given in AU, and their orbital period given in years.

| P ms | \dot{P} | DM $\text{cm}^{-3} \text{ pc}$ | S mJy | M_{BH} M_{\odot} | M_{NS} | a AU | e | P_{orb} yr |
|-----------|-----------|-----------------------------------|------------|--------------------------------|-----------------|-----------|------|------------------------|
| 834.6 | 10.3 | 196.0 | 1.04 | 7.5 | 1.3 | 330 | 0.36 | 2000 |
| 616.3 | 1.2 | 591.0 | 0.54 | 8.2 | 1.1 | 0.5 | 0.68 | 0.12 |
| 382.0 | 3.1 | 328.6 | 0.79 | 7.5 | 1.3 | 160 | 0.35 | 700 |
| 338.3 | 1.1 | 550.1 | 0.79 | 7.8 | 1.3 | 1200 | 0.59 | 14000 |
| 478.6 | 1.1 | 183.2 | 0.15 | 7.8 | 1.3 | 590 | 0.75 | 4800 |
| 782.3 | 6.9 | 174.5 | 0.12 | 7.4 | 1.3 | 150 | 0.82 | 650 |
| 226.1 | 0.2 | 340.3 | 0.31 | 7.5 | 1.3 | 330 | 0.36 | 2000 |
| 432.4 | 1.1 | 335.5 | 1.4 | 7.8 | 1.3 | 0.5 | 0.68 | 0.12 |
| 330.3 | 0.7 | 267.1 | 0.09 | 7.5 | 1.3 | 160 | 0.35 | 700 |
| 899.1 | 7.4 | 590.9 | 0.64 | 7.8 | 1.3 | 1200 | 0.59 | 14000 |

Timing

The next stage of the experiment was to create fake timing data for each pulsar. Ten pulsars were randomly picked from the catalog, and 3000 days' worth of data was generated by a pulsar timing software, Tempo2 [5]. Tempo2 is used to compare a model for a pulsar with actual observations of pulse arrival times; the difference between these are referred to as 'timing residuals' of the pulsar. Thus, Tempo2 was used to create the time of arrivals (TOAs) of our ten pulsars and corresponding black hole companion. Then, we attempted to analyze these TOAs with and without the knowledge of black hole binary parameters. That is to say, we removed the black hole orbital parameters from the pre- and post-fit parameters, to simulate what the pulses would appear as sans knowledge of the black hole orbital parameters.

RESULTS

When analyzing the Tempo2 graph for the timing residuals as a function of time with the binary parameters fit, the result was as expected. The pulse residuals were primarily consistent around zero – indicative of white noise. This is to say that Tempo2 accounted for the TOA pulses and adjusted accordingly, ultimately covering the signal of the black hole.

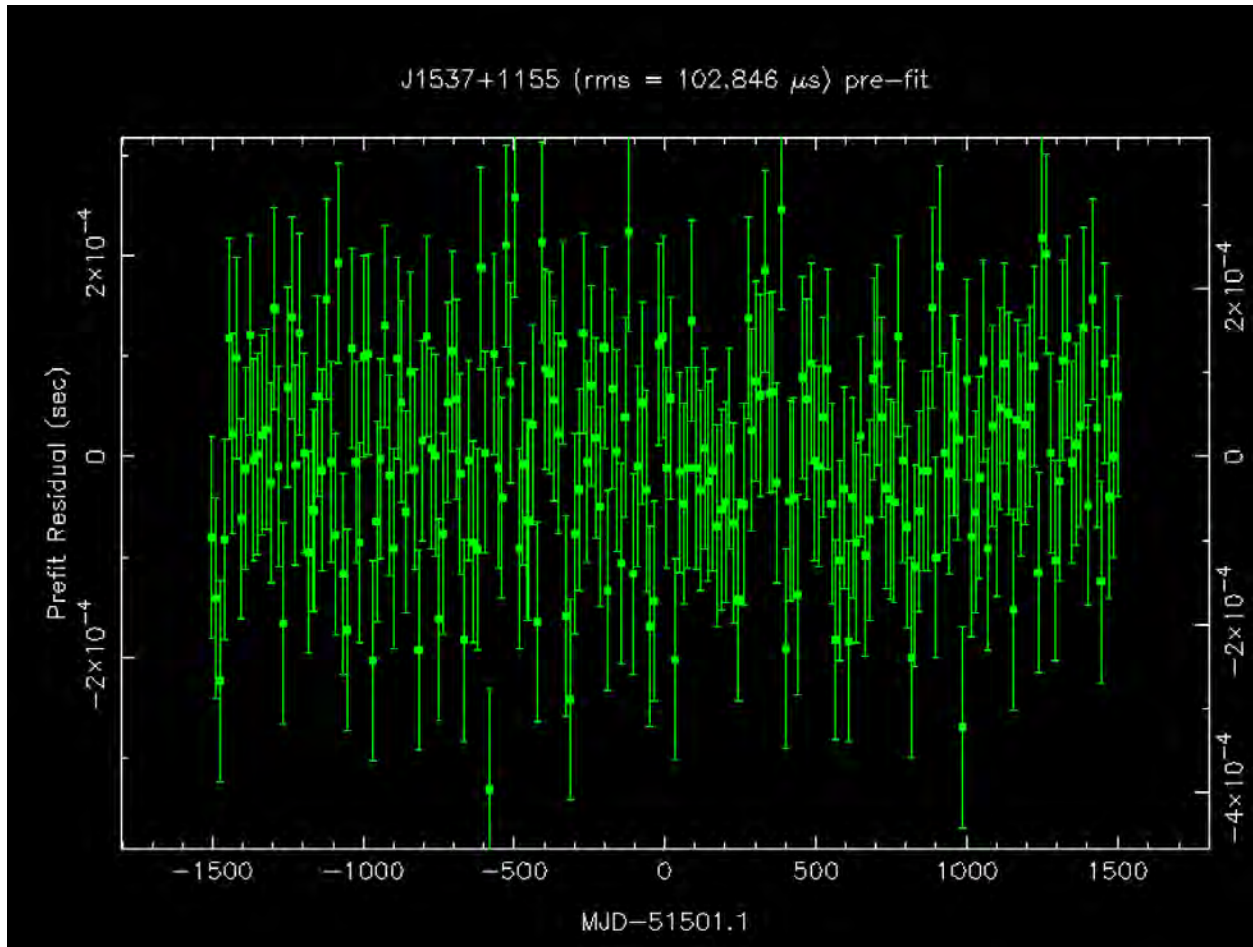


Figure 1. Pictured above is residual timings of pulsar TOAs as a function of time, with black hole binary orbital parameters fit to a model. The residuals are primarily centered around zero, which means this graph is indicative of white noise, such that the black hole signature is removed from the data.

On the other hand, when removing the black hole orbital parameters and re-fitting the data, the simulation was assuming the data was an orbit of an isolated pulsar. The corresponding graph of the TOAs as a function of time were in agreement of an isolated pulsar, that is to say, the resulting graph is characteristic of what we actually observe. Most noticeably, the graph also exhibited pulsar timing noise, which is found in some pulsars when observed over a long period of time.

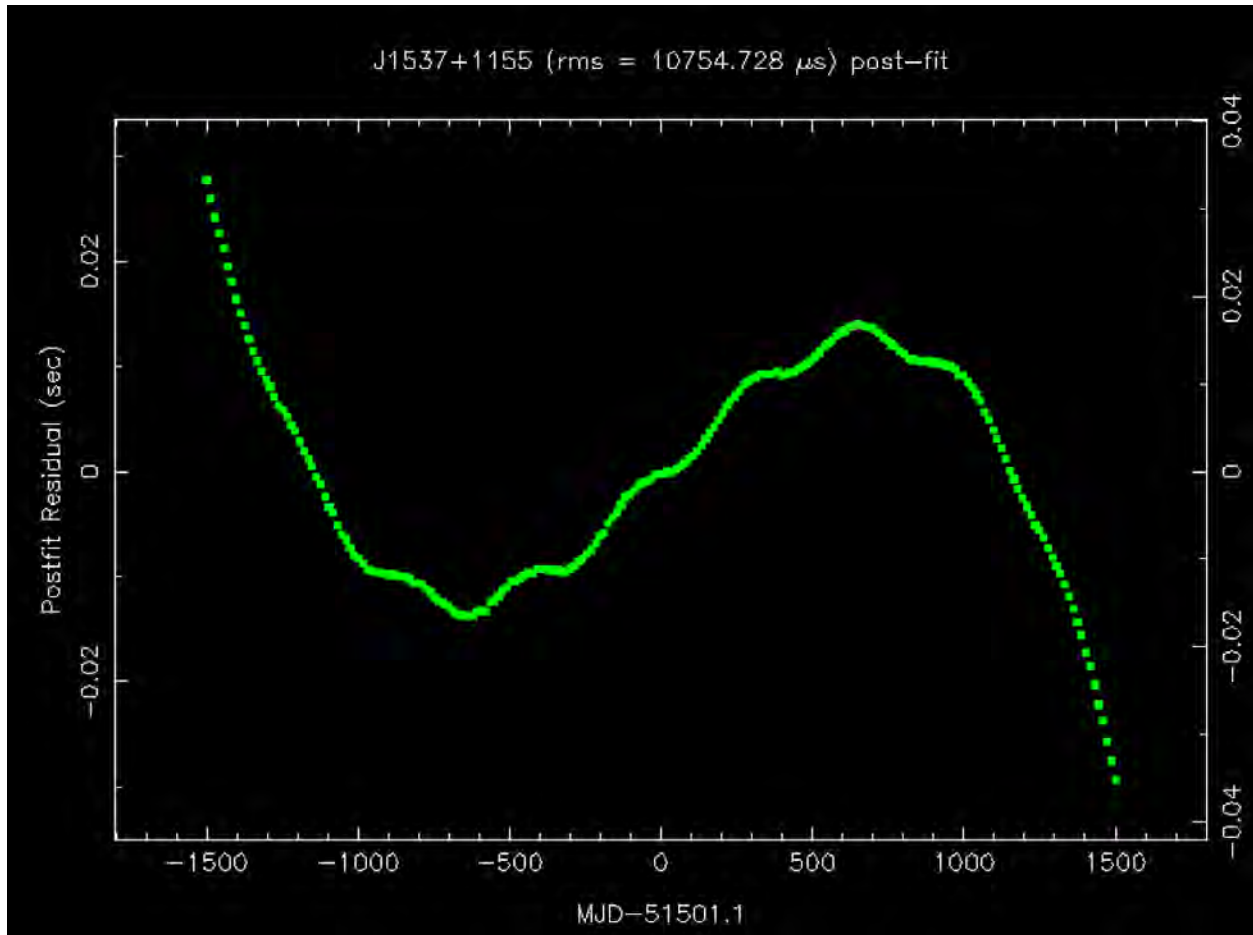


Figure 2. Pictured is the residual timings of a neutron star as a function of time, with the black hole binary orbital parameters unfit to the timing model. The trend of this graph is what we observe of a actual isolated pulsars, including the slight deviations of TOAs, referred to as timing noise.

DISCUSSION

Black hole binary parameters have an observational signature that is seen in residuals of the isolated pulsar model. Surprisingly, the resulting residuals of the unfit black hole binary parameters looked very similar to pulsar timing noise. Pulsars, and millisecond pulsars especially, are most notable for their predictable, consistent spin-down rates – with precision comparable to the best atomic clocks. However, some pulsars exhibit semi-random fluctuations in TOAs after some long period of time, also referred to as ‘timing noise’. A definite reason for timing noise has not been uncovered, but speculation has attributed the noise to perhaps the strangeness in spin. However, as a result of this experiment, another speculation arises: could some fraction of pulsar timing noise be the result of a black hole signature?

CONCLUSION

When attempting to analyze the graph of TOAs as a function of time by unfitting the black hole orbital parameters to a neutron star binary system, the resulting graph is characteristic of what is actually observed when timing an isolated pulsar. A bold suggestion that is in need of further study

is that black hole signatures may be the cause of the pulsar timing noise. This also suggests that neutron star black hole binary systems may have already been detected and been written off as isolated pulsars with this characteristic noise. Moving forward, it is essential to show what other effects these binary systems exhibit.

ACKNOWLEDGEMENTS

A special thank you is reserved for the NASA WVU Space Grant Consortium for funding this experiment and generously providing the grant. Another special thanks goes to Dr. Duncan Lorimer, whose guidance and patience as a mentor was essential and greatly appreciated.

Also, I would like to extend my gratitude to our collaborators who proved instrumental in providing the parameters for our binary systems, which was the foundation for this experiment.

REFERENCES

- [1] D. R. Lorimer, “Binary and Millisecond Pulsars”, *Living Rev. Relativity* 11, (2008), 9. 5 Mar 16.
- [2] B.P Abott et al. (LIGO Scientific Collaboration and Virgo Collaboration). 2016. Observation of Gravitational Waves from a Binary Black Hole Merger. *Phys. Rev. Lett.* 116, 061102. 5 Mar 16.
- [3] K. Belczynski, “Compact Object Modeling with the StarTrack Population Synthesis Code”. *Astrophysics* v3, (2007). 5 Mar 16.
- [4] D. R. Lorimer, S. Bates, A. Rane, J. Swiggum, “PsrPopPy: An open-source package for pulsar population simulations”. *Instrumentation and Methods for Astrophysics* v2, (2014). 5 March 16.
- [5] G. Hobbs, “Using the pulsar timing software package, TEMPO2”. arXiv:1205.6273v1. CSIRO Astronomy and Space Science, Australia Telescope National Facility. 29 May 2012.

PREPARATION AND STABILITY OF CIS-DICARBONYLBIS(DIORGANODITHIOCARBAMATO)IRON(II) COMPLEXES

Brett Szeligo
Chemistry
Wheeling Jesuit University
Wheeling, WV

ABSTRACT

Iron(II) dithiocarbamate complexes are known to be stable; however, recent ^1H NMR analysis of our sample of *cis*-dicarbonylbis(dibenzylidithiocarbamato)iron(II) revealed, in addition to the expected peaks for the iron(II) complex, a broad peak in the range of 24 ppm. This peak corresponds to the location of the CH_2 peak for the corresponding paramagnetic iron(III) complex, thus calling into question the extent of decomposition over time of the numerous other previously prepared *cis*-dicarbonylbis(diorganodithiocarbamato)iron(II) complexes. The stability of these compounds has been investigated using TGA, ^1H NMR, and magnetic susceptibility. At ambient temperature, traces of the corresponding paramagnetic tris(diorganodithiocarbamato)iron(III) complex have been found for some derivatives, indicating possible room temperature decomposition of iron(II) to iron(III) or contamination during preparation. The extent of this contamination was determined by ^1H NMR and magnetic susceptibility and found, for the most part, to be minor. Alternative methods of preparation were attempted and analysis is still in progress. These observations will be discussed, along with the implications of the validity of earlier studies.

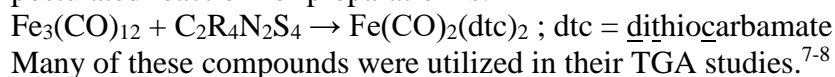
INTRODUCTION

Since their first reported preparation in 1964, the *cis*-dicarbonylbis(diorganodithiocarbamato)iron(II) complexes (Figure 1) have been the subject of continuing research.¹ These early studies reported preparation, infrared spectroscopy, ^1H NMR, Mössbauer spectra, UV photoelectron spectroscopy, and a crystal structure of derivatives with various organic substituents.²⁻⁶ The Chemistry Department at WJU has been collaborating with Dr. Aloysius Hepp at NASA Glenn Research Center for a number of years on the thermal decomposition of metal dithiocarbamate complexes to form sulfur containing minerals.^{7,8} These sulfur complexes have numerous applications including a simulated chemical lunar environment, production of electrical current, and acceleration of chemical reactions. Addition of the carbonyl ligands produces a stable iron(II) complex allowing for the study of its thermal decomposition. The postulated mode of decomposition was first a loss of carbon monoxide, followed by loss of dithiocarbamate ligands and fragments, resulting in the formation of iron sulfides.

Much of physical science research is directed at better understanding fundamental mechanisms. This basic research can later be applied to the long-term application to the sciences. An example of better understanding of fundamental mechanisms is found in the stability of the biological functional protein hemoglobin. The prosthetic group of hemoglobin, heme, is the functional part of the protein that binds oxygen and carbon dioxide. Heme is constructed from a central iron atom

and an organic molecule called protoporphyrin. Attached to protoporphyrin are various substituents. Our basic science research on iron dithiocarbamate carbon monoxide complex decomposition can later be applied to better understand the stability of the Fe-CO bond in heme. Carbon monoxide poisoning kills on average around 450 people pre year in the United States and a better understanding of the iron interaction with CO, CO₂, and O₂ could provide insight to treatment or prevention. The iron in heme preferentially bonds to CO rather than O₂ or CO₂, resulting in death.

The initial preparation of these complexes reported in the literature involved iron(II), carbon monoxide gas, and dithiocarbamate salts.¹ Duffy and his students introduced an easier, safer preparation which did not involve toxic carbon monoxide gas, but, instead, utilized triiron dodecacarbonyl (Fe₃(CO)₁₂) and the corresponding thiuram disulfide (C₂R₄N₂S₄), yielding compounds with the appropriate elemental analyses, infrared light analysis, and NMR.⁴ The postulated reaction for preparation is:



In 2014, Roffey published her Ph.D. thesis, carried out under the direction of Dr. Graeme Hogarth, University College (London), in which she reported that the preparative method involving triiron dodecacarbonyl (Fe₃(CO)₁₂) resulted in paramagnetic impurities, which were very difficult to separate from the resulting iron(II) dicarbonyl complexes.⁹ This led us to re-examine these previously prepared complexes.

Currently, various *cis*-dicarbonylbis(diorganodithiocarbamato)iron(II) complexes have been re-examined and their stability investigated using TGA, ¹H NMR, and magnetic susceptibility. At ambient temperature, traces of the corresponding paramagnetic tris(diorganodithiocarbamato)iron(III) complex have been found for some derivatives, indicating possible room temperature decomposition of diamagnetic iron(II) to paramagnetic iron(III) or contamination during preparation. Parallel TGA studies have indicated a variety of paths for thermal decomposition, simultaneous loss of both carbon monoxide or step-wise loss of carbon monoxide at two distinct temperatures, leading to intermediates of varying thermal and kinetic stability.⁸

RESULTS AND DISCUSSION

1. Nuclear Magnetic Resonance

Examination of the Nuclear Magnetic Resonance spectra, an analytical procedure which involves placing a solution of a sample in a strong magnetic field and then observing its response to electromagnetic radiation of varying frequencies, our sample of *cis*-dicarbonylbis(dibenzylthiocarbamato)iron(II) revealed, in addition to the expected peaks for the iron(II) complex, a broad peak in the range of 24 ppm (Figure 1.1). This peak corresponds to the location of the CH₂ peak for the corresponding paramagnetic iron (III) complex.¹⁰

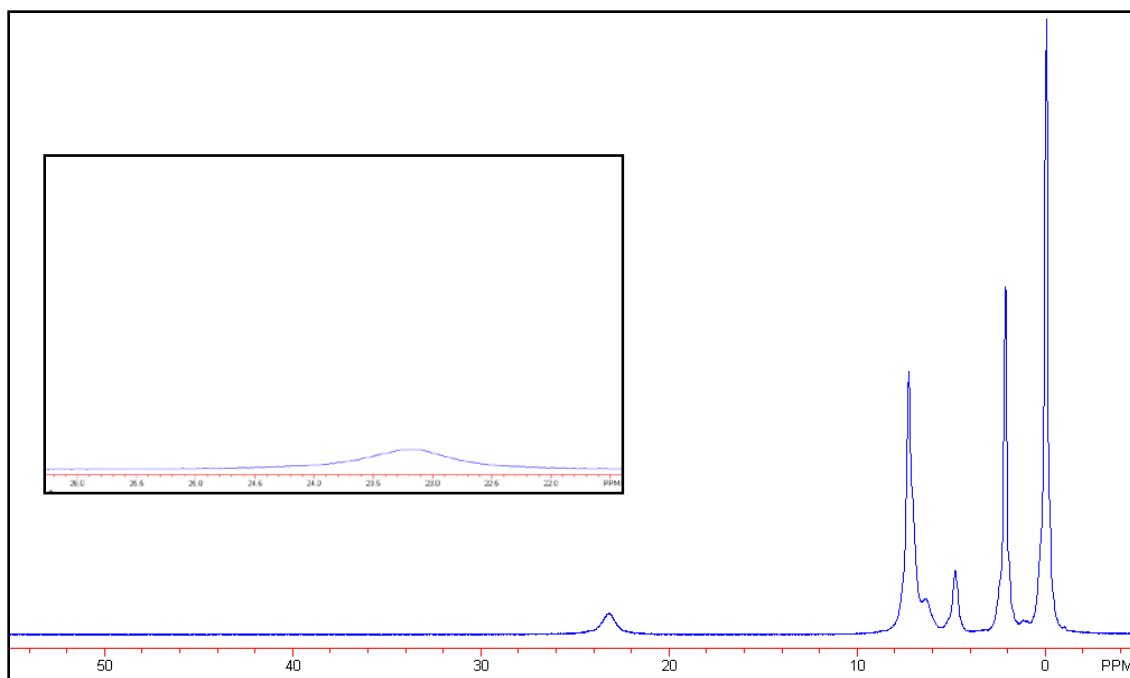


Figure 1.1: ^1H NMR spectra of *cis*-dicarbonylbis(dibenzylthiocarbamato)iron(II) inset shows peak at 24 ppm.

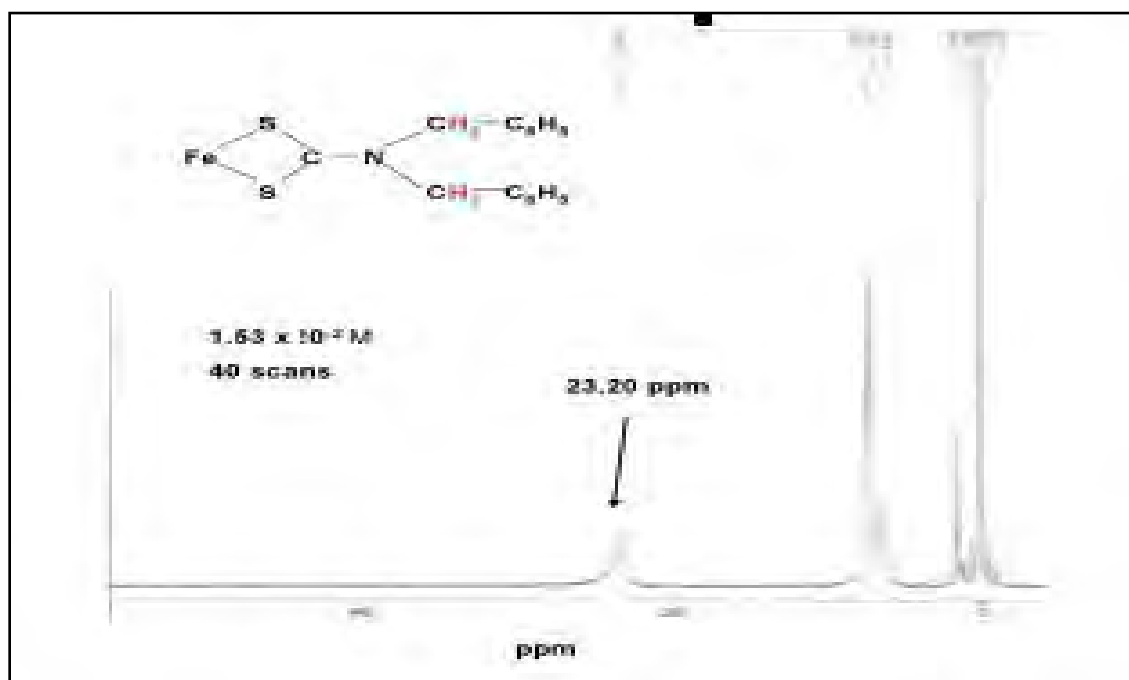


Figure 1.2: Proton NMR of tris-(dibenzylthiocarbamato)iron(III).

This calls into question the extent of decomposition over time of the numerous other *cis*-dicarbonyl-bis(diorganodithiocarbamato)iron(II) which have been used for TGA studies.

Previous work by other student researchers has investigated the exchange of ligands between different tris(diorganodithiocarbamato)iron(III) complexes (Figure 1.2).¹⁰ Because the iron(III) in

the complexes is paramagnetic, it shifts the NMR signal for the closest protons to the iron(III). This shift is influenced by the nature of the other ligands, allowing the use of the NMR to determine the extent of the iron(III) impurity. The appearance of iron(III) signals in the NMR spectra of some previously prepared samples of the iron(II) dicarbonyl complexes has raised concern about the long-term thermal stability of these samples. While the iron(II) is diamagnetic and does not interact with the protons on the ligand, we should be able to examine the broadened proton signals from the paramagnetic iron(III) impurity to determine the extent of contamination or decomposition of the iron(II) complex.

Parallel studies ^1H NMR of tris(diorganodithiocarbamato)iron(III) complexes gave insight into the bonding of these spin-crossover complexes and their distinctive ^1H NMR spectra. Several iron(II) dithiocarbamates (methylphenyl, piperidyl, ethylphenyl, dimethyl and diphenyl derivatives) have been examined by ^1H NMR and analyzed for the extent of possible decomposition (Table 1). Each of these spectra were taken recently and are of samples prepared more than four decades ago and stored under ambient conditions.

| Compound, R organic substituent | ^1H NMR of Decom. Product (ppm) | ^1H NMR of tris Product (ppm) |
|---------------------------------|--|--|
| Dimethyl | 50.1 | 49.6 |
| 2,6 Dimethylpiperidyl | 9.4 | - |
| Ethyl Benzyl | 28.3, 32.9 | - |
| Diphenyl | No α hydrogen | - |
| Ethyl Phenyl | 25.5 | - |
| Morpholine | 31.3 | 30.8 |
| Methyl Phenyl | 32.6 | - |
| Piperidyl | 31.1 | 29.0 |
| Dibenzyl | 24.0 | 23.0 |

Table 1: Proton NMR chemical shifts of the impurity signals from the *cis*-dicarbonylbis(diorganodithiocarbamato)iron(II) samples and the corresponding signals from previously prepared tris-(diorganodithiocarbamato)iron(III)

2. Magnetic Susceptibility

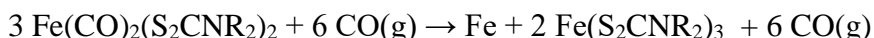
The next step of the experimental work was determining the magnetic attraction of each and the apparent magnetic moment of the various compounds. Diamagnetic compounds have no unpaired electrons, and are slightly repelled when introduced to a magnetic field. Paramagnetic compounds have one or more unpaired electrons, and are attracted to a magnetic field. Iron(III) dithiocarbamate compounds are paramagnetic and iron(II) dithiocarbamate compounds are diamagnetic, by determining the magnetic susceptibility, their repulsion or attraction to a magnetic field, we can calculate the extent of contamination with magnetically attracted iron(III) by comparing how the magnitude of the attraction of the sample to the magnetic field.¹¹ This allowed us to determine the extent of the decomposition products or contamination on preparation over the past four decades (Table 2).

| Compound, R | Apparent Magnetic Moment, μ_B | Magnetic Moment of tris, μ_B | Spectral Evidence of Decomposition |
|-----------------------|-----------------------------------|----------------------------------|------------------------------------|
| Dimethyl | 0.83 | 4.17 | Measureable |
| 2,6 Dimethylpiperidyl | 0.96 | 2.46 | Measureable |
| Ethyl Benzyl | 0.96 | 4.50 | Two Trace Peaks |
| Diphenyl | 1.55 | 2.52 | No α Hydrogen |
| Ethyl Phenyl | 2.05 | 4.70 | Substantial |
| Morpholine | 2.11 | 5.21 | Substantial |
| Methyl Phenyl | 2.65 | 2.99 | Substantial |
| Piperidyl | - | 4.01 | Trace |

Table 2: Apparent magnetic moment of samples of diamagnetic $\text{Fe}(\text{CO})_2(\text{S}_2\text{CNR},\text{R}')_2$ contaminated with paramagnetic $\text{Fe}(\text{S}_2\text{CNR},\text{R}')_3$

Iron(II) complexes are diamagnetic compounds, meaning that all electrons are paired and their opposing spins cancel, making the compounds be repelled by the magnet. However, Iron(III) complexes possess unpaired electrons, which makes these compounds attracted to the magnet. Since the dicarbonyl compounds contain iron(II), it can be expected that if the compounds are pure, (i.e. no contamination by iron(III)), then there should be a minimal magnetic moment. Thus, the magnitude of the magnetic moment will allow us to determine how much of the sample is contaminated with iron(III). As reported in Table 3, the piperidyl and ethylbenzyl derivative showed trace contamination, the dimethyl and 2,6 dimethylpiperidyl derivative showed measurable contamination, and the ethylphenyl, morpholine, and methylphenyl derivative showed substantial contamination. The extent of contamination of diphenyl could not be determined since there is no hydrogen attached to the adjacent carbon atom.

The greater the apparent magnetic moment of the sample, the more significant the decomposition. One cannot assume however that the upper limit of the observed magnetic moment of the contaminated sample is the magnetic moment which corresponds to the tris complex since one of the proposed decomposition is metallic iron:



These results do indicate that either some decomposition has taken place over time or that the sample of the dicarbonyl was initially contaminated by the tris complex.

3. High-Speed Ball Mill

Recently, an alternative preparation synthesis method has been explored. Dithiocarbamate synthesis without the use of solvent is being investigated by utilizing mechanochemistry and the same reactants used in earlier preparations, $\text{Fe}_3(\text{CO})_{12}$ and the corresponding thiuram disulfide. As reported by Roffey, the current preparation utilizing a solvent has led to a contamination with the tris-dithiocarbamate complex. In this experiment, the reactants are placed in a 3-4 cm^3 stainless steel vial with stainless steel pellets. The vial is shaken at a high frequency, and the impact of the pellets with the reactant provides the energy necessary to initiate the reaction.

It was hypothesized that the following reaction would take place stepwise and that samples taken

at various times during the preparation would reveal first the dicarbonyl and then the tris decomposition product. The progress of the desired reaction would be monitored by recording IR spectra at 16 hour intervals and comparing the infrared spectra to the reported spectra for the corresponding dicarbonyl.¹ The reaction has been performed and spectral analysis suggests failure to form the dicarbonyl.

CONCLUSION

Evidence from two experimental methods not previously utilized yielded, ¹H NMR, and magnetic susceptibility, confirmed reports of varying amounts of contamination. Our sample of iron(II) dithiocarbamates are in fact contaminated with iron(III), since Fe(S₂CNRR')₃ was found in most samples. Previously utilized experimental methods, elemental analysis, infrared light analysis, ¹³C and ¹⁵N NMR, UV photoelectron spectroscopy, and TGA, did not reveal the presence of these impurities. The following reaction is the postulated reaction for contamination:



It should be noted that the contamination was minor, this does not call into serious question results reported previously. It is not clear whether the samples were contaminated with iron(III) through synthesis or during slight decomposition over the past four decades. The minor contamination detected does confirm the postulation that dithiocarbamate complexes are especially stable in ambient environments.

One of the future steps of this research project is to attempt alternative methods of preparation that would limit the amount of iron(III) contamination. Another possible preparation would use Fe₂(CO)₉ or Fe₃(CO)₁₂ with less of the oxidizing agent, thiuram disulfide, under a nitrogen atmosphere.

ACKNOWLEDGEMENTS

I would like to take this opportunity to thank the faculty of the Chemistry Department at Wheeling Jesuit University, especially Norman V. Duffy Ph.D., Jason F. Fuller Ph.D, and James E. Coffield Ph.D. for their help and guidance. I would also like to thank the NASA West Virginia Space Grant Consortium for helping to support this research and for their continued support with the award of Undergraduate Research Fellowships. Without WVSGC funding and my mentors' assistance and guidance, this research would not have been feasible.

PRESENTATIONS

This work was presented at Wheeling Jesuit University Research Symposium.

REFERENCES

1. F.A. Cotton and J.A. McCleverty, *Inorg. Chem.* 1964, 3, 1398.
2. J.S. Ricci, Jr., C.A. Eggers, and I. Bernal, *Inorg. Chim. Acta*, 1972, 6, 97.

3. H. Buettner, and R.D. Feltham, *Inorg. Chem.* 1972, 11, 971.
4. J.B. Zimmerman, T.W. Starinshak, D.L. Urich, and N.V. Duffy, *Inorg. Chem.* 1977, 16, 3107.
5. N.V. Duffy, C. Cauletti, and C. Furlani, *Inorg. Chim. Acta*, 1973, 23, 181.
6. M.R. Houchin, *Inorg. Chim. Acta*, 1984, 83, 103.
7. C.C. Jack, M.D. Hoops, A.F. Hepp and N.V. Duffy, *J. Undergrad. Chem. Res.* 2012, 11-14.
8. J.E. Coffield, N.V. Duffy, M.D. Hoops and R.Z. Beck, *J. Undergrad. Chem. Res.* 2012, 12, 7-10.
9. A. Roffey, PhD thesis, Univ. College (London) 2013.
10. N. Barker, M. Logan, J.E. Coffield, and N.V. Duffy, *J. Undergrad. Chem. Res.* 2015. 14, 60-63.
11. G. Hogarth, *Transition Metal Dithiocarbamates; 1978-2003; in Progress in Inorganic Chemistry*, 53, p.71-585; K.D. Karlin, ed. (2005).

Graduate Research Fellowships Reports

EXERCISE REGULATES BRAIN-ADIPOSE TISSUE CROSSTALK IN THE “STRESS LESS” MOUSE MODEL

Debbie Amos
Biomedical Science
Marshall University
Huntington, WV

ABSTRACT

Oxidative stress plays a key role in modulating lipid and glucose homeostasis which can lead to obesity and its comorbidities. Exercise causes both an increase in redox stress which in-turn signals antioxidant protection by stimulating antioxidant defense. In obese mouse models, exercise was shown to lower fat mass and regulate adipose function. I previously showed the impact of exercise on oxidative stress levels as well as body composition, metabolic parameters, and skeletal muscle function. With noted alterations in fat mass and key metabolic parameters that reflect overall energy metabolism, the impact of exercise was analyzed on brain-adipose cross talk. We hypothesized reducing redox stress lowered body and fat mass and improved metabolic parameters by modulating adipose-brain cross talk and ultimately enhancing energy metabolism. To study this hypothesis, we used two ‘stress-less’ mouse models (i) catalase (**Cat-tg**), that expresses 4-fold higher catalase, and (ii) **Bob-Cat**, a hybrid between Cat-tg and obese mice (Ob/Ob),. These two “stress-less” models along with their parent strains were subjected to moderate exercise (8 weeks of treadmill running) or sedentary regimen. Body weight, food intake, fat and lean mass (ECHO-MRI) were measured in addition to metabolic parameters (CLAMS). Changes in molecules secreted by adipose (adipokines) in addition to appetite regulating genes (brain) were also determined. Results showed both Bob-Cat and Cat-tg groups lost weight compared to C57 sedentary group, and exercised groups also showed decreased fat mass. CLAMS showed an increase in energy expenditure and food intake with exercise in all groups except the Bob-Cat group. Within adipose tissue, exercise trended to increase the mRNA expression of *adiponectin* and *catalase* in all groups and increase in catalase activity in C57 and Cat-tg groups in addition to a trend of exercise to further increase *catalase* gene expression and catalase activity. Also, exercise induced PPAR γ expression in C57 group. Leptin, is a key hormone secreted by adipose tissue that modulates appetite. Pearson correlation revealed a significant association between fat mass changes and adipose leptin expression (dCT values) at $p < .0025$. Within the brain, exercise trended to increase satiety gene *POMC* and decrease *NPY* gene expression (increased appetite). However, fold change values were higher for all mice overexpressing antioxidant catalase. Overall, we have seen a positive influence by exercise on energy metabolism and obesogenic pathways (brain-adipose crosstalk) in the novel “stress-less” mouse model.

INTRODUCTION

Oxidative stress plays a key role in the metabolic syndrome, which includes obesity, Type II diabetes, and cardiovascular diseases [1]. Exercise has shown to both cause an increase in the production of reactive oxygen species (ROS) as well as induction of antioxidant defense [2] [3] [4]. Exercise results in lower fat mass [3] and allows for normal adipose and hypothalamic signaling [5]. Being a post-collegiate athlete, I desired to continue my research funded by NASA in 2015-2016 and determine the effects of exercise on oxidative stress levels, body composition,

metabolism, and appetite regulation by investigating the adipose-brain axis. To study my objectives, I continued to breed and maintain two different “stress-less” mouse models: (i) Catalase Transgenic (Cat-tg) mice: that express 3-4 fold higher human catalase levels compared to its parent strain C57Bl6 mice (thus ‘stress-less’) and (ii) Bob-Cat mice: a hybrid between Cat-tg and Ob/Ob leptin deficient mice. C57BL6 and Ob/Ob mice were control groups. Sixteen week old Cat-tg ($n \geq 7$) and Bob-Cat mice ($n=8$) were assigned to a sedentary or exercise group. The exercise group ran 30 min., 5 days per week for 8 weeks at 15 m/min (moderate rate) on a mouse treadmill (Mice 3/6 Animal Treadmill, Columbus Instruments, Columbus, OH). The IACUC committee of Marshall University approved this study. Weekly food and body weights were measured. ECHO-MRI (magnetic resonance imaging) was performed at the beginning, 4 week, and 8 week time points to analyze fat and lean body mass percentages. CLAMS (Comprehensive Laboratory Animal Monitoring System) was performed at the end of the 8 weeks to measure Respiratory Exchange Rate (RER), Heat Production (Kcal/h), Food Intake (g/24h), and Locomotor Activity (X-Ambulatory Counts/day). At the end of 8 weeks, mice were fasted, anesthetized, and then blood was obtained by cardiac puncture. Blood was centrifuged 10 minutes to obtain plasma. 35 μ L of plasma was then used in an LDX Cholestech machine to obtain the lipid profile for each mouse. A glucometer was used to determine fasting blood glucose level. Tissues were collected, weighed, and flash frozen in liquid nitrogen then stored at -80°C . Milliplex Mouse Adipokine Magnetic Bead Panel was used to measure levels of Leptin using 10 μ L of thawed plasma from each mouse according to manufacturer’s protocol in a Luminex 200 system. Adipose tissue from all groups of mice (exercise and sedentary) was evaluated in terms of catalase enzymatic activity (measured on a Shimadzu UV-1800 Spectrophotometer according to the method of Aebi [6], oxidized proteins (Millipore OxyBlotTM Protein Oxidation Detection Kit according to company protocol), and mRNA expression of catalase and key adipokines including leptin, adiponectin, and PPAR γ using Real Time PCR (RT-qPCR). A Pearson Correlation was then performed to determine if Leptin mRNA expression was correlated with body fat mass. The hypothalamic region from each brain was sectioned and used to determine differences in the gene expression of primary appetite regulating genes NPY, AgRP, POMC, and the Leptin Receptor (LepR) by RT-qPCR. Results were calculated by 1 or 2 WAY ANOVA with post-hoc tests and plotted using Excel and GraphPad Prism as mean \pm SEM $p < .05$ was considered statistically significant. All gene expression levels were represented as fold change determined by the $\Delta\Delta\text{Ct}$ method. All associated personnel had passed the CITI Certification Tests for Mouse and Rodent Handling. Animals were treated in compliance with Marshall University Animal Committee (Institutional Animal Care and Use Committee) regulations.

BACKGROUND

Obesity is a rising global epidemic [7]. The brain directly controls body composition as a pivotal regulator of appetite, metabolism, and energy homeostasis [8]. The orexigenic and anorexigenic signaling pathways are located within the hypothalamus which primarily controls the appetite regulation system. The orexigenic pathway contains neurons that co-express Neuropeptide Y (NPY) and Agouti Related Peptide (AGRP), which decreases satiety and energy expenditure, while the anorexigenic pathway contains Proopiomelanocortin (POMC) and Cocaine-Amphetamine Related Transcript (CART) that suppress appetite and increase energy expenditure [8]. Numerous regulatory factors stimulate these neuronal populations including the hormone leptin, an adipokine (signaling molecule secreted by adipose tissue). Leptin reflects the body’s fat

mass and triggers neurons by activating POMC and inhibiting NPY leading to decreased appetite by the JAK/STAT3 (Janus kinase/signal transducers and activators of transcription) pathway (adipose-brain axis) [9]. Nevertheless, during obesity, excess body fat alters levels of adipokines, and results in increased production of reactive oxygen species (ROS) primarily by the mitochondrial electron transport chain and peroxisomal oxidation of fatty acids [10]. High levels of ROS disrupt metabolic pathways involved in glucose and lipid signaling [11] and compromise hypothalamic neuronal signaling [1]. Research has revealed that oxidative stress (OS) levels are increased as rodents and humans travel to space and remain elevated upon return to earth [12]. Though aerobic exercise increases the production of ROS, benefits are related to its induction of antioxidant defense over time [2] [3] [4]. Exercise also lowers fat mass [3] allowing for normal adipose and hypothalamic signaling [5].

EXPERIMENT

In my previous studies, funded by NASA, I showed the impact of exercise on the level of oxidative stress, body composition, and skeletal muscle function. With noted alterations in fat mass and metabolic parameters, I hypothesized oxidative stress levels were also impacting brain-adipose cross talk. Therefore, I planned to increase my population of mice and further evaluate the same two mouse models previously used that overexpress antioxidant catalase (I) **Cat-tg mice**: that expresses 3-4 fold higher catalase levels compared to its parent strain C57Bl6 mice (hence are stress less mice) and (II) **Bob-Cat mice**: a hybrid between Cat-tg and Ob/Ob leptin deficient mice and compare them to the wildtype C57Bl6 (C57) and Ob/Ob mice and determine the impact of redox stress on adipose function and hypothalamic appetite regulation.

PROJECT

To test the proposed hypothesis, my **first aim** was to investigate the impact of exercise on adipose signaling. My **second aim** entailed analyzing the impact of exercise on hypothalamic gene expression and adipose-brain cross talk to determine whether to see if there is any evidence of altered appetite regulation comparing the exercise group to the sedentary group.

METHODS

Animal Models and Exercise

As in my previous NASA funded project, C57Bl6, Catalase Transgenic (Cat-tg), “Bob-Cat,” and Ob/Ob mice were continued to be analyzed. Animals were housed in cages of 3 to 4 mice according to their respective groups. C57Bl6 mice ($n \geq 6$) and Ob/Ob ($n=7$) were bought from Hilltop Laboratories and acclimated to mouse facilities at Marshall University prior to beginning each study. All groups were fed Normal Rodent Chow (Lab Diet 5001) ad libitum. A breeding pair of Cat-tg mice, a gift from Arlan Richardson’s Laboratory [13] were bred and housed in Marshall University Animal Facility. “Bob-Cat” ($n=8$) mice, a novel mouse model generated and bred in our laboratory, by crossing Cat-tg mice with Ob-Ob (obese, leptin deficient, JAX Labs). All guidelines were followed according to IACUC rules and regulations in accordance with approved study protocol. Each of the mouse models were divided into exercise and sedentary groups. Sedentary mice remained in their respective cages in the same environment as the exercised mice. Exercised mice were acclimated to the treadmill (Columbus Instruments) one week prior to

beginning the exercise protocol: 8 weeks of exercising, 5 days per week for 30 minutes at a rate of approximately 15 m/min. Animals were treated in compliance with Marshall University IACUC (Institutional Animal Care and Use Committee) regulations.

Body Weight and Food Consumption

Body mass (g) and total food intake (g) were measured per week. Calculations were conducted to determine the average weekly body weight per mouse group as well as food intake per mouse.

ECHO-Magnetic Resonance Imaging (ECHO-MRI)

Body fat and lean mass composition of the eight groups of mice: C57Bl6, Cat-tg, Bob-Cat, and Ob/Ob (sedentary and exercise) were determined using ECHO-MRI (Houston, TX). Mice were weighed and individually placed into the MRI machine. Five MRI readings were conducted per mouse with regard to fat and lean mass. Calculations were made using Microsoft Excel for the median values of each parameter.

Comprehensive Laboratory Animal Monitoring System (CLAMS)

Metabolic parameters were measured indirectly by assessing O₂ consumption (VO₂) and CO₂ production, respiratory exchange rate (RER), as well as physical activity. Mice were provided ground rodent chow (Lab Diet 5001) for three days during analysis. Metabolic parameters were analyzed for the middle 48 hours the mice were subjected to CLAMS, which is approximately 0600 hour of the first day to 0600 hour of the third day. Heat production (energy expenditure), RER average, average food intake per day, as well as X-ambulatory locomotor activity (physical movement made across the cage) per day were calculated.

Tissue Collection

After 24h fasting, mice were anesthetized using Isoflurane. Blood was obtained by cardiac puncture; red blood cells (RBCs) and plasma were separated by centrifugation for 10 min. Mice were perfused intracardially with cold phosphate buffered saline (PBS). Tissues including adipose, brain, etc. were removed, weighed, and flash frozen in liquid nitrogen. To preserve tissues, all were stored in -80°C.

Lipid Profile/Glucometer

Whole blood was used to measure fasting glucose levels by Precision Xtra Glucometer. The lipid profile (LDL, HDL, total cholesterol, and triglyceride levels) was determined using 35 µL of plasma LDX Cholestech Machine. The remaining plasma was frozen at -80°C.

Mouse Adipokine Magnetic Bead Panel

Luminex 200, laser technology was used to determine IL-6, MCP-1, TNF- α , Leptin, Insulin, and Resistin levels using the Milliplex Mouse Adipokine Array (Millipore) in each mouse's plasma according to manufacturer's protocol.

RT-qPCR

RNA was isolated from both 100 mg of abdominal adipose tissue and the hypothalamic region of each mouse brain using TRI Reagent according to the manufacturer's recommended protocol (Sigma). Concentrations of RNA were measured by use of the NanoDrop 1000 (NanoDrop Technologies Inc., Thermo Scientific, Wilmington, DE, USA). Reverse transcription of total RNA

(1 µg) was performed using iScript™ cDNA Synthesis Kit (Bio-Rad Hercules, CA, USA). RT-qPCR was conducted using iQ SYBR™ Green Supermix (Bio-Rad). The mouse primers for catalase, leptin, adiponectin, and β-Actin used to determine gene expression levels in adipose tissue include: Catalase (Accession Number: NM-009804) Forward: 5'- agtcttctgtcccagatctctc -3' and Reverse: 5'- ctggctcggtcttgaatggaa -3'. Leptin (Accession Number: NM-008493) Forward: 5' - ctcatgccagcactcaaaaa -3' and Reverse: 5'- agcaccacaaaacctgatcc -3.' Adiponectin (Accession Number NM-009605) Forward: 5'- gcagagatggcactcctgga -3 and Reverse 5' - cccttcagctcctgtcattcc -3," and β-Actin (Accession Number NM-007393) Forward: 5'- ctacctcatgaagatcctcaccga -3' and Reverse: 5'- ttctcctaatgtcacgcacgatt - 3.' To analyze gene expression within the hypothalamic region of the brain, the identical primers for catalase and B-Actin (previously noted) were used as well as: POMC, NPY, AgRP, and LepR: POMC (Accession Number: NM_001278584.1) Forward: 5'– gcgacggaagagaaaagaggt -3' and Reverse: 5'– gtcaggcctagtctctgtcg –3.' NPY (Accession Number: NM_023456.2) Forward: 5'- cgctctgacactacatca –3' and Reverse: 5' – ttgttctggggcgcttttct –3,' AgRP (Assession Number: NM_001271806.1) Forward: 5'– ctccaccttgcagcattcc – 3' and Reverse: 5'– gtgactgcttctgtagcca –3.' LepR: (Accession Number: NM_146146.2) Forward: 5' –cttctggagcctgaacctat –3' and Reverse: cagggtctggtgtggtcaaa –3.' RT-qPCR was performed in the Bio-Rad MyiQ or Bio-Rad CFX Connect™ instrument. All samples were run in duplicate or triplicate. Results were calculated using the Pfaffl Equation ($2^{-\Delta\Delta C_t}$) [14, 15], and expressed as fold change compared to the control C57Bl6 mice.

Catalase Activity

The Shimadzu UV-1800 Spectrophotometer was used to determine the enzymatic activity of catalase according to the method of Aebi [6]. Approximately 50 mg of abdominal adipose tissue was homogenized and 8 µL of each sample was added to 1mL of 25mM Hydrogen Peroxide (H₂O₂) solution and analyzed for one minute in duplicate or triplicate. Change in absorbance was recorded at 240nm and specific activity (U/mg protein) was calculated based on protein estimation by the Lowry Method.

OxyBlot

Analysis of oxidized proteins (within adipose tissue) was performed using the Millipore OxyBlot™ Protein Oxidation Detection Kit according to company Protocol. A memcode stain of total protein was used for normalization and images were analyzed using the Biorad ChemiDoc Analysis Tools.

Statistical Analysis

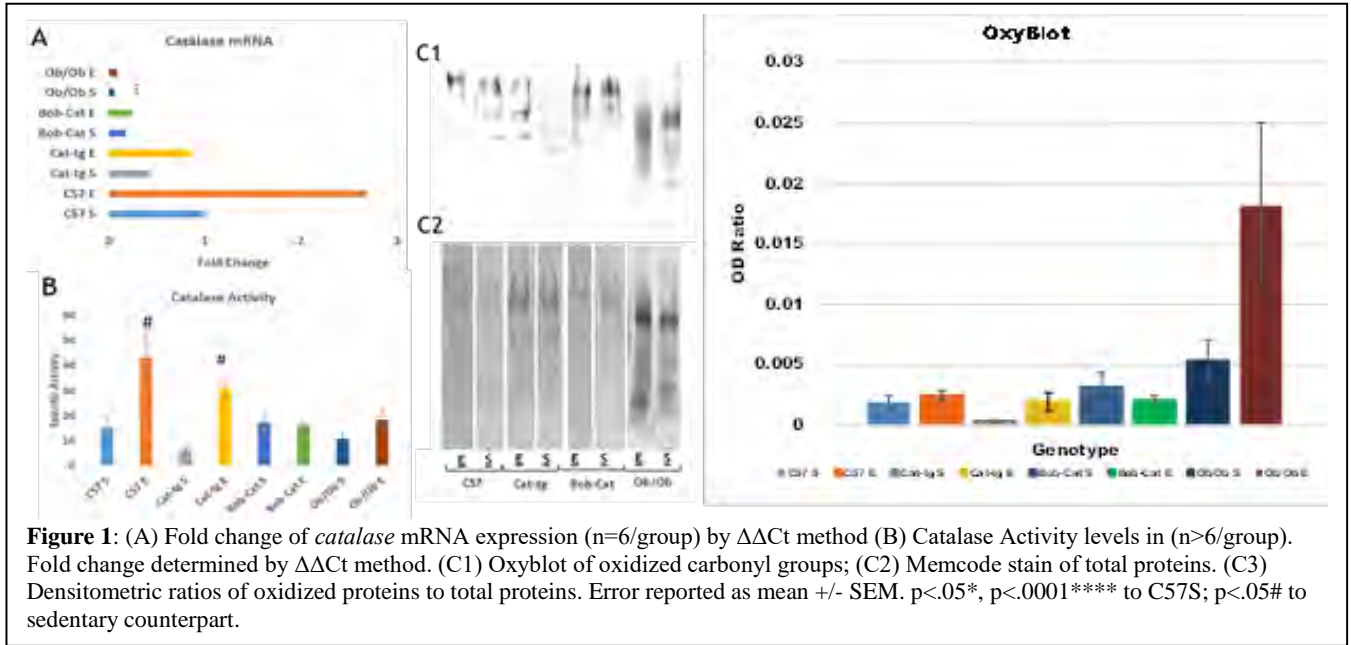
Results are expressed as mean +/- SEM. The difference in each group was evaluated by Pearson Correlation or One Way or Two Way ANOVA followed by Bonferonni Post-Hoc tests when applicable with GraphPad Prism. Statistical significance was accepted at p<0.05.

RESULTS

Adipose Tissue Antioxidant and Oxidative Stress Levels

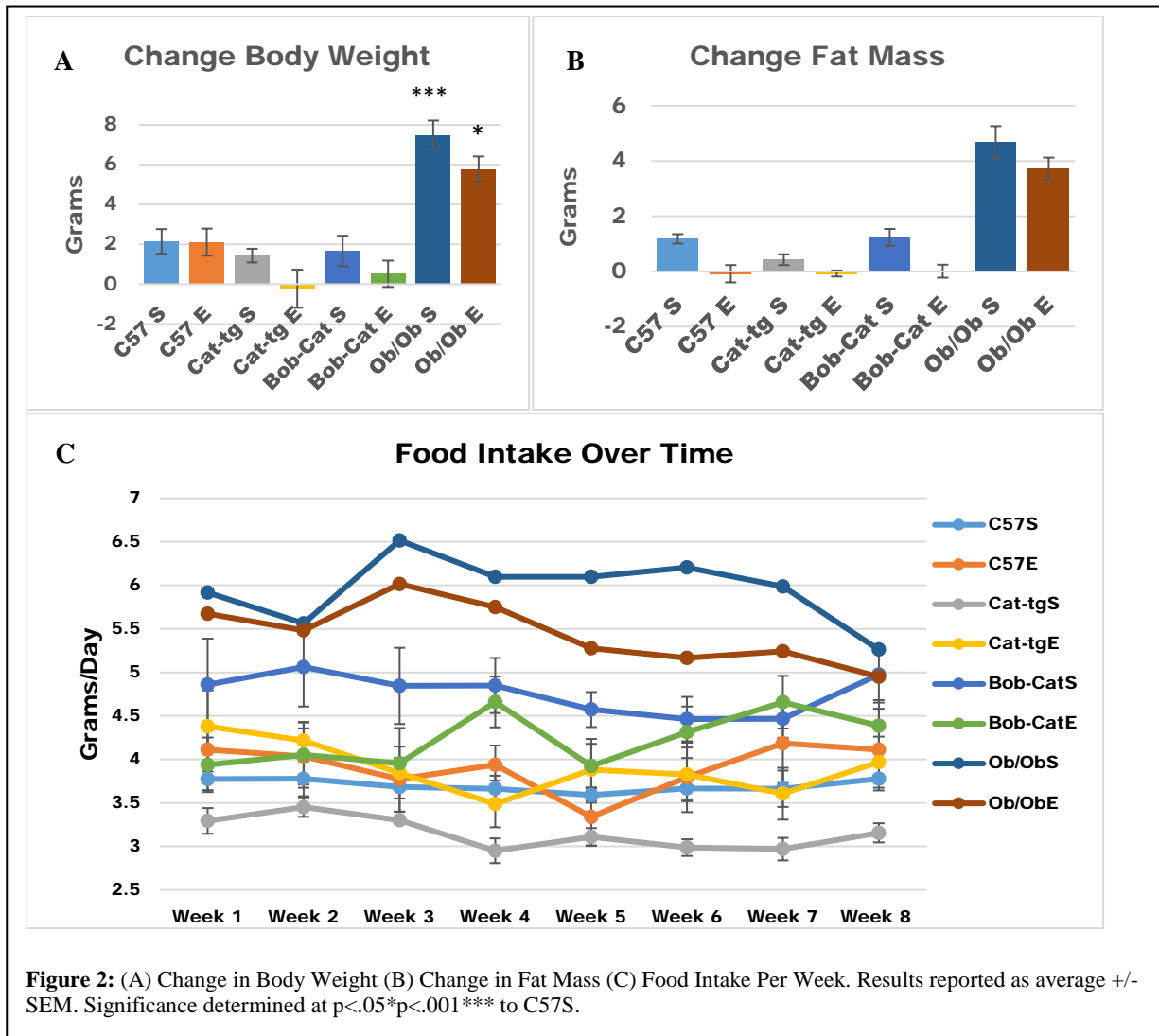
Ob/Ob mice had a significantly lower expression level of catalase than C57S mice (Fig. 1A) Catalase activity analysis revealed that exercise groups all trended to have higher activity levels than their sedentary counterparts with C57E and Cat-tgE having significantly higher levels (p<.05) (Fig. 1B). Densitometric ratios of oxidized proteins to total proteins revealed Ob/Ob E groups had

significantly higher oxidative stress levels than C57S controls. From the combined results it is evident that overexpression of catalase has modified oxidative stress levels within the adipose tissue of mice overexpressing catalase and mice that have been put on exercise regimen.



Body Weight, Fat Mass (ECHO MRI), and Food Intake

All mouse groups either had no change or a decrease in body weight (Fig. 2A) compared to C57 Sedentary (C57S) except the Ob/Ob mouse group. Exercise trended to exacerbate this effect. This same effect was noted in change in fat mass (Fig. 2B) indicating the beneficial effects of exercise and catalase overexpression on body composition. Weekly food intake (Fig. 2C) was measured in all groups, and results indicate all exercised mice trended to have greater food intake except the Ob/Ob mice compared to sedentary counterparts.



Blood Profile and Comprehensive Animal Monitoring System (CLAMS)

As depicted in Table 1, there was an overall trend for exercised mice to have higher levels of HDL (LDX Cholestech machine). Cat-tg Exercise mice had significantly lower levels of insulin and a trend for higher levels of leptin, with the opposite effect in Bob-Cat mice in comparison to their sedentary counterparts. Ob/Ob mice had very low levels of leptin yet high levels of insulin in comparison to all other mouse groups. (Milliplex Adipokine Array). All exercised mice showed an increase or no difference in RER (Respiratory Exchange Rate) in comparison to sedentary counterparts. Cat-tg mice showed an increase in RER vs C57 exercised mice while Bob-Cat mice showed a decrease. (higher RER indicates a greater use of carbohydrates vs fat for energy.) Bob-

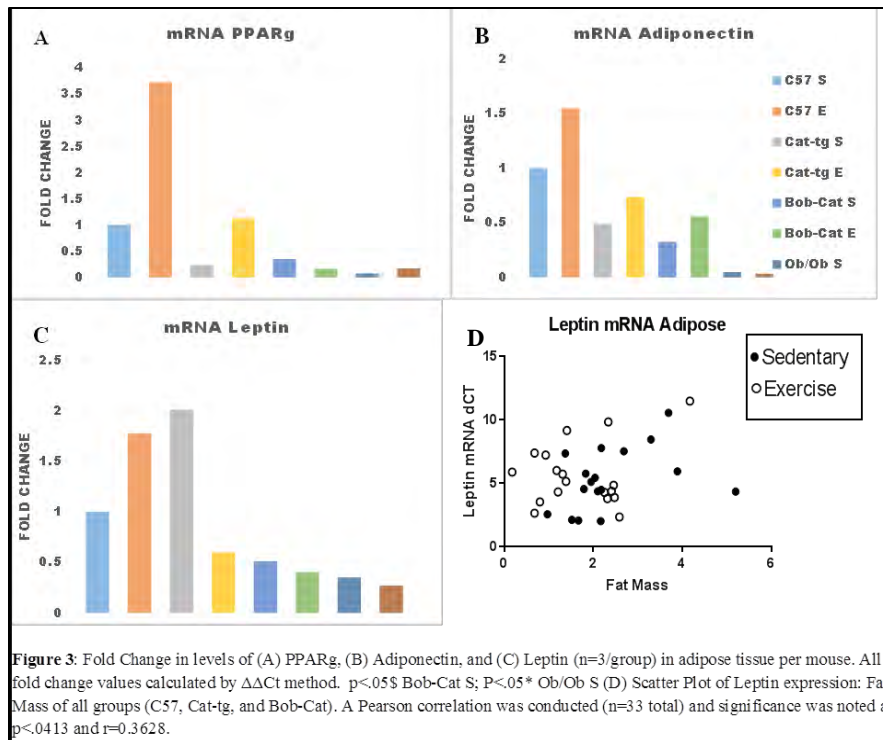
Cat mice trended to show the highest energy expenditure (EE). However, exercise affected energy expenditure of Cat-tg and Bob-Cat mice differently.

| Table 1 | HDL (mg/dl) | Insulin (pg/ml) | Leptin (pg/ml) | RER (VCO₂/VO₂) | EE (Kcal/h) |
|------------------|----------------------|-------------------------------------|----------------------------------|---|-----------------------------------|
| C57 S | 61.8 +/- 22.4 | 287.1 +/- 211.6 | 29.60 +/- 13.8 | 0.93 +/- .015 | 0.40 +/- .02 |
| C57 E | 54.3 +/- 11.1 | 150.2 +/- 88.8 | 84.2 +/- 18.8 | 0.95 +/- .01 * | 0.42 +/- .02 |
| Cat-tg S | 58 +/- 8.2 | 67.20 +/- 20.9 | 14.93 +/- 5.3 | 0.94 +/- .01 | 0.40 +/- .03 |
| Cat-tg E | 53 +/- 15.3 | 17.52 +/- 6.2^{sss} | 113 +/- 46.8^{**} | 0.98 +/- .02 ### | 0.44 +/- .04 |
| Bob-Cat S | 61.8 +/- 9.3 | 47.83 +/- 16.2 | 43.51 +/- 6.5 | 0.88 +/- .03 * | 0.49 +/- .02 ** |
| Bob-Cat E | 59.3 +/- 9.4 | 146 +/- 41.0^{***ss} | 27.50 +/- 5.5 | 0.92 +/- .02 \$# | 0.44 +/- .03 \$ |
| Ob/Ob S | 98.8 +/- 1.08 | 1182 +/- 401 | 1.34 +/- .622 | 0.89 ± 0.01 | 0.55 ± 0.01^{****} |
| Ob/Ob E | 77 +/- 4.35 | 468 +/- 210 | 0.97 | .89 ± 0.01 | 0.56 ± .02^{****} |

(n≥3) * p<.05 ** p<.01 *** p<.001 p<.0001**** compared to C57 sedentary # p<.05 ## p<.01 compared to C57 exercise \$ p<.05 \$\$ p<.01 \$\$\$ p<.001 compared to sedentary counterpart.

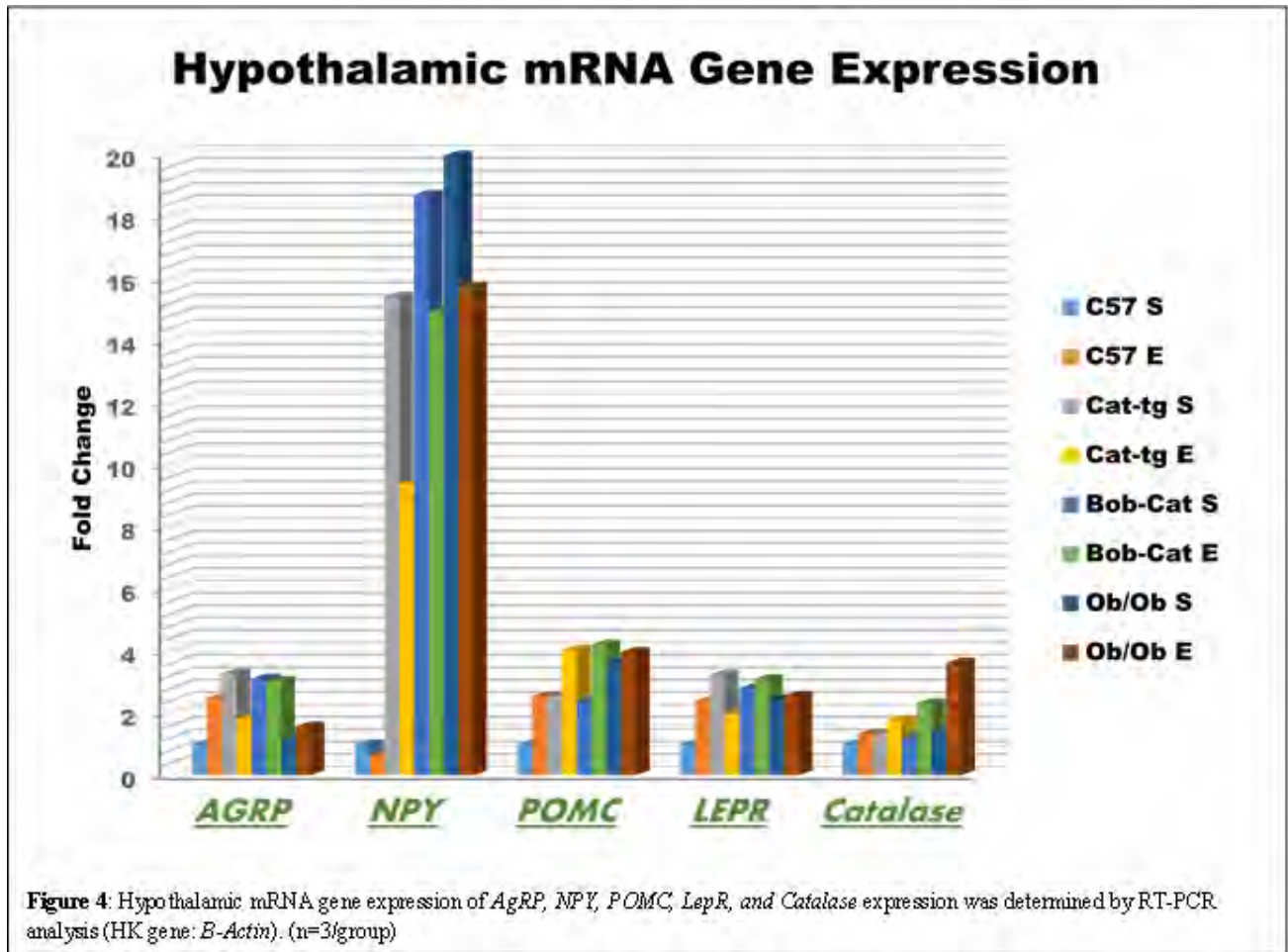
Key Adipokine Fold Change (RT-qPCR) and Correlation to Fat Mass

There was no significant changes in adiponectin expression. However exercise induced PPAR γ expression in C57 group. Leptin, is a key hormone secreted by adipose tissue that modulates appetite. Pearson correlation revealed a significant association between fat mass changes and adipose leptin expression (dCT values) at p<.0413 (Figure 3).



Hypothalamic mRNA Gene Expression

Post sectioning the hypothalamic region of the brain and RNA isolation, mRNA gene expression was determined for *AgRP*, *NPY*, *POMC*, *LepR*, and *Catalase* expression was determined by RT-PCR analysis (HK gene: *B-Actin*). Fold Change is depicted in comparison to C57S (Figure 4). Exercise and catalase overexpression trended to increase gene expression in all genes analyzed. However, most notably, exercise increased satiety gene *POMC* and decreased *NPY* gene expression (increased appetite). Most intriguingly the effect was exacerbated in mice overexpressing catalase on exercise regimen in the case of *POMC*. Fold change values were higher for all mice overexpressing antioxidant catalase. Further investigation of a larger population of mice will provide more conclusive results. (n=3/group)



DISCUSSION

Moderate exercise and overexpression of catalase (antioxidant) has resulted in a decrease of body weight and fat mass in all groups of mice compared to the wildtype C57 sedentary control mouse. However, Bob-Cat and Cat-tg lean mass changes were affected differently when comparing exercise and sedentary groups. In addition to body composition, metabolic parameters with regard to energy expenditure and food intake were also differentially affected along with plasma analysis of insulin and leptin levels and key adipokines which play pivotal roles in appetite and energy regulation. Furthermore, we have seen interesting trends in the combined beneficial effects of moderate exercise and antioxidant excess in adipocyte gene expression/enzymatic activity and appetite regulation. With the combined effects of exercise and antioxidant, we saw an overall increase in POMC compared to C57 and Cat-tg sedentary mice and decrease in NPY in comparison to Cat-tg sedentary counterparts which would increase satiety. This effect reflected in an overall increase in RER and decrease in body weight and fat mass in comparison to both C57 sedentary/exercise and Cat-tg sedentary groups. Therefore, it will be important to further study other endocrine organs and systems effecting energy metabolism to fully understand the mechanisms of exercise in combination with catalase overexpression.

OUTCOMES

Based on our results, it is evident that the effects of exercise and overexpression of antioxidant catalase has an additive influence on body composition, metabolic parameters, and adipose tissue function thus altering appetite regulation and energy metabolism. The novel “stress-less” mice are a good model to study the beneficial impact of redox regulation in obese individuals, athletes, space traveling rodents, and astronauts.

FUTURE PLANS

Based on our results, it is evident the effect of exercise and overexpression of antioxidant catalase has had an additive influence on energy expenditure. This effect is also known to be influenced by energy harvest of the gut microbiome. Therefore, assessment of microbial species in the fecal samples between all genotypes on exercise and sedentary regimen will be analyzed.

ACKNOWLEDGEMENTS

I acknowledge the generous support by WV-NASA Space Grant Consortium. I would also like to acknowledge Dr. Jung Han Kim for training and use of ECHO-MRI and CLAMS machinery, as well as my lab members, and most of all, my PhD Committee Members including: 1) my research mentor, Dr. Nalini Santanam, 2) Dr. Mohan, Dr. Mangiarua, Dr. Kim, and Dr. Lamendella for their time and continual advice/support throughout my academic career.

VALUABLE ASPECTS

Not only did the WV-NASA Grant provide me funds to continue my education at Marshall University, it also allowed me to develop further as a young researcher and advance the skills required in becoming an excellent science professor. I was able to enhance my knowledge on techniques I had previously learned, as well as learn new methods to analyze and calculate experimental results. It also enabled me to present multiple poster presentations, one of which I received first prize at last year’s NASA S.P.A.C.E. Day, and another at a regional conference (Appalachian Regional Cell Conference October 2016 – 2nd Place). I am also grateful for the experience I have had teaching and training undergraduates and graduate students rotating through our laboratory about techniques and protocols related to my project. I am truly thankful for the experience and hope to continue to be funded by NASA as I complete my PhD thesis.

PUBLICATIONS AND PRESENTATIONS

- Poster Presentation: Marshall University Biomedical Science (BMS) program, “Exercise modulates fat mass in a ‘stress-less’ mouse model” Research Retreat: August 26, 2016
- Poster Presentation: Appalachian Regional Cell Conference (ARCC): “Exercise modulates fat mass in a ‘stress-less’ mouse model” October 1, 2016 *Second Place Poster Presentation

- Oral Presentation: Marshall University Biomedical Science (BMS) program: Exercise, Redox Regulation, and Appetite” March 7, 2017
- Publication in Review: “Catalase overexpression modulates metabolic parameters in stress-less leptin-deficient mice” BBA: Molecular Basis for Disease; March 9, 2017 *1st Author
- Poster Presentation: Joan C. Edwards School of Medicine Research Day: “Exercise Modulates Energy Metabolism in an Obese ‘Stress-less’ Mouse Model” March 24, 2017
- Poster Presentation: CCTS Conference: “Exercise Modulates Energy Metabolism in an Obese ‘Stress-Less’ Mouse Model” March 30, 2017

REFERENCES

1. Luque-Contreras, D., et al., *Oxidative stress and metabolic syndrome: cause or consequence of Alzheimer's disease?* Oxid Med Cell Longev, 2014. **2014**: p. 497802.
2. Golbidi, S., A. Mesdaghinia, and I. Laher, *Exercise in the metabolic syndrome*. Oxid Med Cell Longev, 2012. **2012**: p. 349710.
3. Shern-Brewer, R., et al., *Exercise and cardiovascular disease: a new perspective*. Arterioscler Thromb Vasc Biol, 1998. **18**(7): p. 1181-7.
4. Meilhac, O., et al., *Role of arterial wall antioxidant defense in beneficial effects of exercise on atherosclerosis in mice*. Arterioscler Thromb Vasc Biol, 2001. **21**(10): p. 1681-8.
5. Caruso, V., H. Bahari, and M.J. Morris, *The beneficial effects of early short-term exercise in the offspring of obese mothers are accompanied by alterations in the hypothalamic gene expression of appetite regulators and FTO (fat mass and obesity associated) gene*. J Neuroendocrinol, 2013. **25**(8): p. 742-52.
6. Aebi, H., *Catalase in vitro*. Methods Enzymol, 1984. **105**: p. 121-6.
7. Furukawa, S., et al., *Increased oxidative stress in obesity and its impact on metabolic syndrome*. J Clin Invest, 2004. **114**(12): p. 1752-61.
8. Wee, N.K., et al., *The brain in bone and fuel metabolism*. Bone, 2016. **82**: p. 56-63.
9. Wauman, J. and J. Tavernier, *Leptin receptor signaling: pathways to leptin resistance*. Front Biosci (Landmark Ed), 2011. **16**: p. 2771-93.
10. Fernandez-Sanchez, A., et al., *Inflammation, oxidative stress, and obesity*. Int J Mol Sci, 2011. **12**(5): p. 3117-32.
11. Ballal, K., et al., *Obesogenic high fat western diet induces oxidative stress and apoptosis in rat heart*. Mol Cell Biochem, 2010. **344**(1-2): p. 221-30.
12. Stein, T.P., *Space flight and oxidative stress*. Nutrition, 2002. **18**(10): p. 867-71.
13. Chen, X., et al., *Catalase transgenic mice: characterization and sensitivity to oxidative stress*. Arch Biochem Biophys, 2004. **422**(2): p. 197-210.
14. Pfaffl, M.W., *A new mathematical model for relative quantification in real-time RT-PCR*. Nucleic Acids Res, 2001. **29**(9): p. e45.

15. Edgar, R.C., *Search and clustering orders of magnitude faster than BLAST*. *Bioinformatics*, 2010. **26**(19): p. 2460-1.

NUMERICAL ANALYSIS OF BIRD WING CROSS SECTIONS

Stephen Birt
Aerospace Engineering
West Virginia University
Morgantown, WV

ABSTRACT

The most common mode of transportation we see when crossing large distances is flight. When most wish to attend conferences or celebrations air vehicles take us from one coast to the other. This mode of transportation brings about the desire to create a more efficient mode of transportation. If the airline that you purchase your ticket from has less costs to consider when in transit, the cost of your ticket could very well reduce. In an effort to contribute to this front, and to present another resource for computational fluid dynamists to use when creating their models, presented in this paper are the methodologies, implementation, and results of a project brought to fruition due to the help of the NASA West Virginia Space Grant Consortium.

INTRODUCTION

During the course of the past year, there has been a focus on the biomimetic application of bird wings. The focus mainly came from the desire to represent, as accurately as possible, the flow pattern around a bird's wing and how this may better the design of an air vehicles wing. The main topics that will be covered in this paper are the experimental study, the results, and the outcomes made available due to the work completed. The experimental portion of this paper will outline the methods and procedures taken to ensure the data collected for the biomimetic work to be relevant to the engineering community at large. The results section will focus on the data collected and how this may impact the way we consider airfoil designs. Lastly, the outcomes section is geared towards the gains this research has produced, whether it is involving others to learn about new resources available or giving an opportunity to present this to the community at large.

BACKGROUND

Computational fluid dynamics (CFD) is the analysis of systems involving fluid flow, heat transfer, and associated phenomena such as chemical reactions by means of computer-based simulation (*Anderson, J, 1995*). This simulation is solved using numerical analysis methods to account for error terms and to somewhat simplify the solution depending on the algorithm used. The way that this is done is mainly through the discretized continuum mechanics functions, which are used to reduce from a three-dimensional case to a two-dimensional case for the purposes of this research (*Ragheb, M.,1976*). In the case of this research, the focus is on the fluid flow around an object in a designated plane.

The way that the computation is done is through three main components: the software's pre-processor, the solver, and the post-processor (*Anderson, J, 1995*). The pre-processor is where those initial conditions are set and the geometry of the object to be considered is placed to ensure the regions are adequately defined for the solver. The solver embodies the numerical analysis methods

used to determine the solution for the flow field state variables (e.g., pressure, velocity, temperature, etc.). Finally, the post-processor allows the user to interpret the data collected (e.g., integrate over a surface to solve for spanwise lift and drag). The post-processor can also be used to check for irregularities and correct for tested conditions (e.g., check the dimensionless wall distance, y^+ , to ensure adequate mesh size is used to model turbulence at its lowest spatial scales) With this understanding of computational fluid dynamics in mind, the experimental configuration can be better understood.

EXPERIMENT

The best way to obtain the data necessary to conduct the numerical test on the wing cross sections is to first convert the wing into digital data that can be input into computational fluid dynamics software. This was completed by scanning via a three-dimensional DAVID SLS-3 structured light scanner. The experimental configuration represented in the Figure 14.

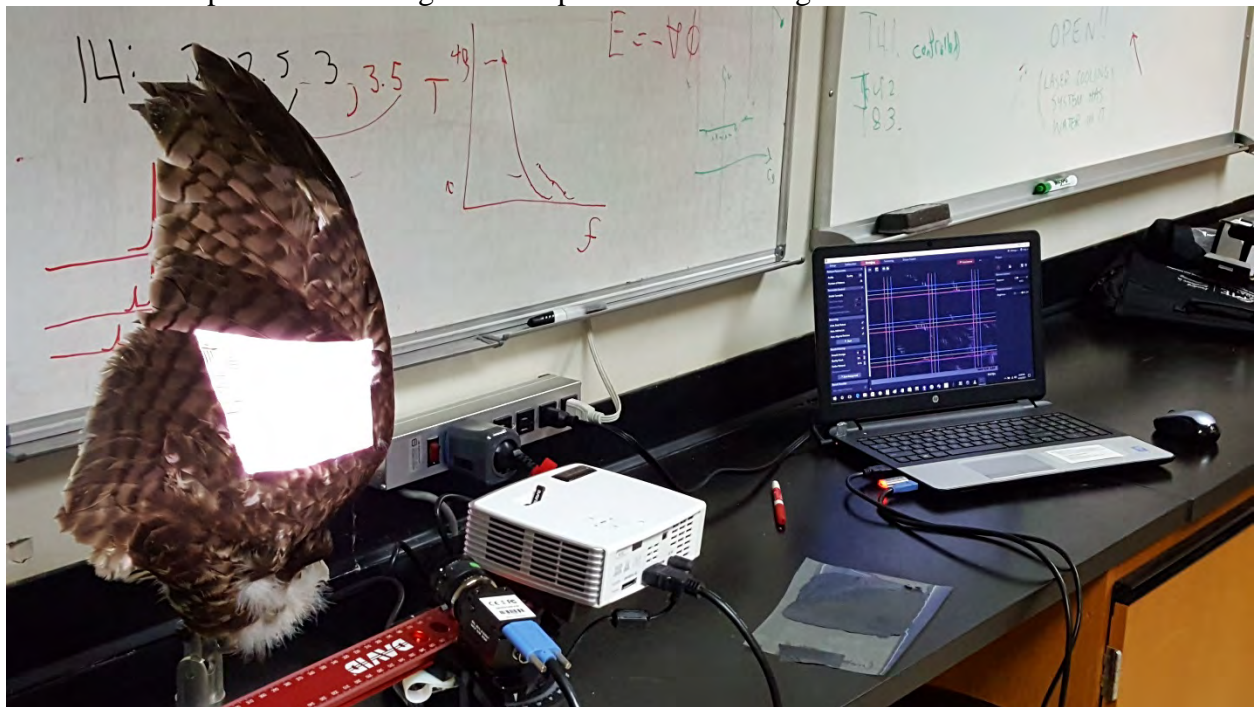


Figure 14: The DAVID SLS-3 structured light scanner is used in the laboratory to create a three dimensional numerical model of a preserved bird wing.

The scanner takes individual scans of the wing at different angles, where the wing is rotated along the base of a table to render a complete three-dimensional image of the wing (Figure 15).

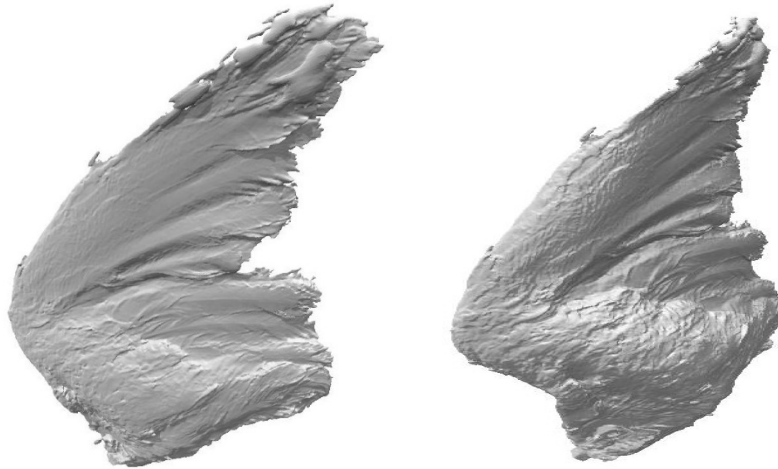


Figure 15: Resultant 3D scan of the bird wing model in a standard tessellation language (STL) format.

From this, we import the completed three-dimensional scan into MATLAB and split the scan into individual two-dimensional slices oriented normally to the spanwise direction of the model. These slices range between the scapular (wing root) feathers to the primary (wing tip) feathers. This was done to compare flows past the sections and how this may help to understand the full span of a bird's wing for testing. A figure of the slicing process is noted in Figure 16.

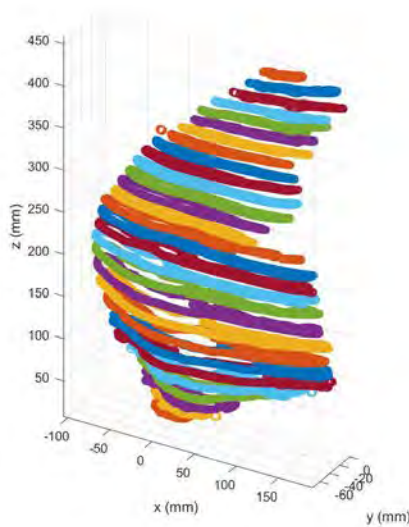


Figure 16: Array of 2D wing section slices taken from a 3D bird wing STL file.

For the focus of the project, there was a sample set chosen from the wing of a red-tailed hawk (*Buteo jamaicensis*) taken along the span-wise length of the wing. Four wing section selections were chosen from the original set of slices. These slices were located at the scapulars, the marginal coverts-secondary coverts region, the transition point between the marginal coverts-secondary coverts-coverts, and finally the alula-primary coverts-primaries region. These sections were selected due to their relatively different geometric forms. The numerical experiment

consisted of passing these wing sections through varying angles of attack to assess their overall performance as a function of orientation of the section to the oncoming flow.

Procedure

The wing airfoils are first imported into ANSYS Fluent. In order to create a region that would fit the airfoil, the necessary surrounding area needed to be found first. Based on the work done in "Laminar-turbulent transition of a low Reynolds number rigid or flexible airfoil", the investigated case can be considered linear for analysis purposes (*Lian, Y., 2007*). Insight into the proper size for the airfoil to be considered without interference of the walls of the structure was also gleaned using this text source.

There are different regimes of flow when dealing with flight. The use of the dimensionless variable called the Reynolds number helps to determine the general flow behavior in which the airfoil is immersed. Reynolds number is defined as the ratio of the inertial-to-viscous forces and may be calculated as the product of the fluid density, velocity, and characteristic length divided by the fluid dynamic viscosity, or

$$\text{Re} = \frac{\rho V l}{\mu}$$

The flow behavior is typically described as having two particular regimes: laminar flow, where the fluid behaves more like sheets of material stacked upon itself, is commonly found when the Reynolds number is less than 100,000; when the Reynolds number exceeds 1,000,000, the flow is commonly found to be fully turbulent, where the behavior exhibits large and small scale fluid “tumbling”, high mixture rates, and increased shear stress on objects held within the flow. The periodic changing from laminar to turbulent flow between Reynolds numbers of 100,000 and 1,000,000 is commonly referred to as transitional flow. For the particular case investigated based upon the cruise velocity and wing chord length of an adult red-tailed hawk flying in standard sea level air, the Reynolds number was calculated to be approximately 44,000, which clearly placed it in the laminar flight regime.

The correct size of the computational grid domain found for this work’s flow regime was twenty-five chord lengths away from the airfoil. Therefore, if the bird wing airfoil were one centimeter it would need twenty-five centimeters worth of space in all directions in order for the resulting upwind and downwind pressures to have no influence on the data set. The solution that was best found for testing was to create a box around the bird wing airfoil to prevent the building of the pressure and disruption of the data collected. Moving on from defining the geometry in the pre-processing stage, the use of a mesh for the solver to operate was created.

Meshing

The meshing styles for the CFD approach vary depending on the structure being observed. The best method found in the case of the bird wing section was the triangular mesh method. The quadrilateral could not be used in this case due to the irregularity of the shape of the bird wing section. To better account for the irregularities along the bird wing section, the triangular-mesh method allows for more points to be given to refine it. This saves processing power when trying to complete multiple runs on data sets at varying initial conditions (*Tu, Jiyuan, 2012*). For the purpose of the experiment, the zones where taken as inlet, outlet, wall, and surface for the ease of

comparison between different data sets.

Initialization

Once the meshing has been completed, the next step was initial conditions needed and the solver that would best work for the case study. The red-tailed hawk is known to fly at approximately 64 miles per hour, converting that to meters per second would be 28.6. The airfoil is considered to be at cruising altitude with the wing fully extended and no additional thrust being produced by the hawk. Another condition placed on this experiment was that cruising altitude could be considered as sea level for the pressure needed in the experiment.

The solver used for this case was the pressure implicit with splitting of operator (PISO) algorithm. This algorithm was chosen due to the restriction in processing power and for the advantages found involving laminar regimes. The calculations were completed by varying angles of attack between zero and thirty degrees with two degree incremental steps. Figure 17 shows the velocity profile of the bird wing section at 10° angle of attack and Figure 18 shows the same flow (also at 10° angle of attack) over a NACA 6409 airfoil. The NACA 6409 airfoil was selected for this comparison due to its similar camber – the avian wing section has a maximum camber of 6% at 34.5% chord, and the NACA 6409 has a maximum camber of 6% at 39.6 % chord.

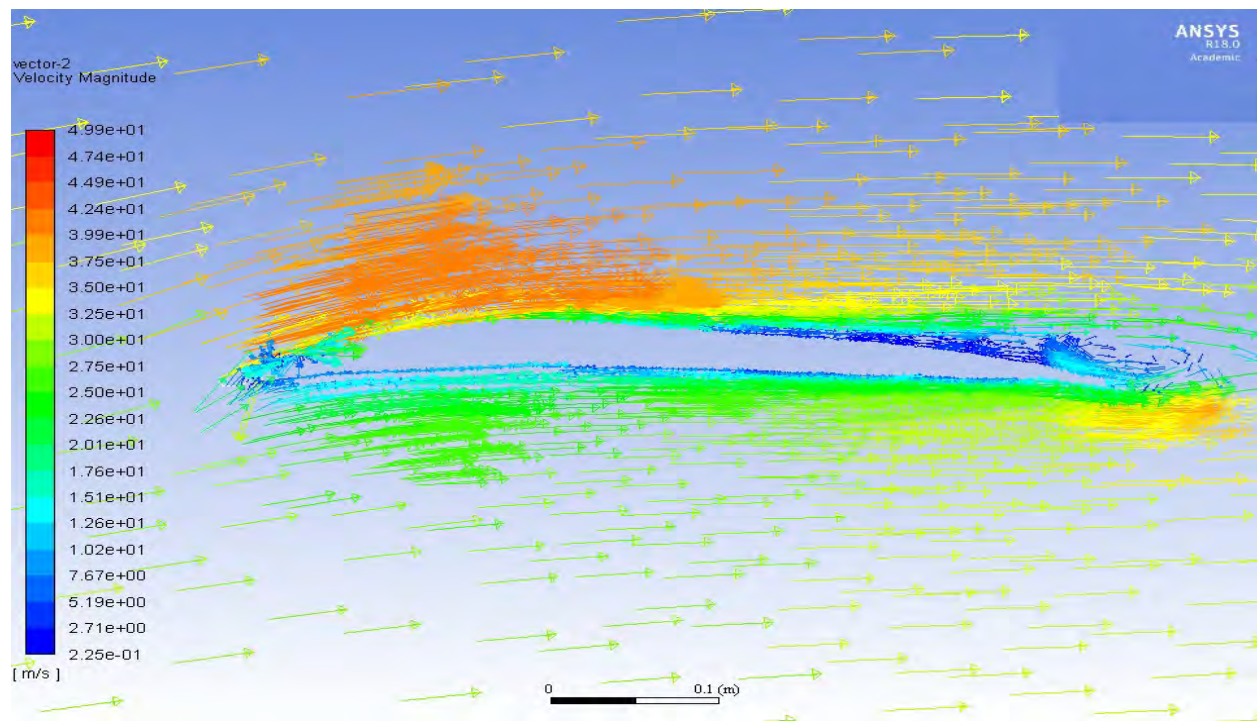


Figure 17: Bird wing section with 35cm chord length taken at 24° angle of attack at 28.6m/s

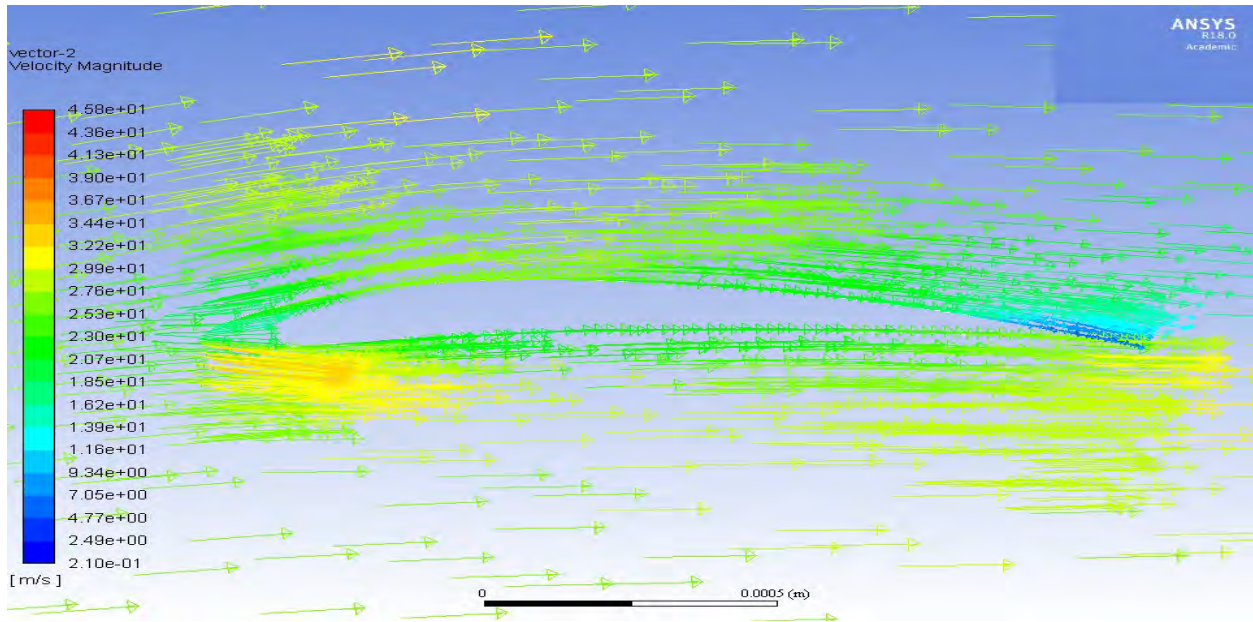


Figure 18: NACA 6409 at 24° angle of attack at flow Re of 44,000 with velocity=28.6m/s

RESULTS

Analysis

One major difference between an avian wing section and a similarly-cambered manmade airfoil is the relative irregularity of the avian wing section's upper and lower surfaces. If we were to compare the scapular region to a NACA 6409, which has a similar camber as noted in the figure below, it is noted that the sharpness of the bird wing airfoil creates greater velocity change over the upper surface of the wing as opposed to the NACA 6409 airfoil.



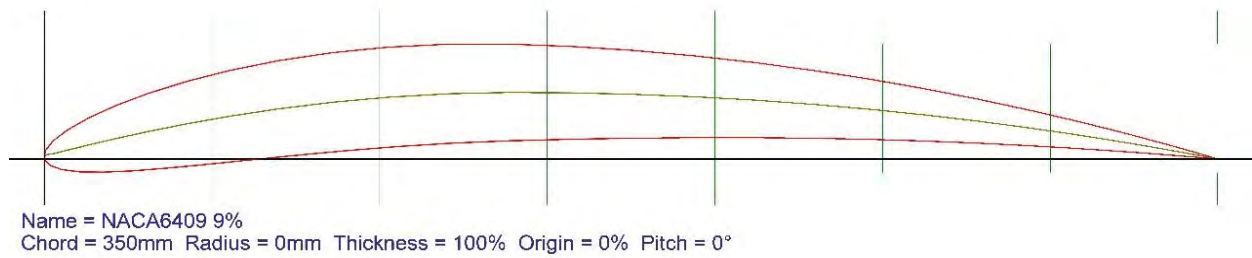


Figure 19: Camber Comparison between Bird Wing Section and NACA 6409

Post-Processing

Comparing the results of the avian and manmade wing sections, the best way for an accurate comparison was found through comparing the drag and lift polars of each. Figure 20 shows the drag polar of the tested bird wing section and the NACA 6409 airfoil. Following the drag polar is the lift curve comparison shown in Figure 21.

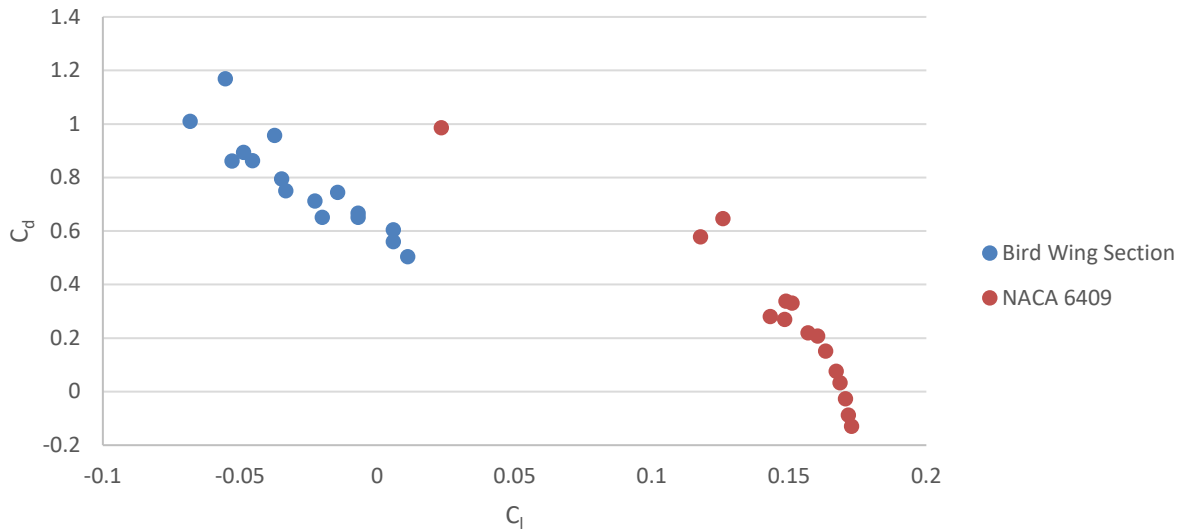


Figure 20: The bird wing section shows higher efficiency at lower C_l values compared to NACA 6409.

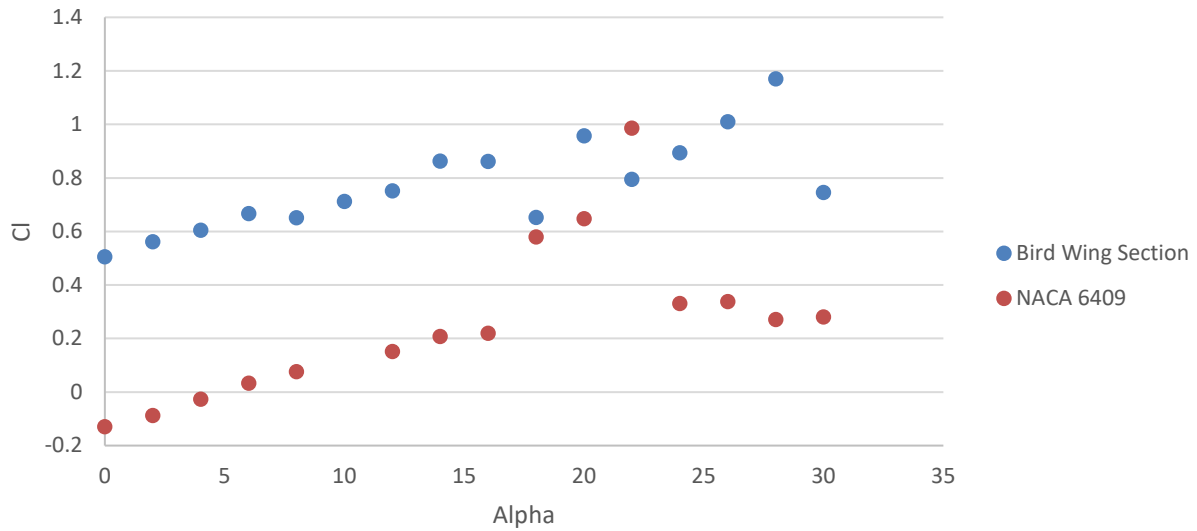


Figure 21: The bird wing section shows more lift per the given alpha compared to the NACA 6409.

These results show that in some cases the bird wing section is more efficient than a comparable manmade airfoil. It should also be noted that during the calculation of the drag and lift coefficients, there were more iterations necessary to achieve a converged result for the bird wing section.

Impact

Applications

There appears to be a need to further consider the two-dimensional profile of a bird's wing. It should, however, also be noted that the reason birds fly so well is due to the varied structure of the wing. There has been interest in the biomimetic flight of bird prior to this research in the forms of ornithopters. Ornithopters are mechanisms that simulate flight, whether this flight is completed by bird, bat, or insect (*Park, Joon Hyuk, 2008*). The majority of studies have focused on the flapping flight of the animal and how this power is generated.

Researchers may also have interest in the differences in morphology of the bird wing, particularly in the study of morphing wing structures. Morphing wings allow for changes in camber during different regimes of flight, thus mimicking the way that a bird changes the camber of its wing in flight.

There has also been work done involving maneuvering flight, where the bird is changing lift coefficients at various speeds (*Warrick, D. R., 2002*). For such studies, instead of considering a steady-state solution for the flight, the flow is taken as unsteady, which complicates the solution process by adding temporal variation of the bird wing morphology.

Website

The project undertaken was not simply a way to complete numerical work on the bird wing. There has been a push to get this information out to the public via a website data bank where the 3D STL files and the resultant slices can be downloaded and tested in a variety of different initial conditions. The website has been online since late November 2016 and there are plans in place to continue the maintenance of the website and the addition of new data sets resulting from future work. The website, found at mae.wvu.edu/bird_wing_database/, will host data that is categorized based on the name of the bird with additional data concerning the age and sex of the bird from which the original wing was collected.

Publications

A Conference presentation and subsequent publication is currently being prepared for the 2017 SAE Aerotech Congress and Exhibition from September 26th through the 28th in Fort Worth, Texas. The paper will present the method of 3D and 2D avian wing geometry collection, two-dimensional study of the bird wing, and a comparison between the avian results and those of similar manmade airfoils.

CONCLUSION

The primary goal of this research was to investigate a process for determining avian wing section flight performance by scanning and numerically slicing an avian wing and then importing the geometry into a CFD package for numerical analysis of the shape at appropriate operating conditions. Another goal was to create a medium that would enable data sets, like the one used for research experimentation, to be accessible for all who held an interest in computational fluid dynamics, or for those who wished to investigate new mechanisms for biomimetic flight. The data samples were collected through a 3D scan and converted to 2D slices in order to focus on the bird

wing sections. Then research conducted focused on the use of computational fluid dynamics software, ANSYS Fluent, to complete the data collection and numerical solutions. This process involved designating the geometry and the region that it would operate in completed through the pre-processing period. From this, the solution was given after validating and testing mesh refinement. Lastly, the post-processor allowed for the interpretation of the data collected.

ACKNOWLEDGEMENTS

The author would like to recognize the NASA West Virginia Space Grant Consortium, who gave the opportunity to contribute to the computational fluid dynamics sphere and an opportunity to learn under the WV SGC Graduate Research Fellowship Program (GFRP). This research could not have been completed without the help of my research advisor, Dr. Patrick Browning, who assisted in bringing me through the first few months of understanding necessary to accurately represent an airfoil in virtual space. It was also under Dr. Browning's guidance that the different variables and considerations necessary to being able to process the scans taken from the DAVID SL-3 scanner. There is also a need to recognize Dr. Christopher Griffin who helped with the finer details of meshing sizes and computational processing of the airfoil and practices necessary to achieve the optimal result.

REFERENCES

1. Ragheb, M. "Computational fluid dynamics." (1976).
2. Anderson, John David, and J. Wendt. *Computational fluid dynamics*. Vol. 206. New York: McGraw-Hill, 1995.
3. Lian, Yongsheng, and Wei Shyy. "Laminar-turbulent transition of a low Reynolds number rigid or flexible airfoil." *AIAA journal* 45.7 (2007): 1501-1513.
4. Tu, Jiyan, Guan Heng Yeoh, and Chaoqun Liu. *Computational fluid dynamics: a practical approach*. Butterworth-Heinemann, 2012.
5. Park, Joon Hyuk, and Kwang-Joon Yoon. "Designing a biomimetic ornithopter capable of sustained and controlled flight." *Journal of Bionic Engineering* 5.1 (2008): 39-47.
6. Warrick, D. R., M. W. Bundle, and K. P. Dial. "Bird maneuvering flight: Blurred bodies, clear heads1." *Integrative and Comparative Biology* 42.1 (2002): 141-148.

CHARACTERIZING THE INNATE AND ADAPTIVE RESPONSES OF IMMUNIZED MICE TO *BORDETELLA PERTUSSIS* INFECTION USING *IN VIVO* IMAGING AND TRANSCRIPTOMICS ANALYSES

Dylan Boehm
Immunology and Microbial Pathogenesis
West Virginia University
Morgantown, WV

Bordetella pertussis (*Bp*) is the causative agent of pertussis (whooping cough). Acellular pertussis vaccines (ACV) replaced whole cell vaccines (WCV) in the US immunization schedule in the early 1990s. Since that time, there has been a resurgence of pertussis cases in the US despite 95% vaccine coverage. WCV vaccines induced cell-mediated responses, which include neutrophil recruitment, whereas ACV vaccines induce Th2 responses. Our goal was to characterize the macrophage and neutrophil response in the context of vaccination with a bioluminescent neutrophil mouse model (NECre luc) and a macrophage specific GFP reporter mouse strain (MacGreen). MacGreen mice were challenged with isogenic mutant strains of *Bp* lacking adenylate toxin and pertussis toxin. NECre luc mice were immunized with WCV, ACV, or a truncated adenylate cyclase toxoid (RTX). Neutrophil recruitment was studied in live mice across the experimental time course and corroborated by flow cytometry and other data. WCV immunization resulted in neutrophilia in response to *Bp* challenge, and immunization with RTX did not protect mice against *Bp* challenge. To further understand the response to *Bp* challenge in vaccinated mice, RNA sequencing was performed on total lung tissue RNA and the immunoglobulin clonal repertoire directed by each vaccine was determined. Collectively our data show that WCV immunization induces increased neutrophil recruitment and activation, and a robust cell mediated response compared to ACV immunization. These data also illustrate how *in vivo* imaging and next generation sequencing can be used to further expand our knowledge of how vaccines induce protective responses against invading pathogens.

INTRODUCTION

Pertussis is a human disease primarily caused by a respiratory infection of the Gram-negative pathogen *Bordetella pertussis* (*Bp*). The hallmark of pertussis is a distinctive whooping cough. Aerosolized *Bp* bacterium are inhaled and adhere to airway respiratory epithelial cells through bacterial adhesins such as filamentous hemagglutinin (FHA), fimbriae and pertactin¹. After bacterial colonization, the bacteria expresses multiple toxins including pertussis toxin (PT) and adenylate cyclase toxin (ACT). *Bp* releases PT, which dysregulate the immune response through ADP-ribosylation of the G-protein α -subunit of cytokine receptors present on a range of leukocytes²⁻⁵. While the secretion of PT has long range effects, ACT is thought to act locally on host cells by converting ATP into supraphysiological levels of cAMP, further dysregulating the host immune response^{6,7}.

In the 1940s an effective whole cell vaccine (WCV) was developed which indirectly slowed basic research on *Bp* compared to other bacterial pathogens. The WCVs were highly reactogenic, and caused prolonged and unusual crying after administration⁸, hyporesponsiveness⁹, and febrile convulsions¹⁰. These issues lead to the development of acellular vaccines (ACV) known today as DTaP/tdap. The pertussis WCV vaccine is composed of killed whole *Bp* bacteria, while the ACV

is composed of detoxified *Bp* antigens. Due to these differences in composition, the vaccine induced protection differs as well. The ACV vaccines utilize alum adjuvant and induce a Th2 responses to several key virulence factors such as PT, FHA, fimbriae, and pertactin depending on vaccine formulations. Whereas the aP induces a Th2 response in human and mice, WCV immunization and *Bp* infection promote a Th1/Th17-type response¹¹⁻¹⁴.

Since the replacement of the WCV with the ACVs, there has been a remarkable increase in the number of cases in the US, with the number of cases in 2012 equaling that of 1954, the date after which the WCVs were first introduced in the US. There are potentially multiple factors that resulted in the return of pertussis in the US. It has been documented that the Th2 response induced by ACV immunization may be inferior to the Th1/Th17 response of the WCV¹⁵. Additionally, ACV protection wanes significantly as early as one year after vaccination, and by 4 years after vaccination vaccine effectiveness is only 9%¹⁶. Furthermore, in a non-human primate model it has been shown that ACV immunized baboons challenged with *Bp* are capable of carrying the infection and transmitting aerosolized *Bp* to naïve baboons¹⁷. Recently, the findings of an epidemiological study suggest that asymptomatic transmission of pertussis is indeed occurring in the human population, and has a role in the increase of pertussis incidents¹⁸.

These recent findings demonstrate the shortcomings of the ACV and urge us to reevaluate the differences between WCV and ACV induced protection with new technologies that were not available in during the developments of the WCV or ACVs. Adenylate cyclase toxin (ACT) an essential virulence factor of *Bp* and is also a known protective antigen¹⁹⁻²¹. ACT contains two main domains: adenylate cyclase and the Repeats in Toxin. In the absence of the AC domain, the protein is non-toxic and referred to simply as RTX²². In a previous study, sera from mice immunized with RTX contained antibodies capable of neutralizing ACT²². ACT is not included in any commercial formulations of ACVs and many have proposed that its inclusion could improve protection⁷.

Immune protection through a Th1 response induces the release of proinflammatory cytokines and chemokines that stimulate the activation and recruitment of innate immune cells such as macrophages, neutrophils, and dendritic cells to the site of infection. Similarly, induction of a Th17 response results in robust activation and recruitment of primarily neutrophils. In Th1/Th17 immune responses these cell populations aid the clearance of the pathogen by phagocytosis of opsonized pathogens. Neutrophils and macrophages play roles in both the innate and adaptive arms of the immune system. Surprisingly, it has been suggested that *Bp* is capable of persisting intracellularly inside of host macrophages by an unknown mechanism²³. Following *Bp* infection of a naïve mouse, neutrophils and macrophages reach peak recruitment between 5 and 7 days after challenge^{24,25}. This occurs after the bacterial burden has begun to decrease. Subsequent studies have determined that neutrophil depletion prior to *Bp* infection in naïve mice does not increase bacterial burden. However, when immunized mice were challenged with *Bp* following depletion of neutrophils the *Bp* bacterial burden increased, demonstrating a protective role of neutrophils in immunized mice²⁶. As previously mentioned, *Bp* toxins PT and ACT both affect innate immune cell activation and their recruitment^{6,27,28}. These toxins contribute to a significant rise in the number of circulating white blood cells in severe cases, known as leukocytosis, and has been attributed as the cause of mortality in fatal cases¹. Leukocytosis was first described in pertussis patients as early as the 1890s^{29,30}. In the 1960's, Morse observed leukocytosis following WCV immunization³¹,

which he hypothesized was caused by PT, then known as leukocytosis-inducing factor³². Therefore, it can be assumed that the toxin associated effects on innate immune cells would be neutralized following ideal *Bp* immunization, and raises the question of where and when are neutrophils and macrophages recruited in an ACV or WCV protected mouse?

Macrophage recruitment was determined using MacGreen mice, a mouse strain in which the macrophages were labelled with a GFP reporter. Our objective for this study was to determine the spatiotemporal location of macrophage distribution in response to *Bp* infection. To accomplish this we challenged MacGreen mice with a WT *Bp* strain (Tahoma 1), or isogenic mutant strains lacking PT or ACT. Following challenge we determined 1) viable bacterial levels, and 2) spatiotemporal localization of macrophages and neutrophils. Additionally, we sought to elucidate the intercellular survival of these strains *in vivo* using a mouse strain incapable of undergoing autophagy and *in vitro* using an autophagy inhibitor.

To address the neutrophil responses following immunization, we utilized *in vivo* imaging systems (IVIS) to characterize the neutrophil responses to *Bp* challenge in the context of various vaccines such as ACV or WCV. We implemented NECre luc mice, a luminescent neutrophil reporter mouse strain has been used in a *Bacillus anthracis* infection model³³, to track neutrophil recruitment following *Bp* challenge. To do so, we: 1) validated the NECre luc mouse as a model for tracking neutrophil recruitment in response to *Bp* infection, 2) tracked the spatiotemporal localization of neutrophils in the context of acellular and whole cell vaccines, and 3) and characterized vaccine associated gene expression profiles using RNA sequencing. The NeCRE luc mouse³³ was used to measure the presence and relative quantities of neutrophils in live mice during *Bp* challenge. We then corroborated our findings with flow cytometry analysis to quantify neutrophils and macrophages in the blood and airway of naïve and immunized mice. WCV immunization resulted in robust neutrophil recruitment and clearance of *Bp*, but also resulted in morbidity of the NeCre luc mice. While the naïve, WCV, or ACV primed adaptive responses to *Bp* are known, we sought to also discover new effects of *Bp* challenge and vaccination on respiratory tract tissues. RNAseq analysis was performed on the lungs of naïve or immunized mice at both early and late time points after challenge with *Bp*. We observed specific gene signatures for each vaccine, and we also identified gene expression profiles that had not been associated with *Bp* or immunization. Neutrophil specific gene expression corroborated our cellular analysis of the respiratory tract demonstrating increased expression of neutrophil specific genes in WCV immunized mice. Furthermore, we determined T-helper cell gene expression profiles of lung transcriptomes and corroborated the activation of Th1 specific gene expression to increased levels of Th1 associated cytokine production in the lungs of WCV immunized mice. Utilizing the depth of data generated through RNAseq we could classify specific B cell clonotypes present in the lung of each immunization group. This technique allowed for analysis of the diversity and frequency of the immunoglobulin repertoire of immunized groups. We hypothesize that these approaches can continue to be applied to other pathogen to host interactions to characterizing the underpinnings to disease progression and immunological responses.

METHODS

Bacteria and culture conditions

B. pertussis strains were cultured on Bordet-Gengou (BG) agar (1906) supplemented with 15% de-fibrinated sheep blood (Hemostat Laboratories) for 48 h at 36°C. *B. pertussis* was then transferred from BG plates to three flasks of 12 ml of modified Stainer-Scholte liquid medium (SSM)³⁴. SSM cultures were not supplemented with cyclodextrin (Heptakis(2,6-di-O-methyl)- β -cyclodextrin). SSM cultures were grown for ~22 h at 36°C with shaking at 180 rpm until the OD₆₀₀ reached 0.5 on a 1 cm path width spectrophotometer (Beckman Coulter DU 530). The cultures were then diluted to 1 x 10⁹/ ml with SSM.

Mouse Strains

All mouse strains used were bred in a specific pathogen-free experimental conditions within the Office of Laboratory Animal Resources vivarium at West Virginia University. Mice were aged 8 – 12 weeks, male and female sex mice were equally assigned to all vaccination groups. 129-Elane^{tm1(cre)Roes}/H mice (Medical Research Council, London, UK) were crossed with FVB.129S6(B6)-Gt(ROSA)26Sortm1(luc)kael/J mice (Jackson labs; 0051225) resulting in NECre luc progeny. NECre luc mice were injected with CycLuc 1 luciferin³⁵ (EMD Millipore, Darmstadt, Germany) and confirmed to be luminescent using Xenogen Lumina II. Upon intraperitoneal injection of a luciferase substrate (luciferin), neutrophils emit luminescence that is detectable using a high sensitivity live animal imaging system (Xenogen IVIS Lumina II). MacGreen mice (Tg(Csf1r-EGFP)1Hume) were purchased (Jackson labs; 018549) and bred in WVU vivarium. LC3B^{-/-} (B6;129P2-Map1lc3btm1Mrab/J) were purchased (Jackson labs; 009336) and bred in WVU vivarium.

Vaccines used in study and administration

All vaccines were formulated into 200 μ l doses with the antigen content described below. 100 μ l of INFANRIX (GSK) human vaccine (DTaP) which is 1/5 human dose of the vaccine, was mixed in 100 μ l of PBS. The NIBSC WHO standard *Bordetella pertussis* whole-cell vaccine (NIBSC code 94/532) was received lyophilized and reconstituted in 1ml of PBS. At this concentration one human dose is 100 μ l therefore, 20 μ l was mixed with 180 μ l of PBS, which is 1/5 of the human dose (66 μ g of total protein). A truncated ACT protein (RTX) was purified as previously described (Wang and Maynard, 2015) 5.6 μ g of RTX was combined with 100 μ l alum adjuvant (Alhydrogel®, InvivoGen) corresponding to 1 mg of aluminum hydroxide. All immunizations occurred by intraperitoneal injection. Unvaccinated mice received 200 μ l of sterile PBS.

Vaccination and Challenge with *Bordetella pertussis*

NECre luc mice were bred to ages ranging from (8-12 weeks). Mice were vaccinated at day 0, and then boosted 21 days later. Thirty-five days post initial vaccination, *B. pertussis* UT25 was grown as described above, and provided as a challenge dose at 2 x 10⁷ CFU in 20 μ l. Mice were anesthetized by intraperitoneal injection of 200 μ l of ketamine (6.7 mg/ml) and xylazine (1.3 mg/ml) in 0.9% saline. Two 10 μ l doses of bacteria were administered through nasal inhalation into each nostril of the mouse. Mice from each of the groups were challenged WCV (8), ACV (8), RTX (6), and naïve control (PBS injection) (5).

Collection of murine samples and determination of bacterial burden

On days 1,2,4,6, and 9 pc, mice were euthanized by intraperitoneal injection of pentobarbital and dissected in a biosafety cabinet under BSL-2 conditions. Blood was collected by cardiac puncture, serum was separated by centrifugation through a BD Microtainer SST blood collector (BD), or blood for complete blood cell counts were collected in BD Microtainer Tubes with K₂EDTA (BD). Trachea and lungs were removed, placed in 1 ml PBS, and then homogenized. Trachea tissue was homogenized by a Brinkman Homogenizer (Polytron), while lung tissue was dissociated using a Dounce homogenizer (Kimble Chase). To determine viable *B. pertussis* in the nares, 1 ml of PBS was flushed through the nares and collected. In order to determine bacterial burden 100 µl of homogenate or nasal lavage was serially diluted in sterile PBS. Four 10 µl aliquots of each serial dilution were plated on BG containing streptomycin (100 µg/ml) to ensure only UT25 *B. pertussis* grew on the plates. After 72 h at 36°C colony forming units (CFUs) were counted and the bacterial burden per tissue was calculated. Due to the serial dilutions plated our limit of detection was 10³ CFUs per ml or organ. CFUs from experimental groups at each time point were compared to the naive (PBS injected) and challenged group by a two-tailed unpaired t test using the software package Prism 7 (GraphPad, La Jolla, CA). All murine infection experiments were performed per protocols approved by the West Virginia University Animal Care and Use Committee (protocol number 14-1211).

IVIS imaging

NECre luc mice received 83 mg/kg of CycLuc1 luciferin by IP injection (100 µl). Five minutes after injection mice were anesthetized with 3% isoflurane, mixed with oxygen from the XGI-8 gas anesthesia system supplied with a Xenogen IVIS Lumina II. Luminescent signals were acquired during a five-minute exposure. Acquisition was performed using Living Image 2.5 software (Xenogen). Images were acquired with a binning of 4. Following imaging, mice were either euthanized for dissection and extraction of tissue samples or returned to the vivarium. Luminescence was determined by quantification of photons emitted per second generated in each region of interest (ROI): whole mouse image or nasal cavity. The background of each image was subtracted from the ROI, background photons were defined by the average of two ROIs away from the mouse, for the same image. Data was expressed as relative fold change between target ROIs from experimental groups to an average of ROIs from control mice that were not vaccinated or challenged. Group comparisons were analyzed by one-way analysis of variance (ANOVA) followed by a Tukey's multiple-comparison test using Prism 7.

Preparation of tissue and flow cytometry analysis

Blood, lung, and cells isolated from nasal lavage were analyzed by flow cytometry. A 100 µl sample was removed from lung homogenate of all samples and filtered through a 70 µm cell strainer, then centrifuged at 1000 x g for 5 mins to pellet cells. Supernatant was removed, and RBC lysis buffer (BD Pharm lysis) added incubated at 37°C for 2 min, then pelleted using the same centrifugation conditions. Cells were resuspended in 500 µl of PBS + 1% FBS, 100µl was aliquoted for antibody staining. After cardiac puncture blood was placed in EDTA containing tube (BD Bioscience), RBC were lysed using Pharmlyse (BD Biosciences) with a 15 min room temperature incubation and then prepared in a similar manner to other tissues. All cell suspension samples were incubated on ice in PBS and 1% FBS for blocking. Antibodies against specific cell surface markers: PE-conjugated GR-1 (BD, 553128) Alexa Fluor 700-conjugated CD11b (Biolegend, 101222) were added to cell suspensions and incubated in the dark for 1 h at 4°C. Lung, blood, and nasal wash suspensions were pelleted, and resuspended in PBS prior to analysis.

Samples were read using LSR Fortessa (BD), and analyzed using FlowJo v10 (FlowJo, LLC). PMNs were classified as CD11b⁺Gr-1⁺ single, live cells.

Cytokine Quantification

Lung homogenates were pelleted by centrifugation and then supernatant was collected and stored at -80°C until analysis. Concentration of cytokines in the lungs of vaccinated and challenged mice were determined by quantitative sandwich immunoassays, Meso Scale Discovery (Rockville, MD) V-PLEX Proinflammatory Panel (K15048G-1) and Mouse IL-17 Ultra-Sensitive kits (K152ATC-1), following manufacturer's instructions. Data was analyzed by one-way ANOVA, with a Tukey's multiple-comparison test for each time point.

Serology

Vaccinated and challenged mouse serological responses to RTX, and PT were determined by qualitative ELISA. High-binding 96-well ELISA plates were coated overnight at 4°C with 50 µl of purified RTX or Pt in PBS at a concentration of 1 µg/mL. Purified *Bp* antigens, were obtained from Dr. Jennifer Maynard. Serum samples from NVNC, PBS, ACV, and WCV serum titers were analyzed for PT, as the RTX group had no PT in vaccine. Samples from NVNC, PBS, WCV, and RTX were analyzed for serum antibody titers to RTX, as ACV would not be expected to have RTX titers because no RTX was included in vaccine. Plates were then washed with PBS + 1% Tween 20 (PBS-T), then blocked with 5% milk in PBS-T for 1 hour at room temperature. Sera were diluted to a concentration in the linear dose range for each antigen. Plates were incubated for 2 h at 37°C with serial diluted serum samples from vaccinated groups. Following 3 PBS-T washes, 1:4000 goat anti-mouse IgG-AP (Southern Biotech), secondary antibody was added and incubated 1 h at 37°C. Plates were washed, then developed for 30 min with 100 µl p-nitrophenyl phosphate. Colorimetric signal was measured using Spectramax i3 (Molecular Devices) at 450nm. An average of blanks was subtracted from all absorbances and used as a baseline detection limit. The minimum detection limit above the baseline was analyzed by one-way ANOVA, with a Tukey's multiple-comparison test for each time point using Prism 7.

Isolation of Lung RNA, illumina library preparation, and sequencing

Lung RNA was prepared similar to previously reported³⁶ with the following modifications. The freshly isolated NECre luc mice lungs were homogenized and RNA was prepared immediately using RNeasy purification kit (Qiagen). Each lung was placed in 1 ml of sterile PBS and then 2 ml of TE lysozyme (1mg/ml) was added and allowed to incubate for 10 min on ice. 2 ml of RLT buffer was added and incubated for another 10 min on ice. The homogenate was then pushed through a syringe needle. The homogenates were pelleted by centrifugation at 20,800g (max speed microfuge) for 10 min. The supernatant was extracted and then 2.8ml of 100% EtOH was added to each tube. This supernatant of each mouse sample was then disturbed to four RNeasy tubes for RNA isolation. The RNA was eluted and pooled into one sample per mouse. The resulting RNA was quantified on a Qubit 3.0 (ThermoFisher) with the high intensity assay kit. Next, the RNA integrity was assessed using Agilent BioAnalyzer RNA Pico chip. All samples were then submitted Ribo-zero rRNA depletion (illumina) and reassessed for RNA integrity. rRNA depleted mRNA samples were then fragmented and prepared into libraries using illumina ScriptSeq Complete Gold (Epidemiology). Libraries were checked for quality control with KAPA qPCR QC assay (KAPA Biosystems). The libraries (33 total) were then sequenced on an illumina HiSeq at the Marshall University Genomics Core facility on 2 lanes of 2x50bp. Sequencing data were

deposited to the Sequence Read Archive (SRA) and are available under the reference number SRA587785, BioProject number PPJNA394758.

RNAseq bioinformatics analyses

The reads were analyzed using the software CLC Genomics workbench 9.5. *Mus musculus* genome was downloaded from NCBI. Reads were mapped against the genomes using the following settings for mapping: mismatch cost = 2, insertion cost = 3, deletion cost = 3, length fraction = 0.8, similarity fraction = 0.8. RPKM values were generated using default parameters for CLC Genomics. On average ~20 million reads were obtained for each sample and with stringent parameters ~73% mapped to the murine genome with our mapping parameters. Fold changes in gene expression and statistical analyses were performed using an Extraction of Differential Gene Expression (EDGE) test p value. Expression data for each gene was considered significant if the p value was less than 0.05. Venn diagrams were generated using Venny 2.1³⁷. Fold-change of gene expression data was plotted relative to non-challenged control groups at each time point. Gene list were created using GO terms acquired through AmiGO 2 database³⁸ including neutrophil (CL:000075), neutrophil activation (GO:0042119), neutrophil migration (GO:1990266), innate immune response (GO: 0045087), T-helper 1 type immune response (GO:0042088), type 2 immune response (GO:0042092), and T-helper 17 type immune response (GO:0072538).

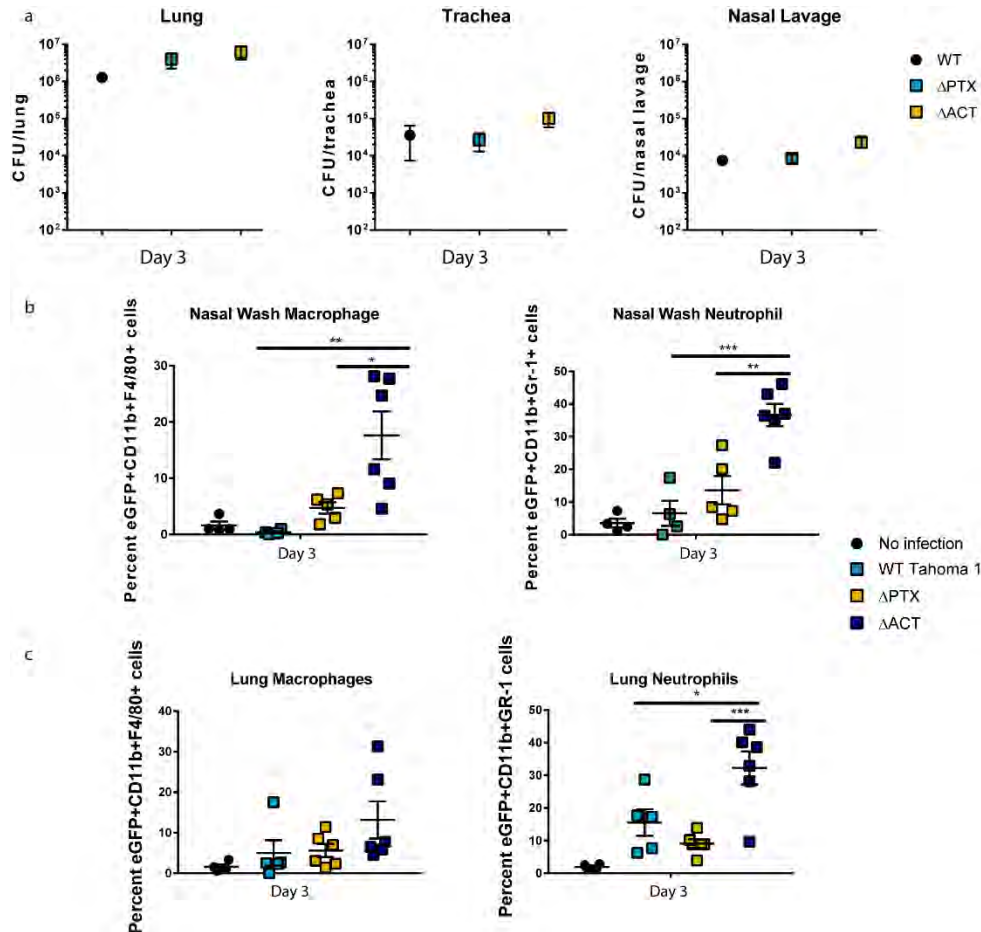
Immunoglobulin and T-cell receptor profiling

B cell clones were identified using MiXCR software (MiLaboratory)³⁹, capable of generating quantitated clonotypes of immunoglobulins. The same paired-end Illumina sequenced reads mentioned above were merged using concatenation, then imported into MiXCR software. Merged reads were aligned to each other to generate clonotypes of based on VDJ segment regions of unique immunoglobins specific to each sample. Clone data for each sample was grouped based on vaccine received, and time point. Clonotypes from each sample were then separated into T and B cells, based on T-cell receptor or B-cell receptor specific sequences. Prepared data files were then imported into VDJtools (MiLaboratory), for data representation according to established protocol⁴⁰. Briefly, data was represented to show V-J diversity, and quantify unique clonotypes using dendrograms and chord diagrams.

RESULTS

Macrophage recruitment in MacGreen mice following *Bp* challenge

In previous studies it has been shown that macrophages and neutrophils play a protective role in the clearance of *Bp* during naïve infection, and mice immunized with WCV or ACV vaccines. In this study we first visualized macrophage to the site of infection using MacGreen mice. MacGreen mice and C57B6 mice were challenged with a 10^7 dose of WT *Bp* strain. Following challenge we determined an increase in GFP+ cells in the nasal lavage and lung homogenate compared to MacGreen mice that were not challenged (data not shown). We next choose to challenge MacGreen mice with *Bp* isogenic mutant strains lacking either of the main toxins of *Bp* Δ PPT or



Δ ACT to mimic the effect of antibody-mediated neutralization of these antigens. Challenge with

Figure 22: *Bp* challenge of MacGreen mice. (a) Viable bacterial levels of isogenic *Bp* mutant strains were determined by counting of CFUs. (b) Flow cytometric analysis of live, single cells that expressed CD11b+F4/80+GFP+ (macrophages), or CD11b+Gr-1+ (neutrophils) from nasal lavage. (c) Flow cytometric analysis of macrophages and neutrophils from a single cell suspension of lung homogenate. Results are mean \pm SEM (n=4-6) *** p< 0.001, **p<0.01, * p<0.05 determined by one-way ANOVA with Tukey post hoc test.

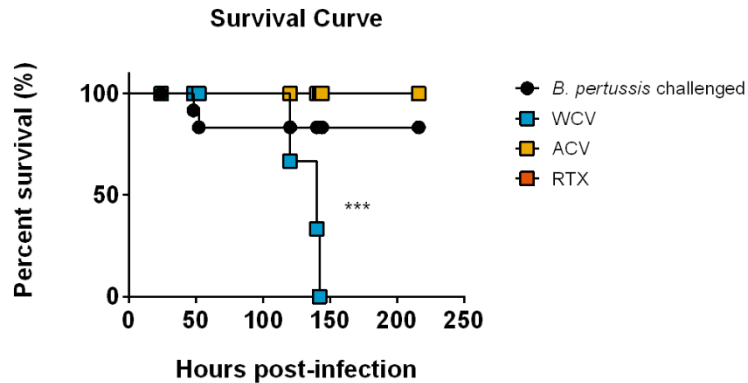


Figure 2: Kaplan- Meier survival curves of NECre luc mice according to immunization group. The survival percentage of remaining NECre luc mice (prior to scheduled euthanasia) immunized with WCV, ACV, RTX, and Bp challenged, or not vaccinated and challenged with Bp. Log-rank (Mantel-Cox) test: *** $p < 0.0005$. In Fig. 1 the time points where mice were euthanized for analysis are indicated. In this survival curve, we are only showing the mice became morbid throughout the study timeframe. Therefore we are showing survival data for 12 of 47 total mice in the final timepoint.

a 10^7 dose of *Bp* resulted in no significant differences in viable bacterial levels, as determined by colony forming units (CFUs) (Fig. 1a). To compare macrophages and neutrophils present at the site of infection we used flow cytometry. The largest differences were seen in the nasal wash where the highest proportion of cells present are immune cells. Mice challenged with the Δ ACT strain had the largest increase in the percentage of macrophages and neutrophils, 27% and 32% higher than non-challenged mice, respectively (Fig1b). Analysis of lung tissue homogenate showed a similar trend in macrophage accumulation however the Δ ACT challenged mice were not significantly different. Lung neutrophils however, were again significantly higher in mice challenge with Δ ACT mutant compared to other stains (Fig1c). The role of autophagy was analyzed using a mouse strain deficit in LC3B, a protein involved in initialization of an autophagosome and a chemical inhibitor of autophagy, chloroquine. Unfortunately, we did not observe significant differences in viable bacterial levels or cell populations (data not shown). Together these data suggest that when ACT is not present there is a higher percentage of live macrophages and neutrophils present.

ACV and WCV immunization of NECre luc mice result in clearance of *Bp*, however WCV immunized mice experienced increased morbidity and mortality.

To characterize the effects of the vaccination on neutrophil recruitment, NECre luc mice were immunized with the vaccines as indicated in Supplementary Table S1, and then boosted with the same vaccine 21 days later by intraperitoneal injection. We sought to compare the neutrophil recruitment in naïve, ACV, WCV, and RTX-only vaccinated NECre luc mice during *Bp* challenge.

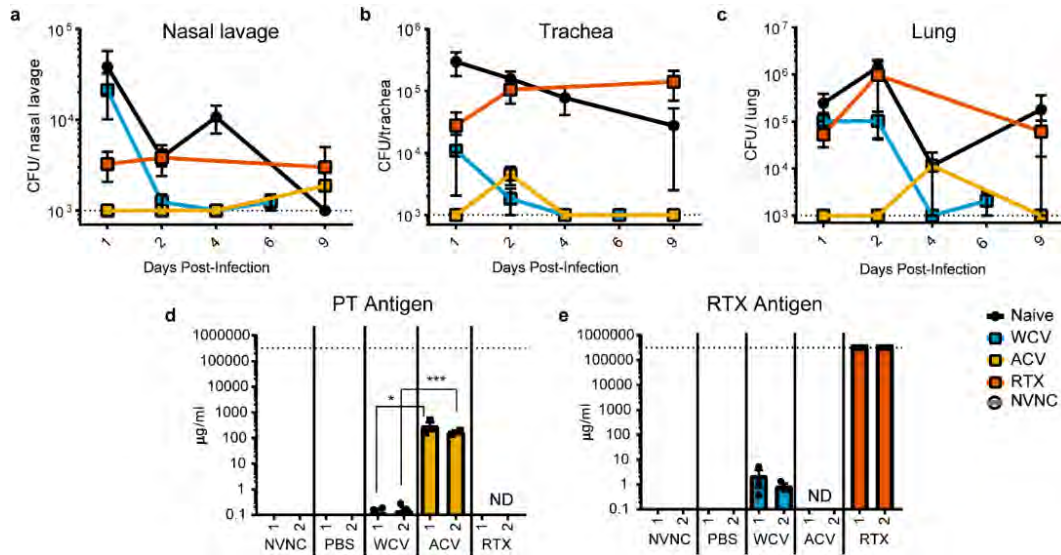


Figure 23: Bacterial burden in respiratory tissue and serological responses to *Bp* challenge of immunized and naïve NECre luc mice. Mice were vaccinated with PBS control vehicle, WCV, ACV, or RTX then *Bp* challenged. At days 1,2,4,6 and 9 p.c. the bacterial burdens were determined by culturing of (A) nasal lavage, homogenates of (B) trachea and (C) lung on BG agar. The dashed line at 1000 CFUs represents the lower limit of detection. Data in each group were compared to PBS control using a two-tailed paired t-test. Bacterial limits in the (A) nasal lavage, (B) trachea, and (C) lungs of NECre luc mice vaccinated with WCV were significantly lower than PBS control at day 2 pc ($p < 0.05$), while ACV followed a similar trend in the (B) trachea ($p = 0.059$) and (C) lung ($p = 0.07$) at day 2 pc. Significant differences are not indicated on the graphs for clarity.

At day 35 post initial immunization, NECre luc mice were challenged with virulent *B. pertussis* strain UT25, by intranasal instillation. A challenge dose of 2×10^7 CFUs *Bp* does not typically cause morbidity in immunocompetent mice (data not shown). We originally planned to euthanize 4 mice per group per experimental day (1, 2, 4, and 9). However, 2 of 13 naïve challenged NECre luc mice were euthanized at day 2 due to morbidity (Fig. 2). At day 6, we unexpectedly observed morbidity, which required euthanasia of all remaining WCV immunized NECre luc mice (Fig. 2). Conversely, no morbidity was observed in the ACV and RTX immunized mice 9 days post *Bp* challenge (Fig. 2). We were surprised to observe morbidity in the WCV immunized mice. Upon determining viable bacterial burden from lung, trachea, and nasal lavage, we observed clearance of *Bp* to our limits of detection in both ACV and WCV immunized mice compared to naïve infection (Fig. 3abc). Taken together, these data suggests that morbidity of the WCV immunized mice was not fully attributed to bacterial burden. Additionally, we determined that vaccination with RTX resulted in 100 percent survival out to 9 days post-challenge (pc), while bacterial burden was similar to naïve infected mice, suggesting that RTX immunization did not improve bacterial clearance (Fig. 3abc) but these data suggest RTX immunization may have protective capacity.

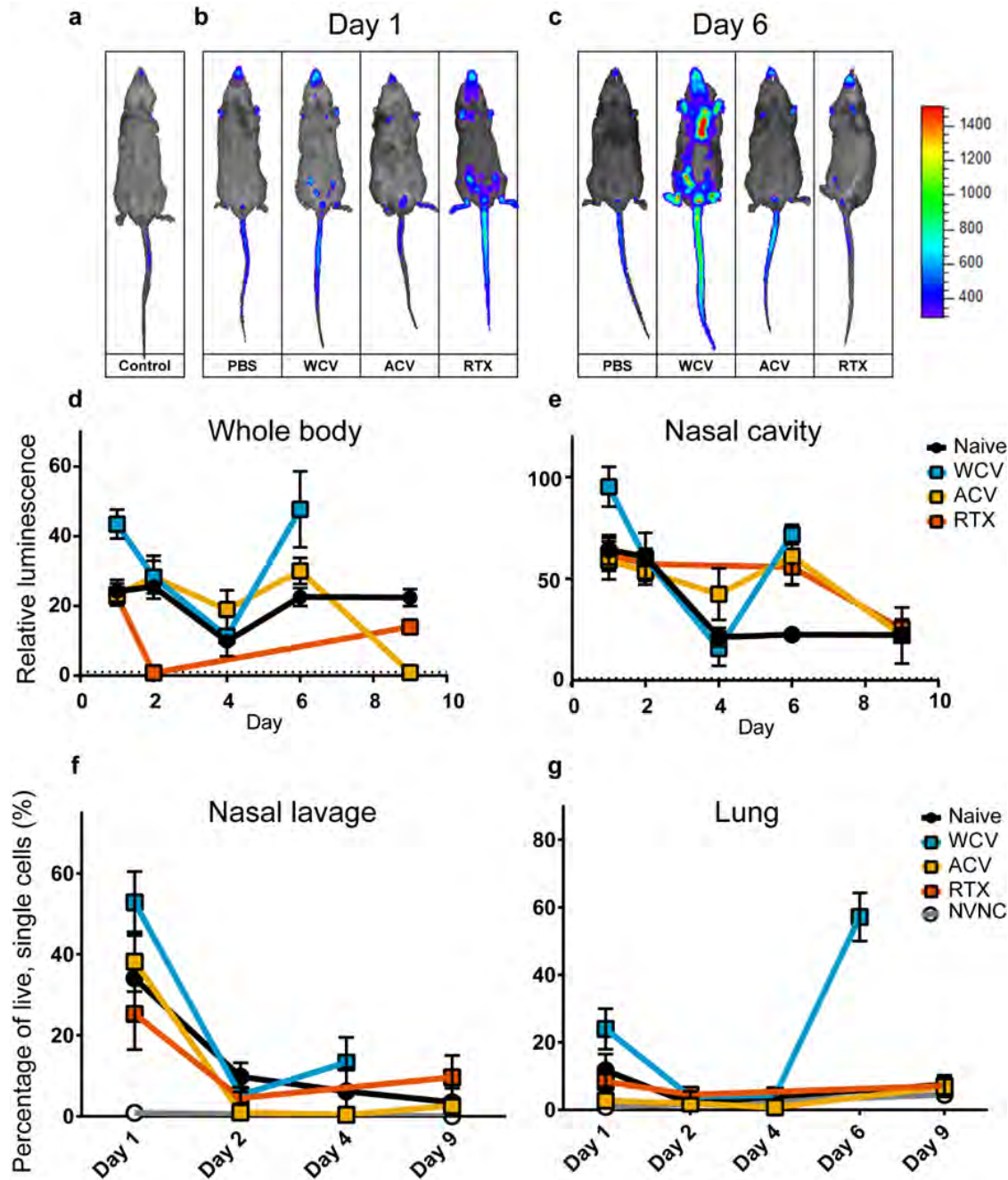


Figure 4: (A) Representative images of naïve, not Bp challenged NECre luc mice. (B) Representative images of PBS control, WCV, ACV, and RTX immunized and Bp challenged NECre luc mice at day 1 pc and (C) day 6 pc (D and E). Luminescence was measured on Xenogen IVIS Lumina II. Relative luminescence levels quantified by fold change of emitted photons/second of NECre luc mice following Bp challenge (N=3-5) compared to average luminescence of naïve, not challenged NECre luc mice (N=5). Neutrophil luminescence of (D) whole animal signal and (E) nasal cavity was determined at days 1,2,4,6, and 9 pc. (f) Quantification of the percentage of live, single cells classified as neutrophils (GR-1+CD11b+) detected in nasal lavage (f) and lung homogenate (g).

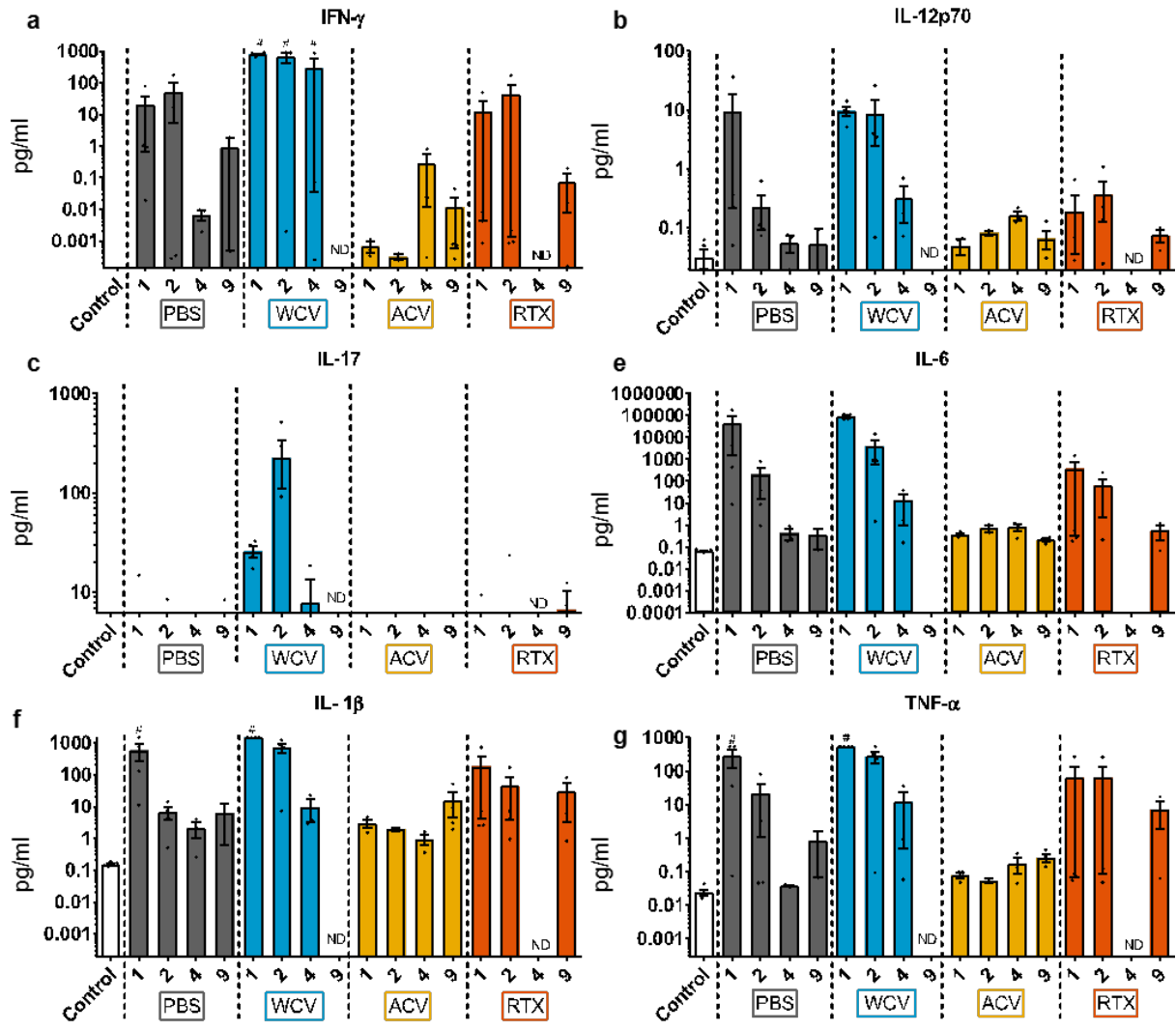


Figure 5: Analysis of cytokine profiles from lungs of naïve and immunized NCRre luc mice post challenge with *Bp*. Th1 associated cytokines from the supernatant of lung homogenates were analyzed at days 1,2,4 and 9 pc. Cytokines (a) IFN- γ , (b) IL-12p70, (c) IL-17, (d) IL-6, (e) IL-1 β , (f) TNF- α were quantified using electrochemiluminescence immunoassays. ND: Sample not determine, #: data above upper limits of detection

Analysis of serological responses of immunized mice.

As expected, the ACV immunized mice were protected against challenge as they rapidly cleared *Bp* (Fig. 3abc). WCV immunized mice did clear *Bp* but this response was delayed compared to the ACV mice. To determine the efficacy of immunization on antibody production, we performed serology analysis. PT is a common antigen of both the ACV and WCV and we observed a significantly higher concentration of anti-PT in the ACV mice compared to the WCV (Fig. 3d). It is possible that this contributes to the difference in rate of *Bp* clearance. Immunization of NCRre mice with RTX with alum adjuvant resulted in high anti-RTX despite the fact that we did not see increased clearance due to RTX immunization. In another study, we immunized CD1 mice with

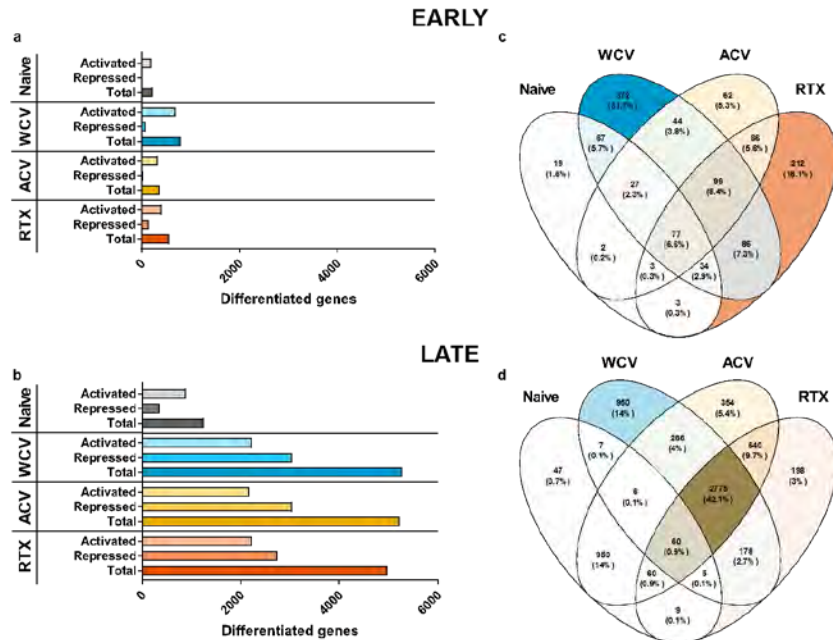


Figure 6: Lung transcriptome profile of vaccinated and challenged NCR luc mice. RNA sequencing was performed on total RNA from homogenized lung on days 1 (Early) or 6/9 (Late) following challenge with *Bp*. (a) The total number of statically differentiated genes found in lung transcriptome at early (a) or late (c) time points. Statistically differentiated genes were categorized as those that were activated or repressed. Venn diagram of statistically differentiated genes either unique or common to vaccinated or naïve groups at early (b) or late (d) time points.

RTX and alum adjuvant and we also saw no clearance of *Bp* compared to non-vaccinated mice (data not shown). Our data suggest that, while immunization with RTX induces antibody production, it is not sufficient to protect mice from *Bp* infection as a single, antigen vaccine.

Spatiotemporal IVIS imaging of neutrophils in naïve and vaccinated NCR luc mice.

Neutrophil accumulation in NCR luc mice were visualized on days 1, 2, 4, 6 and 9 pc. Prior to imaging each day, mice were IP injected with CycLuc1, which is a high sensitivity synthetic luciferin³³. A Lumina II IVIS (Xenogen) was used to capture luciferase driven neutrophil luminescence at indicated time points (Fig. 4 and). Luminescent signal of whole mouse (Fig. 4d) or nasal cavity (Fig. 4e) of vaccinated mice was then compared to signal from naïve, non-infected mice and calculated as fold change. At day 1 pc, we detected significantly higher luminescence in naïve challenged mice compared to naïve non-challenged mice suggesting higher neutrophil accumulation in challenged mice. Furthermore, whole mouse luminescence in WCV immunized and challenged mice luminescence signal was significantly higher than naïve *Bp* challenged mice, ACV and RTX groups at day 1 (Fig. 4d). In general, luminescence signals of all groups decreased across days 2 and 4. However, in the WCV group at day 6, we detected an increase in nasal cavity signal (71-fold) and whole animal luminescence signal (47-fold) compared to naïve not challenged mice (Fig. 4de). Due to variability, this increase was not significant compared to other groups. At this point WCV immunized mice were morbid and required euthanasia. Taken together this data suggests that WCV immunization prior to challenge resulted in increased neutrophil accumulation compared to other vaccination groups. We next aimed to corroborate our IVIS luminescence data with flow cytometric analysis of respiratory tissues.

Validation of neutrophil infiltration in respiratory tissue by flow cytometry

Luminescent signal of luciferase expressing cells typically correlates with the localization of responding cell populations and this has been demonstrated with NECre luc mice³³. To confirm this, we needed to corroborate the luminescent signal by neutrophils, to the number of neutrophils in the respiratory tissues. This was accomplished by performing flow cytometric analysis on respiratory tissue following IVIS imaging. Single cell suspensions from lung tissue or nasal lavage were labelled with antibodies recognizing cell surface markers. We defined neutrophils as CD11b+GR-1+ live cells. Similar to the IVIS data, all *Bp* challenged groups had significantly higher neutrophil percentages in nasal lavage compared to naïve non-challenged mice (Fig. 4f). At day 1 post *Bp* challenge, WCV immunized mice had a significantly higher percentage of neutrophils than ACV immunized mice in nasal lavage. The percentages of neutrophils decreased from day 1 to day 2 in all vaccinated groups as well as the naïve group. At day 4, WCV immunized mice exhibited higher levels of neutrophils than observed at day 2 (Fig. 4g). Correlating with the nasal lavage, WCV mice exhibited significantly higher percentages of neutrophils in the lungs than ACV mice. Lung neutrophils at day 4 were not statistically significant between any of the groups. However, by day 6 there was a 53% increase in lung neutrophils compared to day 4 in the WCV group which directly correlates with the increased luminescent signals measured by IVIS imaging (Fig. 4g).

WCV immunized NECre luc mice induce stronger Th1 immune response compared to ACV immunized mice.

It has been previously documented that upon *Bp* challenge, WCV immunized mice induce a primarily Th1/Th17 immune response, similar to a naïve infection^{12,13,41}. Whereas, ACV immunized mice generate primarily a Th2 response¹¹. We hypothesized that similar to previous murine models, NECre luc mice would induce these immune profiles. To determine cytokine profiles of immunized and challenged mice we determined the concentration of cytokines in lungs of mice using electrochemiluminescent sandwich immunoassays. As expected, our data corroborated with previous data demonstrating an increased Th1 response seen in WCV vaccinated NECre luc mice compared to the ACV group. As expected, we also determined an increased Th1 response in naïve challenged mice. The Th1 response was determined by increased levels of IFN- γ , IL-12p70, and TNF- α (Fig. 5ab), while the Th17 response was qualified by increased IL-17A, IL-6, and IL-1 β (Fig. 5cde) cytokine levels in the lungs of mice. Interestingly, at the time points we observed lung cytokines only, the WCV group produced detectable levels of IL-17A in the lungs of NECre luc mice (Fig. 5c). We also measured similar levels of cytokines related to a Th2 response, IL-5 and IL-4, between WCV and ACV groups (data not shown). The lung cytokine profile from NECre luc mice immunized with RTX resembled a profile of naïve *Bp* challenged mice with the exception of IL-6, which was lower in the RTX group. Taken together these data from the NECre luc mouse model corroborates with previous findings suggesting a strong Th1/Th17 in WCV immunization, which we did not detect in ACV immunization NECre luc mice.

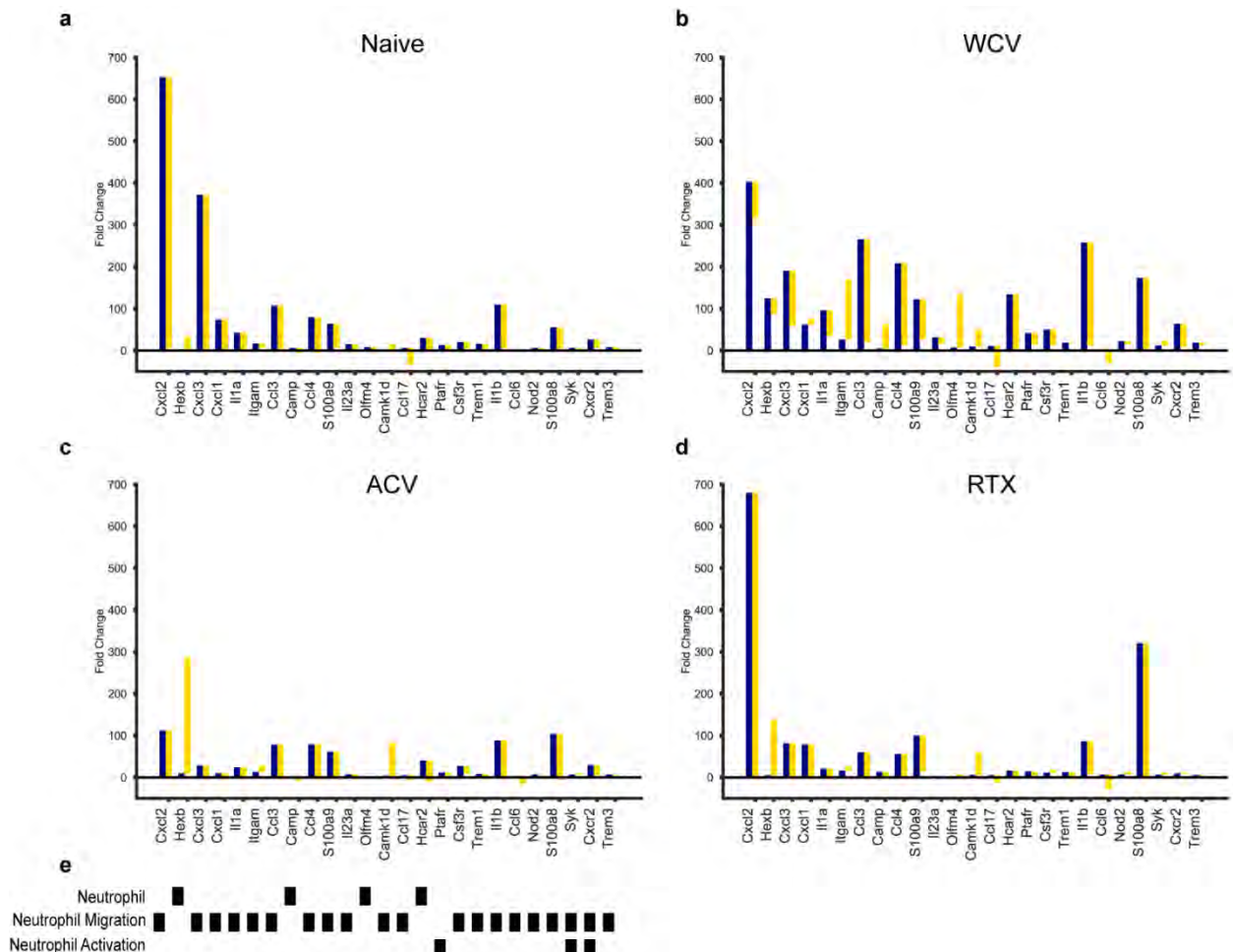


Figure 7: (a) Relativeness of immunoglobulin profiles between vaccinated and challenged, challenged, or non-challenged groups at late time point. (b) Immunoglobulin diversity and frequency of non-challenged control, experimental groups at late time points. Chord diagrams are used to visualize variable – joining segment diversity. Outer arcs demonstrate overall count of a particular variable (upper portion of chord diagram) or joining segment (lower portion of chord diagram) in each group. Inner ribbons represent the linked segments of a clonotype, while the thickness of the ribbon signifies frequency of the clonotype.

Characterizing the gene expression profiles of the lungs of immunized and naïve mice after *Bp* challenge

Current and past *Bp* immune response studies have focused on a limited set of known immunological responses to *Bp* challenge such as: bacterial burden, antibody response, recruitment of phagocytes, cytokine profiles, and others^{11,42}. Whooping cough is classified as a toxin mediated disease, due mainly to the activity of pertussis and adenylate cyclase toxins which affect a wide array of host cells^{3,43}. It is then conceivable that *Bp* infection would have a broader effect on the respiratory tissue as a whole system beyond the predictable individual immune response factors. To address this, we employed RNA sequencing (RNAseq) to observe the effect of *Bp* challenge on the lungs of immunized and naïve NECre luc mice at a transcriptomic level. This would enable us to characterize the response to infection, as well as the vaccine induced responses. We expected that we would observe a distinct set of genes among

all challenged groups that corresponded to *Bp* infection. Additionally, we sought to discern the unique gene expression profiles in response to each of the immunized groups.

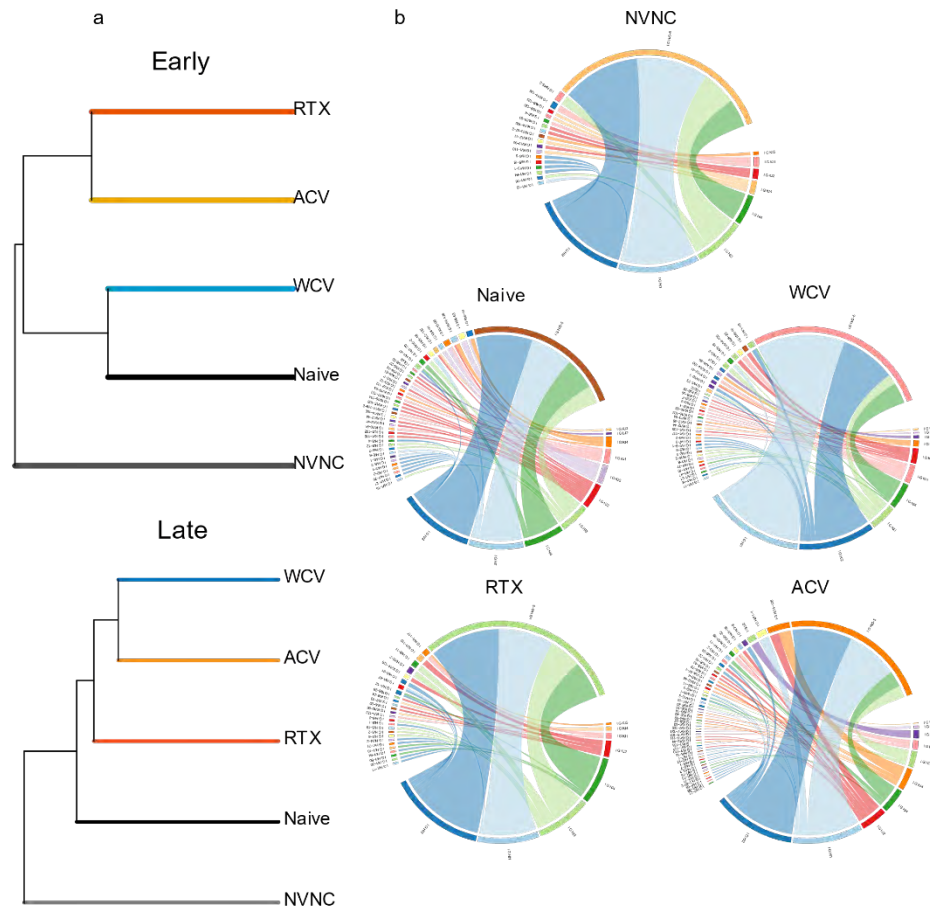


Figure 8: Differentiated genes associated with neutrophil recruitment at early and late time points following *Bp* challenge. Gene expression profiles are shown for (a) Naïve, (b) WCV, (c) ACV, and (d) RTX immunized and challenged mice. Blue and gold bars are the fold change compared to control non-challenge non-vaccinated mice at early and late time points, respectively. Genes shown are the 25 genes with the highest variance across all groups between early and late time point. Genes were ranked based on variance in fold change across groups for the early and late time points, separately. Then, to get a list that better represented genes with an overall fold change throughout the experiment, calculated ranks from both time points were combined to generate comprehensive ranks.

To perform RNAseq analysis, lungs from NECre luc mice were

harvested at an early time point (day 1) following *Bp* challenge and at a late time point (day 6 or 9). RNA from the lungs of the mice were isolated. Libraries were prepared and sequenced on the Illumina HiSeq 1500 platform. To characterize transcriptional responses to *Bp* challenge in naïve or vaccine mice (ACV, WCV, RTX), we compared the challenged samples to control mice that were not immunized and not challenged. Based on this, we expected to be able to determine the both the immunological (innate and adaptive) and the non-immunological responses to *Bp* challenge. We determined the differentially expressed genes (DEGs) for both early (day 1) and late (day 6 or 9 depending on group) time points. The total numbers of dysregulated genes are shown in Fig. 6. Overall, there were more dysregulated genes at the later time point than early after

challenge (Fig. 6ac). At 1 day pc, the WCV group had the most genes activated (Fig. 6a). Of the genes that were differentially expressed at day 1 in the WCV, 54% were unique and not differentially regulated in the other groups (372 of 686). At the late time points, there were more common dysregulated genes and only 18% were unique to the WCV. We found that 6.6% of DEGs (77) were common to all groups either challenged with *Bp* following immunization or naïve challenge, suggesting these genes were common to infection (Fig. 6b). A comparison between naïve challenged mice and immunized challenged mice showed 8.4% of DEGs (99) common to all immunized groups. At the later time point, 42% of total DEGs (2775 of 6595) were in common with the WCV, ACV, RTX groups unlike the early time which only had 8.4% of DEGs (99 of 1173) of in common among all vaccinated groups (Fig. 7bd). Cumulatively, this data suggests that 1) WCV vaccination induces a more diverse early response to *Bp* challenge due to the higher number of unique genes compared to other groups and 2) at the later time point all vaccination groups have a more similar lung transcriptome.

Analysis of neutrophil specific gene signatures

Due to the neutrophil accumulation seen following *Bp* challenge of WCV immunized NECre luc mice, we first chose to investigate genes related to neutrophil activity. We selected genes with neutrophil related GO terms and then plotted the relative fold changes for this subset of genes for each immunization group (Fig. 7). The fold change of these genes from either the naïve challenged, or immunized and challenged groups was compared to naïve, not infected control mice. The expression levels of these genes is shown in relation to the early and late time points (Fig. 7). *Cxcl2* is a chemokine that is produced by monocytes and neutrophils at sites of infection⁴⁴ Convalescent mice that have been previously challenged with *Bp*, express lower amounts of *Cxcl2* when re-challenged with *Bp* than naïve mice⁴⁵. We observed that ACV immunized mice expressed less *Cxcl2* than naïve mice (Fig. 7ac) and ACV mice returned to uninfected levels of *Cxcl2* by the late time point whereas naïve mice remained 314-fold higher than uninfected mice. High expression of *Cxcl2* occurred in the WCV mice, but *Cxcl2* expression remained high at the late time point (Fig. 7b). The RTX immunized group had the highest expression of *Cxcl2* and it completely decreased to below uninfected levels by day 9 (Fig. 7d). All of the groups showed increases in a number of C-X-C and C-C family chemokines (*Cxcl3*, *Cxcl1*, *Ccl3*, *Ccl4*, *Ccl6* and *Ccl17*). Interestingly *Cxcl1* gene expression was increased at day 1 in all groups (Fig. 7). IL-23 is a cytokine involved in the IL-17 response and here we detected increased IL-23 in only the WCV group as would be expected (Fig. 7b). Tumor necrosis factor (*Tnf*) gene expression was increased in WCV, RTX, and ACV mice, but in ACV mice it returned to lower than uninfected expression levels at day 9 (data not shown). Ross *et al.* demonstrated that IL-17A promotes production of CXCL1 during *Bp* challenge¹¹. In our cytokine analysis, only the WCV mice had sufficient IL-17 to be detected in the lung homogenates (Fig. 5c). Taken together these data suggest that although we did not observe high *IL-17A* gene expression in the transcriptome or in the IL-17 cytokine analysis, there could still be sufficient IL-17A in the Naïve, ACV, and RTX challenged mice that could account for the increased *CXCL1* gene expression.

Overall the WCV mice had higher expression of more neutrophil genes than any of the other groups (Fig. 7). Expression of these neutrophil signatures did not return to uninfected levels which corroborates IVIS (Fig. 4) and flow cytometry analyses (Fig. 4fg). Neutrophil gene expression in ACV mice was dynamic and returned to levels lower than uninfected mice by day 9, which correlates with the fact that the ACV mice did not have detectable *Bp* in their lungs at day 9

indicating the initial challenge does had been cleared (Fig. 3). Overall the ACV and WCV signatures were the most dissimilar and yet the RTX and Naïve mice were the most similar (Fig. 7) which correlates with the fact that RTX mice still have detectable *Bp* in their nares, trachea and lungs at day 9. These data confirm our neutrophil observations but also enhance our analysis of the neutrophil dynamic in the context of vaccination status and *Bp* challenge.

Analysis of immune response from NECre luc lung transcriptome

As mentioned previously, we measured elevated levels of Th1 immune response cytokines following challenge of WCV and naïve NECre luc. We corroborated these findings upon analysis of the lung transcriptome, by observing distinct T helper cell gene signatures between WCV, ACV, and RTX vaccination. We observed 15 significantly upregulated genes related to a Th1 immune response in our data set, out of these 12 were highest in the WCV vaccinated group. As expected, Th17 associated genes were consistently higher in the WCV vaccinated group.

B cell expansion between vaccinations

It has been established that B cells are required for the clearance of *Bp* in mice^{46,47} and that ACV immunization protects through neutralizing antibodies. However; passive immunized mice by transfer of serum from a convalescent mouse did not significantly reduce *Bp* burden⁴⁷. To further investigate antibody production between WCV and ACV immunized mice, we aimed to determine the diversity of B cell clone expansion between vaccinated and non-vaccinated challenged mice. Using MiXCR software, the same illumina sequenced reads mentioned above were analyzed specifically for immunoglobulin profiling³⁹. Individual B cell clones were identified by B cell receptor sequence and clonal expansion was accessed by immunoglobulin diversity and frequency between the vaccinated and challenged, naïve challenged, and non-challenged control groups. At the early time point day 1 pc, immunoglobulin diversity and frequency of B cells depicted a close relation between the ACV and RTX vaccination groups, as also did WCV and naïve challenged mice (Fig. 8a). This response shifted by the late time point (days 6 or 9), when we observed that WCV and ACV groups were more similar. Using this approach, we were able to determine the individual variable and joining segments abundance, and the frequency of which a particular was found. Not surprisingly, we observed the highest degree of diversity at the late time point. WCV and ACV were the most similar due to a higher number and abundance of clonotypes, (Fig. 8b). We focused our analysis on the diversity of the third complementarity-determining region (CDR3) of the heavy Ig chain, because this region has been shown to be necessary for antigen specificity⁴⁸. The highest abundant CDR3 region, NQHLEW, was present only in the WCV immunized mice, while the other 10 highest CDR3 regions were shared across vaccine groups. Together this data suggests that clones generated from acellular based vaccines (ACT and RTX) are more closely related because they are generated to a limited number of antigens. However, by the late timepoint proliferation of specific B cell clones generated from WCV has created the same diversity seen in the ACV clones.

DISCUSSION

In this study, we compared the early innate immune response to isogenic mutant strains and adaptive immune responses of immunized NECre luc mice vaccinated with ACV or WCV vaccines, to mice immunized with a truncated ACT toxin absorbed to alum (RTX), or non-vaccinated naïve mice following challenge with *Bp*. ACV and WCV immunized mice cleared *Bp*

challenge but distinctive immune responses for observed. We also determined that the RTX antigen alone was not protective as a single antigen vaccine with alum adjuvant. We utilized IVIS imaging to track the recruitment of neutrophils to the respiratory tract of challenged mice from days 1-9 pc. Thereby demonstrating a dramatic increase in the amount of neutrophils recruited to the lungs and nasal cavity of WCV immunized mice compared to ACV immunized mice when followed by *Bp* challenge. These data were also supported by flow cytometry and cytokine analysis. Furthermore, by performing RNA sequencing on the lung transcriptome during infection in vaccinated or naïve mice we described unique gene expression profiles depending on the vaccination status of the mice. We also used the RNA sequencing to begin to describe the immunoglobulin diversity induced by each vaccine.

Upon initial *Bp* challenge, we observed activation of neutrophil associated genes in all groups, however it was only in the WCV immunized mice that we saw increased neutrophil genes still elevated at the late time point. Neutrophilia and elevated neutrophil related genes at the late time point when bacterial numbers are greatly reduced indicates either over activation of neutrophil “chemokine storm,” or possibly a lack of neutralization of bacterial toxins. Multiple studies suggest that PT is responsible for neutrophilia and leukocytosis following *Bp* infection^{32,49-51}. Immunization with the ACV induced 1146-fold more anti-PT than WCV immunization at day 2 (Fig. 3d). It is possible that this lack of antibody production resulted in not sufficient neutralization of PT within the mice which exacerbated the neutrophilia. Surprisingly, the highest neutrophil accumulation was determined at day 6 pc when bacterial levels were similar to those of ACV protected mice (Fig. 3). These findings suggest that while WCV immunization is protective at clearing infection in NECre luc mice; however it induced severe neutrophilia. It is also interesting to point out that the neutrophil response in WCV mice decreased at days 2 and 4 but highly returned at day 6 (Fig. 4). At day 2 we observed a significant increase in IL-17 in the lungs of WCV mice (Fig. 5c). These data suggest that IL-17 production leads to the high neutrophil recruitment observed at day 6. Stephen Morse observed dose-dependent leukocytosis in mice following vaccination with killed *Bp*³¹. In this study, NECre luc mice were immunized with 1/5th the human dose of WCV. We now realize that this dose is likely well above the proportional weight of a mouse compared to a human. It is possible that this high vaccine dose induced the hyper leukocytosis, similar to dose-dependent increase that Morse observed. It is known that hyperleukocytosis is associated with death in infant cases^{1,52-54}, and that PT is responsible for inducing leukocytosis. Furthermore, mice and baboons infected with *Bp* then treated with anti-PT antibodies had lower levels of leukocytosis compared to non-infected controls⁴⁹. An epidemiological study found that in unvaccinated individuals with pertussis 72% of patients experienced leukocytosis⁵⁵. Here in our study, we observed that WCV immunized NECre luc mice experienced neutrophilia and morbidity which highlights the potential issues of using WCVs. It would be interesting to determine the relationship of neutrophilia and WCV immunization in epidemiological past studies, but we have not been successful in finding a study that specifically looked at neutrophilia because most note general leukocytosis.

In MacGreen mice we observed a higher percentage of macrophages and neutrophils present in lung homogenates and nasal lavage. In these experiments the isogenic mutants represented what could be expected from complete neutralization of one of the major *Bp* toxins. These data suggest that neutralization of ACT could lead to greater leukocyte survival at early time points following infection. This finding is supported though previous studies in which ACT has been found to lead

to cell apoptosis^{6,56}.

In NECre luc mice, the ACV was clearly more protective and less detrimental to the mice than the WCV. Truncated²¹ and full length ACT²¹ purified from *Bp* culture has been shown to be a protective antigen. Wang *et al.* described the RTX region of ACT as highly immunogenic and easily purified as a recombinant protein²². We have observed that immunization of CD1 mice with RTX and alum adjuvant results in high anti-RTX titers (data not shown). Here we immunized NECreluc mice with RTX and alum, but no protection was observed (Fig. 3abc). The previous studies^{21,57} were performed with strain 18323 and the antigen was directly isolated from *Bp*. It is now known that strain 18323, is an outlier compared to most other global *B. pertussis* strains and Guiso *et al.* noted that strain 18323 produces less PT than the Tohama I type strain²¹. From our work, we know that UT25 produces more PT and ACT than Tohama I (data not shown). It is possible that due to the increased PT levels produced by UT25, vaccination with RTX was not sufficient to block colonization and proliferation *in vivo*. Although RTX immunization did not result in clearance of *Bp* from NECre luc mice, we did observe a reduction in the proinflammatory cytokine IL-6 in the RTX group compared to not vaccinated and WCV vaccinated and challenged mice (Fig. 5e). PT and ACT have both been shown to induce the production of IL-6 in human cell lines^{58,59}. The anti-ACT antibodies generated by RTX vaccination may play a role in reducing the levels of IL-6 due to reducing the activity of ACT. We hypothesize that it is necessary to neutralize both PT and ACT to provide optimal protection and in future studies we will test RTX as an antigen in a multivalent ACV containing PT antigen.

Using standard immunological analyses, we observed typical Th2 and Th1/17 responses in ACV and WCV immunized mice respectively. *Bp* utilizes PT and ACT to facilitate survival in the host and most studies about the PT/ACT specific effects have been performed on cell cultures *in vitro*. Microarray analysis has been used to profile the lung transcriptome of mice challenged with *Bp*^{45,60}. Here, we sought to use RNAseq to investigate the overall gene expression profiles of the murine lung in response to *Bp* challenge. Consistent with other studies we observed an increase in cytokines response for innate immune cell recruitment such as KC, TNF- α , IL-12p70, IL-6^{43,45,61} as early as day 1 pc in naïve and WCV immunized mice, although this response was higher in the WCV group (Fig. 5).

Analysis of the lung transcriptome 1 day after *Bp* challenged exhibited a distinct profile of WCV vaccination compared to ACV, RTX, or naïve infected mice. This response was consistent with our WCV cytokine profile demonstrating a strong proinflammatory response. Similarly, transcriptome data from others during early *Bp* infection noted an increase in chemokines such as Cxcl2, Cxcl10, Cxcl3, Ccl3, Cxcl1, and Ccl4^{45,61}. In Raeven *et al.*, convalescent mice previously infected with *Bp* exhibited higher expression of these chemokines compared to naïve mice, similar to our whole cell transcriptome where these chemokines are consistently higher than the naïve mice (Fig. 7). Genes related to neutrophils revealed a similar profile between naïve mice and RTX vaccinated mice further suggesting that RTX and alum alone did not induce protection.

Our overall transcriptomic profiling revealed thousands of significant gene expression changes (Fig. 6). After analyzing the neutrophil (Fig. 7), the T cell specific, and innate gene changes we then sought to specifically characterize B cell clone diversity. The RNAseq reads were re-processed with the MiXCR algorithm and we analyzed the abundance and diversity of VDJ

clonotypes (Fig. 8). Besides the T cell response differences of the ACV and WCV (Th2 v. Th1/Th17) another significant difference between these two vaccines is the number of antigens. ACVs have 2-5 antigens (PT, FHA, PRN, FIM2/3) but the WCV hypothetically has ~3,000 antigens. In light of this, it would be logical to hypothesize that the WCV would induce a vast antibody repertoire as measured by many VDJ clonotypes. However, we observed a greater diversity and abundance in the ACV group compared to the WCV at both early and late time points (Fig. 7). It is important to point out that this analysis was performed on total lung RNA. If we were to isolate B cells and sequence deeper we would expect to more thoroughly characterize the repertoire. These data are interesting but we do not know which clone types result in functional antibodies that protect against *Bp*. Further analysis is required to bridge the gap between clonotypes and functional/protective antibodies.

Using NeCRE luc mice we demonstrated a mouse model that is capable of tracking neutrophil migration throughout a *Bp* respiratory infection. These data demonstrate how analysis of cellular responses through *in vivo* imaging can be used to provide a quantitative parameter throughout a study. This model can be applied to other bacterial infection models or cancer tumor progression models where following the same mouse throughout a study would be beneficial. We chose to vaccinate NeCRE luc mice with 1/5th the human dose consistent with previous studies^{11,42}. In light of the responses observed in this study and by simple mouse to human weight calculations, we hypothesize that the 1/5th human dose is not physiologically correct. In an effort to determine an appropriate dose, we are currently titrating the ACV and WCV doses to better model *Bp* challenge in mice. Here in this study, we also added next generation sequencing technology to expand upon the immunological findings. RNAseq analysis can be further employed to understand key cell populations and how they are impacted by both immunization and *Bp* challenge. Our current goal is to continue to refine the murine challenge models with new technological approaches in order to facilitate formulation of new pertussis vaccines.

These findings suggest that by corroborating specific RNAseq analysis with data from classic immunological techniques such as CFUs, cellular responses, and cytokine profiles we can discover novel intricacies of vaccine induced immunity to *Bp*.

PRESENTATION AND PUBLICATION OF THE FINDINGS

This work has been presented at the International *Bordetella* Society meeting in New Orleans, LA., the Mid-Atlantic Microbial Pathogenesis Meeting in Wintergreen, VA, the Alleghany branch of the American Society of Microbiology, Erie, PA, and at the Van Liere Research Conference Morgantown, WV. This fall this manuscript will be sent to a peer-reviewed journal for publication.

ACKNOWLEDGEMENTS

I would like to thank the NASA WV Space Grant Consortium for a contribution to the funding this work and the experience of managing grant funding. The funding for this project has set the ground work for my dissertation research and allowed our project to fully develop. I would like to thank my mentor Dr. F. Heath Damron for his gracious support and patience in my research and career development. I would also like to thank WVU Core facilities directors for their training. Finally, I thank Dr. Mariette Barbier, and the members of the Damron and Barbier labs for their support and help with experiments. I would also to acknowledge the Marshall University CORE

facilities and RNA sequencing which was funded by the WV InBRE grant P20 GM103434.

REFERENCES

- 1 Paddock, C. D. *et al.* Pathology and pathogenesis of fatal *Bordetella pertussis* infection in infants. *Clin Infect Dis* **47**, 328-338, doi:10.1086/589753 (2008).
- 2 Spangrude, G. J., Sacchi, F., Hill, H. R., Van Epps, D. E. & Daynes, R. A. Inhibition of lymphocyte and neutrophil chemotaxis by pertussis toxin. *J Immunol* **135**, 4135-4143 (1985).
- 3 Carbonetti, N. H., Artamonova, G. V., Andreasen, C. & Bushar, N. Pertussis toxin and adenylate cyclase toxin provide a one-two punch for establishment of *Bordetella pertussis* infection of the respiratory tract. *Infect Immun* **73**, 2698-2703, doi:10.1128/IAI.73.5.2698-2703.2005 (2005).
- 4 Andreasen, C., Powell, D. A. & Carbonetti, N. H. Pertussis toxin stimulates IL-17 production in response to *Bordetella pertussis* infection in mice. *PLoS One* **4**, e7079, doi:10.1371/journal.pone.0007079 (2009).
- 5 Carbonetti, N. H. Pertussis toxin and adenylate cyclase toxin: key virulence factors of *Bordetella pertussis* and cell biology tools. *Future Microbiol* **5**, 455-469, doi:10.2217/fmb.09.133 (2010).
- 6 Confer, D. & Eaton, J. Phagocyte impotence caused by an invasive bacterial adenylate cyclase. *Science* **217**, 948-950, doi:10.1126/science.6287574 (1982).
- 7 Sebo, P., Osicka, R. & Masin, J. Adenylate cyclase toxin-hemolysin relevance for pertussis vaccines. *Expert Review of Vaccines* **13**, 1215-1227, doi:10.1586/14760584.2014.944900 (2014).
- 8 Howson CP, H. C., Fineberg HV. *Histories of pertussis and rubella vaccines. Adverse effects of Pertussis and Rubella Vaccines.* 9-31 (National Academy Press, 1991).
- 9 Gold, M. S. Hypotonic-Hyporesponsive Episodes Following Pertussis Vaccination. *Drug Safety* **25**, 85-90, doi:10.2165/00002018-200225020-00003 (2002).
- 10 Donnelly, S., Loscher, C. E., Lynch, M. A. & Mills, K. H. G. Whole-Cell but Not Acellular Pertussis Vaccines Induce Convulsive Activity in Mice: Evidence of a Role for Toxin-Induced Interleukin-1 β in a New Murine Model for Analysis of Neuronal Side Effects of Vaccination. *Infection and Immunity* **69**, 4217-4223, doi:10.1128/IAI.69.7.4217-4223.2001 (2001).
- 11 Ross, P. J. *et al.* Relative contribution of Th1 and Th17 cells in adaptive immunity to *Bordetella pertussis*: towards the rational design of an improved acellular pertussis vaccine. *PLoS Pathog* **9**, e1003264, doi:10.1371/journal.ppat.1003264 (2013).
- 12 Mills, K. H. G., Ryan, M., Ryan, E. & Mahon, B. P. A murine model in which protection correlates with pertussis vaccine efficacy in children reveals complementary roles for humoral and cell-mediated immunity in protection against *Bordetella pertussis*. *Infection and Immunity* **66**, 594-602 (1998).
- 13 Warfel, J. M. & Merkel, T. J. *Bordetella pertussis* infection induces a mucosal IL-17 response and long-lived Th17 and Th1 immune memory cells in nonhuman primates. *Mucosal Immunol* **6**, 787-796, doi:10.1038/mi.2012.117 (2013).
- 14 Fedele, G. *et al.* *Bordetella pertussis* commits human dendritic cells to promote a Th1/Th17 response through the activity of adenylate cyclase toxin and MAPK-pathways. *PLoS One* **5**, e8734, doi:10.1371/journal.pone.0008734 (2010).
- 15 Mills, K. H., Ross, P. J., Allen, A. C. & Wilk, M. M. Do we need a new vaccine to control the re-emergence of pertussis? *Trends Microbiol* **22**, 49-52, doi:10.1016/j.tim.2013.11.007 (2014).
- 16 Klein, N. P., Bartlett, J., Fireman, B. & Baxter, R. Waning Tdap Effectiveness in Adolescents. *Pediatrics* **137**, e20153326, doi:10.1542/peds.2015-3326 (2016).
- 17 Warfel, J. M., Beren, J. & Merkel, T. J. Airborne transmission of *Bordetella pertussis*. *J Infect Dis* **206**, 902-906, doi:10.1093/infdis/jis443 (2012).
- 18 Althouse, B. M. & Scarpino, S. V. Asymptomatic transmission and the resurgence of *Bordetella pertussis*. *BMC Medicine* **13**, 146, doi:10.1186/s12916-015-0382-8 (2015).
- 19 Betsou, F., Sebo, P. & Guiso, N. CyaC-mediated activation is important not only for toxic but also for protective activities of *Bordetella pertussis* adenylate cyclase-hemolysin. *Infection and Immunity* **61**, 3583-3589 (1993).
- 20 Cheung, G. Y. *et al.* Effect of different forms of adenylate cyclase toxin of *Bordetella pertussis* on protection afforded by an acellular pertussis vaccine in a murine model. *Infect Immun* **74**, 6797-6805, doi:10.1128/IAI.01104-06 (2006).

- 21 Guiso, N., Szatanik, M. & Rocancourt, M. Protective activity of Bordetella adenylate cyclase-hemolysin against bacterial colonization. *Microbial Pathogenesis* **11**, 423-431, doi:[http://dx.doi.org/10.1016/0882-4010\(91\)90038-C](http://dx.doi.org/10.1016/0882-4010(91)90038-C) (1991).
- 22 Wang, X. & Maynard, J. A. The Bordetella Adenylate Cyclase Repeat-in-Toxin (RTX) Domain Is Immunodominant and Elicits Neutralizing Antibodies. *The Journal of Biological Chemistry* **290**, 3576-3591, doi:10.1074/jbc.M114.585281 (2015).
- 23 Lamberti, Y. A., Hayes, J. A., Perez Vidakovics, M. L., Harvill, E. T. & Rodriguez, M. E. Intracellular Trafficking of Bordetella pertussis in Human Macrophages. *Infection and Immunity* **78**, 907-913, doi:10.1128/iai.01031-09 (2010).
- 24 Harvill, E. T., Cotter, P. A. & Miller, J. F. Pregenomic Comparative Analysis between Bordetella bronchiseptica RB50 and Bordetella pertussis Tohama I in Murine Models of Respiratory Tract Infection. *Infection and Immunity* **67**, 6109-6118 (1999).
- 25 Kirimanjeswara, G. S., Agosto, L. M., Kennett, M. J., Bjornstad, O. N. & Harvill, E. T. Pertussis toxin inhibits neutrophil recruitment to delay antibody-mediated clearance of Bordetella pertussis. *J Clin Invest* **115**, 3594-3601, doi:10.1172/JCI24609 (2005).
- 26 Andreasen, C. & Carbonetti, N. H. Role of neutrophils in response to Bordetella pertussis infection in mice. *Infect Immun* **77**, 1182-1188, doi:10.1128/IAI.01150-08 (2009).
- 27 Goodwin, M. S. & Weiss, A. A. Adenylate cyclase toxin is critical for colonization and pertussis toxin is critical for lethal infection by Bordetella pertussis in infant mice. *Infection and Immunity* **58**, 3445-3447 (1990).
- 28 Locht, C., Coutte, L. & Mielcarek, N. The ins and outs of pertussis toxin. *FEBS Journal* **278**, 4668-4682, doi:10.1111/j.1742-4658.2011.08237.x (2011).
- 29 Froehlich. Beitrag zur pathologie des Keuchhustens. *Jahrb fur Kinderheilkunde* **44** (1897).
- 30 Meunier, H. De la leucocytose dans la coqueluche. *CR Soc Biol* **50** (1898).
- 31 Morse, S. I. Studies on the lymphocytosis induced in mice by Bordetella pertussis. *The Journal of experimental medicine* **121**, 49-68 (1965).
- 32 Morse, S. I. & Riester, S. K. Studies on the leukocytosis and lymphocytosis induced by Bordetella pertussis : I. Radioautographic analysis of the circulating cells in mice undergoing pertussis-induced hyperleukocytosis. *The Journal of experimental medicine* **125**, 401-408 (1967).
- 33 Weiner, Z. P. *et al.* Circulating lethal toxin decreases the ability of neutrophils to respond to Bacillus anthracis. *Cellular Microbiology* **16**, 504-518, doi:10.1111/cmi.12232 (2014).
- 34 Stainer, D. W. & Scholte, M. J. A simple chemically defined medium for the production of phase I Bordetella pertussis. *J Gen Microbiol* **63**, 211-220 (1970).
- 35 Evans, M. S. *et al.* A synthetic luciferin improves bioluminescence imaging in live mice. *Nat Meth* **11**, 393-395, doi:10.1038/nmeth.2839 (2014).
- 36 Damron, F. H. F. H., Oglesby-Sherrouse, A. G., Wilks, A. & Barbier, M. Dual-seq transcriptomics reveals the battle for iron during Pseudomonas aeruginosa acute murine pneumonia. *Scientific reports* **6** (2016).
- 37 Venny. An interactive tool for comparing lists with Venn's diagrams (2007-2015).
- 38 Carbon, S. *et al.* AmiGO: online access to ontology and annotation data. *Bioinformatics* **25**, 288-289, doi:10.1093/bioinformatics/btn615 (2009).
- 39 Bolotin, D. A. *et al.* MiXCR: software for comprehensive adaptive immunity profiling. *Nat Meth* **12**, 380-381, doi:10.1038/nmeth.3364 (2015).
- 40 Shugay, M. *et al.* VDJtools: Unifying Post-analysis of T Cell Receptor Repertoires. *PLoS Computational Biology* **11**, 1-16, doi:10.1371/journal.pcbi.1004503 (2015).
- 41 Higgs, R., Higgins, S. C., Ross, P. J. & Mills, K. H. Immunity to the respiratory pathogen Bordetella pertussis. *Mucosal Immunol* **5**, 485-500, doi:10.1038/mi.2012.54 (2012).
- 42 Alvarez Hayes, J. *et al.* Bordetella pertussis iron regulated proteins as potential vaccine components. *Vaccine* **31**, 3543-3548, doi:<http://dx.doi.org/10.1016/j.vaccine.2013.05.072> (2013).
- 43 Andreasen, C. & Carbonetti, N. H. Pertussis toxin inhibits early chemokine production to delay neutrophil recruitment in response to Bordetella pertussis respiratory tract infection in mice. *Infection and Immunity* **76**, 5139-5148, doi:10.1128/IAI.00895-08 (2008).
- 44 Alves-Filho, J. C. *et al.* Regulation of chemokine receptor by Toll-like receptor 2 is critical to neutrophil migration and resistance to polymicrobial sepsis. *Proceedings of the National Academy of Sciences* **106**, 4018-4023, doi:10.1073/pnas.0900196106 (2009).

- 45 Raeven, R. H. M. *et al.* Immunological Signatures after *Bordetella pertussis* Infection Demonstrate Importance of Pulmonary Innate Immune Cells. *PLoS ONE* **11**, e0164027, doi:10.1371/journal.pone.0164027 (2016).
- 46 Mahon, B. P., Sheahan, B. J., Griffin, F., Murphy, G. & Mills, K. H. G. Atypical Disease after *Bordetella pertussis* Respiratory Infection of Mice with Targeted Disruptions of Interferon- γ Receptor or Immunoglobulin μ Chain Genes. *The Journal of experimental medicine* **186**, 1843-1851 (1997).
- 47 Kirimanjesswara, G. S., Mann, P. B. & Harvill, E. T. Role of Antibodies in Immunity to *Bordetella* Infections. *Infection and Immunity* **71**, 1719-1724, doi:10.1128/iai.71.4.1719-1724.2003 (2003).
- 48 Xu, J. L. & Davis, M. M. Diversity in the CDR3 Region of V_H Is Sufficient for Most Antibody Specificities. *Immunity* **13**, 37-45, doi:10.1016/S1074-7613(00)00006-6 (2000).
- 49 Nguyen, A. W. *et al.* A cocktail of humanized anti-pertussis toxin antibodies limits disease in murine and baboon models of whooping cough. *Science translational medicine* **7**, 316ra195-316ra195, doi:10.1126/scitranslmed.aad0966 (2015).
- 50 Im, S.-Y. *et al.* Dual effects of pertussis toxin on murine neutrophils in vivo. *Inflammation* **13**, 707-726, doi:10.1007/bf00914314 (1989).
- 51 Carbonetti, N. H. Pertussis leukocytosis: mechanisms, clinical relevance and treatment. *Pathog Dis* **74**, doi:10.1093/femspd/ftw087 (2016).
- 52 Winter, K. *et al.* Risk Factors Associated With Infant Deaths From Pertussis: A Case-Control Study. *Clinical Infectious Diseases* **61**, 1099-1106, doi:10.1093/cid/civ472 (2015).
- 53 Briand, V., Bonmarin, I. & Lévy-Bruhl, D. Study of the risk factors for severe childhood pertussis based on hospital surveillance data. *Vaccine* **25**, 7224-7232, doi:<http://dx.doi.org/10.1016/j.vaccine.2007.07.020> (2007).
- 54 Mattoo, S. & Cherry, J. D. Molecular pathogenesis, epidemiology, and clinical manifestations of respiratory infections due to *Bordetella pertussis* and other *Bordetella* subspecies. *Clin Microbiol Rev* **18**, 326-382, doi:10.1128/CMR.18.2.326-382.2005 (2005).
- 55 Heininger, U., Klich, K., Stehr, K. & Cherry, J. D. Clinical findings in *Bordetella pertussis* infections: results of a prospective multicenter surveillance study. *Pediatrics* **100**, e10-e10, doi:10.1542/peds.100.6.e10 (1997).
- 56 Skopova, K. *et al.* cAMP-elevating capacity of the adenylate cyclase toxin-hemolysin is sufficient for lung infection but not for full virulence of *Bordetella pertussis*. *Infect Immun*, doi:10.1128/IAI.00937-16 (2017).
- 57 Guiso, N., Rocancourt, M., Szatanik, M. & Alonso, J.-M. *Bordetella* adenylate cyclase is a virulence associated factor and an immunoprotective antigen. *Microbial Pathogenesis* **7**, 373-380, doi:[http://dx.doi.org/10.1016/0882-4010\(89\)90040-5](http://dx.doi.org/10.1016/0882-4010(89)90040-5) (1989).
- 58 Torre, D. D. Production and release of tumor necrosis factor alpha, interleukin-1B and interleukin-6 by human mononuclear leukocytes stimulated with pertussis toxin. *The new microbiologica* **16**, 309-314.
- 59 Bassinet, L., Fitting, C., Housset, B., Cavaillon, J.-M. & Guiso, N. *Bordetella pertussis* adenylate cyclase-hemolysin induces interleukin-6 secretion by human tracheal epithelial cells. *Infection and Immunity* **72**, 5530-5533, doi:10.1128/iai.72.9.5530-5533.2004 (2004).
- 60 Raeven, R. H. M. *et al.* Molecular Signatures of the Evolving Immune Response in Mice following a *Bordetella pertussis* Infection. *PLoS ONE* **9**, e104548, doi:10.1371/journal.pone.0104548 (2014).
- 61 Moreno, G. *et al.* Toll-like receptor 4 orchestrates neutrophil recruitment into airways during the first hours of *Bordetella pertussis* infection. *Microbes and Infection* **15**, 708-718, doi:<http://dx.doi.org/10.1016/j.micinf.2013.06.010> (2013).

PRECISE ORBIT DETERMINATION USING DUTY CYCLED GPS DATA

Sean Lantto
Aerospace Engineering
West Virginia University
Morgantown, WV

ABSTRACT

GPS provides an opportunity to achieve centimeter level accurate, precise orbit determination (POD). This is achieved through the use of carrier phase measurements which require continuous tracking, which is difficult to obtain on small satellites, such as CubeSats, due to power limitations, requiring the GPS receiver to be duty cycled. This work investigates combining the duty cycled GPS observables with a dynamic model through an extended Kalman filter (EKF), to achieve high accuracy POD. Tests were done on simulated duty cycled observables generated for 10 different satellite orbit, with varying percentages of on time in 10 minute intervals over a 3 hour observation time. Both a pure kinematic approach and a reduced dynamic approach were investigated, with the reduced dynamic approach having a 3D root mean square error (RMSE), tens of meters better than the kinematic approach.

INTRODUCTION

Simulation to Flight 1 (STF-1) is a 3U CubeSat being built in at NASA Independent Verification and Validation (IV&V) facility in Fairmont, WV to demonstrate the capability of using software only simulations during the developmental lifecycle of a CubeSat [5]. STF-1 hosts multiple payloads from West Virginia University (WVU) as well, including a Novatel OEM615 GNSS receiver. The receiver will be used for precise orbit determination of the spacecraft, however the receiver will be duty cycled. Duty cycling of the GPS receiver will reduce the overall accuracy of the precise orbit determination. To alleviate the effects of the duty cycling, a dynamic model can be applied to estimate the spacecraft's position and velocity, which will then be updated with the GPS measurement inside an extended Kalman filter (EKF). This combination of dynamic model and kinematic measurements in the EKF, is called a reduced dynamic approach. While the work in this paper has been applied only to simulated data, when STF-1 launches, it will be applied to the actual on orbit spacecraft, for both post processing and on orbit precise orbit determination.

BACKGROUND

GPS has been used to provide centimeter level accurate precise orbit determination (POD) for low earth orbiting (LEO) spacecraft such as Jason-1 [1]. This is achieved by using the carrier phase measurements of the GPS signal, instead of the less accurate code ranging. When using carrier phase measurements, the phase ambiguities (N) must be solved for, and can be seen below in **Equation 1** [2]. The phase ambiguities are the integer number of wavelengths between the GPS satellite and receiver. Solving for the phase ambiguities requires continuous tracking of the GPS satellites, and requires time to solve upon first acquiring a satellite.

Equation 1: Carrier Phase Measurement Equation

$$\phi^{(k)} = \lambda^{-1}[r^{(k)} - I^{(k)} + T^{(k)}] + F(\delta t_u - \delta t) + N^{(k)} + \epsilon_\phi$$

On small spacecraft, such as CubeSats, power cannot always be supplied to all instruments at once. Therefore, duty cycling (powering a device on and off at regular predetermined intervals), is performed to ensure all instrumentation has the ability to run, though not continuously. When the GPS receiver is duty cycled it loses tracking of the GPS satellites, and when turned back on, it must solve for the carrier phase ambiguities again. Another consequence of the duty cycling, is that when the receiver is powered on, it tries to estimate the position using its last known location, which for most receivers on Earth is no problem. However due to speeds required to orbit the Earth, when the receiver is powered on, it will be in a completely new location, with potentially an entire new set of satellites. Depending on the duty cycle, the amount of time spent on, may be severely limited. To help estimate the position when the receiver is turned back on, a dynamic model can be used to propagate an estimated position and velocity while the receiver is off. For a spacecraft, the dynamic model should take into account the forces due to gravity, which include zonal harmonics, third-body effects, and relativistic effects. The forces in the model will also include atmospheric drag and radiation pressure both from the Sun and reflected off the Earth. These forces cause perturbations in the Keplerian elements of the spacecraft's orbit, causing the orbit to deviate, and thus the spacecraft's position will not be predictable without accounting for the forces.

To combine the dynamic models estimate, with the measured position and velocity from the GPS, an extended Kalman filter can be used. An extended Kalman filter (EKF), is a non-linear version of the Kalman filter. The EKF has two parts, a prediction, or time update, and a measurement update. During the prediction step, the last estimated state is propagated into the current state, and the error covariance is updated. To bring the last state into the current one, it is multiplied against a state transition matrix, which contains partial the partial derivatives of the equations used to model the system, such as the partial derivative of the position with respect to the accelerations due to the forces acting on a system. The measurement update changes the predicted current state based off of some observation model, in this case the GPS acts as the observation model. The resulting estimated state after the measurement update is then used in the next prediction step, and this process is repeated until some criteria is met, likely to be the end of the set of data used to model for either measurement or prediction. The EKF used in this work is an error state EKF, which means it does not find the total state, but instead it finds the difference between the last state and the current state.

Equation 2: Basic Equations for an EKF

$$\begin{aligned}
 \textbf{Prediction: } X_{K|K-1} &= f(X_{K-1|K-1}, \mathbf{u}_{K-1}), \mathbf{P}_{K|K-1} = \mathbf{F} * \mathbf{P}_{K-1|K-1} * \mathbf{F}^T + \mathbf{Q} \\
 \textbf{Measurement Update: } \mathbf{K} &= \mathbf{P}_{K|K-1} * \mathbf{C}^T * (\mathbf{C} * \mathbf{P}_{K|K-1} * \mathbf{C}^T + \mathbf{R})^{-1}, \\
 X_{K|K} &= X_{K|K-1} + \mathbf{K} * [\mathbf{y}_K - \mathbf{C}X_{K|K-1}], \mathbf{P}_{K|K} = (\mathbf{I} - \mathbf{K} * \mathbf{C}) * \mathbf{P}_{K|K-1}
 \end{aligned}$$

METHODS

The EKF has only been applied to simulated GPS observables so far, which in turn were generated

for simulated orbits. Each simulated orbit has an observation time of three hours, starting at noon on January first of 2017. The ephemeris is calculated every tenth of a second for the next three hours. This generated ephemeris is used to generate the GPS observables, as well as the truth positions and velocities to compare the estimates from the EKF against.

Ephemeris Calculation and the Generation of the GPS Observables

The ephemeris for a three hour, 10 Hz, observation period, starting on January 1st, 2017 at noon, was calculated for seven different CubeSats [3]. STF-1, ISS (provides ephemeris for CubeSats launched from ISS NanoRacks CubeSat Deployer), RAVAN-XB3, Athenoxat-1, SNAP-3, Lemur-2, and SMDC-ONE. The date and time of the observation period is important to keep track of, so that the position of the spacecraft can be rotated from an Earth Centered Inertial (ECI) frame into an Earth Centered, Earth Fixed (ECEF) frame, through a direction cosine matrix (DCM). The DCM used includes compensation for the leap seconds between international atomic time (TAI) and coordinated universal time (UTC). A DCM is created for each timestep of the ephemeris calculation. This will be more useful later when the generation of the GPS observables is concerned.

The Keplerian elements are used to generate the initial state (position and velocity in ECI) of the spacecraft using methods from *Montenbruck* [4]. The parameters to be used for modeling forces on the spacecraft are placed into a structure that will be called later. For the seven previously listed satellites, only the geopotential forces (zonal harmonics, etc.) and third-body effects from the Sun and Moon are considered, ignoring effects from radiation pressure and atmospheric drag. The ephemeris is then calculated for each time step of the observation period using Matlab functions from *Montenbruck* [4]. The functions calculate the accelerations from the desired forces to be modeled, and solves the differential equations of motion using numerical integration methods.

With the generated ephemeris, the position and velocity are rotated from ECEF into latitude, longitude, and height (LLH); as well as a “local” East, North, Up (ENU) frame. These coordinate frames are the ones directly used to generate the GPS observables. While generating the GPS observables the spacecraft is currently treated as just a receiver moving through space, not account for the spacecraft’s attitude at all, and thus errors imposed by the spacecraft (multipath, blocking of signals, etc) are ignored. Error due to the ionosphere is included in the generated observables. Unlike a GPS receiver on the ground, a spacecraft in LEO can see satellites that are orbiting on the opposite side of the Earth, with limitations. An elevation angle (angle from receiver to GPS satellite, with respect to a local flat plane at the receiver) mask is used to determine how far behind the Earth the receiver can track satellites, and is calculated using **Equation 3** below, where h is the altitude from the surface of Earth. The GPS observables are then generated for the spacecraft using a function written by Ryan Watson. The function saves a MAT file with the generated observed code range, carrier phase measurements, satellite IDs, which will all be used in estimating the position in the EKF.

Equation 3: Equation to find the elevation mask angle for a satellite in LEO

$$\theta = \arccos\left(\frac{R_{Earth}}{(R_{Earth} + h)}\right)$$

After generating the GPS observables a copy of them are made. This copy is ran through a function

that adds the effects of duty cycling to the generated phase observables. For all the satellites used in this work, the duty cycle takes place over 10 minute intervals. This means that every 10 minutes the receiver will be powered on again, and will remain on for some percentage of the 10 minute cycle time. The function adds a random integer value between -100 and 100 to the phase observables to represent the change in the carrier phase integer ambiguity. The function also places a flag that will signal to the EKF that a phase break has taken place, and a measure must be taken to find the new ambiguity.

EKF Structure

The error state extended Kalman filter used in this work, estimates the changes in position and velocity of the spacecraft, as well as the clock bias, clock bias drift, and the carrier phase integer ambiguity. The EKF takes the desired duty cycle on percentage, and the desired state transition matrix as inputs before running. The duty cycle on percentage for this work is in increments of 10% of 10 minutes. The results section shows the impact of having a longer or shorter duty cycle on time. After the duty cycle time is applied, the number of satellites per time step is modified to add the satellites in gradually when the receiver is “powered on” during the cycle. This stops the EKF from reaching a solution too quickly, making the estimation more applicable to a real situation. The rate at which the satellites are added was determined by the rate in which satellites were acquired during hardware in the loop simulation and testing, which is discussed later in this paper. The duty cycle determines when measurement updates occur during the EKF so, when the receiver is said to be off, the EKF skips the measurement update, and solely relies on the prediction step to estimate the state. The model used during the prediction step determines how detrimental, to the accuracy of the EKF’s estimation, the duty cycle is.

The selection of the model used in the prediction step, or the state transition matrix, determines whether or not the EKF will follow a kinematic or reduced dynamic approach. The kinematic approach relies solely on the measurement update, as the prediction step simply says that the current state is equivalent to the previous state. This causes issues when the receiver is duty cycled, because when the receiver is turned off, the EKF will continue to use the last state from when the receiver was on as the current one. Once the receiver is turned back on, the difference in position is very large due to the spacecrafts movement, increasing the time to acquire a good solution and the amount of overall error. To help alleviate this error, a least squares estimator is used to estimate the position as soon as four satellites are being tracked. This will decrease the time for the EKF to estimate a good solution, and is similar to what an actual receiver will do.

Comparison of Estimated and Truth Position for STF-1(Kinematic approach 50% duty cycle)

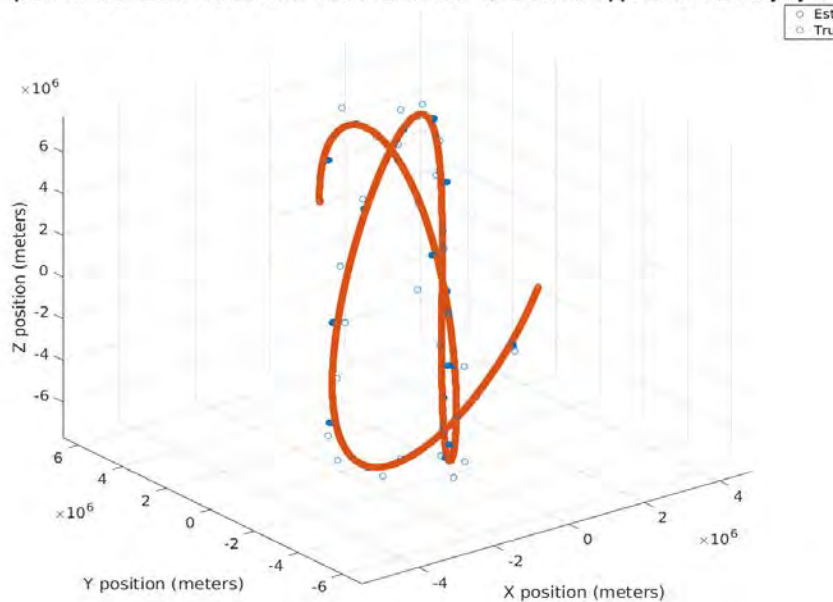


Figure 24: Comparison of estimated and truth position using a purely kinematic approach to the EKF. (Duty Cycled 5 minutes on, 5 minutes off)

If the EKF is told to use a reduced dynamic approach, the state transition matrix uses the partial derivatives of the equations of motion to model the spacecraft dynamics. This means that even when the receiver is off, the position and velocity can still be estimated, and depending on the model used, will decrease the error incurred during the duty cycle off time. For this work a two-body model is used to model the system dynamics and form the state transition matrix. The function that does this, developed by *Montenbruck [4]*, takes the previously estimated state and the time since the last update (0.1 seconds in this case), and propagates the state forward. During the measurement update, differences between the two body state and the actual state are estimated and the state is updated. Using this reduced dynamic approach greatly reduces overall error as can be seen in the results section. The equation below shows the calculation of the position and velocity from the Keplerian elements. Here \underline{a} is the semi-major axis, \underline{e} is the eccentricity, \underline{E} is the eccentric anomaly, and $\underline{\mu}$ is the gravitational parameter of Earth.

$$R = a * (1 - e * \cos(E))$$

$$V = \frac{\sqrt{\mu * a}}{R}$$

While it is possible to use a reduced dynamic method in the EKF with a higher fidelity force model to propagate the state and form the state transition matrix, it is not done in this work due to the large increase in computational time this requires. Longer computational time is detrimental to real time orbit determination on board a spacecraft. However methods of using a higher fidelity model without a significant increase in computational time are being investigate for the future of this work, as it could further reduce the overall error.

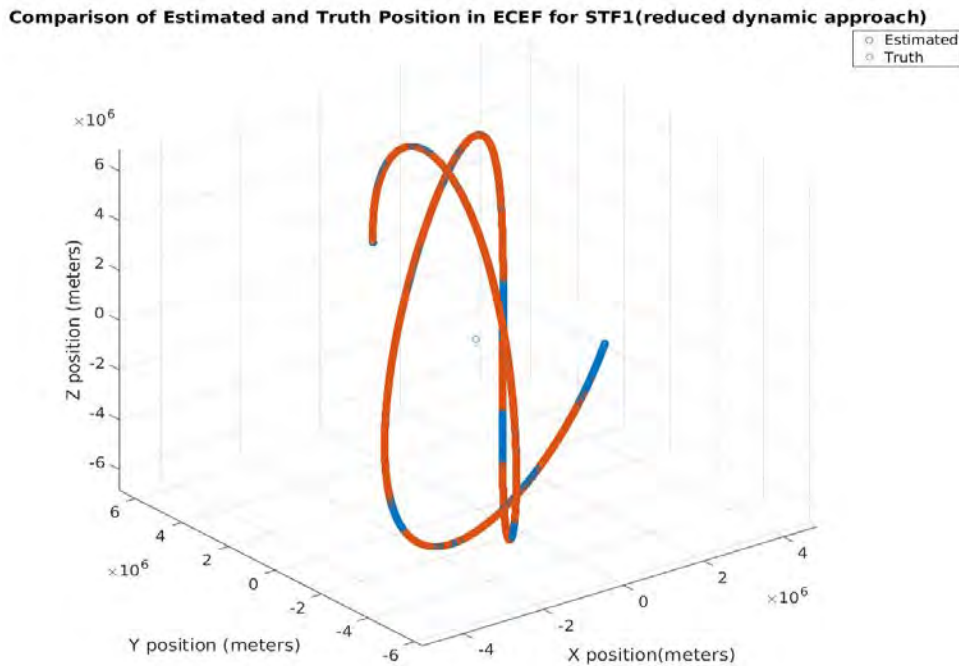


Figure 25: Comparison of estimated and truth position using a reduced dynamic approach to the EKF. (Duty Cycled 5 minutes on, 5 minutes off)

Hardware in the Loop Simulation and Testing

In the summer months of 2016 NASA Goddard Space Flight Center (GSFC), provided a Spirent Signal generator and software to simulate a spacecraft in orbit. Using the provided signal generator and software, the flight GPS receiver for STF-1 was used to collect the simulated GPS data under various duty cycle conditions. The collected data was processed using GIPSY-OASIS, to get positioning of the spacecraft, and will later be used with GIPSY to do POD.

RESULTS

The figure below shows the results of averaging together the root mean square (RMS) of the 3D position error from all seven satellites. It is apparent that the reduced dynamic approach significantly improves on the error, as well as the fact that the longer the receiver is on during its duty cycle interval, the smaller the error. The benefit of using a reduced dynamic approach is even apparent when the receiver is allowed to be powered continuously. The bars on each point show the standard deviation of the RMS. Due to the randomness built in of acquiring and tracking satellites when the receiver is powered on, these results will vary, but should produce the same trend as shown in the figure below.

Mean 3D RSOS of Kinematic and 2-body model for various on times of all sats

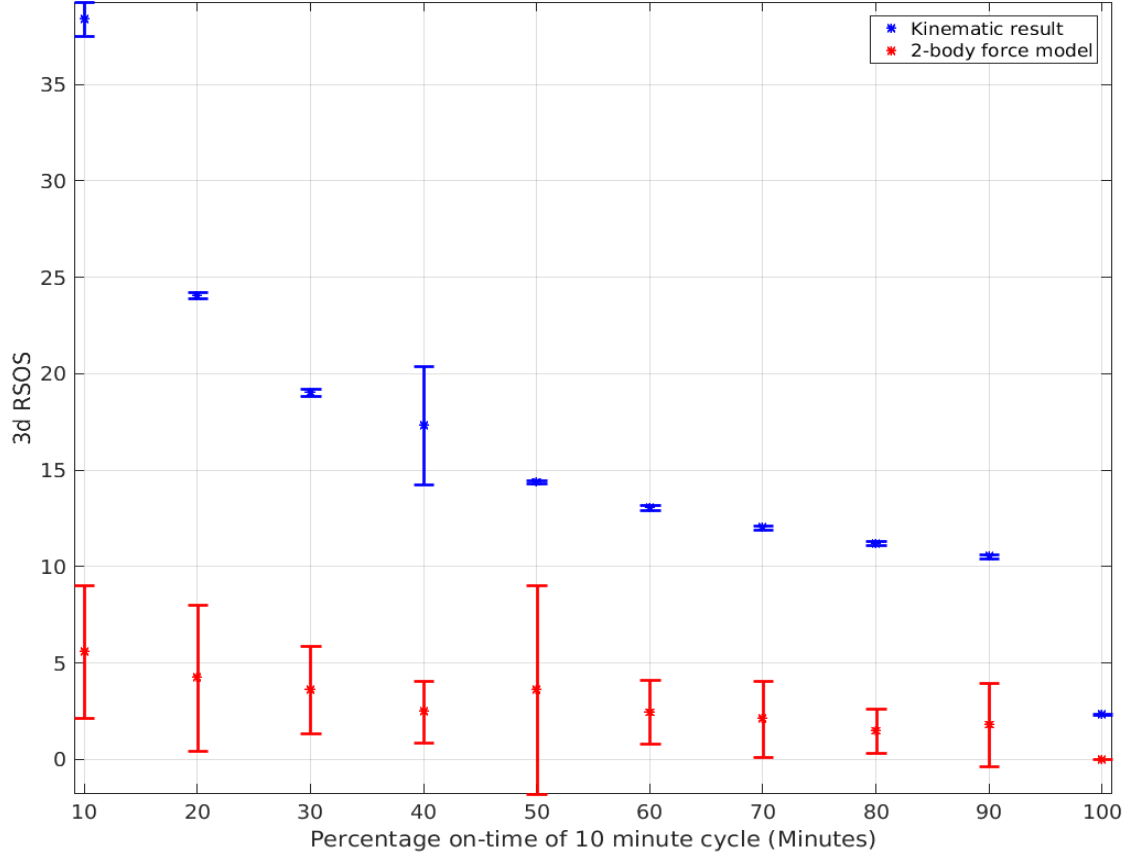


Figure 26: Comparison of the average RSOS for both the kinematic approach, and the reduced dynamic approach using a 2-body force model

FUTURE PLANS

Currently I am working towards writing a conference paper to submit for the American Institute for Aeronautics and Astronautics (AIAA) SciTech 2018 Forum and Exposition. This will detail the work in shown in this paper as well as further results. The next step is to attempt to use GIPSY OASIS to modify real spacecraft data from previous missions (such as Jason-1, TOPEX/Poseidon, and GRACE) to represent duty cycled data. Then using the included dynamic models in GIPSY, precise orbit determination will be attempted to attempt to match the results from the EKF developed in Matlab.

STF-1 is scheduled to launch later this year and when data is collected from the CubeSat, it will be processed using the same methods developed and explained in this paper. This will give the opportunity to validate with real, current data. If it is deemed feasible, it is possible to attempt to apply these POD methods on board STF-1 for real time onboard POD.

CONCLUSIONS

While so far only attempted using simulated data, the beneficial impact of a reduced dynamic approach, over a purely kinematic approach, to precise orbit determination using GPS is obvious, even when the GPS receiver is allowed to remain on continuously instead of being duty cycled. If validated with real data from STF-1, this work will benefit other small satellites that wish to have an inexpensive way of precise positioning that will benefit scientific payloads onboard the spacecraft.

Prior to starting this project my knowledge on GPS and precise orbit determination was very limited, and I had no knowledge of tools such as Kalman filters. This project has allowed me to develop the critical problem solving and self-teaching skills that not only have benefitted my work this past year, but will be of great use to me in my future career, as I may encounter subjects of which I have no knowledge. The tools that I have gained experience in, are not solely used to for this application and would be useful to a variety of scientific and engineering fields, should I find myself working in one of them. By far one of the greatest opportunities of this work, is the chance to work directly with flight hardware on STF-1, and be involved with the GPS payload objectives.

ACKNOWLEDGMENTS

NASA West Virginia Space Grant Consortium

Without their grant of the fellowship, I would not have had the opportunity to work with STF-1, let alone be able to work towards my master's degree in aerospace engineering.

Dr. Jason Gross, Research Mentor and Advisor

Without Dr. Gross's guidance, I would not have been totally lost on this project and unsure of where to start if I had started at all. Also without him, I would not have considered graduate school nor had the opportunity to work with STF-1.

Ryan Watson

Ryan's previous work under Dr. Gross has provided tools that have allowed this project to progress as far as it has

REFERENCES

1. Haines, Bruce, et al. "One-centimeter orbit determination for Jason-1: new GPS-based strategies." *Marine Geodesy* 27.1-2 (2004): 299-318.
2. Kaplan, Elliott D., and Christopher J. Hegarty. *Understanding GPS: principles and applications*. Boston, Artech House, 2006.
3. Kulu, Erik. "World's largest database of nanosatellites, more than 1600 nanosats and CubeSats." *Nanosatellite & CubeSat Database*, www.nanosats.eu/. Accessed 21 Apr. 2017.
4. Montenbruck, Oliver, and Gill Eberhard. *Satellite orbits: models, methods, and applications*. Berlin, Springer, 2001.
5. Morris, Justin, et al. "Simulation-to-flight (stf-1): A mission to enable cubesat software-based validation and verification." (2016).
6. Tapley, Byron D., et al. *Statistical orbit determination*. Amsterdam, Elsevier: Academic Press, 2004.

MECHANISMS OF OXIDATIVE DAMAGE ASSOCIATED WITH

TENOFOVIR NEPHROTOXICITY

Rachel Murphy
Biomedical Sciences
Marshall University
Huntington, WV

ABSTRACT

Tenofovir (TFV) is a reverse transcriptase inhibitor that is FDA approved to treat HIV and chronic Hepatitis B. It has a long half-life, allowing for once a day dosing and is effective in both treatment novel and treatment experienced patients. It is administered orally as tenofovir disoproxil fumarate (TDF) and is deesterified in the intestine to the active drug TFV. However, renal impairment is associated with its use; TFV can induce decreased glomerular filtration rate (GFR) and free calcitriol, renal failure, and Fanconi Syndrome. The exact mechanism of toxicity currently remains unknown, largely due to limited experimental models. Our laboratory has established that clinically relevant concentrations of TFV are toxic within 24 h in an immortalized human proximal tubule cell line (HK-2). The purpose of this specific study was to further investigate the mechanisms of cytotoxicity and oxidative damage observed in HK-2 cells following treatment with TFV and to determine if managing oxidative damage mitigates toxicity. TFV is the active form of Viread and was used for all studies. HK-2 cells were grown to confluency for 48 h and then exposed to 0-28.8uM TFV for 24, 48, or 72 h. The vehicle used for all studies was phosphate buffered saline (PBS). Tenofovir induces a loss of cell viability compared to the control within 24h as shown by an MTT assay, Trypan Blue Exclusion cell counts, and LDH leakage. Oxidative stress and mitochondrial damage were assessed in different cell fractions using OxyBlot and western blot for MnSOD, ATP Synthase, and Cytochrome C and showed an increase in protein carbonylation and loss of mitochondrial membrane integrity following 72 h exposure to 28.8uM TFV. Studies were conducting using a 1 h pretreatment of antioxidants resveratrol, N-acetylcysteine, or ascorbic acid and showed protection of cell viability following 24 h TFV exposure. These studies suggest that mitochondrial damage and oxidative stress occur in HK-2 cells treated with TFV and that controlling oxidative damage may help prevent toxicity from developing. Additional knowledge of subcellular events associated with tenofovir nephrotoxicity can be used to develop clinical methods to mitigate toxicity.

INTRODUCTION

Tenofovir (TFV) is a reverse transcriptase inhibitor that is approved in the United States to treat HIV and chronic Hepatitis B. Although TFV is a first line drug used to treat HIV (WHO Model List 2015), renal impairment remains an adverse effect associated with its use. The exact mechanism of toxicity currently remains unknown, largely due to limited experimental models. Our laboratory has established that clinically relevant concentrations of TFV are toxic within 24 h in an immortalized human proximal tubule cell line (HK-2). The overall purpose of this study was to further investigate the mechanisms of cytotoxicity and oxidative damage observed in HK-2 cells following treatment with TFV and to determine if managing oxidative damage mitigates toxicity.

Oxidative stress and mitochondrial damage were evaluated using Oxyblot and western blotting. OxyBlot is a method kit established by Millipore that evaluates protein carbonylation as a result

of exposure to reactive oxygen and nitrogen species (ROS, RNS). Oxyblot and western blotting were done on mitochondrial and cytosolic fractions following 72 h exposure to 28.8uM TFV. Western blotting specifically probed for leakage of cytochrome c, ATP Synthase, and Manganese Superoxide Dismutase (MnSOD) from the mitochondrial fraction to the cytosolic fraction; these proteins are normally sequestered in the mitochondria and leakage into the cytosolic fraction indicates a loss in mitochondrial membrane integrity.

Our previous study indicated that cell death is occurring in HK-2 cells within 24 h TFV exposure, however markers of apoptosis such as caspase 3 and 9 activation was not observed until 72 h exposure. We hypothesized that there may be multiple mechanisms of toxicity, and that necrosis may be occurring at earlier time points. We probed for necrosis using western blotting for lactate dehydrogenase (LDH) leakage into the cytosol following 24-48 h exposure to 14.5 and 28.8uM TFV.

Due to the observed oxidative damage in our last study, we hypothesized that toxicity may be mitigated through pretreatment with antioxidants. Prior to 24 h treatment with 3 or 14.5uM TFV, HK-2 cells were incubated with resveratrol (5, 7.5, or 10uM), N-acetylcysteine (NAC, 0.5 or 1mM), or ascorbic acid (10 or 25uM) for 1 h. Protection was assessed by measuring cell viability following the treatment period via the MTT assay.

All experiments were analyzed using SigmaStat software. A one-way ANOVA was run on each experiment, followed by a Holm Sidak post hoc test as appropriate. Statistical significance was set to a threshold of $p < 0.05$ and all data is presented as mean \pm SEM (standard error of the mean). Additional detail regarding procedures and experiments can be found in the “Methods” section below.

This study shows that TFV induces a loss of cell viability compared to the control within 24h as shown by an MTT assay, Trypan Blue Exclusion cell counts, and LDH leakage. OxyBlot and western blots for MnSOD, ATP Synthase, and Cytochrome C on mitochondrial and cytosolic fractions showed an increase in protein carbonylation and loss of mitochondrial membrane integrity following 72 h exposure to 28.8uM TFV. Antioxidant pretreatment studies showed protection of cell viability following 24 h TFV exposure. These results suggest that mitochondrial damage and oxidative stress occur in HK-2 cells treated with TFV and that antioxidant pretreatment may mitigate toxicity. Additional discussion of the observed results can be found in the “Discussion” and “Conclusions” sections below.

BACKGROUND AND SIGNIFICANCE

Tenofovir disoproxil fumarate (TDF) is an antiretroviral agent that is approved in the United States to treat Human Immunodeficiency Virus (HIV) and chronic Hepatitis B (HBV). Tenofovir (TFV) is a nucleotide analogue of adenosine 5'-monophosphate that competes for incorporation into the growing viral strand during chain elongation and blocks reverse transcriptase, leading to chain termination [1, 2]. To improve oral bioavailability, it is administered as the prodrug tenofovir disoproxil fumarate (TDF) which is deesterified in the intestine to the active drug TFV [3, 4]. TFV has a long half-life, allowing for once a day dosing and is more efficacious when given orally rather than as a subcutaneous injection; both of these factors are important for clinical HIV

management and compliance [5-7]. TFV is also effective in patients who have resistant HIV-1, making it an essential drug in the treatment of HIV according to the World Health Organization [8, 9].

While TFV has many positive attributes, renal toxicity remains an adverse effect associated with its use. TFV can induce increases in serum creatinine and plasma vitamin D protein binding, decreases in glomerular filtration rate (GFR) and free calcitriol, Fanconi Syndrome, and renal failure [10-12]. Fanconi syndrome is a disorder of renal tubular function that results in excess excretion of potassium, phosphate salts, protein, urate, and glucose.

Though TFV induced renal toxicity has been documented, very little is known about the mechanism; this knowledge gap may be due in part to limited experimental models. In vitro studies have used primary renal proximal tubule cells treated for up to 22 days and in vivo mouse and rat models were treated with oral gavage for 5-8 weeks [13-16]. The duration of these experiments can hamper mechanistic studies, and the added stress of daily oral gavage can complicate mechanistic studies using animal models. Cell lines with better responsiveness to TFV could circumvent these issues.

In our previous study, our lab determined that Human Kidney-2 cells (HK-2) are a suitable model to study tenofovir induced renal cytotoxicity. HK-2 cells retain similar activity and biochemical properties to in vivo cells and are commonly used in renal mechanistic studies [17-20]. Using clinically relevant concentrations, we determined that TFV causes oxidative stress, reduces cellular ATP, and induces apoptosis within 24-72 h. The purpose of this study was to further investigate the oxidative damage associated with TFV induced cytotoxicity as well as to begin preliminary tests on toxicity prevention.

METHODS

Chemicals and Reagents

TFV was purchased from Cayman Chemicals (Item No. 13874, Ann Arbor, MI) and was used for all studies. The cell treatment vehicle was phosphate buffered saline (Invitrogen, Carlsbad, CA, Item No. 14175095). Resveratrol, N-acetyl-cysteine (NAC) and other chemicals were purchased from Sigma Aldrich (St. Louis, MO) or Fisher Scientific (Pittsburg, PA). Antibodies and kits were purchased as indicated in the sections below.

Cell Lines and Tenofovir Treatment

Human immortalized epithelial HK-2 cells were purchased from the American Type Culture Collection (ATCC) and were cultured according to ATCC guidelines. In brief, cells were grown in a keratinocyte-free media with 50ug/ml bovine pituitary extract and 5ng/ml recombinant epithelial growth factor from Invitrogen in a warm humidified incubator with constant settings of 37^o C and 5% CO₂. HK-2 cells were plated into six-well tissue culture plates or 75mL tissue culture flasks at a concentration of 750,000 cells/ml and allowed to grow for 48 h. Media was replaced and cells were treated with a final concentration of 0, 1.5, 3, 4.75, 14.5, or 28.8 uM TFV for 24, 48, or 72 h. The vehicle was an equal volume of phosphate buffered saline (PBS). Following each treatment period, cells were collected with Trypsin-EDTA (0.25%) for sample analysis.

Mitochondrial Isolation

Following collection with Trypsin-EDTA, mitochondria were isolated using a Mitochondrial Isolation Kit for Cultured Cells (Thermo Scientific) and differential centrifugation. Briefly, cells were centrifuged at 850g for 10 min and resuspended in 800uL of Reagent A with added protease inhibitor. Samples were vortexed for 5 sec at maximum speed and then incubated on ice for 2 min. 10uL of Reagent B was added and samples were vortexed for 5 sec at maximum speed and incubated on ice for 10 minutes, vortexing every minute. Next, 800uL of Reagent C with added protease inhibitor was added and the samples were centrifuged at 750g for 10 min. The supernatant was transferred to new samples tubes and centrifuged at 12,000g for 15 min at 4⁰C. The supernatant (cytosolic fraction) was transferred to a new tube and the pellet (mitochondrial fraction) was resuspended in 75uL cell lysis buffer.

Cell Viability

Cells were plated into 48-well tissue culture plates (39,000 cells/ml) and allowed to grow for 48 h followed by treatment with vehicle or TFV (see “Cell Lines and Tenofovir Treatment”). Following the treatment period, cell viability was assessed using the MTT assay [21]. This assay relies on the conversion of tetrazolium dye 3-(4,5-dimethylthiazol-2-yl)-2,5-diphenyltetrazolium bromide (MTT) to formazan by NAD(P)H-dependent oxidoreductases.

To ensure that results of the MTT Assay were not due to mitochondrial damage rather than cell death, a trypan blue exclusion test for membrane integrity was conducted based on a previously published protocol [22]. An aliquot of collected cells are diluted 1:10 with 40% w/v Trypan Blue solution. The suspension was mixed via pipetting and allowed to sit for approximately 2 min. A 10ul aliquot of suspension was transferred to a hemocytometer and total cells, live cells, and dead cells were counted.

When cells lose membrane integrity as necrosis develops following exposure to a toxicant, LDH is released from the cell into the extracellular space. This leakage can be used as a quantification of cell death via necrosis. Western blot analysis was also used to evaluate LDH leakage from HK-2 cells into the media. Following the 24-48 h treatment period with vehicle or TFV, cells were pelleted, rinsed with 500ul PBS, and centrifuged. The pellet was then disrupted with lysis buffer. Media samples were centrifuged at 2,000g for 10 min to remove any cell debris. Protein content was measured, and each lane was loaded with 10ug of protein. Membranes were probed using a rabbit polyclonal antibody for LDH (1:500 dilution in 5% BSA/TBST). Results were analyzed with BioRad Chemidoc densitometry software (version 4.0.1) with n=6 samples/group.

Oxyblot and Western Blot

Western blot analysis was conducted to assess expression of manganese superoxide dismutase (MnSOD), ATP Synthase, and cytochrome C in mitochondrial and cytosolic cell fractions. Protein concentration in each sample was determined using the Bradford protein assay [23]. A 40 ug aliquot of each sample was boiled for 5 min to denature it. Proteins were then separated on a 12.5% polyacrylamide gel and transferred to a nitrocellulose membrane; successful transfer and protein loading were verified using Memcode Reversible Protein Stain. Membranes were blocked using either a 5% w/v milk/TBST solution (10mM Tris-HCl, 150mM NaCl, 0.1% Tween-20; pH 8.0) or a 3% Bovine Serum Albumin (BSA)/PBST solution for 1hour. Membranes were next

incubated with continual shaking overnight at 4⁰C with a rabbit polyclonal antibody for MnSOD (1:5000 dilution), ATP Synthase (1:1000 dilution) or cytochrome C (1:250 dilution). The membranes were washed four times with TBST and goat anti-rabbit HRP-linked secondary antibodies (1:5000 dilution in 5% milk/TBST) and added for 1 hour. Membranes were washed again with TBST and then developed using Amersham ECL Western Blotting Detection Agent (GE Healthcare Life Sciences). A BioRad chemic-doc system was used to capture the gel image and used for densitometry analysis. All gels were analyzed with n=7 samples/group.

There are several markers of oxidative stress including protein carbonylation, which can produce and aldehyde or ketone side chain on cellular proteins. Protein carbonylation was analyzed using the Oxyblot Protein Oxidation Detection Kit (EMD Millipore). 25µg aliquots of sample were derivatized as previously described and protein loading was verified using the MemCode Protein Stain [24]. Briefly, protein carbonyl moieties on cellular proteins generated by oxidative stress are derivatized in the presence of 2,4-dinitrophenylhydrazine (DNPH) to stable 2,4-dinitrophenylhydrazone groups; the primary antibody (1:150 dilution in 1% BSA/PBST) recognizes these 2,4-dinitrophenylhydrazone groups on proteins. Results were analyzed with BioRad Chemidoc densitometry software (version 4.0.1) with n=7 samples/group.

Antioxidant Protection Studies

A series of studies examined whether various antioxidants could provide protection from TFV. HK-2 cells were allowed to grow for 48 h followed by a 1 h pretreatment with resveratrol (5, 7.5, or 10uM in DMSO), N-acetylcysteine (NAC, 0.5 or 1mM in sterile water), or ascorbic acid (10 or 25uM in sterile water) followed by a 24 h incubation with 0, 3, or 14.5 uM TFV. Viability of cells was assessed using the MTT assay (See “Cell Viability”). All media and MTT were removed from the cells prior to the addition of DMSO to prevent any interaction of antioxidants with formazan.

Statistical Analysis

Data are presented as Mean ± SEM with 2–4 independent experiments with 2–4 biological replicates. Differences between groups were determined with a one-way ANOVA followed by a Holm–Sidak post-hoc test with $p < 0.05$ (SigmaStat, SSPS).

RESULTS

Effects of TFV on Cell Viability

TFV reduced cell viability within 24 h at all tested concentrations ($p < 0.05$) as shown by the MTT Assay (Figure 1). Cell viability continued to be reduced at 48 and 72 h at all concentrations relative to vehicle control, and 4.75 and 28.8uM TFV showed additional loss in cell viability compared to other treatment groups ($P < 0.05$). To ensure that the results of the MTT assay accurately showed a decrease in cell viability rather than a direct effect of TFV on mitochondrial reductase enzymes, concurrent Trypan Blue cell exclusion counts were conducted. Trypan Blue cell counts confirmed that TFV causes a reduction in cell viability at all concentrations relative to control from 24-72 h ($p < 0.05$); there was no difference between groups (Figure 2).

Western blot analysis on media and cell lysate samples following 24 and 48 h TFV exposure were conducted to assess cellular release of LDH. At 24 and 48 h exposure, TFV induced release of LDH into the media at all concentrations tested relative to control ($p < 0.05$, Figure 3). At 24 h,

14.5 uM TFV showed additional LDH release compared to other treatment groups ($p < 0.05$). However, at 48 h exposure, 28.8uM TFV showed additional LDH release compared to other treatment groups ($p < 0.05$). Intracellular expression of LDH was not different at any time point or concentration tested (Figure 3).

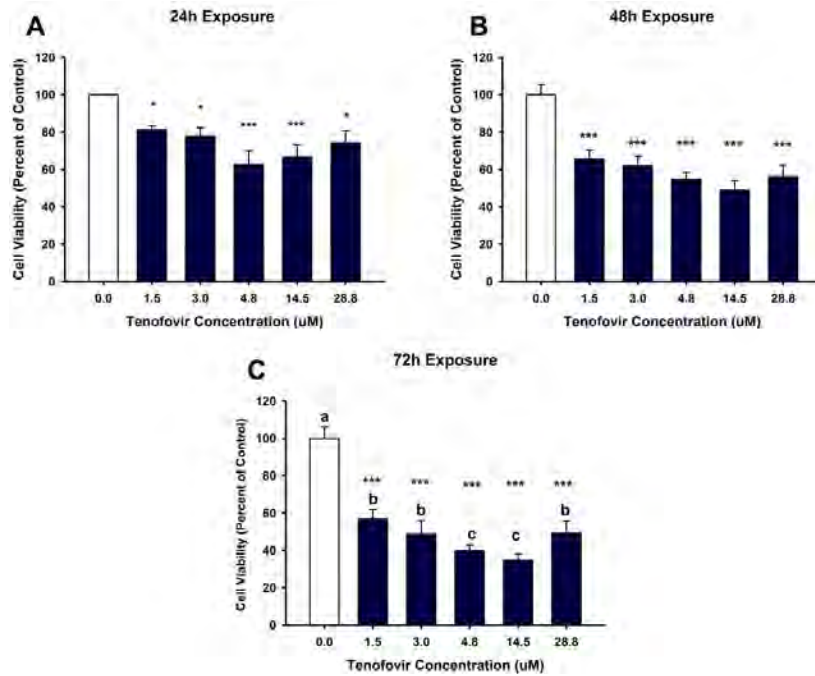


Figure 1 Tenofovir effects on HK-2 cell viability using MTT. TFV diminished cell viability at 24 (A), 48 (B) and 72 h (C). Statistical difference from 0 uM tenofovir depicted in (A,B) by asterisks (* $p < 0.05$, *** $p < 0.001$). Different superscript letters (C) indicate groups that are different from each other ($p < 0.05$). Each bar represents Mean \pm SEM for three independent experiments with two biological replicates.

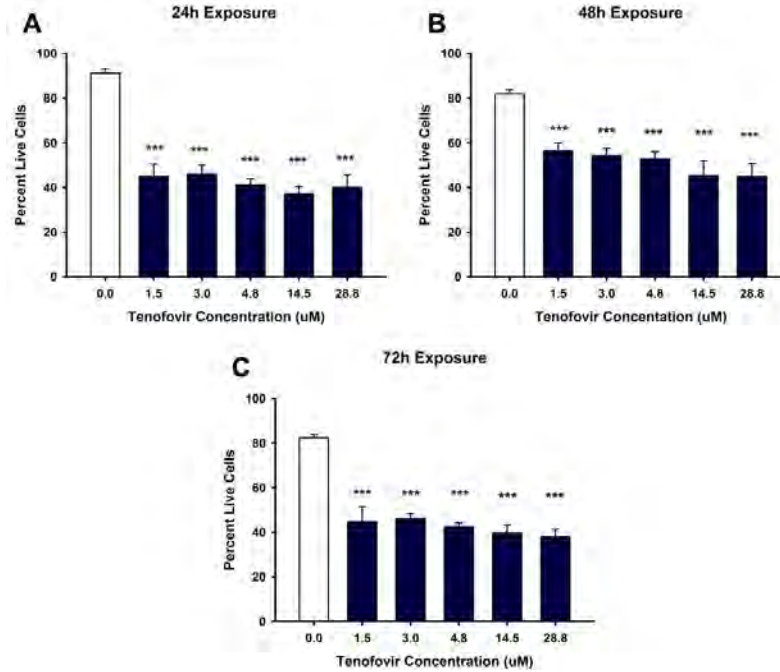


Figure 2 Tenofovir effects on HK-2 cell viability using Trypan Blue cell exclusion counts. TFV decreased cell viability at 24 (A), 48 (B) and 72 h (C). Statistical difference from 0 µM tenofovir is denoted by asterisks (***) $p < 0.001$. Each bar represents Mean \pm SEM for three independent experiments run with two biological replicates.

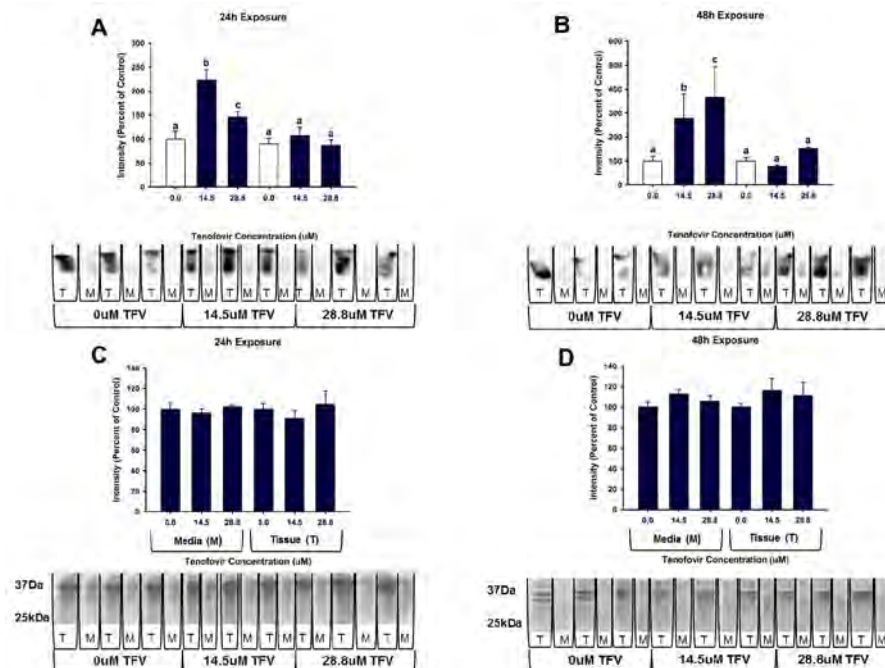


Figure 3 Tenofovir effects on LDH release from HK-2 cells. LDH release was measured in media and HK-2 cell lysate following 24 (A) and 48 h (B) exposure to TFV. Representative gel

and cumulative densitometry are included in each panel. Representative blot with Memcode Reversible staining for equal 10ug protein loading depicted for 48 (C) and 72 h (D) exposure. Different superscript letters indicate differences between groups ($p < 0.05$). Each bar represents Mean \pm SEM for two independent experiments run with three biological replicates.

TFV Effects on Mitochondrial Membrane Integrity

Cytochrome C and ATP Synthase are normally sequestered in the mitochondria of cells; release of these proteins into the cytosolic fraction indicate a loss of mitochondrial membrane integrity. 28.8uM TFV induced release of cytochrome c to the cytosolic fraction at 72 h exposure ($p < 0.001$) (Figure 4). However, TFV did not induce the release of ATP synthase to the cytosol (Figure 4). The differences in the release of these two proteins may be due to the fact that ATP Synthase is bound to the inner mitochondrial membrane.

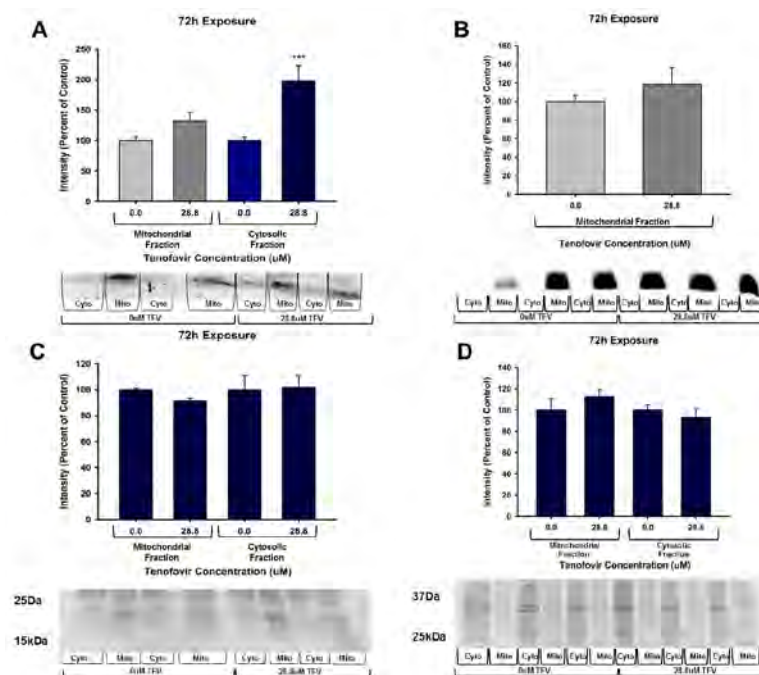


Figure 4 Tenofovir Effects on Cytochrome C and ATP synthase expression. Cytochrome c (A) and ATP synthase (B) release were measured in mitochondrial and cytosolic fractions following 72 h exposure to TFV. Representative gel and cumulative densitometry are included in each panel. Representative blot with Memcode Reversible staining for equal 40ug protein loading depicted for cytochrome (C) and ATP synthase (D). Asterisks indicate statistical differences between groups (***) $p < 0.001$). Each bar represents Mean \pm SEM for three independent experiments run with three biological replicates.

TFV Effects on Oxidative Stress in the Mitochondria

TFV induced oxidative stress in mitochondria following 72 h exposure to 28.8uM TFV (Figure 5) relative to control ($p < 0.05$) as shown by protein carbonylation. 72 h exposure to 28.8uM TFV also induced leakage of MnSOD from the mitochondrial fraction to the cytosolic fraction ($p < 0.001$) relative to control (Figure 5). Loss of this enzyme within the mitochondrial antioxidant system may further contribute to the observed oxidative damage.

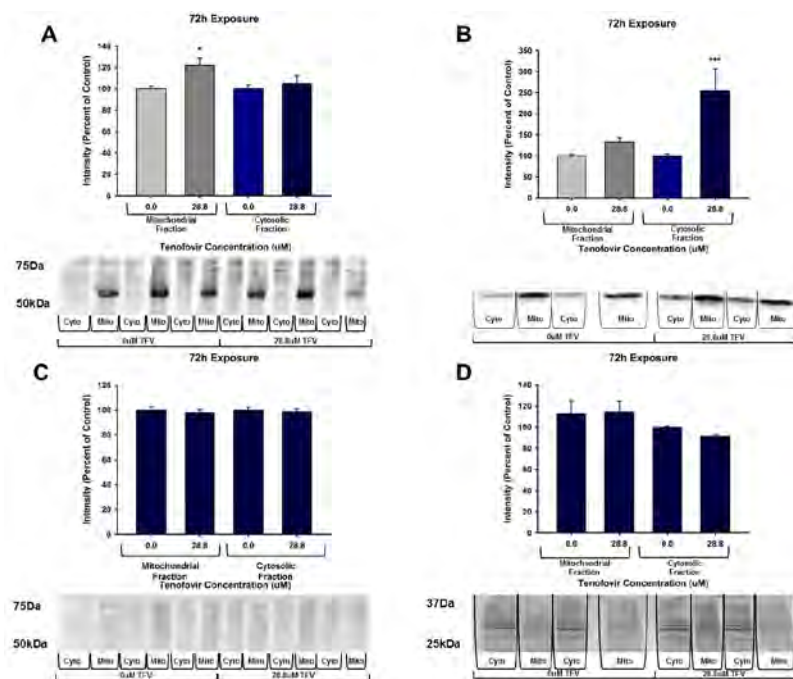


Figure 5 Tenfiovir effects on protein carbonylation and MnSOD expression. Protein carbonylation (A) and MnSOD expression (B) were measured in mitochondrial and cytosolic fractions following 72 h exposure to TFV. Representative gel and cumulative densitometry are included in each panel. Representative blot with Memcode Reversible staining for equal protein loading depicted for Oxyblot (25ug) (C) and MnSOD (40ug) (D). Asterisks indicate statistical differences between groups (* $p < 0.05$, *** $p < 0.001$). Each bar represents Mean \pm SEM for three independent experiments run with three biological replicates.

Antioxidant Protection of TFV Toxicity

Our previous study showed that oxidative stress was increased by TFV resulting in increased protein carbonylation and 4-hydroxynonenol (4-HNE) adduct formation. This suggests that a rise in reactive oxygen species occurs with TFV cytotoxicity. Pretreatment with ascorbic acid, resveratrol, and NAC reduced TFV toxicity in HK-2 cells; cell viability was higher in cells exposed

to TFV in the presence of antioxidants compared to TFV alone (Figure 6). While 0.5mM ascorbic acid did protect from TFV cytotoxicity, it did not provide enough protection to return viability to the same level as control (Figure 6). These findings suggest that use of an antioxidant pretreatment can reduce TFV cytotoxicity in HK-2 cells.

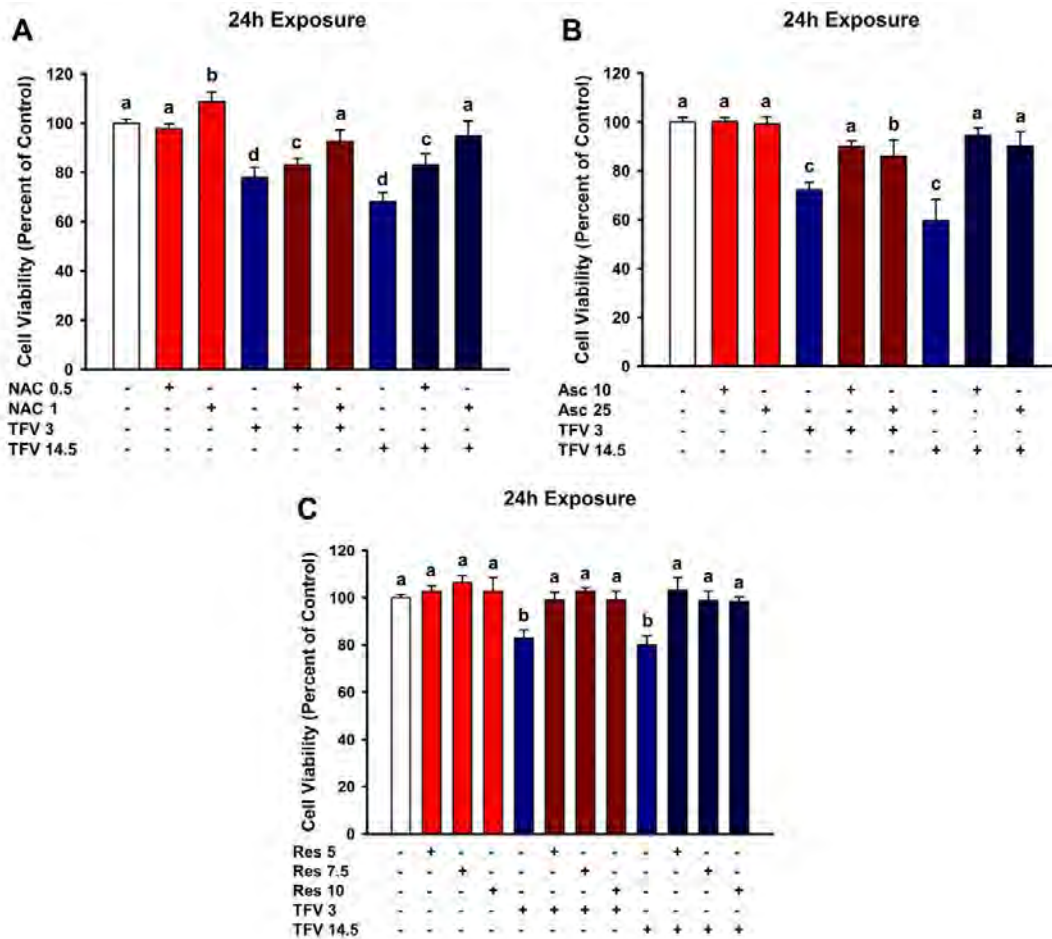


Figure 6 Effects of antioxidant pretreatment on TFV cytotoxicity. N-acetylcysteine (NAC) (A), ascorbic acid (B) and resveratrol (C) protected HK-2 cells from tenofovir cytotoxicity as assessed by MTT viability. **A)** Cells were treated with 0 (-), 0.5mM (+), or 1mM (+) NAC followed by a 24 h exposure to 0 (-), 3uM (+) or 14.5 μM TFV (+). **B)** Cells were treated with 0 (-), 10uM (+), or 25uM (+) ascorbic acid followed by a 24 h exposure to 0 (-), 3uM (+) or 14.5 μM TFV (+). **C)** Cells were treated with 0 (-), 7.5uM (+), 10uM (+), or 10uM (+) resveratrol followed by a 24 h exposure to 0 (-), 3uM (+) or 14.5 μM TFV (+). Different superscript letters (a-d) indicate statistical difference from all other groups (p<0.05). Values represent Mean ± SEM for three independent experiments run with three biological replicates.

DISCUSSION

TFV is a very effective antiviral nucleotide reverse transcriptase inhibitor prescribed worldwide in the treatment of HIV and Hepatitis B. Patients treated with TFV have an increased incidence of renal impairment [25, 26]. Renal TFV toxicity in humans is characterized by Fanconi Syndrome, and depending on the dose, development of irreversible impaired renal function. There is a positive correlation between increased TFV plasma concentration, renal toxicity and the duration that patients were treated with TFV [27, 28]. Because treatment with TFV is chronic, examination of the mechanism of renal toxicity is clinically relevant. Understanding the mechanism is essential for the development of methods to mitigate TFV renal impairment.

Our studies are the first to show that HK-2 cells are an effective model to study tenofovir cytotoxicity. In a previously published paper, we showed that treatment with clinically relevant concentrations of TFV reduced cell viability in HK-2 cells within 24 h. We also showed that TFV increases protein carbonylation and 4-HNE adduct formation in whole cell lysate at 72 h exposure and induces apoptosis via activation of caspase 3 and 9. There is also marked reduction in intracellular ATP at 72 h, but not 24 or 49 h TFV exposure [29]. These data provide insight to the mechanism of TFV induced cytotoxicity, but also leave many questions.

Our previous study indicated that mitochondrial damage and oxidative stress play a role in TFV induced cytotoxicity; the current study expands details of this mechanism. While TFV induced apoptosis at 72 h exposure as shown by caspase 3 and 9, activation of these proteins was not observed in lower time points. Additionally, intracellular ATP was not affected until 72 h exposure. This is indicative that multiple mechanisms of toxicity may be involved. When cells undergo necrosis, organelles swell and break down, which leads to breakdown of the plasma membrane [30-32]. This loss in membrane integrity leads to the release of intracellular contents. Lactate dehydrogenase (LDH) is a stable enzyme that is expressed in every cell type; it is commonly used as a marker of necrosis [33, 34]. Our study showed an increase in LDH release from HK-2 cells into the media following 24 and 48 h exposure (Figure 2); this is indicative that TFV induces necrosis in HK-2 cells within 24 h exposure. These findings are in line with clinical data of patients with TDF induced renal injury, which show marked tubular necrosis [35].

The results of our previous study also indicated that the mitochondria are the target of TFV renal cytotoxicity. Clinical studies indicate that the mitochondria of the proximal tubules are the target of TFV induced toxicity as shown by enlarged and malformed mitochondria in electron microscopy cross sections [10, 35-37]. Cytochrome c excretion into urine is observed clinically in HIV patients who have developed tenofovir induced nephropathies [38]. Proximal tubular mitochondrial toxicity has also been described in mice and rats treated with TFV as shown by disruptions in mitochondrial cristae and a reduction in mtDNA levels [15, 16]. The results of our current study are in line with these findings. TFV increases oxidative damage in the mitochondrial fraction of HK-2 cells, but not the cytosolic fraction (Figure 5). Additionally, there is a loss in mitochondrial membrane integrity, as indicated by the presence of cytochrome c and MnSOD in the cytosolic fraction following 72 h TFV exposure (Figure 4 and 5). Release of cytochrome c to the cytosol induces apoptosis via binding to Apaf-1 to form an apoptotic complex that activates caspase 9 [39, 40].

Cytochrome c is a key component of the electron transport chain; its leakage from the mitochondria into the cytosol may contribute to the loss cellular ATP production observed in our previous study. Interestingly, analysis of ATP synthase expression showed no leakage into the cytosolic fraction; ATP synthase is a membrane bound protein in the inner mitochondrial membrane and membrane breakdown may not be severe enough to induce release of ATP synthase. It is unlikely that loss of ATP synthase from the mitochondrial membrane contributes to a reduction in cellular ATP following TFV exposure.

MnSOD is a genomically encoded mitochondrial antioxidant enzyme that is essential in maintaining the balance of generation and detoxification of reactive oxygen species (ROS). MnSOD functions mainly via detoxifying superoxide free radicals that are generated during mitochondrial respiration. Oxidative stress occurs when there is an imbalance between the generation and detoxification of ROS and reactive nitrogen species (RNS)[41]. The role of MnSOD in toxicity development in HIV patients has not been extensively studied. However, one study has shown that Blood Urea Nitrogen (BUN) is elevated in wild type mice treated with 50mg/kg TDF but not in transgenic mice that overexpress MnSOD [42]. Our study shows that following 72 h exposure with 28.8uM TFV, MnSOD leakage into the cytosol increased 1.5-fold (Figure 5). This data indicates a loss in mitochondrial membrane integrity following TFV exposure and may indicate a decreased ability to respond to oxidative stress. Whether MnSOD leakage contributes to the observed oxidative damage is not yet clear as there was no change in mitochondrial expression following TFV treatment. Additional study needs to be conducted to determine more fully what role MnSOD plays in the development of TFV renal cytotoxicity.

Resveratrol and ascorbic acid are widely known as antioxidants and have been shown to prevent renal toxicity of a number of chemotherapeutic agents that induce oxidative stress in vitro and in vivo rodent models, including cisplatin and cadmium [43-47]. N-acetylcysteine (NAC) is the precursor to glutathione (GSH), an important cellular antioxidant. NAC is most notably used to treat acetaminophen overdose by providing cysteine for glutathione synthesis to mitigate hepatic toxicity, but has been shown to protect hepatocytes from oxidative damage induced by cadmium and mercury in rats [48, 49].

Our study shows that an hour pretreatment with resveratrol, NAC, or ascorbic acid protects HK-2 cell viability when exposed for 24 h to 3 or 14.5uM TFV (Figure 6). It should be noted that high concentrations of NAC (0.5-1mM) were required to induce a protective effect; resveratrol may be the best choice in prevention of TFV induced cytotoxicity as it required the lowest concentration to induce a protective effect (5uM). It is unclear by what mechanism antioxidants protect against TFV toxicity. Our previous studies did not show markers of oxidative damage (protein carbonylation and 4-HNE adduct formation) until 72 h exposure, but protection was observed in our current study within 24 h TFV exposure. Additional study needs to be done to determine the role of reactive oxygen and nitrogen species at lower time points as well as to elucidate the mechanism of antioxidant protection.

CONCLUSIONS

This study provides additional insight into the mechanism of TFV induced renal cytotoxicity. TFV induces necrosis within 24 h as shown by LDH release from HK-2 cells. Oxidative stress is

increased in mitochondria, and there is a loss of mitochondrial membrane integrity, resulting in the release of MnSOD and cytochrome c into the cytosol. Cytochrome c release further validates that TFV induces apoptosis at 72 h exposure. The role of MnSOD in TFV induced cytotoxicity remains unclear. However, antioxidant pretreatment attenuates TFV induced cytotoxicity, but the mechanism by which this occurs is unknown at this time. Additional studies need to be conducted to determine to what degree TFV modulates the mitochondrial antioxidant system, as well as investigate the mechanism by which antioxidants protect against TFV induced oxidative damage.

The generous funding I have received through the NASA West Virginia Space Grant Consortium has allowed me to generate the data presented in this report, which has won at national and regional poster presentation competitions. This fellowship has enabled me to conduct research that has led to a first author publication in the International Journal of Molecular Sciences (see Ref. 29). I have also had the opportunity to present my research both nationally and internationally at Experimental Biology 2016, The British Pharmacological Society 2016 Annual Meeting, and the Society of Toxicology 2017 Annual Meeting. It was at the SOT 2017 meeting that I secured my postdoctoral fellowship at Michigan State University that will begin in July 2017.

ACKNOWLEDGEMENTS

I would like to extend my sincerest thanks to the NASA West Virginia Space Grant Consortium for funding this work and allowing me to pursue my training as a researcher. I would also like to thank my mentor, Dr. Monica Valentovic for her guidance and mentorship. I would not have gotten as far as I have without her help at every step in my graduate career at Marshall University.

REFERENCES

1. Balzarini, J., et al., *Differential antiherpesvirus and antiretrovirus effects of the (S) and (R) enantiomers of acyclic nucleoside phosphonates: potent and selective in vitro and in vivo antiretrovirus activities of (R)-9-(2-phosphonomethoxypropyl)-2,6-diaminopurine*. Antimicrob Agents Chemother, 1993. **37**(2): p. 332-8.
2. Robbins, B.L., et al., *Anti-human immunodeficiency virus activity and cellular metabolism of a potential prodrug of the acyclic nucleoside phosphonate 9-R-(2-phosphonomethoxypropyl)adenine (PMPA), Bis(isopropylloxymethylcarbonyl)PMPA*. Antimicrob Agents Chemother, 1998. **42**(3): p. 612-7.
3. Shaw, J.P., et al., *Metabolism and pharmacokinetics of novel oral prodrugs of 9-[(R)-2-(phosphonomethoxy)propyl]adenine (PMPA) in dogs*. Pharm Res, 1997. **14**(12): p. 1824-9.
4. Choi, S.U., T. Bui, and R.J. Ho, *pH-dependent interactions of indinavir and lipids in nanoparticles and their ability to entrap a solute*. J Pharm Sci, 2008. **97**(2): p. 931-43.
5. Deeks, S.G., et al., *Safety, pharmacokinetics, and antiretroviral activity of intravenous 9-[2-(R)-(Phosphonomethoxy)propyl]adenine, a novel anti-human immunodeficiency virus (HIV) therapy, in HIV-infected adults*. Antimicrob Agents Chemother, 1998. **42**(9): p. 2380-4.
6. Barditch-Crovo, P., et al., *Phase i/ii trial of the pharmacokinetics, safety, and antiretroviral activity of tenofovir disoproxil fumarate in human immunodeficiency virus-infected adults*. Antimicrob Agents Chemother, 2001. **45**(10): p. 2733-9.

7. Durand-Gasselín, L., et al., *Nucleotide analogue prodrug tenofovir disoproxil enhances lymphoid cell loading following oral administration in monkeys*. *Mol Pharm*, 2009. **6**(4): p. 1145-51.
8. Miller, M.D., et al., *Antiviral activity of tenofovir (PMPA) against nucleoside-resistant clinical HIV samples*. *Nucleosides Nucleotides Nucleic Acids*, 2001. **20**(4-7): p. 1025-8.
9. Squires, K., et al., *Tenofovir disoproxil fumarate in nucleoside-resistant HIV-1 infection: a randomized trial*. *Ann Intern Med*, 2003. **139**(5 Pt 1): p. 313-20.
10. Hall, A.M., et al., *Tenofovir-associated kidney toxicity in HIV-infected patients: a review of the evidence*. *Am J Kidney Dis*, 2011. **57**(5): p. 773-80.
11. Del Palacio, M., S. Romero, and J.L. Casado, *Proximal tubular renal dysfunction or damage in HIV-infected patients*. *AIDS Rev*, 2012. **14**(3): p. 179-87.
12. Havens, P.L., et al., *Association of higher plasma vitamin D binding protein and lower free calcitriol levels with tenofovir disoproxil fumarate use and plasma and intracellular tenofovir pharmacokinetics: cause of a functional vitamin D deficiency?* *Antimicrob Agents Chemother*, 2013. **57**(11): p. 5619-28.
13. Wang, F. and O.P. Flint, *BMS-986001, an HIV nucleoside reverse transcriptase inhibitor, does not degrade mitochondrial DNA in long-term primary cultures of cells isolated from human kidney, muscle, and adipose tissue*. *Antimicrob Agents Chemother*, 2013. **57**(12): p. 6205-12.
14. Vidal, F., et al., *In vitro cytotoxicity and mitochondrial toxicity of tenofovir alone and in combination with other antiretrovirals in human renal proximal tubule cells*. *Antimicrob Agents Chemother*, 2006. **50**(11): p. 3824-32.
15. Kohler, J.J., et al., *Tenofovir renal toxicity targets mitochondria of renal proximal tubules*. *Lab Invest*, 2009. **89**(5): p. 513-9.
16. Lebrecht, D., et al., *Mitochondrial tubulopathy in tenofovir disoproxil fumarate-treated rats*. *J Acquir Immune Defic Syndr*, 2009. **51**(3): p. 258-63.
17. Ryan, M.J., et al., *HK-2: an immortalized proximal tubule epithelial cell line from normal adult human kidney*. *Kidney Int*, 1994. **45**(1): p. 48-57.
18. Paolicchi, A., et al., *gamma-Glutamyl transpeptidase catalyses the extracellular detoxification of cisplatin in a human cell line derived from the proximal convoluted tubule of the kidney*. *Eur J Cancer*, 2003. **39**(7): p. 996-1003.
19. Gunness, P., et al., *Comparison of the novel HK-2 human renal proximal tubular cell line with the standard LLC-PK1 cell line in studying drug-induced nephrotoxicity*. *Can J Physiol Pharmacol*, 2010. **88**(4): p. 448-55.
20. Miyamoto, Y., et al., *A uremic toxin, 3-carboxy-4-methyl-5-propyl-2-furanpropionate induces cell damage to proximal tubular cells via the generation of a radical intermediate*. *Biochem Pharmacol*, 2012. **84**(9): p. 1207-14.
21. Humphrey, M.L., et al., *Mitochondrial mediated thimerosal-induced apoptosis in a human neuroblastoma cell line (SK-N-SH)*. *Neurotoxicology*, 2005. **26**(3): p. 407-16.
22. Strober, W., *Trypan blue exclusion test of cell viability*. *Curr Protoc Immunol*, 2001. **Appendix 3**: p. Appendix 3B.
23. Bradford, M.M., *A rapid and sensitive method for the quantitation of microgram quantities of protein utilizing the principle of protein-dye binding*. *Anal Biochem*, 1976. **72**: p. 248-54.

24. Terneus, M.V., et al., *Comparison of S-Adenosyl-L-methionine and N-acetylcysteine protective effects on acetaminophen hepatic toxicity*. J Pharmacol Exp Ther, 2007. **320**(1): p. 99-107.
25. Verhelst, D., et al., *Fanconi syndrome and renal failure induced by tenofovir: a first case report*. Am J Kidney Dis, 2002. **40**(6): p. 1331-3.
26. Fux, C.A., et al., *Tenofovir use is associated with a reduction in calculated glomerular filtration rates in the Swiss HIV Cohort Study*. Antivir Ther, 2007. **12**(8): p. 1165-73.
27. Quesada, P.R., et al., *Incidence and risk factors for tenofovir-associated renal toxicity in HIV-infected patients*. Int J Clin Pharm, 2015. **37**(5): p. 865-72.
28. Ezinga, M.W., J.F.M; Bosch, M.E.W; van der Ven, A.J.A.M; Burger, D.M, *Long-term treatment with tenofovir: prevalence of kidney tubular dysfunction and its association with tenofovir plasma concentration* Antivir Ther, 2014. **19**: p. 765-771.
29. Murphy, R.A., et al., *Establishment of HK-2 Cells as a Relevant Model to Study Tenofovir-Induced Cytotoxicity*. Int J Mol Sci, 2017. **18**(3).
30. Schweichel, J.U. and H.J. Merker, *The morphology of various types of cell death in prenatal tissues*. Teratology, 1973. **7**(3): p. 253-66.
31. Moquin, D. and F.K. Chan, *The molecular regulation of programmed necrotic cell injury*. Trends Biochem Sci, 2010. **35**(8): p. 434-41.
32. Challa, S. and F.K. Chan, *Going up in flames: necrotic cell injury and inflammatory diseases*. Cell Mol Life Sci, 2010. **67**(19): p. 3241-53.
33. Burd, J.F. and M. Usategui-Gomez, *A colorimetric assay for serum lactate dehydrogenase*. Clin Chim Acta, 1973. **46**(3): p. 223-7.
34. Chan, F.K., K. Moriwaki, and M.J. De Rosa, *Detection of necrosis by release of lactate dehydrogenase activity*. Methods Mol Biol, 2013. **979**: p. 65-70.
35. Herlitz, L.C., et al., *Tenofovir nephrotoxicity: acute tubular necrosis with distinctive clinical, pathological, and mitochondrial abnormalities*. Kidney Int, 2010. **78**(11): p. 1171-7.
36. Cote, H.C., et al., *Exploring mitochondrial nephrotoxicity as a potential mechanism of kidney dysfunction among HIV-infected patients on highly active antiretroviral therapy*. Antivir Ther, 2006. **11**(1): p. 79-86.
37. Woodward, C.L., et al., *Tenofovir-associated renal and bone toxicity*. HIV Med, 2009. **10**(8): p. 482-7.
38. Maggi, P., et al., *Early markers of tubular dysfunction in antiretroviral-experienced HIV-infected patients treated with tenofovir versus abacavir*. AIDS Patient Care STDS, 2012. **26**(1): p. 5-11.
39. Liu, X., et al., *Induction of apoptotic program in cell-free extracts: requirement for dATP and cytochrome c*. Cell, 1996. **86**(1): p. 147-57.
40. Jiang, X. and X. Wang, *Cytochrome c promotes caspase-9 activation by inducing nucleotide binding to Apaf-1*. J Biol Chem, 2000. **275**(40): p. 31199-203.
41. Fridovich, I., *Superoxide radical and superoxide dismutases*. Annu Rev Biochem, 1995. **64**: p. 97-112.
42. Glover, M., et al., *Overexpression of mitochondrial antioxidant manganese superoxide dismutase (MnSOD) provides protection against AZT- or 3TC-induced endothelial dysfunction*. Antiviral Res, 2014. **111**: p. 136-42.
43. Do Amaral, C.L., et al., *Resveratrol attenuates cisplatin-induced nephrotoxicity in rats*. Arch Toxicol, 2008. **82**(6): p. 363-70.

44. Valentovic, M.A., et al., *Resveratrol attenuates cisplatin renal cortical cytotoxicity by modifying oxidative stress*. *Toxicol In Vitro*, 2014. **28**(2): p. 248-57.
45. Fu, B., et al., *Resveratrol rescues cadmium-induced mitochondrial injury by enhancing transcriptional regulation of PGC-1alpha and SOD2 via the Sirt3/FoxO3a pathway in TCMK-1 cells*. *Biochem Biophys Res Commun*, 2017. **486**(1): p. 198-204.
46. Maliakel, D.M., T.V. Kagiya, and C.K. Nair, *Prevention of cisplatin-induced nephrotoxicity by glucosides of ascorbic acid and alpha-tocopherol*. *Exp Toxicol Pathol*, 2008. **60**(6): p. 521-7.
47. Koyuturk, M., et al., *The potential role of combined anti-oxidants against cadmium toxicity on liver of rats*. *Toxicol Ind Health*, 2007. **23**(7): p. 393-401.
48. Joshi, D., et al., *N-acetyl cysteine and selenium protects mercuric chloride-induced oxidative stress and antioxidant defense system in liver and kidney of rats: a histopathological approach*. *J Trace Elem Med Biol*, 2014. **28**(2): p. 218-26.
49. Wang, J., et al., *N-acetylcysteine protects against cadmium-induced oxidative stress in rat hepatocytes*. *J Vet Sci*, 2014. **15**(4): p. 485-93.

“FENCE-LINE” CONTRAST SOUNDSCAPE STUDY OF FORESTED LANDS IN ALLEGANY STATE PARK AND ALLEGHENY NATIONAL FOREST: IS THERE AN IMPACT OF OIL AND GAS DEVELOPMENT ON AN EASTERN FOREST SOUNDSCAPE?

Kasey Lynne Osborne
Biological Sciences
Marshall University
Huntington, WV

ABSTRACT

“Natural resources” – an inclusive term indiscriminate of splendor or conservation status – require proper management, be it for forest, oil, water, wildlife, or even soundscapes. The soundscape, or all sounds (biophony, anthrophony, geophony) characterizing an area, is both an ecological monitoring tool and a resource itself – a component of the landscape. As energy demands surge, the oil/gas region of the Appalachian Plateau adjusts to unconventional extraction concurrent with traditional drilling operations. Energy development leaves enduring spatial footprints on the landscape, such as fragmentation from well-pad matrices. Soundscape patterns may not be as readily observed as visual cues, but their analysis can reveal temporal landscape changes and ecological integrity. This study examined the soundscape of a contiguous eastern deciduous temperate forest located across the “fence-line” of a federally-managed forest (Allegheny National Forest, PA), an area with ongoing energy development, and a state-managed park (Allegheny State Park, NY), an area without energy development. Using comparable sites in each state, I deployed ten Wildlife Acoustics SM2 recorders in a north-south line across the PA-NY border. The devices recorded for one minute every thirty minutes, and these data were collected every two months. The indices used reveal how complex or uniform the sound is, the ratio of biophony relative to anthrophony, and ultimately show how biodiversity may wane in response to ecosystem health. The literature generally finds higher biophony and acoustic complexity in undisturbed areas, which the undeveloped NY sites are predicted to reflect. The expected results imply that the infrastructure, land disturbance, and compromised natural soundscape associated with energy development can negatively impact wildlife occupancy, communication, reproductive success, vegetation composition, and ecological integrity as represented by acoustic niches in the soundtope. Incorporating soundscapes into modern landscape assessment ensures comprehensive and informed natural resource management. Results indicated no significant difference in any index between the two forest management plans; this could be explained by a lack of temporal distinctions in analysis and an influx of species associated with edge on lands with energy development.

INTRODUCTION

This study examined the effects of general (conventional and unconventional) natural gas extraction on eastern deciduous forests by analyzing and comparing the soundscapes in sites in a state park without energy development and a national forest with energy development. The study area was a contiguous forest in northcentral Pennsylvania, the Allegheny National Forest, extending into southern New York in the Allegheny State Park. Natural gas extraction has a long

history in this region and the more recent Marcellus shale extraction dots the landscape, as well. The Pennsylvania sites have historical and current energy development, while the New York sites do not. The disparate management goals and surface-mineral rights ownership of the two states provide a unique stage for a fence-line contrast study, which examines two contiguous landscapes undergoing different management regimes (Hongslo 2010). The biophony in these areas is dominated primarily by birds, then insects and amphibians. Because continuous, passive long-term monitoring of landscapes is both feasible and potentially informative with soundscape ecology, I used this method to investigate what, if any, differences in the soundscape occur between two adjacent forest sites with different natural gas management regimes (Deichmann, Hernandez-Serna, and Delgado 2017). This study examined the soundscape of the two forest treatments using the following acoustic indices: Acoustic Complexity (ACI), Normalized-Difference Sound (NDSI), and Acoustic Evenness (AEI). I hypothesized the Pennsylvania sites would have lower complexity and biophony, and have higher evenness, with the inverse prediction for the New York sites.

I placed 10 Wildlife Acoustics Song Meter SM2+ (Wildlife Acoustics 2012) autonomous recorders in the study area—5 in NY and 5 in PA. I programmed the devices to record for one minute every thirty minutes from June 2016 until June 2017 (although this report only includes data analyzed until March 2017). The data were collected on a 2-month cycle and analyzed incrementally. The three indices used were then run through a mixed effects model with autoregressive (corAR1) covariance structure, and showed no significant difference between forest management in NY and PA in any of the indices.

BACKGROUND

“New World” of America astounded early surveyors with the land’s variform and abundant natural resources – from great and sturdy trees, wide, flowing rivers, bounteous feathered and furred game, to untapped energy just below fruitful soil. She remains a natural resource hub, with the stewardship of her lands perpetuating abundance to the current day. However, the coexistence of both scenic horizons rich with life and resources vital to human civilization has not been attained without a balancing act. Sustainably using natural resources while promoting economic and societal growth is the key to continued enjoyment of nature and services for generations to come. However, this balance is contentious and complicated to both determine and implement. The political climate of natural resource management is increasingly impassioned as both public environmental awareness and energy demands surge (USDE 2005); this discord is particularly evident in the Allegheny Plateau. Pennsylvania is the home to many thriving historical and modern energy industries as well as its namesake, “Penn’s Woods”, which makes the state the second-most forested in the northeast (Smith, Miles, Perry, and Pugh 2009).

Energy Development Background

The Allegheny National Forest (ANF), covering Pennsylvania’s Elk, Forest, McKean, and Warren counties, is entrenched in the history of energy extraction, for it is but 40 miles away from Titusville, PA, where the first commercial oil well, the Drake well, in the United States was drilled in August 1859 (Ross 1996). The oil fields of Bradford, PA supplied an astounding 90% of the entire world’s oil demand into the early 1900s (Fettke 1938). Since this historical explosive phase in energy exploration, Pennsylvania has remained a chief source of domestic energy products,

including coal, natural gas, and oil. Many of the oil fields beneath the ANF are still producing today, with new wells between 1986-2005 increasing four-fold (Thomas, Brittingham, and Stoleson 2014; USFS 2007b, 2008). Further, in the past decade, a new layer of fuel, namely the Marcellus shale, in the Allegheny Plateau, has become newly accessible in the advent of unconventional drilling techniques such as high-volume hydraulic fracturing and horizontal drilling, wherein the shale is fractured to release gas (Brittingham, Maloney, Farag, Harper, and Bowen 2014; Engelder and Lash 2008; Drohan, Finley, Roth, Schuler, Stout, Brittingham, and Johnson 2012a; Slonecker, Milheim, and Roig-Silva 2012).

Pennsylvania residents own approximately 76% of the land developed for shale-play, non-residents own 7%, and the Commonwealth owns 17%, leading to booms in the regional economies of those towns near the developed sites (Kelsey, Shields, Ladlee, and Ward 2011). In 2009, around 24 000 new jobs and \$3.1 to \$3.2 billion in new income came into Pennsylvania (Kelsey et al. 2011). State agencies, including the Pennsylvania Game Commission and Department of Conservation and Natural Resources, have also reaped the economic benefits of owning mineral rights in shale-play regions, receiving millions of dollars toward their agency missions (Kelsey et al. 2011; Drohan et al. 2012a).

Since the mid-2000s, Pennsylvania has undergone rapid landscape change to accommodate the influx of this new energy development. According to the Pennsylvania Department of Environmental Protection (PA DEP), the agency tasked with managing energy resources, the number of historical and modern well reports amount to around 325,000 wells drilled since 1859 (PA DEP 2011), with about 51,000 unconventional and conventional wells formed in the past decade, per the PA DEP's self-reporting system records (PA DEP 2017). Numbers obtained from this system can have an element of ambiguity to them due to the nature of self-reporting by energy companies, the variety in types of wells and operations, historical and modern production, and the inclusion of both permitted and future wells (Drohan et al. 2012a).

Conventional wells and unconventional Marcellus shale wells often exist in the same area, though they regularly have different spatial footprints (Drohan et al. 2012a; Drohan, Brittingham, Bishop, and Yoder 2012b). The abundant conventional wells are shallow and typically 1 ha or less, but occur in clusters over large swathes of land (Slonecker et al. 2012; USFS 2007a). Traditional wells outnumber Marcellus shale operations, though the latter have a footprint anywhere between 2 and 12 ha, and are comprised of well pad matrices and substantial infrastructure (PA DEP 2011; Drohan et al. 2012b). However, the horizontal wells employed for Marcellus shale, which can reach 2 438 m in subterranean length and, thus, access a wider area for gas, can result in fewer overall wells drilled (Drohan et al. 2012a). While the peak of the current Marcellus shale drilling has passed and new drilling permit applications have presently slowed, the potential short- and long-term impacts eastern forests will experience are not yet well understood, for research has been unable to keep up with the expanding gas exploration (Thomas et al. 2014, Drohan et al. 2012b); however, effects can be partially predicted by studying similar landscape disturbance in ecosystems from other anthropogenic processes (Brittingham et al. 2014).

Ecological and Ecosystem Impacts

Civilization depends on functioning, interconnected ecosystems for many daily items, or goods and services: food, water, living space, medicines, building materials, recreation, aesthetics,

energy, and countless other products and activities. An ecosystem's health is often defined and assessed in terms of its ecological integrity and condition, which are intricate qualities encompassing features such as the ecosystem's ability to reach its natural biological potential, its ability to recover following disturbance, how stable its patterns are, and the diversity, composition, and functions of the species and communities it supports and sustains (Karr and Dudley 1981; Karr, Fausch, Angermeier, Yant, and Schlosser 1986; Parkes and Lyon 2006).

As with any large-scale anthropogenic disturbance, the opportunity for compromised ecological integrity is increased (Noss 1990; Drever Aitken, Norris, and Martin 2006; Parrish, Braun, and Unnasch 2003; Williams 2002; Andreasen, O'Neill, Noss, and Slosser 2001). Many types of disturbance and landscape change occur with energy development, including: forest fragmentation and clearing; access roads and road systems; well pads and associated well matrices; vertical and horizontal drilling operations; gathering and main transmission lines; construction machinery; compressor stations; freshwater and flowback water storage ponds; equipment storage areas; pipelines; increased human traffic and occupancy for site maintenance; and other anthropogenic disturbances (Drohan et al. 2012b; Slonecker et al. 2012;). Habitat alteration, particularly linear clearings used for roads and pipelines, can have marked impacts on habitat and inhabitants, such as edge effects, barrier effects, and road mortality (Laurance and Yensen 1991; Laurance, Goosem, and Laurance 2009; Fahring 2003; Murcia 1995; Brittingham et al. 2014; Segers and Broders 2014).

Because natural gas development in the Allegheny Plateau, and specifically on the ANF, is frequently in forested areas (Ritters et al. 2002), core forest habitat (>100 m from edge) (Abrahams, Griffin, and Matthews 2015; Souther et al. 2014) is often compromised by fragmentation. Core habitat is particularly critical on the ANF, because it harbors most of the remaining interior forest in Pennsylvania (USFS 2007b). Fragmentation also alters forest patch size and isolation, solar penetration, and temperature, moisture, and other abiotic elements, which in turn affects biotic components, such as making way for expanding invasive plant species (Brittingham et al. 2014; Mortensen, Rauschert, Nord, and Jones 2009; Harper et al. 2005).

Wildlife Impacts

Being the only national forest in the state, and a large, contiguous one at that, means the ANF supports a great diversity of forest wildlife, particularly forest-interior species including neotropical migrant songbirds and species of concern (Thomas et al. 2014; Steele, Brittingham, Maret, and Merritt 2010). Because continuous and core forest is often fragmented to make way for natural gas and oil development, forest-interior specialists, particularly songbirds, can suffer from the loss of these areas. Nesting recruitment and mortality of birds can occur when development coincides with breeding season (Wilgenburg, Hobson, Bayne, and Kiper 2013).

Pipelines and access roads create linear corridors in the forest, which can either serve as a barrier or an avenue (Laurance et al. 2009). Movement can be impeded or facilitated; the latter often being the case with predatory or invasive mammals and birds such as the brown-headed cowbird (*Molothrus ater*) (Brittingham et al. 2014), leading to higher predation rates (Bayne, Boutin, Tracz, and Charest 2005). Movement patterns, species interactions, distribution, occupancy, and abundance can all be altered from the introduction of linear fragmentation (Laurance et al. 2009; Brittingham et al. 2014).

Despite the lack of literature pertaining to amphibians and unconventional gas development, forest-dwelling amphibians can suffer deleterious effects from forest fragmentation, particularly in community diversity and abundance, depending on forest and anuran assemblage type (Gibbs 1998; Cushman 2006; Bell and Donnelly 2006; McCracken and Forstner 2014). Amphibians associated with a moist microclimate, detritus, and coarse woody debris, such as Plethodontidae, the woodland salamanders, can be negatively impacted by the artificially sustained successional habitat left by gas wells and the increased salinity associated with roads and fracturing water (Moseley, Ford, Edwards, and Adams MB 2010; Russell, Wigley, Baughman, Hanlin, and Ford 2004). Species whose ranges largely overlap or are even restricted to the areas underlain by the shale-play are most at risk (Gillen and Kiviat 2013), particularly coupled with increased access roads and amphibians' poor dispersal abilities (Moseley et al. 2010; Storfer 2003).

Chronic noise pollution from natural gas development and production and oil wells can negatively affect wildlife (Francis and Barber 2013; Barber, Crooks, and Fristrup 2010; Barber et al. 2011; Blickley, Blackwood, and Patricelli 2012; Proppe, Sturdy, and St. Clair 2013). While the development and drilling process can take several months to years, the production period and compressor stations can contribute to anthropogenic sound for many years beyond this timeframe (Brittingham et al. 2014). Many taxa rely on sound to communicate, be it for mating, territorial establishment, awareness of predation or prey, inter- and intra-specific interaction, or other uses. The long-term source of noise pollution in energy development are compressor stations, which can cause acoustical masking and negatively affect species abundance, site avoidance, pairing and reproductive success, altered avian communities, and prey-predator interactions (Brittingham et al. 2014; Francis and Barber 2013; Blickley et al. 2012).

Unlike the sparse research conducted in the eastern forests, the sagebrush ecosystem in the western US has experienced extensive oil and gas development and subsequent research, primarily on the greater sage-grouse (*Centrocercus urophasianus*), which is treated as an umbrella species (Brittingham et al. 2014; Lendrum, Andersen, Long, Kie, and Bowyer 2012. 2012; Blickley et al. 2012). Concurrent with gas exploration in Wyoming, the sage-grouse population has decreased substantially since over several decades with a negative association with gas development (Rowland, Wisdom, Suring, and Meinke 2006). Mule deer habitat selection, density, and migration routes were all found to be impacted by unconventional gas development (Sawyer, Kauffman, and Nielson 2009; Lendrum et al. 2012). While the sagebrush ecosystem is not directly comparable to the eastern temperate forest, similar patterns can exist in response to the same disturbance types.

Inversely, many wildlife species associated with edge and early successional habitat can be associated with natural gas development, where canopy removal and forest fragmentation are common. Diversity and species richness of small mammals and reptiles is often improved by the introduction of edge habitat and canopy removal (Moseley et al. 2010; Russell et al. 2004; Menzel, Ford, Laerm, and Krishon 1999; Ross et al. 2000; Greenberg 2001; Kjoss and Litvaitis 2001). Game species may flourish from properly managed natural gas openings transformed into wildlife openings (Moseley et al. 2010).

Soundscapes

Understanding interactions of human-natural systems at different scales requires assessing ecosystem health with a modern and comprehensive approach that takes advantage of innovative ecological monitoring tools (Pijanowski, Farina, Gage, Dumyahn, and Krause 2011a; Dumyahn and Pijanowski 2011a). One of these relatively recent tools is acoustic ecology, or soundscape assessment, which combines elements from landscape ecology, bioacoustics, community ecology, and engineering (Gasc, Francomano, Dunning, and Pijanowski 2017). A “soundscape” (Pijanowski and Farina 2011b; Schafer 1977) is an entity regarded as the collection of all the sounds that exist in a certain landscape, such as a forest, city, desert, marine reef, and so on. These sounds are assembled into three classifications: biophony, geophony, and anthrophony (Pijanowski et al. 2011c). Biophony is the sound emitted from living organisms, often as communication of birds, amphibians, insects, mammals, and other fauna. Geophony includes abiotic environmental sounds, like rainfall, flowing water, thunder, wind, earth, and rustling leaves. Anthrophony refers to sounds generated by humans or human-related activities, such as trucks and cars, planes, sirens, construction machinery, and other anthropogenic sources. These distinct categories, fluctuating over time and space, synthesize to form a single soundscape, which is a distinct object that reflects the informative properties of the items comprising it (Farina, Lattanzi, Malavasi, Pieretti, and Piccioli 2011a; Bedoya, Isaza, Daza, and López 2017), and is considered a natural resource – something to be conserved, as well (Pilcher 2010; Krause and Ellen 2001).

The use of sound to assess landscape change and ecological integrity is growing as a modern monitoring tool within the realm of landscape ecology (Farina and Belgrano 2004; Brown and Williams 2016; Truax and Barrett 2011). While soundscape ecology certainly integrates and builds upon parallel fields, unlike the humanities/species-centric and behavioral approach of bioacoustics and acoustic ecology, soundscape ecology largely follows the tenets of landscape ecology (Turner 1989), with an emphasis on spatial-temporal patterns of sound with respect to biophony, geophony, and anthrophony (Villanueva-Rivera et al. 2011; Bormpoudakis, Sueur, and Pantis 2013), while maintaining bioacoustics’ conservation ethic (Pijanowski et al. 2011a). Landscape change has traditionally been studied by static visual means (Farina and Belgrano 2004) like surveys; however, in addition to being both a natural resource (Dumyahn and Pijanowski 2011) and an ecological pattern, the soundscape reflects landscape-level shifts in pattern and process and can detect landscape disturbance over spatial and temporal spectrums (Matsinos et al. 2008). While analysis of sonic facets in the environment may initially seem abstract, the soundscape contains quantifiable properties: acoustic composition, temporal and frequency patterns, spatial variability, and acoustic interactions (Pijanowski et al. 2011a; Villanueva-Rivera et al. 2011; Smith and Pijanowski 2014). The acoustic patterns of a soundscape can reflect the biological diversity that exists in an area by way of signatures or occupation of sound frequency ranges, the levels of complexity of sound signals, and other quantifiable properties of collected audio, while explaining ecological and evolutionary processes as manifested in sound (Mazaris et al. 2009).

The biophony portion of the soundscape is especially telling of a habitat’s ecology, as it is what carries all communication from wildlife. Birds are a major biophonic presence, and beyond being a main contributor to biophony, birds are also considered indicators of ecosystem health due to traits that make them an excellent study taxon, such as: high trophic positions, low reproductive rates (Maurer 1999 Hausner, Yoccoz, and Ims 2003), detectability and existing knowledge base, their presence over many landscape types and levels of vegetative structure (Furness and

Greenwood 1993; Bradbury et al. 2005; Drever, Aitken, Norris, and Martin 2008), response to vegetative structure (Eglington 2012), and their many life history traits and habitats (Chace and Walsh 2006). Many birds are gregarious and exhibit coordinated vocalizations within and between species groups in order to convey information to both like-species and intruders (Mazaris, Kallimanis, Chatzigiandis, Papadimitriou, and Pantis 2009; Gasc et al. 2017). Amphibians are also a major natural sound contributor. Because they are often quite sensitive to any nuanced changes in their immediate environment, they are considered ecological indicators of sustainable forest management (Moseley et al. 2010; Welsh and Droege 2001).

METHODS

Recorders

To ensure comparable conditions and keep the fence-line component relevant, I restricted my study area in Pennsylvania to the northern extent of the forest. I arranged the recorders along a rough north-south line perpendicular to the PA-NY boundary with respect to a disturbance gradient (Gibbs 1998; Fischer and Lindenmayer; Joo, Gage, and Kasten 2011; Kleist, Guralnick, Cruz, and Francis 2017; Pieretti and Farina 2013); 9 of these occupied an area of approximately 26 km² (4920 hectares), with the tenth recorder 10 km south of the main study area at a hydraulic fracturing site so more unconventional samples were obtained. In both treatment areas (non-energy and energy development), I affixed the recorders to trees of 60 to 80 cm diameter at breast height by wire and about 3.5 to 4 m above the ground.

I named the recorders “AF#”, the pound sign signifying Allegheny Forest ‘Unit Number’. Units 1 through 5 were in the Allegheny National Forest (PA, energy development), and units 6 through 10 were in the Allegany State Park (NY, no energy development). I initially used a random point generator for recorder placement, and I adjusted on-site in response to surface ownership, travel concerns, and degree of forest cover. I used a comparable mix of land uses within the umbrella of either treatment, including deeper forest, forest proximate to trails and roads, and near buildings. I placed each recorder approximately 25 to 50 m from the edge.

Statistical Analyses

I performed statistical analyses in the R Statistical Program (R Core Team 2015) with packages tuneR (Ligges Preusser, Thieler, and Weihs 2015) and Soundecology (Villanueva-Rivera and Pijanowski 2015). To prepare the data, faulty or empty WAV files were omitted from the analysis. I calculated hourly means for each index (Normalized-Difference Sound, Acoustic Complexity, Acoustic Evenness), resulting in 24 values per day per site, and were processed without further temporal separations. I treated each hourly value as a repeated sample instead of an independent observation (Gutzwiller and Riffell 2007). The average samples for each recorder were approximately 6,600.

The Normalized Difference Soundscape Index (NDSI) was developed by the Remote Environmental Assessment Laboratory (REAL) at Michigan University (Kasten, Gage, Fox, and Joo 2012). The NDSI determines possible anthropogenic auditory disturbance based on the biophony relative to anthrophony ratio, with results ranging from -1 (pure anthrophony) to +1 (pure biophony). I used the Acoustic Complexity Index (ACI) (Farina and Morri 2008; Pieretti et al. 2011a) to help discriminate between sounds that do not share the inherent patterns of biophony,

particularly geophonies and anthrophonies. The output of ACI combines the complexity of sound over both temporal and frequency spectrums, and can be used as an acoustic signature of a specific soundscape at a given time. Higher ACI values suggest greater acoustic complexity. The Acoustic Evenness Index (AEI) (Villanueva-Rivera, Pijanowski, Doucette, and Pekin 2011) is analogous to species evenness. The audio dominance and occupancy per each frequency band are calculated and represented as the Gini coefficient, wherein a value of 0 is perfect unevenness and 1 is total evenness. Evenness can fluctuate greatly over time, with higher evenness generally indicative of less diversity represented in the spectrogram, and low evenness signifying a greater number of entities producing auditory signals, and thus, higher species richness (Sueuer, Farina, Gasc, Pieretti, and Pavoine 2014; Ström 2013).

After comparing model scores and ruling out other tests based on missing assumptions, I performed a mixed-effects (random and fixed) model relating each index to forest management type fit by restricted maximum likelihood estimation (REML) without a covariance structure, followed by another mixed-effects model including an AR-1 autocorrelation structure, which is an auto-regressive model of order 1. The form argument was the hourly sequence per recorder to account for temporal autocorrelation, since the samples were not independent (Gutzwiller and Riffell 2007). The fixed effects were the acoustic index and forest treatment, and the random effects were the hour and site per treatment. Based on AIC model selection, the mixed model with AR-1 autocorrelation outperformed the GLS and the mixed model without autocorrelation.

DISCUSSION

While the New York sites were expected to show higher biophony, higher acoustic complexity, and lower evenness, when examined as two groups, no significant difference existed between the two states. This could be explained by several factors, including the small study area and short distance between the national forest and state park. Although the difference in spatial characteristics of the two forest regimens is stark when viewed from aerial satellite imagery, the on-ground footprint and level of fragmentation were relatively similar, so habitat use by organisms between the two areas could be comparable or contain overlap. If the Pennsylvania recorders were placed further south amid denser oil fields checkered with well pad matrices and with less continuous forest proximate to the energy study area, the soundscape may be more influenced by energy development; however, this could invalidate the fence-line component of the study since forest condition can shift with distance. Some recorders in New York were placed near sources of water, which could mask biophony and cause misinterpretation of geophony as anthrophony in analysis. Many wildlife species are enticed by or associated with energy development due to synanthropy, edge effects, early successional habitat, or linear corridor use (Alverson, Waller, and Solheim 2010; Moseley et al. 2010; Harper 2007).

Because sound wave attenuation and reception depend on many circumstances, such as terrain features, vegetative structures, distance, frequency, intensity, and source, the analysis and interpretation of sound data can be muddy (Villanueva-Rivera et al. 2011). Further, this study examined energy development as a whole, including both the more abundant conventional well areas and unconventional together on a landscape – as they often occur together. So, the soundscape analysis cannot necessarily be attributed to either one type of energy development, but a combination of the two in spatial distribution, depending on their distance and area effect.

The data for most recorders were replete with outliers and significant spreads. This can be explained by several scenarios. The seasonal (spring versus winter) and hourly (dawn versus midnight) difference in sound sources and abundance of biophony, analyzed as if there were no difference, could contribute to this condition. Further, the periodic but severe noise from the compressor station may be affecting some averages.

Since the forests of Pennsylvania are estimated to have once dominated the great majority of land, and with current estimates at a substantial 61% of total land area (USFS 2011), forest resources are a vital focus for both policymakers and stakeholders, including agencies, numerous industries, nature enthusiasts, hunters, and anyone who may use or be affected by forest resources. Ideal regulations should be friend to both ecology and economy, striking a balance between conservation and industry that is often difficult to achieve. While the purpose of state parks – such as the case with the New York segment – is typically oriented toward recreation, national forests bear the motto “Land of Many Uses” (USFS 2011). This entails a more multifaceted approach to land management in order to sustainably support anything from wildlife habitat, watershed protection, and wood products, to hunting and recreational opportunities. The breadth of factors both influencing and influenced by forests and forest-related activities and products is outside the scope of this study, but sustainability is a comprehensive practice that requires a collective mission and collaboration by disparate entities. Common sense management practices can benefit from incorporating information generated by emerging ecological monitoring tools, such as soundscape ecology.

Natural gas forest openings are not necessarily negative introductions for all wildlife, as they can serve as wildlife openings. As stated, many reptiles and small mammal populations increase in diversity and species richness (Moseley et al. 2010; Russell et al. 2004; Menzel et al. 1999; Ross et al. 2000; Greenberg 2001; Kjoss and Litvaitis 2001) due to edge habitat and canopy removal. Managed wildlife openings and early-successional vegetation are beneficial for game species like the eastern wild turkey (*Meleagris gallopavo*), American black bear (*Ursus americanus*), ruffed grouse (*Bonasa umbellus*), American woodcock (*Scolopax minor*), and white-tailed deer (*Odocoileus virginianus*) (Moseley et al. 2010; Kammermeyer and Moser 1990; Parker, Kammermeyer, and Marchington 1992; DeGraaf and Yamasaki 2003). Passerines such as eastern meadowlarks (*Sturnella henslowii* Audubon), field sparrows (*Spizella pusilla* Wilson), and other songbird species (Moseley et al. 2010) can also take advantage of these openings and successional habitat with enhanced habitat heterogeneity, foraging, and nesting habitat (Parker et al. 1992; DeGraaf and Yamasaki 2003; Northrup and Wittemeyer 2013). These concepts can also explain the high levels of biophonic influence in the energy development sites.

However, taking the opportunity to make these natural gas clearings into ecological assets will require surface management that focuses on reducing soil compaction (Moseley et al. 2010), and improving species composition and vegetative structure of the surrounding plant communities (Harper 2007; DeGraaf and Yamasaki 2003). Further research examining the effects of increasing cover materials like coarse woody debris, rocks, and vegetation, and how the natural gas openings are maintained to possibly benefit wildlife, should be conducted.

The Allegheny National Forest hosts a unique blend of beauty and utility, and while examining temporal landscape change and the potential associated ecological impacts, landscape disturbance

has been an integral force in the historical and current development and maintenance of eastern forests, and Pennsylvania is no exception. The condition and growth status of forests in Pennsylvania are not static, but in constant flux from use of ecosystem services, as the ANF has been both a main source of timber and energy (Flaherty and Flaherty 2014). Current forest composition and ecological conditions are merely a result of over a century of continued natural resource use.

Future Plans

I intend to reassess the dataset using temporal distinctions. Further, including the data from the spring and summer seasons between March and June 2017 (therefore, analyzing an entire 12 months) in the analysis may produce more informative results.

CONCLUSION

Because the magnitude of the sound data is so great and may not be very ecologically informative when considered as a whole, I intend to subset the data temporally to yield potentially more relevant results. Because we used no temporal separation in the current analyses, patterns may appear if seasonal or choral times are considered. In temperate deciduous forests, most organisms are vocally active in the spring and summer months, and in the morning and evening choruses (Gasc, Francomano, and Dunning 2017; Farina et al. 2011a). Because soundscape ecology is a new and growing field, current acoustic indices are being improved and new indices are being developed, so using other metrics may examine other aspects of the soundscapes and offer new insights.

ACKNOWLEDGEMENTS

I would like to thank my research mentor, Dr. Anne C. Axel, and the rest of my graduate committee, Drs. Jayme L. Waldron and Shane Welch, for being supportive, informative, and very helpful to me. I am also grateful for the NASA WV Space Grant Consortium fellowship in allowing me to fund and present my research at the 2017 United States – International Association of Landscape Ecology conference, “People, Places, Patterns: Linking Landscape Heterogeneity and Socio-Environmental Systems” in Baltimore, Maryland.

REFERENCES

- Abrahams LS, Griffin WM, Matthews HS (2015) Assessment of policies to reduce core forest fragmentation from Marcellus shale development in Pennsylvania. *Ecol Indic* 52:153–160. doi: 10.1016/j.ecolind.2014.11.031
- Alverson WS, Waller DM, Solheim SL (2010) Northern tree deer: Wisconsin Edge in. 2:348–358
- Andreasen JK, O’Neill R V., Noss R, Slosser NC (2001) Considerations for the development of a terrestrial index of ecological integrity. *Ecol Indic* 1:21–35. doi: 10.1016/S1470-160X(01)00007-3
- Barber JR, Crooks KR, Fristrup KM (2010) The costs of chronic noise exposure for terrestrial organisms. *Trends Ecol. Evol.* 25:180–189
- Barber JR, Burdett CL, Reed SE, Warner KA, Formichella C, Crooks KR, Theobald DM, and Fristrup KM (2011) Anthropogenic noise exposure in protected natural areas: Estimating the scale of ecological consequences. *Landscape Ecol* 26:1281–1295. doi: 10.1007/s10980-011-9646-7
- Bodoya C, Isaza C, Daza JM, López JD (2017) Automatic identification of rainfall in acoustic recordings. *Ecol Indic* 75:95–100. doi: 10.1016/j.ecolind.2016.12.018
- Bell KE, Donnelly MA (2006) Influence of forest fragmentation on community structure of frogs and

- lizards in northeastern Costa Rica. *Conserv Biol* 20:1750–1760. doi: 10.1111/j.1523-1739.2006.00522.x
- Blickley JL, Blackwood D, Patricelli GL (2012) Experimental evidence for the effects of chronic anthropogenic noise on abundance of greater sage-grouse at Leks. *Conserv Biol* 26:461–471. doi: 10.1111/j.1523-1739.2012.01840.x
- Bormpoudakis D, Sueur J, Pantis JD (2013) Spatial heterogeneity of ambient sound at the habitat type level: Ecological implications and applications. *Landsc Ecol* 28:495–506. doi: 10.1007/s10980-013-9849-1
- Bradbury RB, Hill RA, Mason DC, Hinsley SA, Wilson JD, Balzter H, Anderson GQA, Whittingham MJ, Davenport IJ, Bellamy PE (2005) Modelling relationships between birds and vegetation structure using airborne LiDAR data: A review with case studies from agricultural and woodland environments. *Ibis (Lond. 1859)*. 147:443–452
- Brittingham MC, Maloney KO, Farag AM, Harper DD, Bowen ZH (2014) Ecological risks of shale oil and gas development to wildlife, aquatic resources and their habitats. *Environ Sci Technol* 48:11034–11047. doi: 10.1021/es5020482
- Brown ED, Williams BK (2016) Ecological integrity assessment as a metric of biodiversity: are we measuring what we say we are? *Biodivers. Conserv.* 25:1011–1035.
- Canterbury GE, Martin TE, Petit DR, Petit LJ, Bradford DF (2000) Bird communities and habitat as ecological indicators of forest condition in regional monitoring. *Conserv Biol* 14:544–558. doi: 10.1046/j.1523-1739.2000.98235.x
- Chace JF, Walsh JJ (2006) Urban effects on native avifauna: a review. *Landscape Urban Plann* 74:46-78
- Cho SH, Bowker JM, Roberts RK, Kim S, Kim T, Lambert DM (2015) Effects on consumer welfare of visitor satisfaction with recreation information availability: A case study of the Allegheny National Forest. *Tour Econ* 21:853–869. doi: 10.5367/te.2014.0383
- Cushman SA (2006) Effects of habitat loss and fragmentation on amphibians: A review and prospectus. *Biol Conserv* 128:231–240. doi: 10.1016/j.biocon.2005.09.031
- DeGraaf RM, Yamasaki M (2003) Options for managing early-successional forest and shrubland bird habitats in the northeastern United States. *For Ecol Manage* 185:179–191. doi: 10.1016/S0378-1127(03)00254-8
- Deichmann JL, Hernandez-Serna A, Delgado C. JA (2017) Soundscape analysis and acoustic monitoring document impacts of natural gas exploration on biodiversity in a tropical forest. *Ecol Indic* 74:39–48. doi: 10.1016/j.ecolind.2016.11.002
- Drever MC, Aitken KEH, Norris AR, Martin K (2008) Woodpeckers as reliable indicators of bird richness, forest health and harvest. *Biol Conserv* 141:624–634
- Drohan PJ, Finley JC, Roth P, Shuler TM, Stout SL, Brittingham MC, Johnson NC (2012a) Perspectives from the Field: Oil and Gas Impacts on Forest Ecosystems: Findings Gleaned from the 2012 Goddard Forum at Penn State University. *Environ Pract* 14:394–6. doi: 10.1017/S1466046612000300
- Drohan PJ, Brittingham M, Bishop J, Yoder K (2012b) Early trends in landcover change and forest fragmentation due to shale-gas development in Pennsylvania: A potential outcome for the northcentral Appalachians. *Environ Manage* 49:1061–1075. doi: 10.1007/s00267-012-9841-6
- Dumyahn SL, Pijanowski BC (2011) Soundscape conservation. *Landsc Ecol* 26:1327–1344. doi: 10.1007/s10980-011-9635-x
- Eglinton SM, Noble DG, Fuller RJ (2012) A meta-analysis of spatial relationships in species richness across taxa: birds as indicators of wider biodiversity in temperate regions. *J Nat. Conserv* 20:301-309
- Engelder T, Lash GG (2008) Marcellus shale play's resource potential creating stir in Appalachia. *The American Oil and Gas Reporter* 51:87
- Farina A, Belgrano A (2004) The eco- field: A new paradigm for landscape ecology. *Ecol Res* 107–110
- Farina A, Lattanzi E, Malavasi R, Pieretti N, Piccioli L (2011a) Avian soundscapes and cognitive landscapes: Theory, application and ecological perspectives. *Landsc Ecol* 26:1257–1267. doi: 10.1007/s10980-011-9617-z
- Farina A, Pieretti N, Piccioli L (2011b) The soundscape methodology for long-term bird monitoring: A Mediterranean Europe case-study. *Ecol Inform* 6:354–363. doi: 10.1016/j.ecoinf.2011.07.004
- Fettke, CE (1938) The Bradford oil field, Pennsylvania and New York. *Topographic and Geological Survey: Bulletin M21*. Harrisburg, PA
- Fischer J, Lindenmayer DB (2006) Forum: Beyond fragmentation: the continuum model for fauna research and conservation in human-modified landscapes. *Oikos* 112:473–480. doi: 10.1111/j.0030-1299.2006.14148.x
- Flaherty KJ, Flaherty T, III (2014) Oil and gas in Pennsylvania (3rd ed.) Pennsylvania Geological Survey, 4th ser., Educational Series 8, p. 36

- Francis CD, Barber JR (2013) A framework for understanding noise impacts on wildlife: An urgent conservation priority. *Front Ecol Environ* 11:305–313. doi: 10.1890/120183
- Francis CD, Paritsis J, Ortega CP, Cruz A (2011) Landscape patterns of avian habitat use and nest success are affected by chronic gas well compressor noise. *Landsc Ecol* 26:1269–1280. doi: 10.1007/s10980-011-9609-z
- Fuller S, Axel AC, Tucker D, Gage SH (2015) Connecting soundscape to landscape: Which acoustic index best describes landscape configuration? *Ecol Indic* 58:207–215. doi: 10.1016/j.ecolind.2015.05.057
- Furness RW, Greenwood JJ (1993) *Birds as monitors of environmental change*. Springer. pp 86–143. doi 10.1007/978-94-015-1322-7
- Gasc A, Francomano D, Dunning JB (2017) Future directions for soundscape ecology : The importance of ornithological contributions *Future directions for soundscape ecology : The importance of ornithological contributions*. 134:215–228. doi: 10.1642/AUK-16-124.1
- Gibbs JP (1998) Distribution of woodland amphibians along a forest fragmentation gradient. *Land Ecol* 4:263-268
- Gillen JL, Kiviat E (2012) Hydraulic Fracturing Threats to Species with Restricted Geographic Ranges in the Eastern United States. *Envir Rev and Cas Studies*. 14:320–331.
- Google Earth Pro (2006). Wuthrich D, *Geospatial Solut* 16:30–32
- Gutzwiller KJ, Riffel SK (2007) Using Statistical Models to Study Temporal Dynamics of Animal–Landscape Relations. In: *Temporal Dimensions of Landscape Ecology: Wildlife Responses to Variable Resources*. pp 93–118.
- Greenberg CH (2001) Response of reptile and amphibian communities to canopy gaps created by wind disturbance in the southern Appalachians. *Forest Ecol and Manage* 148:135-144
- Harper KS, MacDonald PB, Chen J, Brosofske K, Saunders S, Euskirchen E, Roberts D, Jaiteh M, and Esseen P (2005) Edge influence on forest structure and composition in fragmented landscapes. *Conser Biol* 19:768-782.
- Harper CA (2007) Strategies for Managing Early Succession Habitat for Wildlife. *Weed Technol* 21:932–937
- Hausner VH, Yoccoz NG, Ims RA (2003) Selecting indicator traits for monitoring land use impacts: Birds in northern coastal birch forests. *Ecol Appl* 13:999–1012. doi: 10.1890/1051-0761(2003)13[999:SITFML]2.0.CO;2
- Honglo E (2015) An ecology of difference : fence-line contrast photographs as scientific models in ecology. *J Polit Ecol* 22:339–356.
- Jones NF, Pejchar L (2013) Comparing the ecological impacts of wind and oil & gas development: A landscape scale assessment. *PLoS One*. doi: 10.1371/journal.pone.0081391
- Joo W, Gage SH, Kasten EP (2011) Analysis and interpretation of variability in soundscapes along an urban-rural gradient. *Landsc Urban Plan* 103:259–276. doi: 10.1016/j.landurbplan.2011.08.001
- Johnson N (2010) Pennsylvania energy impacts assessment report 1: Marcellus shale natural gas and wind. The Nature Conservancy, Pennsylvania. http://www.nature.org/media/pa/tnc_energy_analysis.pdf Accessed 10 Oct 2016.
- Karr JR, Dudley DR (1981) Ecological perspective on water quality goals. *Environmental Management* 5:55-68
- Karr JR, Fausch D, Angermeier PL, Yant PR, Schlosser IJ (1986) *Assessing biological integrity in running waters: a method and its rationale*. Illinois Natural History Survey, Champaign, Illinois, Special Publication 5
- Kasten EP, Gage SH, Fox J, Joo W (2012) The remote environmental assessment laboratory’s acoustic library: An archive for studying soundscape ecology. *Ecol Inform* 12:50–67. doi: 10.1016/j.ecoinf.2012.08.001
- Kelsey TW, Shields M, Ladlee JR, Ward M (2011) Economic impacts of Marcellus shale in Pennsylvania: employment and income in 2009. Marcellus Shale Education and Training Center (MSETC), Pennsylvania College of Technology and Penn State Extension. <http://www.msetc.org/docs/EconomicImpactFINALAugust28.pdf#zoom=75>. Accessed 21 June 2016
- Kjoss VA, Litvaitis JA (2001) Community structure of snakes in a human-dominated landscape. *Biol Cons* 98:285-292
- Kleist NJ, Guralnick RP, Cruz A, Francis CD (2017) Sound settlement : noise surpasses land cover in explaining breeding habitat selection of secondary cavity- - nesting birds. *Ecol Applic* 27:260–273. doi: 10.1002/eap.1437
- Krause B, Ellen G (2001) Loss of natural soundscape: global implications of its effect on humans and other creatures prepared for San Francisco World Affairs Council, 31 January 2001
- Krause BL (1987) Bioacoustics, habitat ambience in ecological balance. *Whole Earth Rev* 14–16.

- Laurance WF, Yensen E (1991) Predicting the impact of edge effects in fragmented habitats. *Biol Conserv* 55:77–92
- Laurance WF, Goosem M, and Laurance SGW (2009) Impacts of roads and linear clearings on tropical forests. *Trends in Ecol and Evol* 24:659–669
- Lendrum PE, Anderson CR, Jr., Long RA, Kie JG, Bowyer T (2012) Habitat selection by mule deer during migration: effects of landscape structure and natural-gas development. *Ecosphere* 3:art82. doi: 10.1890/ES12-00165.1
- Ligges U, Preusser A, Thieler A, Weihs C (2015) Package tuneR. <https://cran.r-project.org/web/packages/tuneR/tuneR.pdf>. Accessed 01 November 2016).
- Litvaitis JA (2001) Importance of early successional habitats to mammals in eastern forests. *Wildlife Society Bulletin*. 29: 466-473
- Maurer BA (1999) Biological diversity, ecological integrity, and neotropical migrants: new perspectives for wildlife management NCASI Technical Bulletin. 328: 24-31
- Mazaris AD, Kallimanis AS, Chatzigiannidis G, Papadimitriou K, Pantis JD (2009) Spatiotemporal analysis of an acoustic environment: Interactions between landscape features and sounds. *Landsc Ecol* 24:817–831. doi: 10.1007/s10980-009-9360-x
- McCracken SF, Forstner MRJ (2014) Oil road effects on the anuran community of a high canopy tank bromeliad (*Aechmea zebrina*) in the upper Amazon Basin, Ecuador. *PLoS One*. doi: 10.1371/journal.pone.0085470
- Menzel MA, Ford WM, Laerm J, Krishon D (1999) Forest to wildlife opening: habitat gradients in the southern Appalachians. *Forest Ecol and Manage.* 114: 227-232
- Mortensen DA, Rauschert ESJ, Nord AN, and Jones BP (2009) Forest roads facilitate the spread of invasive plants. *Inva Plant Sci and Manag* 2:191-199
- Moseley KR, Ford WM, Edwards JW, Adams MB (2010) Reptile, amphibian, and small mammal species associated with natural gas development in the Monongahela National Forest, West Virginia. *U S For Serv Res Pap NRS* 10:1–14. doi: 3
- Murcia C (1995) Edge effects in fragmented forests: implications for conservation. *Trends in Ecol and Evol* 10:58-59
- Northrup JM, Wittemyer G (2013) Characterising the impacts of emerging energy development on wildlife, with an eye towards mitigation. *Ecol Lett* 16:112–125. doi: 10.1111/ele.12009
- Noss R (1990) Indicators for monitoring biodiversity: a hierarchical approach. *Conserv Biol* 4:355–364.
- PA Dept. of Environmental Protection (PADEP) (2011) Marcellus shale fact sheet. Pennsylvania Department of Environmental Protection. <http://www.elibrary.dep.state.pa.us/dsweb/Get/Document-77964/0100-FS-DEP4217.pdf>. Accessed 15 July 2016.
- PA Dept. of Environmental Protection (PADEP) (2017) Commonwealth of Pennsylvania Office of Oil and Gas Management, Division of Compliance and Data Administration, Oil and Gas Reports Data. <http://www.dep.pa.gov/DataandTools/Reports/Oil%20and%20Gas%20reports/Pages/default.aspx>. Accessed 1 April 2017
- Parker JR, Kammermeyer KE, Marchington RL (1992) Wildlife usage of clover plots in the Chestatee wildlife management area. *Georgia J of Science* 50:160-169
- Parkes D, Lyon P (2006) Towards a national approach to vegetation condition assessment that meets government investors' needs: A policy perspective. *Ecol Manage Restor* 7:53-55
- Parrish JD, Braun DP, Unnasch RS (2003) Are we conserving what we say we are? Measuring ecological integrity within protected areas. *Bioscience* 53:851. doi: 10.1641/0006-3568(2003)053[0851:AWCWWS]2.0.CO;2
- Pieretti N, Farina A, Morri D (2011) A new methodology to infer the singing activity of an avian community: The Acoustic Complexity Index (ACI). *Ecol Indic* 11:868–873. doi: 10.1016/j.ecolind.2010.11.005
- Pieretti N, Farina A (2013) Application of a recently introduced index for acoustic complexity to an avian soundscape with traffic noise. *J Acoust Soc Am* 134:891–900. doi: 10.1121/1.4807812
- Pijanowski BC, Farina A (2011a) Introduction to the special issue on soundscape ecology. *Landsc Ecol* 26:1209–1211. doi: 10.1007/s10980-011-9655-6
- Pijanowski BC, Farina A, Gage SH, Dumyahn SL, Krause BL (2011b) What is soundscape ecology? An introduction and overview of an emerging new science. *Landsc Ecol* 26:1213–1232. doi: 10.1007/s10980-011-9600-8
- Pijanowski BC, Villanueva-Rivera LJ, Dumyahn SL, Farina A, Krause BL, Napoletano BM, Gage SH, Pieretti N (2011c) Soundscape ecology: the science of sound in the landscape. *Bioscience* 61:203–216. doi: 10.1525/bio.2011.61.3.6

- Pilcher E (2010) Soundscape Workshop Planning 11-4-05. 1–40
- Pinheiro J, Bates D, DebRoy S (2015) nlme: linear and nonlinear mixed effects models. R Packag version 3.1-122 R package:1–3
- Proppe DS, Sturdy CB, St. Clair CC (2013) Anthropogenic noise decreases urban songbird diversity and may contribute to homogenization. *Glob Chang Biol* 19:1075–1084. doi: 10.1111/gcb.12098
- R Core team (2015) R Core Team. *R A Lang. Environ. Stat. Comput. R Found. Stat. Comput.*, Vienna, Austria. ISBN 3-900051-07-0, URL <http://www.R-project.org/>. 55:275–286.
- Ritters KH, Wickham JD, O'Neill RV, Jones KB, Smith ER, Coulston JW, Wade TG, Smith JH (2002) Fragmentation of continental United States forests. *Ecosystems* 5:815–822
- Ross PW (1996) Allegheny oil: the historical petroleum industry on the Allegheny National Forest, Allegheny National Forest Heritage Publication No. 1
- Ross B, Fredericksen T, Ross E, Hoffman W, Morrison ML, Beyea J, Lester MB, Johnson BN, Fredericksen NL (2000) Relative abundance and species richness of herpetofauna in forest stands in Pennsylvania. *Forest Service* 46:139–146
- Rowland MM, Wisdom MJ, Suring LH, Meinke CW (2006) Greater sage-grouse as an umbrella species for sagebrush-associated vertebrates. *Biol Conserv* 129:323–335. doi: 10.1016/j.biocon.2005.10.048
- Russell KR., Wigley TB, Baughman WM, Hanlin HG, Ford WM (2004) Responses of southeastern amphibians and reptiles to forest management: a review. In: Rauscher, H. M., K. Johnsen, eds. *Southern forest science: past, present, future*. Gen. Tech. Rep SRS-75. Asheville, NC: U. S. Department of Agriculture, Forest Service, Southern Research Station 319:334
- Sawyer H, Kauffman MJ, Nielson RM (2009) Influence of well pad activity on winter habitat selection patterns of mule deer. *J Wildl Manage* 73:1052–1061. doi: 2
- Schafer RM (1977) The Tuning of the World. *First Soundscapes* 15–67. doi: 10.2307/3345272
- Segers JL, Broders HG (2014) Interspecific effects of forest fragmentation on bats. *Can J Zool* 92:665–673. doi: 10.1139/cjz-2014-0040
- Slonecker E, Milheim L, Roig-Silva C (2012) Landscape consequences of natural gas extraction in Bradford and Washington counties, Pennsylvania, 2004–2010. *US Geol Surv Open* 2004–2010
- Smith WB., Miles PD, Perry CH, Pugh SA (2009) *Forest Resources of the United States, 2007*. USDA Forest Service General Technical Report WO-78. USDA Forest Service, Washington, D. C., USA
- Smith JW, Pijanowski BC (2014) Human and policy dimensions of soundscape ecology. *Glob Environ Chang* 28:63–74. doi: 10.1016/j.gloenvcha.2014.05.007
- Souther S, Tingley MW, Popescu VD, Hayman DTS, Ryan ME, Graves TA, Hartl B, Terrell K (2014) Biotic impacts of energy development from shale: Research priorities and knowledge gaps. *Front Ecol Environ* 12:330–338. doi: 10.1890/130324
- Steele MA, Brittingham MC, Maret TJ, and Merritt JF (2010) *Terrestrial vertebrates of Pennsylvania a complete guide to species of conservation concern*. John Hopkins University Press, Baltimore, Maryland
- Storfer A (2003) Amphibian declines: Future directions. *Divers. Distrib.* 9:151–163
- Ström C (2013) Rapid biodiversity assessment of a Neotropical rainforest using soundscape recordings. 24. Master's Thesis, Umea University
- Sueur J, Farina A, Gasc A, Pieretti N, and Pavoine S (2014) Acoustic indices for biodiversity assessment and landscape investigation. *Acta Acust united with Acust* 100:772–781. doi: 10.3813/AAA.918757
- Thomas EH, Brittingham MC, Stoleson SH (2014) Conventional oil and gas development alters forest songbird communities. *J Wildl Manage* 78:293–306. doi: 10.1002/jwmg.662
- Towsey M, Wimmer J, Williamson I, Roe P (2014) The use of acoustic indices to determine avian species richness in audio-recordings of the environment. *Ecol Inform* 21:110–119. doi: 10.1016/j.ecoinf.2013.11.007
- Truax B, Barrett GW (2011) Soundscape in a context of acoustic and landscape ecology. *Landsc Ecol* 26:1201–1207. doi: 10.1007/s10980-011-9644-9
- Tucker D, Gage SH, Williamson I, Fuller S (2014) Linking ecological condition and the soundscape in fragmented Australian forests. *Landsc Ecol* 29:745–758
doi 10.1007/s10980-014-0015-1
- Turner MG (1989) *Landscape Ecology: The effect of pattern on process*. *Annu Rev Ecol Syst* 20:171–197. doi: 10.1146/annurev.es.20.110189.001131
- US Dept. of Agriculture - Forest Service (USFS) (1996) Allegheny National Forest final environmental impact statement to accompany the land and resource management plan Allegheny National Forest.
- US Dept. of Agriculture - Forest Service (USFS) (2007a) Allegheny National Forest record of decision for

final environmental impact statement and the land and resource management plan.

<http://www.fs.usda.gov/Internet/FSE_-DOCUMENTS/stelprdb5044088.pdf> Accessed 10 July 2011.

US Dept. of Agriculture - Forest Service (USFS) (2007b) Allegheny National Forest record of decision for final environmental impact statement and the land and resource management plan. Appendix F—oil, gas, and mineral development on the Allegheny National Forest. http://www.fs.usda.gov/Internet/FSE_DOCUMENTS/stelprdb5044096.pdf. Accessed 13 October 2016

US Dept. of Agriculture - Forest Service (USFS) (2008) Oil and gas issues. United States Forest Service Northeast and Midwest Forests Oil and Gas Exploration Workshop, 12–13 November 2008, Milwaukee, Wisconsin, USA

US Dept. of Agriculture - Forest Service (USFS) (2011) Pennsylvania forest resource fact sheet. http://na.fs.fed.us/ra/factsheets/pa_brief.pdf Accessed 10 July 2016

US Dept. of Energy (USDE) (2005) Mature region, youthful potential, oil and natural gas resources in the Appalachian and Illinois basins. Washington, DC

Villanueva-Rivera MLJ, Pijanowski BC, Doucette J, Pekin B (2011) A primer of acoustic analysis for landscape ecologists. *Landsc Ecol* 26:1233–1246. doi: 10.1007/s10980-011-9636-9

Villanueva-Rivera MLJ (2016) R Package “soundecology.”

Welsh H, Droege S (2001) A case for using Plethodontid salamanders for using ecosystem integrity Monitoring Biodiversity and Ecosystem Integrity of North American Forests. *Conserv Biol* 15:558–569

Wilgenburg SL Van, Hobson KA, Bayne EM, Koper N (2013) Estimated avian nest loss associated with oil and gas exploration and extraction in the western Canadian sedimentary basin estimation. *Avian Conserv Ecol* 8:9. doi: 10.5751/ACE-00585-080209

Wildlife Acoustics (2013) Available from <http://www.wildlifeacoustics.com>

Zuur AF, Ieno EN, Walker NJ, et al (2009) Mixed effects models and extensions in ecology with R. 1431-8776(print)r978-0-387-87457-9(H)

DIET-IFI202B INTERACTIONS IN A NOVEL CONGENIC MOUSE MODEL OF OBESITY

Jacaline Parkman
Biomedical Science
Marshall University
Huntington, WV

ABSTRACT

Obesity is an international health crisis and is considered the leading cause of preventable death. The development of obesity is most likely due to interactions of many genes with obesity-promoting environments such as high fat diets (HFD). These interactions lead to an expansion of adipose tissue through hyperplasia, increase in cell number (also known as adipogenesis) and/or hypertrophy, increase in cell size. In addition, adipose tissue is an endocrine organ that secretes cytokines and recruits macrophages, which also secrete cytokines. Adipose tissue in those who are obese recruit many more macrophages than those who are lean, which contributes to low grade inflammation, a common characteristic associated with obesity. Previously, we identified a quantitative trait locus (QTL) linked to obesity and hyperlipidemia on mouse chromosome (Chr) 1 in an intercross of obese and diabetic TALLYHO/Jng (TH) mice with C57BL/6 (B6). To confirm the QTL, a congenic mouse strain was developed through the introgression of a 128Mb TH-derived genomic interval into B6 background (B6.TH-Chr1-128Mb). The congenic mice were found to be more susceptible to diet-induced obesity and hyperlipidemia than B6 mice. The purpose of this study was to characterize the congenic mice by studying adipogenesis and inflammation and identify a prime mediator that played a role in developing obesity under HF diets. We hypothesized that upregulation of the obesity susceptibility gene interferon activated gene 202B (*Ifi202b*), which mapped in the distal portion of our congenic interval, was a molecular mechanism underlying the HF diet-induced obesity in B6.TH-Chr1-128Mb congenic mice and was associated with alterations in adipogenesis and inflammation. Expression for different markers for adipocyte differentiation and inflammation were examined through mRNA and protein levels in white adipose tissue and liver. B6.TH-Chr1-128Mb and B6 mice weaned onto chow and HFD at 4 weeks and maintained until 16 weeks of age. mRNA levels were measured from cDNA from adipose tissue by real-time quantitative RT-PCR (qPCR). Protein levels were measured by western blots. Gene expression of peroxisome proliferator-activated receptor gamma (PPAR γ), a master regulator of adipogenesis, showed statistically significant expression in the B6.TH-Chr1-128Mb on a HFD compared to B6 on a HFD or on Chow. Western blotting showed a similar trend but did not reach statistical significance. There were no significant differences in gene expression levels of *Pref-1*, an upstream repressor to adipocyte differentiation, and *Cebpb*, a transcription factor during the early stages of adipogenesis, in adipose tissue between congenic and B6 mice on chow and HFD. *There was decreased gene expression of 11 β -Hsd1 in our congenic model compared to B6 on chow. Expression of 11 β -Hsd1 increased when B6 and the congenic mice were on a HFD.* Interleukin 6 (*Il6*), a cytokine secreted by macrophages and adipose tissue, gene expression was higher for congenic mice compared to B6 on a HFD. IL6 protein expression showed a similar trend. These did not reach statistical significance. In conclusion, we found that obesity in congenic mice is accompanied by increased gene expression of *Pparg*. *Pparg* may be a potential downstream target of *Ifi202b*.

INTRODUCTION

Obesity is a worldwide epidemic and is considered the leading cause of preventable death. It is associated with an increased risk of type 2 diabetes, hypertension, hyperlipidemia, cardiovascular disease, and various cancers (1,2). Obesity is a complex disease that is attributed to interactions between obesogenic environmental factors, for example high fat (HF) diets, and genetic factors (2,3). The etiology of obesity, however, is not well understood and more research needs to be done (1).

Obesity is characterized as excess accumulation of adipose tissue. A Body Mass Index (BMI), weight (kg) divided by height squared (m), of 30.0 or higher, is considered obese (4). Adipose tissue is an endocrine organ that stores excess energy as lipids and is predominately composed of adipocytes. It also contains preadipocytes, fibroblasts, mesenchymal stem cells, blood vessels, and macrophages (5). Adipocytes contain a large lipid droplet that adapts to changes in nutritional needs. When there is excess energy, free fatty acids are esterified to triacylglycerides (TAGs) by adipocytes and are stored. When energy is required, TAGs are hydrolysed to release free fatty acids (lipolysis) to be used for β -oxidation (6). When adipose tissue expands, it undergoes hypertrophy, increase in size, and/or hyperplasia, increase in number from de novo differentiation from preadipocytes (adipogenesis) (7). Adipogenesis involves a complex transcriptional cascade. CAAT/enhancer binding protein β (C/EBP β) expression is transiently induced by an increase in intracellular cyclic adenosine monophosphate (cAMP) and mitogens. C/EBP β then induces the expression of C/EBP α and peroxisome proliferator-activated receptor gamma (PPARG), master regulators of adipogenesis (8). These are necessary for producing the biochemical and functional properties of adipocytes (9).

Obesity is also associated with chronic low-grade systemic inflammation. Macrophages and other immune cells like T-cells are recruited to adipose tissue and play a role in inflammation as well as housekeeping, such as angiogenesis and clearing apoptotic cells. As the tissue expands, more immune cells are recruited, driving a pro-inflammatory response (10). The number of macrophages are highly increased in obese tissue compared to lean tissue, 45-60 % vs 10-15 % respectively (11). Macrophages release pro-inflammatory cytokines, as can adipose tissue itself (12).

Genetic research with humans can be difficult and complicated, so animal models that share physiologic and genetic similarity with humans are used (13). Animal models can also be used to limit genetic complexities by isolating individual loci in congenic strains. Congenic strains are created by moving a gene or region of interest from one inbred (donor) strain to another inbred (recipient) strain. The name of congenic strain is designated using the format: Recipient.Donor-Introgressed region. We generated a congenic mouse strain that carries an obesity quantitative trait locus (QTL) on chromosome 1 (Chr1), 128 Mb in size, derived from TALLYHO (TH), a polygenic mouse model for obesity and type 2 diabetes, on a C57BL/6 (B6) background (B6.TH-Chr1-128Mb). The QTL was found through a genome-wide mapping study using F2 population of B6 and TH mice and was associated with increased fat mass in Chr 1 (14). The congenic mice were generated to confirm the QTL and develop a strategy for positional cloning of the responsible gene(s). Using B6.TH-Chr1-128Mb, we generated a second congenic strain carrying only the proximal segment, 92 Mb in size, of the original congenic interval (B6.TH-Chr1-92Mb). We found that B6.TH-Chr1-128Mb congenic mice exhibited a significant increase in body fat

mass compared with B6.TH-Chr1-92Mb congenic and B6 mice. Since body fat mass between B6.TH-Chr1-92Mb congenic mice and B6 mice were similar, the results suggested that the Chr1 obesity QTL candidate region was most likely within the distal segment of the TH congenic interval. Through positional cloning, the obesity susceptibility gene interferon activated gene 202B (*Ifi202b*) was identified in different studies and mapped within the distal segment of our interval. The *Ifi202b* gene encodes p202, a nuclear DNA-binding protein that is able to affect transcription by interacting with many transcription factors involved in cell proliferation, apoptosis, inflammation, and cell differentiation (15,16,17). Gene expression of *Ifi202b* was found to be absent in the adipose tissue of C57BL/6 (B6) mice due to a microdeletion in the 5'-flanking region of *Ifi202b* in B6. *Ifi202b* gene expression was present in the adipose tissue of obese NZO mice. The gene expression of *IFI16*, a human orthologue of *Ifi202b*, was found to be increased in white adipose tissue of obese adults compared to lean adults (18). One study showed that upregulation of *Ifi202b* promoted lipid accumulation in adipocytes via increasing *11 β -hydroxysteroid dehydrogenase type 1 (11 β -Hsd1)*, an enzyme that converts cortisone to cortisol (18,19). *Ifi202b* was also seen to be expressed in early stages of adipocyte differentiation (20).

Based on our preliminary data, we hypothesized that upregulation of *Ifi202b* is a molecular mechanism underlying the HF diet-induced obesity in B6.TH-Chr1-128Mb congenic mice and is associated with alterations in adipogenesis and inflammation. By investigating differentially expressed genes between B6 mice and B6.TH-Chr1-128Mb congenic mice, we could identify downstream genes of *Ifi202b*. We could also compare chow and HF diets to determine which downstream genes of *Ifi202b* contributed to the *Ifi202b*-diet interactions in the developing obesity in B6.TH-Chr1-128Mb mice. We used adipose tissue that we had collected from our preliminary studies. B6 and B6.TH-Chr1-128Mb mice were weaned onto chow and HF diets and maintained till 16 weeks of age before they were sacrificed. We focused on genes involved with adipogenesis and inflammation, including CCAAT/enhancer binding protein- β (*C/EBP β*), peroxisome proliferator-activated receptor- γ (*PPAR γ*), preadipocyte factor-1 (*Pref-1*), *11 β -Hsd1*, and interleukin 6 (*Il6*). We ran real-time quantitative RT-PCR (qPCR) where total RNA from white adipose tissue was extracted using RNeasy Midi Kit (Qiagen). 2 μ g of RNA was reverse-transcribed with SUPERScript[®] RT using oligo d(T)12-18 as primer to synthesize first-strand cDNA. qPCR was performed using 1x SYBR Green PCR core reagents (Qiagen) using StepOne[™] Real-Time PCR system (Thermo Fisher Scientific). We also performed western blots. Tissue was homogenized in RIPA buffer with proteinase inhibitor. BCA assay (Pierce Inc.) was used to determine the protein concentration with various amounts of bovine serum albumin (BSA) as standards. 30 ng of protein were mixed with 15 μ l loading buffer and β -mercaptoethanol and protein samples were separated on a 10% SDS-PAGE and transferred to a PVDF membrane. Membranes were probed with specific antibodies, primary and secondary. Enhanced chemiluminescence was used to develop the blots. Results were calculated with one-way ANOVA and plotted using Excel as mean \pm SEM with $p < .05$ considered statistically significant.

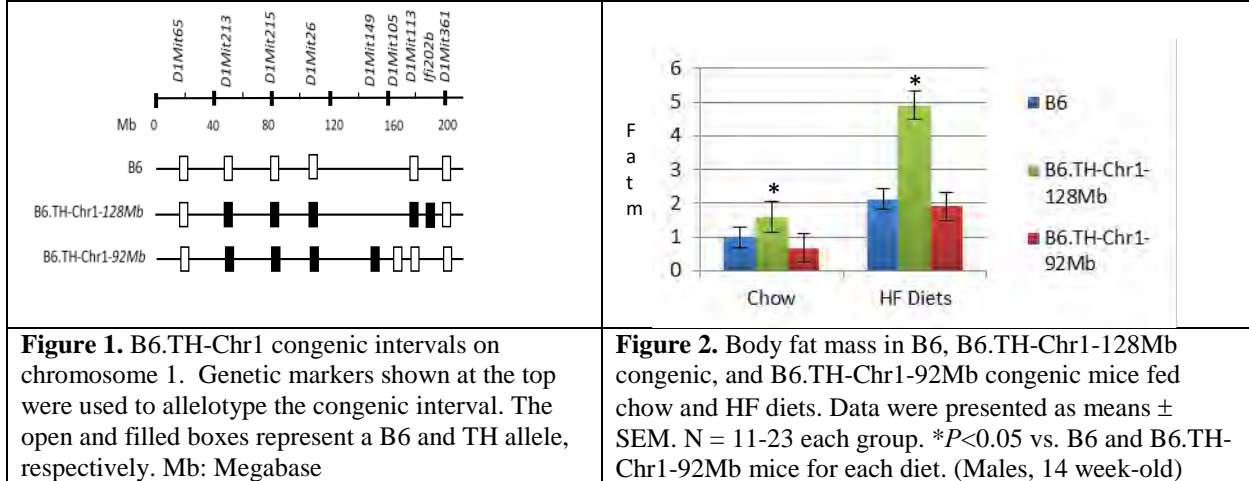
EXPERIMENT

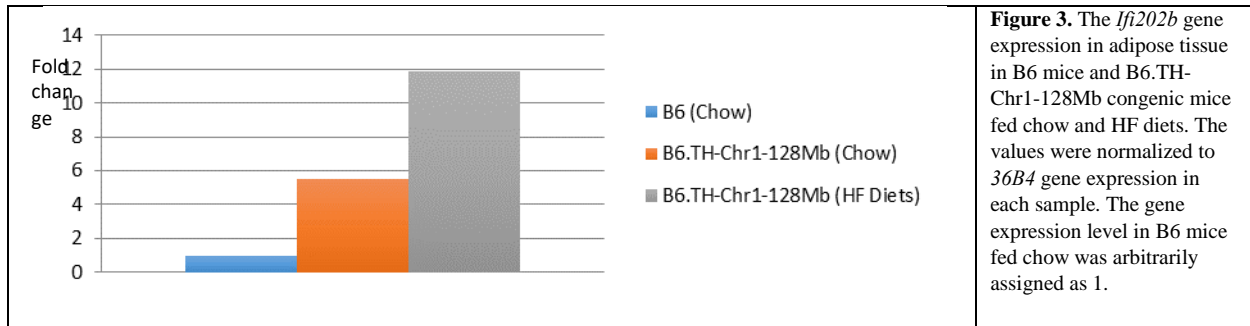
For this study, we hypothesized that upregulation of *Ifi202b* is a molecular mechanism underlying the HF diet-induced obesity in B6.TH-Chr1-128Mb congenic mice and it is associated with alterations in adipogenesis and inflammation. By using our novel congenic mouse model, we aim to identify a prime mediator that plays a role in developing obesity under HF diets in order to

understand the mechanism of gene-diet interactions. The role of *Ifi202b* related to dietary obesity has not been investigated. We investigated differentially expressed genes between B6 mice and B6.TH-Chr1-128Mb congenic mice to identify downstream genes of *Ifi202b*. We also compared chow and HF diets to identify downstream genes of *Ifi202b* that contributed to the *Ifi202b*-diet interactions in B6.TH-Chr1-128Mb mice.

PRELIMINARY DATA

We previously identified a quantitative trait locus (QTL) associated with increased fat mass in chromosome (Chr) 1 (14) through a genome-wide mapping study using F2 population of B6 and TH mice. To confirm the QTL and to identify responsible gene(s), we generated the congenic mouse strain B6.TH-Chr1-128Mb derived from TH on a B6 background. This mouse carries the Chr1 QTL which is 128 Mb in size. We then generated B6.TH-Chr1-92Mb using the proximal segment of the 128Mb interval (Fig. 1). On a standard rodent chow, B6.TH-Chr1-128Mb congenic mice had a significant increase in body fat mass compared with to B6.TH-Chr1-92Mb congenic and B6 mice (Fig. 2). Body fat mass between B6.TH-Chr1-92Mb congenic mice and B6 mice were not statistically different. This suggested that the QTL candidate region was most likely located in the distal segment of the TH congenic interval (Fig.1). *Ifi202b* maps in the distal region. On a high fat diet (HFD), in B6.TH-Chr1-128Mb congenic mice had increased fat mass and hypercholesterolemia compared to B6 mice. *Ifi202b* mRNA levels were increased in adipose tissue of B6.TH-Chr1-128Mb congenic mice compared to B6 mice on chow. Expression became higher on HF diets (Fig. 3).





PROJECT

To test our hypothesis, we investigated downstream molecules of *Ifi202b* involved with adipogenesis and inflammation in the adipose tissue in B6.TH-Chr1-128Mb mice and B6 mice. We also compared B6 mice and congenic mice fed chow and HF diets. B6 mice have no expression of *Ifi202b* in their adipose tissue due to a microdeletion, so we could investigate differentially expressed genes between B6 mice and B6.TH-Chr1-128Mb to find downstream genes of *Ifi202b*. We could also compare chow and HF diets to find which downstream genes of *Ifi202b* contributed to *Ifi202b*-diet interactions in developing obesity.

We used previously collected adipose tissue from B6 and B6.TH-Chr1-128Mb mice. These mice were weaned onto chow and HF diets and maintained till 16 weeks of age. Since p202, *Ifi202b* protein, can modulate transcription by interacting with transcription factors, we expected expression of its downstream genes to be affected in the B6.TH-Chr1-128Mb mice. We focused on genes involved with adipogenesis and inflammation.

METHODS

Real-time quantitative RT-PCR (qPCR)

Total RNA from white adipose tissue was extracted using RNA purification columns from RNeasy Midi Kit (Qiagen). RNA (2 µg) was reverse-transcribed with SUPERScript® RT using oligo d(T)12-18 as primer to synthesize first-strand cDNA. qPCR was performed in a 25-µl volume in 1x SYBR Green PCR core reagents (Qiagen) containing 1 µl cDNA template dilute (1:5, v/v) and 6 pmol primers for genes of interest using the StepOne™ Real-Time PCR system (Thermo Fisher Scientific). For each sample, duplicate amplifications were performed. Relative changes in gene expression were calculated using the $2^{-\Delta\Delta CT}$ formula. acidic ribosomal phosphoprotein P0 (36B4) mRNA levels served as control.

Western blot analysis

Tissue was homogenized in RIPA buffer with proteinase inhibitor (Sigma). BCA assay (Pierce Inc.) was used to determine the protein concentration with various amounts of bovine serum albumin (BSA) as standards. 30 ng of protein were mixed with 15ul Laemmli sample buffer (BIO-RAD) buffer and β-mercaptoethanol and protein samples were separated on a 10% SDS-PAGE and transferred to a PVDF membrane. After blocking, the membranes were incubated in primary and the corresponding secondary antibodies and washed with TBST. Detection of immunoreactive bands were performed using the enhanced chemiluminescence kit (Perkin Elmer).

Statistical Analysis

Image Lab was used to quantify bands in Western blot. Results are expressed as mean \pm SEM. The difference in each group was evaluated one-way ANOVA. Statistical significance was set at $p < 0.05$.

RESULTS

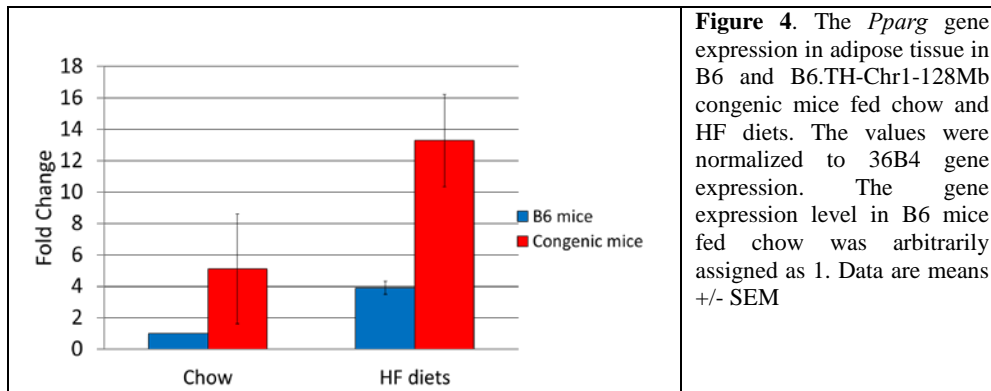


Figure 4. The *Pparg* gene expression in adipose tissue in B6 and B6.TH-Chr1-128Mb congenic mice fed chow and HF diets. The values were normalized to 36B4 gene expression. The gene expression level in B6 mice fed chow was arbitrarily assigned as 1. Data are means \pm SEM

Gene expression levels of *Pparg*, a master regulator of adipogenesis, significantly increased in adipose tissue on HFD in congenic mice compared to chow and compared to B6

on HFD (Fig 4). This trend of increased expression on HFD was also seen in PPARG protein expression levels in adipose tissue (Fig. 5a) and liver tissue (Fig. 5b), but it did not reach statistical significance.

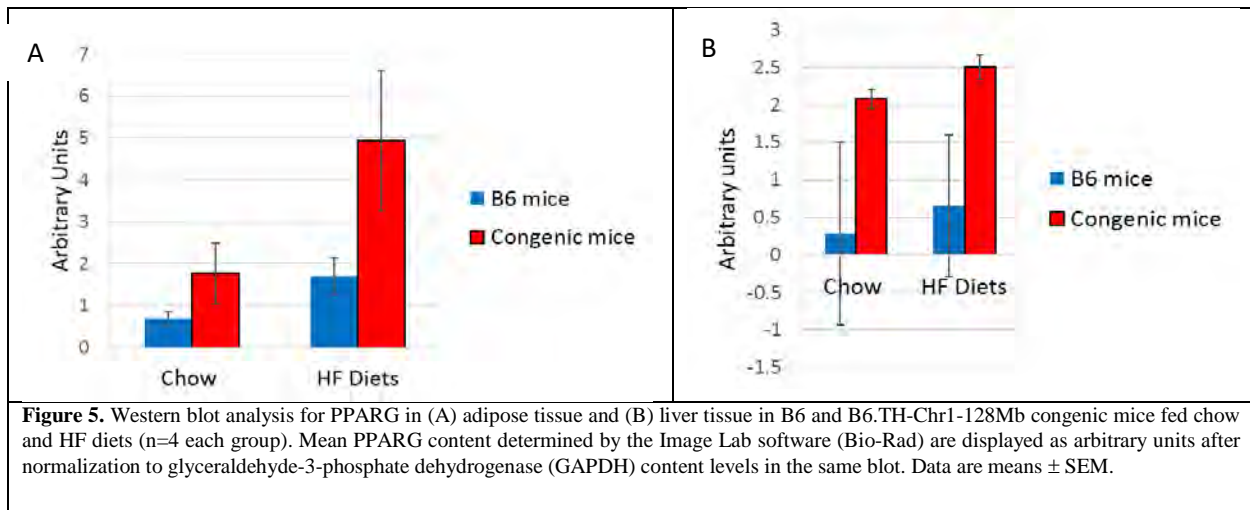


Figure 5. Western blot analysis for PPARG in (A) adipose tissue and (B) liver tissue in B6 and B6.TH-Chr1-128Mb congenic mice fed chow and HF diets (n=4 each group). Mean PPARG content determined by the Image Lab software (Bio-Rad) are displayed as arbitrary units after normalization to glyceraldehyde-3-phosphate dehydrogenase (GAPDH) content levels in the same blot. Data are means \pm SEM.

There were no significant differences in gene expression levels of *Pref-1*, an upstream repressor to adipocyte differentiation, and *Cebpb*, a transcription factor during the early stages of adipogenesis, in adipose tissue between congenic and B6 mice. This was true for both chow and high fat diet. We saw decreased gene expression of *11 β -Hsd1* in our congenic model compared to B6 on chow. We saw increased expression of *11 β -Hsd1* when B6 and the congenic mice were on a HFD.

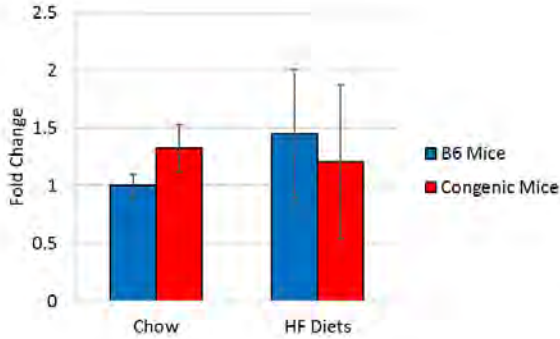


Figure 6. The *Il-6* gene expression in adipose tissue in B6 and B6.TH-Chr1-128Mb congenic mice fed chow and HF diets. The values were normalized to *36B4* gene expression. The gene expression level in B6 mice fed chow was arbitrarily assigned as 1. Data are means \pm SEM

The gene expression level of *Il6*, a pro-inflammatory marker, was increased by HFD in B6 mice, without genotype difference. A similar trend was also shown in IL6 protein levels in adipose tissue and liver, including increased expression in the congenic mouse model between chow and HFD, but it was not statistically significant.

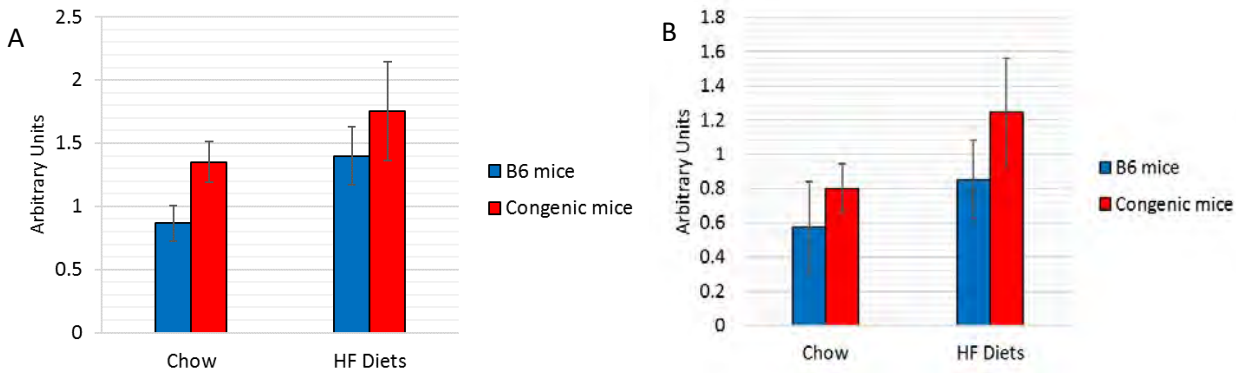


Figure 7. Western blot analysis for IL6 in (A) adipose tissue and (B) liver tissue in B6 and B6.TH-Chr1-128Mb congenic mice fed chow and HF diets (n=4 each group). Mean IL6 content determined by the Image Lab software (Bio-Rad) are displayed as arbitrary units after normalization to glyceraldehyde-3-phosphate dehydrogenase (GAPDH) content levels in the same blot. Data are means \pm SEM.

DISCUSSION

Ifi202b transcribes the protein p202 which is involved in cell differentiation, cell proliferation, and apoptosis through interactions with different transcription factors (15,16,17). Through this study, we saw an upregulation on *Pparg* in B6.TH-Chr1-128Mb congenic mice on a HFD. This may be the result of gene-diet interactions in the congenic mouse model. *Pparg* may be a potential downstream target of *Ifi202b*. PPARG transcriptionally regulates proteins involved in adipogenesis, lipid and carbohydrate metabolisms, and insulin sensitivity (21,22). PPARG is inhibited by the Wnt/beta-catenin pathway which also plays a role in adipogenesis. Wnt and beta-catenin inhibit PPARG during adipogenesis, preventing the formation of mature adipocytes and the presence of Wnt also inhibits mesenchymal stem cells from becoming preadipocytes. The PPARG pathway and the Wnt/beta-catenin pathway need further study for the development of obesity in B6.TH-Chr1-128Mb congenic mice.

We did not see a genotype difference for the other adipogenic or inflammatory markers that were

tested. There was a diet effect seen with *Il6* and *11 β -Hsd1*. Expression for the markers increased on a HFD compared to chow. Previous studies of *Ifi202b* and obesity suggested that upregulation of *Ifi202b* promoted lipid accumulation in adipocytes through *11 β -Hsd1*. We, however, saw decreased gene expression of *11 β -Hsd1* in our congenic model compared to B6 on chow. *11 β -Hsd1* does not seem to be the mechanism underlying lipid accumulation in our congenic model. The congenic mouse model in their study involved NZO x B6 and the introgressed region differed in size from our congenic model involving TH x B6. Our mice were also had hyperlipidemia while the other mouse model did not. This may be due to a polymorphism in Apolipoprotein A2 (*Apoa2*) which plays a role in lipid metabolism (23). We are currently studying this further.

CONCLUSION

For this study, the *Ifi202b* gene, a nuclear DNA binding protein, had been proposed as a positional candidate gene for our Chr1 obesity QTL. We hypothesized that upregulation of *Ifi202b* was the molecular mechanism underlying the HF diet-induced obesity in B6.TH-Chr1-128Mb congenic mice and was associated with alterations in adipogenesis and inflammation. We investigated multiple adipogenic genes and *Il6* which were potential downstream effectors of *Ifi202b*. We found that obesity in congenic mice is accompanied by increased gene expression of *Pparg*. *Pparg* may be a potential downstream target of *Ifi202b* and may be part of the underlying mechanism of obesity in the congenic mouse model.

FUTURE DIRECTIONS

Pparg may be part of the underlying mechanism of obesity in the congenic mouse model since it is a potential downstream target of *Ifi202b*. This pathway needs to be explored further. We also want to look at the morphology of the adipose tissue to see if hypertrophy and/or hyperplasia are occurring in the fat tissue of the congenic mouse models. This can be furthered studied by looking at the mitochondria. Mitochondria in white adipose tissue plays a key role in energy production. Adipogenesis is accompanied by a stimulation of mitochondrial biogenesis. Biogenesis and adipogenesis both require some of the same transcription factors including *Pparg* (24).

ACKNOWLEDGEMENTS

I would like to thank and acknowledge the generous support by WV-NASA Space Grant Consortium. The funding allowed me to start my thesis work at Marshall University. I would also like to acknowledge Dr. Jung Han Kim for her help and support during the year.

PRESENTATIONS

This work was presented at Research day at Marshall University in March 24, 2017 and will be presented at the Experimental Biology Conference in Chicago on April 23, 2017.

REFERENCES

1. McAllister E et al. Ten Putative Contributors to the Obesity Epidemic. *Crit Rev Food Sci Nutr*. 2009, 49(10): 868–913.
2. Reaven GM. Insulin resistance: the link between obesity and cardiovascular disease. *Med Clin North Am*. 2011, 95: 875–892.
3. Wilborn C et al. Obesity: prevalence, theories, medical consequences, management, and research directions. *J Int Soc Sports Nutr*. 2005, 2: 4-31.
4. Lee WJ et al. The Effect and Predictive Score of Gastric Bypass and Sleeve Gastrectomy on Type Diabetes Mellitus Patients with BMI>30kg/m². *Obes Surg*. 2015 Oct;25(10):1772-8.
5. Ali A et al. Adipocyte and adipogenesis. *Eur J Cell Biol*. 2013, 92(6-7): 229-236.
6. Frühbeck G et al. Regulation of adipocyte lipolysis. *Nutr Res Rev*. 2014 Jun;27(1):63-93.
7. Spalding KL et al. Dynamics of fat cell turnover in humans. *Nature* 2008, 453: 783–787
8. Yeh WC et al. Cascade regulation of terminal adipocyte differentiation by three members of the C/EBP family of leucine zipper proteins. *Genes Dev*. 1995 Jan 15;9(2):168-81.
9. Rosen ED, MacDougald OA. Adipocyte differentiation from the inside out. *Nat Rev Mol Cell Biol*. 2006 Dec;7(12):885-96.
10. Cooke AA et al. Fatty acids and chronic low grade inflammation associated with obesity and the metabolic syndrome. *Eur J Pharmacol*. 2016 Aug 15;785:207-14.
11. Weisberg SP et al. Obesity is associated with macrophage accumulation in adipose tissue. *J. Clin. Investig.*, 112 (2003):1796–1808.
12. Majdoubi A et al. Role of antigen presentation in the production of pro-inflammatory cytokines in obese adipose tissue. *Cytokine*. 2016, pii: S1043-4666(16)30023-0.
13. McMurray F et al. From mice to humans. *Curr Diab Rep*. 2012, 12(6): 651-658.
14. Stewart T et al. Genetic and Genomic Analysis of Hyperlipidemia, Obesity and Diabetes Using (C57BL/6J × TALLYHO/JngJ) F2 Mice. *BMC Genomics* 2010, 11: 713.
15. Joost H et al. The Genetic Basis of Obesity-Associated Type 2 Diabetes (diabesity) in Polygenic Mouse Models. *Mamm Genome* 2014, 25 (9-10): 401–412.
16. Flati V et al. The murine p202 protein, an IFN-inducible modulator of transcription, is activated by the mitogen platelet-derived growth factor. *J Interferon Cytokine Res*. 2001, 21(2):99-103.
17. Choubey D et al. Interferon-inducible Ifi200-family genes in systemic lupus erythematosus. *Immunol. Lett*. 2008, 119:32-41.
18. Vogel H et al. Loss of function of Ifi202b by a microdeletion on chromosome 1 of C57BL/6J mice suppresses 11β-hydroxysteroid dehydrogenase type 1 expression and development of obesity. *Hum Mol Genet*. 2012, 1;21(17):3845-3857.
19. Nakata T et al. The Increased Ratio of 11β-Hydroxysteroid Dehydrogenase Type 1 versus 11β-Hydroxysteroid Dehydrogenase Type 2 in Chronic Periodontitis Irrespective of Obesity. *SpringerPlus* 5 2016: 40.
20. Li H et al. Jiao Role of interferon-inducible protein 202 (p202) in the regulation of adipogenesis in mouse adipose-derived stem cells *Mol. Cell. Endocrinol*. 2014, 382: 814–824.
21. Leońska-Duniec et al. Genetic Variants Influencing Effectiveness of Exercise Training Programmes in Obesity – an Overview of Human Studies. *Biology of Sport* 33.3 (2016): 207–214.

22. Echeverria et al. Long-chain polyunsaturated fatty acids of PPARs, signaling:relationship to tissue development and aging. *Prostaglandins, Leukotrienes and Essential Fatty Acids*. 2016, 114: 28-34.
23. Zaki ME, Amr KS, Abdel-Hamid M. APOA2 Polymorphism in Relation to Obesity and Lipid Metabolism. *Cholesterol*. 2013;2013:289481.
24. De Pauw A et al. Mitochondrial (dys)function in adipocyte (de)differentiation and systemic metabolic alterations. *The American Journal of Pathology*. 2009, 175(3): 927–939.

INVESTIGATION OF PLASMA EXHAUST PROFILE MANIPULATION USING MAGNETIC FIELDS

Bryan Shambaugh
Aerospace Engineering
West Virginia University
Morgantown, WV

ABSTRACT

In this research, the magnetoplasmadynamic (MPD) effects of applying a toroidal magnetic field around an ionized exhaust plume were investigated to manipulate the exhaust profile of the plasma jet under near vacuum conditions. Tests for this experiment were conducted using the West Virginia University (WVU) Hypersonic Arc Jet Wind Tunnel. A series of twelve N52 grade neodymium magnets were placed in different orientations around a steel toroid mounted around the arc jet's exhaust plume. Four different magnet orientations were tested in this experiment. Two additional configurations were run as control tests without any imposed magnetic fields surrounding the plume. Each test was documented using a set of 12 photographs taken from a fixed position with respect to the flow. The photographic data was analyzed by comparing images of the exhaust plume taken 10, 20, and 30 seconds after the plasma jet was activated. Analysis of the collected images revealed that configurations where the magnetic field lines were tangential to the toroid's central axis had very little influence on the size of the exhaust profile across all time steps. In contrast, the configurations where magnetic field lines ran parallel to the toroid's central axis expanded the exhaust profile across all time steps.

INTRODUCTION

This project investigated the possibility that a toroidal magnetic field can control the exhaust flow emitting from a plasma jet moving at hypersonic speeds. The ultimate objective was to determine if applying the toroidal magnetic field outside the exhaust nozzle of an arc jet thruster could act as a magnetic nozzle by manipulating the plasma flow profile through a vacuum.

Tests for this experiment were conducted using the West Virginia University (WVU) Hypersonic Arc Jet Wind Tunnel, in which a series of twelve N52 grade neodymium magnets were placed in different orientations around a steel toroid mounted around the arc jet plume. Four different magnet orientations which produced different magnetic fields around the plume were tested in this experiment: two of the configurations held the magnetic poles aligned with the flow direction with north or south facing the nozzle; two configurations held the magnetic poles in a tangential orientation to the flow with north or south facing in a clockwise direction. All magnets in each of the magnetized cases were positioned equidistant to one another and equidistant to the toroid's central axis. Two additional configurations were run as control tests without any imposed magnetic fields surrounding the plume. Each test was documented using 12 sets of photographs taken from a fixed position with respect to the flow, and the photographic data was analyzed by comparing images of the exhaust plume taken 10, 20, and 30 seconds after the plasma jet was activated.

Two separate numerical analysis techniques were performed to determine the effectiveness and practicality of this design. First, a MATLAB script was written to predict what effects a given magnetic field would have on the ions and electrons within the argon plasma exhaust plume. A heat transfer analysis was then performed using ANSYS Mechanical to determine the radiation heat transfer effects of the argon exhaust plume on the toroidal structure. This analysis was performed to ensure the neodymium magnets would not exceed their maximum operating temperature.

Several tasks had to be accomplished before attempting this experiment. First, the WVU Hypersonic Arc Jet wind tunnel needed to be serviced, and ultimately repaired, before it could run properly. Having a fully functional wind tunnel was crucial because the experiment would not have been possible without it. A literature review was also conducted and several numerical analyses were completed to demonstrate project feasibility. The test apparatus was designed and constructed both physically and digitally using a 3D modeling software prior to completing these analyses. Once the test apparatus was completed, the equipment and procedures necessary for accurate data collection were identified. The experiment metric was also finalized based on the wind tunnel's most effective operating conditions for this project. From there all the necessary equipment was gathered to perform the experiment. Tests of identical operating condition were performed on different test dates and analyses of the experimental results were performed to evaluate the system's sensitivity to repeatability. Results were analyzed using image processing software to determine which magnetic field configuration would have the most significant effect on the flow expansion.

PROBLEM STATEMENT

When rockets are launched within the Earth's atmosphere gravity and atmospheric pressure induce forces on the expelled gas. However, in the vacuum of space gravitational and atmospheric pressure forces become negligible. Without ambient back pressure the nozzle flow is considered under-expanded. That is, the nozzle exit area is insufficient to establish equilibrium between exit static pressure and ambient pressure [1]. When this happens, the compressed gases exiting the nozzle expands both axially and radially. Such expansion produces thrust in a direction contrary to the rocket's trajectory, decreasing its effective thrust capacity and increasing the amount of propellant required for a given mission [1]. This project investigates the possibility if using magnetic fields to reduce overexpansion for applications involving electric propulsion systems.

BACKGROUND

Magnetoplasmadynamics and Magnetic Nozzles

Electric and magnetic fields are a fundamental part of electric propulsion systems [1]. "Electric propulsion can produce thrust by electrically heating propellant, electrostatically accelerating charged particles, or manipulating the flow of charged particles with electromagnetic fields" [2]. "One method to increase the thrust of an MPD thruster is to operate it in an externally applied magnetic field" [3]. Such applied magnetic fields are known as magnetic nozzles. Magnetic nozzles create thrust by using electric or magnetic fields to direct the flow of ionized particles. This is done by converting thermal and non-directional kinetic energy to directional kinetic energy

[2]. The electrostatic force propagated by the field directs a charged propellant through an exhaust nozzle. This is known as electrostatic acceleration.

The magnetic fields in these nozzles can be placed in a variety of different locations within the rocket design. The electric or magnetic field can be applied either in the ionization chamber, in the exhaust nozzle, or outside the exhaust nozzle [4]. In this experiment the magnetic field was applied to the flow after it exits the exhaust nozzle.

WVU Hypersonic Arc Jet Wind Tunnel

A significant amount of time was spent understanding the wind tunnel operating procedures and gathering all the historic documents and other operational notes related to the wind tunnel. The hypersonic arc jet wind tunnel at WVU was designed and built by Dr. John Loth during the late 1960s [5]. In its most basic description the tunnel comprises an arc jet assembly (Figure 27), a vacuum chamber (Figure 28), a control console, a dual stage vacuum pump and roots blower system, and a model SR-1500-F7 Miller DC power supply [5].



Figure 27: Dismantled arc jet assembly with (a) cathode and (b) anode

The necessary operating procedure was pieced together primarily from a 1973 thesis transcript by Leonard E. Graham titled, “Feasibility Study of Enthalpy, Density, and Velocity Probe for Low Density Supersonic Flows” [5]. This document was treated as a user manual because it contains a detailed description of the tunnel and its operating procedures.

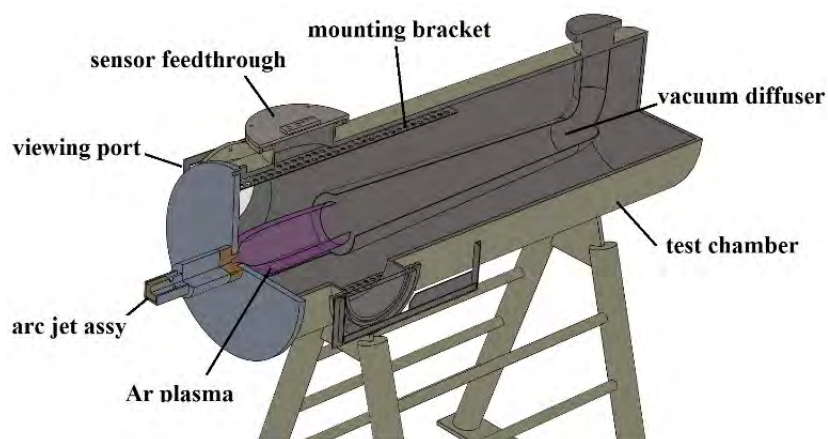


Figure 28: Cutaway CAD view of the WVU Arc Jet Hypersonic Wind Tunnel

An arc jet rocket is a type of MPD thruster that converts electrical energy into thermal energy by passing a propellant gas through an electric arc [1]. Arc jet rockets operate as low thrust propulsion systems that have a high specific impulse [3]. The arc jet depicted in Figure 27 acts as a “point-plane” wind actuator to propel the ionized gas into the vacuum chamber [6]. In this actuator, the point is the tungsten tipped cathode (Figure 27a) and the plane is the anode converging nozzle (Figure 27b) [5]. A corona discharge forms at the point of the cathode and reaches toward the anode producing an electric arc. This arc heats and ionizes the surrounding gas producing plasma. The same electric field also serves to accelerate the plasma toward the anode until it exists the exhaust nozzle [6]. “The plasma flow is assumed to be governed by the Navier-Stokes equations coupled with the magnetohydrodynamics (MHD) equations for [radio frequency] electromagnetic field” [7]. “Plasma flow velocity and Mach number increase downstream as the ion temperature decreases” [2].

Once the plasma exits the exhaust nozzle it enters the vacuum chamber for a distance of approximately 41cm before entering the diffusion nozzle. The water-cooled diffusion nozzle connects the dual stage vacuum and roots blower system and is responsible for evacuating the vacuum chamber [5]. The vacuum chamber pressure is calculated by subtracting the gage pressure on the console from the ambient pressure.

METHODOLOGY

The purpose of this project was to manipulate the flow profile of an ionized exhaust plume under near vacuum conditions using a toroidal magnetic field. Specifically, the study investigates the argon plasma jet produced by the WVU Hypersonic Arc Jet Facility. During this experiment the argon plasma was directed through a steel toroid before entering a diffusion nozzle connected to the vacuum pump. The toroid was located approximately 24.2 cm from the exhaust nozzle and 14.5 cm from the diffuser nozzle for all tests.

The test apparatus was designed and constructed both physically and digitally using the SolidWorks 3D modeling software. Developing a 3D computer-aided design (CAD) model of the testing apparatus prior to its physical construction helped determine the best way to mount the toroid within the wind tunnel and what size to make each part. A full CAD model of the apparatus bolted to mounting brackets found within the WVU Hypersonic Arc Jet Wind Tunnel is displayed in Figure 29.

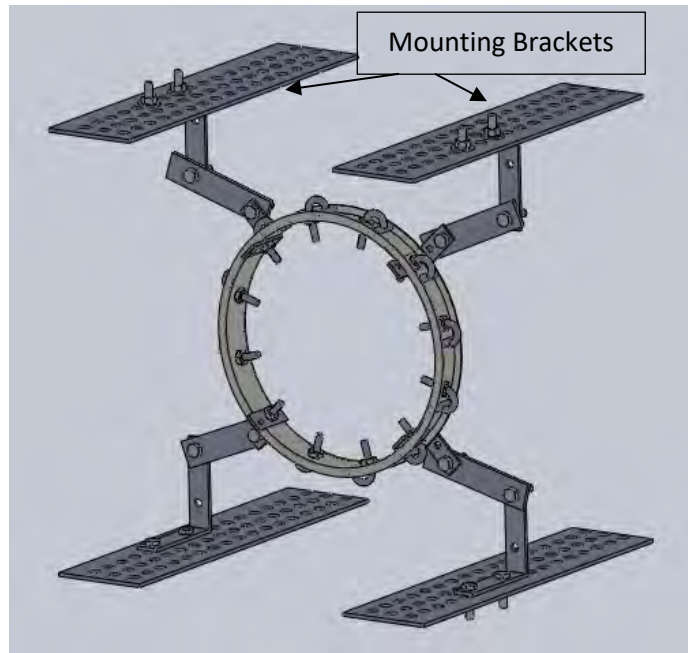


Figure 29: Full scale CAD model of the test apparatus

The toroid was modified from a shopping cart wheel with an inner diameter of about 21.6 cm. Twelve J bolts which were used to secure the magnets in place and mount the toroid to its support structure as seen in Figure 29

The test apparatus utilized a series of twelve N52 grade neodymium magnets mounted on the steel toroid. Six different apparatus configurations were tested in this experiment. Two configurations were run as control tests without any magnetic interference. The control tests were run with and without the steel toroid to determine if deploying a toroidal structure alone would influence the exhaust flow independently of a magnetic field. Two data sets were collected with the north and south magnetic poles, respectively, facing the exhaust nozzle so the magnetic field lines would run parallel to the toroid's central axis. For each of these tests the north poles of all magnets were oriented in the same direction as seen in Figure 30.



Figure 30: Toroid with axial magnetic field

The fifth and sixth data sets involved orienting the magnets tangentially with respect to the exhaust flow. For these tests the magnets' north or south poles uniformly faced either clockwise or counterclockwise around the toroid so the magnetic field lines would always be tangential to the toroid's central axis as seen in Figure 31.

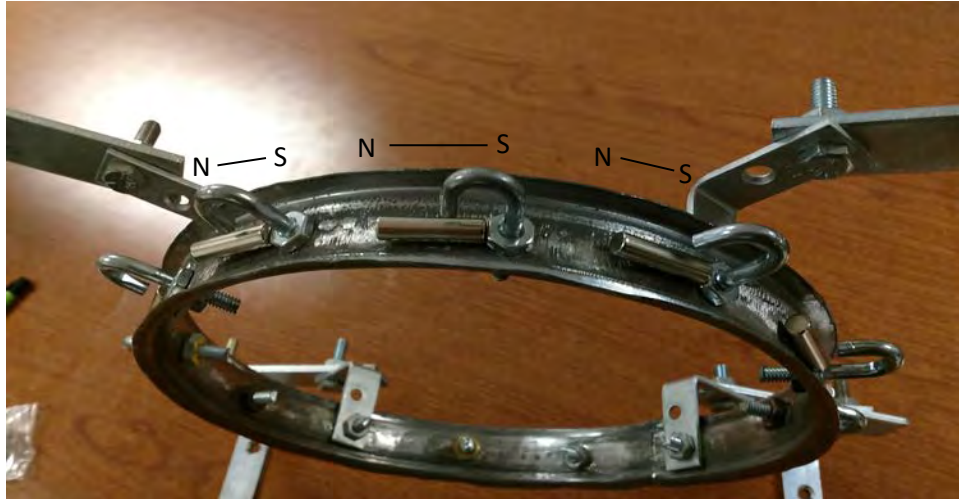


Figure 31: Toroid with tangential magnetic field

All magnets in each data set were positioned equidistant to one another and equidistant to the toroid's central axis. A test matrix representing the order in which tests were performed is presented in Table 1.

Table 1: Test matrix

| | <i>Magnet Orientation</i> | <i>Test Numbers</i> | <i>Time Steps (sec.)</i> |
|--|---------------------------|---------------------|--------------------------|
| Control Test (no magnets) (no toroid) | N/A | 19-24, 67-72 | 10, 20, 30 |
| Toroid Test (no magnets) | N/A | 1-6, 43-48 | 10, 20, 30 |
| Axial Tests | <i>Axial North</i> | 7-12, 55-60 | 10, 20, 30 |
| | <i>Axial South</i> | 13-18, 31-36 | 10, 20, 30 |
| Tangential Tests | <i>Tangential North</i> | 37-42, 61-66 | 10, 20, 30 |
| | <i>Tangential South</i> | 25-30, 49-54 | 10, 20, 30 |

This method of using permanent magnets in different orientations also permitted testing under various magnetic field configurations without constructing an entirely different apparatus. Multiple electro magnets would have been required to study the same number magnetic fields shown in Table 1

NUMERICAL ANALYSIS

MATLAB Analysis

A numerical analysis was performed to verify concept feasibility. Figure 32 reveals a significant difference in the effect magnetic fields have on negatively charged electrons versus the positively charged ions within the argon plasma.

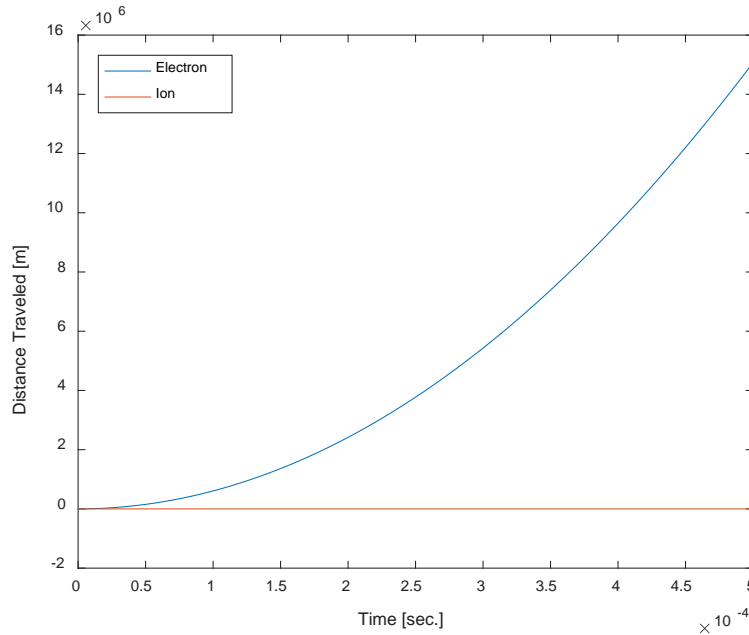


Figure 32: Movement of charged particles based on a 0.7343 Tesla magnetic field

These calculations were based primarily on Newton's second law of motion:

$$a = \frac{F}{m} \quad (1)$$

where the acceleration of a particle is equal to the total force applied to that particle divided by its mass. Electrons are much more susceptible to velocity changes from applied magnetic fields because they are considerably less massive than the positive ions.

Further analysis also revealed an exponential decay in magnetic field strength as distance from the magnet increased linearly. This analysis was based on the equation for magnetic field strength:

$$B = \frac{BrV}{2\pi d^3} \quad (2)$$

where d is the distance away from the magnet. Results from this analysis are depicted in Figure 32 where the magnet radius is approximately 0.003 meters.

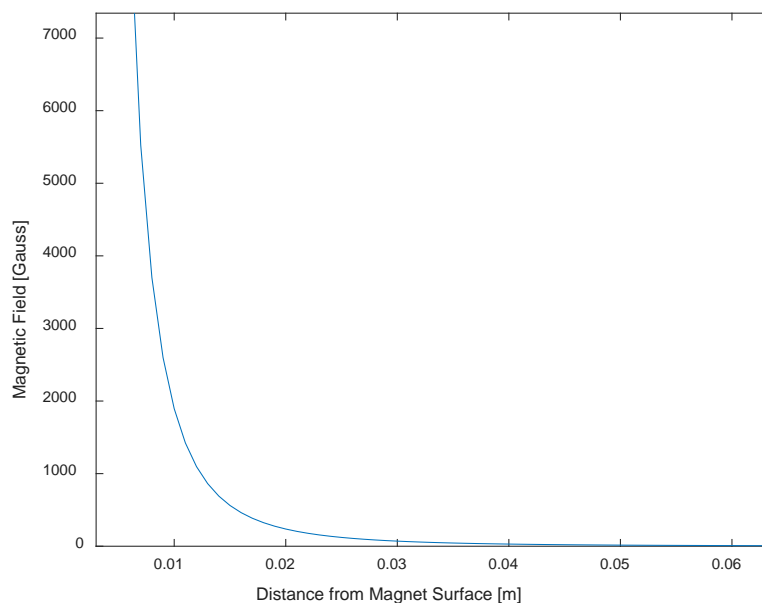


Figure 33: Decay of a magnetic field [Gauss] as distance [m] from the magnet's central axis increases

However, this analysis only accounts the magnetic field of one cylindrical magnet used in this investigation. The magnetic field through the toroid is stronger because opposing sides on the interior of the magnet interact with one another. The magnetic field through a toroid also spans a much greater area than the magnetic field from a single magnet for the same reason. Since the numerical analysis described in this section only considers the field due to a single magnet, the wider magnetic field through the toroidal test apparatus should have a greater influence on the plasma.

Heat Transfer Analysis

A heat transfer numerical analysis was completed to determine the test apparatus temperature profile due to the ionized exhaust plume using ANSYS Mechanical. However, before any numerical analysis could begin a three-dimensional model of the test apparatus had to be developed. This was done using SolidWorks. The SolidWorks assembly was then imported to ANSYS Workbench as a SAT file as depicted in Figure 34.

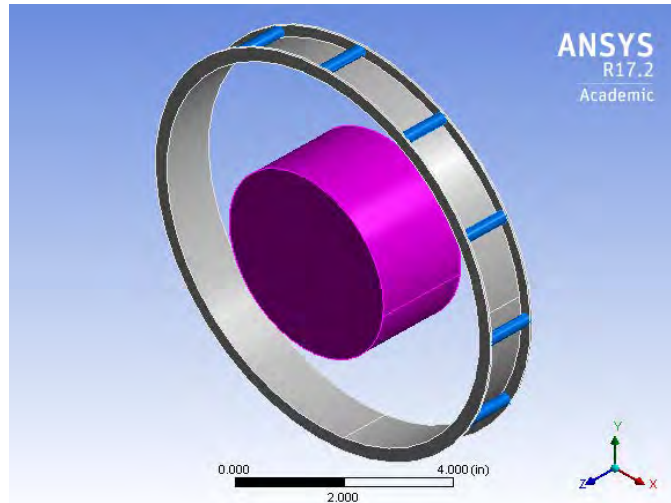


Figure 34: Analysis geometry

The purple section in Figure 34 represents the argon plasma and each blue cylinder represents a neodymium magnet. The material properties of neodymium were manually inserted into ANSYS as a custom material using an online database [8] in conjunction with material specifications listed on the K&J Magnets website where physical specimens were purchased [9]. These for all materials used in this analysis are provided in

Table 2: Material properties for heat transfer analysis

| | <i>Argon</i> | <i>Neodymium</i> | <i>Structural Steel</i> |
|--|--------------|------------------|-------------------------|
| Density [kg/(m ³)] | 1.62 | 7003 | 7850 |
| Reference Temperature [K] | 877.59 | 290.37 | 290.37 |
| Specific Heat [J/(kg*K)] | 520.64 | 190.08 | 434 |
| Isotropic Thermal Conductivity [W/(m*K)] | 0.02 | 13 | 60.5 |

The ANSYS simulation was run using a total of 15301 nodes and 4922 elements. The argon plasma plume maintained a constant temperature of 877 K while the initial temperature of the toroid was set at 306 K. Radiation heat transfer was evaluated between the argon plume and the innermost surface of the steel toroid using emissivities of 0.2 and 0.07, respectively.

The results of this analysis showed that, without convection heat transfer, a toroid positioned approximately 5 cm outside the plasma jet will not reach the magnet’s maximum operating temperature within a 30 second time span. This is because the mounting toroid insulates the magnets by absorbing most of the direct radiation heat transfer and transferring it to the magnets convectively. This process decreases the effective heat transfer rate from the plume to the magnets, allowing for more exposure time. The decreased heat transfer rate allows the toroidal apparatus to run for approximately 2.5 minutes with continuous radiation exposure before reaching the magnet’s maximum operating temperature.

THE EXPERIMENT

Experiment Metric

Data was collected using one type-K thermocouple connected to a multichannel thermometer, a Nikon D5300 camera with an adjustable lens connected to a tripod, a second camera for recording gauge measurements, the toroidal test apparatus previously described, a laptop equipped with digital photography (Digicam Control) and image processing software (MATLAB), one size 300 cylinder of argon gas with two pressure gauges, an ambient temperature thermometer, and a barometer to measure atmospheric pressure. The wind tunnel control console also contains a vacuum pressure gauge, an injector pressure gauge, a flow meter, an ammeter, and a volt meter. The Nikon camera used an adjustable 18-55 mm lens. For this experiment the camera's aperture was set at 4.5, the ISO was 100, and the shutter speed was 1/160 sec. The operating conditions for the wind tunnel are displayed in Table 3.

Table 3: Hypersonic Wind Tunnel Operating Conditions

| <i>Operating Condition</i> | <i>Value</i> |
|--|---------------------|
| <i>Argon Regulator Pressure [kPa (psig)]</i> | <i>308.20 (40)</i> |
| <i>Argon Mass Flow Rate [SLPM]</i> | <i>34.52</i> |
| <i>Average Vacuum Tank Pressure [kPa (mmHg)]</i> | <i>1.52 (11.38)</i> |
| <i>Voltage [v]</i> | <i>400</i> |
| <i>Current [amp]</i> | <i>300</i> |
| <i>Electric Start Capacity [%]</i> | <i>50</i> |

Experimental Procedure

The purpose of the procedure was to obtain photographic evidence of how an argon plasma jet interacts with a toroidal magnetic field.

Setup

First, all the materials had to be collected. The thermocouple was connected to the multichannel thermometer which was plugged into an external power supply. One end of the pressure gauge was connected to the release valve of the argon tank. The other end of the pressure gauge was connected to plastic piping leading to the flow meters within the wind tunnel's control consol. A tripod was erected and attached to the camera so it faced one of the viewing ports within the hypersonic wind tunnel. The other viewing port was covered with an opaque fabric to prevent optical interference. The laptop was turned on and connected to the Nikon camera via a USB line. An external battery pack connected the camera to a power outlet. After starting the laptop, a program called Digicam Control was activated so the camera settings could be manipulated remotely through the USB connection. The final step in setting up the full apparatus was to install the magnetic field configuration for each test.

Before any testing could begin the Nikon camera lens needed to be properly focused for optimal image clarity. To do this a ruler was positioned in the wind tunnel near the central location of the exhaust plume. The ruler was mounted on several wooden blocks and supported by mounds of clay so the numbers were clearly visible. The digital zoom was maximized through the laptop and the camera lens was adjusted manually to focus on the ruler. Adjusting the camera settings in this

way ensured an accurate point of focus within the argon plume allowing for a clearer image. Once the camera was properly focused it could not be moved for any reason until all data was collected. Altering the camera's focus or physical position by any amount would skew any results from the image processing techniques described in later sections. This is partially why images were captured remotely rather than using the physical shutter button on the camera.

Testing

The first step in each test was to activate the vacuum interlock, start the cooling system, and start the duel stage vacuum pump and roots blower system. The duel stage system had to be run for a minimum of 10 minutes before the vacuum chamber reached optimal pressure for the experiment. During this time the computer program controlling the Nikon camera was set to capture four images per test. Photographs were taken 10 seconds apart with the first image being captured 10 seconds after the digital shutter button was clicked on the computer screen. After the necessary vacuum was reached the argon tank was opened and the output pressure gauge was set to 308 kPa (40 psig). The flow meter was set at 34.5 SLPM [10] and images of all gauge measurements were recorded photographically using the second camera.

Each testing sequence contained six runs for a single magnet orientation. The toroid temperature was recorded before and after each run. To ensure the magnets did not reach their maximum operating temperature a 5-10 minute cool down period was observed between tests. The starting temperature for any given test was between 300-311 K. This period also prevented the arc jet from overheating due to the temperature build-up from each test. The cool down time between each test was also recorded. After each sequence an additional five-minute cool down period was observed before closing the argon release valve and shutting down the wind tunnel completely. Once the vacuum interlock was deactivated the wind tunnel was opened and the magnet orientation was changed to begin another sequence. After each sequence, all photographs were collected into a single folder which was titled based on the magnet orientation of that sequence.

RESULTS AND DISCUSSION

To analyze my experimental data each image for a particular data set was uploaded into MATLAB as a matrix. Once an image was uploaded any unnecessary pixels were eliminated so only relevant data was analyzed. This process also converted the image to grayscale with black pixels having a value of zero and white pixels having a value of one. A thresholding technique was then used to round any element in the matrix above 0.3 to one and any element below that value to zero. This process is called binarization. The average of all these binary images was calculated and used that as the comparison image. A single comparison image was calculated at each time step for each magnetic field configuration.

By subtracting an image with magnets from one of the control tests a false color image could be such as the one in Figure 35 could be displayed. This image shows the 20 second comparison between the control test and the test with a toroid but no magnets. Here, the red areas indicate a reduction in the flow profile and green areas indicate an expansion. The red area in the middle indicates where the toroid was located. These images provide a visual representation of the average change in any two time steps or magnet orientations.

Image comparisons against the control test were inconclusive due to a uniform change in exhaust trajectory between the control test and all other tests using the toroidal structure. As a result, comparisons to the control test did not provide an accurate representation of the effects caused by magnetic fields.

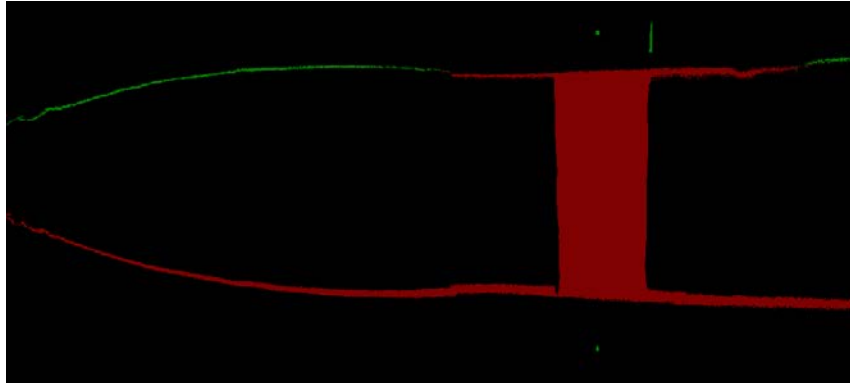


Figure 35: Control vs. toroid test (20 sec.)

To provide a more accurate representation of the affects caused by magnetic fields other each magnetic field orientation was compared to the toroid test without magnets. Table 4 presents the percent change in area between the toroid test and each magnetic field configuration.

Table 4: Exhaust plume percent expansion trends in comparison to the toroid test

| | 10 seconds | 20 seconds | 30 seconds |
|--|------------|------------|------------|
| <i>Toroid vs. tangential north [%]</i> | +1.01 | -0.12 | +0.04 |
| <i>Toroid vs. tangential south [%]</i> | +1.30 | +0.53 | +0.50 |
| <i>Toroid vs. axial (north or south) [%]</i> | +3.29 | +3.44 | +4.57 |
| <i>Toroid STD [%]</i> | +1.42 | +1.52 | +1.99 |

In Table 4 positive numbers indicate the exhaust profile was larger than the toroidal test and negative numbers indicate the profile was smaller than the toroidal test. Results from both axial orientations were nearly identical and are presented together. This table reveals that the most significant change in area is due to the axial configurations. For a visual comparison, the false color image of the axial tests at the 30 second time step is displayed in Figure 36.

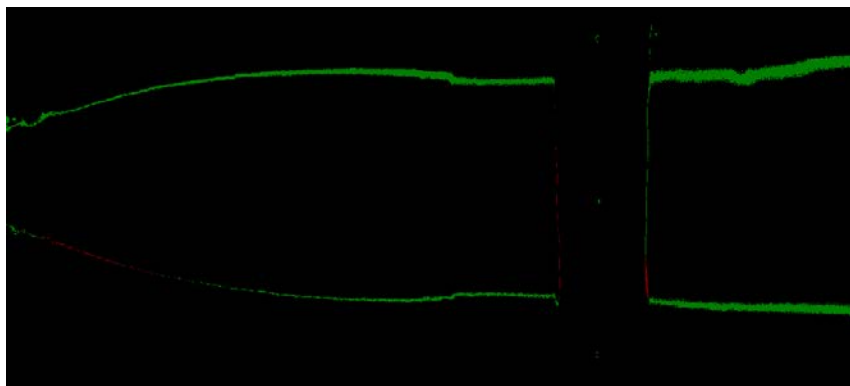


Figure 36: Toroid test vs. axial test (30 sec.)

CONCLUSION

After thorough analysis of the experimental findings described in the Results and Discussion section of this paper several observations were made. First, data from Table 4 clearly shows that manipulating the exhaust profile of a hypersonic plasma jet is possible under near vacuum conditions. Comparisons with the control test and the toroid test revealed that the axial configurations provided the most significant exhaust profile expansion across all time steps. For applications where constricting the exhaust flow is most desirable the numerical analysis from Table 4 revealed that a toroidal structure alone, without the influence of a magnetic field, would produce the best results. In conclusion, this study was successful in demonstrating that a toroidal magnetic field can manipulate the exhaust profile of a plasma jet was achieved under near vacuum conditions. However, for the purposes of reducing overexpansion, implementing a toroidal magnetic field around the exhaust plume is not practical. The current research is being presented at the SAE AeroTech Conference in September 2017 in Fort Worth, Texas. Future research may investigate why the trajectory of the plume changed with the presence of a toroidal structure. This line of research may present a different potential solution to reducing overexpansion.

THE PROGRAM

The NASA West Virginia Space Grant Consortium (WVSGC) has provided a tremendous amount of support for this project. The most significant area of assistance came in the form of time and financial support. Prior to receiving this grant, I worked as a teaching assistant to offset the cost of tuition and living expenses. However, the additional time required for grading papers and helping students left very little room for conducting research for my thesis. After receiving this grant I was able to complete my research and defend my thesis in a single academic year. This would not have been possible without the graduate research fellowship I received from the NASA WVSGC.

ACKNOWLEDGEMENTS

I would like to acknowledge:

The NASA WVSGC for their financial support in the form of a graduate research fellowship.

My research advisor, Dr. Patrick Browning, for his support and guidance throughout this entire project.

Clayton Clouse for assistance in wind tunnel diagnostics and collecting experimental data.

REFERENCES

- [1] J. Sellers, W. Astore, R. Giften and W. Larson, *Understanding Space: An Introduction to Astronautics*, 3rd ed., D. Kirkpatrick, Ed., New York: McGraw-Hill Higher Education, 2005.
- [2] F. Ebersohn, S. Girimaji, D. Staack, J. Shebalin, B. Longmier and C. Olsen, "Magnetgic Nozzle Plasma Plume: Review of Crucial Physical Phenomena," in *48th AIAA/ASME/SAE/ASEE Joint Propulsion Conference & Exhibit*, Atlanta, Georgia, 2012.
- [3] M. Inutake, A. Ando, F. Hori, T. Sugimura, K. Fukushi, T. Ochiai, M. Yamamoto, T. Yagai, A. Imasaki and M. Yoshinuma, "Supersonic Plasma Flow in a Magnetic Nozzle," in *Japan Society for Aeronautical and Space Sciences*, Aoba, Sendai, 1999.
- [4] M. Coletti, "A Thrust Formula for an MPD Thruster with Applied-Magnetic Field," *Acta Astronautica*, vol. 81, no. 2, pp. 667-674, 2012.
- [5] L. Graham, "Feasibility Study of Enthalpy, Density, and Velocity Probe for Low Density Supersonic Flows," 1973.
- [6] A. Drews, L. Cademartiri, G. Whitesides and K. Bishop, "Electric Winds Driven by Time Oscillating Corona Discharges," *Journal of Applied Physics*, vol. 114, no. 14, p. 143302, 2013.
- [7] S. Utyuzhnikov, A. Konyukhov, D. Rudenko, S. Vasil'evskii, A. Kolesnikov and O. Chazot, "Simulation of Subsonic and Supersonic Flows in Inductive Plasmatoms," *AIAA Journal*, vol. 42, no. 9, pp. 1871-1877, 2004.
- [8] J. Matthey, "Neodymium, Nd," MatWeb - The Online Materials Information Resource, [Online]. Available: <http://www.matweb.com/search/datasheet>. [Accessed 8 December 2016].
- [9] K&J Magnetics, Inc., "Neodymium Magnet Physical Properties," [Online]. Available: <https://www.kjmagnetics.com>. [Accessed 23 November 2016].
- [10] Brooks Instrument, LLC, "Industrial Glass Tube, Variable Area Flowmeters," 2014.

WEIHRAUCH REDUCIBILITY AND FINITE-DIMENSIONAL SUBSPACES

Sean Sovine
Mathematics
Marshall University
Huntington, WV

ABSTRACT

In this work, we study several principles involving subspaces and decompositions of vector spaces, matroids, and graphs from the perspective of Weihrauch reducibility. We study the problem of decomposing a countable vector space or countable matroid into 1-dimensional subspaces. We also study the problem of producing a finite-dimensional or 1-dimensional subspace of a countable vector space, and related problems for producing finite-dimensional subspaces of a countable matroid. This extends work in the reverse mathematics setting by Downey, Hirschfeldt, Kach, Lempp, Mileti, and Montalbán (2007) and recent work of Hirst and Mummert (2017). Finally, we study the problem of producing a nonempty subset of a countable graph that is equal to a finite union of connected components and the problem of producing a nonempty subset of a countable graph that is equal to a union of connected components that omits at least one connected component. This extends work of Gura, Hirst, and Mummert (2015). We briefly investigate some of these problems in the reverse mathematics setting.

INTRODUCTION

Weihrauch reducibility and reverse mathematics are two frameworks for classifying the logical strengths of mathematical principles. Weihrauch reducibility, based on computability theory, involves formalizing mathematical principles as mappings taking functions from \mathbb{N} to \mathbb{N} to other functions from \mathbb{N} to \mathbb{N} , where \mathbb{N} represents the set of natural numbers, while reverse mathematics involves formalizing principles within second-order arithmetic. Our work deals with the Weihrauch reducibility and reverse mathematics classifications of some mathematical principles related to dependence. More specifically, we investigate the logical strengths in the two settings of principles involving the existence of subspaces and decompositions of vector spaces, graphs, and matroids.

We show that the Weihrauch principle D_M that takes as input an e-matroid and returns a decomposition of that matroid into 1-dimensional subspaces is strongly Weihrauch equivalent to the Weihrauch principle LPO-hat. In the proof of this result we use another result that we obtained, which says that the principle DEP, which takes as input an e-matroid and returns the characteristic function for its dependence relation, is strongly Weihrauch equivalent to LPO-hat. This work builds on work of Hirst and Mummert (2017). We show that the reverse mathematics equivalent to D_M is equivalent to the subsystem ACA_0 over RCA_0 .

We also show that the Weihrauch principle PS_W that takes as input a countable vector space and returns as output a nontrivial proper subspace is at least as strong as the principle WKL_W , where WKL_W is the Weihrauch principle corresponding to Weak Koenig's Lemma. To obtain this proof

we adapt a proof given by Downey, Hirschfeldt, Kach, Lempp, Mileti, and Montalbán (2007) in the computability setting to the Weihrauch setting. This proof reduces the principle SEP, which takes as input two disjoint enumerated sets and returns a separating set, to PS_W . However, by standard techniques one can show that SEP and WKL_W are strongly Weihrauch Equivalent. We also show that the principle that is given by the compositional product of C_N into WKL_W is an upper bound for PS_W .

Finally, we obtain several classification results for principles involving saturated subgraphs. We define a principle $\text{PSG}_W\text{-finite}$ that takes as input a countable graph and returns a set that is equal to a finite union of connected components. We show that this principle is strongly Weihrauch equivalent to LPO-hat. We also define a principle PSG_W that takes as input a countable graph with more than one connected component and returns a nontrivial proper saturated subgraph, which is a set that is a union of connected components in the input graph that omits at least one connected component. This is the graph analogue to the principle PS_W . We show that this principle has the same upper and lower bounds as PS_W , i.e., that WKL_W is reducible to PSG_W , and that PSG_W is reducible to the principle given by the compositional product of C_N into WKL_W . We show that these upper and lower bounds are not equal. This extends work of Gura, Hirst, and Mummert (2015).

Our method of obtaining these results was the standard method used in mathematical research. We first spent time reading papers and textbooks to learn about the current state of the art in the field and to gain facility with the concepts and techniques relevant to the results we intended to study. Then we spent time thinking about the problems of interest and trying various approaches to obtaining their solutions. We presented some of the results of our work at the Joint Mathematics Meetings in Atlanta, GA, in January of 2017. We plan to extend and revise the results of this work into a paper, which we plan to submit to a peer-reviewed publication.

BACKGROUND

Weihrauch reducibility and reverse mathematics are two frameworks within mathematical logic for determining the logical strengths of mathematical principles. In classifying the logical strength of a theorem A, we set out to answer the following question: If we are given another theorem B and if we assume A, then can we prove B, or vice-versa? It turns out that the answer to this question depends on the framework in which one carries out proofs. Weihrauch reducibility and reverse mathematics are two such frameworks. Some benefits of using these frameworks to classify of theorems are: they allow one to establish relationships between apparently different mathematical problems; classifications suggest when certain proof techniques are required to prove particular theorems; these classifications can be used to discover which axioms are needed for mathematics; and, classifications can be used discover alternate proofs to known theorems. Both of these frameworks have close connections to computability theory. Hence, we briefly introduce computability theory.

Computability Theory

Computability theory is the subfield of mathematical logic that studies the properties of functions that can be computed algorithmically. The first step in this study is to formally define what it means for a function to be “algorithmically computable”. Informally, an algorithmically

computable function is one whose output on a given input can be determined by a human or a machine using a finite number of steps – where there is a clearly-defined set of rules that determines what action is taken at each step, and each rule and each action is mechanical in nature – using a finite amount of memory or scratch paper, and taking a finite amount of time to complete. During the 1930's, several formal models of computation were introduced which were intended provide a mathematical characterization of those functions that can be algorithmically computed. The most important of these early models were the λ -calculus introduced by Alonzo Church, the Turing machine introduced by Alan Turing, and the theory of μ -recursive functions introduced by Stephen Cole Kleene. In particular, a Turing machine is a mathematical description of a simple device that can be physically constructed, making it clear that functions computable by Turing machine can be mechanically computed by a machine.

It was proved during the 1930s and 1940s that these three and other models of computation were equivalent, in the sense that a function is computable by one of these models if and only if it is computable by each of the others. The resulting set of functions characterized by these models is referred to as the set of computable (or sometimes Turing computable) functions. The equivalence of these formal models lends support to the Church–Turing Thesis, which says that any function that is “algorithmically computable” in the informal sense is a computable function, and vice-versa.

As would be expected from the informal definition of an algorithm, in each model of computation the formal algorithm that specifies how a function is computed can be described by a finite string in a finite language. In fact, modern programming languages are “Turing equivalent”, meaning that the set of functions they can compute is exactly the set of computable functions. Hence, when thinking of an algorithm for a computable function, one may think of an implementation of that algorithm in a modern programming language, such as C++, Java, or Python. Beware that our concept of algorithm assumes that the input and output of an algorithmically computable function both consist of a finite amount of information. It is for this reason that computable functions are required to have domain and codomain as the set \mathbb{N} of natural numbers. However, we can also represent functions from and to other countable sets as computable functions, as long as appropriate codings for the domain and codomain sets are available.

In computability theory, in addition to studying the computability of particular functions from \mathbb{N} to \mathbb{N} , one also studies the computability of sets of natural numbers. In fact, one can show that these are essentially equivalent problems. Alan Turing showed in 1936 that there is a set of natural numbers that is not computable, meaning there is no computable procedure that can determine if a given natural number is in that set or not, using a finite amount of computation time. One can define a relationship between sets of natural numbers wherein one set A is called *Turing reducible* to another set B if there is a computable procedure that, given access to B , determines whether or not a given natural number is in A (we say that A is *computable from* B in this case). Turing reducibility is used to define a system of relationships between subsets of the natural numbers based on whether particular sets can or cannot be computed from other particular sets of natural numbers. The classes of equivalent sets in this system are called the *Turing degrees*.

Weihrauch Reducibility

Weihrauch reducibility is a framework for comparing theorems based on computability. In this

framework, mathematical objects are represented by elements in Baire space, i.e., by functions from \mathbb{N} to \mathbb{N} . A theorem is formalized in this setting as a mapping from a domain set to a codomain set, referred to as a Weihrauch principle, and these domain and codomain sets are represented as subsets of Baire space. Work in Weihrauch reducibility typically deals with relationships between principles by quantifying over all representations of a given problem. A more detailed description of the methodology of Weihrauch reducibility is given by Brattka and Gherardi (2011) and by Dorais, Dzhafarov, Hirst, Mileti, and Shafer (2016). In this work we follow the approach of Hirst and Mummert (2017) and do not work directly with representations. We instead identify mathematical objects with functions from \mathbb{N} to \mathbb{N} . In this way, we assume that each object has been encoded as a function from \mathbb{N} to \mathbb{N} , and we make comparisons between principles involving such functions. This approach is in line with the approach of reverse mathematics, in which we assume that the mathematical objects under consideration have been encoded using natural numbers and sets of natural numbers. For our purposes, principles in Weihrauch reducibility are given by sets of ordered pairs of the form (A, B) , where A is a function from \mathbb{N} to \mathbb{N} which is an instance of a problem and B is a function from \mathbb{N} to \mathbb{N} which is a solution to the instance A .

A principle P is said to be *Weihrauch reducible* to a principle Q if there are computable functionals Φ and Ψ such that:

- 1) For each instance A of P , Φ^A is an instance of Q .
- 2) Given a solution B to the instance Φ^A of Q , $\Psi^{A, B}$ is a solution to the instance A of P .

If there exists a functional Ψ satisfying (2) that is independent of the input A , then we say that P is *strongly Weihrauch reducible* to Q .

Informally, the Weihrauch reduction of P to Q consists of two computable procedures, one that takes an instance of P and from it computes an instance of Q and another that takes a solution to this instance of Q and from it computes a solution to the original instance of P . In this way, a Weihrauch reduction is like a proof of the principle P starting from the assumption of Q , in which the method of proof that is allowed is greatly restricted, so that the only allowable proofs are those that can be expressed as pairs of computable procedures. This restriction results in a more fine-grained classification of logical strength than would be obtained if stronger proof techniques were allowed.

Reverse Mathematics

In reverse mathematics, we formalize mathematical theorems in the language of second-order arithmetic, which is a theory in two-sorted first-order logic, with one sort of variables intended to represent natural numbers and the other sort intended to represent sets of natural numbers. This two-sorted logic can be interpreted within the usual, one-sorted version of first-order logic, and we have at our disposal all of the fundamental theorems concerning first-order logic, including Gödel's Completeness Theorem, which ensures that a proposition which is true in all models of a theory is syntactically provable. When working in reverse mathematics, we work with subsystems of second-order arithmetic, which are subsets of the full set of axioms of second-order arithmetic along with weakened versions of some axioms of second-order arithmetic and possibly some additional axioms, and principles, which are represented by additional axioms in the language of

second-order arithmetic. A standard and comprehensive reference for reverse mathematics is Stephen Simpson's text *Subsystems of Second-Order Arithmetic* (2009).

Because the only objects in the language of second-order arithmetic are natural numbers and sets of natural numbers, other mathematical objects that appear in theorems studied in reverse mathematics must be coded either as natural numbers or as sets of natural numbers. As a corollary to this fact, in reverse mathematics we may only deal with objects that are countable or that can be represented by sets of countable objects. For example, any complete, separable metric space can be represented by a set of countable objects, since each point in such a space can be represented by a member of an equivalence class of Cauchy sequences with terms in a countable, dense subset. In contrast, an uncountable, discrete topological space cannot be represented in second-order arithmetic.

In order to ensure the availability of enough logical tools to complete mathematical proofs, in reverse mathematics we work over a base system of relatively weak axioms. By this we mean that there is a particular subsystem – called the base system – that is assumed along with the other principles and subsystems under consideration, so that implications among subsystems and principles are obtained relative to this base system. The most common base system for reverse mathematics is RCA_0 , which consists of basic arithmetical axioms plus weakened induction and comprehension axioms. Most results in reverse mathematics have the form “A implies C over B”, where A, B, and C are subsystems of second-order arithmetic. The meaning of this statement is that every model of both A and B is also a model of C. Here the B is the base system.

PRINCIPLES RELATED TO DEPENDENCE

Most of the principles we study involve the existence of subspaces or decompositions into subspaces, where the meaning of ‘subspace’ depends on which mathematical dependence structure the principle refers to. The structures we work with are matroids, graphs, and vector spaces. Throughout this work we assume that all graphs are simple, meaning that in any graph discussed here there is at most one edge between any two distinct vertices and there are no self-loops. Matroids axiomatize a form of dependence between objects that generalizes forms of dependence that arise in several settings in mathematics, including linear dependence within vector spaces and connectedness within graphs. With respect to a matroid, a graph, or a vector space one can define a subspace to be a set that is saturated under the corresponding dependence relation. Within the graph, vector space, and matroid structures one can also define the concept of a basis, and then one can define the dimension of a subspace to be the cardinality of any basis.

Our notion of dependence within a graph is based on connectedness, and as a result a subspace of a graph in this setting is a union of connected components. There is a large body of work on graphical matroids, in which a set of vertices is considered to be dependent if it contains a cycle. We follow Gura, Hirst, and Mummert (2015) in studying dependence within graphs in terms of connectedness. This study is motivated by the fact that problems pertaining to connected components in graphs have interesting logical properties, particularly in relation to computability.

The principles studied in this work are related to those studied by Hirst and Mummert (2017) and Gura, Hirst, and Mummert (2015). We are interested in the following general principles, where M

represents a graph, vector space, or matroid:

- 1) Decomposition into subspaces: Given an object M equipped with a notion of dependence, there is a decomposition of M into 1-dimensional subspaces.
- 2) Existence of subspaces: Given an object M equipped with a notion of dependence and with dimension greater than 1, there exists a nontrivial proper subspace S of M .
- 3) Existence of finite-dimensional subspaces: Given an object M equipped with a notion of dependence and with dimension greater than 1, there exists a finite-dimensional nontrivial proper subspace S of M .
- 4) Existence of 1-dimensional subspaces: Given an object M equipped with a notion of dependence and with dimension greater than 1, there exists a 1-dimensional subspace S of M .

As can be readily seen, a given principle of type (4) will imply the analogous principles of type (2) and type (3), since within a matroid, a vector space, or a graph with dimension greater than 1, a 1-dimensional subspace will always be nontrivial and proper. We are interested in whether the additional specificity in (3) and (4) makes a principle of type (3) or (4) logically stronger than the analogous principle of type (2) or (3).

CLASSIFICATION RESULTS OBTAINED

Here we present the key results of our work in slightly more detail than in the introduction section above. For the full details of this result, please see Sean Sovine's master's thesis, which is also titled *Weihrauch Reducibility and Finite-Dimensional Subspaces* (2017).

We show that the Weihrauch principle D_M that takes as input an e-matroid and returns a decomposition of that matroid into 1-dimensional subspaces is strongly Weihrauch equivalent to the Weihrauch principle LPO-hat. In the proof of this result we use another result that we obtained, which says that the principle DEP, which takes as input an e-matroid and returns the characteristic function for its dependence relation, is strongly Weihrauch equivalent to LPO-hat. This work builds on work of Hirst and Mummert (2017). We show that the reverse mathematics equivalent to D_M is equivalent to the subsystem ACA_0 over RCA_0 . As a corollary to this result we obtain that the reverse mathematics principle that formalizes "every countable vector space has a decomposition into 1-dimensional subspaces" is equivalent to ACA_0 over RCA_0 .

We also show that the Weihrauch principle PS_W that takes as input a countable vector space and returns as output a nontrivial proper subspace is at least as strong as the principle WKL_W , where WKL_W is the Weihrauch principle corresponding to Weak Koenig's Lemma. To obtain this proof we adapt a proof given by Downey, Hirschfeldt, Kach, Lempp, Mileti, and Montalbán (2007) in the computability setting to the Weihrauch setting. This proof reduces the principle SEP , which takes as input two disjoint enumerated sets and returns a separating set, to PS_W . However, by standard techniques one can show that SEP and WKL_W are strongly Weihrauch Equivalent. We also show that the principle that is given by the compositional product of C_N into WKL_W is an upper bound for PS_W .

We obtain several classification results for principles involving saturated subgraphs. We define a principle PS_{G_W} -finite that takes as input a countable graph and returns a set that is equal to a finite union of connected components. We show that this principle is strongly Weihrauch equivalent to LPO -hat. As a corollary to this result, we show that the principle that takes as input a nontrivial e-matroid and returns a nontrivial finite-dimensional subspace is also strongly Weihrauch equivalent to LPO -hat. This extends work of Gura, Hirst, and Mummert (2015).

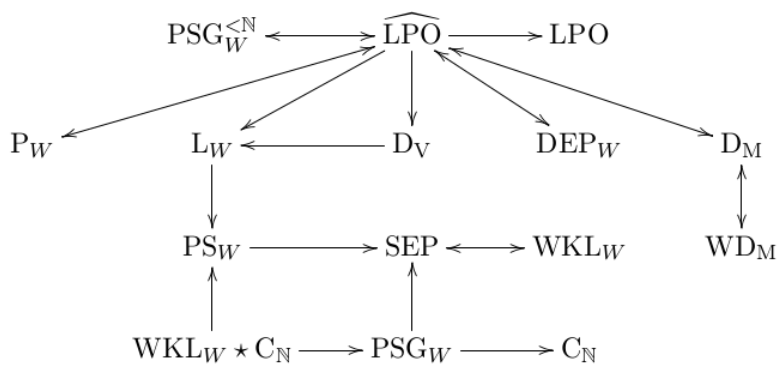


Figure 1.2: Weihrauch reducibility relationships between principles studied here.

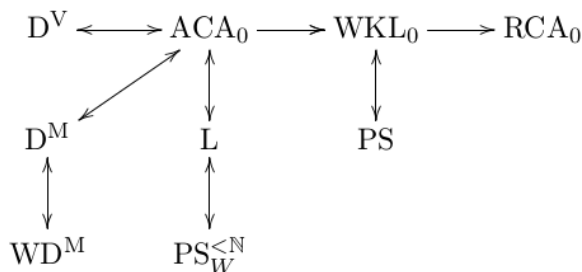


Figure 1.3: Reverse mathematics relationships between principles studied here.

We also define a principle PSG_W that takes as input a countable graph with more than one connected component and returns a nontrivial proper saturated subgraph, which is a set that is a union of connected components of the input graph that omits at least one connected component. This is the graph analogue to the principle PS_W . We show that this principle has the same upper and lower bounds as PS_W , i.e., that WKL_W is reducible to PSG_W and that PSG_W is reducible to the compositional product of C_N into WKL_W . We show that these upper and lower bounds are not equivalent.

The two diagrams above display the relationships between of the principles we study in this work, in the Weihrauch reducibility and reverse mathematics settings, respectively.

PRODUCTS OF THIS RESEARCH

The main product of this research was Sean Sovine's master's thesis (2017). We also presented some of the results of our work at the Joint Mathematics Meetings in Atlanta, GA, in January of 2017. We plan to extend and revise the results of this work into a paper, which we plan to submit to a peer-reviewed publication.

FUTURE WORK

Downey, Hirschfeldt, Kach, Lempp, Mileti, and Montalbán (2007) give the reverse mathematics classification of the principle that formalizes “every countable vector space of dimension greater than one has a finite-dimensional nontrivial proper subspace”, which corresponds to a finite-dimensional version of the principle PS_W . We would like to obtain the classification of the Weihrauch reducibility analogue to this principle. We obtained upper and lower bounds for the principles PS_W and PSG_W , however we have also shown that these bounds are not tight. Hence, we would like to obtain an exact classification of these principles. Finally, Hirst and Mummert (2017) and Gura, Hirst, and Mummert (2016) define principles related to the principles we study, in which the input object either has a known finite dimension or comes with a finite upper bound on for its dimension. We would like to investigate the strengths of finite-dimensional or bounded-dimension versions of the subspace and decomposition principles we have studied in this work.

ACKNOWLEDGEMENTS

I would like to acknowledge my thesis advisor, Dr. Carl Mummert. Without his guidance, this work would not have been possible. I would also like to acknowledge Dr. Jeffrey Hirst for his feedback on several early drafts of my thesis and for serving as a member of my thesis committee. I would like to acknowledge Dr. Michael Schroeder for serving as a member of my thesis committee. Finally, I would like to acknowledge the NASA West Virginia Space Grant Consortium, which provided financial support while I worked on this project through the Graduate Research Program fellowship.

VALUABLE ASPECTS OF THE GRADUATE RESEARCH FELLOWSHIP PROGRAM

The Graduate Research Fellowship program provided financial support while I worked on this project. In particular, it allowed me to devote much of my time during the summer of 2016 to working on this project. I believe that having this time was a significant factor in its successful outcome. The funding from the Graduate Research Fellowship program also allowed me to attend the Joint Mathematics Meetings in Atlanta, GA in January, 2017, where I presented some of the results of this work.

REFERENCES

Vasco Brattka and Guido Gherardi, *Effective choice and boundedness principles in computable analysis*, *Bulletin of Symbolic Logic* 17 (2011), no. 1, 73–117.

Francois G. Dorais, Damir D. Dzhafarov, Jeffrey L. Hirst, Joseph R. Mileti, and Paul Shafer, *On uniform relationships between combinatorial problems*, *Trans. Amer. Math. Soc.* 368 (2016), no. 2, 1321–1359. MR 3430365

Rodney G. Downey, Denis R. Hirschfeldt, Asher M. Kach, Steffen Lempp, Joseph R. Mileti, and Antonio Montalbán, *Subspaces of computable vector spaces*, *J. Algebra* 314 (2007), no. 2, 888–894. MR 2344589

Kirill Gura, Jeffrey L. Hirst, and Carl Mummert, *On the existence of a connected component of a graph*, *Computability* 4 (2015), no. 2, 103–117. MR 3393974

Jeffrey L. Hirst and Carl Mummert, *Reverse mathematics of matroids*, *Computability and Complexity: Essays Dedicated to Rodney G. Downey on the Occasion of His 60th Birthday (Cham)* (Adam Day, Michael Fellows, Noam Greenberg, Bakhadyr Khoussainov, Alexander Melnikov, and Frances Rosamond, eds.), Springer International Publishing, 2017, pp. 143–159.

Stephen G. Simpson, *Subsystems of second order arithmetic*, second edition ed., *Perspectives in Logic*, Cambridge University Press, Cambridge; Association for Symbolic Logic, Poughkeepsie, NY, 2009. MR 2517689

Sean R. Sovine, *Weihrauch Reducibility and Finite-Dimensional Subspaces*. Master's thesis, 2017. Available through Marshall Digital Scholar at <http://mds.marshall.edu/etd/>.

CHARACTERIZATION AND FLIGHT TESTING OF MULTI-ANTENNA GNSS, MULTI-SENSOR ATTITUDE DETERMINATION FOR STRATOSPHERIC BALLOON PLATFORMS

Nathan Tehrani
Aerospace Engineering
West Virginia University
Morgantown, WV

ABSTRACT

In this paper, a multi-antenna Global Navigation Satellite System (GNSS), multi-sensor attitude estimation algorithm is outlined, and its sensitivity to various error sources is assessed. The attitude estimation algorithm first estimates attitude using multiple GNSS antennas, and then fuses a host of other attitude estimation sensors including tri-axial magnetometers, Sun sensors, and inertial sensors. This work is motivated by the attitude determination needs of the Antarctic Impulse Transient Antenna (ANITA) experiment, a high-altitude balloon-lofted science platform. In order to assess performance trade-offs of various algorithm configurations, the attitude estimation performance of various approaches is tested using a simulation that is based on recorded ANITA III flight data. For GNSS errors, attention is focused on multipath, receiver measurement noise, and carrier-phase breaks. For the remaining attitude sensors, different grades of sensor are assessed. Through a Monte-Carlo simulation, it is shown that, under typical conditions, sub-0.1 degree attitude accuracy is available when use multiple antenna GNSS data only, but that this accuracy can degrade to degree-level in some environments warranting the inclusion of additional attitude sensors to maintain the desired level of accuracy.

INTRODUCTION

This document outlines the development, simulation, and testing of an attitude determination algorithm. It is motivated by the requirements of the Antarctic Impulse Transient Antenna (ANITA) experiment. ANITA is an ongoing project that uses a balloon-lofted platform to detect radio impulses from high-energy particle collisions in the ice below. Ultra-high energy neutrinos (UHEN) and ultra-high energy cosmic rays (UHECR) have both been detected by IceCube, a ground-based neutrino observatory which uses detectors embedded in ice.¹ ANITA, with its high operating altitude, can observe possible particle collisions in a significantly-larger volume of ice.²

The ANITA I, II, and III flight platforms have made successful radio transient discoveries.^{2,3} ANITA uses several feed-horn antennas with narrow observation beams and a high degree of pointing precision for each antenna. For any airborne sensing platform, the pointing accuracy is dependent on the accuracy of the onboard attitude solution.⁴ As such, a key to high pointing accuracy is a robust attitude-determination system.

Attitude determination using multi-antenna GNSS observations is an established process, first proposed by Cohen in 1991.⁵ It was also adapted for aircraft use⁶ and tested by the same author.⁷ Multi-antenna GNSS attitude determination has been tested on ground, waterborne, and flight

vehicles,⁸ and the technology has matured to multiple commercially-available products.^{9,10} There has been considerable effort to simulate gyroscope-free attitude determination using 3-axis magnetometers, 2-axis Sun sensors, or both, for spacecraft applications.¹¹ Highlights include the use of a magnetometer-only Sun-pointing algorithm by Ahn, 2003.¹² This method did not include filtering and was used to estimate an attitude vector which was being corrected. Magnetometer-derived attitude was within 3° of gyroscope-derived truth for the entire investigated flight.

Psiaki (1991) modeled an orbit- and attitude-determination algorithm.¹³ Using a 10nT 3-axis magnetometer and a 0.005° Sun sensor, this method showed less than 0.1° error in all axes. Crassidis (1996) created a Sun sensor and magnetometer Kalman filter and showed that a magnetometer-only attitude estimate is markedly improved (error reduced by approximately half) with the inclusion of Sun sensor data.¹¹ The Balloon-borne Large Aperture Submillimeter Telescope for Polarimetry (BLASTPol) is a similar stratospheric platform that uses Kalman filtering of multi sensor data for post-flight attitude determination.⁴

Multi-antenna GNSS has been used for remote sensing platforms since shortly after its proposal,¹⁴ and it is in use on multiple stratospheric balloon platforms.⁴ This paper outlines the design and performance evaluation of a GNSS-based attitude estimator that is then augmented with various other attitude sensors to offer a proposed algorithm for the ANITA project, or other similar balloon-based payloads.

DATA SIMULATION

Flight Profile

The simulated flight data used in this study is based upon the recorded flight data of ANITA III. That is, to simulate a balloon flight, the onboard position and attitude solutions were accepted as truth for simulation purposes, and sensor readings with realistic measurement noise were simulated.

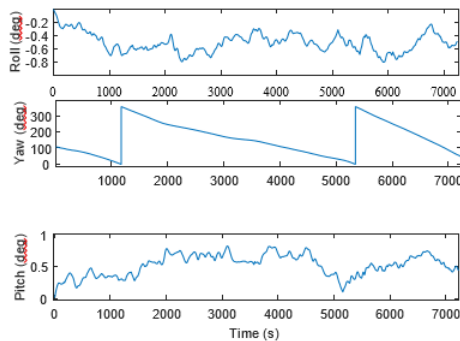


Figure 1. Attitude profile used in this work.

Figure 1 shows the Euler angle time histories during a two-hour segment of the ANITA III flight. As indicated in Fig. 1, the platform had a small ($< 1^\circ$) oscillation in the roll and pitch axes and a constant rotation about the yaw axis.

GNSS Observables Simulation

For each simulation run, four GNSS receivers were simulated with baseline separations of one-meter each, such that they are arranged in a square configuration. That is, the antennas were placed

according to the following matrix R_b :

$$R_b = \begin{bmatrix} x_{2,b} & y_{2,b} & z_{2,b} \\ x_{3,b} & y_{3,b} & z_{3,b} \\ x_{4,b} & y_{4,b} & z_{4,b} \end{bmatrix} \quad (1)$$

where $x_{i,b}$, $y_{i,b}$, and $z_{i,b}$ are the body-centric coordinates of the i^{th} antenna $i = 1$ denoting the master antenna, as was done by Cohen in the first paper describing multi-antenna attitude determination.⁵ GNSS carrier-phase data was simulated for each flight profile at a rate of 10 Hz using the MATLAB SatNav Toolbox,¹⁵ which was modified by Watson et al. (2016)¹⁶ to include additional GNSS error sources.

A number of deterministic and non-deterministic error sources are associated with GNSS measurements.¹⁷ Fortunately, for attitude estimation applications, several of the primary GNSS error sources, including satellite and receiver clock biases and atmospheric delays, are canceled through the use of double differenced GNSS observations.¹⁷ However, two important error sources, namely multipath reflections and carrier-phase breaks (AKA cycle-slips) remain present. In particular, when a metallic object reflects a GNSS signal onto the antenna, the multiple paths induce errors.¹⁷ This could be a large problem on balloon-based scientific platforms, as the antennas are spaced closely and in close proximity to science payload. Thermal measurement noise in the receiver is another error source; it is actually amplified by double differencing GNSS data. As such, for this simulation study, multipath, carrier-phase breaks, and receiver thermal errors were assessed with respect to their effect on the attitude estimator's performance using the distributions indicated in Table 1.

Inertial Measurement Simulation

In addition to GNSS measurements, inertial measurement unit data was simulated for each flight profile and data at a sampling rate of 200 Hz. In particular, four grades of IMU tri-axial rate gyroscope and accelerometers were simulated assessed. In this case, ideal gyroscope readings were generated by accepting the truth attitude solution of the ANITA III flight. These ideal measurements were then polluted with both a time-varying bias and a white noise component. The magnitude of these two noise terms were selected based on the grade of the inertial sensors assumed, which were varied as indicated in Table 1.

Sun Sensor & Magnetometer Simulation

Two-axis Sun-sensor data and tri-axial magnetometer data were also simulated for each flight based on the measurement models and uncertainties of the sensors current installed on the ANITA IV balloon. In particular, the apparent Sun position and the Earth's magnetic field along the flight profile were calculated and sensor measurements were simulated by polluting these true values with random noise based on the measurement noises quoted by the manufacturers' spec. sheets as indicated in Table 1.

The magnetometer data consists of magnetic field intensity measurements (B_b) in three orthogonal directions corresponding to the North, N , East, E , and down D axes in the body frame, b . This begins with B_E , a vector constraining the simulated magnetic field intensities in the navigation

frame, generated at each location along the flight path:

$$\vec{B}_E = \begin{pmatrix} B_{b,N} \\ B_{b,E} \\ B_{b,D} \end{pmatrix}. \quad (2)$$

Body-frame magnetic field measurements are generated by multiplying truth attitude (represented by the direction-cosine matrix C_n^b) by the navigation-frame magnetic field:

$$\vec{B}_b = C_n^b \vec{B}_E. \quad (3)$$

With three contributing error sources added: hard and soft iron errors and measurement noise, in a simplified method as described by Gebre-Egziabher et. al.:¹⁸

$$\hat{B} = A_{si} \vec{B}_b + \vec{B}_{hi}, \quad (4)$$

where A_{si} is a 3×3 matrix which describes the soft-iron error effect and \vec{B}_{hi} is a 3×1 vector containing the hard-iron offset, a magnetic field generated by ferromagnetic material on the platform. For this study, nominal values for A_{si} and \vec{B}_{hi} were used, based on the calibrations in the Gebre-Egziabher paper. Simulated measurement noise was then added to \hat{B} , corresponding to precision level of the modeled magnetometer.

The simulated Sun sensor data consists of solar incidence angles θ_{X} and θ_{Y} relative to the two horizontal body-frame axes X_b and Y_b . These were generated using the apparent solar azimuth θ_{Sun} and elevation φ_{Sun} calculated for each epoch of the flight duration. First, the solar azimuth and elevation values are transformed into a unit vector representing the Sun's position in the sky with respect to the navigation frame, n :

$$V_{Sun,n} = \begin{pmatrix} Sun_{x,n} \\ Sun_{y,n} \\ Sun_{z,n} \end{pmatrix}. \quad (5)$$

This unit-vector is then transformed using the nav-to-body direction cosine matrix, C_n^b :

$$V_{Sun,b} = C_n^b V_{Sun,n} \quad (6)$$

and the solar incidence angles in the X and Y body coordinates are then calculated:

$$\angle_X = \pi/2 + atan2(Sun_{z,b}/Sun_{x,b}), \quad (7)$$

$$\angle_Y = \pi/2 + atan2(Sun_{z,b}/Sun_{y,b}); \quad (8)$$

where $atan2$ is the four-quadrant tangent inverse.

As with the magnetometer measurements, simulated measurement noise was added to the Sun sensor measurements. However, in the case of a Sun sensor, as measurement noise increases at low solar elevations, the measurement noise was scaled according to solar elevation angle. Sun sensor measurements were simulated at 10Hz intervals.

Simulation Overview

For this study, a total of 50 one-hour flight profiles were simulated in a Monte-Carlo manner. In particular, the ECEF starting positions, magnitude of GNSS error sources, and quality of IMU, Magnetometer and Sun sensor data were varied as indicate in Table 1. Note that by randomly varying the starting location, the GNSS constellation satellite geometry was randomized as well.

ATTITUDE ESTIMATION

Algorithm Overview

Figure 2 shows the overall algorithm used. First, a carrier-phase differential GNSS filter, as detailed in Section III.B, estimates the baselines between antennas. Next, this information is used as a measurement update for a GNSS-only multiple antenna attitude estimator as described in Section III.C, in which the attitude estimates are smoothed by assuming typical low-dynamic balloon flights. Finally, the resulting estimated attitude state is optionally fused with a multi-sensor estimator that also incorporates inertial, magnetometer, and Sun sensor data, as discussed in Section III.D.

Table 1. Sensor Error-Source Monte-Carlo Simulation Distribution Parameters

| Error-Sources | Model Parameters | Notes |
|----------------------------|---|--|
| Thermal Noise | $\sigma_\rho = 0.32m$, $\sigma_\phi = 0.16\lambda$ | linear scale factor randomly selected between [0,1] |
| Multipath | 1.0 intensity: $\sigma = 0.4m, \tau = 15sec$ | linear scale factor randomly selected between [0,2] |
| Tropospheric Delay | Percent of error assumed handled by broadcast correction | Modified Hopfield with linear scale factor randomly selected between [0.95,1.05] |
| Ionospheric Delay | First order ionospheric effects mitigated with dual-frequency | linear scale factor randomly selected between [0.7,1] |
| Carrier phase break | Likelihood set to 1 phase break per 24 minute to 1 phase break per 240 minutes. | |
| Gyroscope | In-run Bias $\sigma = 9.6e^{-6} \frac{rad}{sec}$, $ARW = 0.2 \frac{deg}{\sqrt{hr}}$ | Scaled Honeywell HG1700AG72 SF = $(\frac{1}{50}, \frac{1}{200}, \frac{1}{400})$ |
| Sun Sensor | Zenith measurement noise $\sigma = 0.1$ deg. | Scaled SolarMEMS ISSDX-60 SF = (1, 2, 3, 4) |
| Magnetometer | Measurement noise $\sigma = 2.67$ nT terms scaled between [0.005, A_{si} 0.01] B_{hi} terms scaled between [25nT, 50nT] | Scaled ST LSM9DS0 SF = (1, 5, 10) |

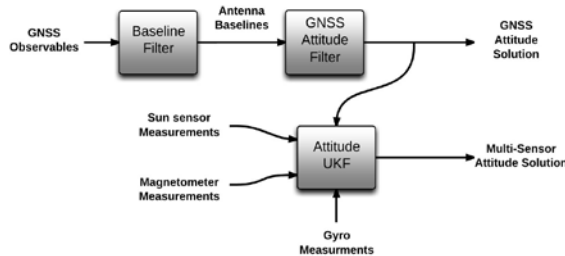


Figure 2. Block diagram showing the three main estimators: baseline-estimation filter, GNSS-only attitude estimator, and multi-sensor attitude estimator.

Antenna Baseline Estimation Filter

A Kalman filter is used to estimate the relative position between each of the antennas and a single master antenna at each of the 10 Hz measurement epochs. In particular, this Kalman filter uses Carrier-phase Differential GNSS (CD-GNSS) measurements to estimate the relative position vectors between the antennas.¹⁷ The state vector, x , for this filter consists of the relative position vector components between antenna's A and B , and a set of double-difference carrier-phase biases $N_{A,B}$.

$$x = \begin{bmatrix} x_{A,B} \\ y_{A,B} \\ z_{A,B} \\ N_{A,B}^{1,k} \\ \vdots \\ N_{A,B}^{j,k} \end{bmatrix}$$

The measurement models used to model the double-differenced carrier-phase observables follow the same approach outlined in,¹⁹ as is discussed next.

First, the model for an undifferenced GNSS carrier-phase measurement, ϕ , (with units of carrier cycles) is given as:¹⁷

$$\phi = \lambda^{-1}[r + I_\phi + T_\phi] + \frac{c}{\lambda}(\delta t_u - \delta t_s) + N + \epsilon_\phi, \quad (10)$$

where λ is the wavelength corresponding to the frequencies $L1$ and $L2$ and expressed in meters. The geometric range r between the receiver and GNSS satellite is also expressed in meters, as are the ionospheric and tropospheric delays I and T . The speed of light c is expressed in meters per second. The clock biases of the receiver and satellite, δt_u and δt_s , respectively, are expressed in seconds. The un-modeled error sources, which include multipath and thermal noise, are included in ϵ_ϕ in units of meters.

First, carrier-phase measurements for the master antenna A (antenna 1) and B (antennas 2, 3, or 4) are differenced to form single-differenced phase measurements:

$$\Delta\phi_{A,B}^j = \lambda^{-1}r_{A,B}^j + \frac{c}{\lambda}\delta t_{A,B} + N_{A,B}^j + \epsilon_{\phi,A,B}^j \quad (11)$$

Within Eq. 11, due to the very short baseline separation between the antennas, the atmospheric delays completely cancel along with the any satellite clock bias and ephemeris errors. Next, the single differenced measurements are then differenced between satellites. For example, between satellite j and a reference satellite k :

$$\nabla\Delta\phi_{A,B}^{j,k} = -\lambda^{-1}(\mathbf{1}_A^j - \mathbf{1}_A^k)^T \Gamma_{A/B_{k|k-1}} + N_{A,B}^{j,k} + \epsilon_{\phi,A,B}^{j,k} \quad (12)$$

where the remaining receiver clock bias errors are eliminated, leaving only the unknown phase

bias $N_{A,B}^{j,k}$, which is known to be an integer.

Within this filter, the measurement vector, z , consists of double-differenced phase measurements for each satellite relative to the reference satellite, including measurements for each the $L1$ and $L2$ frequencies:

$$z = \begin{bmatrix} \nabla\Delta\phi_{L1A,B}^{i\dots n,k} & \nabla\Delta\phi_{L2A,B}^{i\dots n,k} \end{bmatrix}. \quad (13)$$

In parallel with this Kalman filter, the floating point estimated phase bases, $N_{A,B}^{j,k}$ and their estimated error-covariance are fed into an integer ambiguity resolution algorithm. In particular, the Least-squares AMBIGUITY Decorrelation Adjustment (LAMBDA) method²⁰ is used to determine the integer biases and adjust the estimated relative positions.

GNSS-only Attitude Determination

Once the antenna relative baselines with respect to a master antenna are estimated using the baseline estimation filter, an ECEF antenna relative position matrix, R_{ECEF} is generated at each epoch by vertically concatenating the estimate relative vectors of each of non-master antenna, as adopted from Cohen:⁵

$$R_{ECEF} = \begin{bmatrix} x_{2,ECEF} & y_{2,ECEF} & z_{2,ECEF} \\ x_{3,ECEF} & y_{3,ECEF} & z_{3,ECEF} \\ x_{4,ECEF} & y_{4,ECEF} & z_{4,ECEF} \end{bmatrix} \quad (14)$$

This matrix is then fed to a parallel estimator to estimate the platform attitude given the antenna baseline vectors, in which the state vector x contains the attitude state expressed in Euler angles that represent the rotation from the body to navigation-frame:

$$x = \begin{pmatrix} \phi \\ \theta \\ \psi \end{pmatrix}. \quad (15)$$

Using Horn's Method,²¹ the rotation matrix between body and Earth-fixed frames is found using the estimated the ECEF configuration, R_{ECEF} and the known body-axis antenna configuration R_b . Horn's method is a variant of the sum of least squares,²¹ where R_b and R_{ECEF} are both centered about their respective centroids, yielding $R_{b'}$ and $R_{ECEF'}$, where a matrix, M , is equal to the product of the two centered coordinate matrices:

$$M = R_b * R_{ECEF} \quad (16)$$

The elements of this matrix are defined as follows:

$$M = \begin{bmatrix} S_{xx} & S_{xy} & S_{xz} \\ S_{yx} & S_{yy} & S_{yz} \\ S_{zx} & S_{zy} & S_{zz} \end{bmatrix}. \quad (17)$$

The matrix N is constructed using the elements from the above matrix:

$$N = \begin{bmatrix} (S_{xx} + S_{yy} + S_{zz}) & S_{yz} - S_{zy} & S_{zx} - S_{xz} & S_{xy} - S_{yx} \\ S_{yz} - S_{zy} & (S_{xx} - S_{yy} - S_{zz}) & S_{xy} + S_{yx} & S_{zx} + S_{xz} \\ S_{zx} - S_{xz} & S_{xy} + S_{yx} & (-S_{xx} + S_{yy} - S_{zz}) & S_{yz} + S_{zy} \\ S_{xy} - S_{yx} & S_{zx} + S_{xz} & S_{yz} + S_{zy} & (-S_{xx} - S_{yy} + S_{zz}) \end{bmatrix}. \quad (18)$$

The eigenvector V corresponding to the highest eigenvalue of N is normalized to form a unit quaternion, and the imaginary component is omitted. The resulting real quaternion is converted to a rotational matrix, C_b^E , the body-frame to Earth-frame transformation matrix, which is in turn multiplied by the Earth-frame to navigation-frame transformation C^n_E . This is converted into the measured Euler angles, and the filter state is updated.

This filter's measurement update consists of the Euler angles from the baseline vectors. The error-state covariance matrix P is initialized as a diagonal matrix containing the error magnitudes for each Euler angle, in this case 0.1° . The process noise matrix Q is set as the identity matrix, as roll, pitch, and yaw rates are very low for this platform.

Multi-Sensor Attitude Unscented Kalman Filter

Finally, a third Kalman filter estimator is used for attitude determination using all sensor data. In this step, an unscented Kalman filter (UKF) was chosen for its ability to handle the nonlinear transformation between platform attitude and solar incidence angles in the Sun sensor measurements. The details of the UKF implementation followed in this study are offered the tutorial paper by Rhudy and Gu²² and as such, these details are not discussed in detail herein. In this paper, an outline of the state vector, state prediction $f(x)$, and observation functions $h(x)$ for each measurement update are discussed.

The state vector, x estimated in the Multi-Sensor filter is given as:

$$x = \begin{pmatrix} \phi \\ \theta \\ \psi \\ b_p \\ b_q \\ b_r \end{pmatrix}.$$

where ϕ , θ , and ψ are the platform's roll, pitch and yaw, and $b_{p,q,r}$ are the time-varying biases of the IMU's roll rate, p , pitch rate, q , and yaw rate r gyroscopes.

Within the UKF framework, at each epoch, the the state vector is expanded into a group of $2L+1$ sigma points, χ , where $L = 6$ is the length of the estimated state vector. For each group of sigma points l , the attitude states are predicted by integrating the IMU gyro data through the attitude kinematic equations:²³

$$f(\phi, \theta, \psi) : \begin{bmatrix} \phi_i \\ \theta_i \\ \psi_i \end{bmatrix} = \begin{bmatrix} \phi_{i-1} \\ \theta_{i-1} \\ \psi_{i-1} \end{bmatrix} + \begin{bmatrix} 1 & t(\theta_{i-1})s(\phi_{i-1}) & t(\theta_{i-1})c(\phi_{i-1}) \\ 0 & c(\phi_{i-1}) & -s(\phi_{i-1})c(\theta_{i-1}) \\ 0 & \frac{s(\phi)}{c(\theta_{i-1})} & \frac{c(\phi_{i-1})}{c(\theta_{i-1})} \end{bmatrix} \left(\begin{bmatrix} p \\ q \\ r \end{bmatrix} - \begin{bmatrix} b_p \\ b_q \\ b_r \end{bmatrix} \right) \Delta t,$$

(20) where $s(\cdot)$ represents sine, $c(\cdot)$ represents cosine, and $t(\cdot)$ represents tangent. Furthermore,

φ_{i-1} , θ_{i-1} , and ψ_{i-1} are the previous epoch's roll, pitch, and yaw sigma points, are the first three elements of each column of χ , and $b_{p,q,r}$ are the the sigma points corresponding to the IMU bias states, which are predicted as random walk parameters.

$$f(b_{p,q,r}) : \begin{bmatrix} b_{pi} \\ b_{qi} \\ b_{ri} \end{bmatrix} = \begin{bmatrix} b_{pi-1} \\ b_{qi-1} \\ b_{ri-1} \end{bmatrix} + \begin{bmatrix} w_{bp} \\ w_{bq} \\ w_{br} \end{bmatrix} \quad (21)$$

The measurement-prediction matrix Ψ is populated by the predicted measurement vectors using each set of sigma-points in χ . Because measurements occur at different rates in this filter, it is necessary to have different measurement updates occur at different rates. For epochs coinciding with Sun sensor and GNSS attitude measurements, each column Ψ_i is as follows:

$$\Psi_i = \begin{pmatrix} B_{b,x} \\ B_{b,y} \\ B_{b,z} \\ \angle_X \\ \angle_Y \\ \phi' \\ \theta' \\ \psi' \end{pmatrix}, \quad (22)$$

where B_b , $\hat{6}_{-X}$, and $\hat{6}_{-Y}$ are predicted magnetometer and Sun sensor measurements based on the i^{th} sigma point. The observation models, $h(x)$ used to predict the magnetometer and Sen sensor measurements based upon estimate attitude sigma points are identical to those used to generate the data as discussed in Section II, with the exception that no magnetometer biases are estimated in the filter. That is, the observation equations use \hat{C}_n^b , the direction-cosine representation of the predicted attitude states $\hat{\phi}$, $\hat{\theta}$, and $\hat{\psi}$:

$$h_B(\phi, \theta, \psi) : \vec{B}_b = \hat{C}_n^b \vec{B}_n. \quad (23)$$

$$V_{Sun,b} = \hat{C}_n^b V_{Sun,n} \quad (24)$$

$$h_{\angle_X}(\phi, \theta, \psi) : \angle_X = \pi/2 + atan2(Sun_{z,b}/Sun_{x,b}); \quad (25)$$

$$h_{\angle_Y}(\phi, \theta, \psi) : \angle_Y = \pi/2 + atan2(Sun_{z,b}/Sun_{y,b}) \quad (26)$$

As GNSS attitude and Sun sensor measurements occur at 10Hz rate, the remaining (50Hz) measurement updates consist only of magnetometer measurement predictions:

$$\Psi_i = \begin{pmatrix} B_{b,x} \\ B_{b,y} \\ B_{b,z} \end{pmatrix}, \quad (27)$$

The measurement update matrix z consists of the simulated sensor measurement at each filter epoch. These are similar in form the the columns of Ψ :

$$z = \begin{bmatrix} B_{b,x} \\ B_{b,y} \\ B_{b,z} \\ \angle X \\ \angle Y \\ \phi_{GNSS} \\ \theta_{GNSS} \\ \psi_{GNSS} \end{bmatrix}, \quad (28)$$

for filter epochs with GNSS, magnetometer, and Sun sensor measurements, and

$$z = \begin{bmatrix} B_{b,x} \\ B_{b,y} \\ B_{b,z} \end{bmatrix}, \quad (29)$$

for epochs with magnetometer measurements only.

Assumed Stochastic Parameters

The Kalman filter process noise, Q and measurement noise, R , and initial error-covariance P_0 , assumptions selected for the differential GNSS baseline estimator are outlined in Table 2:

Table 2. Baseline filter assumed parameters.

| Filter Parameter | Assumed Values |
|----------------------------------|---|
| State error covariance P_0 | Baseline states: 1 m Ambiguity states: 225 m |
| Measurement noise covariance (R) | $\sigma_\phi = 4 \cdot 10^{-4}$ m |
| Process noise covariance Q | Attitude states: In-run Bias $\cdot 10^{-2}$ m/ \sqrt{s} Ambiguity states: 0 m/ \sqrt{s} |

The multi-sensor, unscented Kalman filter was developed to run in multiple modes (GNSS-inertial, inertial, magnetometer and Sun sensor only, and all sensors). The different modes required different tuning parameters for adequate performance. These are outlined in Table 3:

Table 3. Multi-sensor attitude filter parameters.

| Filter Parameter | Assumed Values |
|--------------------------------|---|
| State error covariance P_0 | INS+Mag+SS: 10^{-2} deg. attitude states, 10^{-6} deg. bias states; INS+GNSS: 10^{-3} deg. attitude states, 10^{-5} deg. bias states; INS+all: 10^{-2} deg. attitude states, 10^{-6} deg. bias states |
| Measurement noise covariance R | $\sigma_{Mag} = 25$ nT $\sigma_{Sun} = 0.1$ deg $\sigma_{GNSS}(\phi, \theta) = 0.1$ deg. $\cdot ADOP$ $\sigma_{GNSS}(\psi) = 0.01$ deg. $\cdot ADOP$ |
| Process noise covariance Q | Attitude states: In-run Bias $\cdot 10^{-2} \frac{rad}{\sqrt{s}}$ Bias states: ARW $\cdot 10^2 \frac{rad}{\sqrt{s}}$ |

RESULTS

Results Overview

To summarize the results of the Monte-Carlo study, Figure 3 shows the cumulative distribution of

the 3D attitude error for the various filter configurations over the 50 simulated flights. As is

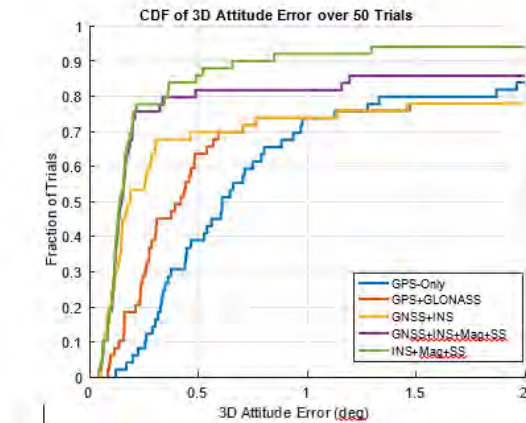


Figure 3. Comparison between GNSS-only filter and multi-sensor attitude filter in different modes (CDF truncated to 2 degrees)

evident in Figure 3, in general, the additional sensors yield improved performance. Furthermore, there is a clear advantage to adding GLONASS data into the estimator. When all sensors are fused, attitude estimation less than 0.2 degrees is available for approximately 75% of the data. The CDF plot cuts off at two degrees as a small number of trials for which the filter diverged and are not shown for clarity.

GNSS-only Attitude Filter

The GNSS-only attitude filter was run in two modes, the first using GPS data only, and the second adding GLONASS observables. The pitch, roll, and heading error statistics for both filter modes are presented in Tables 4 and 5. These results include two simulations for which the baseline filter solution failed to converge, presumably due to carrier-phase break.

Using GLONASS as well as GPS satellites yielded a median performance improvement of 40 percent lower attitude error. Considering ANITA’s Antarctic flight regime, fewer GNSS satellites are observable, and these are seen at lower elevations.²⁴ This can negatively impact the Geometric Dilution of Precision (GDOP), a metric that describes the geometric diversity of satellite-receiver vectors.¹⁷ The attitude dilution of precision, as proposed by Yoon (2001) is a similar metric which assesses the ability to measure Euler angles.²⁵ It is defined as:²⁵

$$ADOP = \sqrt{\text{tr}[(nI - SS^T)^{-1}]},$$

where n is the number of satellites in view, I is the 3×3 identity matrix, and S is a $3 \times N$ matrix comprising the unit vectors to each satellite, including the reference satellite.²⁵ A variable starting location was used to investigate the effect of the lower GDOP and ADOP at high latitudes. Figure 4 shows error performance using GPS satellites only and using both GPS and GLONASS satellites, as well as the ADOP calculated in each case, for a polar flight profile:

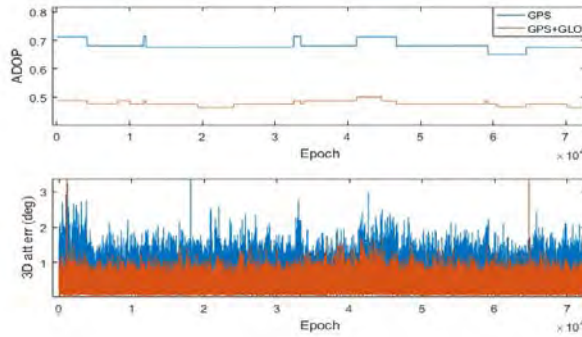


Figure 4. Comparison between GPS-only mode and GPS+GLONASS mode for a polar flight profile.

GNSS Multi-Sensor Attitude Filter

Tables 6, 7, and 8 present overall error statistics for the 50 trials (including the two convergence failures) for the GNSS+INS, GNSS+ All sensors, and All sensors without GNSS, respectively. The filter failed to converge two times when the magnetic hard-iron bias was close to the magnetic process noise parameter in the measurement covariance matrix.

Table 6. GNSS+INS Error Statistics

| | Roll (deg.) | Pitch (deg.) | Heading (deg.) |
|--------|-------------|--------------|----------------|
| Min | 0.0332 | 0.0339 | 0.0160 |
| Max | 104.1555 | 51.9770 | 347.5273 |
| Median | 0.1078 | 0.1064 | 0.0505 |

Table 6. GNSS+INS Error Statistics

| | Roll (deg.) | Pitch (deg.) | Heading (deg.) |
|--------|-------------|--------------|----------------|
| Min | 0.0332 | 0.0339 | 0.0160 |
| Max | 104.1555 | 51.9770 | 347.5273 |
| Median | 0.1078 | 0.1064 | 0.0505 |

Table 7. GNSS+INS+Mag+SS Error Statistics

| | Roll (deg.) | Pitch (deg.) | Heading (deg.) |
|--------|-------------|--------------|----------------|
| Min | 0.0277 | 0.0220 | 0.0209 |
| Max | 6.14e+4 | 0.0189e+4 | 3.57e+4 |
| Median | 0.1078 | 0.1064 | 0.0505 |

Using additional sensors in addition to GNSS can markedly improve performance. For example, Figure 5 shows the attitude estimation error for one example trial, in which the GNSS-only attitude is shown alongside the multi-sensor filters for comparison.

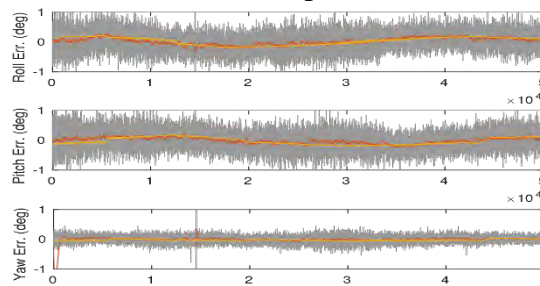


Figure 5. Roll, pitch, and heading errors for multi-sensor filter in GNSS+INS mode (red), GNSS+INS+Mag+SS mode (yellow), with GNSS-only filter result (gray) for comparison.

Of great interest is the algorithm's ability to handle carrier-phase breaks. For example, phase breaks could occur due to radio-frequency interference, such as during a data transmission over the Iridium satellite constellation which operates very close to the GPS L1 frequency.²⁶ When a carrier-phase break occurs, it can fortunately be detected easily by a data editor.²⁷ As such, whenever this occurs, the baseline estimation filter re-sets the error-covariance for the impacted carrier-phase ambiguities to a large value. The result is a momentary spike in attitude error, not longer than five filter time steps, but often with multi-degree magnitude. The multi-sensor filter

attitude determination performance was lower across the range of phase break likelihoods as shown in Figure 6. Notably, the multi-sensor UKF yielded a low error-level attitude solution for the two trials with GNSS-attitude convergence failure.

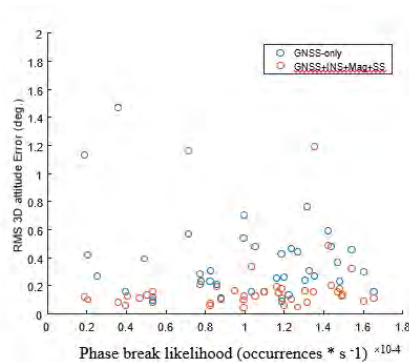


Figure 6. RMS attitude vs. phase break likelihood for each trial.

Also of interest is the filter’s performance with high receiver measurement thermal noise and multipath errors. Figures 7 and 8 show that the multi-sensor filter yields lower-magnitude errors than the GNSS-only filter across both error scale ranges. Although an increasing level of multipath error did not noticeably affect the result of the GNSS-only filter performance, the multi-sensor filter performed better in nearly all trials.

Flight Verification

To verify the performance of the GNSS baseline filter, GNSS attitude filter, and full multisensory algorithm, a flight test experiment was developed, leveraging the research lab’s existing *Phastball Zero* unmanned flight platform.



Figure 7. WVU Phastball Zero UAV outfitted with GNSS receivers.

The flight experiment uses the same attitude determination algorithm (as it is a post-processing algorithm) as the simulation study. The aircraft has been outfitted with three GNSS receivers and their respective antennas. One dual-frequency, GLONASS-enabled NovAtel 615-series receiver is mounted with its antenna at the aircraft’s nose. Two lower-cost Ublox M8T receivers are mounted within the fuselage with an antenna at each wing tip. An Analog Devices IMU provides accelerometer, gyroscope, and magnetometer readings at each 50Hz timestep, as in the simulation study. One sun sensor, identical to the modeled sensor, is mounted on the rear fuselage. These sensors’ data are time-matched using a GPS-time aligned pulse-per-second signal from one

receiver.



Figure 8. Inertial measurement unit (left), sun sensor (right)

Because the algorithm relies on GNSS receivers which are mounted on a rigid body (ei: the balloon-suspended platform), modification must be made to support the experiment on the aircraft, which has varying wing flex during flight.

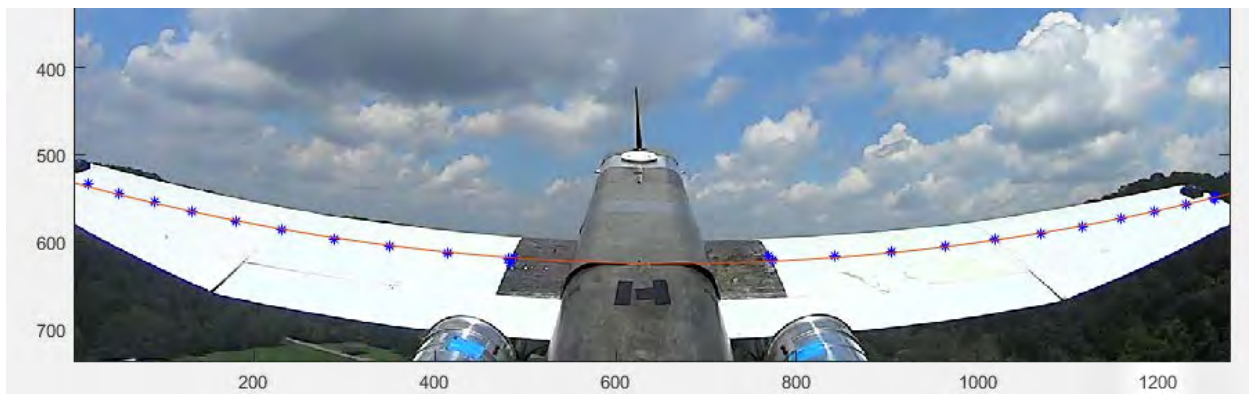


Figure 9. Wing flex fit using fiducial markers

In order to provide precise aircraft body-frame coordinates for the antennas, a camera was added to the aircraft tail to record the flight. Optical markers, added to the wing surface, provide a convenient wing measurement solution. An image processing algorithm was adapted to track the positions of the markers, then convert to body-frame coordinates using the geometry of the system. At each time step, the wing marker positions are fit to a polynomial to approximate the actual shape of the wing. This information is used in conjunction with the measured GNSS baselines to find the aircraft attitude. Modification of the GNSS baseline filter to support single-frequency observations, as taken during flight testing, is ongoing.

CONCLUSION

This study outlined the design and testing of a GNSS-based attitude determination algorithm, as well as its augmentation with additional sensor data. GNSS-only attitude solutions are consistently improved when GLONASS satellites are included in addition to GPS, owing to more observables and lower dilution of precision (especially in polar regions). Furthermore, adding inertial measurements, Sun sensor and magnetometer data further improves attitude-determination performance and reliability.

ACKNOWLEDGMENTS

The author thanks the West Virginia Space Grant Consortium for enabling and funding this project, and Dr. Jason Gross for providing mentorship. Working on this project had a profound positive effect on the author's education, enabling him to gain a strong programming background as well as an introduction to hardware integration. These skills include, but are not limited to, C++, Python, and MATLAB programming, physical system simulation, binary data manipulation, and flight vehicle assembly and repair. In addition, work has been published in the form of one conference paperⁱ with plans to compete two aerospace journal papers.

REFERENCES

- ¹Collaboration, I. et al., "Evidence for high-energy extraterrestrial neutrinos at the IceCube detector," *Science*, Vol. 342, No. 6161, 2013, pp. 1242856.
- ²Hoover, S. et al., "Observation of Ultrahigh-Energy Cosmic Rays with the ANITA Balloon-Borne Radio Interferometer," *Phys. Rev. Lett.*, Vol. 105, Oct 2010, pp. 151101.
- ³Gorham, P. W. et al., "Observational constraints on the ultrahigh energy cosmic neutrino flux from the second flight of the ANITA experiment," *Phys. Rev. D*, Vol. 82, Jul 2010, pp. 022004.
- ⁴Gandilo, N., Ade, P., Amiri, M., Angile, F., Benton, S., Bock, J., Bond, J., Bryan, S., Chiang, H., Contaldi, C., et al., "Attitude determination for balloon-borne experiments," *SPIE Astronomical Telescopes+ Instrumentation*, International Society for Optics and Photonics, 2014, pp. 91452U–91452U.
- ⁵Cohen, C. E. and Parkinson, B. W., "Expanding the performance envelope of GPS-based attitude determination," *ION GPS-91; Proceedings of the 4th International Technical Meeting of the Satellite Division of the Institute of Navigation*, Vol. 1, 1991, pp. 1001–1011.
- ⁶Cohen, C. E. and Parkinson, B. W., "Aircraft applications of GPS-based attitude determination," *Proceedings of the 5th International Technical Meeting of the Satellite Division of The Institute of Navigation (ION GPS 1992)*, 1992, pp. 775–782.
- ⁷Cohen, C. E., Parkinson, B. W., and McNally, B. D., "Flight tests of attitude determination using GPS compared against an inertial navigation unit," *Navigation*, Vol. 41, No. 1, 1994, pp. 83–97.
- ⁸Teunissen, P. J., Giorgi, G., and Buist, P. J., "Testing of a new single-frequency GNSS carrier phase attitude determination method: land, ship and aircraft experiments," *GPS solutions*, Vol. 15, No. 1, 2011, pp. 15–28.
- ⁹Magellan Professional, *ADU5*, 6 2007, Rev. C.
- ¹⁰NovAtel, "Attitude-Pitch/Roll/Yaw, What We Offer <http://www.novatel.com/solutions/attitude/#whatWeOffer>," .
- ¹¹Crassidis, J. L. and Markley, F. L., "Predictive Filtering for Attitude Estimation Without Rate Sensors," *ADVANCES IN THE ASTRONAUTICAL SCIENCES*, Vol. 93, 1996, pp. 1021–1038.
- ¹²Ahn, H.-S. and Lee, S.-H., "Gyroless Attitude Estimation of the Sun-Pointing Mode Satellite," *International Conference on Control, Automation and Systems*, October, 2003, pp. 22–25.
- ¹³Psiaki, M. L., "Autonomous low-earth-orbit determination from magnetometer and sun sensor data," *Journal of Guidance, Control, and Dynamics*, Vol. 22, No. 2, 1999, pp. 296–304.
- ¹⁴Toth, C. K. and Grejner-Brzezinska, D. A., "Performance analysis of the airborne integrated mapping system (AIMS)," *International Archives of Photogrammetry and Remote Sensing*, Vol. 32, 1997, pp. 320–326.
- ¹⁵GPSsoft, "Satellite Navigation TOOLBOX 3.0 User's Guide," 2003.
- ¹⁶Watson, R. M., Sivaneri, V., and Gross, J. N., "Performance Characterization of Tightly-Coupled GNSS Precise Point Positioning Inertial Navigation within a Simulation Environment," *AIAA Guidance, Navigation, and Control Conference*, 2016, p. 1869.
- ¹⁷Misra, P. and Enge, P., *Global Positioning System: Signals, Measurements and Performance Second Edition*, Lincoln, MA: Ganga-Jamuna Press, 2006.
- ¹⁸Gebre-Egziabher, D., Elkaim, G. H., David Powell, J., and Parkinson, B. W., "Calibration of strapdown magnetometers in magnetic field domain," *Journal of Aerospace Engineering*, Vol. 19, No. 2, 2006, pp. 87–102.

- ¹⁹Gross, J. N., Gu, Y., and Rhudy, M. B., "Robust UAV relative navigation with DGPS, INS, and peer-to-peer radio ranging," *IEEE Transactions on Automation Science and Engineering*, Vol. 12, No. 3, 2015, pp. 935–944.
- ²⁰Teunissen, P., De Jonge, P., and Tiberius, C., "The lambda method for fast GPS surveying," *International Symposium GPS Technology Applications Bucharest, Romania*, 1995.
- ²¹Horn, B. K., "Closed-form solution of absolute orientation using unit quaternions," *Journal of the Optical Society of America*, Vol. 4, No. 4, 1987, pp. 629–642.
- ²²Rhudy, M. and Gu, Y., "Understanding Nonlinear Kalman Filters, Part II: An Implementation Guide," *Interactive Robotics Letters*, 2013.
- ²³Stevens, B. L., Lewis, F. L., and Johnson, E. N., *Aircraft Control and Simulation: Dynamics, Controls Design, and Autonomous Systems*, John Wiley & Sons, 2015.
- ²⁴Cojocaru, S., Birsan, E., Batrinca, G., and Arsenie, P., "GPS-GLONASS-GALILEO: a dynamical comparison," *Journal of Navigation*, Vol. 62, No. 01, 2009, pp. 135–150.
- ²⁵Yoon, S., "Euler angle dilution of precision in GPS attitude determination," *Aerospace and Electronic Systems, IEEE Transactions on*, Vol. 37, No. 3, 2001, pp. 1077–1083.
- ²⁶Maine, K., Devieux, C., and Swan, P., "Overview of IRIDIUM satellite network," *WESCON/95. Conference record. 'Microelectronics Communications Technology Producing Quality Products Mobile and Portable Power Emerging Technologies'*, IEEE, 1995, p. 483.
- ²⁷Blewitt, G., "An automatic editing algorithm for GPS data," *Geophysical Research Letters*, Vol. 17, No. 3, 1990, pp. 199–202.

PUBLICATION

- ⁱ Tehrani, Nathan, and Jason N. Gross. "Characterization of Multi-Antenna GNSS, Multi-Sensor Attitude Determination for Stratospheric Balloon Platforms." *AIAA Modeling and Simulation Technologies Conference*. 2017.

MECHANISMS OF RADIOCONTRAST NEPHROTOXICITY

Dakota Ward
Biomedical Sciences
Marshall University
Huntington, WV

ABSTRACT

Contrast Induced-Acute Kidney Injury (CI-AKI) is the third most common causes of acute renal failure in hospitalized patients. CI-AKI is the result of exposure to iodinated contrast media which are required for many diagnostic procedures including: computed tomography, angiography, and cardiac catheterization. The risk of renal injury increases if a patient has a predisposing factor such as chronic kidney disease, congestive heart failure, or diabetes. Although the exact mechanism of toxicity of CI-AKI is not known, the current theories suggest: oxidative stress, changes in renal hemodynamics, and direct cytotoxicity are contributing to CI-AKI nephrotoxicity. This project tested the hypothesis that the radiocontrast agent diatrizoic acid (DA) will induce direct cellular cytotoxicity in the form of oxidative stress and mitochondrial dysfunction in the absence of hemodynamic influence. Immortalized human adult proximal tubular epithelial (HK-2) cells (ATCC) were incubated with clinically relevant concentrations (0-18 mg I/mL) of DA for 24 hours. All treatment groups had a sample size of $n \geq 6$. Viability was assessed using the conversion of (3-(4,5-Dimethylthiazol-2-yl)-2,5-Diphenyltetrazolium Bromide) (MTT) to formazan and trypan blue exclusion assays. Toxicity was evident in HK-2 cells exposed to 2, 5, 10, 15, and 18 mg I/ml relative to phosphate buffered saline used as vehicle control ($p < 0.05$) at 24 hours as measured by the MTT assay and trypan blue exclusion. Oxidative stress was quantitated using Western blot analysis for 4-hydroxynonenal (4-HNE) and protein carbonylation (OxyBlot). The effects of DA exposure on tumor necrosis factor alpha (TNF- α) release was also quantified. The results of this study showed that the HK-2 cells are sensitive to clinically relevant concentrations of DA within 24 hours.

INTRODUCTION

Iodinated contrast media are required for many diagnostic procedures including: computed tomography, angiography, and cardiac catheterization. Contrast-induced acute kidney injury (CI-AKI) can occur following exposure to contrast media and is the third most common cause of acute kidney injury (AKI) in hospitalized patients (Pattharanitima et al., 2016). Renal toxicity and proximal tubule damage are serious side effects of radiocontrast media; however, the exact cellular mechanisms of nephrotoxicity have not been fully elucidated. In turn, there are multiple proposed hypotheses to explicate these mechanisms, three of which are moderately supported. The first is an increase in reactive oxygen species (ROS) production leading to oxidative stress and cellular damage. Second, alterations of renal hemodynamics resulting in decreased renal perfusion and glomerular filtration rate (GFR). The third is direct toxic effects of contrast media on renal proximal tubular cells. The purpose of this study was to investigate the mechanism of diatrizoic acid (DA) induced cytotoxicity in an immortalized human epithelial cell line (HK-2), therefore; eliminating hemodynamic and inflammatory responses induced by radiocontrast media. The overall purpose can be divided into two specific aims: evaluation of oxidative stress in HK-2 cells following DA exposure and investigation into the source of this oxidative stress and cytotoxicity.

Oxidative stress was evaluated by determining protein carbonylation and 4-hydroxy-2-nonenal (4-HNE) adduct formation. OxyBlot is a method kit established by Millipore that evaluates protein carbonylation due to exposure to excess reactive oxygen species (ROS). 4-HNE adduct formation on proteins is a common result of exposure to ROS, and thus can also be used to evaluate oxidative stress. It is possible that the source of reactive oxygen species could be contributed to an increase in the release of TNF- α due to exposure to DA. TNF- α has been shown to induce ROS generation via a number of different pathways including the activation of NADPH oxidases and inducing mitochondrial ROS production. It was hypothesized that exposure to DA would result in an increase in release of TNF- α into the cellular growth media resulting in activation of TNF- α receptors. This hypothesis was evaluated by determining levels of TNF- α found in cellular lysate via Western blot using an antibody from Abcam and the levels of TNF- α released into the media via an ELISA Assay kit from Abcam. All blots were exposed on a Chemi-Doc (BioRad) and appropriate densitometry was performed using Image Lab software (BioRad).

These experiments were conducted by exposing HK-2 cells to various concentrations for 24 hours. HK-2 cells were plated with the concentration of 750,000 cells/mL and allowed to grow to confluency over the course of 48 hours. The cells were then exposed to 0, 2, 5, 10, 15, and 18 mg I/mL of DA dissolved in phosphate buffered saline (PBS) as a vehicle control. The cells were exposed to these treatments for 24 hours. At the end of the treatment period, cells were collected using Trypsin (Gibco Life Technologies) and lysed with Cell Lysis Buffer (Santa Cruz). At this point total protein content was assessed and the appropriate experiments were run as stated above.

All experiments were analyzed using SigmaStat software. A one-way ANOVA was run on each experiment, followed by a Holm Sidak or Tukey post hoc test as appropriate. Statistical significance was set to a threshold of $\alpha < 0.05$ and all data is presented as mean \pm SEM (standard error of the mean). Additional detail regarding procedures and experiments can be found in the “Methods” section below.

This study showed that exposure to DA reduced cell viability within 24 hours as demonstrated by an increase in protein carbonylation and 4-HNE adduct formation across all concentrations. There was a decrease in TNF- α in cellular lysate for all 5 concentrations of DA when compared to vehicle control. At 15 and 18 mg I/mL DA, there was an increase in TNF- α found in the cellular growth media. These results indicate that exposure to DA results in oxidative stress in the absence of hemodynamic and inflammatory responses to radiocontrast media. Additional research based on this data can lead to a method to clinically mitigate or prevent DA induced nephrotoxicity.

BACKGROUND

Radio-opaque contrast media are FDA approved to increase the visibility of internal bodily structures in x-ray based imaging techniques such as computed tomography (CT), angiography, and radiography. Radiocontrast media are administered intravenously and are typically used to visualize blood vessels and the gastrointestinal tract but are also indicated in visualizing the urinary tract, fallopian tubes, and uterus. A major adverse effect associated with the radiocontrast agent diatrizoic acid (DA) is acute kidney injury (AKI) followed by acute renal failure. Contrast-induced AKI (CI-AKI) is responsible for a third of AKI in hospitalized patients (Pattharanitima et al., 2016)

affecting between 1-2% of the general population and up to 50% of high-risk subgroups (Mehran et al., 2006). High risk groups include patients with congestive heart failure (CHF), diabetes mellitus, hypotension, low hematocrit, presence of an intra-arterial balloon pump, and age > 75 years according to the Mehran CI-AKI risk scale. Although the exact mechanism of nephrotoxicity induced by contrast media is unknown, alterations of renal hemodynamics leading to decreased glomerular filtration rate (GFR) and renal perfusion, decreases in function of antioxidant enzymes leading to oxidative stress, and direct toxic effects of contrast media on proximal tubular cells are the three most supported hypotheses.

Diatrizoic acid (DA), also known as Hyapaque, Gastrographin, or Urografin, is an iodinated radiocontrast agent used in many medical imaging procedures such as intravenous pyelography, computed tomography, angiography, and gastrointestinal imaging. DA is classified as a high-osmolality contrast agent whose osmolality ranges from 1500-2000mOs/kg H₂O depending on the preparation. Contrast agent osmolality is defined as the number of particles dissolved in one kilogram of water (Bucher 2016). One of the most widely proposed mechanisms for CI-AKI is decreased blood flow following administration of radiocontrast agents. Following intravenous infusion of contrast media, renal blood flow initially increases and is followed shortly after by a prolonged period of vasoconstriction and reduced renal perfusion (Karstoft et al, 1995). Ischemia is therefore thought to play a major role in the pathophysiology of CI-AKI. Although high-osmolar contrast media (HOCM) have an osmolality that is up to 8 times the osmolality of blood, there is no overall difference in CI-AKI incidence when compared to patients that were administered low-osmolar contrast media (LOCM) as shown in a large randomized double blind study led by Moore et al (Moore et al 1992). It is apparent that decreased renal perfusion and ischemia do play a role in CI-AKI, however; the direct toxic effects of contrast media are a major factor in CI-AKI. It is important to determine the effects of the older contrast media on mitochondrial function, oxidative stress, and UPR in order to determine if their ionic nature is playing a role in the incidence of CI-AKI.

METHODS

HK-2 Model

An immortalized noncancerous human kidney epithelial cell line (HK-2) was used. HK-2 cells maintain activity and biochemical properties similar to proximal tubule cells in an *in vivo* model (Gunnes et al., 2010, Paolicchi et al., 2003). Using this cell line allows for a comprehensive mechanistic study of subcellular changes following diatrizoic acid (DA) exposure lacking extra-renal interactions, hemodynamic, or inflammatory components that would be found in an *in vivo* system. DA has been shown to be taken up in the rat proximal tubule cells by the Oat1 and Oat3 transporters (Mudge et al., 1971). HK-2 cells were purchased from the American Type Culture Collection (ATCC); they were cultured according to ATCC guidelines in a keratinocyte-free medium with 50ug/ml bovine pituitary extract (BPE) and 5ng/ml recombinant epithelial growth factor (EGF) from Invitrogen (Carlsbad, CA).

Diatrizoic Acid Treatment

HK-2 cells will be exposed to varying concentrations of DA for all studies. HK-2 cells were plated into 6-well tissue culture plates (750,000 cells/ml) (Corning, Sigma-Aldrich) and allowed to grow for 48 hours in a humidified incubator with constant settings of 37°C and 5% CO₂. Cells were

treated with 0, 2, 5, 10, 15, and 18 mg I/ml of DA (Sigma-Aldrich) for all experiments. The vehicle used in all studies is phosphate buffered saline (Invitrogen). Plasma concentrations of DA for most imaging procedures range from ~2 mg I/ml to 6 mg I/ml, however, plasma levels can reach up to ~23 mg I/ml for procedures such as intravenous pyelography and angiography. The range of concentrations used in the experiments include the normal plasma concentrations of DA found in plasma of human subjects, therefore, the concentrations used in these studies are of clinical relevance. Preliminary studies determined in this lab have shown that exposure to DA leads to decreased cell viability consistently at 24 hours (Figure 1). Following the treatment period, cells were trypsinized (Invitrogen) and collected along with the cell culture media to be used for analysis by Western blot. All treatments in this study have an n=2/group and were replicated in triplicate using a different cellular passage to give a total of n=6/group.

Cell Viability

Cell viability assays were performed alongside every experiment to ensure treatment success. Cells were plated on 48-well tissue culture plates (39,000 cells/ml) (CytoOne, USA Scientific) and allowed to grow for 48 hours in a humidified incubator with constant settings of 37°C and 5% CO₂. Cells were treated with 0, 2, 5, 10, 15, and 18 mg I/ml of DA (Sigma-Aldrich) for all experiments. The vehicle used in all studies is phosphate buffered saline (Invitrogen). After the treatment period, cell viability was assessed in two ways. The first was an MTT assay which relies on the conversion of the tetrazolium dye 3-(4,5-dimethylthiazol-2-yl)-2,5-diphenyltetrazolium bromide (MTT) to formazan by NAD(P)H-dependent oxidoreductases (Humphrey et al., 2005). The second cell viability assay was the trypan blue exclusion method. In this test, a cell suspension is mixed with the trypan blue dye and then visually examined to determine whether cells take up or exclude dye. A viable cell will have a clear cytoplasm whereas a nonviable cell will have a blue cytoplasm (Strober 2001). All treatments will have an n = 4/group and will be repeated with different cellular passages for a total of n = 8/group.

Cell Isolation

Following DA treatment (see above), cells were incubated in 2ml of 0.25% Trypsin (Gibco) for 10 minutes prior to being washed with two aliquots of 1ml Renal Krebs Ringer Solution (7.39 g/L NaCl, 0.385 g/L KCl, 0.318 g/L MgSO₄•7H₂O, 0.852 g/L Na₂HPO₄, 0.149 g/L CaCl₂•H₂O; pH 7.4). The cells were then centrifuged at 1000 x g for 10 minutes. The resultant supernatant is discarded and the pellet is washed once again with 500ul of Krebs Ringer Solution and centrifuged at 1000 x g for 10 minutes. The resultant supernatant is discarded and the pellet containing HK-2 cells is suspended in 120 µL 1x Cell Lysis Buffer (Cell Signaling) containing Halt™ Protease Inhibitor (Thermo Scientific) prior to being placed in a -80°C freezer. The cellular protein fraction was then thawed and aliquoted for various assays such as Oxyblot and Western blot.

OxyBlot and Western Blot

Cell lysates were run on a 12.5% polyacrylamide gel at concentrations of 15-40ug protein/well at 55V for 18h. Gels were then transferred to a nitrocellulose membrane at 100V for 90min. Memcode staining (Thermo-Scientific) was done to ensure transfer success and consistent loading concentration. OxyBlot primary antibodies bind to carbonylated proteins, a process that occurs when there is excessive ROS in the cell. Appropriate antibody for OxyBlot (Millipore, CellBio Labs) were diluted in 1% BSA in PBST, appropriate antibodies for 4-HNE (Abcam) and TNF-α (Abcam) were diluted in 1% BSA in TBST, and appropriate antibodies for caspase 3 (Abcam) were diluted in 5% dry milk in PBST. Appropriate secondaries were used and all blots were

analyzed using enhanced chemiluminescence from Amersham™ ECL™ Western Blotting Detection Kit (GE Healthcare, Buckinghamshire, UK) on a Chemi-Doc (BioRad). Densitometry was performed for each blot and is presented as intensity as a percent of control.

ELISA

Following exposure to DA for 24hr, cellular growth media was collected in order to determine the release of TNF- α . The media was centrifuged at 1000x g for 10 minutes to remove cellular debris. 50 μ L of sample and 50 μ L of a TNF- α antibody cocktail containing a TNF- α Detector antibody and a TNF- α Capture antibody were incubated in the supplied microplate for 1 hour on a plate shaker set to 400 RPM. The microplate wells were then washed with a supplied wash buffer 3 times before the addition of TMB substrate and further incubation for 10 minutes on a plate shaker set to 400 RPM. After the incubation period, a stop solution was added and the optical density was measured at 450nm using a microplate reader. The concentration of TNF- α was assessed using a concentration curve of known standards.

Statistical Analysis

All experiments were analyzed using SigmaStat software. A one-way ANOVA was run on each experiment, followed by a Holm Sidak post hoc test as appropriate. Statistical significance was set to a threshold of $p < 0.05$ and all data is presented as mean \pm SEM (standard error of the mean).

RESULTS

Cell viability following DA exposure

To determine cell viability, absorbance values were normalized to control with control groups set to 100%. Cell viability is expressed as percent of control as mean \pm SEM with $N \geq 6$. Cell viability was reduced at 2, 5, 10, 15, and 18 mg I/mL of DA at 24hr exposure (Fig. 1). Based on this data, all treatment concentrations were used for the remainder of the experiments

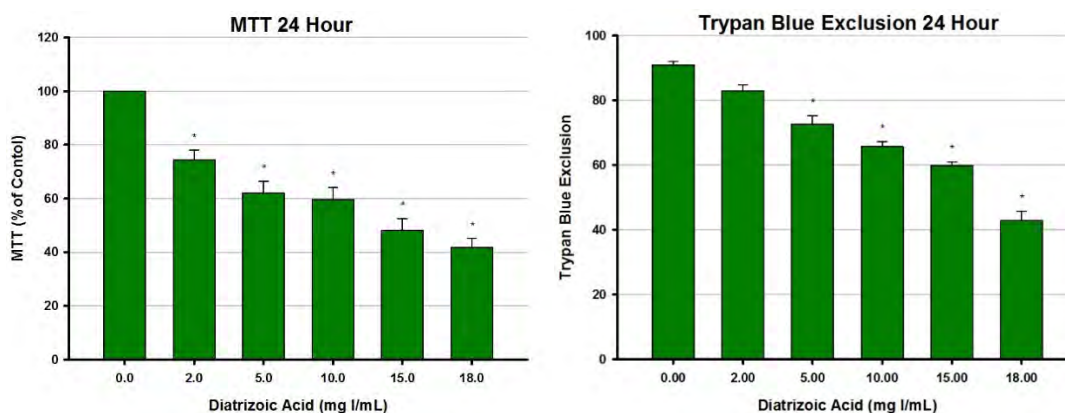


Figure 1. MTT/Trypan Blue Exclusion following 24hr exposure to DA. Viability was assessed using the MTT assay and Trypan Blue Exclusion and expressed as % of Vehicle (PBS) control and cells per ml ($\times 10^6$), respectively. Assays were evaluated following a 24-hour exposure to DA. Values represent mean \pm S.E.M. with 3 independent experiments. An (*) denotes statistical ($p < 0.05$) differences between DA treatment group and control (0 mg I/mL).

Oxidative stress following DA exposure

To evaluate oxidative stress after DA exposure, protein carbonyl analysis (Millipore) and 4-HNE adduct formation (CellBio Labs) were performed. Protein carbonylation was increased at 2, 5, 10, 15, and 18 mg I/mL after 24hr exposure (Fig. 2). 4-HNE adduct formation was increased at 2, 5,

10, 15, and 18 mg I/mL after 24hr (Fig. 2). Densitometry is presented as Intensity Percent of control as mean \pm SEM with N>6.

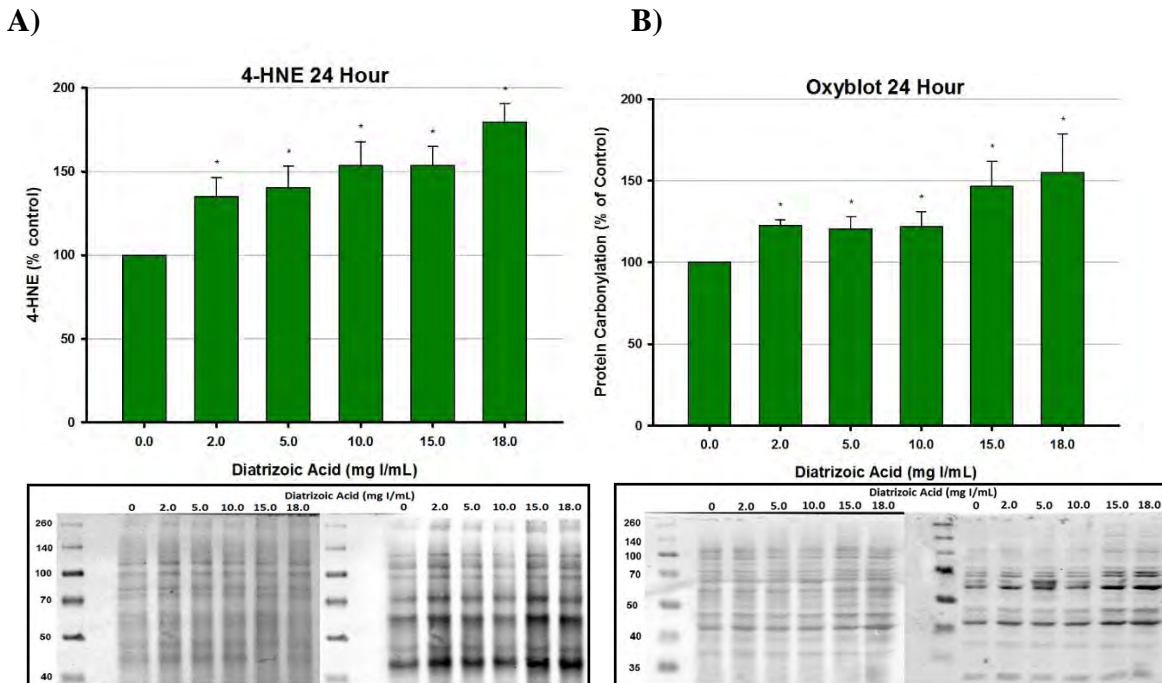
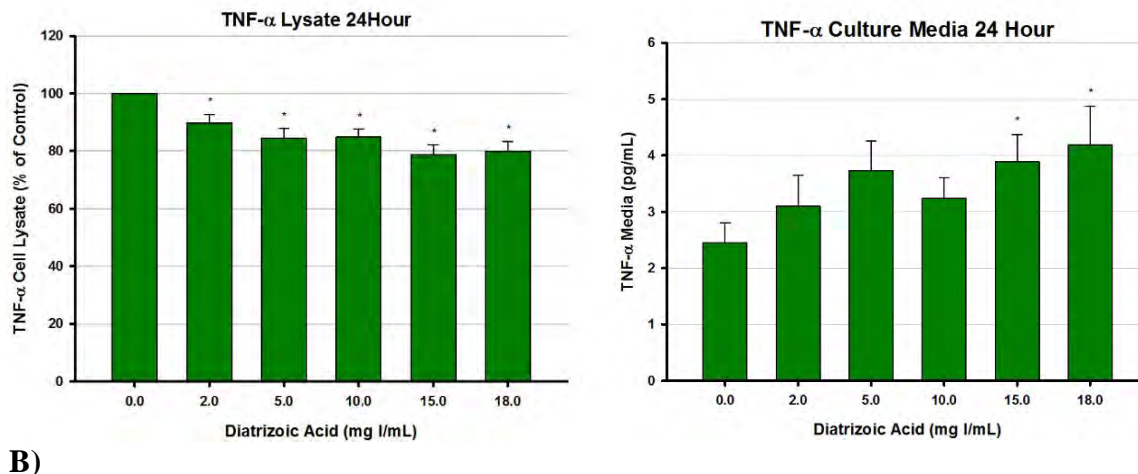


Figure 2. 4-HNE and Protein Carbonylation in HK-2 Cells following DA exposure for 24 h. Representative gels depict protein loading and 4-HNE (Panel A) or Oxyblot (Panel B). Cumulative densitometry represent mean \pm S.E.M. Experiment was repeated 3 times. Asterisks denote statistical ($p \leq 0.05$) differences between group and control (0.00 mg I/mL).

TNF- α release following DA exposure

To evaluate TNF- α release after DA exposure, levels of TNF- α were determined in both cellular lysate and cellular growth media. Levels of TNF- α in cellular lysate were decreased at 2, 5, 10, 15, and 18 mg I/mL after 24hr exposure as determined by Western blot(Fig. 3). Levels of TNF- α released into the growth media were increased at 15 and 18 mg I/mL DA after 24hr as determined by ELISA (Fig. 3). Densitometry is presented as Intensity Percent of control as mean \pm SEM with N>6.

Figure 3 A)



B) Figure 3. TNF- α in Cell Lysate and Culture Media following DA exposure for 24h. Bar graphs denote TNF- α in lysate and cell media (Panel A). Panel B contains representative gel for protein loading and TNF- α in cell lysate. Values represent mean \pm S.E.M. from 3 separate experiments. (*) denotes different ($p \leq 0.05$) from control.

DISCUSSION

The results obtained from these experiments give a great insight to the mechanism of toxicity of DA induced cytotoxicity. We have shown that DA is toxic to HK-2 cells at *clinically relevant concentrations* within 24 hours. Also, DA increases oxidative stress within 24 hours in the form of increased protein carbonylation and 4-HNE protein adduct formation. The levels of TNF- α are significantly decreased in cellular lysate and increased in the cellular media at 15 and 18 mg I/mL of DA after 24 hour exposure. Lastly, Preliminary studies indicate that exposure to DA increases the expression of cleaved caspase 3 within 24 hours relative to control.

The on data obtained from this study shines new light on the exact mechanisms of DA induced cellular toxicity. We now know that exposure to DA induces oxidative stress in the absence of changes in renal hemodynamics and inflammatory response that occur in a clinical setting. We have also learned that exposure to DA induces the release of the inflammatory cytokine TNF- α which could play a role in the oxidative stress and induction of the apoptotic pathways.

At this juncture in the research, there are still more questions than answers. We know that exposure to DA results in an increase in oxidative stress which eventually leads to apoptotic cell death, however; we do not know the exact source of the excessive reactive oxygen species. More experiments need to be performed and at different time points in order to determine the overall effects of DA. From the data obtained, two hypotheses can be deduced: exposure to DA results in activation of TNF- α pathways that induces ROS generation, or oxidative stress is generated from another source, such as mitochondrial dysfunction or a decline in the cellular antioxidant systems, resulting in release of TNF- α . It is unclear which hypothesis is more likely, however; additional studies characterizing the effects of DA on mitochondrial function are currently being performed

by this lab.

Additional studies at 8 hours and 16 hours need to be performed in order to build a clear picture as to when and how the oxidative stress is occurring and by what mechanisms. It is important to explore the effects of DA on the antioxidant system within the cell which can be done by evaluating levels of the free antioxidant glutathione and determining expression and activity of antioxidant enzymes such as superoxide dismutase. The effects of DA on other cellular compartments is also an area of interest, such as, the endoplasmic reticulum (ER). It is possible that exposure to DA could result in alterations to the ER's microenvironment which is tightly regulated. Changes in cellular energy levels, calcium regulation, or redox status all play a role in maintaining ER homeostasis. If this balance is altered, protein folding can be affected resulting in an accumulation of unfolded or misfolded proteins leading to activation of the unfolded protein response (UPR) and ER stress. This lab is prepared to explore this area of interest by measuring levels UPR specific proteins such as glucose related protein 78 (GRP78), C/EBP homologous protein (CHOP), activating transcription factor 4 (ATF4), and the ER stress specific caspase, caspase 12, (Wang et al., 2009, Yu et al., 2015) after exposure to DA.

CONCLUSION

This series of experiments has shown to be successful at looking into the effects of DA exposure on human kidney epithelial cells in the absence of hemodynamic and inflammatory variables. Knowing that DA decreased cellular viability, induces oxidative stress and the release of the inflammatory cytokine TNF- α , and seemingly leads to apoptosis provides a sturdy foundation to more detailed experiments. The generosity of the NASA West Virginia Space Grant Consortium has allowed for the advancement of knowledge in this particular area of interest. The data from these experiments have been used in multiple poster presentation competitions including the Joan C. Edwards School of Medicine 29th Annual Research Day held at Marshall University and the 2016 West Virginia IDEa Network of Biomedical Research Excellence Summer Research Symposium held at West Virginia University.

The amount of knowledge that I have gained as a researcher and student is considered invaluable to me and is partly due to the financial support of the NASA West Virginia Space Grant Consortium. From this experience, I will be able to further my goals and dreams to become a research scientist in my future professional life.

ACKNOWLEDGEMENTS

I would like to extend my deepest gratitude to the NASA West Virginia Space Grant Consortium for funding this work and allowing me to pursue my training as a researcher. I would also like I would also like to thank my mentor, Dr. Monica Valentovic for her guidance and mentorship. Without her help and ability to push me to my fullest potential, the opportunities that I have been grateful enough to accept would not be possible. Finally, I would like to acknowledge my lab mates such as my laboratory technician, Katie Brown, our undergraduate research assistant, Mason Dial, and my lab partner, Rachel Murphy. Without the culmination of everyone's efforts, I would not be where I am today.

REFERENCES

1. [Bucher A](#), [De Cecco CN](#), [Schoepf UJ](#), [Meinel FG](#), [Krazinski AW](#), [Spearman JV](#), [McQuiston AD](#), [Rui Wang](#), [Bucher J](#), [Vogl TJ](#), [Katzberg RW](#). Is Contrast Medium Osmolality a Causal Factor for Contrast-Induced Nephropathy?. [Biomed Res Int](#). 2014; 2014: 931413.
2. [Gunness P1](#), [Aleksa K](#), [Kosuge K](#), [Ito S](#), [Koren G](#). Comparison of the novel HK-2 human renal proximal tubular cell line with the standard LLC-PK1 cell line in studying drug-induced nephrotoxicity. [Can J Physiol Pharmacol](#). 2010 Apr;88(4):448-55.
3. [Karstoft J](#), [Bååth L](#), [Jansen I](#), [Edvinsson L](#). Vasoconstriction of isolated arteries induced by angiographic contrast media. A comparison of ionic and non-ionic contrast media iso-osmolar with plasma. [Acta Radiol](#). 1995;36(3):312-6
4. [Mehran R](#)¹, [Nikolsky E](#). Contrast-induced nephropathy: definition, epidemiology, and patients at risk. [Kidney Int Suppl](#). 2006; 100:S11-5.
5. [Moore RD](#), [Steinberg EP](#), [Powe NR](#), [Brinker JA](#), [Fishman EK](#), [Graziano S](#), [Gopalan R](#). Nephrotoxicity of high-osmolality versus low-osmolality contrast media: randomized clinical trial. [Radiology](#). 1992;182(3):649-55.
6. [Mudge GH](#), [Berndt WO](#), [Saunders A](#), [Beattie B](#). Renal transport of diatrizoate in the rabbit, dog, and rat. [Nephron](#). 1971; 8(2):156-72.
7. [Paolicchi A](#), [Sotiropoulou M](#), [Perego P](#), [Daubeuf S](#), [Visvikis A](#), [Lorenzini E](#), [Franzini M](#), [Romiti N](#), [Chieli E](#), [Leone R](#), [Apostoli P](#), [Colangelo D](#), [Zunino F](#), [Pompella A](#). Gamma-Glutamyl transpeptidase catalyses the extracellular detoxification of cisplatin in a human cell line derived from the proximal convoluted tubule of the kidney. [Eur J Cancer](#). 2003; 39(7):996-1003.
8. [Pattharanitima P](#), [Tasanarong A](#). Pharmacological strategies to prevent contrast-induced acute kidney injury. [Biomed Res Int](#). 2014; 2014:236930.
9. [Samali A](#), [Fitzgerald U](#), [Deegan S](#), [Gupta S](#). Methods for Monitoring Endoplasmic Reticulum Stress and the Unfolded Protein Response. [Int J Cell Biol](#). 2010; 2010: 830307
10. [Strober W](#). Trypan blue exclusion test of cell viability. [Curr Protoc Immunol](#). 2001; Appendix 3:Appendix 3B.
11. [Valentovic M](#), [Ball J](#), [Brown M](#), [Terneus MV](#), [McQuade E](#), [Van Meter S](#), [Hedrick HM](#), [Roy AA](#), [Williams T](#). Resveratrol Attenuates Cisplatin Renal Cortical Cytotoxicity by Modifying Oxidative Stress. [Toxicol In Vitro](#). 2014; 28(2): 248-257
12. [Wang M](#), [Wey S](#), [Zhang Y](#), [Ye R](#), and [Lee A.S](#). Role of the Unfolded Protein Response Regulator GRP78/BiP in Development, Cancer, and Neurological Disorders. [Antiox Redox Signal](#). 2009; 11(9): 2307-2316
13. [Yu Lou](#), [Wang Z](#), [Xu Y](#), [Zhou P](#), [Cao J](#), [Li Y](#), [Chen Y](#), [Sun J](#). Resveratrol prevents doxorubicin-induced cardiotoxicity in H9c2 cells through the inhibition of endoplasmic reticulum stress and the activation of the Sirt1 pathway. [Int J Mol Med](#). 2015; 36(3): 873-880.
14. [Zhong H](#), [Yin H](#). Role of lipid peroxidation derived 4-hydroxynonenal (4-HNE) in cancer: Focusing on mitochondria. [Redox Biology](#). 2015; 4:193-199.